Technische Universität München

Lehrstuhl für Nukleartechnik

Forschungs-Neutronenquelle Heinz Maier-Leibnitz (FRM II)

AREVA CERCA

REP Atomizer Engineering

&

UMo Fuel-Powder Fabrication

Robert Schenk

Vollständiger Abdruck der von der Fakultät für Maschinenwesen der Technischen Universität München zur Erlangung des akademischen Grades eines

Doktor-Ingenieurs (Dr.-Ing.)

genehmigten Dissertation.

Vorsitzender:		Univ.-Prof. Dr. Dr. h.c. Ewald Werner
Prüfer der Dissertation:	1.	Univ.-Prof. Rafael Macián-Juan, Ph.D.
	2.	Univ.-Prof. Dr. Winfried Petry

Die Dissertation wurde am 17.11.2015 bei der Technischen Universität München eingereicht und durch die Fakultät für Maschinenwesen am 08.03.2016 angenommen.

Abstract

FRM II has to convert its nuclear fuel to a uranium enrichment, which is significantly lower than the current 93 %. As part of this conversion, new fuel types are being evaluated such as uranium-molybdenum (UMo) powder. Industrial fabrication of UMo powders is conducted by means of atomization. The powder production technique was not available for UMo in Europe. Therefore, German FRM II and French fuel manufacturer AREVA CERCA have launched a common project for the design, engineering, and operation of a prototype UMo fuel-powder production facility in France. The key component of this facility is a UMo atomizer.

In the course of this work, atomization system and process requirements were defined and summarised. Based on the requirements, a prototype UMo atomizer was designed, dimensioned, constructed, assembled, and commissioned. The atomizer principle is based on the rotating electrode process (REP), a centrifugal atomization technique for high purity metals and specialty alloys. The prototype was granted the nuclear operating licence and was experimentally parameterised. UMo fuel-powder was fabricated using different system parameters. The produced powder was characterised using granulometry, chemical analysis, and microscopy.

More than 60 experimental atomization runs were performed, out of which 24 hot runs involving UMo were conducted. Parameter sets were found that allowed for the production of almost entirely spherical particles in the target size ranges. These particles had generally smooth surfaces without intra-porosity and were free of satellites, internal voids, inclusions or shells. REP atomization of UMo demonstrated to yield high purity powder for high purity ingot material. The fabricated UMo fuel-powder thus fully complied with fuel specifications. The implemented atomizer can produce 25 % of the annual UMo target production-capacity of the prototype within one working day. The yield efficiency regarding usable UMo powder reached about 77 % and 25 % for target particle diameter ranges $< 125\,\mu$m and $< 40\,\mu$m, respectively. Particle size distributions with median diameters as low as $62\,\mu$m were obtained. The median diameter of stainless steel powders was reproduced with a standard deviation of about 1 %, indicating high process repeatability. A relationship between the UMo mass flow rate generated in REP and input electric arc power was established. It was found that the U8Mo mass flow rate in REP had a lower threshold. It was also observed that UMo melting range, rotating electrode geometry, and alloy homogeneity had influence on the atomization process and experimental results, notably powder quality. Moreover, it was found that REP-atomized UMo particles had a dendritic microstructure. Also, an influence of carbon impurities on the mass flow rate and particle microstructure was observed. Potential surrogate materials for further development were briefly evaluated on a theoretical basis. Existing models with respect to REP and centrifugal atomization were summarised, adjusted, and compared to experimental results of this work showing good agreement.

To my parents

„Damit das Mögliche entsteht, muss immer wieder das Unmögliche versucht werden.“

Hermann Hesse

Contents

Contents....IX
Notation....XV

1 Introduction 1

1.1 About FRM II....1
1.2 Reactor Core and Fuel Element....2
1.3 Fuel Plate....3
1.4 Reactor Conversion....4
1.5 UMo Fuel Types....5
1.6 UMo Fuel Powder Fabrication....6
1.7 FRM II/CERCA UMo Atomizer Project....7

I Engineering....9

2 Process and System Requirements 11

2.1 Nuclear Safety and Radiation Protection....11
2.2 Conventional and Occupational Safety....12
2.3 Repeatability....13
2.4 Powder Quality....13
2.5 Modelling....14
2.6 Process Efficiency....15
2.7 Maintenance....15
2.8 Laboratory-Scale and Scalability....15
2.9 Production Capacity....16
2.10 Automation....16
2.11 Differential Design....16

3 Atomizer 19

3.1 Concept 19

3.1.1 Rotating Electrode Process (REP) 19

3.1.2 Laboratory-Scale Design 23

3.1.3 System Architecture 23

3.1.4 Process Control 29

3.1.5 Commissioning 30

3.2 Infrastructure for Hot Operation 31

3.3 System Components 34

3.3.1 Make or Buy 34

3.3.2 Glovebox 36

3.3.3 Gas Purifier 43

3.3.4 Framework (34) 46

3.3.5 Argon 47

3.3.6 Arc Welder 48

3.3.7 Welding Torch (15) 54

3.3.8 Tungsten Electrode (21) 55

3.3.9 Infeed Linear Guide Rails (1) and Slider (19) 57

3.3.10 Torch Adapter (16) 58

3.3.11 Drill-Rig (20) with Cantilever (18) 59

3.3.12 Rotating Electrode (9) 60

3.3.13 High Frequency Spindle (11) 62

3.3.14 Carbon Brushes (23) 71

3.3.15 Brass Pipes (24) 73

3.3.16 Collector Ring (25) with Screw Insulation (26) 74

3.3.17 Graphite Dust Seal (22) 75

3.3.18 Insulator and Retention Depot (27) 75

3.3.19 Variable-Frequency Drive 76

3.3.20 Motor (6) 79

3.3.21 Belt (8) 82

3.3.22 Motor Carrier (31) 83

3.3.23 Tension Spring (29) 84

3.3.24 Linear Guide Rails (30) and Hybrid Bearings (32) 85

3.3.25 Winch (28) 86

3.3.26 Bump Stop (33) 87

3.3.27 Powder Collection Chamber (4) 87

3.3.28 Powder Seal Screw (3) 89

II Experimental 91

4 Process Repeatability ... 93

4.1 Experimental Setup ... 93
4.2 Results and Discussion ... 94
4.3 Measurement Uncertainty ... 99
4.4 Comparison ... 99
4.5 Conclusion ... 100

5 Mass Flow Rate ... 101

5.1 Background ... 101
  5.1.1 Definitions ... 101
  5.1.2 Electric Arc ... 103
  5.1.3 Model ... 108
5.2 Experimental Setup ... 108
5.3 Results and Discussion ... 109
  5.3.1 Arc Welder Operating Range ... 109
  5.3.2 Electric Arc Power ... 110
  5.3.3 Rotating Electrode Length ... 113
  5.3.4 Rotating Electrode Diameter ... 115
  5.3.5 Impurities ... 117
  5.3.6 Model Evaluation ... 120
5.4 Comparison ... 122
5.5 Conclusion ... 123

6 Atomization Regime ... 127

6.1 Background ... 127
  6.1.1 Direct Droplet Formation (DDF) ... 128
  6.1.2 Ligament Disintegration (LD) ... 131
  6.1.3 Film Disintegration (FD) ... 132
  6.1.4 Model ... 132
6.2 Experimental Setup ... 135
6.3 Results and Discussion ... 136
  6.3.1 Particle Shape and Model Evaluation ... 136
  6.3.2 Surrogate Material ... 142
6.4 Comparison ... 144
6.5 Conclusion ... 147

7 Particle Size and Process Efficiency ... 149

7.1 Background ... 149

7.1.1 Powder Screening 149
7.1.2 Particle Size Distribution 151
7.1.3 Characteristic values 155
7.1.4 Efficiencies 158
7.1.5 Models 159
7.2 Results and Discussion 162
7.2.1 Yield Efficiency and Parameter Sets 162
7.2.2 Production Capacity 169
7.2.3 Particle Size Distribution 169
7.2.4 Model Evaluation 185
7.3 Comparison 191
7.4 Conclusion 192

8 Particle Morphology and Chemistry 195

8.1 Background 195
8.1.1 Phase Diagrams 195
8.1.2 Primary Crystallisation in Alloys 200
8.1.3 Microsegregation 203
8.1.4 Classification of Particles and Impurities 204
8.2 Results and Discussion 207
8.2.1 Powder Chemistry 207
8.2.2 Surface Morphology 211
8.2.3 Microstructure 214
8.2.4 Irregular Particles 226
8.3 Comparison 230
8.4 Conclusion 231

III Summary 235

9 Summary, Outlook, and Conclusion 237

9.1 Summary 237
9.1.1 Nuclear Operating Licence 237
9.1.2 Design 238
9.1.3 Dimensioning 238
9.1.4 General Parameterisation 238
9.1.5 Surrogate Material 240
9.1.6 Maintenance 240
9.1.7 Repeatability 241
9.1.8 Powder Quality 241

9.1.9 Process Efficiency 243
9.1.10 Production Capacity 244
9.1.11 Modelling....244
9.1.12 Rotating Electrodes 245
9.2 Outlook 246
9.3 Conclusion 249

IV Appendix....251

A Dimensioning 253

A1 HF Spindle Design Point 253
A2 Brushes....254
A3 Motor Pulley Diameter 255
A4 Belt....255
A5 Winch 258
A6 Tension Spring....258
A7 Motor Carrier 260

B Granulometry 261

B1 Stainless Steel....262
B2 UMo....291

List of Figures....317
List of Tables 333
Publications....337
Bibliography....339
Acknowledgement....349

Notation

Abbreviations

AC	Alternating current
Al	Aluminium
Ar	Argon
at	Atomic
B	Backlash
BSE	Back-scattered electrons
C	Carbon
Ca	Calcium
CAD	Computer-aided design
CERCA	Compagnie pour l'Etude et la Réalisation de Combustibles Atomiques
CCHEN	Comisión Chilena de Energía Nuclear
CS	Crystallisation speed
Cu	Copper
DC	Direct current
DCEN	Direct current (tungsten) electrode negative
DCEP	Direct current (tungsten) electrode positive
DDF	Direct droplet formation
EDX	Energy-dispersive X-ray spectroscopy

FD	Film disintegration
FRM II	Forschungsreaktor München II
Fe	Iron
H_2	Hydrogen
H_2O	Humidity or water
HC	High current
HEPA	High-efficiency particulate absorption
HEU	Highly enriched uranium
HF	High frequency
HFIR	High Flux Isotope Reactor
IDL	Interdiffusion layer
IGSD	Inclusive graphic standard deviation
ILL	Institut Laue-Langevin
INL	Idaho National Laboratory
Inox	Stainless steel (French: inoxydable)
ISO	International Organization for Standardization
KAERI	Korea Atomic Energy Research Institute
KF	Klein Flange
L	Liquid phase in phase diagrams
LC	Low current
LEU	Low-enriched uranium
LF	Ligament formation
Mg	Magnesium
Mo	Molybdenum
N_2	Nitrogen
NBR	Nitrile butadiene rubber
Ni	Nickel
NN	Number of nuclei
O	Rotation offset
O.C.V.	Open-circuit voltage

ORNL	Oak Ridge National Laboratory
O_2	Oxygen
PC	Personal computer
PE	Polyethylene
PMMA	Poly(methyl methacrylate) or Plexiglas
PREP	Plasma rotating electrode process
PSD	Particle size distribution
PU	Polyurethane
REP	Rotating electrode process
RHF	Réacteur à Haut Flux
S	Solid phase in phase diagrams
SE	Secondary electrons
SEM	Scanning-electron microscopy
SD	Standard deviation
Si	Silicon
U	Uranium
^{235}U	Uranium-235 isotope
U(x,y)	Element(s) x, y dissolved in uranium, e.g. U(C) or U(C,Mo)
UC	Uranium carbide, intermetallic compound
uc	Uncertainty (div. units)
UMo	Uranium-molybdenum alloy in general
USB	Universal serial bus
UxMo	Uranium with x wt.-% of molybdenum, e.g. U8Mo
VFD	Variable-frequency drive
W	Tungsten
wt	Weight
Zn	Zinc
Xe	Xenon
1.4301	Stainless steel X5CrNi18-10 according to EN-10088-3

Latin Alphabet

Symbol	**Unit**	**Quantity**
b	mm	Circular arc length
C	div.	Constant
c	at.-% or wt.-%	Concentration
D	mm or m	Rotating electrode diameter
D	µm or m	Particle or droplet diameter
E	V m^{-1}	Electric field strength
e	-	Euler number
e	mm	Shaft centre distance
e'	mm	Minimum shaft centre distance
F	N	Force
F_{Ar}	-	Argon fraction
F_0	N	Inherent spring pre-tension
g	N kg^{-1}	Gravitational acceleration
H	kJ kg^{-1}	Enthalpy
h	mm	Height
I	A	Electric current
i	A cm^{-2}	Arc current density
K	V	Linear functions of arc length
k	N mm^{-1}	Spring rate
L'	mm	Theoretical belt length
l	mm	Electric arc length
l_t	mm	Total belt length due to centrifugal force
l_0	mm	Belt length (tensionless)
l_1	mm	Belt length after pre-tension
m	kg	Mass
$m(D)$	µm^{-1} or m^{-1}	Normalised mass distribution

$\dot{m}$	kg s^{-1} or g s^{-1}	Mass flow rate
m_{cus}	%	Cumulative undersize distribution
M_p	$\{\sigma^{0.88}\rho_{\text{l}}^{-0.71}\mu_{\text{l}}^{-0.17}\}$	Material parameters referring to the atomization regime in centrifugal atomization
n	rpm	Rotational speed
$n(D)$	µm^{-1} or m^{-1}	Normalised number distribution of particle diameters
O_p	$\{Q\omega^{0.6}D_{\text{re}}^{-0.68}\}$	Operating parameters referring to the atomization regime in centrifugal atomization
P	W	Power
p	mm	Perimeter
Q	m^{3} s^{-1}	Volume flow rate
$\dot{Q}$	W	Heat flow or transfer rate
R	µm or m	Range
r	-	Coarse-to-fine (mass) ratio
R^2	-	Coefficient of determination
S	mm^{2}	Surface area
s	mm	Spring length
Sp	-	Relative span
T	°C or K	Temperature
T_{f}	h^{-1}	Leak-rate
t	s	Time
U	V	Electric voltage
v	m s^{-1}	Speed
X	-	Characteristic number describing the atomization regime

Greek Alphabet

Symbol	Unit	Quantity
α	-	Refers to the α-phase in phase diagrams
β	-	Refers to the β-phase in phase diagrams
γ	-	Refers to the γ-phase in phase diagrams
Δ	-	Interval or difference
δ	-	Refers to the δ-phase in phase diagrams
ε	-	Refers to the ε-phase in phase diagrams
ε_{t}	%	Total belt elongation
ε_1	%	Belt elongation after pre-tension of the belt
ε_2	%	Belt elongation due to centrifugal force
η	%	Efficiency or yield efficiency
μ_{l}	$\mathrm{kg\,m^{-1}\,s^{-1}}$	Dynamic viscosity
μ_{st}	-	Static friction coefficient
π	-	Pi
ρ	$\mathrm{kg\,m^{-3}}$	Density
σ	$\mathrm{N\,m^{-1}}$	Surface tension
σ_{ig}	µm or m	Inclusive graphic standard deviation
σ_{ln}	-	Log-normal standard deviation
ω	$\mathrm{rad\,s^{-1}}$	Angular velocity

Subscripts

a	Atomization
a1	Refers to particle diameter
app	Apparent
av	Average
b	Belt
brush	Carbon brush

b1	Refers to particle cross-section area
c	Calculated
c	Coarse, refers to the coarse-to-fine ratio
carrier	Motor carrier
cf	Centrifugal force
d	Droplet
e	Refers to cathode energy loss in electric arc welding
el	Electric
exp	Expected, refers to total belt elongation
f	Fine, refers to the coarse-to-fine ratio
f, st	Refers to static friction force
i	Size interval
lb	Refers to radiation loss of the electric arc
Li, l	Liquid
m	Melt
m, m	Refers to the mass mean diameter
m, x	Value, smaller than which there is 100x% of particles by mass
m, 0.5	Refers to mass median diameter
max	Maximum value
min	Minimum value
mode	Peak of a curve
motor	Atomizer motor
op	Operation
p	Particle or powder
p	Moment order in generalised mean particle diameter relationship
pt	Pre-tension
pu	Pulley
q	Moment order in generalised mean particle diameter relationship
r	Relative
re	Rotating electrode

Real	Refers to the real temperature of a melt
rest	Refers to the rest of a rotating electrode after atomization
rp	Restoring pull
s	Spring
ses	Shaft extension screw
sphere	Refers to a spherical particle
spindle	High frequency spindle
t	Total
u	Usable, refers to yield efficiency
w	Welding
wc	Worst case
0.01	Refers to a belt elongation of 1 %
10, 30, 32 etc.	Different definitions of mean diameters

Note on Units

All equations are presented in SI units unless stated otherwise. Other units may be used if more convenient or common, and their use is always made clear.

1

Introduction

This introductory chapter gives an overview of the project's background, beginning with a brief presentation of FRM II and its current nuclear fuel, followed by the presentation of the reactor conversion program and U8Mo fuel types currently under investigation. U8Mo fuel-powder fabrication processes investigated in the past are then briefly presented. The chapter concludes with a presentation of this work's underlying project and corresponding objectives.

1.1 About FRM II

The Forschungs-Neutronenquelle Heinz Maier-Leibnitz (FRM II) is a scientific high flux neutron source operated by Technische Universität München (TUM). It is dedicated to the research with and application of neutrons in science, industry, and medicine. FRM II provides users with an undisturbed thermal neutron flux density $\Phi_{\mathrm{th,max}}$ of approximately $8 \cdot 10^{14}$ neutrons $\mathrm{cm}^{-2}\,\mathrm{s}^{-1}$ at 20 MW nominal thermal power. FRM II exhibits the world's highest thermal flux-to-power ratio. The neutron energy-spectrum ranges from 10^{-7} eV to 25 meV to 10 MeV for ultra-cold (minimum value), thermal (average), and fission neutrons (maximum value), respectively. FRM II offers operation cycles of 60 consecutive days and typically a total of 240 days of operation per year.

1.2 Reactor Core and Fuel Element

FRM II is a combined light and heavy water compact-core reactor powered by one single fuel element (Figure 1-1). While light water (H_2O) serves as coolant and neutron moderator, heavy water (D_2O) serves as moderator and neutron reflector. Due to the compact core design, the thermal neutron density flux reaches a maximum outside the fuel element in the D_2O tank where beam tubes and some intermediate applications are situated. As a result, extraction of thermal neutrons for user applications is maximised. At present, the total uranium inventory of the fuel element is 8.1 kg with an enrichment of 93 at.-% in ^{235}U. Therefore, the current uranium inventory is considered highly enriched uranium, HEU (> 20 % of ^{235}U).

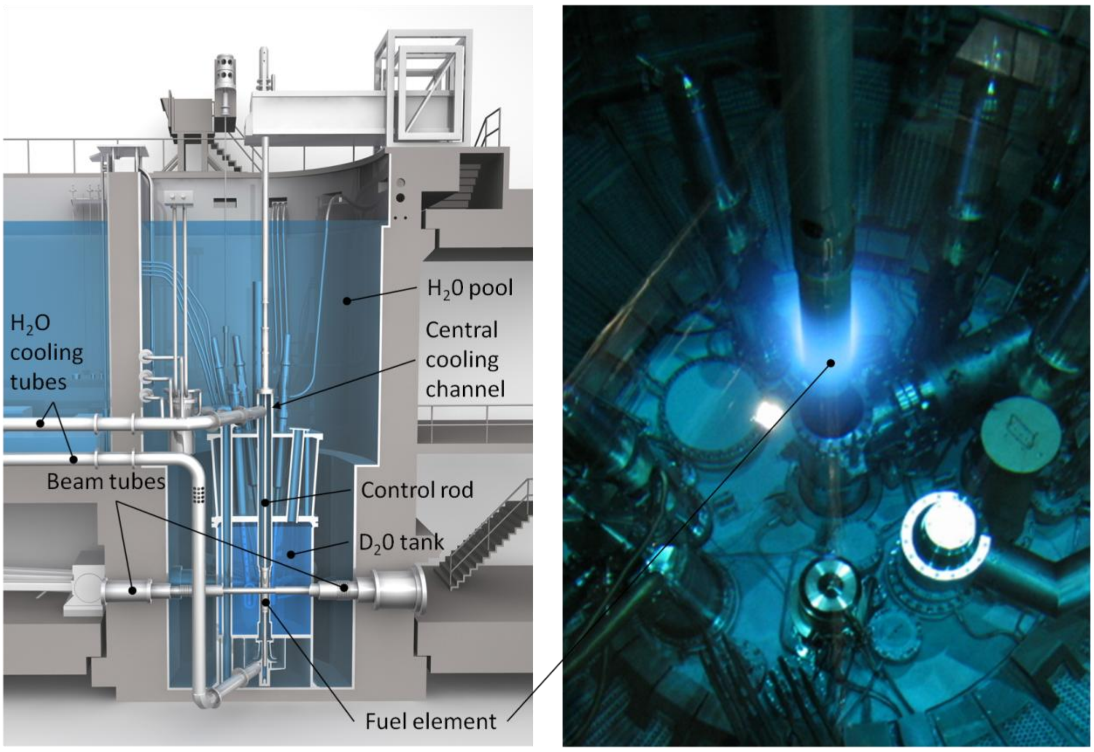

Figure 1-1 Sectioned schematic view of the primary circuit of FRM II (left) and fuel element during replacement (right); both pictures property of TUM.

The current fuel element design is based on the fuel elements of RHF (Réacteur à Haut Flux) at the Institut Laue-Langevin (ILL), France, and HFIR (High Flux Isotope Reactor) at Oak Ridge National Laboratory (ORNL), USA. It has the form of a hollow cylinder and is composed of 113 radially arranged fuel plates that are separated by cooling channels with constant size of 2.2 mm (Figure 1-2). The latter is achieved through involute-shaped fuel plates that promote consistent heat removal.

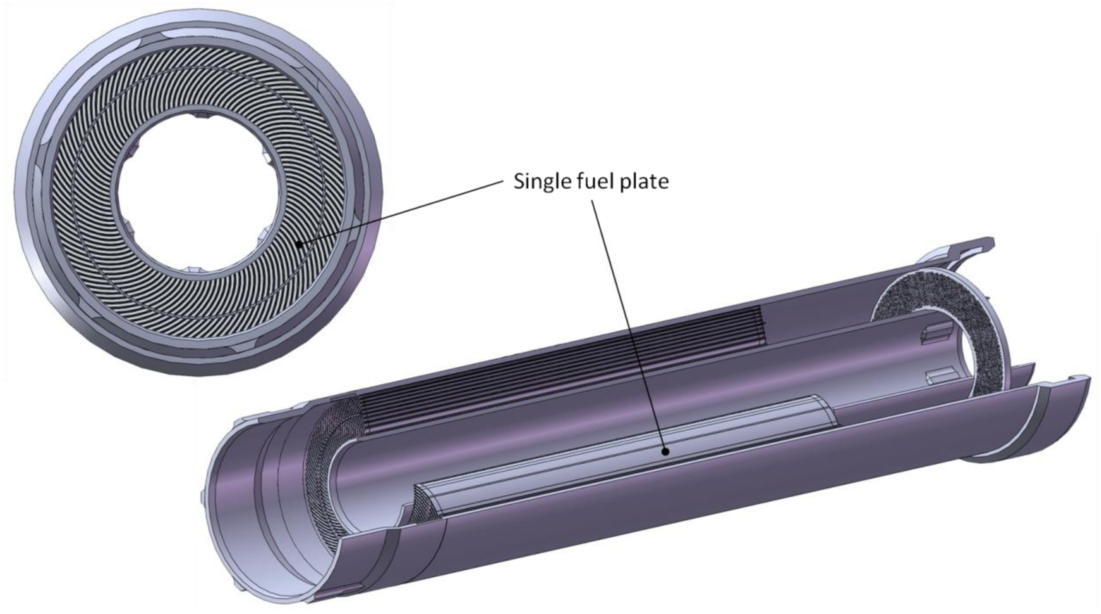

Figure 1-2 Top view (left) and sectioned view (right) of the FRM II fuel element [Breitkreutz 2011].

1.3 Fuel Plate

Each fuel plate (Figure 1-2) consists of a fuel plate core (“meat”), a frame made of AlMg2, and two claddings made of AlFeNi (Figure 1-3). At present, the meat consists of ground U_3Si_2 (uranium silicide) powder which is dispersed in a matrix of pure aluminium powder. Uranium silicide exhibits a uranium density of $11.3\,\mathrm{gU\,cm^{-3}}$ [Schmid 2011]. While the meat contains the fissile material, the cladding prevents the coolant from contamination with fission products, provides thermal contact between coolant and meat, and protects the meat from coolant-induced chemical erosion[1]. Pure aluminium is used for the meat matrix as it exhibits superior malleability and has a high thermal conductivity ($235\,\mathrm{W\,m^{-1}\,K^{-1}}$), resulting in a large contact area between fuel particles and matrix after fuel plate fabrication, i.e. hot and cold rolling. Thus, efficient heat removal from the U_3Si_2 fuel particles ($15\,\mathrm{W\,m^{-1}\,K^{-1}}$) to the cladding is provided. In addition, aluminium is used in nuclear applications as it has one of the smallest absorption cross section for thermal neutrons ($\sigma_\gamma = 0.23\,\mathrm{b}$)[2] among structural materials [Emendörfer and Höcker 1982].

---

[1] The average flow speed of the coolant is about $16\,\mathrm{m\,s^{-1}}$.

[2] $1\,\mathrm{b}$ (barn) = $10^{-28}\,\mathrm{m}^2$

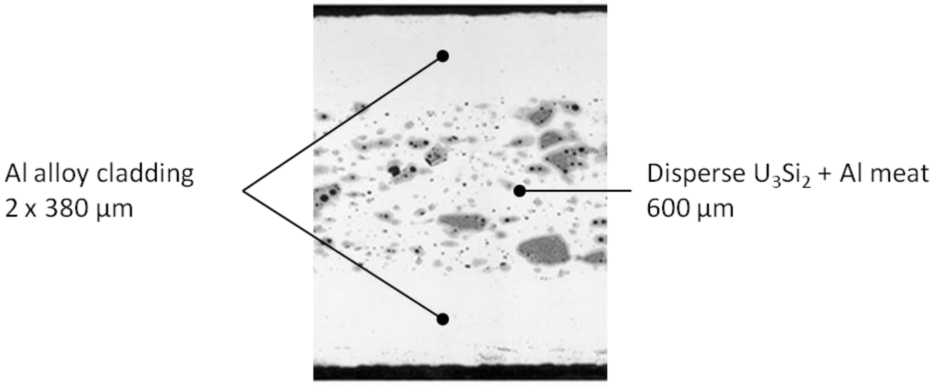

Figure 1-3 Fuel plate section showing the meat and cladding zones [Schmid 2011].

Height, length, and thickness of the meat zone extent to 700 mm, 2.4 mm, and 0.6 mm, respectively. The volume fuel loading (U_3Si_2-to-Al ratio) of the fuel plate increases radially. It is 14 vol.-% in the outer and 27 vol.-% in the inner fuel plate zone. Thus, the corresponding uranium density in the meat is 1.5 gU cm^{-3} and 3 gU cm^{-3}, respectively [Breitkreutz 2011].

1.4 Reactor Conversion

According to the third partial operating license "3. Teilerrichtungsgenehmigung" of FRM II, the currently used HEU fuel has to be replaced by a lower enriched fuel as soon as a suitable fuel is available. That is, the relative amount of fissile ^{235}U has to be reduced with respect to the total uranium inventory. Therefore, FRM II has created its own scientific project group for reactor conversion covering reactor physics simulation, material science, and nuclear engineering. The group contributes to worldwide efforts to reduce enrichment.

Conversion must not compromise the nuclear safety of the reactor, has to guarantee the aforementioned operating cycle length, and may only marginally affect neutron flux density and quality. Changing geometry or size of the fuel element would require conceptual and constructional changes to the reactor core. This in turn is associated with enormous costs and long downtime due to reconstruction in a radioactive environment and a new qualification procedure for the nuclear operating license. As a consequence, conversion efforts concentrate on increasing the total uranium inventory in the fuel element in order to decrease the fraction of ^{235}U and thus enrichment. Hence, an increase in both uranium density and volume fuel loading is currently being pursued.

Here, an upper limit is given by the density of pure metallic uranium in the orthorhombic α-phase, which is 19.06 gU cm^{-3}. For the current FRM II fuel element geometry, this would mean a theoretical decrease in enrichment to about 31 % [Röhrmoser *et al.* 2005]. However, pure metallic α-uranium is dimensionally unstable under irradiation and thermal load and therefore cannot be used [Holden 1958, Paine and Kittel 1955, Rest *et al.* 1998]. In fact, only the high temperature, body-centred cubic γ-phase of uranium may be used as nuclear fuel [Paine and Kittel 1955]. Dimensional stability of uranium, notably its γ-phase, may be promoted through alloying [Wilkinson 1962a]. Accordingly, several binary and ternary uranium alloys as well as intermetallic compounds were investigated in the past [Jungwirth 2011, Van Den Berghe and Lemoine 2014]. As a result, uranium-molybdenum alloys with a molybdenum mass fraction between 7 wt.-% (U7Mo) and 10 wt.-% (U10Mo) were identified as best compromise between high uranium density, γ-phase stability at room temperature before and during irradiation, and thermal neutron absorption cross section[3] [Van Den Berghe and Lemoine 2014]. The corresponding uranium densities vary from 16.5 gU cm^{-3} (U7Mo) to 15.3 gU cm^{-3} (U10Mo) [Schmid 2011].

1.5 UMo Fuel Types

At present, two types of UMo fuel are being investigated in parallel with regard to fabrication process and irradiation behaviour, namely monolithic UMo fuel as well as UMo fuel powder dispersed in an aluminium matrix.

Monolithic fuel offers the highest possible fuel volume loading in the meat, i.e. 100 %, and less interaction potential between the fuel and structural material (e.g. no aluminium matrix, less contact area).

Fuel powder dispersed in a structural matrix allows for a superior heat removal due to the high thermal conductivity of the aluminium matrix. However, a commercially reasonable fuel plate fabrication process limits the fuel volume loading to 55 vol.-% [Snelgrove *et al.* 1997]. In addition, thermal conductivity of the meat was shown to decrease strongly with increasing UMo content [Huber *et al.* 2015] due to its relatively low thermal conductivity (e.g. 12 W m^{-1} K^{-1} for U10Mo). Recent studies have shown that the highest reasonably achievable uranium density in a disperse fuel using U7Mo alloy is 8 gU cm^{-3}, resulting in an enrichment of 30 % [Röhrmoser *et al.* 2012].

The present work is a key part of the dispersed UMo fuel type program.

---

[3] The absorption cross section for thermal neutrons of molybdenum is σ_γ = 2.6 b and therefore tenfold higher than for aluminium. Nevertheless, it is one of the lowest among structural materials [Emendörfer and Höcker 1982].

1.6 UMo Fuel Powder Fabrication

Commercially, metal powders are produced by chemical, electrolytic, mechanical, and atomization processes from bulk material [Lawley 1992, Yule and Dunkley 1994]. Thus, different fabrication processes of UMo fuel powder were evaluated in the past including grinding, cryogenic milling, the hydride-dehydride process, gas atomization [Clark *et al.* 1998], as well as centrifugal atomization [Clark *et al.* 2007, Kim *et al.* 1997b, Kim *et al.* 2007, Oh *et al.* 2006]. More recently and in parallel to this work, magnesiothermic reduction was investigated [Champion *et al.* 2013].

Mechanical comminution techniques such as grinding and (cryogenic) milling and their combination proved to be ineffective due to UMo ductility. Chilling UMo with liquid argon (87.3 K) was ineffective in increasing alloy brittleness, therefore not improving the process. Production rates were reported as "extremely" low. The resulting powder consisted of coarse UMo shavings (grinding) or flakes (cryogenic milling) and high contamination from grinding and milling tools due to mechanical wear.[Clark *et al.* 1998]

The hydride-dehydride process is a common uranium powder production technique that is based on the difference in density of uranium hydride (11 $\mathrm{g\,cm^{-3}}$) and uranium (19 $\mathrm{g\,cm^{-3}}$). Bulk uranium, namely its surface, is exposed to and reacts with hydrogen at temperatures below 300 °C. Due to the difference in density, uranium hydride spalls off the bulk material surface as fine powder. Uranium hydride is then heated and reduced under vacuum. The process was applied to pure uranium resulting in 29 wt.-% and 17 wt.-% in the particle-diameter target size-ranges of 45-150 µm and below 45 µm, respectively. High-energy ball milling allegedly increased the fraction in the target size range of the coarser particles to 82 %. However, scanning-electron microscopy (SEM) analysis revealed that the particles had a "blocky" form and had agglomerated during milling. As a result, particles were "much" smaller than indicated by sieve analysis. Besides theses issues, safety concerns with respect to containment and reactivity of heated hydrogen were stated as disadvantages. The potential explosion danger in hydrogen applications is of even more concern in nuclear facilities as radioactive and fissile material is being handled.[Clark *et al.* 1998]

Recent investigations into the process showed a lack of process repeatability and control for large charges. Production rate and efficiency were not stated. Also, the aforementioned inherent process shortcomings were not addressed.[Durazzo *et al.* 2014]

Gas atomization is the dispersion of a bulk liquid melt into fine droplets by means of pressurised gas. The process was evaluated using gold as surrogate material as it has a similar surface tension, viscosity, density, and melting point compared to uranium. The produced particles met target size requirements and were spherical in shape with satellites. Its potential to meet program needs was stated, but further investigation, in particular with uranium or UMo, has not been reported to this day.[Clark *et al.* 1998]

General concerns with gas atomization are powder collection-chamber lengths of typically 10 m (if no liquid-gas quenching is used), particle internal porosity due to insoluble gas entrapment, and lack of scalability with respect to both gas and melt flow rate [Yule and Dunkley 1994]. Furthermore, the process necessitates superheat of about 75-150 K [Lawley 1992] in order to avoid premature solidification. Considering that relevant UMo alloys have a liquidus > 1200 °C, practical target melting temperatures may rise beyond 1300 °C. The melting point of gold lies around 1069 °C, though. This is of major concern as the crucible (melt tundish) and atomization nozzle cannot be cooled with water as commercially practiced due to criticality concerns. Thus, refractory crucibles and nozzles have to be used that withstand the temperature, uranium chemical reactivity, and typical pressure differences from 0.5 MPa (5 bar) to 9 MPa [Lawley 1992] at the same time. The latter is also a concern to nuclear safety with respect to the containment that requires operation at negative pressure.

For completeness, it is mentioned that another fabrication method was investigated in parallel to this work using magnesiothermic reduction. It involved the chemical reduction of UO_2 powder with Mg chips at elevated temperatures and subsequent reaction of metallic uranium with present molybdenum powder. The obtained particles were irregular in shape and tended to agglomerate. With increasing temperatures during heat treatment, agglomerates showed a tendency to spheroidise, though. A homogeneous distribution of molybdenum in the particle and small porosities were reported (0-3 µm). The obtained particle size distributions corresponded to the target size range.[Champion *et al.* 2013]

Ultimately, centrifugal atomization has been identified as a suitable and the most promising fabrication process as UMo powders were successfully produced at industrial scale at KAERI (Korea Atomic Energy Research Institute) and through a proof of principle at INL (Idaho National Laboratory) in the past.

1.7 FRM II/CERCA UMo Atomizer Project

In early 2010, German FRM II and French fuel manufacturer AREVA CERCA agreed to launch a common project for the design, engineering, and operation of a prototype UMo fuel-powder production facility in France.

General objective of the collaboration is to provide feedstock atomized UMo fuel powder for irradiation tests. Besides, gathering expertise, notably in centrifugal atomization, is of vital interest with regard to potential UMo production at industrial scale. In this respect, both the prototype development and operation allow for evaluation of the practical feasibility of such a project in a highly regulated nuclear environment within Europe while keeping both development costs low and time short in case of technical or licensing failure. In addition, the project aims at significantly reducing shipping costs, logistics, and lead times associated with powder coming from external non-European sources, in particular for changes in both alloy composition and customer demands. Furthermore, the only industrially viable process of KAERI is limited to an enrichment of 20 %.

In the position of a project engineer of FRM II, the author planned, designed, implemented, commissioned, and tested the entire prototype UMo fuel-powder production facility (Figure 1-4). The implemented production facility includes a prototype atomizer, an induction furnace, two gloveboxes, analytical equipment, and a dedicated uranium laboratory. The work was accomplished in close collaboration with representatives from AREVA CERCA. In addition, INL provided insight to its atomization and casting process and delivered pre-fabricated UMo for atomization experiments.

The key component of the production facility is the prototype UMo REP atomizer. This thesis summarises the author's accomplished work with regard to the engineering of the prototype atomizer, experimental atomizer parameterisation, and characterisation of fabricated U8Mo and U7Mo fuel powder.

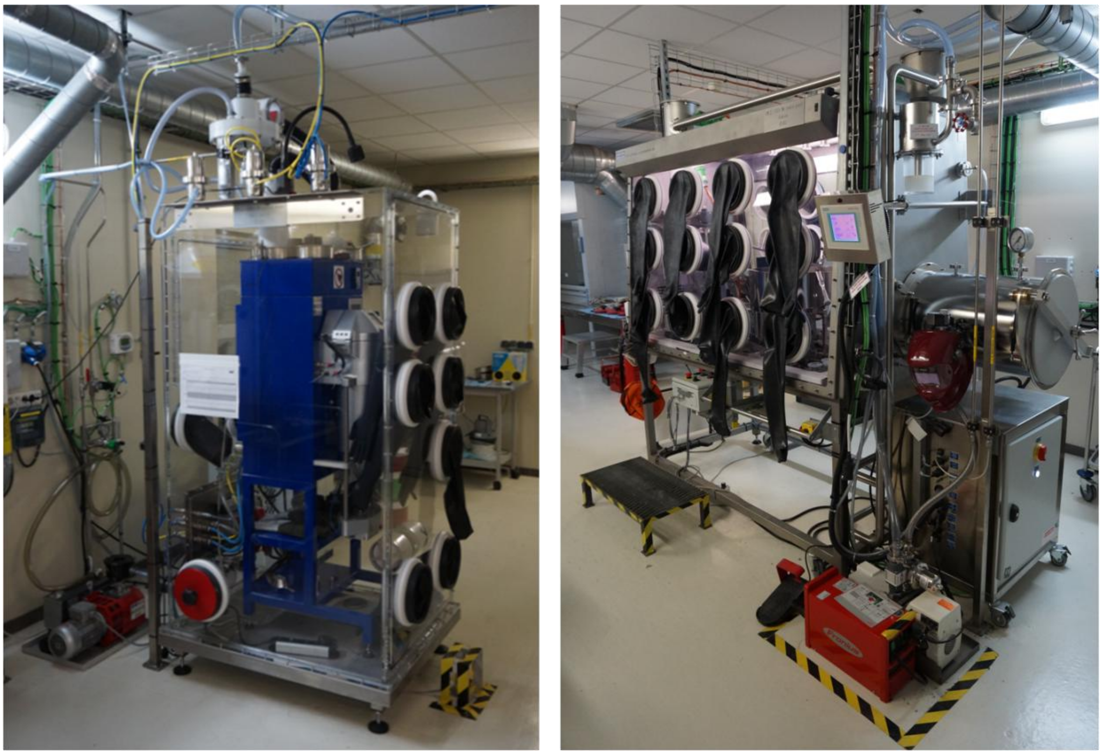

Figure 1-4 Implemented prototype UMo fuel powder production facility including induction furnace (left) and atomizer (right).

I

Engineering

2

Process and System Requirements

The process and system requirements were primarily derived from the desired UMo fuel-powder properties. In addition, nuclear safety, occupational safety, and radiation protection requirements as well as financial aspects had to be respected. As the relationship between atomized UMo fuel-powder quality and the atomization process is still under investigation, system flexibility instead of process automation was emphasised. The following chapter summarises in detail the respective requirements.

2.1 Nuclear Safety and Radiation Protection

The new powder production facility including the atomizer is being operated on the Areva FBFC (Franco-Belge de Fabrication du Combustible) fuel-element production site in Romans-sur-Isère, France, and is legally part of the stationary nuclear installation INB 63 (Installation nucléaire de base); it is thus subject to the French nuclear regulator ASN (Autorité de sûreté nucléaire). Therefore, an important aspect of engineering was to ensure the reception of a nuclear operation licence with respect to the atomization process and atomizer design. As the project planning, build-up, and operation of the atomizer as well as its auxiliary installations and equipments represent a change to the operating licence of the INB 63, the entire project is subject to article 26 of the INB related act ["Décret no. 2007-1557" 2014]. The corresponding change documents [Cadoret 2013, Denet 2010] include a description of the installation and relevant processes as well as an evaluation of both the related nuclear and conventional risks.

Resultant constraints having a direct impact on both the atomizer and production facility design are stated in Table 2-1.

Table 2-1 Excerpt of the most important maximum operating limitations of the powder production facility with respect to criticality and radiation protection [Cadoret 2013].

Installation service life	Atomizer glovebox leak-rate	Oxygen content in atomizer glovebox	Processing of U	Processing of ^{235}U	Total production of ^{235}U powder	Enrichment in ^{235}U	Atomizer glovebox negative pressure
[years]	[h^{-1}]	[%]	[g]	[g]	[kg]	[%]	[Pa]
5	0.01	4	300	150	2	50	10

* Values given for U or ^{235}U are valid for metallic U or U-based alloys, e.g. U8Mo.

According to [Cadoret 2013], the atomizer has to be housed in an inert atmosphere containment in order to guarantee the oxygen limit with respect to inflammability of UMo alloys, in particular in powder form. In addition, the containment has to prevent from dissemination of and contamination with radioactive material. To ensure safety in case of a containment rupture, the total amount of uranium is limited (Table 2-1). In terms of criticality, enrichment of uranium in ^{235}U as well as the amount of ^{235}U is limited to 50 % and 150 g, respectively; the latter limitation accounts for dissemination and contamination risks as well. Also, a decreasing pressure cascade towards the glovebox has to ensure that all nuclear material is kept within the installation in case of confinement rupture. The use or presence of water or other moderators in the atomizer or its glovebox is not covered by the article 26 and thus strictly prohibited.

The current version of the article 26 concerning the UMo atomizer [Cadoret 2013] is based on both the atomizer concept as well as purpose that is presented in this work. Any changes – e.g. in process, design, equipment, enrichment, type of fissile fuel etc. – will be subject to another evaluation.

2.2 Conventional and Occupational Safety

An evaluation of conventional and occupational risks with respect to both the atomization device and process was conducted [Cadoret 2013], stating risks due to rotating parts, earthquakes, calorific values of materials, and hot parts, that have to be considered. Furthermore, risks arising from electromagnetic fields, electric arcs (light-intensity, spectrum, and temperature), and electrified components must be accounted for in the atomizer design and are subject to external technical control [Boulanger 2012].

2.3 Repeatability

Repeatability or precision is the consistency of experimental results across successive experiments, carried out by the same operator under the same conditions, using the same machine and parameter set, the same measuring instrument and procedure over a short period of time [Taylor and Kuyatt 1994]. Initially defined for experiments, this definition equally applies to production and constitutes an important machine feature regarding industrial processes. In fact, it has a direct impact on significance of production result, process modelling, and process efficiency.

The atomizer prototype is intended to serve as precursor for the industrialisation of UMo fuel powder production. It must therefore provide repeatable parameter settings as well as production results. As a consequence, repeatability was accounted for in prototype design (chapter 3) and experimental process evaluation (chapter 4).

Current production specifications [Harbonnier 2002, Vanvor and Zill 2003] define neither Upper Limit (UL) nor Lower Limit (LL) for the variation of production results to each other.

2.4 Powder Quality

The definition of powder quality varies with different applications. According to the current fuel specification of AREVA [Gery 2011], UMo fuel powder has to meet constraints regarding the isotopic composition, radioactivity, chemical impurities as well as molybdenum fraction, and granulometry (both Table 2-2 and Table 2-3). Also, the U_3Si_2 fuel specification [Vanvor and Zill 2003] was used for orientation.

Table 2-2 Excerpt of desired U8Mo fuel powder characteristics with respect to atomization according to the material supply specification G183 [Gery 2011].

Mo fraction [wt.-%]	Powder type	Particle shape	Maximum particle diameter [µm]	Mass fraction of particles with diameter ≤ 40 µm [wt.-%]
8 ± 0.5	Atomized	Spherical	125	30-50

In addition to the particle diameter ranges of < 40 µm and < 125 µm presented in Table 2-2, particle diameters < 180 µm have to be considered as well since coarser particles may become an option for fuel element production.

Other fuel powder properties of interest are typically related to particle morphology, notably particle shape (sphere, ellipsoid, filament, flake, or irregular), particle diameter, surface pores (voids, channels), surface roughness (smooth, irregular surface, e.g. dendrites), internal voids (vacuum) or porosity (gas), alloy homogeneity and phase, grain size, segregation, surface oxidation, impurities, shells, and satellite particles [Yule and Dunkley 1994]. In addition, bulk properties such as particle size distribution, mechanical properties, tap density, and flowability are relevant.

Powder quality is mainly determined by the material to be atomized, the atomization process, the atomizer design, and the applied parameter set. While the material used in this work was predefined (U8Mo and U7Mo), process and prototype design choice (chapter 3) as well as experimental parameterisation (chapters 5, 6, 7, 8) were accomplished in this work.

Table 2-3 Excerpt of regulated chemical impurities of U8Mo fuel powder according to the material supply specification G183 [Gery 2011]; stated are elements that may occur in the casting and atomization process.

Element	Limit value [ppm or μg/g]
C	2000
Cu	500
Fe	1500
H	500
N	2500
Ni	500
O	7000
Al	5000
Si	2000

2.5 Modelling

An important aspect when aiming at producing fuel powder at an industrial scale is the prediction or estimation of production results from a given parameter set. It is hence advantageous to implement an atomization process that is merely understood through empiric models, physically derived models or numeric algorithms.

In this work, existing models are summarised and compared to experimental results (chapters 5, 6, 7). In addition, experimental correlations are established for relationships that have not been modelled yet with respect to atomization of UMo in general and U8Mo in particular (chapter 5).

2.6 Process Efficiency

In general, productivity or process efficiency is defined as the ratio of system input to output. The definition of this factor, though, may differ depending on what one is interested in. For atomizer performance evaluation, characteristic numbers such as

+ the mass ratio of atomized powder to employed material,
+ the mass ratio of conform (usable) atomized powder to atomized powder,
+ the mass ratio of usable atomized powder to employed material
+ the mass ratio of coarse to fine powder

are generally of interest, and were thus considered during prototype design (chapter 3) and experimentally evaluated (chapter 7).

2.7 Maintenance

Generally, maintenance effort should be kept as low as possible in order to guarantee high availability of the facility and to save manpower and working time. Therefore, the use of approved technologies and concepts as well as certified industrial components was preferred for the prototype design. In addition, it was paid attention that wear parts are accessible and removable (chapter 3).

2.8 Laboratory-Scale and Scalability

In the present work, lab-scale design refers to a prototype process that has limited production capacities and dimensions in contrast to a potential industrial facility (chapter 3). Lab-scale allows for gathering expertise with regard to industrial scale UMo production by means of centrifugal atomization, validation of the technical feasibility, and evaluation of the practical feasibility in a highly regulated nuclear environment within Europe. Also, this approach allows for reasonable risk management in terms of nuclear safety as well as development costs and time in case of technical or licensing failure. Finally, lab-scale also allows for quick changes in alloy composition or enrichment during fuel development as cleaning procedures are faster. In case of failure, dismantling of a lab-scale facility comes at lower costs.

Since the atomizer is meant to serve as a prototype for industrialisation of UMo production, the lab-scale design must allow scalability to increase production capacities while providing same results for same parameter sets. Generally, this may be achieved by larger system dimensions or by increasing the number of systems in operation. Whereas the latter is a question of infrastructure and automation level or available operating personnel, dimensional changes have impact on the atomization process, system architecture, and component choice. To keep both options open, a scalable atomization process was chosen (chapter 3.1). In addition, system components that were commercially available or that could be customised on larger scale for industrialisation were purchased and implemented (chapter 3.3).

2.9 Production Capacity

The atomizer prototype is meant to produce 1 % of the actual sighted industrial production capacity of $100\,\mathrm{kg\,year^{-1}}$ – that is $1\,\mathrm{kg\,year^{-1}}$. Thus, the prototype was dimensioned accordingly (chapter 3) and its performance verified (chapter 7).

2.10 Automation

Partial automation of certain atomizer functions may decrease maintenance effort, facilitate operation, enhance process control, and increase repeatability. Full automation, notably at prototype level, is not aimed at in order to keep costs and technological risk moderate (chapter 3). As a consequence, only prototype functions with direct influence on the atomization process were automated.

2.11 Differential Design

This design approach tries to decrease the number of functions executed by one component in contrast to integral design or function integration [Ponn and Lindemann 2008]. The primary advantage of this approach is the exchangeability of single components without (greater) impact on the overall design in case of malfunction or wear or conceptual change; it thereby accounts for prototype related uncertainties concerning component behaviour under operating load and conditions. It is also beneficial to limiting component complexity, thus rendering single parts more robust and decreasing technological risk, especially when developing a prototype. Therefore, atomizer systems executing main functions with respect to REP (chapter 3.1.3) were subdivided into multiple structurally and functionally independent as well as exchangeable system components (chapter 3.3).

A disadvantage of differential design is that the number of interfaces and component suppliers to manage is increased as – given a certain number of functions to execute – the amount of separate components rises.

3

Atomizer

This chapter presents the design of the atomizer prototype, which is based on the previously defined process and system requirements. First, the concept including the underlying atomization technique, the laboratory-scale approach, the system architecture, the general atomization process control, and the commissioning approach is described. Second, the atomizer infrastructure for hot operation is shown. The chapter concludes with a detailed presentation of all atomizer system components including their function, characteristics, specific features, and potential alternatives. Main intention of the following chapter is to provide a detailed understanding of the atomizer mode of operation as well as the implemented technical solutions in order to allow for reconstruction and further development.

3.1 Concept

3.1.1 Rotating Electrode Process (REP)

Based on earlier research on UMo fuel-powder fabrication methods stated in chapter 1.6, the rotating electrode process was chosen due to features that are summarised in the following paragraphs.

Principle

Atomization is the dispersion of a bulk liquid or metal melt into fine droplets. In centrifugal atomization, dispersion is achieved through centrifugal force while metal melting is subject to different technologies. The rotating electrode process (REP) is such a centrifugal atomization technique, which is based on the simultaneous rotation and melting of an ingot, the rotating electrode, and its subsequent atomization due to centrifugal force (Figure 3-1). In REP, rotating electrode melting is achieved by means of an electric arc, i.e. tungsten arc welding. A similar principle is used in the plasma rotating electrode process (PREP), where a transferred plasma arc is used for melting [Roberts and Loewenstein 1980]. Patents for REP were issued in 1963 and 1974 by Nuclear Materials, Inc. for a short and long bar design, respectively [Lawley 1992].

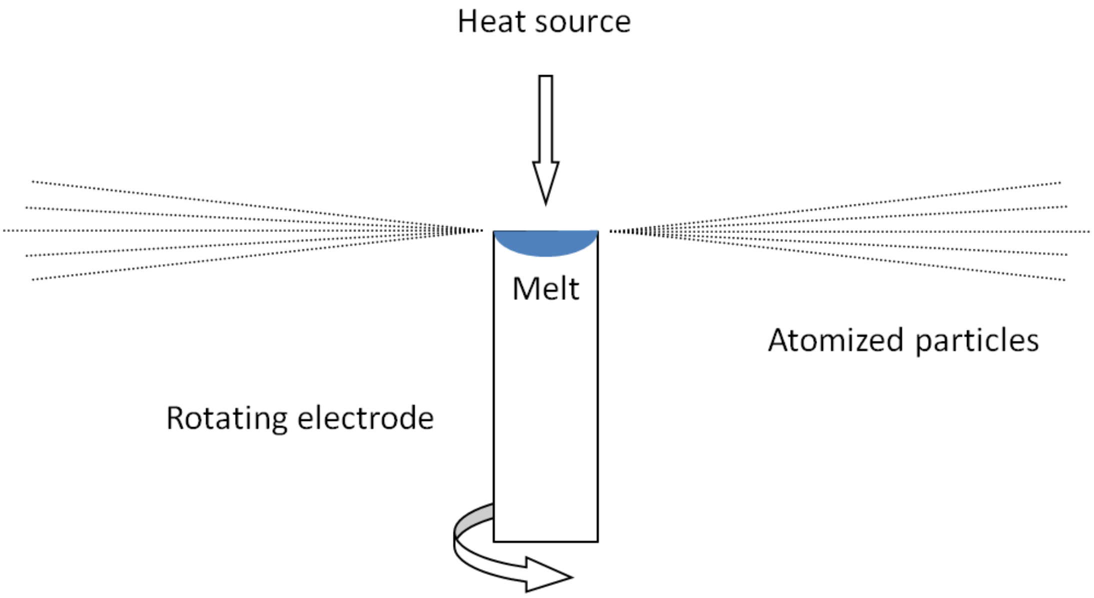

Figure 3-1 Physical principle of the rotating electrode process (REP) [Schenk *et al.* 2013].

Process Flexibility

Due to the use of an electric arc and its inherently high temperatures, a wide range of elemental metals and metal alloys may be melted. As the melt is not in contact with other materials, REP is independent from the metal's chemical reactivity or melting point. As a result, a large variety of elemental metals and metal alloys can be atomized – a beneficial feature offering flexibility in fuel development.

An additional advantage of REP is that it can be conducted with other melting technologies such as plasma arc (PREP), laser or electron beam. It may also be transformed into other centrifugal atomizing systems such as centrifugal shot casting, rotary electrode disc atomization, and the rotating disk or rapid spinning cup process – thus offering high flexibility.

Safety

Inert gas atmospheres used in REP are also important in terms of safety (chapters 2.1, 2.2), considering the chemical reactivity of uranium-molybdenum, in particular at molten state and in powder form.

As REP uses centrifugal force for atomization of the liquid melt, the use of moderating media such as water or oil as in liquid atomization is avoided. Also, the process does not necessitate critical amounts of uraniferous material to function. Therefore, REP reduces criticality concerns with respect to nuclear safety (chapter 2.1) and thus facilitates the licensing process.

Powder Quality

REP is generally conducted under inert atmosphere (e.g. argon, helium) which is detrimental in terms of product quality (chapter 2.4). Indeed, inert atmospheres may inhibit corrosion, particularly oxidation, of the chemically highly reactive UMo and thus reduce powder impurities [Lawley 1992]. In addition, inert atmospheres promote the production of spherical particles as oxygen is critical to particle spheroidisation since oxide layers may oppose surface tension [Lawley 1992]. A typical spheroidisation time in centrifugal atomization is $< 2 \cdot 10^{-5}\,s$ as reported for Sn particles with diameters from 149 to 420 µm [Lawley 1992].

Also, REP is used in high purity applications as the molten metal is not in contact with other materials, thus substantially reducing contamination of powder with impurities (chapter 2.4). In fact, REP may reproduce the ingot chemical composition [Lawley 1992].

REP-atomized particles have neither satellites nor shells and their surface is generally smooth. Depending on the atomization regime (chapter 6.1), REP-atomized particles can be entirely spherical in shape. They generally exhibit neither internal voids nor porosity. As a consequence, REP powders may reach the highest packing density [Lawley 1992] and thus fuel loading before and after fuel plate fabrication. Indeed, it was reported that fuel plates made from spherical UMo particles had lower void porosity than fuel plates from mechanically fabricated powders [Clark *et al.* 2007].

The particle size distribution is considered narrow and the standard deviation (SD) is typically smaller than for gas atomization [Lawley 1992, Lefebvre 1989, Yule and Dunkley 1994]. The particle mean size in REP can meet the particle diameter target ranges < 125 µm and < 40 µm of this work [Yule and Dunkley 1994].

In general, rapid solidification conditions prevail in REP, resulting in fine particle microstructures. Cooling rates in REP of $10^{2}\,K\,s^{-1}$ for a particle median diameter of 200 µm [Lawley 1992] and in centrifugal atomization of $10^{2}\,K\,s^{-1}$ to $10^{4}\,K\,s^{-1}$ [Yule and

Dunkley 1994] were stated. Rapid solidification also stabilises the high temperature γ-phase of UMo at room temperature [Clark *et al.* 2007, Kim *et al.* 1997b, Kim *et al.* 2007].

Modelling

Basic governing process phenomena of REP are well enough understood to allow for simplified modelling (chapter 2.5) – be it empiric models, be it physically derived models (chapters 5.1, 5.3.6, 6.1.4, 7.1.5). Even though existing models predict neither particle size distribution nor particle morphology nor atomization mass flow, they were reported to meet characteristic distribution parameters [Lawley 1992, Yule and Dunkley 1994].

Process Efficiency

It is stated that in REP at least 80 % of the rotating electrode is atomized to powder [Lawley 1992].

Lab-Scale and Scalability

The rotating electrode process (REP) offers process scalability (chapter 2.8). That is, the underlying physical models apply irrespective of machine dimensions and production capacities[4] amongst others. In addition, this feature allows for process evaluation and feasibility studies at lab scale, i.e. production of decreased powder quantities compared to industrial scale (chapter 2.8). REP also provides lab-scale in terms of machine dimensions as the collection chamber diameter is substantially smaller than in vacuum atomization. This is due to the increased cooling rate that is mainly determined by forced convection [Lawley 1992, Yule and Dunkley 1994] and thus the surrounding medium, e.g. argon or helium.

Disadvantages

Shortcomings of REP are its demand for high precision (e.g. machined) rotating electrodes and its limited amount of superheat [Lawley 1992]. In fact, rotating electrode imbalance may cause vibration that in turn may affect machine lifetime, safety, and process stability. Since in REP the material is instantaneously ejected as it is molten, atomization of alloys with a large melting range may not result in the desired particles properties [Lawley 1992].

At high arc currents, tungsten inclusions from the stationary tungsten electrode were reported [Eylon *et al.* 1980b, Roberts and Loewenstein 1980]. Also, it was reported that REP atomized powders show poor compressibility and green strength due to their spherical shape and intrinsic hardness [Lawley 1992], therefore potentially affecting fuel plate fabrication. That is, powder densification may necessitate processes such as hot extrusion or hot isostatic pressing [Lawley 1992].

---

[4] Both parameters can be connected but do not necessarily have to.

Technological Risk Management

From a development point of view, the use of REP increased the probability of success and decreased investment risks since proof of principle of UMo atomization by means of REP was already provided and showed promising results [Clark *et al.* 2007].

Although the rotating disk atomization process was industrialised by KAERI with respect to UMo fabrication, not all relevant operating parameters have been published yet. In addition, the reported batch size per run is 4 kg [Kim *et al.* 1997b] and the powder collection chamber has a diameter of 2.5 m [Kim *et al.* 2007]. Thus, this industrial process exceeds both the imposed nuclear safety limitations (chapter 2.1) as well as the demands for lab-scale (chapter 2.8). Scalability of this process as required for implementation at lab-scale has not been reported yet.

3.1.2 Laboratory-Scale Design

Production Capacity

The prototype atomizer is designed to handle around 40 g of U8Mo per atomization run. It thus fulfils the required annual prototype production capacity of 1 kg (chapter 2.9). The target mass of 40 g was adopted as starting point from the successful proof of principle by INL [Clark *et al.* 2007].

Dimensions

The containment (glovebox) dimensions (chapter 3.3.1) were so chosen as to provide full and direct accessibility to the prototype through gloves in order to facilitate operation, maintenance, potential component changes, and prototype extension. Accordingly, the dimensions of the prototype, in particular of the powder collection chamber, were adjusted to the glovebox.

Axis of Rotation

The axis of electrode rotation is vertically implemented as it was found to allow for easier operation at lab-scale [Clark *et al.* 2007]. In contrast, industrial REP designs generally favour horizontal arrangements [Champagne and Angers 1981, Lawley 1992].

3.1.3 System Architecture

For construction purposes such as dimensioning, (internal and external) component integration, fabrication, assembly, and documentation, the atomizing unit of the atomizer was designed and modelled by means of computer-aided design (CAD), Figure 3-2.

The atomizing unit was divided into several interacting systems that execute main functions with respect to REP (Figure 3-3). They are presented in the following paragraphs. As each system is composed of multiple components that execute specific functions following the differential design approach (chapter 2.11), all system components are presented and discussed in chapter 3.3.

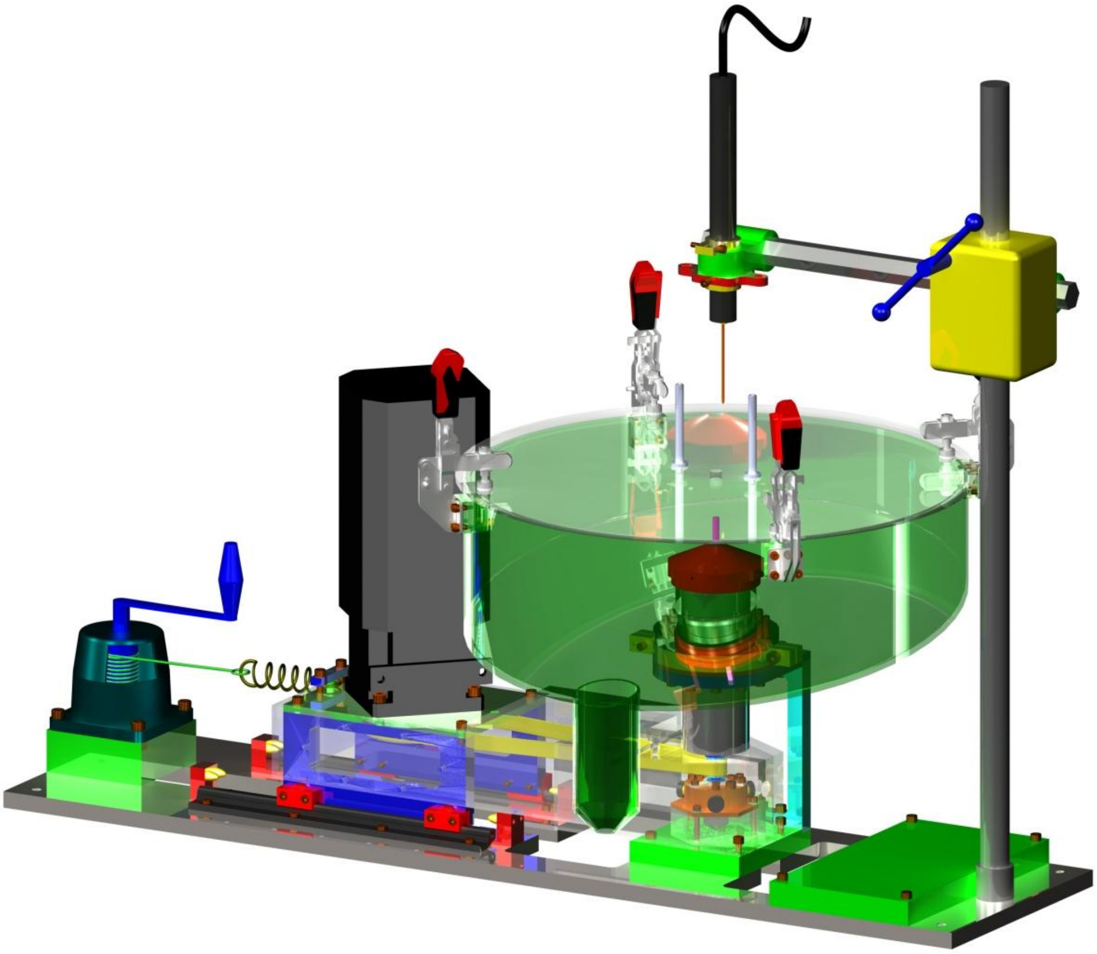

Figure 3-2 CAD model of the atomizing unit of the REP atomizer (the collection chamber is transparent).

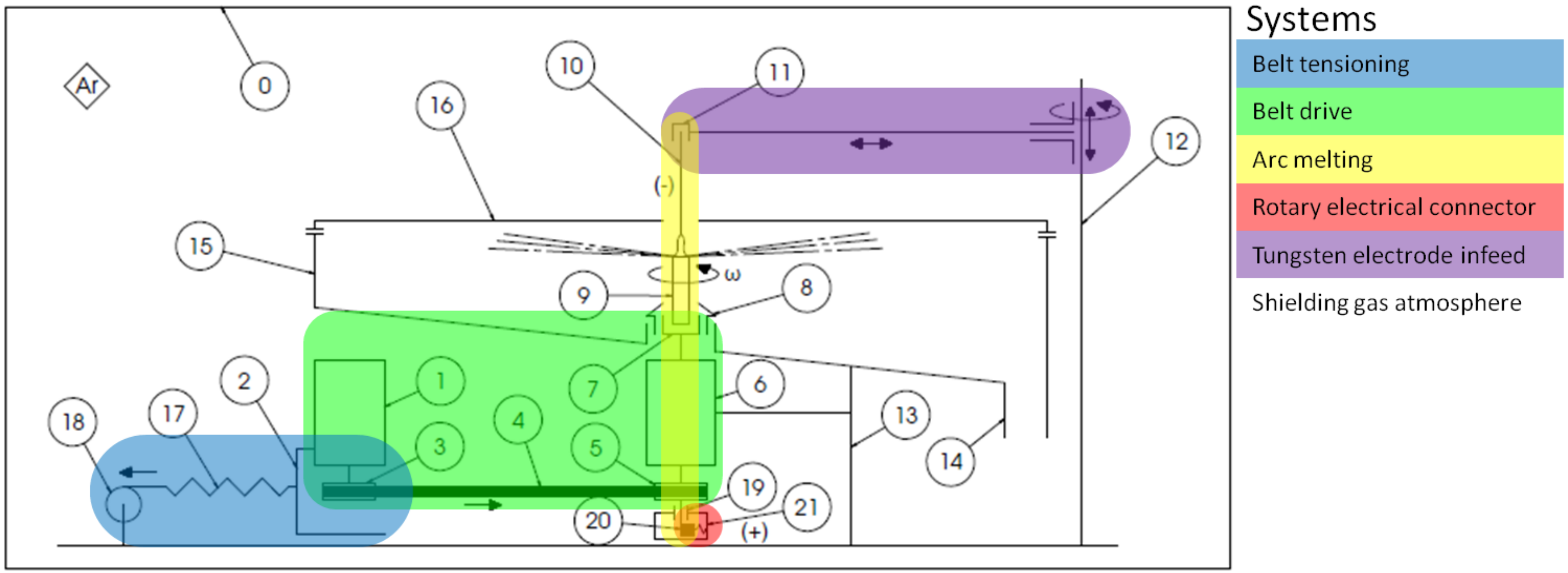
Ar
0
1
2
3
4
5
6
7
8
9
10
11
12
13
14
15
16
17
18
19
20
21
(-)
(+)
ω
Systems
🟦 Belt tensioning
🟩 Belt drive
🟨 Arc melting
🟥 Rotary electrical connector
🟪 Tungsten electrode infeed
Shielding gas atmosphere

System components: (0) containment under Argon, (1) motor, (2) motor carrier, (3) motor pulley, (4) belt, (5) spindle pulley, (6) spindle, (7) collet chuck, (8) powder seal screw, (9) rotating (U8Mo) electrode, (10) tungsten electrode, (11) welding torch, (12) drill rig, (13) framework with base plate, (14) collection chamber outlet, (15) collection chamber, (16) cover hood, (17) tension spring, (18) winch, (19) graphite dust seal, (20) carbon brush, and (21) collector ring.

Figure 3-3 Schematic of the prototype atomizer system architecture.

Shielding Gas System

This system contains the entire atomizing unit and protects the operator from potentially hazardous material (chapter 2.1) while protecting corrodible substances such as U8Mo from oxidation (chapter 2.4). It consists of an external shielding as well as regeneration gas supply, gas purifier (chapter 3.3.3), and glovebox (chapter 3.3.2).

The shielding gas atmosphere consists of high purity argon that is constantly reprocessed. Consequently, it is cleaned from oxygen and moisture.

Design point of the system is an oxygen as well as moisture level below 10 ppm, respectively, as well as operation under negative pressure (> 10 Pa, Table 2-2).

Belt-Drive System

The belt-drive system (Figure 3-3, green) is responsible for the rotation of the consumable (U8Mo) electrode (9). It consists of a variable-frequency drive (VFD, Figure 3-7), motor (1), motor and spindle pulley (3, 5), belt (4), and high frequency spindle (6) with collet chuck (7). The rotating electrode is carried by the high frequency spindle, which is powered by the motor through the belt. In turn, the motor and thus rotation speed is governed by the VFD. The VFD is situated outside the containment (0) and may be controlled by two operator interfaces: potentiometer or personal computer (Figure 3-7). It is connected to the spindle rotary sensor that monitors rotation speed. The sensor’s signal is displayed on the control panel for operator information as well (Figure 3-7).

Belt drive arrangements offer multiple advantages such as flexibility in motor and spindle combination as well as their arrangement, high and alterable mechanical advantage by changing motor or spindle pulley, elastic power transmission, no lubricants, high radial speeds, and noiseless operation [Wittel *et al.* 2009].

The VFD offers a variable rotational speed range as well as closed-loop control of the motor rotation. Thus, a wide range of particle sizes can be covered and constant atomization conditions promoted, respectively.

Design point of the system is a 40 g consumable electrode with 10 mm diameter rotating at 40’000 rpm ± 5’000 rpm. This parameter set yielded promising results with respect to powder quality (target size) and process efficiency [Clark *et al.* 2007].

Belt-Tensioning System

In support of the belt-drive system, the belt tensioning system (Figure 3-3, blue) provides belt pre-tension and assures belt fit throughout the entire speed range (Figure 3-3). The latter function is vital to a constant rotational speed as pre-tension is reduced with increasing speed due to centrifugal force. It consists of a winch (18), tension spring

(17), and motor carrier (2) sliding on linear hybrid bearings while interacting with the belt (4). Though using a tension spring and winch instead of a weight, it resembles the tension slide arrangement described in [Wittel *et al.* 2009].

Pre-tension is applied at standstill by retracting the wrench's wire rope whereupon the connected tension spring is stretched and its pull increased. The latter acts on the mobile carrier, dragging it towards the winch and thus increasing the centre axis distance between the two pulleys. As a consequence, the transmission belt is lengthened and thus tensioned until balance of forces with the tension spring is reached (Figure 3-4).

During operation, the belt gains speed. As a result, the initial balance of forces at standstill is disturbed. In fact, an arising centrifugal force compensates the initial belt pre-tension force. Accordingly, the tension spring is decreasingly opposed by the belt. As the difference in spring pull force and belt pull force exceeds the static friction of the motor carrier (chapter A7), the motor carrier is dragged towards the winch until a new balance of forces is reached (Figure 3-4). Conversely, as belt speed decreases, centrifugal force decreases as well, allowing the belt to relocate the motor carrier towards its initial standstill position.

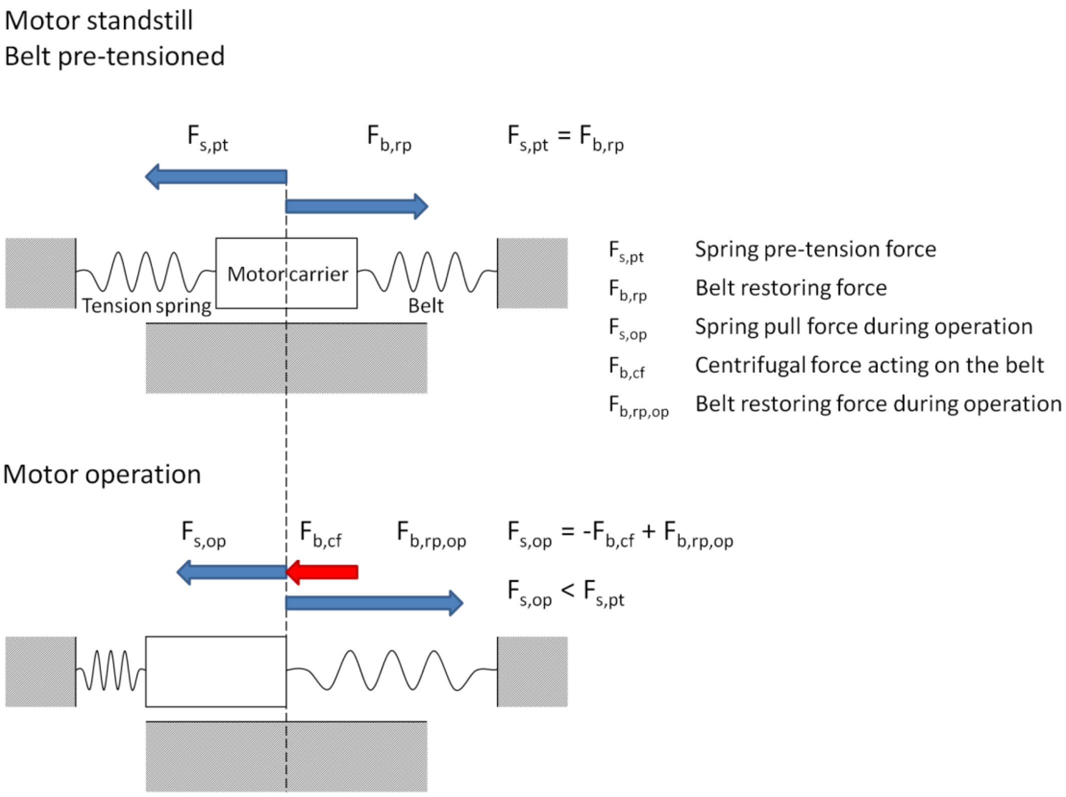
Motor standstill
Belt pre-tensioned
$F_{s,pt}$
$F_{b,rp}$
$F_{s,pt} = F_{b,rp}$
Motor carrier
Tension spring
Belt
$F_{s,pt}$ Spring pre-tension force
$F_{b,rp}$ Belt restoring force
$F_{s,op}$ Spring pull force during operation
$F_{b,cf}$ Centrifugal force acting on the belt
$F_{b,rp,op}$ Belt restoring force during operation
Motor operation
$F_{s,op}$
$F_{b,cf}$
$F_{b,rp,op}$
$F_{s,op} = -F_{b,cf} + F_{b,rp,op}$
$F_{s,op} < F_{s,pt}$

Figure 3-4 Schematic showing equilibrium conditions of the belt-tensioning system – at motor standstill and during atomizer operation.

In general, tension slide systems are self-adjusting, vibrationless, independent from load changes, and minimise slippage [Wittel *et al.* 2009]. In addition, the modified and implemented system is more compact and offers variable belt pre-tension (by more or less retracting the winch's wire rope) than the arrangement described in [Wittel *et al.* 2009].

Design point of the system is a radial speed of 40'000 rpm and belt speed of 65 $m\,s^{-1}$.

Arc-Melting System

The consumable is melted by means of an electric arc that is powered by an arc welder (Figure 3-7) and established between a static and the consumable rotating (U8Mo) electrode. The arc-melting system (Figure 3-3, yellow) consists of a welder, welding torch (11), tungsten electrode (10), rotating electrode (9), the shaft of the high frequency spindle module (6), and the rotary electrical connector (Figure 3-3, red).

The welding current is conducted through the welding torch and tungsten electrode as well as rotating consumable electrode, collet and collet chuck, spindle shaft, pulley, and finally shaft extension screw. The electric circuit is closed by the rotary electrical connector that is situated below the spindle pulley.

Electric arcs readily melt every (conducting) alloy [Matthes and Schneider 2012] and hence U8Mo as well. In addition, the arc-melting system provides contactless arc ignition and arc current feedback control.

Design point for this system is an electric arc current of 70 A with respect to the INL proof of principle [Clark *et al.* 2007].

Tungsten Electrode Infeed System

The tungsten electrode infeed system (Figure 3-3, purple) allows for a follow-up movement of the tungsten electrode, since the rotating (U8Mo) electrode is consumed during atomization and subsequently loses its initial length. Thereby, a breakdown of the electric arc due to an excessive electric arc length is avoided. Besides the follow-up movement, initial positioning of the tungsten electrode for both centrical melting and contactless ignition are additional functions. It consists of a drill rig with cantilever (12), drill and torch adapter, linear guide rails, and slide with linear bearings.

The infeed is situated on the collection-chamber cover-hood (16) in order to decrease the cover hood's mass and thus facilitate its manual handling. The guided path of the infeed allows for both full compensation of the loss in rotating electrode length due to atomization and some flexibility in rotating electrode length.

Rotary Electrical Connector

The rotary electrical connector (Figure 3-3, red) provides transmission of the electrical current between the rotating spindle shaft (and thus rotating electrode) and the stationary welding machine. It consists of brass pipes that contain carbon brushes (20), a brass collector ring (21), an aramid/NBR seal (19), seal holder, screw insulation, and insulator with retention depot.

Three brushes are arranged radially around the spindle-shaft extension-screw and mounted on a conductive and stationary collector ring that is connected to the electrical circuit of the welding machine. Below the collector ring, the depot for metallic graphite powder retention is placed.

Slip ring arrangements were favoured because of their capacity to withstand both relatively high current densities and radial speeds. However, extensive brush wear due to high purity inert atmospheres [Hayward 1990, Slawecki *et al.* 1966] causes the brushes to lose shaft-connection and atmospheric pollution by sublimated brush particles. This is accounted for by self-adjustment of the brushes and a combined sealing and retention system, respectively.

Design point is a rotation speed and electric arc current of 40.000 rpm and 70 A, respectively.

Powder Collection

The atomized (U8Mo) powder is collected in a closed chamber made of steel and polycarbonate. Besides powder collection, the chamber protects against accidentally ejected rotating electrodes and powder dissemination within the glovebox.

Design point of the powder collection chamber is a diameter of 600 mm as particle adhesion to the chamber walls was reported for a collection chamber diameter of 300 mm [Clark *et al.* 2010]. Also, glovebox dimensions were taken into account.

Framework

All systems are carried through and merged in the atomizer framework. The framework is mounted to the glovebox structure to ensure stable atomizer operation. All connections between the system components and framework are detachable as they were made with screws.

3.1.4 Process Control

Main process parameters in REP may be divided into two categories: operating and material parameters. They control particle shape (chapter 6), particle size distribution and mean particle size (chapter 7), and particle oxidation (chapter 8). Operating parameters consist of rotational speed, volume flow rate (electric arc power), rotating electrode diameter, and atmosphere. Material parameters consist of dynamic viscosity, liquid density, surface tension, and enthalpy of melt (Table 6-2).

While material parameters were determined by the target materials, i.e. U8Mo and U7Mo, the atomizer is so designed as to allow for automatic control of the operating parameters in order to promote constant atomization conditions.

The Rotational speed may be set before each atomization run via an operator interface (chapter 3.3.19). In order to keep the parameter constant, it is monitored and closed-loop-controlled. For operator information and verification, the speed of the rotating electrode is displayed.

The volume flow rate is indirectly controlled through the electric arc current. An interface enables the operator to set the value of the electric arc current before each atomization run. The electric arc voltage is automatically controlled (chapter 3.3.6).

Different rotating electrode diameters may be used for atomization (chapter 3.3.13). The shape and diameter of the rotating electrode is determined during casting.

The atomization atmosphere, however, is fixed. That is, the gas purifier system inherently operates at full capacity, thus extracting the maximum possible amount of oxygen and moisture. Corrosive impurities such as oxygen and moisture are monitored and displayed for operator information.

For atomization, the atomizing unit is brought to the nominal rotational speed. At full rotational speed, the electric arc is ignited. During atomization, the electric arc length is maintained manually. The electric arc is extinguished prior to full atomization of the consumable rotating electrode for protection of the collet chuck.

3.1.5 Commissioning

Commissioning of the atomizer prototype was divided into two phases: cold and hot. Cold commissioning (Figure 3-5) was conducted with non-radioactive and non-fissile surrogate material and outside the hot zone. As U8Mo surrogate 1.4301 stainless steel was used due to its availability, market price, partially similar material properties (chapter 6.3.2), and workability in terms of rotating electrode fabrication. The cold commissioning phase aimed at verifying operations readiness of the REP prototype atomizer before machine contamination with radioactive material [Schenk *et al.* 2013]. This approach guaranteed free access to the prototype in case of constructional modifications and exchange of system components. Also, procedures to pass material and tools into or out from the hot zone were avoided and radioactive waste reduced.

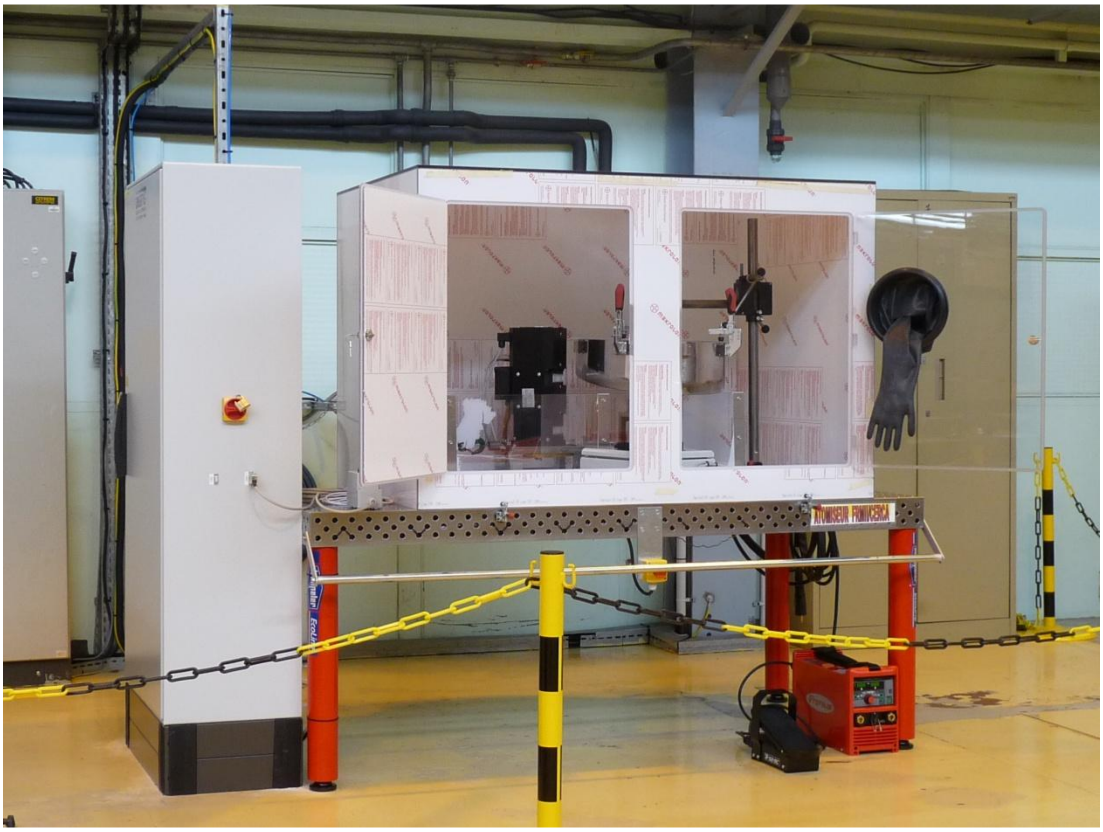

Figure 3-5 Atomizer installation during cold commissioning.

Hot commissioning was conducted with the target material, i.e. U8Mo. For this purpose, the prototype was moved to the dedicated uranium laboratory.

3.2 Infrastructure for Hot Operation

Hot atomizer operation (Figure 3-6) required an infrastructure that exceeds the presented atomizing unit and cold commission installation. In fact, a uranium laboratory was reconstructed for and fully dedicated to the atomizer project. In addition, a shielding inert gas glovebox was customised in order to house the atomizing unit and particle analysis equipment. The planning and construction works included adjustment of power as well as gas supply, re-dimensioning of the laboratory exhaust ventilation, and nuclear safety analysis – all performed in co-operation with AREVA CERCA.

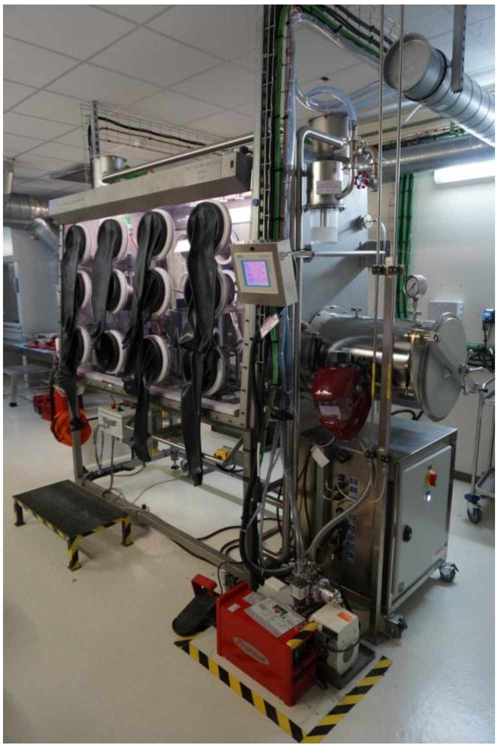

Figure 3-6 Atomizer infrastructure during hot operation in the UMo laboratory.

In support of these works, an installation plan of the entire atomizer (Figure 3-7) was elaborated accounting not only for the atomizing unit itself, but also for the entire auxiliary atomizer process equipment. The auxiliary equipment includes the inert gas glovebox, gas purifier, vacuum pump, sieving machine, scales, pressure as well as oxygen sensors and alarms, switch cabinets, operator interfaces, arc welder, lighting, glovebox feed-throughs, vacuum locks and filters. Moreover, necessitated power supply, shielding as well as regeneration gas supply, and exhaust ventilation are part of the infrastructure.

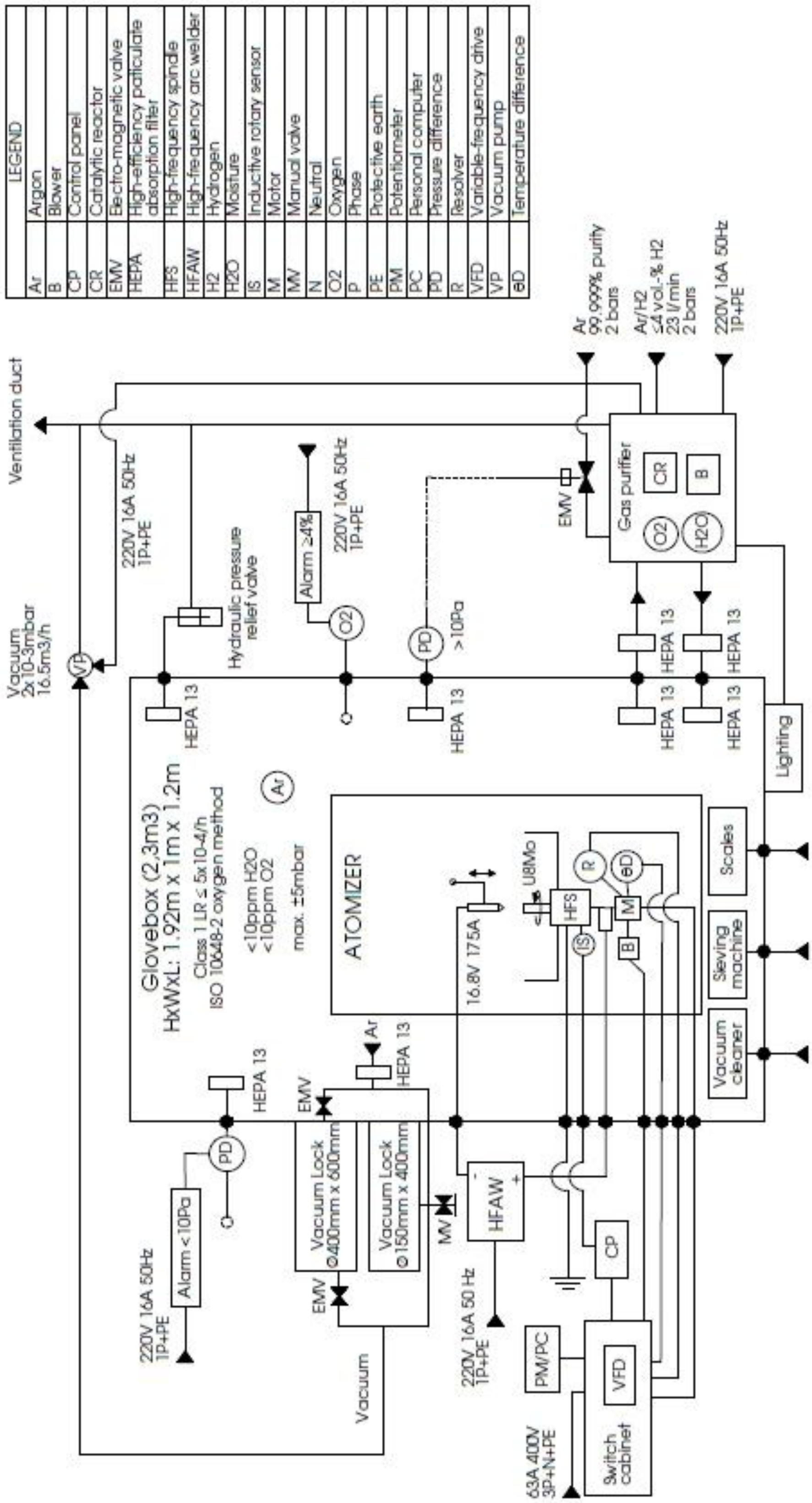
LEGEND
Ar Argon
B Blower
CP Control panel
CR Catalytic reactor
EMV Electro-magnetic valve
HEPA High-efficiency particulate absorption filter
HFS High-frequency spindle
HFAW High-frequency arc welder
H2 Hydrogen
H2O Moisture
IS Inductive rotary sensor
M Motor
MV Manual valve
N Neutral
O2 Oxygen
P Phase
PE Protective earth
PM Potentiometer
PC Personal computer
PD Pressure difference
R Resolver
VFD Variable-frequency drive
VP Vacuum pump
ϑD Temperature difference
Ventilation duct
Vacuum 2x10-3mbar 16.5m3/h
VP
220V 16A 50Hz 1P+PE
Hydraulic pressure relief valve
Alarm ≥4%
O2
PD
>10Pa
EMV
Gas purifier
CR
B
O2
H2O
Ar 99,999% purity 2 bars
Ar/H2 ≤4 vol.-% H2 23 l/min 2 bars
HEPA 13
Glovebox (2,3m3)
HxWxL: 1.92m x 1m x 1.2m
Class 1 LR ≤ 5x10-4/h ISO 10648-2 oxygen method
<10ppm H2O <10ppm O2
max. ±5mbar
Ar
ATOMIZER
16.8V 175A
U8Mo
HFS
IS
R
M
ϑD
B
Lighting
Scales
Sieving machine
Vacuum cleaner
Vacuum Lock ⌀400mm x 600mm
Vacuum Lock ⌀150mm x 400mm
MV
HFAW
CP
PM/PC
VFD
Switch cabinet
63A 400V 3P+N+PE
220V 16A 50 Hz 1P+PE
Alarm <10Pa
Vacuum

Figure 3-7 Installation schematic of the atomizer facility for hot operation including the atomizing unit, auxiliary equipment, supply requirements, and interfaces.

3.3 System Components

3.3.1 Make or Buy

Figure 3-8 shows the components of the atomizing unit. The entire atomizer consists of additional components (Figure 3-7). All components were either (i) commercially available or (ii) customised to system requirements or (iii) in-house designed, dimensioned, and constructed. The atomizer components are listed in the following paragraphs with respect to the three categories.

Commercially available and directly purchased components include quick release clamps (Figure 3-8, 5), arc welder, welding torch (15) and control pedal, static tungsten electrode (21), drill rig (20) including cantilever (18) and drill adapter (17)), winch (28), tension spring (29), linear guide rails (30) and hybrid bearings (32), carbon brushes (24) in brass pipes (25), screw insulation (26), bump stops (33), sieving machine, weighing scales as well as 220 V, gas, and data feed-throughs.

Customised[5] components involve VFD, motor (6), switch cabinet, potentiometer, control panel including display, motor pulley (7), glovebox, gas purifier, belt (8), high frequency spindle (11, including collet and collet chuck (10), inductive sensor, bearings, lubrication, pulley (13), and shaft extension screw (14)), and power feed-throughs (arc welder, motor).

In-house designed, dimensioned and constructed components[6] include infeed linear guide rails (1) and linear slider (19), cover hood (2), powder collection chamber (4), powder seal screw (3), spindle clamps and spacer (12), torch adapter (16), graphite dust seal (22) and its holder (23), brass collector (25), motor carrier (31), atomizer framework (34), and belt-drive protection cover (35).

---

[5] Customised components were in-house dimensioned, though designed on demand and adapted or entirely new built by sub-contractors.

[6] The fabrication of these components was partially subcontracted depending on component complexity and in-house know-how.

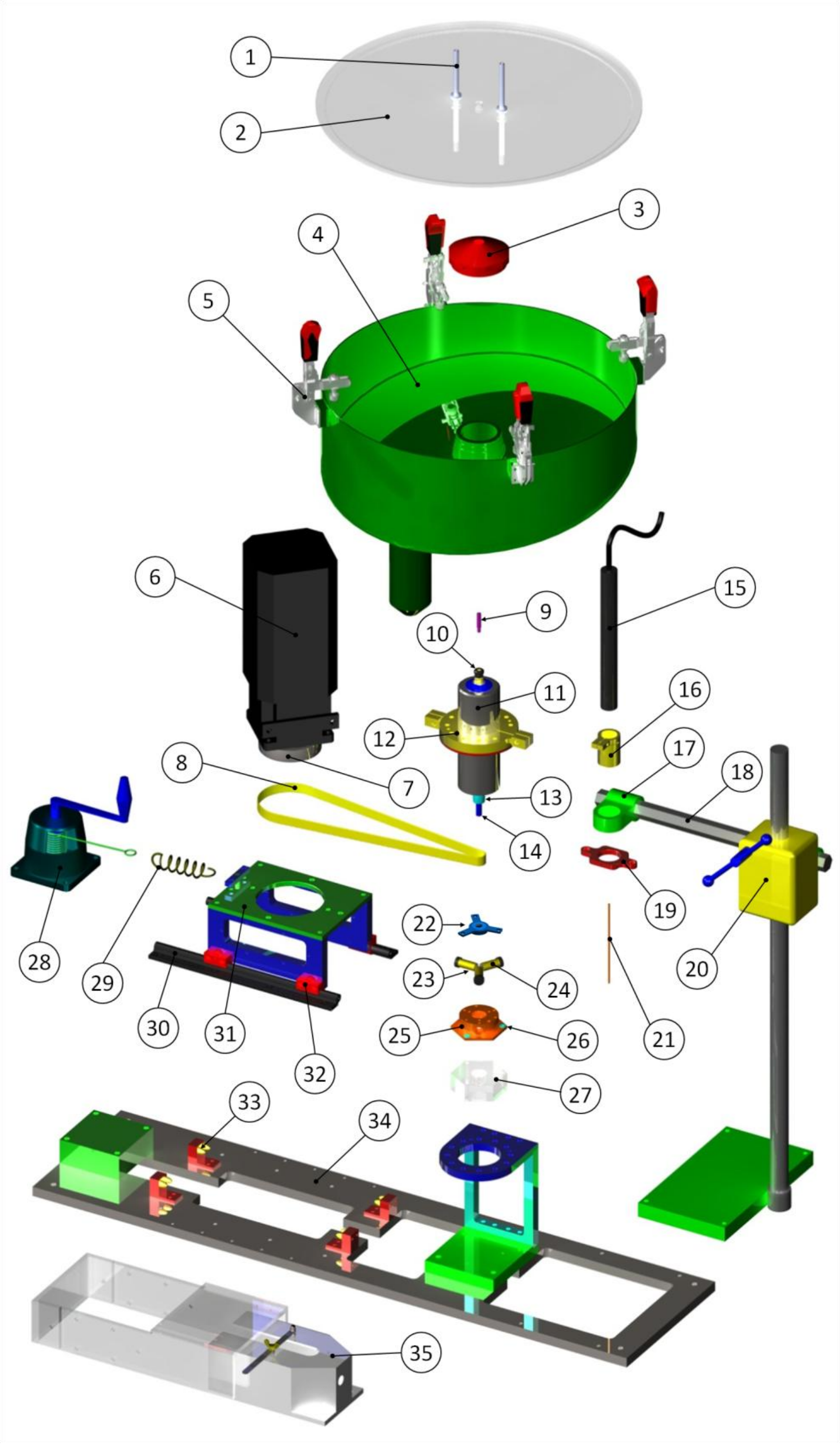

Figure 3-8 Exploded CAD model of the atomizing unit consisting of (1) infeed linear guide rails, (2) cover hood, (3) powder seal screw, (4) powder collection chamber, (5) quick release clamps, (6) motor, (7) motor pulley, (8) belt, (9) rotating (U8Mo) electrode, (10) collet and collet chuck, (11) high frequency spindle, (12) spindle clamps and spacer, (13) spindle pulley, (14) shaft extension screw, (15) welding torch, (16) torch adapter, (17) drill adapter, (18) cantilever, (19) linear slider, (20) drill rig, (21) static (tungsten) electrode, (22) graphite dust seal, (23) carbon brushes, (24) brass pipes, (25) brass collector ring, (26) screw insulation, (27) insulator with retention depot, (28) winch with handle bar, (29) tension spring, (30) linear guide rails, (31) motor carrier, (32) hybrid bearings, (33) bump stop, (34) atomizer framework, and (35) belt-drive protection cover.

3.3.2 Glovebox

Function

The shielding gas glovebox (Figure 3-9 and Figure 3-10) contains the atomizer, sieving machine, scales, as well as radioactive and fissile material, e.g. U8Mo. It is a sealed containment under inert gas atmosphere and therefore prevents the uraniferous material from any reaction with air, notably oxygen. Moreover, the glovebox constitutes a protection barrier against dissemination of and contamination with radioactive material. As a side effect, the glovebox constitutes a barrier against the danger of asphyxia related to the presence of a considerable amount (~ $2.5\,\mathrm{m}^3$) of Ar in the laboratory. It also serves as protective earth for the atomizing unit.

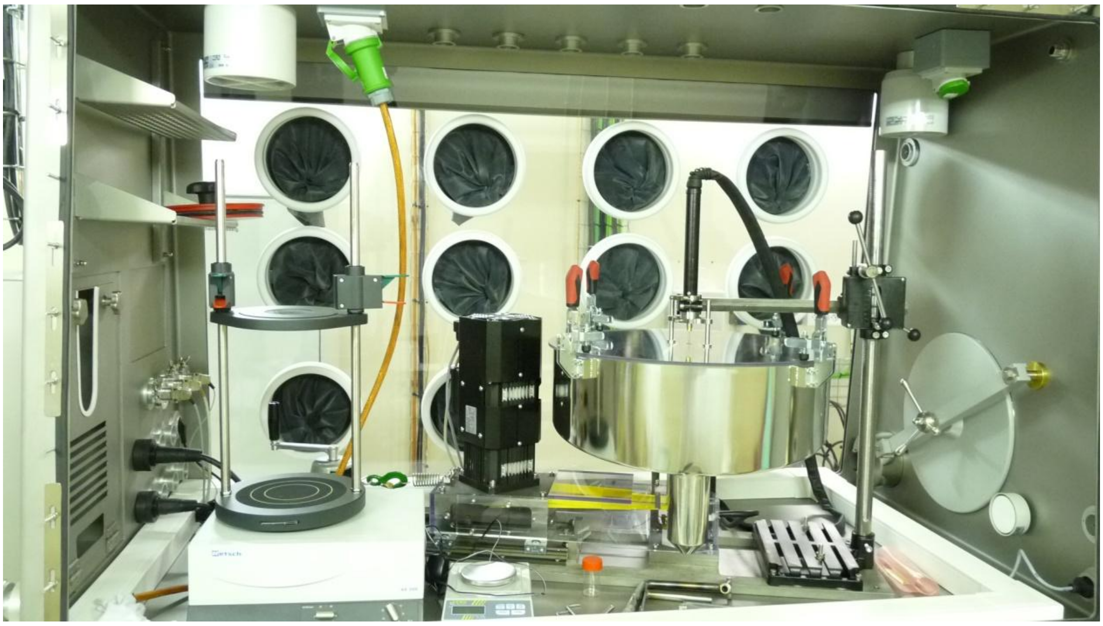

Figure 3-9 Inside view of the atomizer glovebox before hot commissioning, showing the atomizing unit, sieving machine for powder granulometry, and weighing scales.

Characteristics

Its framework is built up of stainless steel bars while the box itself is composed of stainless steel plates and two polycarbonate windows. It is equipped with two vacuum locks, an operator interface with display, multiple HEPA H13 (high-efficiency particulate absorption) filters, external electric lighting, two deposition racks, a vacuum pump, two ISO three-phase current plugs, two one-phase welding plugs, several 220 V plugs, multiple ISO KF 40 vacuum flanges. In addition, it is connected to an additional gas treatment system (gas purifier) (chapter 3.3.3).

Box, piping, and gas purifier reach a total leak-tightness or leak-rate of $T_f \leq 5 \cdot 10^{-4}\,\mathrm{h}^{-1}$ making it a class 1 containment certified to ISO 10648-2 (oxygen method).

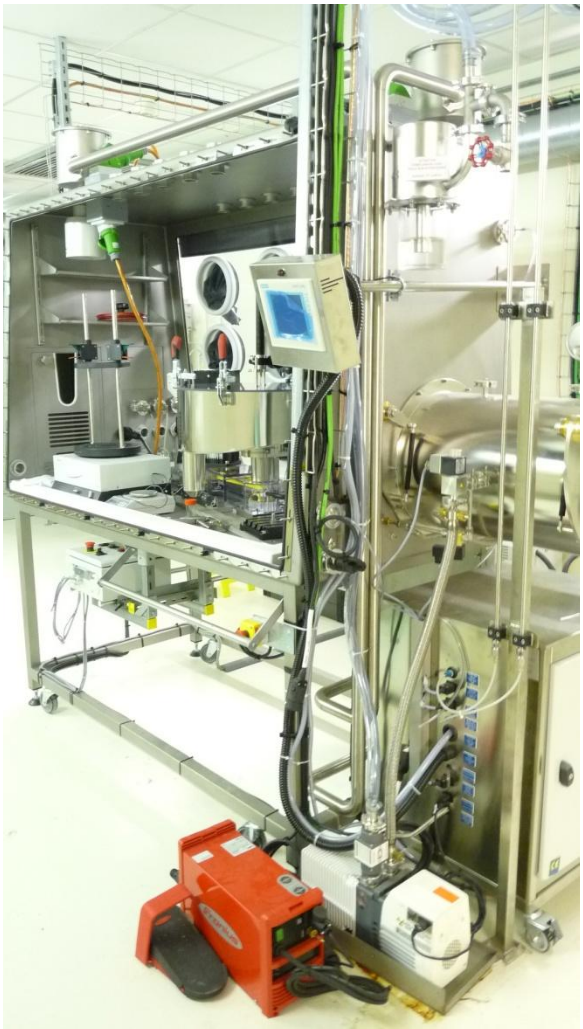

Figure 3-10 Outside view of the atomizer glovebox in the UMo laboratory before hot commissioning [Schenk *et al.* 2014].

Box

Stainless steel plates of 3 mm thickness cover the bottom, top, and short faces of the trapezoid box structure as this material has favourable mechanical properties. However, given the approximate atomizer weight of about 60 kg, the bottom plate is reinforced with steel bars increasing the structural integrity up to 200 kg[7] load. Moreover, screws are so welded to the bottom plate as to provide a fitting for the atomizer bottom plate. This fixation attenuates motor induced vibrations and prevents relocation of the atomizer during operation.

The long glovebox sides, though, are each covered with a window made of transparent polycarbonate (Figure 3-9). The transparency allows for visual control of the rotating electrode mounting, atomization, sieving, and weighing, while protection is provided due to the impact resistance of polycarbonate ["Makrolon® AR" 2014] – in contrast to poly(methyl methacrylate) (PMMA or Plexiglas).

---

[7] Regardless of the rated load, attention must be paid that the load is distributed over the entire bottom plate and thus reinforcement bars.

It measures 1.92 m in height, 1.2 m in length, and 1 m in depth, offering a total volume of around 2.3 m^3. The offered space, though, is intentionally only half-occupied by the present equipment to leave room for future changes to the prototype. The depth was so chosen as to enable the operator to directly reach the glovebox centre line – and hence every point within the glovebox – without auxiliary tools. In order to account for different operator heights and to foster an upright working position, the bottom height of the glovebox was chosen on an average men size (172 cm) and the windows are inclined.

Edges and corners resulting from cover plate junctions are rounded off to prevent retention of fissile and radioactive material.

Two stainless steel shelves are installed on the opposite side of the vacuum locks for storage of wear and spare parts, tools as well as U8Mo electrodes and powder (Figure 3-9). Mesh bottoms account for retention risks of nuclear material.

Vacuum Locks

Material is transferred in or out of the glovebox through two (vacuum) transfer locks made from stainless steel (Figure 3-11). Thereby, exposure of the inert atmosphere to air is avoided. Both vacuum locks are placed outside the glovebox in order to dedicate the entire glovebox space to the atomization process and powder analysis equipment.

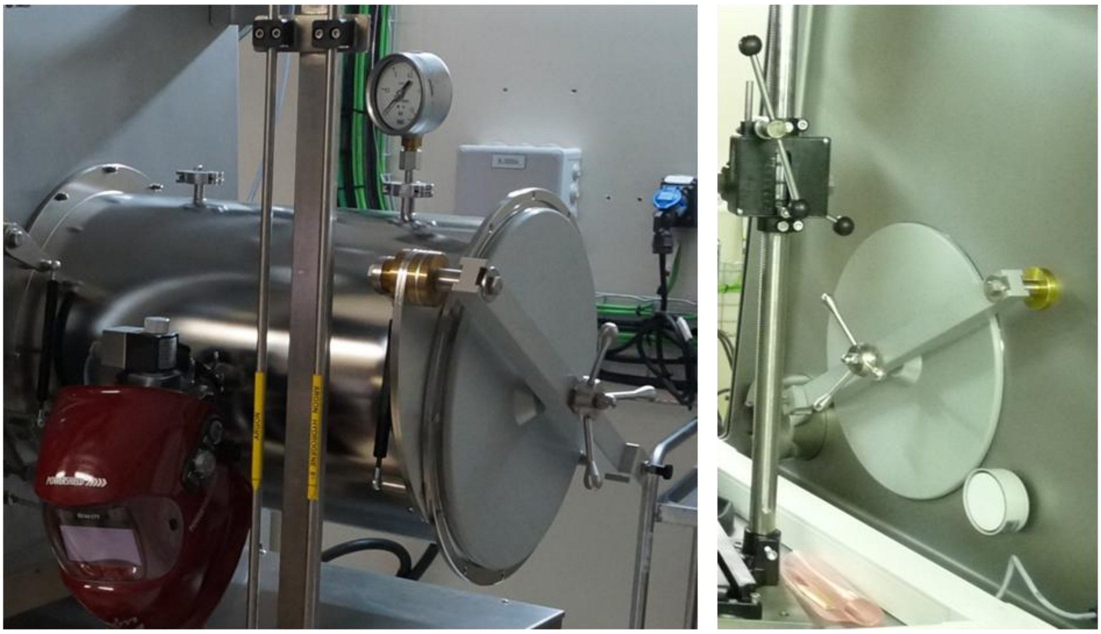

Figure 3-11 Inside and outside view of the large vacuum lock (the small vacuum lock is visible on the right picture, though partially hidden behind the drill rig).

The small one – 150 mm in diameter and 400 mm in length (volume: ~ 0.008 m^3) – can only be operated manually and is used for transfers of wear and spare parts, tools, and fissile material.

The large one – 400 mm in diameter and 600 mm in length (volume: ~ 0.075 m^3) – may be operated manually or automatically. Yet, it is only intended for degassing storage under vacuum and major equipment changes. This is due to its ninefold volume that is a matter of operation costs when taking into account that vacuum pumping and purging consumes energy and Ar.

Vacuum is generated through a vacuum pump, while filtered purging gas comes directly from the glovebox interior.

In order to keep the glovebox atmosphere clean and avoid dissemination, vacuum locks have to be evacuated and purged minimum three times before transfer of material. In addition, both vacuum locks have to be kept under vacuum off operation hours to avoid unintended opening.

Gloves

Accessibility of the atomizer is provided by 24 gloves, 12 per window side (Figure 1-4 and Figure 3-9). Each window is divided into 3 lines – bottom, middle, and top – containing 4 gloves and hence providing access to the whole glovebox. Although compromising the atmosphere due to an increased leak rate, this vast amount of gloves was considered particularly vital for a prototype installation regarding accessibility and manoeuvring.

On grounds of their relatively low permeability to moisture and gases, butyl-based gloves are implemented. Material thicknesses typically vary between 0.4 mm, 0.6 mm, and 0.8 mm, the latter size being more resistant than the former. However, a glove thickness of 0.4 mm was chosen to facilitate work with finger-sized objects and tools.

Glove fittings have a diameter of 215 mm and offer increased arm-mobility in contrast to smaller fittings. A dozen of removable (non-transparent) fitting covers are used to protect gloves and improve glovebox atmosphere. However, fixed transparent fitting covers – while improving the leak-rate as well – would also improve lighting.

Lighting

Two external electric lightings placed on both working window sides in the upper glovebox section provide additional lighting as the vast amount of (non-transparent) gloves dims laboratory light (Figure 1-4).

Vacuum Pump

A rotary vane pump (Figure 3-12) provides a pumping rate and ultimate pressure of $16.5\,m^3 h^{-1}$ and $< 2\cdot10^{-3}$ mbar, respectively. It is primarily used for vacuum lock pumping, but may also be used for reactor regeneration.

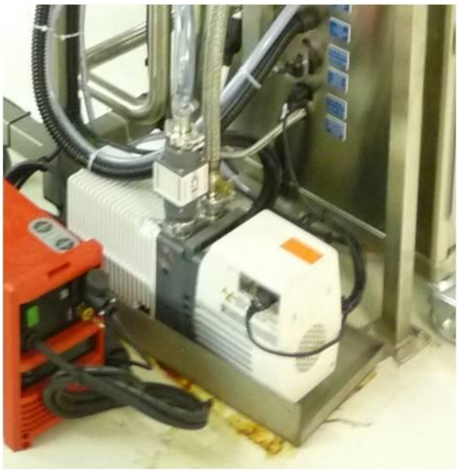

Figure 3-12 Rotary vane vacuum pump of the atomizer glovebox.

Pressure Relief Valve

Glovebox gauge[8] pressure is limited to ± 500 Pa or ± 5 mbar to guarantee its structural integrity; the official operating limit is 3 mbar, though. A passive and hydraulic[9] pressure relief valve (Figure 3-13) protects the glovebox from excessive positive (gauge) pressure in an accidental case.

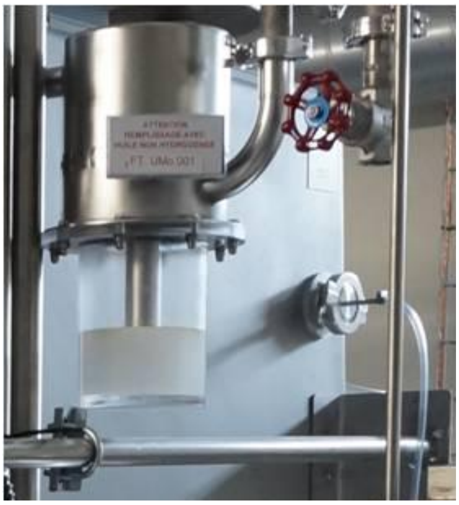

Figure 3-13 Passive pressure relief valve to protect the glovebox from excessive positive pressure.

---

[8] Gauge pressure is referenced against ambient atmospheric pressure.

[9] The pressure relief valve uses dehydrated oil according to site regulations.

For safety reasons, a positive gauge pressure of > 200 Pa triggers the valve and enables excess inert gas extraction through the exhaust ventilation. Regardless of its safety function, the pressure relief valve may also be used for inert gas purging of the glovebox.

Filters

Filtration of inlet and exhaust gas prior to ventilation decreases the risk of external dissemination of and contamination with radioactive material. For this purpose, high-efficiency particulate absorption (HEPA) filters are installed at every gas in- or outlet of the glovebox, thereby also accounting for accidental gas backflow (Figure 3-14). The installed H13 filters have an efficiency or total retention of > 99.95 % for the most penetrating particle size of 0.3 μm.

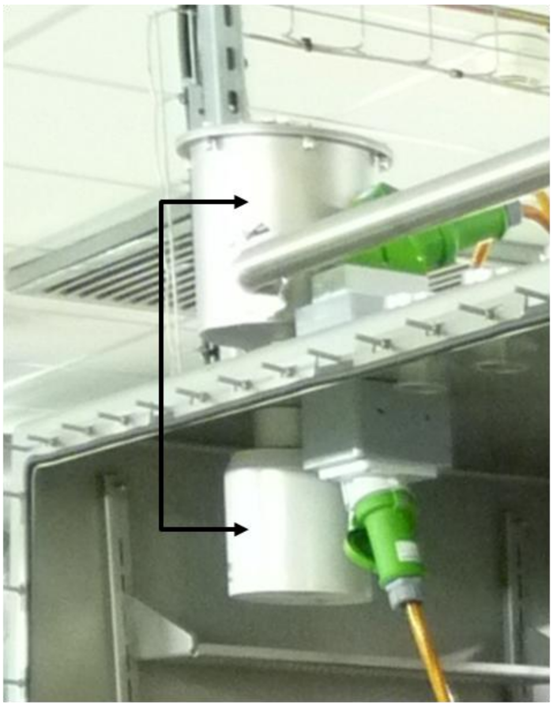

Figure 3-14 Example of HEPA filters installed for argon double-filtration inside and outside the atomizer glovebox.

Feed-Throughs

Over 20 feed-throughs – for gas, vacuum, data, or electricity – are distributed all over the glovebox ensure gas purifier, sensor and atomizer supply. Apart from those of the motor (Figure 3-14, green sockets), welding machine (Figure 3-15, black sockets), and filters, all feed-throughs – custom or standard – can be mounted on standard ISO vacuum KF 40 double-sided flange fittings[10] (Figure 3-15). These fittings have several advantages: While the flange is welded to the glovebox, feed-throughs are not permanently fixed and thus removable. This feature offers flexibility with respect to the prototype facility as removable fittings allow for transposition or substitution of feed-throughs. Although removable, these fittings are designed for applications in vacuum ranges of $\geq 10^{-8}$ Torr ($\approx 1.33 \cdot 10^{-8}$ mbar). Feed-through mounting is simple, quick, and no tools are needed since only a clamp and an elastomeric o-ring are used for fixation. The double-sided configuration allows for feed-through connection inside or outside the glovebox. Procurement costs are decreased since multiple standard KF feed-throughs are already commercially available.

---

[10] ISO standard Klein Flange (KF) with an inner diameter of 40 mm.

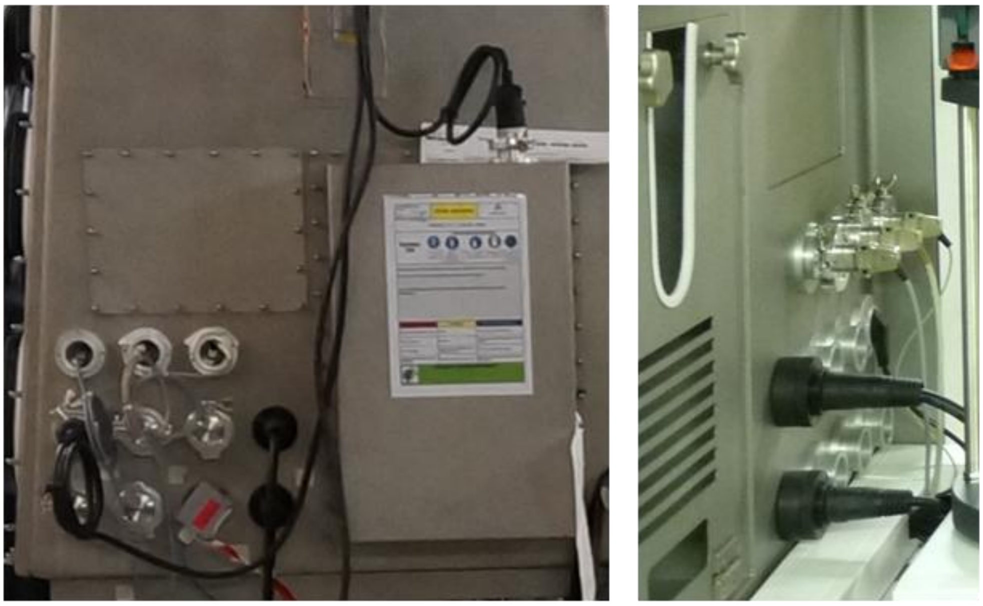

Figure 3-15 Exemplary KF40 flange fittings and feed-throughs at the atomizer glovebox backside.

Safety Sensor

Both UMo and metallic uranium is considered flammable if exposed to oxygen, in particular in powder form. Thus, oxygen content of the glovebox atmosphere is monitored through an oxygen sensor. It is mounted on the upper part of the glovebox in order to avoid underestimation of the oxygen content in case of blower standstill. In this very case, gas purification is ineffective, glovebox atmosphere static and oxygen may accumulate at the top as Ar has a higher density than both air and oxygen.

Sensor resolution is 0.1 % while the allowed oxygen level (within the glovebox) for fire prevention is less than 4 % according to Table 2-1. If this threshold is exceeded, the operator is warned by an audible alarm and must immediately shut down all machines as well as interrupt his work within the glovebox [Cadoret 2013].

3.3.3 Gas Purifier

Function

An additional gas treatment system continuously reprocesses the Ar within the glovebox and thus reduces Ar consumption (Figure 3-16). In addition, the gas purifier comes with integrated functions such as pressure control of the glovebox, automatic glovebox purging, pump and purge control of the large vacuum lock, oxygen and moisture monitoring, and electronic operator interface (touch screen).

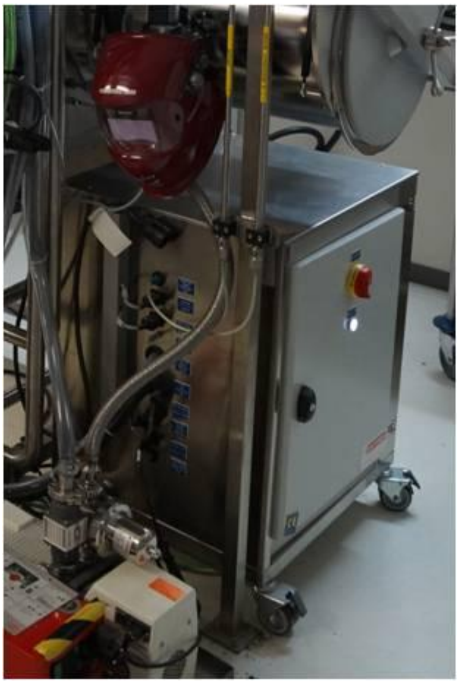

Figure 3-16 Gas purifier for glovebox atmosphere control and reprocessing.

Characteristics

The combination of a glove-box leak-rate of $10^{-4}\,h^{-1}$, an Ar supply with 10 ppm total impurities, and an additional gas purifier, provides in practice constant Ar atmospheres of less than 7 ppm of O_2 and H_2O, respectively. According to [Hodkin *et al.* 1973], this value provided sufficient protection from oxidation of reactive materials like titanium (Ti) and should therefore be a good orientation for the atomization of U8Mo powder.

Oxidation in particular changes material properties of UMo alloys and exposure must therefore be avoided. In particular, as the oxide layer is brittle [Wilkinson 1962a]. Also, oxygen was reported to have influence on spheroidisation during atomization [Lawley 1992, Plookphol *et al.* 2011].

The gas purifier is equipped with an integrated switch cabinet (one-phase, 230 V), a blower, an oxygen as well as moisture sensor, a control panel with touch screen, and a reactor.

As there is an inherent leakage of air into the glovebox, an accumulation of nitrogen occurs over time since it is not removed by the purifier like oxygen and moisture. Therefore, the glovebox must be entirely purged with argon from time to time to avoid excessive concentrations of nitrogen.

Reactor

The Ar is reprocessed in a reactor that consists of a copper-based catalytic converter and a molecular sieve to remove oxygen and moisture, respectively. While the installed molecular sieve adsorbs water molecules, oxygen is extracted from Ar through reduction by metallic copper which in turn is oxidised to copper(II) oxide.

The cleaning capacity of the reactor is 301 and 1440 g for O_2 and H_2O, respectively. Depending on the installation configuration and use, the reactor needed to be regenerated every two to three months due to saturation[11]. For this purpose, the reactor has to be disconnected[12] from the glovebox, heated to 250 °C, and subsequently exposed to a flow of hydrogen-enriched Ar (regeneration gas). Thereby, water present in molecular sieves is evaporated, then mixed with the (dry) regeneration gas flow and vented to the laboratory exhaust. Also, elevated temperatures promote the reduction of copper(II) oxide by hydrogen to metallic copper. This reaction requires typically 2-5 % hydrogen (H_2). The product of this reaction – H_2O – is likewise evaporated and vented. In summary, all extracted water (moisture) is vented and thus no concern to criticality. Typically, regeneration required shutdown of the atomizer installation for approximately one day (16 h).

Since hydrogen may form an inflammable and explosive mixture with oxygen between 4 % and 95 % hydrogen by volume [Marchand 2012], hydrogen enrichment of the regeneration gas is limited to $\leq$ 4 %.

Pressure Control

The glovebox may be operated under positive or negative gauge pressure to protect the reactive material or operator in case of leakage, respectively. The latter, however, is mandatory according to [Cadoret 2013] as operator safety precedes material protection. As a consequence, air present in the laboratory is sucked in by the glovebox in case of a confinement rupture, thereby decreasing the risk of dissemination of or contamination with radioactive material.

---

[11] Saturation depends on glove-box leak-rate, inert gas purity, outgassing of contained material, and exposure to air, and can be seen from an exponential increase of oxygen and moisture over time.

[12] The Ar and Ar/H_2 circuit meet at reactor level. In order to prevent hydrogen from entering the glovebox, the valves which connect the glovebox to the reactor are shut manually.

The allowed operational negative gauge pressure is 3 mbar (300 Pa), though the glovebox was usually operated between 10 Pa and 60 Pa according to constraints imposed by ASN.

Blower

A fan blower is used to force the inert gas to pass through the reactor for cleaning and to generate negative gauge pressure within the glovebox.

Blower power may be controlled automatically or manually but the system should never be shut off; otherwise, gas purification is disabled. Typically, the blower was operated at 80 % rated power in the automatic mode.

Oxygen and Moisture Sensors

Oxygen and moisture are monitored as both may compromise powder quality by oxidising uranium as well as UMo [Wilkinson 1962a]. Since powder quality is already affected at lower oxygen levels than monitored for fire prevention (chapter 3.3.2), an additional oxygen sensor with a smaller target range is installed. Accordingly, the sensors have resolutions that reach 0.1 ppm and 0.01 ppm for O_2 and H_2O, respectively. All values are transmitted to and saved by a visual control panel for observation in order to create both reliable and repeatable production conditions.

Visual and audible alarm was set to 10 ppm.

Control Panel

The control panel (Figure 3-17) shows the operator current oxygen content, moisture content, glovebox pressure, and blower power. Through its touch screen function, pressure mode and thresholds as well as regeneration are controlled. Moreover, oxygen and moisture trend over time are stored and monitored. A visual and audible alarm is available in case impurity thresholds are exceeded.

Alternatives

Instead of operation with gas purifier for inert gas reprocessing, the glovebox may be operated in dynamic or static mode – each without gas purifier. Dynamic operation implies constant inert gas purging to compensate for air leakage to keep oxygen and moisture levels in the order of ppm. In static mode, the glovebox has to be purged down to ppm-levels right before atomization.

Figure 3-17 Control panel of the gas purifier.

3.3.4 Framework (34)

Function

The load-bearing and component-merging framework of the atomizer consists of a bottom plate, several different supports for winch, bump stops, and spindle (Figure 3-18).

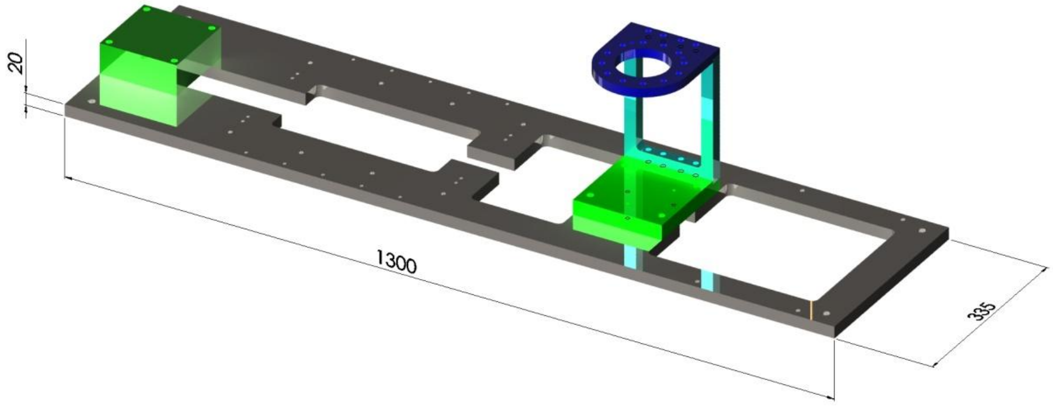

Figure 3-18 CAD model of the atomizer framework.

Characteristics

It was made in-house from stainless steel due to its material properties such as hardness, yield strength, tensile strength, and low corrodibility in comparison with other materials. As a consequence, this material allows for quick and rough estimation of necessary wall thicknesses without detailed calculation.

Bottom plate

The bottom plate of the framework is mounted through screws on the reinforced glovebox bottom plate. This arrangement increases the structural integrity and inhibits atomizer relocation due to vibration. It serves as merging part of all atomizer components and for their alignment. The bottom plate core was removed, though, in order to decrease atomizer weight.

3.3.5 Argon

Function

The atmosphere surrounding the atomization process performs three tasks: Protection of uraniferous materials from corrosion, notably oxidation, with respect to powder quality, in particular sphericity and purity. Enhancement of droplet solidification with regard to both the particle morphology and powder recipient dimensions as well as protection from metal powder inflammability.

Characteristics

An externally installed regular Argon carrier with 11 bottles, each of them containing a volume of 10 m^3 Ar (at normal pressure) assures constant inert gas supply. Bottle pressure is 200 bars. If total bottle pressure falls below 10 bars, Ar supply is semi-automatically switched to a second and similar carrier.

In order to respond to powder quality requirements Ar gas with 99.999 % purity (or 10 ppm total impurity) is used. Higher purities are industrially available, but (exponentially) more expensive at present.

Argon (Ar) was chosen for this application as it is chemically inert – even at elevated temperatures over 300 °C – and therefore does not react with solid or molten uraniferous materials in contrast to other common and cheaper shielding gases like nitrogen (N) or carbon dioxide (CO_2) [Wilkinson 1962a, Wilkinson 1962b]. As Ar is thermally conductive, it allows for particle cooling through forced convection during particle flight in addition to thermal radiation, thereby promoting rapid solidification and decreasing powder collection-chamber dimensions. Ar is ionisable and thus allows for igniting and maintaining the electric arc. Typically, electrode distances from 2 to 5 mm are valid for contactless ignition in Ar.

However, traces of oxygen (10-50 ppm) in argon may cause uranium corrosion above 300 °C [Wilkinson 1962b].

Alternatives

Helium: Pure, dry Helium (He) is a common alternative to Ar as it is an inert gas and does not attack uranium as well [Wilkinson 1962b]; yet, it is more expensive, less ionisable, and with a higher potential drop per unit length [Hodkin *et al.* 1973]. The latter causes a relatively short maintainable arc length [Hodkin *et al.* 1973] and, as a consequence, the necessity of a more powerful welding device than for Ar. However, due to its higher thermal conductivity and thus accelerated particle cooling, He is reported to increase productivity with regard to spherical particles [Hodkin *et al.* 1973] if powder recipient dimensions are limited. Ar/He mixtures are industrially available, merging their different advantages depending on the application and were tested in centrifugal atomization of UMo alloys causing significantly coarser particles than for Ar [Oh *et al.* 2006].

High vacuum[13] may also protect reactive materials due to the absence of corrosive reactants and impurities, but substantially reduces atomized particle cooling rate as thermal radiation remains the only heat transfer mechanism. Another disadvantage of vacuum with regard to inert gas is its non-ionisability, which impedes ignition and maintenance of the electric arc. Therefore, ionisable inert gas has to be continuously injected. From a technical point of view, high vacuum would require an additional vacuum chamber (for atomization) within an inert atmosphere (for powder handling) and supplementary auxiliary installations such as primary pump, turbomolecular pump, inert gas supply, and appropriate tubing and sealing.

3.3.6 Arc Welder

Function

Power supply of the electric arc that melts the rotating U8Mo electrode is provided through an electric arc welder. Besides, electric arc current, current type, polarity, ignition mode amongst other parameters can be controlled (Figure 3-19).

Characteristics

A commercial tungsten inert gas (TIG) welder was purchased (Figure 3-19) providing current and voltage ranges of 2 to 170 A and 10.1 to 16.8 V, respectively, resulting in a nominal electric power of about 3.4 kW. This operating range matched exactly the current-voltage characteristic, equation (5.13), of the electric arc under Argon atmosphere stated in literature [Matthes and Schneider 2012][14]. The open-circuit voltage (O.C.V.) is 93 V.

---

[13] 10^{-1} to 10^{-7} Pa.

The welder was chosen as it leaves the operator enough margins to decrease or increase the electric arc current with respect to a reported reference point of 70 A [Clark *et al.* 2010]. The corresponding mass flow rate for U8Mo was not stated. This, however, is one of the governing parameters regarding particle sphericity [Champagne and Angers 1984, Hinze and Milborn 1950] and may demand adjustments in a wide range. Furthermore, TIG provides a contactless and localised heat source, thus increasing purity and efficiency. The arc welder consists of a power generator and control pedal.

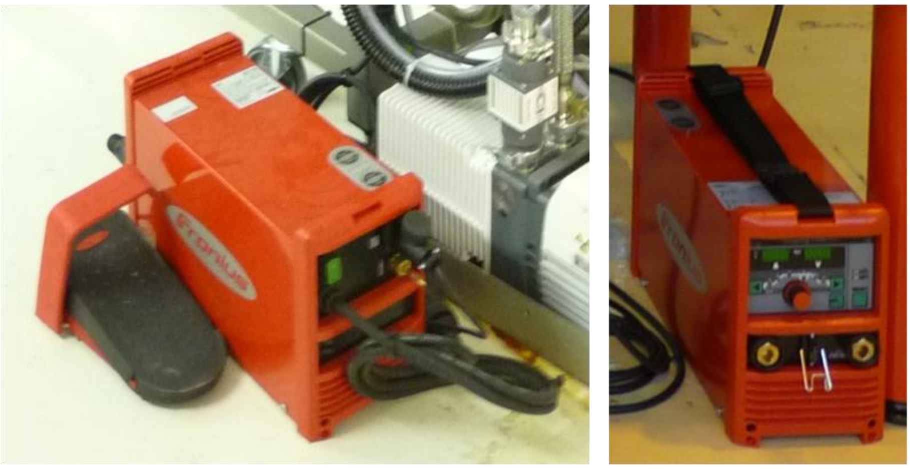

Figure 3-19 Back (left) and front view (right, showing operator interface) of the electric arc welder with food pedal for arc ignition.

Cooling

Due to its nominal power, water cooling of the tungsten electrode is avoided – a vital characteristic regarding criticality and thus nuclear safety. In fact, this welder is so dimensioned as to provide sufficient cooling to the tungsten electrode through an integrated Ar purge flow. However, this purge flow was disconnected from the torch as it would compromise (negative) pressure control within the glovebox, which is a safety feature. As a consequence, cooling is provided by thermal radiation and natural convection[15] only. In order to avoid overheating[16] of the tungsten electrode, larger electrode diameters may be used to decrease the current density.

---

[14] The manufacturer of the arc welder did neither confirm nor contradict the relationship.

[15] The cooling vortex generated by the consumable electrode is considered negligible.

[16] Overheating is indicated on the operator interface through a red LED.

Position

The welder is connected via customised power feed-throughs to both the glovebox and atomizer. The external emplacement allows for maintenance of high performance electronic parts outside the glovebox, avoids contamination, decreases need for space within the glovebox, and facilitates welding operation. Naturally, the torch is situated within the glovebox above the consumable U8Mo electrode.

Polarity

As a rule, the tungsten electrode has a negative polarity (cathode), which leads to (positive) ion movement towards the tungsten electrode [Bourgeois 1989, Correy 1982, Matthes and Schneider 2012]. This setup was also chosen for the UMo atomization in this work. Thereby, pollution of the UMo alloy weld pool by tungsten ion movement is avoided. In addition, temperatures at the anodic consumable electrode are higher than at the cathodic tungsten electrode [Matthes and Schneider 2012] thus promoting melting of the anode and preservation of the cathode. It was also used as it leaves the spindle shaft at zero potential, hence decreasing the risk of arcing within the spindle bearing or labyrinth seal. Positive polarity of the tungsten electrode is used in order to break up oxide layers, e. g. when melting aluminium or magnesium alloys, and often so combined with alternating current (AC) as to allow for cooling of the tungsten electrode during the negative half-wave [Matthes and Schneider 2012]. This option may also be used for an alternative atomization process called centrifugal shot casting (CSC) [Hodkin *et al.* 1973].

HF Ignition

For electric arc ignition, high frequency (HF) ignition mode was used, thereby avoiding contact between the two electrodes – a benefit in terms of weld pool purity and hence fuel powder quality. Moreover, HF ignition enables the operator to accelerate the atomizer to nominal rotation speed before initiating the melting and thus atomization process. In fact, this approach avoided premature droplet formation before the duty point is reached, which would compromise the resulting particle size distribution, process efficiency, modelling, and process repeatability. Technically, high-voltage AC-pulses (9 kV, ≤ 500 Hz, 0.5...1.0 µs) are superimposed over the actual arc melting current for ignition [Matthes and Schneider 2012]. As soon as the arc is ignited, the arc welder automatically switches to DC mode and the set current. Perturbation of other electronic equipment due to the use of HF was not observed. Alternative available ignition modes are scratch start and lift-arc. However, both necessitate direct electrode contact, thus bearing the risk of melt pool contamination with impurities.

DC Current

For REP the arc welder is operated in direct current (DC) mode for it does not induce eddy currents in the spindle housing as it might be the case for AC due to changing magnetic fields. A pulsing arc for both the DC and AC mode is available. The electric arc current of 100 A should not be exceeded permanently due to the limited current density of the carbon brushes (chapter 3.3.14).

Closed-Loop Control

There are two basic types of arc welders that can be distinguished by their means of electric arc control: constant voltage (CV) and constant current (CC) arc welder ["Welding theory and application" 1993]. Their respective static voltage-current characteristics and resulting operating points are shown in Figure 3-20. The intersection of a static voltage-current characteristic of the arc welder with a voltage-current characteristic of an electric arc is referred to as operating point. The operating point is characterised by an electric arc current and voltage, and it varies during melting ["Welding theory and application" 1993].

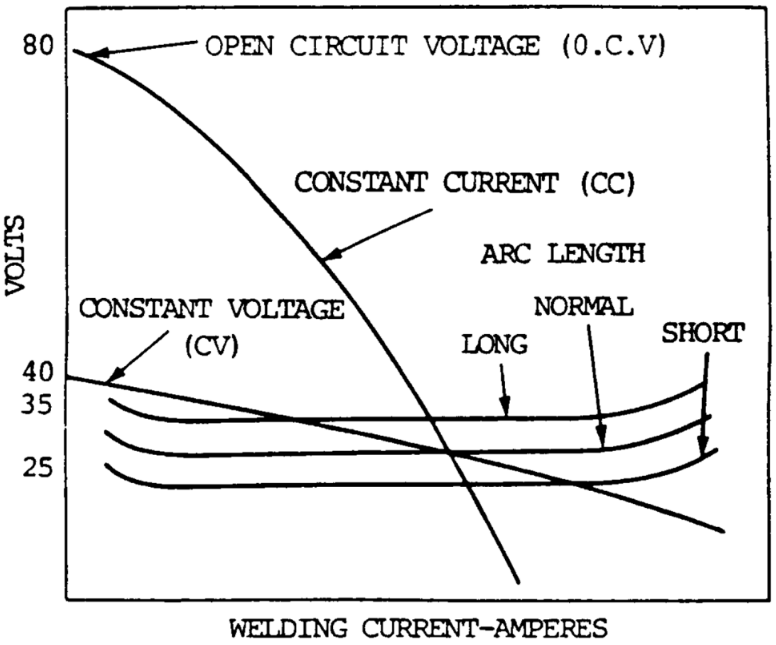

Figure 3-20 Typical voltage-current output characteristic curves of the two basic power source types (arc welders), constant voltage (CV) and constant current (CC) arc welder, and electric arc operating points. The operating point is the intersection of a characteristic of an electric arc and a static characteristic of the arc welder; taken from ["Welding theory and application" 1993].

Single control CC machines enable the operator to adjust the electric current output. For every electric arc current setting, a corresponding static voltage-current characteristic is provided by the arc welder. The CC machine can produce approximately constant electric arc currents with small deviations [Fahrenwaldt *et al.* 2014, "Welding Handbook" 2004, "Welding theory and application" 1993]. The arc voltage, however, is responsive to the electrode-to-work distance, i.e. the electric arc length, for a given electric arc current and a nonconsumable (tungsten) electrode

[Fahrenwaldt *et al.* 2014, "Welding Handbook" 2004, "Welding theory and application" 1993]. The CC arc welder operates with drooping voltage-current characteristics and thus ΔU feedback (closed-loop) control. These characteristics are such that in the vicinity of the operating point, the percent change in current is less than the percent change in voltage ["Welding Handbook" 2004]. As a consequence, a change the in the electric arc current is overcompensated by the adjustment of the electric arc voltage.

CC machines are in particular useful if the electric arc length varies (chapter 5.1.2), for example due to manual operation of the torch, as they provide a fairly constant melting rate [Fahrenwaldt *et al.* 2014, "Welding Handbook" 2004, "Welding theory and application" 1993]. It therefore allows for the implementation of a manual tungsten electrode infeed system. Moreover, this closed-loop control is most suitable for a potential automation of the infeed system since the voltage of a driving infeed motor is usually proportional to the change in electric arc voltage [Matthes and Schneider 2012, "Welding Handbook" 2004].

The installed TIG welder is a single-control CC machine that provides true constant-current. That is, the electric arc current remains constant irrespective of the electric arc length (Figure 3-21). In addition, it has a low current (LC) and high current (HC) option. Accordingly, the electric arc current can be varied between low and high current during melting, for example by using the foot pedal or by programming the pulse option for pulsed melting.

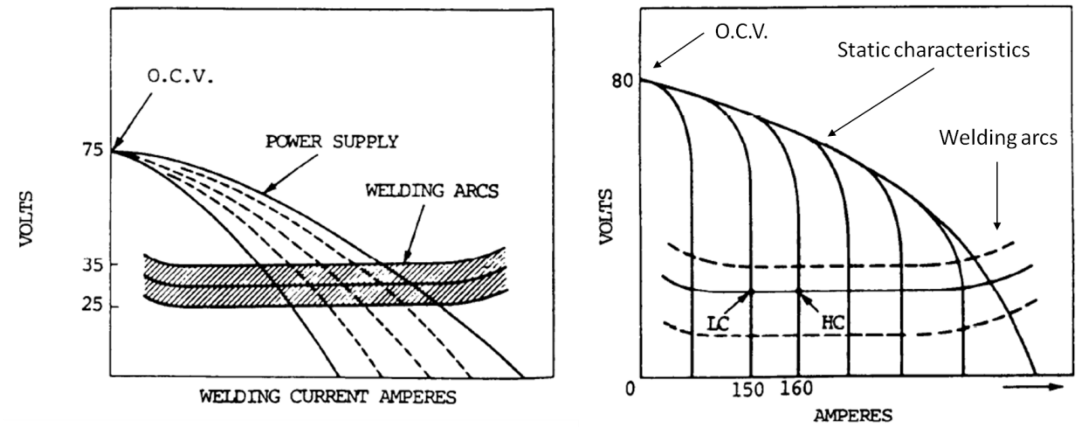

Figure 3-21 Left: Typical static voltage-current characteristics of a traditional CC machine. Right: Typical static voltage-current characteristics of a true constant-current arc welders with low current (LC) and high current (HC) option; both taken from ["Welding theory and application" 1993].

Operator Interface

The arc welder is programmed by means of an integrated operator interface (Figure 3-19) which is placed outside the glovebox. Control is executed through a foot pedal since both the atomizer motor switch and tungsten electrode infeed system requires manual control and thus both operator hands. Two different modes of pedal operation are available: two (on/off) and four (heating/melting/heating/off) step mode. The two and four step mode enables the operator to melt the target directly or to preheat the target before melting, respectively. Electric current increase with time after ignition or pulsing may also be controlled.

Alternatives

Alternative heat sources for REP such as plasma, laser, and ion beam welding as well as induction are briefly evaluated:

Plasma: The combination of plasma torches and REP is known as plasma rotating electrode process (PREP) [Roberts and Loewenstein 1980]. In this application, the thermal plasma generated by the electric arc is confined and directed towards the workpiece. In general, there are two types of plasma torches – transferred and non-transferred [Bourgeois 1989, Matthes and Schneider 2012]. Whereas in the former setup one electrode is outside the torch, in the latter type both electrodes are inside the torch housing. The non-transferred type would render both the rotary electrical connector and the customisation of the high frequency spindle obsolete since the workpiece (rotating electrode) is not part of the electrical circuit[17] – in contrast to the transferred type. Moreover, melting of non-conductive materials would become feasible. However, the non-transferred process offers an efficiency below 30 % [Bourgeois 1989] as the workpiece is only heated by the hot gas flow. On the other hand, the transferred torch type may be used in a twin-torch setup for melting of non-conductive materials. In this setup, one torch is anodic while the other is cathodic [Bourgeois 1989]. Whatever solution seems most applicable, it has to be considered that both torch types are typically water-cooled which is a matter to criticality and thus nuclear safety. Another important aspect is the necessary arc-plasma gas-flow and pressure, in particular for the non-transferred process. In fact, it has to be in accordance with both the mandatory negative pressure in the glovebox and the pressure control system of the glovebox, e.g. gas purifier.

Laser: At present, laser power densities of the same order of magnitude as provided by TIG require considerable larger equipment and/or higher expenses, yet might be an alternative as tungsten electrode infeed, rotary electrical contact, tungsten electrode, and HF ignition would become obsolete. That is, engineering, operation, system complexity, maintenance, and wear parts would be reduced.

---

[17] Although the workpiece is not part of the electric power circuit, the workpiece has to be connected to the protective earth in order to prevent electrostatic charging.

Ion beam: Ion beam welding would require an additional vacuum chamber and auxiliary vacuum equipment – with its already mentioned advantages and inconveniences [Matthes and Schneider 2012] – and not necessarily decrease engineering effort.

Induction: Melting of the rotating, consumable U8Mo electrode through induction is theoretically feasible by adapting the amplitude and frequency of the inducing magnetic field to the physical, magnetic, and electrical properties of U8Mo and thus concentrating the field in the upper electrode area as conducted in induction casting [Davies 1990]. There is little information whether a similar process already exists or not. However, given the scope of the project and schedule, existing and confirmed principles were preferred whenever applicable.

3.3.7 Welding Torch (15)

Function

The welding torch holds the tungsten electrode, allows for adjustment of its overhang, and connects it to the electrical circuit of the welder while electrically insulating it from the metallic drill rig[18] (Figure 3-22).

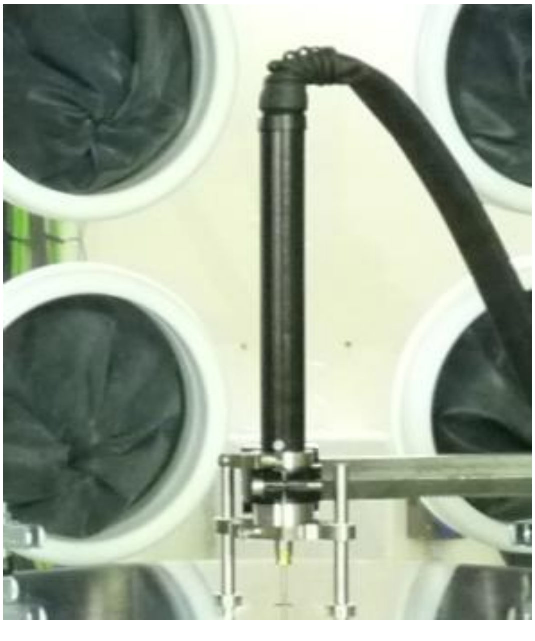

Figure 3-22 Welding torch (black bar) of the tungsten inert gas arc welder.

---

[18] Typically, the torch also directs the shielding gas flow towards the cathode and work piece. This option was disabled (chapter 3.3.6, cooling).

Characteristics

In fact, cathode fixation is provided through an integrated and exchangeable clamp screw that allows for operation of different electrode diameters up to 4.8 mm. In addition, the clamp screw serves as electrical contact between the torch and tungsten electrode as it is made from brass.

3.3.8 Tungsten Electrode (21)

Function

The tungsten electrode (Figure 3-23) creates a difference in electric potential between itself and the rotating electrode in order to establish an electric arc between both of them. For REP, the tungsten electrode must not melt during atomization as it would cause contamination of the U8Mo melt pool and thus atomized particles.

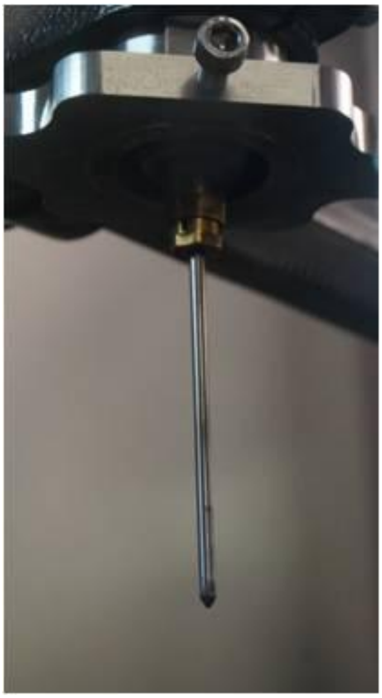

Figure 3-23 Tungsten electrode mounted on the arc welder torch through a brass clamp screw.

Characteristics

For REP, a commercial tungsten electrode with added cerium oxide (CeO_2) served as tungsten electrode for the electric arc as TIG is only feasible with non-melting electrodes with relatively high melting points [Matthes and Schneider 2012]. Notably, tungsten electrodes resist temperatures beyond the liquidus[19] of both U8Mo and stainless steels[20]. Additives like CeO_2 or lanthanum oxide (La_2O_3) increase ignitibility [Matthes and Schneider 2012].

---

[19] Liquidus is the point of full transformation of an alloy from solid to liquid state.

It is mounted on the welding torch and used as cathode having negative electric polarity.

Due to the temperatures created within the electric arc and disabled shielding gas cooling, appropriate electrode diameter with respect to the applied arc current have to be taken into account.

Electrode Tip

Arc stability is improved by paraxial tip pointing [Matthes and Schneider 2012]. The tip angle determines the depth and form of the molten pool. The steeper the tip is, the deeper and more conical the pool [Matthes and Schneider 2012] gets (Figure 3-24).

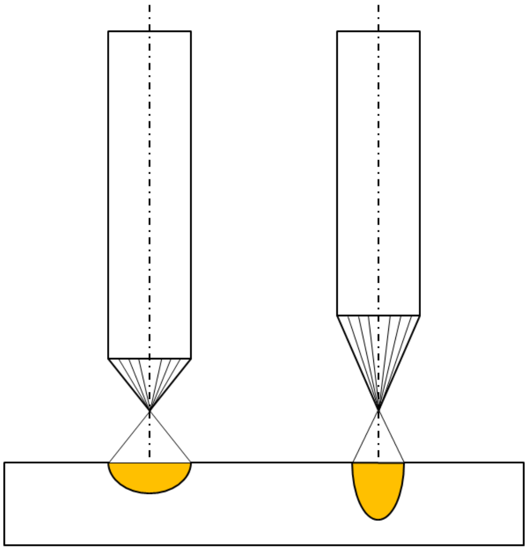

Figure 3-24 Schematic showing the influence of the tip angle. Both electrodes have paraxial tip pointing.

Attention must be paid not to use too steep tips as this might lead to a partial melting of the consumable electrode if the tungsten electrode is not well centred. The resulting imbalance may induce vibration to the spindle and cause damage to the spindle roller bearings if maximum radial load is exceeded. Regarding REP, a relatively shallow, but uniform penetration seemed appropriate for uniform melting and atomization. In fact, a well-balanced form where the tungsten electrode diameter equals tip height was chosen [Matthes and Schneider 2012].

---

[20] During commissioning and parameterization stainless steel served as surrogate material.

Geometry

Typically, electrodes of 175 mm length, 3.2 mm diameter, and 3.2 mm tip height were used. The length enables the operator to position the electrode tip in a close distance to the rotating U8Mo electrode while allowing for a small orifice in the receptacle cover hood.

Polarity

For REP, the standing electrode has negative potential (cathode) and is therefore exposed to lower temperatures than the anode [Matthes and Schneider 2012]. In addition, this polarity avoids contamination of the rotating electrode melt pool with tungsten electrode material [Matthes and Schneider 2012].

3.3.9 Infeed Linear Guide Rails (1) and Slider (19)

Function

This bearing arrangement centres the torch adapter and thus tungsten electrode with respect to the cover hood and rotating electrode (Figure 3-25).

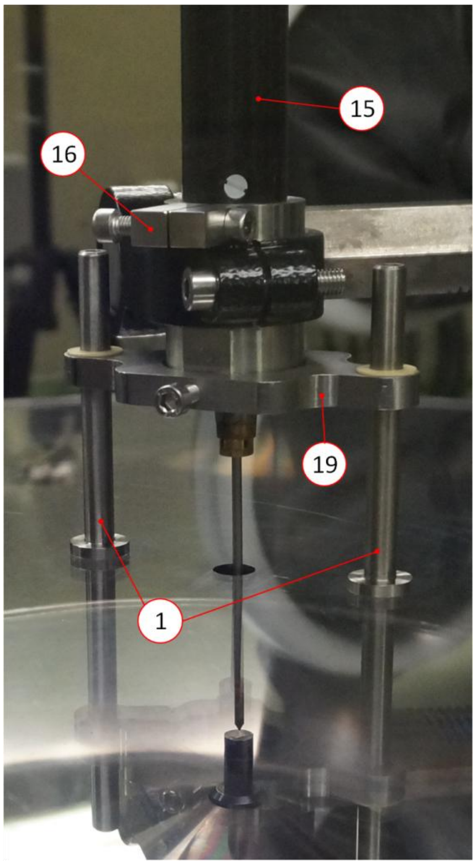

Figure 3-25 Assembly showing the torch adapter (16) that carries the welder torch (15). In addition, the linear slider (19) that runs on the linear guide rails (1) is mounted on the adapter. The numbers correspond to Figure 3-8.

Characteristics

Two linear guide rails were in-house fabricated from stainless steel, mounted on the cover hood and lubricated with vacuum grease. The linear slider is fixed with one screw to the torch adapter. Plastic journal bearings are integrated in the slider for friction reduction.

Mounting Procedure

After mounting of the rotating electrode on the high frequency spindle and closure of the collection-chamber cover-hood, the slider has to be manually mounted on the linear guide rails. Only after centring of the static tungsten electrode, the cover hood can be fixed using the quick release clamps.

3.3.10 Torch Adapter (16)

Function

An in-house torch adapter was so fabricated as to allow for torch mounting on the drill-rig cantilever. In addition, the infeed linear slider is mounted on the torch adapter (Figure 3-25).

Characteristics

It is in-house made from stainless steel and designed as a clamp that is tightened through a screw. A second threaded hole serves as screw intake in order to press the clamp open in case of its plastic deformation Figure 3-26.

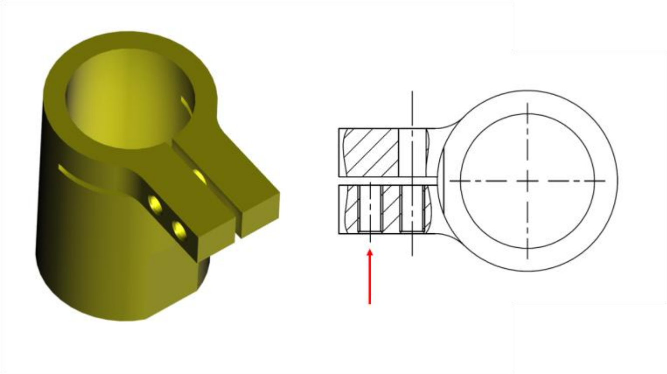

Figure 3-26 CAD model of the torch adapter (left) with front view (right) and cutaway at thread level. The red arrow points to the second screw intake to open the clamp.

3.3.11 Drill-Rig (20) with Cantilever (18)

Function

The implemented drill rig with cantilever allows for manual positioning and relocation of the tungsten electrode with respect to the rotating electrode in order to set the initial arc-ignition gap and electrical arc length as well as to adjust and maintain the latter during atomization.

Characteristics

The drill-rig is placed beside the atomizer recipient – due to its height and cantilever length – instead of placing it on top of the cover hood (Figure 3-27). This allows for better visibility of the atomization process and more lightweight handling of the cover hood.

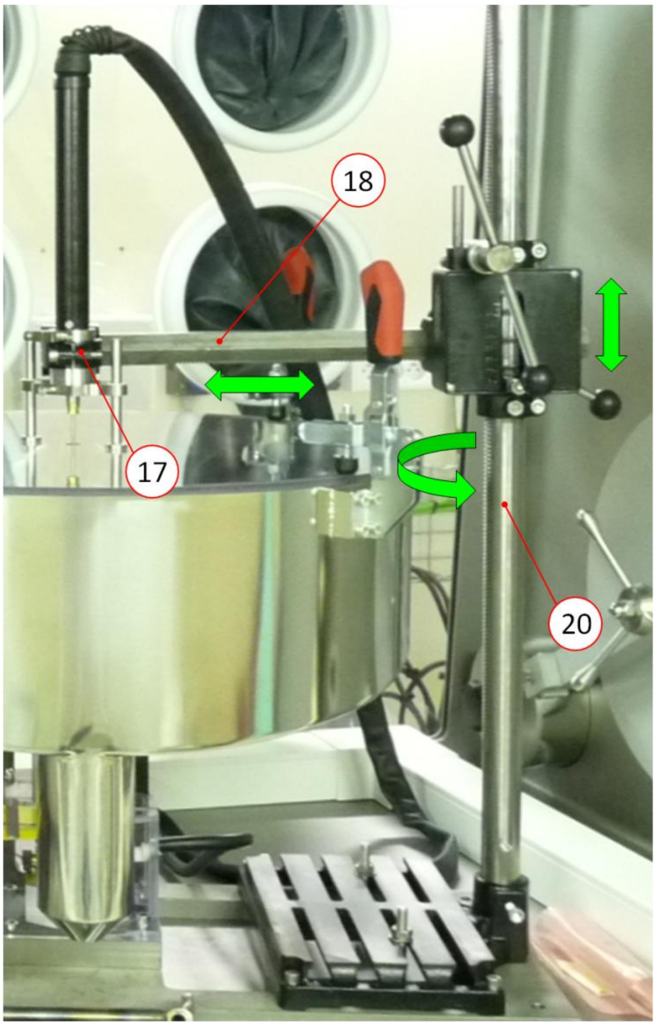

Figure 3-27 Drill rig (20) with cantilever (18) and drill adapter (17). The green arrows indicate moving directions.

It is adjusted and operated manually by means of an Allen key and a feed lever[21]. The drill rig is fixed to the atomizer framework, but may be turned through 360° around its vertical axis while its cantilever can be displaced horizontally. In consequence, the tungsten electrode may be positioned in all three dimensions. This flexibility enables the operator to centre the cathode with respect to the anode since eccentric melting of the anode may induce mechanical imbalance to the rotating electrode, thereby causing potential vibration and/or overload to the spindle roller bearings.

For HF ignition, the tungsten electrode is positioned 2 to 4 mm vertically above the rotating electrode, accounting for both the potential drop per unit length in Ar and the properties of the arc welder. As the anode is consumed during atomization, it loses its initial length. Thereby, the gap between the two electrodes and thus electrical resistance is increased, eventually leading to breakdown of the electric arc. This phenomenon is compensated for by the drill rig that allows for vertical relocation of the cathode in order to follow the burn-up of the anode manually.

Moreover, the drill rig comes with a vertical zero-point fixation to define the initial electrical arc length of about 10 mm after ignition. In addition, it has a depth stop (maximum relocation) to avoid excessive descending of the cathode. A return spring helps the operator to lift the cathode back to the zero point after the operator has released the feed lever.

Due to the length of the cantilever (~ 500 mm), its angular clearance around the drill rig axis becomes important with respect to electrode centring. An in-house designed linear infeed bearing (chapter 3.3.9) is so mounted on top of the cover hood as to guide the drill rig cantilever and thus torch and cathode, eventually reducing clearance and promoting centred melting of the consumable anode.

Alternative

The drill rig and thereby manual infeed system may be extended and automated. For this purpose, the existing arc welder and a commercially available upgrade kit may be used. It consists of a step motor arrangement that carries the welding torch and an electronic closed-loop control.

3.3.12 Rotating Electrode (9)

Function

In REP, the rotating electrode is atomized and therefore a consumable. Inherently, it conducts the electric arc current and has generally anodic polarity.

---

[21] The initially shiftable feed lever was fixed with two welding spots for operator convenience.

Characteristics

For parameterisation purposes, depleted U8Mo as rotating electrode material was used. The electrodes were cast in either an induction furnace (FRM II/ CERCA, Figure 1-4) or an arc-melting furnace (INL). Cold commissioning and repeatability tests were executed with electrodes made from stainless steel (1.4301) that were manufactured on a turning machine.

Geometry

Taking into account its rotation application, the present configuration consists of two (rotation-symmetric) cylindrical bodies – workpiece and stub. The standard rotating electrode has a consumable workpiece length and a diameter of 30 mm and 10 mm, respectively (Figure 3-28). A short version of 20 mm consumable length with the same diameter was used for very high rotational speeds around 50’000 rpm (Figure 3-29). Also, different diameters were used, namely 14 and 20 mm (Figure 3-29).

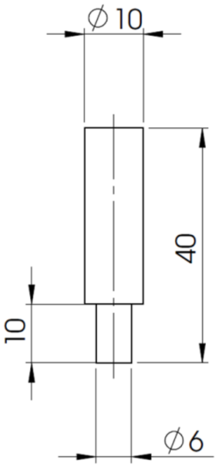

Figure 3-28 Standard rotating electrode dimensions for the REP prototype atomizer.

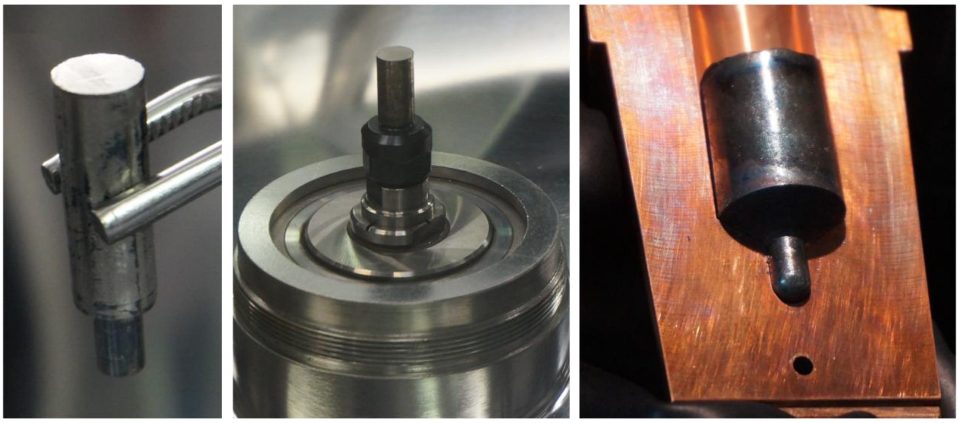

Figure 3-29 Examples of U8Mo and U7Mo rotating electrodes. Left: INL arc-melter cast U8Mo rotating electrode after mechanical polishing. Middle: short rotating U8Mo electrode mounted on the collet chuck. Right: in-house cast U7Mo rotating electrode with 20 mm diameter.

The stub that is inserted into the collet for mounting has smaller dimensions than the consumable workpiece since it cannot be atomized in REP. Overall, electrode masses of around 30 g to 100 g of U8Mo were operated.

Alternatives

Rotating electrode length and diameter may be increased within the operational limits of the spindle (chapter 3.3.13) in order to increase both production capacity and process efficiency.

Cone: Geometries that have a varying diameter, e.g. cones or inversed cones, may also be used. For instance, a cone with increasing diameter towards the stub may constitute a compromise between an increase in production capacity and decrease in rotational stability. However, it must be taken into account that the rotating electrode diameter has influence on the REP parameters and thus atomization regime (chapter 6.1.4), mass flow rate (chapter 5.1), and particle mean size (chapter 7.1.5), therefore influencing production results.

Hollow cylinder: This geometry constitutes a compromise to maintain rotational stability while keeping or even increasing the diameter in order to obtain finer particles.

3.3.13 High Frequency Spindle (11)

Function

A commercial high frequency milling spindle was purchased and customised for both the vibration- and frictionless rotation of the U8Mo reference electrode at constant rotation speed as well as conduction of the electric arc melting current.

Characteristics

The spindle is composed of a shaft, bearings, seals, collet, collet chuck, pulley, customised shaft extension screw, and a rotary sensor (Figure 3-30).

Rotation speeds of 36’000 and 45’000 rpm were reported from [Olivares *et al.* 2012] and [Clark *et al.* 2010, Clark *et al.* 2007], respectively. Yet, these values have to be used carefully as experimental results lack evidence of repeatability [Moore and Archibald 2014], do not always meet powder quality requirements [Olivares *et al.* 2012], and are based on partially estimated parameter sets [Moore and Archibald 2014]. However, they served as an essential reference for design point estimation of this prototype. Besides, the expected U8Mo mean particle size was calculated from equation (7.22) using uranium properties (Table 6-2) in absence of UMo thermophysical properties at liquid state. The results are plotted in Figure 3-31. Operating limits of the high frequency are given in Table 3-1.

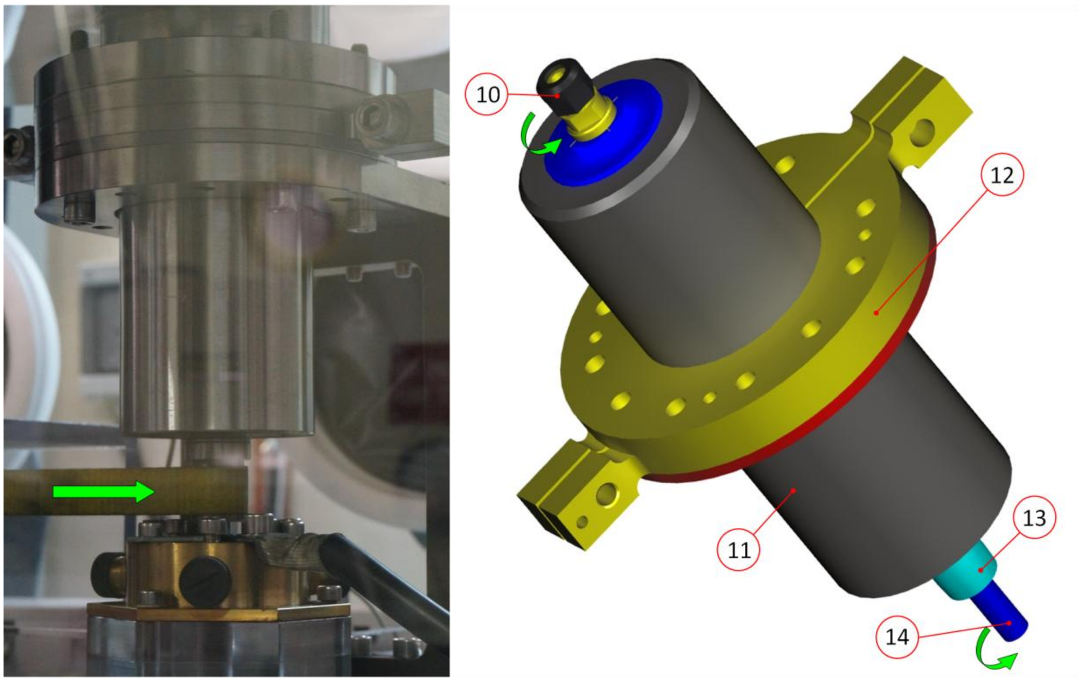

Figure 3-30 High frequency spindle of the atomizer prototype. Left: Spindle as mounted on the atomizing unit. Right: CAD model of the spindle, showing collet chuck (10), two spindle clamps (12, yellow) and spacer (12, red), pulley (13), and shaft extension screw (14).

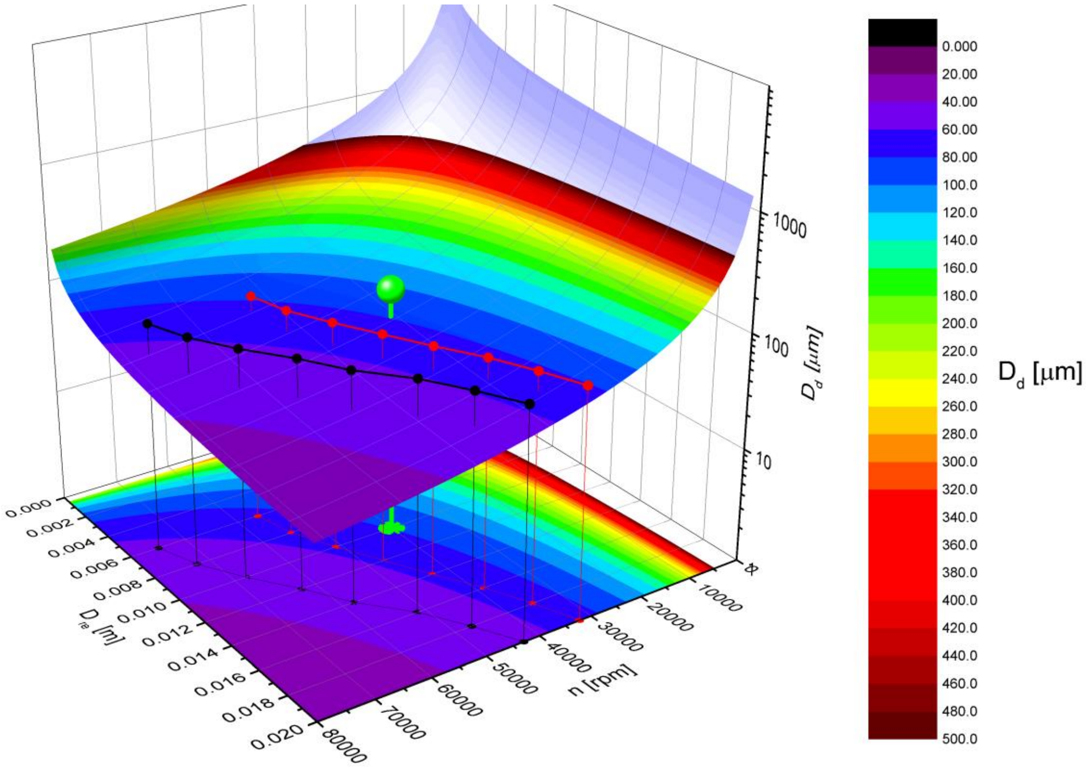

Figure 3-31 Estimated particle mean diameter D_d as a function of rotational speed n and rotating electrode diameter D_{re} using REP model (7.22). The resonance frequency and manufacturer's maximum rotation speed are marked black and red, respectively. The prototype atomizer design-point is marked with a green needle.

Table 3-1 High frequency spindle operating limits according to manufacturer's (Fischer AG) instructions with respect to U8Mo.

Diameter [mm]	Electrode length [mm]	Consumable length [mm]	Maximum rotation speed [rpm]	Resonance frequency [rpm]
10	30	20	55500	73680
	40	30	51000	68000
	50	40	44500	59500
12	30	20	53500	71040
	40	30	47000	62500
	50	40	40000	53000
14	30	20	50500	67380
	40	30	43000	58000
	50	40	36000	48000
16	30	20	47180	62800
	40	30	38590	51480
	50	40	31813	42420
18	30	20	43941	58560
	40	30	35209	46920
	50	40	28791	38400
20	30	20	40878	54480
	40	30	32277	43020
	50	40	26237	34980

* The manufacturer used a 25 % safety margin to calculate maximum rotation speed from resonance frequency for standard U8Mo rotating electrodes.

The design point of the purchased spindle is 40'000 rpm with respect to the standard rotating U8Mo electrode (chapter 3.3.12), resulting in an estimated particle mean diameter of around 81 µm (Figure 3-31 and chapter A1). However, the spindle may exceed this point by 25 % using the standard rotating electrode, resulting in 50'000 rpm and a potential particle mean diameter of around 70 µm.

Moreover, the rotating electrode diameter may be increased by 50 % at design rotation speed. That is, the spindle is designed to tolerate U8Mo electrodes with standard length and diameters up to 15 mm at 40’000 rpm. Also, total U8Mo electrode masses of around 100 g may be reached in this configuration, corresponding to an increase in both production capacity and process efficiency by about 100 % with respect to the design point.

According to Figure 3-31, a droplet mean diameter of 81 μm may also be obtained by atomizing an electrode of 20 mm diameter and 30 mm consumable length at 30’000 rpm. This configuration would increase the production capacity by 400 % with respect to the design point.

Collet and Collet Chuck

The rotating electrode is manually mounted on the high frequency spindle through a screwable collet chuck. Therefore, the electrode is inserted into a taper collet and fastened with a union nut using two wrenches (Figure 3-32).

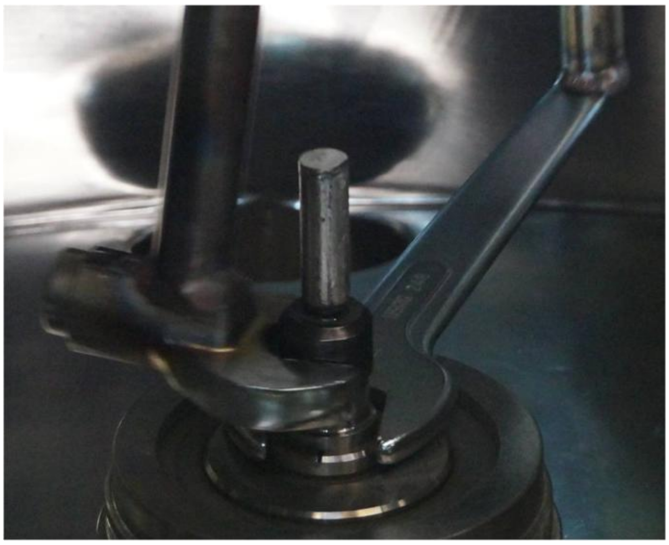

Figure 3-32 Mounting of a U8Mo rotating electrode on the collet chuck.

Besides the mechanical function, the collet and collet chuck benefit from their metallic properties as they have to conduct the electrical current coming from the rotating electrode and running to the shaft.

In addition, both components conduct the heat that is dissipated from the “hot” rotating electrode to the “cold” shaft. Since the collet and collet chuck are made of mild and stainless steel, respectively, they have higher melting points than U8Mo and hence cannot melt[22].

The collet has ISO h12 tolerance and requires a cylindrical clamping surface of 10 mm length and 6 mm diameter.

System inherently, the electrode cannot be fully atomized as one electrode part (stub) is inserted into the collet. However, the stub may be reprocessed for casting and used again for atomization, thus increasing the amount of useable uranium from one batch.

Mounting torques of the collet chuck and collet nut are 16 Nm and 24 Nm, respectively.

Rotary Sensor

In order to ensure repeatability of results and process control, the high frequency spindle is extended with an inductive rotary sensor (Figure 3-33). The sensor is integrated into the spindle housing and generates two signals per shaft revolution. These signals are then transmitted to both the motor-governing frequency inverter and control panel of the control box. As a consequence, closed-loop control of the spindle rotation and thus constant speed throughout the atomization is gained, fostering consisting and repeatable production results. The nominal reacting distance of the sensor is 1 mm. The sensor is designed as a screw and can be removed for maintenance or exchange.

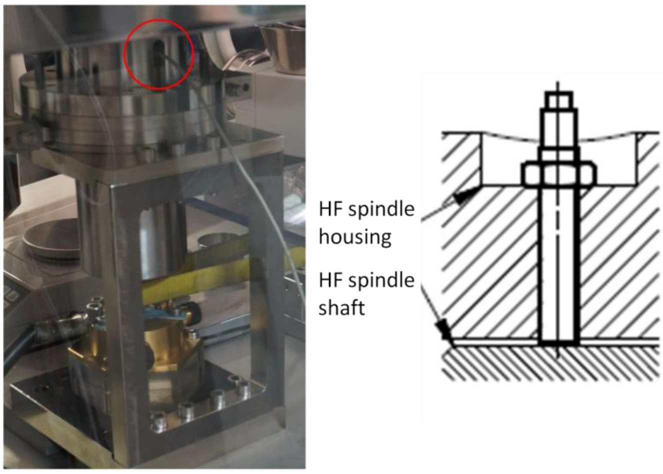

Figure 3-33 Mounting position of the inductive rotary sensor with respect to the high frequency spindle.

Bearing

The spindle shaft is mounted in roller bearings. The latter promote friction- and vibration-less shaft rotation, particularly at high frequencies. As a consequence, the risk of encountering resonances – like reported in [Clark *et al.* 2010] – is minimised and machine safety increased. Also, process control, notably in terms of particle size distribution and repeatability, is promoted as vibration may influence droplet formation.

---

[22] Provided, that the electric arc does not hit these parts directly.

Moreover, hybrid roller bearings composed of metallic races and ceramic (non-conductive) balls were chosen in order to insulate spindle shaft from spindle housing electrically. This is necessary as the melting arc current is conducted through the shaft and bearing configurations using steel balls would thus be prone to arcing. The latter in combination with relatively high arc currents may lead to welding spots on the balls, which in turn will cause untrue running of the spindle, vibration, and eventually destruction of the roller bearings ["Technische Anleitung Nr. 5 - Lagerströme in modernen AC-Antriebssystemen" 2001].

A non-hygroscopic[23] lubricant was chosen and purchased for the roller bearings since moisture may compromise glovebox atmosphere.

As rotating electrodes are atomized as-cast, attention must be paid with respect to their circular runout tolerance (Table 3-2).

Table 3-2 Calculation of the maximum circular runout for U8Mo rotating electrodes for a maximum centrifugal force of about 20 N as provided by Fischer AG.

Diameter [mm]	Consumable length [mm]	Mass [g]	Rotational speed [rpm]	Imbalance [mm]	Centrifugal force [N]	Max. circular runout [mm]
10	30	44	51000	0.7	20	0.03
12	30	62	47000	0.8	19	0.03
14	30	83	43000	1.0	20	0.02
10	40	58	44500	1.0	22	0.04
12	40	82	40000	1.1	19	0.03
14	40	109	36000	1.3	19	0.02

Pulley

The spindle pulley transmits the mechanical power – torque and speed – of the belt to the spindle shaft and thus rotating electrode. It is mounted on the spindle shaft through the shaft extension screw.

---

[23] Hygroscopy (greek): the ability to adsorp / absorp water.

It has a symmetrically convex belt contact area in order to promote belt stress and thus mechanical connection. In fact, tensile stress in the belt is created as it is stretched. As the belt is stretched the most at the pulley's centre line due to its convex form, it is automatically forced to centre on the pulley [Wittel *et al.* 2009].

The standard pulley height, diameter, and curvature radius for the purchased spindle are 25 mm, 22 mm, and 140 mm, respectively.

Shaft

A spindle with an integral[24] shaft that protrudes from both ends of the housing was chosen. While one shaft-end is connected to the consumable electrode and thus electric arc, the other allows for facilitated closing of the electrical circuit of the welding machine outside the spindle housing. In particular, the integral shaft configuration allows for direct conduction of the arc current from one shaft end to the other.

The shaft was additionally machined for the inductive sensor application.

Shaft Extension Screw

The protruding shaft-end is directly followed by the pulley, offering no space for the rotary electrical contact. Hence, it was decided to extend the shaft below the pulley by means of a custom screw that serves as both electrical contact and pulley fastener (Figure 3-34).

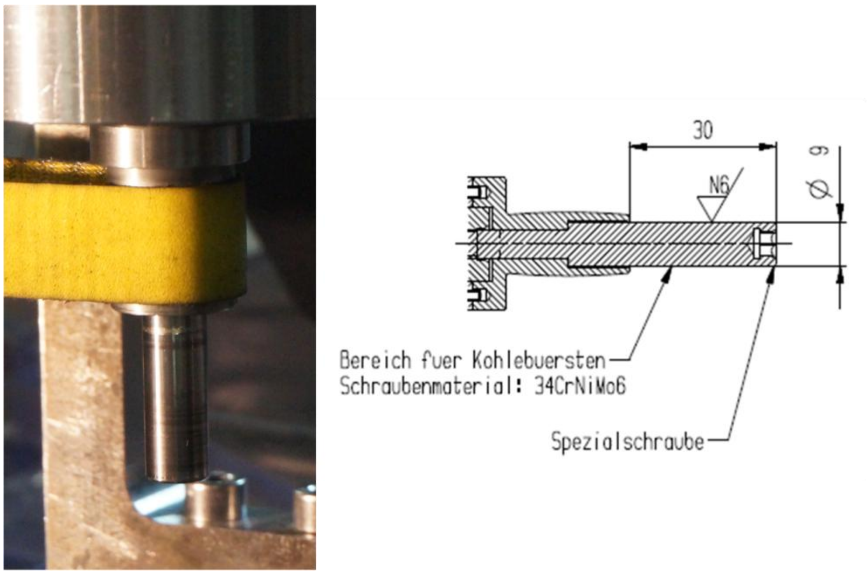

Figure 3-34 Shaft extension screw as mounted (left) and in schematic view (right).

---

[24] Motor spindles, for example, do not have an integral shaft. Actually, a transmission gear connects shaft and integrated motor. This arrangement may cause break sparks at gear level and potential welding spots which, in turn, would disturb gear function.

The shaft extension screw is exchangeable[25] in case of wear, but was made from 15CrNi6 stainless steel and hardened (45-60 HRC) in order to withstand mechanical strain caused by the slip ring brushes.

For the electrical rotary contact, a usable length and diameter of 30 mm and 11 mm, respectively, is provided. A circular runout of 0.02 mm is respected in order to reduce vibration and roller bearing wear. The dimensions of both the brushes and shaft extension screw were iteratively adapted in order to provide sufficient conductive surface while keeping radial speed as low as possible.

The screw was delivered with clockwise sense of rotation, thus leaving the possibility of unscrewing due to the rotation sense of the high frequency spindle shaft. Duly operation is ensured with additional loc-tite fixation and the nominal mounting torque of 10.5 Nm.

Shaft Seals

Radial gap ring seals are positioned at the shaft housing entry and exit by default to exclude contamination from the roller bearings. In the stricter sense, these are pneumatic seals necessitating pressurised gas flow (e.g. argon or air) to fulfil their function since there is a 50-100 µm clearance between housing and shaft – and thus no tight contact. As a matter of fact, the spindle is operated without gas flow since this arrangement, particularly the necessary flow rate, would have compromised pressure control of the gas purifier (chapter 3.3.3) and thus negative pressure operation of the glovebox – a safety feature (chapter 2.1). In return, an in-house designed powder seal screw (chapter 3.3.28) is implemented right before the shaft entry in order to hinder the powder or any other contaminant from entering the spindle during atomization more effectively. A radial shaft seal is positioned at the opposite shaft housing entry to exclude contamination due to graphite and metallic dust (chapter 3.3.17).

Since there is an electric potential difference (max. 16.8 V, chapter 3.3.6) between shaft and seal during atomization, the breakdown voltage for the 50-100 µm gap in Ar at around 1 bar had to be determined. Eventually, a breakdown voltage > 200 V was estimated from publications of [Carazzetti 2009], thus allowing for safe DC operation and atomization. However, electric arcing in the seal was observed during HF ignition (AC) whenever the gap between the rotating and tungsten electrode was too large to establish an electric arc between them.

---

[25] The screw was manufactured with an Allen key intake.

Rotation Sense

The rotation sense of the high frequency spindle is counterclockwise in the current mounting (Figure 3-30).

Collet chuck and union nut have right-hand threads in order to guarantee their tight fit. Otherwise, the arrangement could potentially be unfastened during rotation and cause subsequent loss of the collet chuck and rotating electrode, both constituting a considerable threat due to their rotational kinetic energy.

Spindle Clamps

The high frequency spindle does not possess a fixture and has to be mounted vertically. Thus, it was decided to radially clamp the spindle at housing level, as the housing was made from stainless steel and has about 10 mm wall thickness.

In fact, two identical clamps hold the spindle (Figure 3-30). Although one clamp would be sufficient, a second clamp to secure the spindle is mounted. Both are fastened with one screw using a torque of 20 Nm. A second threaded hole serves as screw intake in order to press the clamp open in case of its plastic deformation, similar to the construction of the torch adapter (Figure 3-25).

Alternatives

There are plenty of commercially available devices such as pressurised (air) turbines, gas turbines, electric motors, and motor-spindles that might fulfil the requirements.

Air turbines are typically powered by pressurised air that drives the turbine blades as it expands, although any other gas would be suitable, e.g. argon. On the one hand, speeds in the order of 100’000 rpm may be reached. On the other hand, power availability is relatively low, because of the over-all design for relatively small pressures (~ 10 mbar); that is, any considerable load on the rotating shaft – be it the electrode itself or any friction – would immediately decrease speed. In our case, off gas ventilation and gas feed would make an external positioning of the spindle necessary with regard to the negative pressure operation of the glovebox.

Gas turbines are driven by expanding gases as well, though the preceding energy supply happens in an internal combustion chamber where the fuel is oxidised. These devices may reach 100’000 rpm and provide considerable torque. By the use of a transmission gear (like for helicopter turbines) a shaft can be rotated. From a practical point of view, exhaust fume ventilation and air feed would make an external positioning necessary.

Direct rotation by an electric motor is another option as it generally provides a lot of torque and do not produce (local) exhaust fumes. Only but important disadvantage is the limitation in rotation speed that rarely exceeds 20’000 rpm while providing enough torque, notably for lab-scale designs. The collet chuck could be directly mounted on the motor shaft.

Integrated motor-spindles require less space and avoid mechanical complexity of a belt-drive, but available motor power is limited. More importantly, the electromagnetic field response of an integrated motor-spindle drive to the arc current that is conducted through the shaft, notably during HF ignition, is unknown. Also, electrical connection to the welding machine circuit would be more complex as motor-spindles do not possess protruding shaft-ends on both sides. Generally, the back-end is occupied by both the gear and motor. However, this spindle type may be an option in non-transferred PREP.

Magnetic bearings (passive or active) may replace mechanical bearings as they run without mechanical friction (and thus exhibit no wear), without lubricant, and at high rotational speeds. Active magnetic bearings are closed-loop controlled and actively control the position of the rotating shaft, e.g. in case of imbalance [Wittel *et al.* 2009].

3.3.14 Carbon Brushes (23)

Function

The carbon brushes were chosen to transmit the electrical arc current from the rotating shaft to the stationary electrical circuit.

Characteristics

Metallic carbon brushes were purchased since they combine both relatively high wear resistance and high current density transmission. In fact, the implemented brushes (type N91, Figure 3-35) withstand radial speeds up to $30\,\mathrm{m\,s^{-1}}$ and current densities up to $35\,\mathrm{A\,cm^{2}}$ (chapter A2), thereby accounting for the maximum rotational speed (chapter 3.3.13) and maximum electric current (chapter 3.3.6), respectively. The high conductivity is due to their metallic additives that consist of 80 % copper (Cu) and 6 % lead (Pb), the rest being graphite.

Carbon brushes are considered consumables, but mechanical wear of carbon or graphite brushes is increased in high purity atmospheres such as applied to the atomizer, actually causing the graphite to sublimate. This phenomenon is due to the reduced presence of oxygen and moisture in the atmosphere. That is, the development of a lubricating film between the brushes and the shaft is hindered, therefore causing dry running and increased wear [Hayward 1990, Slawecki *et al.* 1966].

The brushes have a width, height, and curvature radius of 8 mm, 12 mm, and 5.5 mm, respectively.

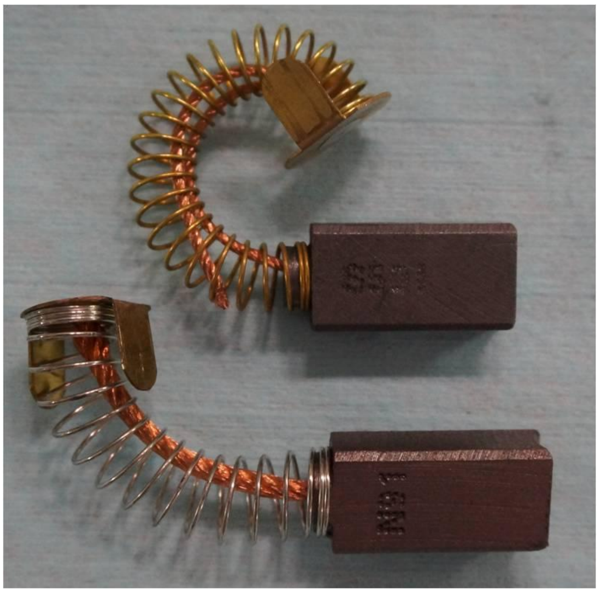

Figure 3-35 Metallic carbon brushes with spring and electric contact. Bottom: type N91.

Preparation

As-fabricated brushes contain enough oxygen and moist to compromise glovebox atmosphere purity due to long-term out-gassing. In fact, brushes are suspected to cause elevated oxygen values ~ 20 ppm. In order to avoid this effect, bake-out of all brushes before mounting was performed at ~ 200 °C for several hours under 2 mbar vacuum.

Alternatives

Given the radial speed of spindle shaft and the electrical current density, different rotary electric transmission options were evaluated. This includes inductive power transmission or liquid rotary connectors.

Induction: This transmission type is contactless and avoids costs related to consumables and maintenance. More importantly, pollution issues due to graphite sublimation would be excluded. However, low current density transmission was the main reason for its non-consideration.

Liquid rotary connectors: They are typically based on liquid metals, namely mercury, gallium-based eutectic alloys (e.g. Galinstan) or eutectic sodium-potassium alloy (NaK) that are considered toxic, metal-corroding, and inflammable, respectively. Nevertheless, mercury-based connectors are being commercialised by Mercotec, but do not exceed 15’000 rpm at present.

Alternative positioning of the brushes inside the spindle housing would have required the construction of a new spindle housing in order to provide access and space for the rotary electrical connector as well as sealing – in comparison with the construction and calculation of a shaft extension screw an incomparably higher effort. Likewise, a positioning of the electrical contact at collet chuck level was ruled out.

3.3.15 Brass Pipes (24)

Function

Brass pipes were purchased in order to contain the carbon brushes. They serve as intermediate conductor of the electrical current from the brush to the collector ring. In addition, they assure constant contact between shaft and carbon brush in combination with the carbon brush spring, thus accounting for brush shortening due to friction-caused mechanical wear (Figure 3-36).

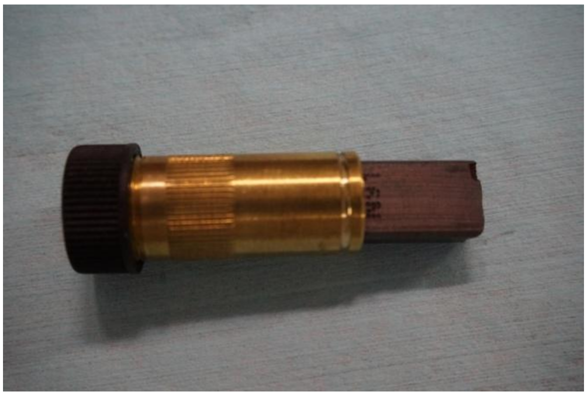

Figure 3-36 Carbon brush mounted on the brass pipe which is closed by a screwable cap at the left end.

Characteristics

Constant shaft-brush-connection is assured by an integrated spring. The spring is fixed in the brass pipe and presses the brush onto the shaft. As a consequence, electrical resistance and break sparks that may alter the welding power and cause electromagnetic perturbations are reduced, respectively. Moreover, the spring provides a constant contact pressure and thus shaft load which, in turn, promoted constant rotation speed and thus both repeatability (chapter 2.3) and powder quality (chapter 2.4).

Maintenance effort is reduced as the brush-pipe arrangement is self-adjusting due to the spring. Also, the brush pipe may be opened at its back-end through a screwable cap nut allowing for exchange of the brush once it is worn out without un-mounting the entire connector. Therefore, the brush pipes are so placed in the collector ring (chapter 3.3.16) as to allow for their accessibility.

3.3.16 Collector Ring (25) with Screw Insulation (26)

Function

Besides holding and fixing the brass pipes, main function of this part is to unify the electric currents coming from the brushes (Figure 3-37).

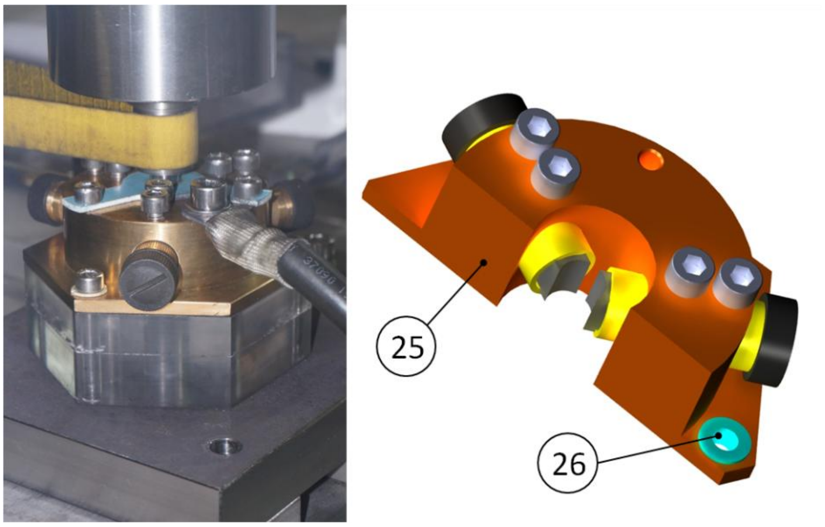

Figure 3-37 Brass collector ring (25) as part of the rotary electrical connector, mounted on the atomizer (left) with carbon brushes and brass pipes. Right: CAD model in sectional view with screw insulation (26).

Characteristics

Altogether three brass pipes are mounted on the collector ring, each of them fixed with two screws. The collector is made from brass and therefore an electrical conductor that allows to join and transmit the three brush currents to the welding machine. Also, the collector design allows free brush positioning and thus contact-pressure adjustment. Typically, a 2 mm distance between brush pipe and rotating shaft was chosen. Moreover, accessibility of the brass pipe back-end for brush maintenance is provided.

The collector ring positions the brushes radially around the shaft extension. The radial arrangement is advantageous as it provides constant brush wear, economy of vertical space, and implementation of three brushes at once and thus a higher applicable electric current.

Plastic journal bearings are used as electrical insulation for the fixing screws that are in direct contact with the atomizer framework (Figure 3-37, 26).

Presuming the DC-mode for standard atomization operations, attention has to be paid when using AC-current for atomization. With regard to the brush arrangement, a three-phase electric motor could be created.

3.3.17 Graphite Dust Seal (22)

Function

Main function of this seal is to prevent graphite or metallic dust – once sublimated from the brushes – from condensation in the spindle roller bearings[26] and on the transmission belt (Figure 3-38). This phenomenon could cause the bearing to fail and would increase belt slip on the spindle pulley (and therefore reduce spindle power), respectively.

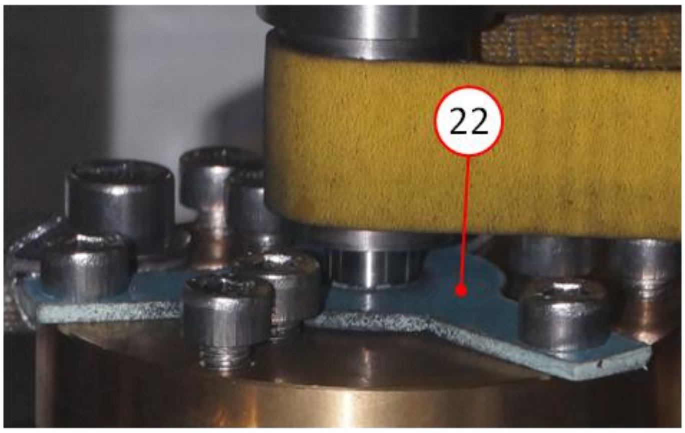

Figure 3-38 Graphite dust seal (22) as mounted on the collector ring.

Characteristics

The seal was designed as radial shaft seal and was made from an aramid fibre and nitrile butadiene rubber (NBR) composite. It is positioned on top of the collector ring below the pulley and spindle shaft housing entry in order to condensate the wear product within the collector ring. The thickness is 2 mm. Thermal treatment at 200 °C under vacuum of 2 mbar was performed for drying and out-gassing.

3.3.18 Insulator and Retention Depot (27)

Function

This part electrically insulates the rotary electrical connector from the atomizer frame and thus glovebox and serves as retention depot for carbon brush wear products, i.e. metallic graphite powder (Figure 3-39).

---

[26] Spindle bearing sealing by pressurized gas was not available.

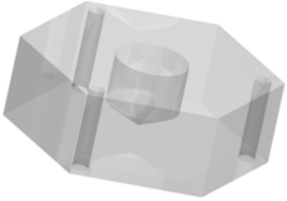

Figure 3-39 CAD model of the insulator and retention depot.

Characteristics

The insulator was made from polycarbonate, which electrically insulates. Its height allows for the exchange of the collector ring and maintenance (dismounting) of the shaft extension screw (Figure 3-37). In addition, a blind hole allows for both collection and removal of the wear products of the brushes.

As the rotary electrical connector assembly is sealed, the sublimated brush material will also deposit on the exposed surfaces including insulator and seal. To which extent this may create an electrically conducting surface on insulating parts, must be examined during prototype operation. The insulator is mounted on the atomizer frame with metallic screws making it necessary to insulate the screws. This is done by plastic journal bearings (chapter 3.3.16).

Alternatives

It is suggested to remove powdery wear products by means of a vacuum cleaner instead of sweeping up as graphite has a tendency to smear.

3.3.19 Variable-Frequency Drive

Function and Setup

The variable-frequency drive (VFD) or frequency inverter allows for control of motor speed and torque of AC powered motors by varying input frequency and voltage. In particular, VFD enables to atomize at different speeds while available torque stays constant over the entire speed range, thereby fostering consistent rotational speed.

Characteristics

The VFD necessitates auxiliary fuses, a power supply unit, filters, and relays and is therefore placed in a switch cabinet (30 kW, 63 A) outside the atomizer glovebox.

The purchased VFD requires a three-phase 400 V and 50 Hz mains supply and may provide a total power of 15 kW (three-phase, 32 A, 400 V, 1600 Hz). This power is intentionally overdimensioned with respect to potential equipment extensions in the future.

Control

In combination with the custom induction sensor of the spindle that provides feedback on the current rotation speed of the spindle, a closed-loop control assuring constant rotational speed of the motor is established. Moreover, the applied Volts-per-Hertz drive control provides constant torque that covers the entire target speed range. Thereby, motor stability in case of load changes is ensured. In fact, torque of AC motors is proportional to U/f [Bose 1981]. The VFD ensures that an increase in frequency and therefore rotational speed results in a proportional rise of voltage to maintain a constant U/f and thus torque[27].

In order to reduce mechanical and thermal stress, VFD automatically and gradually ramps the motor up and down to required speed and standstill, respectively.

Parameter Set

VFD and motor were tuned before delivery (Figure 3-40), but the operator may set all motor parameters by PC using a USB connection to access VFD via the switch cabinet.

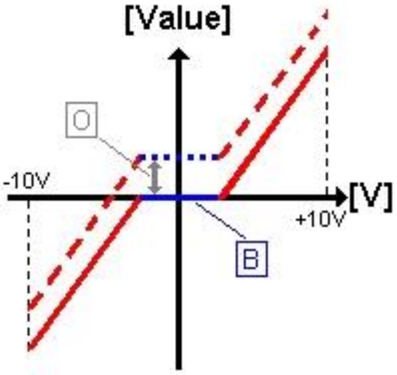

Figure 3-40 Parameterisation diagram of the VFD software. (O) is the rotation offset, (B) is the backlash.

Currently, a potentiometer voltage of 10 V corresponds to a motor speed of 10’310 rpm, resulting in a high frequency spindle speed of about 50’000 rpm. Motor ac- and deceleration ramp are both set to 1000 rpm s^{-1}. The rotation offset and backlash (rotation deadband) are set to 0 rpm and 20 rpm, respectively.

---

[27] Above rated speed, AC motors operate at constant power but lose torque with 1/f as voltage cannot be raised above the nominal value in order to protect motor insulation.

Operator Interface

A customised interface consisting of control panel and potentiometer is implemented to enable the operator to both set and control the rotational speed. Though not installed for prototype operation, both devices may be substituted with a PC with appropriate control software.

The control panel (Figure 3-41) allows for initialisation of the VFD at which the cooling fan is started and drive parameters are loaded. An additional switch is provided to start or stop the motor rotation (using a gradual ramp). The system may also be shut down by pushing the red buzzer. However, VFD will remain in stand-by mode upon this action.

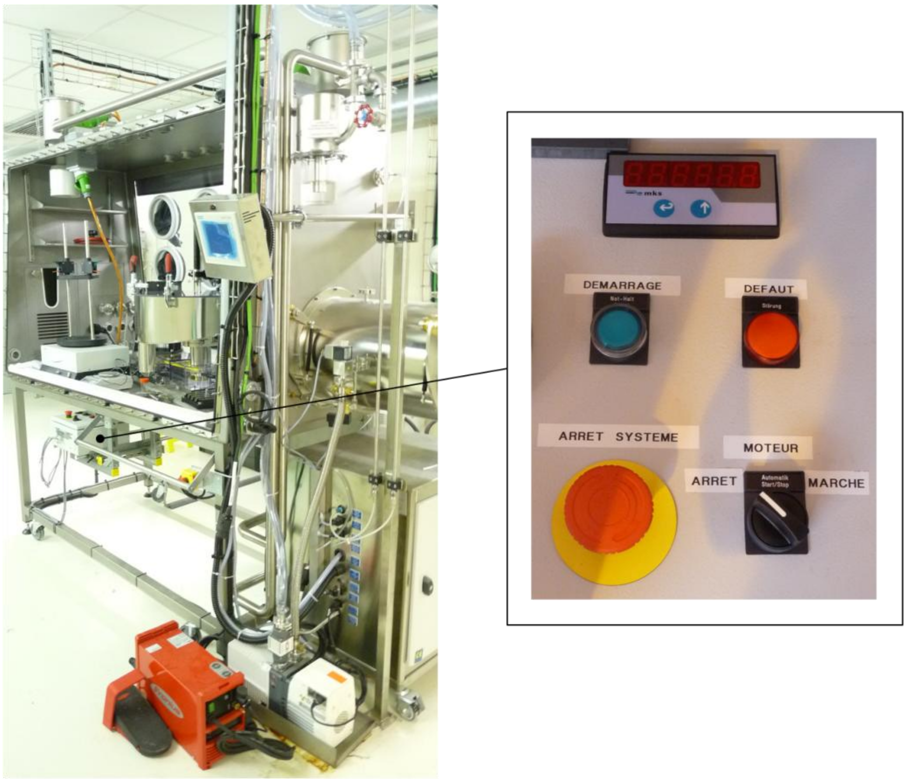

Figure 3-41 Extricable VFD control panel, situated underneath the atomizer glovebox bottom plate.

Rotational speed may be controlled by using the potentiometer as the programmed voltage is proportional to VFD output voltage and thus motor rotational speed. In addition, rotation direction of both the motor and spindle may be determined.

An integrated numeric display (Figure 3-41) allows the operator to monitor the spindle's rotation speed that is transmitted by the inductive sensor. Attention must be paid with respect to the display parameter set as the operator may choose how the sensor signal of the high frequency spindle is interpreted. The display currently receives two signals per rotation from the rotary sensor (chapter 3.3.13) and shows rotational speed in rpm.

3.3.20 Motor (6)

Function and Setup

The motor transforms electric power coming from the variable-frequency drive to both rotational speed and torque in order to power the high frequency spindle (Figure 3-42).

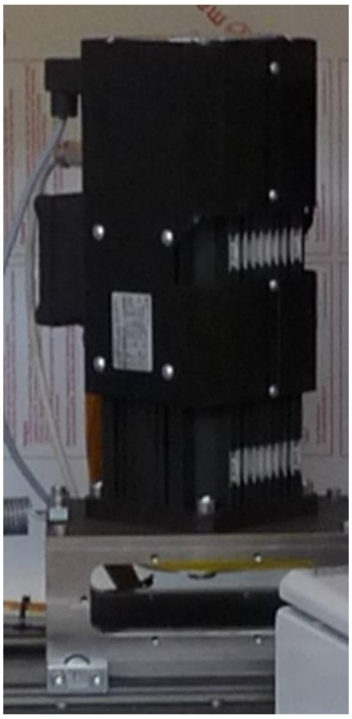

Figure 3-42 Asynchronous induction motor with cooling fan (not visible), mounted on the mobile motor carrier.

Characteristics

The motor has a mountable housing including rotor and stator as well as a custom cooling-fan, integrated encoder, and temperature sensor. The output has a protruding shaft.

A 3 kW electric motor with nominal current, frequency, and voltage of 7.3 A, 339 Hz, and 330 V, respectively, was purchased. It has a rated rotational speed and torque of 9'000 rpm and 3.2 Nm, respectively. Rated torque is available up to 9'000 rpm where it drops to 2.9 kW at 10'000 rpm maximum speed; maximum torque of 9 Nm is reached at 22 A maximum current. Nevertheless, rated torque is so dimensioned as to allow for the acceleration of two shafts, two pulleys, and the rotating electrode to nominal rotation speed within a couple of seconds while overcoming friction of the brushes and aramid/NBR seal as well as additional load. The motor pole-pair number is 2.

The motor including step-motor and pulley weighs about 20 kg. The motor length is 390 mm and the face diagonal measures 190 mm.

Type

An asynchronous motor was chosen as this motor type powers the rotor through electromagnetic induction instead of commutation with brushes, notably graphite brushes. Graphite brushes are subject to excessive wear in high purity atmospheres, e.g. Ar, as reported by [Hayward 1990, Slawecki *et al.* 1966] and may cause the motor to fail.

Mounting

The motor is vertically (upside down) mounted on the mobile motor carrier that is part of the belt-tensioning system (3.3.22). That is, both rotation – motor and spindle – axes are parallel.

Bearings

Hybrid roller bearings for electrical insulation are used.

Shaft

The shaft measures 24 mm and 50 mm in diameter and length, thus providing enough space to mount the custom motor pulley. The shaft provides a keyseat for the keyed joint and it was balanced with half key.

Motor Pulley

The customised motor pulley (Figure 3-43) transmits the motor power to the belt and thus to the high frequency spindle.

It measures 25.4 mm and 120 mm in height and diameter with a circular runout of 0.01 mm. The motor pulley diameter provides a mechanical advantage of about 5.5 with respect to the spindle pulley diameter of 22 mm (chapter A3). Considering motor characteristics, this ratio allows for maximum spindle rotation speeds of up to 55’000 rpm[28] on the one hand. On the other hand, mechanical torque is decreased to around 0.6 Nm at the spindle.

The pulley was made from C45E (Ck45) tempered steel and balanced with half key at 10’000 rpm (rated motor speed). It is mounted on a (conical) taper lock bushing which is a self-locking connection. However, the taper bush itself is coupled by a tight-fit connection to the motor shaft. The key assures non-slip torque transmission between shaft, bushing, and pulley.

The mounting of the pulley to the motor shaft has to be conducted with 17 Nm torque.

---

[28] This value accounts for operating limits of the spindle (~ 50’000 rpm) and estimated belt slip (~ 3,000 rpm at 55’000 rpm).

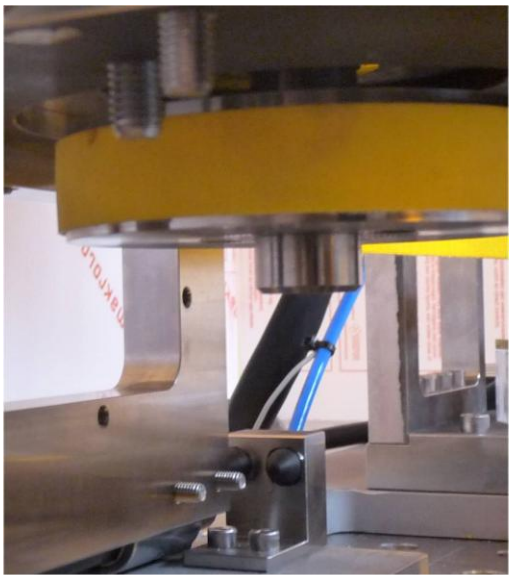

Figure 3-43 Inside view of the motor carrier showing the motor shaft, pulley, and belt (yellow).

Cooling Blower

Forced convection cooling is provided by an integrated brushless 230 V step-motor that is launched automatically when the drive system (VFD) is loaded. This configuration complies with nuclear safety regulations in contrast to cooling systems based on water or oil. Furthermore, the brushless step-motor arrangement avoids problems related to the use of graphite-based brushes in high purity Ar atmospheres that might cause cooling and hence motor to fail.

Sensors

The motor comes with an integrated speed encoder and thermocouple that can be used for closed-loop control of motor rotation and temperature monitoring. The encoder, though, is dispensable since the motor is controlled through the signal of the spindle encoder.

Alternatives

Gas turbines and piston engines – in contrast to electric motors – do not provide full torque over the full speed range. Intrinsically, they do generate (local) exhaust fumes, thereby necessitating the installation of additional exhaust gas ventilation. Moreover, installation of a supply chain for fuel and oxidiser is needed. In contrast, electrical supply is generally available on industrial sites (see also 3.3.13).

Air turbines driven by pressurised air or any other gas offer high rotation speeds, though significantly smaller torques (see also chapter 3.3.13).

3.3.21 Belt (8)

Function

The belt transmits both power and mechanical advantage from the motor pulley to the high frequency spindle's pulley (Figure 3-44).

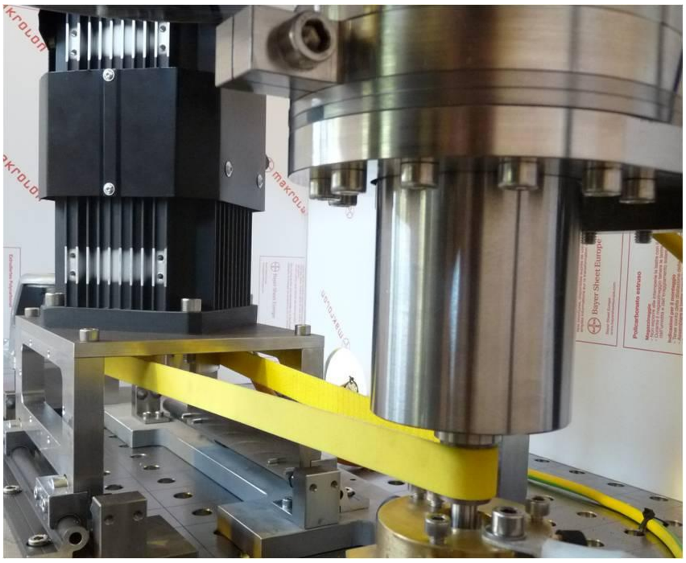

Figure 3-44 Belt-drive arrangement showing motor, motor carrier, belt, and high frequency spindle.

Characteristics

A flat, endless, and coated belt configuration was chosen. An endless belt avoids induction of vibration into the system due to the absence of joints, whereas a flat belt accounts for the applied radial speeds and thus radial force. The belt fabric is made from polyester (PE) which combines elasticity with elongation-resistance while being also anti-static. In order to protect the belt against fraying and wear, the running tread is coated with polyurethane (PU).

A belt that measures 1.5 mm, 25 mm, and 1060 mm in width, height, and length was chosen. Since the current atomizer configuration reaches radial speeds of $63\,\mathrm{m\,s^{-1}}$, a belt enduring speeds up to $70\,\mathrm{m\,s^{-1}}$ was purchased. The belt length accounts for the minimum distance between the spindle and motor axis on the one hand, on the other hand for limited space within the glovebox (chapter A4).

It requires a minimum pre-tension of 0.3 % to 0.4 %, which – for its present length – equals to an elongation of 3 mm to 4 mm, respectively. A higher pre-tension is allowed but increases wear and should not exceed the maximum value of 0.8 % or 8 mm. The belt's stress-strain curve shows linear behaviour between 0 % and 1 % elongation and reaches a restoring force of 400 N at the latter value; the belt's ultimate tensile strength is reached at 3'500 N.

Additional elongation of the belt due to centrifugal force between 50 m s^{-1} and 70 m s^{-1} was reported to reach between 0.5-1 % [Wittel *et al.* 2009]; the supplier suggested 1.5 % for the atomizer application. The latter value was taken for conservative approximation of belt lengthening during operation. Thus, an additional elongation of around 5 mm to 16 mm was taken into account regarding the current belt configuration. For compensation, the belt tensioning system was designed and constructed.

3.3.22 Motor Carrier (31)

Function

It transmits forces and torque caused by the motor to the hybrid bearings and allows for linear relocation of the motor pulley. This latter feature is needed to apply pre-tension to the belt and to keep a constant centre axis distance between motor and spindle and thus a constant belt tension during operation (Figure 3-45).

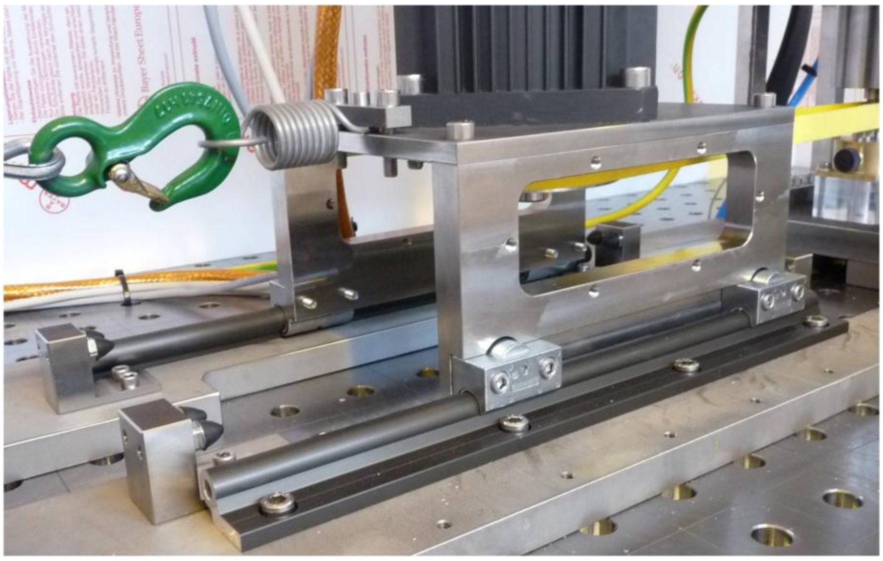

Figure 3-45 Motor carrier mounted to the hybrid bearings and linear guide rails.

Characteristics

The motor carrier was made of stainless steel. It consists of a main plate with a centre hole for motor positioning and mounting, two supporting side plates, four bearing connections, and a clamping connection for the tension spring. The carrier is horizontally moveable on linear guide rails (chapter 3.3.24) in order to adjust the distance between the motor and spindle rotation axis for pre-tension and dynamic belt load control.

Elongation Scale

A metric division scale (mm) is connected to the mobile carrier that allows for control of the applied belt pre-tension (Figure 3-46).

The indicated value corresponds to the change in axis-centre distance between the spindle and motor shaft rotation axis. The difference in belt elongation is approximately twice the difference in axis-centre distance [Wittel *et al.* 2009].

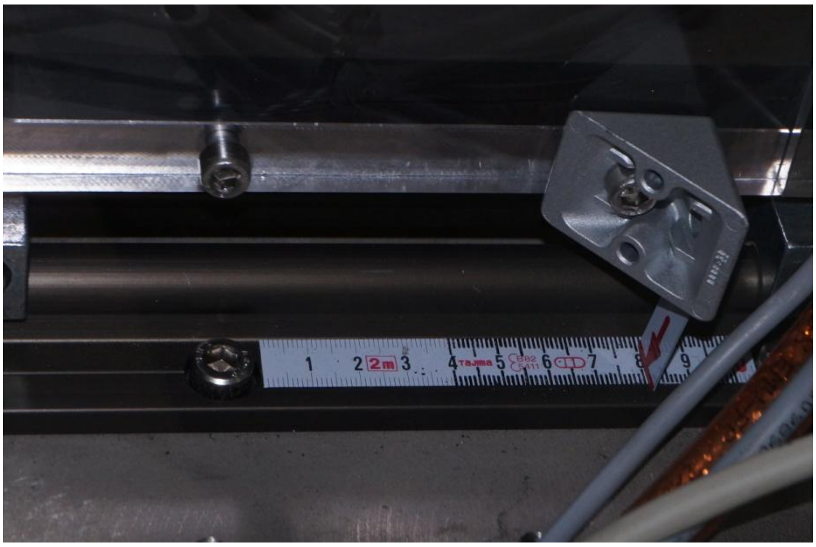

Figure 3-46 Metric division scale on motor carrier backside indicating belt elongation and pre-tension.

3.3.23 Tension Spring (29)

Function and Setup

The customized tension spring in interaction with the belt ensured constant belt-tension and thus belt-fit over the entire atomizer rotational speed range. In addition, power-loss and belt-wear due to slip is decreased.

Characteristics

A spring with an intrinsic pre-tension of 22.91 N at 88.9 mm untensioned length and a spring rate of 5.62 N mm^{-1} until about 130 mm length(or 254 N) was purchased. Figure 3-45 shows the spring in idle state, Figure 3-47 under load.

Pre-Tension

Typically, an axis-centre distance increase by 3 mm was applied for pre-tension, resulting in a belt elongation, lengthening and pre-tension force of 0.6 %, 6 mm and 228 N, respectively (chapter A6). The elongation value is a compromise between required minimum and allowed maximum belt elongation of 0.3 % and 0.8 %, respectively, in order to guarantee fit and increase service life (chapter 3.3.21).

Dynamic Behaviour

Due to centrifugal force, the belt may be exposed to an additional elongation of 1.5 % at maximum rotation speed [Wittel *et al.* 2009]. As this value is more than twice the initial elongation, pre-tension would be levelled. Hence, belt adhesion would decrease, eventually resulting in slippage or detachment of the belt. The former, in turn, would cause loss in power transmission and increased belt-wear.

The spring accounts for this effect by keeping pull on the motor carrier and thus belt. Indeed, the spring rate was so chosen as to guarantee that pull is greater than the minimum pre-tension force of 121 N in any case (chapter A6), even if belt elongation due to centrifugal force exceeds 1.5 %. In addition, the chosen spring rate allows for a moderate decrease in belt tension with increasing rotational speed. As a result, slippage is avoided and system stability in terms of rotation speed and torque promoted – regardless of the electronic closed-loop control.

Alternatives

Instead of using a tension spring, a similar tensioning principle can be realised by a weight hanging on a wire cable that is guided through a pulley system in order to apply a pull force to the motor carrier.

Tensioning systems relying on other principles may be found in [Wittel *et al.* 2009].

3.3.24 Linear Guide Rails (30) and Hybrid Bearings (32)

Function

In order to allow for and guide the movement of the motor carrier, two linear guide rails and four hybrid[29] bearings were purchased and are mounted to the motor carrier and framework. The linear guide rails support the motor carrier mass and allow for its linear movement along the extension of the centre-axis line. The hybrid bearings connect the motor carrier to the guide rails for both motor carrier relocation with minimum friction and motor torque compensation (Figure 3-45).

Characteristics

Linear guide rails and hybrid bearings were made of aluminium, though the sliding surface of the hybrid bearings was made from a special plastic.

---

[29] In this context, hybrid refers to their dual functionality as both roller and linear bearings.

Bearings with a coefficient of static and dynamic friction of < 0.1 and 0.04-0.05, respectively, were chosen. As a result, a pull force of ≤ 30 N (~ 3 kg) is needed for carrier relocation due to the combined motor and carrier mass of about 30 kg.

The static and dynamic bearing load capacity is 400 N, respectively. However, the dynamic load capacity is valid only for a total covered distance of not more than 10 km with respect to the hybrid bearings.

3.3.25 Winch (28)

Function

The purchased aluminium winch allows the operator to apply variable pre-tension to the belt.

Characteristics

The winch's load capacity was chosen to 63 kg or 630 N and thus higher than the sum of maximum pre-tension of the belt and motor carrier bearing friction (Figure 3-47, A5, A7).

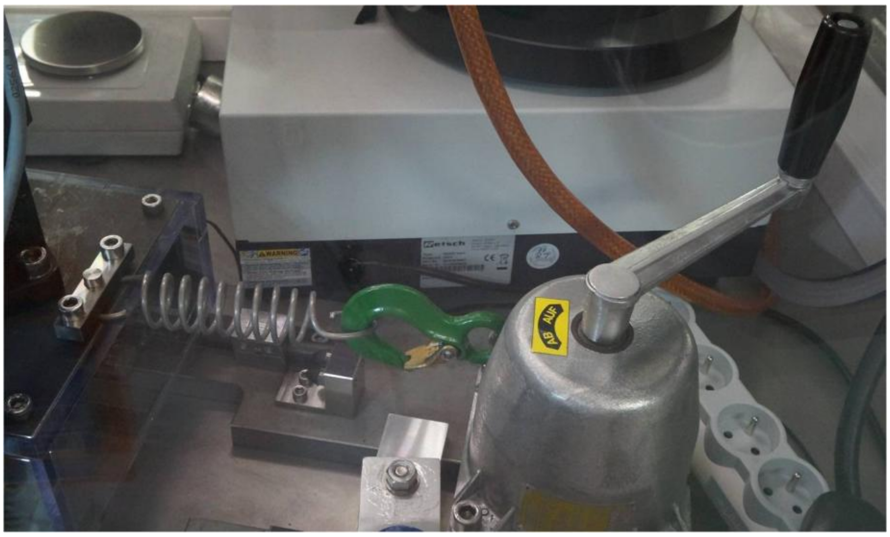

Figure 3-47 Winch with handle bar and tension spring (under load) pulling the motor carrier.

To apply pre-tension to the belt, the wrench's wire rope is pulled in by manual turning of the winch's handle bar. An automatic ratchet pawl brake for load in tow ensures winch position upon operator's absence. For safety, the handle bar may be removed under load to prevent any unintentional altering of the applied belt tension during atomizer operation

Alternatives

A free hanging mass might be used for applying pre-tension instead of the winch. However, for variable pre-tension a change of mass is necessary.

3.3.26 Bump Stop (33)

Function

In case of a belt rupture, the motor carrier will be accelerated towards the winch due to the applied pre-tension force. As to attenuate the subsequent impact and to protect motor and bearings from shock-induced damage, bump stops are placed at the guide rail ends to absorb the carrier's kinetic energy (Figure 3-45).

Characteristics

Bump stops made from attenuating natural rubber were purchased that are parabolic in shape, offering a progressive force–distance characteristic. It is screwed onto a support made of stainless steel that, in turn, is mounted on the atomizer bottom plate (framework).

3.3.27 Powder Collection Chamber (4)

Function

Main function of the powder collection chamber is to serve as a collection repository for atomized powder. In this function, it minimises the dissemination of radioactive and fissile material within the glovebox. In addition, it serves as mechanical protection against the accidental ejection of the rotating electrodes or (thermally) hot and abrasive powder. Also, it provides access for rotating electrode mounting and powder recovery (Figure 3-48).

Characteristics

The entire chamber was made of stainless steel (1.4301) with 3 mm wall thickness for structural integrity and safety, thereby accounting for its own weight and ejection of rotating parts, respectively. Stainless steel was chosen as it is relatively hard, ductile and has a melting point that exceeds the one of U8Mo.

Droplet solidification prior to impingement onto the chamber wall is ensured by the collection chamber diameter that measures 600 mm. The chamber height above the rotating electrode top was estimated to 45 mm in order to allow the spray cone to spread out without interference.

The bottom of the chamber is inclined by 10° and electrically polished to facilitate powder recovery. Attention was paid to ensure that the welding connection is round off and exhibits no pores with respect to particle retention. In addition, a little socket (hollow cylinder) at the lowest point of the recipient enables the operator to empty the collection chamber without dismounting of the entire chamber.

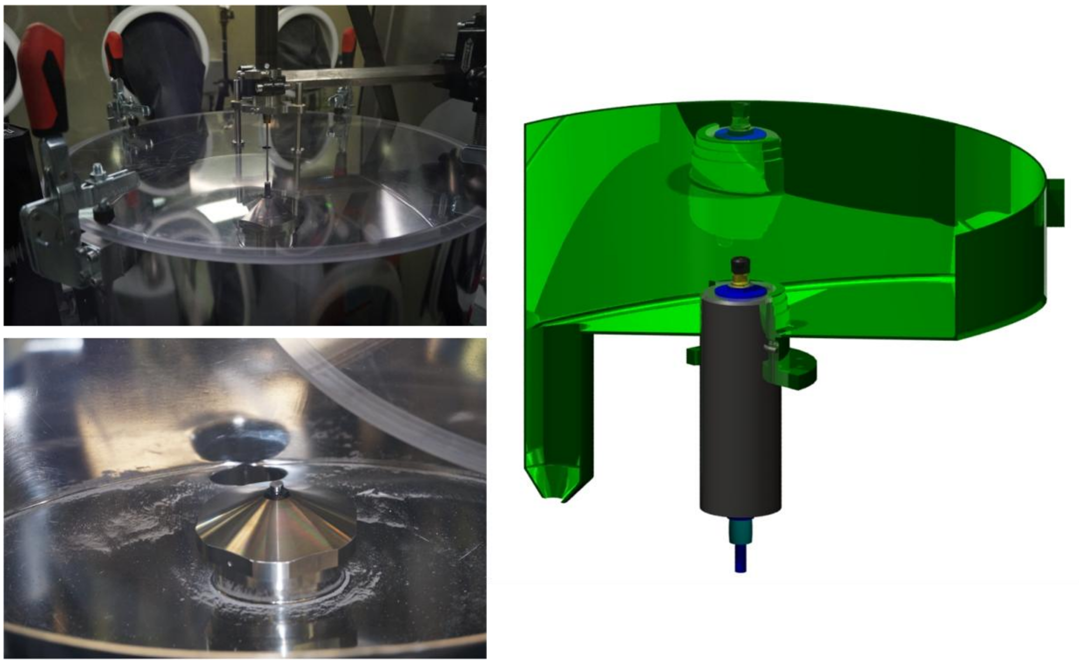

Figure 3-48 Powder collection chamber in operational condition with closed quick release clamps before atomization, after atomization with U8Mo powder, and as sectioned CAD model, showing both the chamber geometry and high frequency spindle positioning.

Cover Hood

For (un-)loading the rotating (U8Mo) electrode, the collection chamber is accessible via the top through a removable cover hood. It was made from polycarbonate (PC) that shows substantial impact strength ["Makrolon® AR" 2014]. Furthermore, a transparent polycarbonate type was chosen giving the operator the possibility of visual control of the atomization procedure.

It has a centred orifice of 10 mm diameter to provide accessibility for the tungsten electrode to the powder production chamber. The orifice is intentionally small to prevent accidentally ejected rotating electrodes from escaping the powder collection chamber. Two threaded holes beside the orifice were drilled for linear guide rails mounting. The thickness of the cover hood is 10 mm and the diameter exceeds the diameter of the powder production chamber to facilitate lifting.

Quick Release Clamps

Fixation of the cover hood to the powder collection chamber is realised be means of four quick release clamps that are self-locking once in closed position.

Alternative

Alternatively, REP may be implemented with a horizontal rotation axis for industrial purposes, i.e. facilitated powder recovery. Also, a customised vacuum cleaner might be used for powder recovery. In addition, an electromagnetic vibrator or imbalance motor, connected to the collection chamber, may be used to support powder recovery.

3.3.28 Powder Seal Screw (3)

Function

The rotating electrode protrudes into the powder collection chamber through the powder seal screw. In addition, this part was designed to give the operator access to the collet chuck for rotating electrode mounting while sealing the high frequency spindle from both powder and dust generated by the atomization process (Figure 3-49).

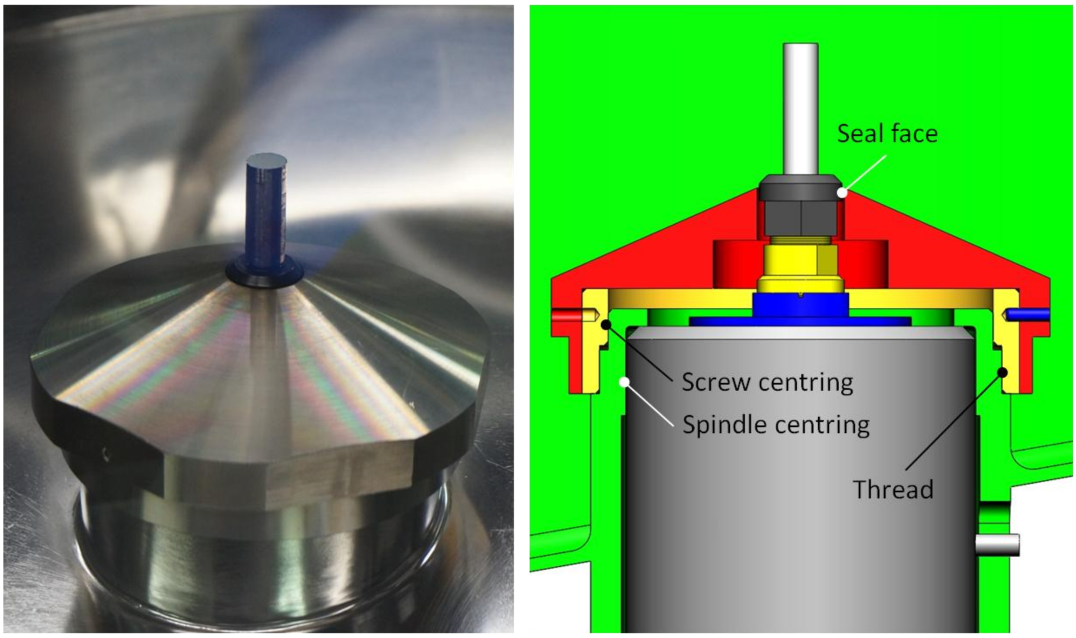

Figure 3-49 Mounted powder seal screw on the atomizer prototype and as a sectioned CAD model for construction.

Characteristics

The powder seal screw was made from stainless steel (1.4301) and has a centred hole through which the collet chuck and rotating electrode protrudes into the powder collection chamber. The thereby created interface needs to be sealed in order to prevent powder from entering the high frequency spindle. For this purpose, the hole of the (stationary) powder seal screw is positioned at collet nut level and designed as a gap ring creating a clearance of about 250 µm around the nut. This arrangement is considered the simplest sealing between stationary and rotating parts [Wittel *et al.* 2009], but accounts for relatively high rotating speeds and limited construction space.

As the spindle shaft's nominal rotation sense is counterclockwise[30], the left-hand thread of the powder seal screw – tightened counterclockwise as well – ensures a firm fit at any time.

In order to provide access to the collet chuck for rotating (U8Mo) electrode mounting, the powder seal was designed as removable and female part of the screw connection. Accordingly, the spindle may be centred at its head in the powder collection chamber while keeping the collet chuck horizontally accessible for tools. The thread of the screw was turned due to its non-standard size. Also, it was made from brass, in contrast to the male thread of the powder collection chamber that was made from harder stainless steel. This combination avoids thread seizing, which may occur in particular for turned workpieces. However, radial centring of the screw with respect to the powder collection chamber is mandatory to ensure a constant gap distance and avoid contact between the screw and rotating parts.

The top of the screw is inclined to account for the droplet trajectory. Moreover, a hexagonal side design was chosen to provide grip for manual screwing.

Alternatives

A fixed or removable seal might be designed and implemented below the collet chuck, thereby enabling the operator to access the collet chuck directly. This design might necessitate a custom collet chuck as the current part does not possess a sufficiently long cylindrical geometry at its food regarding a radial seal arrangement.

---

[30] Technically, rotation in both senses is possible. Yet, safety considerations require the spindle to turn in the opposite sense of the right-hand tightened collet chuck in order to guarantee self-locking in case of radial friction to avoid loss of collet, collet chuck, and rotating electrode.

II

Experimental

4

Process Repeatability

In this chapter, atomizer performance under operating conditions with focus on repeatability of parameter settings and experimental results is investigated. Due to safety considerations, a limitation in UMo supply, and in order to foster a consistent parameter set, experiments were conducted with surrogate material. The results of this study constitute a first quantitative point of reference for process repeatability. The decision whether or not to continue experiments with the presented atomizer design – notably parameterisation involving UMo – was based on the experimental results of this repeatability study.

4.1 Experimental Setup

Stainless steel 1.4301 (EN-10088-3: 1.4301/X5CrNi18-10) rotating electrodes were used in order to evaluate the repeatability of the atomizer prototype's experimental results.

Atomization of electrodes machined from standard stainless steel offered the advantage of electrodes that – in contrast to cast U8Mo electrodes – had the same length, same diameter, same alloy composition, same chemical purity, and that were homogeneous. Moreover, the material was readily available, cheaper, easier to handle (since it is neither radioactive nor fissile), and the electrodes were faster[31] to fabricate than U8Mo electrodes. In this respect it is mentioned, that the amount of available U8Mo electrodes for the project was limited to 25 pieces, of which parameterisation experiments necessitated the majority. Also, purchased U8Mo rotating electrodes proved to be inhomogeneous (Figure 5-14) and were hence not the same, therefore violating the prerequisite of repeatability evaluation.

---

[31] This statement refers to production capacities at TUM and CERCA.

Atomization was conducted at 40'000 rpm and 70 A using a rotating electrode of 10 mm diameter and 30 mm length as well as a WC20 tungsten electrode of 3.2 mm diameter under an atmosphere of < 10 ppm and < 5 ppm moisture and oxygen, respectively. These parameters were reported as being appropriate for producing spherical UMo particles in the targeted size range [Clark *et al.* 2007].

Only varying parameters were the length of the atomized electrode as well as electric arc, since both parameters are controlled manually and visually due to the atomizer design. Nevertheless, it was the objective to maintain an electric arc length of about 10 mm.

4.2 Results and Discussion

The rotational speed of each experiment was repeated with a precision of ± 500 rpm (~ 1 %) for a potentiometer was used to control its set point. It is pointed out, though, that the variation of rotational speed during atomization did not exceed ± 50 rpm (1 ‰).

Due to the manual torch infeed control, the electric arc length may vary from 2 to 20 mm. This variation was levelled through training, though, resulting in an electric arc length of 10 ± 5 mm. Due to the variation in electric arc length, the nominal arc current occasionally decreased by 1 A (~ 1 %) during atomization. This decrease, however, caused an automatic response of the arc welder, which resulted in a rise of the electric arc voltage for compensation (Figure 3-20 and Figure 3-21).

Generally, a bimodal particle size distribution (PSD) was observed for every atomization of 1.4301 conducted under the mentioned conditions (Figure 4-1). This pronounced bimodal distribution is characteristic of atomization in the direct droplet formation regime (DDF, chapter 6.1) where a small and large spherical droplet is produced when the liquid (melt) is ejected from the rotating electrode [Champagne and Angers 1984, Lawley 1992, Yule and Dunkley 1994]. The droplet formation mechanism prevailing in DDF causes the particles to be spherical in shape and also gives rise to a number distribution with equally high peaks as reported by [Champagne and Angers 1984].

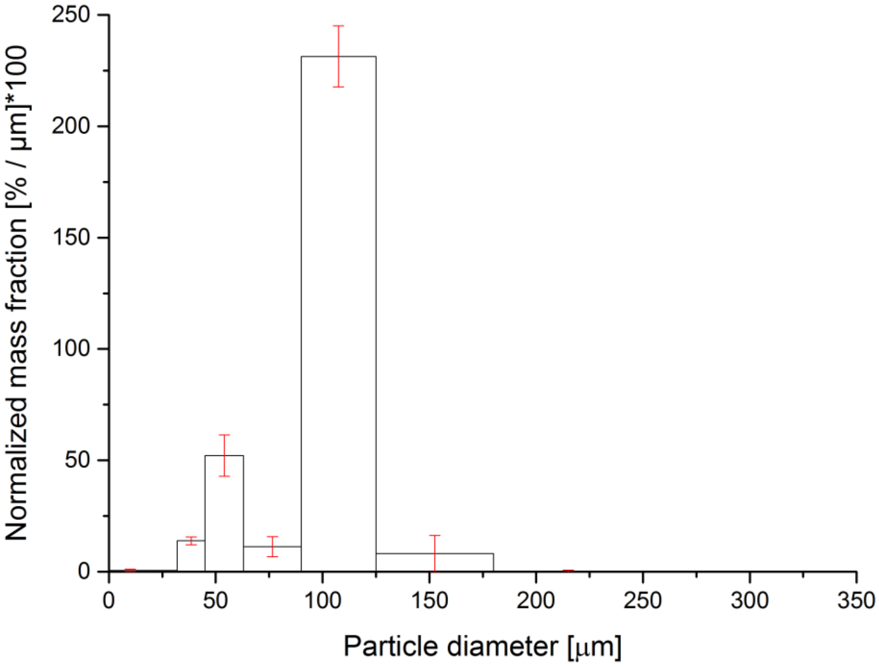

Figure 4-1 Average particle size distribution of 11 atomized stainless steel (1.4301) rotating electrodes with 10 mm diameter and 30 mm consumable length atomized at 40’000 rpm and 70 A, and corresponding standard deviation (red error bars) from Table 4-2.

As predicted in [Lawley 1992, Yule and Dunkley 1994] for REP atomization, a narrow particle size distribution was obtained given an average inclusive graphic standard deviation (chapter 7.1.3) of around 20 µm ± 3 µm with respect to a median and mean of 105 µm, respectively.

All batches consisted of almost entirely spherical or near-spherical particles (Figure 4-2) as indicated by the PSD (Figure 4-1). The smooth and silvery particle surfaces suggest a low surface oxidation, if at all.

In terms of result repeatability, it can be seen from Figure 4-1 and Table 4-1 that the peaks of the average particle-size distribution had a standard deviation of not more than 18 %. In fact, the standard deviation of the global maximum was less than 6 %. Median and mean of the particle size distribution were mostly equal and the standard deviation of their mean values was below 3 % (Table 4-2). However, this does not mean symmetry of the distribution as can be seen from Figure 4-1.

From the initial rotating electrode mass of about 21 g, an average of 14 g was atomized per run, resulting in an average powder yield-efficiency of 67 %. This manually controlled parameter had a standard deviation of 8 % (Table 4-2).

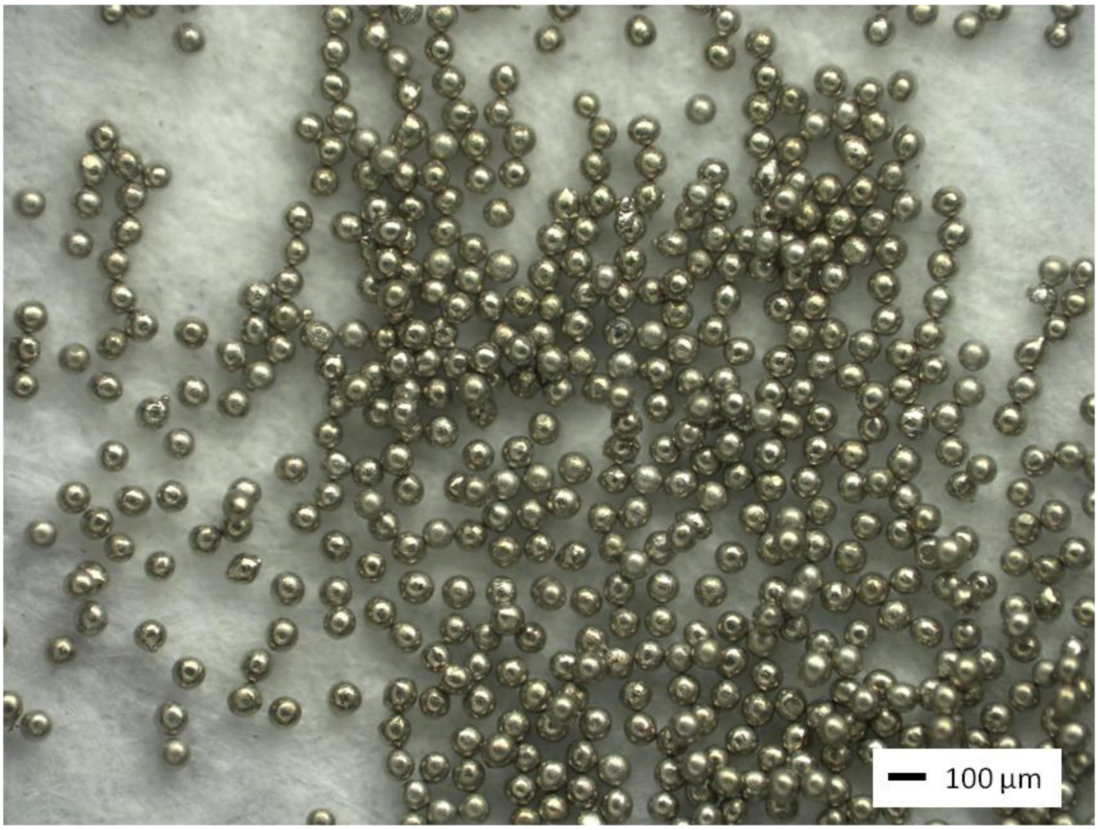

Figure 4-2 Optical micrograph of typical 1.4301 stainless steel atomized powder produced under argon atmosphere using REP. The powder was produced at 35’000 rpm, 60 A, and under argon atmosphere; the electrode had a diameter of 10 mm [Schenk *et al.* 2013].

For the given experimental conditions, the average atomization time was 34 s.

Interestingly, the apparent mass flow rate had a relatively small standard deviation of about 2 % (Table 4-2). This result is worth mentioning as the electric arc length between the electrodes was controlled manually and therefore not constant. The observation hence indicates that the closed-loop control of the arc welder maintained the heat input and thus mass flow rate approximately constant (chapter 5.1.2).

Dry sieving was conducted by two different operators. The procedure did not seem to have considerable influence on the PSD characteristics. Therefore, an extensive study on the influence of the sieving procedure on the PSD was not conducted.

Table 4-1 Particle size distributions of atomized 1.4301 stainless steel (Inox) and resulting mean with corresponding standard deviation. Experiments were conducted at 40’000 rpm ± 500 rpm, 70 A, < 10 ppm moisture, < 5 ppm oxygen, with machined rotating electrodes with 10 mm diameter and 30 mm consumable length. Sieving time and amplitude for each powder batch was 6 min and 1 mm, respectively.

Mesh size	Normalized mass fraction												
	Inox-002	Inox-003	Inox-005	Inox-006	Inox-008	Inox-009	Inox-010	Inox-011	Inox-012	Inox-013	Inox-015*	Mean	SD
[µm]	[%/µm] *100	[%/µm] *100	[%/µm] *100	[%/µm] *100	[%/µm] *100	[%/µm] *100	[%/µm] *100	[%/µm] *100	[%/µm] *100	[%/µm] *100	[%/µm] *100	[%/µm] *100	[%]
0	0.00	0.73	0.00	1.14	0.00	1.15	0.90	1.03	1.06	0.00	1.01	0.64	81.25
32	12.24	11.99	16.45	14.02	16.27	14.17	14.96	13.63	15.59	11.38	11.97	13.88	13.04
45	50.72	57.16	71.29	54.66	52.50	54.86	49.63	52.86	51.05	47.48	31.70	52.17	17.72
63	4.65	5.77	8.87	9.18	7.84	13.37	11.74	13.12	12.51	17.04	19.22	11.21	40.09
90	248.15	244.29	231.21	235.74	241.99	226.76	231.78	228.35	228.76	232.19	196.03	231.39	5.91
125	2.13	1.56	3.11	5.43	2.95	8.98	8.25	8.95	9.09	7.47	31.36	8.12	101.67
180	0.00	0.00	0.00	0.00	0.00	0.00	0.00	0.00	0.00	0.00	1.95	0.18	331.66
250	0.00	0.00	0.00	0.00	0.00	0.00	0.00	0.00	0.00	0.00	0.00	0.00	-
350	0.00	0.00	0.00	0.00	0.00	0.00	0.00	0.00	0.00	0.00	0.00	0.00	-

* Atomization of batch Inox-015 was executed by a different operator.

Table 4-2 Characteristic values of each particle size distribution from Table 4-1 as well as of the corresponding atomization process.

	Inox-002	Inox-003	Inox-005	Inox-006	Inox-008	Inox-009	Inox-010	Inox-011	Inox-012	Inox-013	Inox-015	Mean	SD [%]
Median [µm]	105	105	104	105	105	105	105	105	105	105	109	105	1.21
Mean [µm]	105	105	99	105	105	105	105	105	105	105	111	105	2.56
Inc. gr. stand. deviation [µm]	18	18	23	18	18	19	19	19	19	18	28	20	15.72
Atomized mass [g]	12.25	12.62	14.6	14.32	14.37	13.39	14.05	15.07	14.83	12.89	15.51	13.99	7.59
Powder yield efficiency [%]	57	60	70	68	69	65	67	73	72	59	75	67	8.72
Atomization time [s]	nm	nm	nm	nm	32.1	31.5	33.1	34.9	nm	nm	36.5	33.6	6.13
Apparent mass flow rate [g/s]	nm	nm	nm	nm	0.448	0.425	0.424	0.432	nm	nm	0.425	0.431	2.35

nm: not measured

4.3 Measurement Uncertainty

The variation of particle mass fraction may be due to statistical errors caused by the weighing scale that showed an experimental deviation of up to ± 0.04 g, thus deviating from manufacturer's data that stated a precision of ± 0.01 g. As the atomized powder mass was determined by subtraction of the posterior rotating electrode mass (rest mass) from the prior rotating electrode mass, a systematic uncertainty of ± 0.08 g was used.

Atomization time was manually measured twice – during experiments and through film recordings. A measurement accuracy of ± 0.3 s was postulated.

Powder sieving may cause additional uncertainty as particles can get lost during machine filling, get stuck in the meshes, or due to sieving time, amplitude, and operator [Yule and Dunkley 1994]. Woven meshes below 40 μm are generally avoided [Yule and Dunkley 1994] as they tend to give improper results due to adhesion effects and fabrication precision of the mesh. Nevertheless, an additional sieve below 45 μm was used to get an idea of the complete PSD due to lack of other appropriate options.

Another factor that affected the measurement was the powder collection process. A brush was used to sweep up the powder into a smaller and mobile container. Particles might have been left in the powder collection chamber or adhered to the brush and were collected randomly after following runs.

Furthermore, it was observed that small particles with a diameter below 32 μm tended to adhere to recipient walls – be it plastic, steel, or glass.

4.4 Comparison

Neither INL (Idaho National Laboratory) nor CCHEN (Comisión Chilena de Energía Nuclear) has published data on repeatability studies of their REP atomizers. However, INL released a report based on experiments with U8Mo stating – among other results – a lack of process repeatability [Moore and Archibald 2014]. Namely, two slightly different parameter sets were each repeated once: Thereby, doubling of atomization time and a significant shift of the PSD towards smaller particles was observed at full rotational speed of 45'000 rpm[32] and an electric arc current of 80 A. Though, the opposite behaviour was obtained at 90 % rotational speed using the same electric arc current, resulting in an increased atomization time by 50 % and a slight shift towards coarser particles. The author suspects an insufficient connectivity of the graphite brush arrangement of the INL atomizer to be responsible for the variation of results.

---

[32] The INL atomizer lacks precise information on its rotational speed as the latter is not monitored.

4.5 Conclusion

Requirement fulfilment regarding repeatability was a precondition for costly and time-consuming atomizer parameterisation experiments involving UMo. The repeatability of parameter settings and experimental results of the implemented REP atomizer were quantified using 1.4301 stainless steel. In particular, obtained particle size distributions and their corresponding characteristic values as well as general process characteristics were investigated using a consistent parameter set that was suspected to be suitable for UMo powder production.

Each particle size distribution had the same, bimodal form with a distinct global maximum with little variation. The corresponding median and mean were generally alike with standard deviations of ~ 1 % and ~ 3 %, respectively. The almost negligible variation throughout the study might be due to small variations in the initial parameter set.

Each powder batch consisted almost entirely of spherical or near-spherical particles with smooth and silvery surfaces, indicating a consistent atomization regime and appropriate atmosphere, respectively.

The manual torch infeed had a clear effect on atomized electrode length and thus atomization efficiency. Interestingly, though, the manual operation only marginally affected the apparent mass flow rate given its standard deviation of about 2 % – although the electric arc length varied considerably. Notably, the decrease in electric arc current due to variation of the electric arc length was below ~ 1 A. It is concluded that the ΔU closed-loop control of the arc welder (chapter 3.3.6) worked effectively.

Manual dry sieving seemed to give consistent results with respect to PSD characteristic values. However, the influence of the sieving procedure should be investigated using both a reference powder and different operators in order to quantify its contribution to variations in the PSD. Notably, a lower standard deviation within each mesh size range is needed for industrial production.

To what extent other UMo atomizers provided repeatable results, was not reported in the respective publications. The obtained experimental results, though, allow for the conclusion that the developed system architecture (chapter 3.1.3) and its components (chapter 3.3) are capable of providing both repeatable process parameter settings and repeatable experimental results.

5

Mass Flow Rate

The mass flow rate is an important parameter in centrifugal atomization as it directly influences the droplet formation mechanism and thus particle shape. It also has influence on the mean particle size in certain atomization regimes. Despite its importance, experimental mass flow rates of UMo and uranium generated in REP have not been published to this day. Also, there is no commonly accepted model in REP relating the mass flow rate to process input parameters. Thus, quantification of the mass flow rate and model evaluation with respect to UMo is the main interest of investigation in the following chapter.

5.1 Background

5.1.1 Definitions

Apparent Mass Flow Rate

As the mass flow rate could not be measured directly, it was derived from the ratio of the atomized mass of the rotating electrode and the corresponding atomization time. The atomized mass was obtained by subtracting the rest mass of the rotating electrode (after atomization) from its initial mass (prior to atomization). It is therefore an average value:

$$\dot{m}_{\mathrm{app}} = \frac{m_{\mathrm{re}} - m_{\mathrm{rest}}}{t_{\mathrm{a}}} \tag{5.1}$$

$\dot{m}_{\mathrm{app}}$	Apparent mass flow rate [g/s]
m_{re}	Rotating electrode mass [g]
m_{rest}	Rest mass of the rotating electrode after atomization [g]
t_{a}	Atomization time [s].

Manual measurement of the atomization time started at the ignition of the electric arc and was stopped at its extinction. For traceability and higher precision, it was measured twice – through film recordings and during experiments.

Electric Arc

The electric arc power is defined as:

$$P_{\mathrm{el}} = UI \tag{5.2}$$

P_{el}	Electric arc power [W]
U	Electric arc voltage [V]
I	Electric arc current [I].

Considering equation (5.12) and chapter 3.3.6, the minimum electric power provided by the implemented arc welder for a given electric arc current is:

$$P_{\mathrm{el,min}} = (10\,\mathrm{V} + 0.04\,\frac{\mathrm{V}}{\mathrm{A}} \cdot I) \cdot I \tag{5.3}$$

$P_{\mathrm{el,min}}$	Minimum electric arc power [W]

$$P_{\mathrm{el,min}} = 10\,\mathrm{V} \cdot I + 0.04\,\frac{\mathrm{V}}{\mathrm{A}} \cdot I^2 \ . \tag{5.4}$$

The maximum electric power that can be provided by the TIG arc welder for a given electric arc current is determined by its operating range, notably its maximum electric arc voltage of 16.8 V (chapter 3.3.6):

$$P_{\mathrm{el,max}} = 16.8\,\mathrm{V} \cdot I \tag{5.5}$$

$P_{\mathrm{el,max}}$	Maximum electric arc power [W].

The average electric arc power in this work was defined as:

$$P_{\mathrm{el,av}} = \frac{P_{\mathrm{el,max}} + P_{\mathrm{el,min}}}{2} \tag{5.6}$$

$P_{\mathrm{el,av}}$ Average electric arc power [W].

$$P_{\mathrm{el,av}} = \frac{16.8\ \mathrm{V} \cdot I + (10\ \mathrm{V}\ \cdot I +\ 0.04\ \frac{\mathrm{V}}{\mathrm{A}} \cdot I^2)}{2} \tag{5.7}$$

$$P_{\mathrm{el,av}} = 13.4\ \mathrm{V}\ \cdot I +\ 0.02\ \frac{\mathrm{V}}{\mathrm{A}} \cdot I^2\ . \tag{5.8}$$

The electric arc efficiency is defined as [Katsaounis 1993]:

$$\eta_{\mathrm{w}} = \frac{\dot{Q}_{\mathrm{w}}}{UI} \tag{5.9}$$

η_{w}	Electric arc efficiency [-]
$\dot{Q}_{\mathrm{w}}$	Heat input or flow [W]
U	Electric arc voltage [V]
I	Electric arc current [A].

It is mainly determined by two loss factors: radiation loss and cathode energy loss [Katsaounis 1993]:

$$\eta_{\mathrm{l}} = \frac{\dot{Q}_{\mathrm{lb}}}{UI} \tag{5.10}$$

η_{l}	Radiation loss factor [-],
$\dot{Q}_{\mathrm{lb}}$	Heat flow from the electric arc column [W]

$$\eta_{\mathrm{e}} = \frac{\dot{Q}_{\mathrm{e}}}{UI} \tag{5.11}$$

η_{e}	Cathode energy loss factor [-].
$\dot{Q}_{\mathrm{e}}$	Heat loss at the cathode [W]

5.1.2 Electric Arc

The melting and thus mass flow in REP is generated by means of an electric arc (chapter 3.1.1). Generally, the electric arc is established under shielding gas, i.e. argon or helium atmosphere, through a tungsten inert gas (TIG) welder (chapter 3.3.6).

According to [Correy 1982], about 90% of the electric arc current is carried by electrons. The electrons in turn originate from the cathode. Their transfer from the cathode to the plasma is ascribed to thermal (thermionic) emission due to positive ion bombardment from the positive ion cloud surrounding the cathode[33] [Correy 1982]. The remainder current is carried by the positive ions (Figure 5-1).

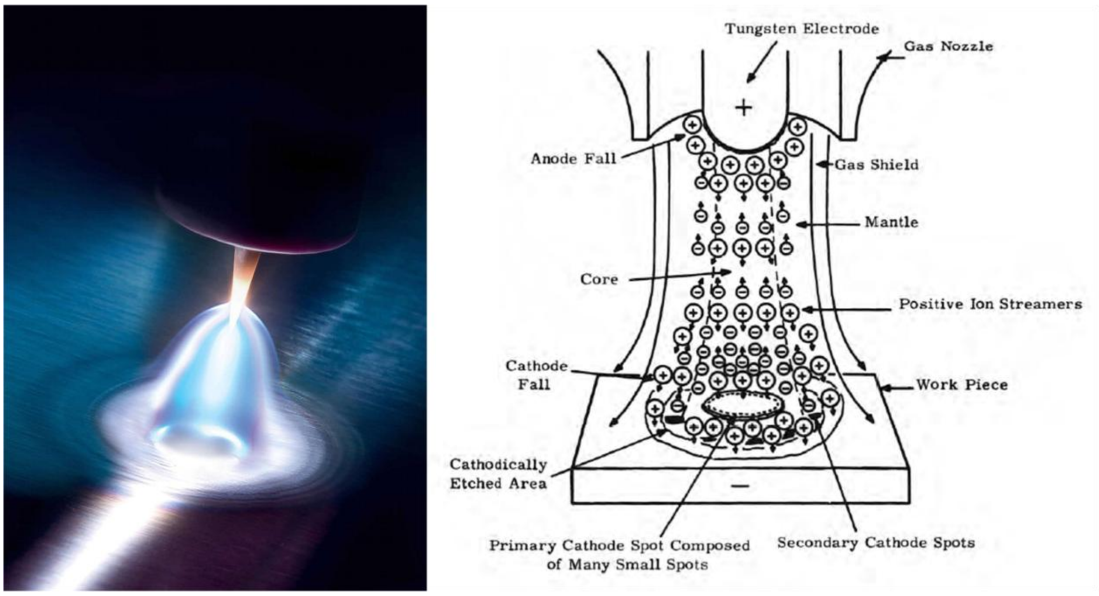
Tungsten Electrode
Gas Nozzle
+
Anode Fall
Gas Shield
Mantle
Core
Positive Ion Streamers
Cathode Fall
Work Piece
Cathodically Etched Area
−
Primary Cathode Spot Composed of Many Small Spots
Secondary Cathode Spots

Figure 5-1 Left: Image of a TIG welding electric arc (property of EWM AG). Right: Schematic of a TIG welding electric arc using direct current (DC) with reverse polarity, i.e. welding with the tungsten electrode positive (DCEP) and the work negative (property of [Correy 1982]). For REP, the inverse polarity with tungsten electrode negative (DCEN) and the work positive is used.

A simple and commonly used model in industrial TIG welding applications for the electric arc voltage-current characteristic in argon under normal pressure is [Matthes and Schneider 2012]:

$$U = 10\,\mathrm{V} + 0.04\,\frac{\mathrm{V}}{\mathrm{A}} \cdot I, \qquad for\, I \leq 600\,\mathrm{A} \tag{5.12}$$

U Electric arc voltage [V]
I Electric arc current [A].

Equation (5.12) corresponds to the minimum voltage provided by the implemented arc welder for a given electric arc current.

---

[33] Besides so-called thermionic cathodes, there are three non-thermionic cathode types: vapour type, tunnelling type, and switching type. The different mechanisms are supposed to occur on non-refractory metals and refractory metals at low current and/or pressure [Lancaster 1986].

However, it is known that the electric arc voltage-current characteristic is a non-linear function of the electric arc current that exhibits a minimum at low electric arc currents where it changes its slope (Figure 5-2). Furthermore, Figure 5-2 shows that the electric arc voltage is a function of the electric arc length.

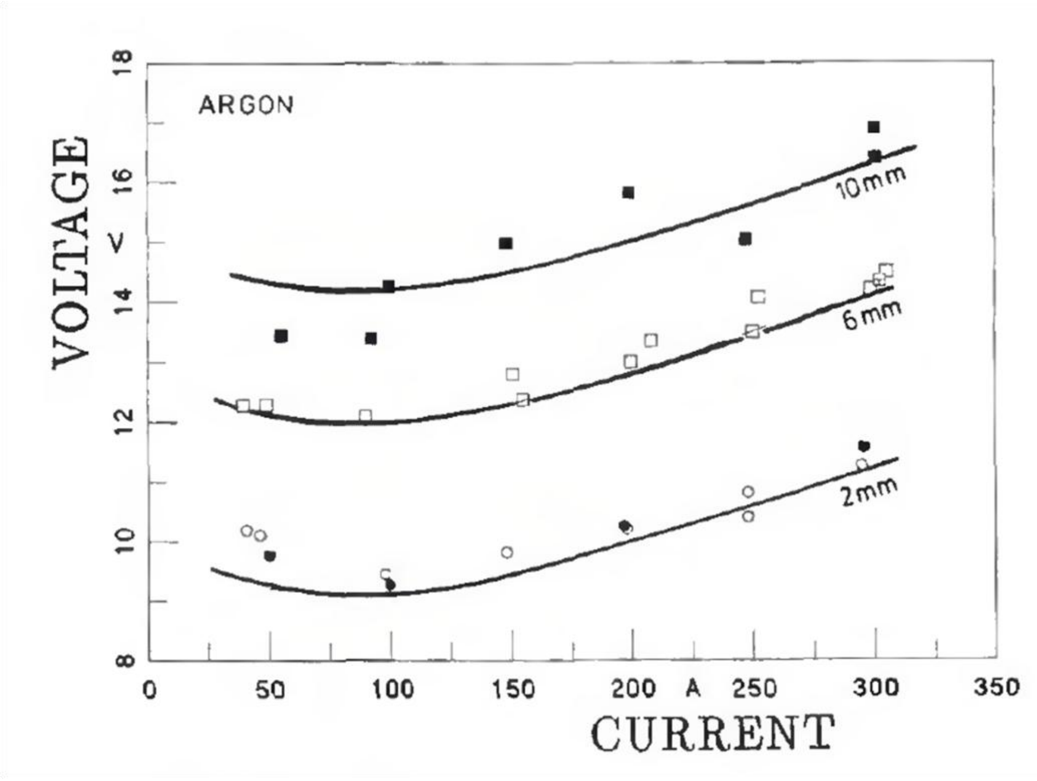

Figure 5-2 Electric arc voltage in argon at atmospheric pressure as a function of electric arc current and electric arc length. The voltage-current electric arc characteristic shows a non-linear behaviour with a minimum towards an electric arc current of about 85 A; property of [Katsaounis 1993].

The location of the minimum, however, depends on multiple parameters, and reported ranges vary accordingly from 2-20 A [Sherrod 1960] to 85 A [Katsaounis 1993]. Namely, electric arc characteristics are determined by the chemical composition of both electrodes, diameter or mass of both electrodes, tip configuration (angle, pointing) of both electrodes, melting or non-melting of the anode, shielding gas type and state (static or dynamic), electrode cooling and shrouding (nozzle), electric current type (AC/DC), and mode of arc operation [Correy 1982].

The aforementioned increase in electric arc voltage due to an increase in electric arc length is non-linear. The electric field strength E decreases with increasing electric arc length (Figure 5-3). The change of the electric field strength, the gradient $\mathrm{d}U/\mathrm{d}l$ (electric arc gain or sensitivity), is in turn a non-linear function of both the electric arc current and voltage (Figure 5-4).

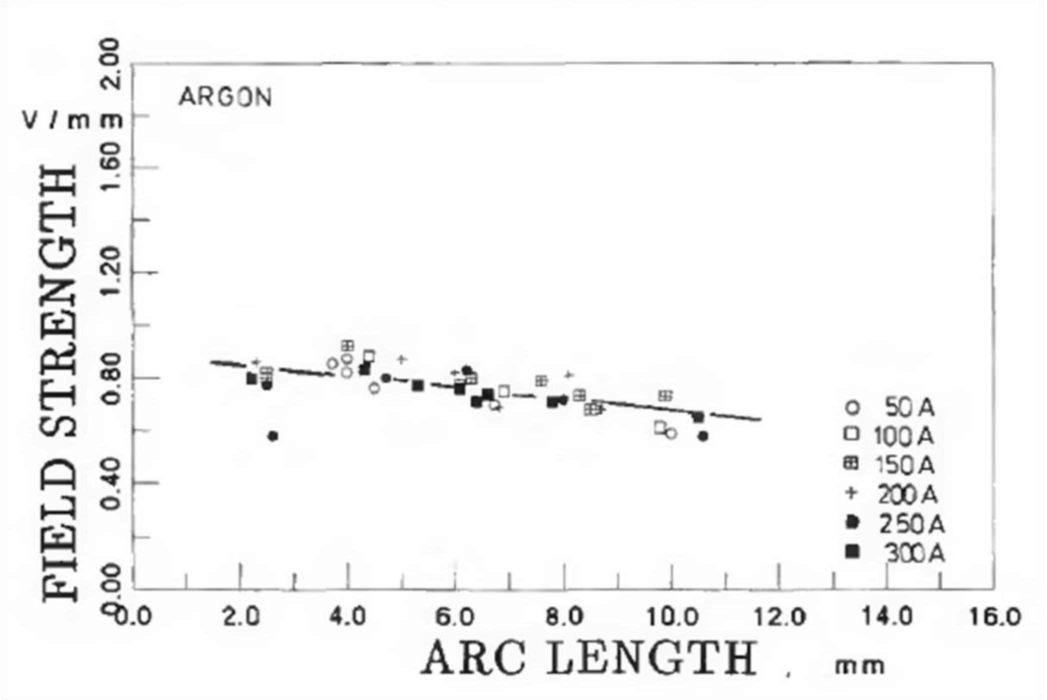

Figure 5-3 Electric field strength as a function of electric arc length at atmospheric pressure; property of [Katsaounis 1993].

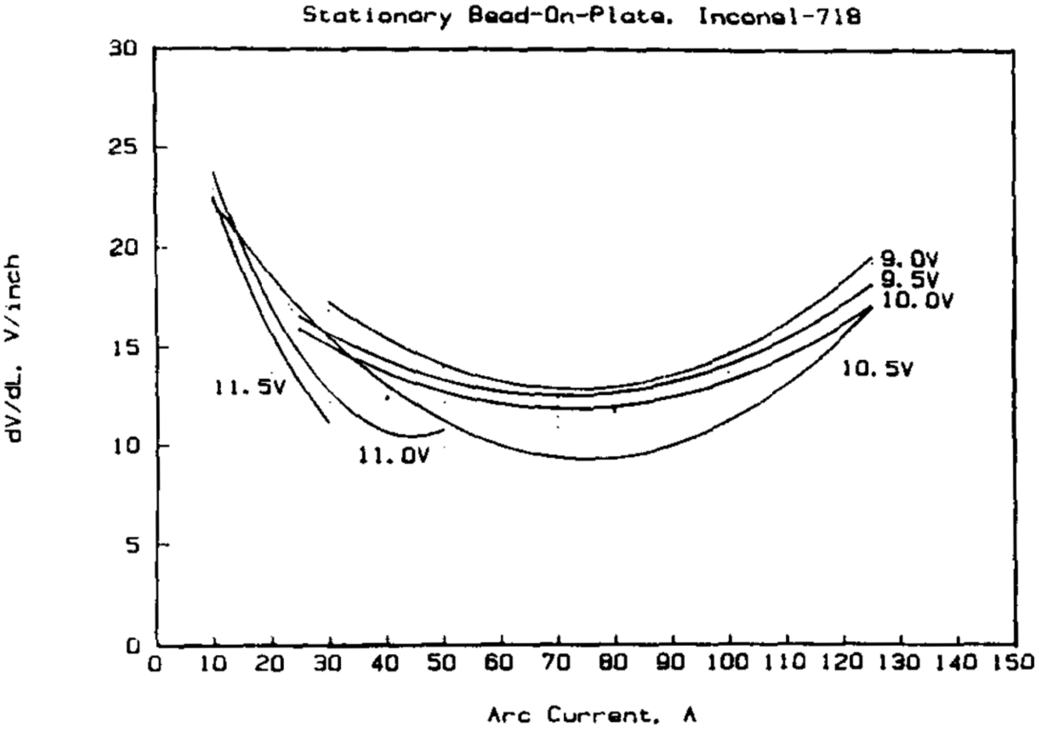

Figure 5-4 Calculated electric arc gain or sensitivity dU/dl as a function of electric arc voltage and electric arc current (1 inch = 25.4 mm); property of [Bjorgvinsson *et al.* 1993].

The heat input of the electric arc to the work is a function of total electric input power (Figure 5-5). While the cathode energy loss factor is 0.08 in argon and approximately constant, radiation loss increases with increasing electric arc length and electric arc current at atmospheric pressure [Katsaounis 1993]. The author found this behaviour for a commercial TIG welder with drooping voltage-current characteristics as was implemented for the prototype atomizer (see chapter 3.3.6).

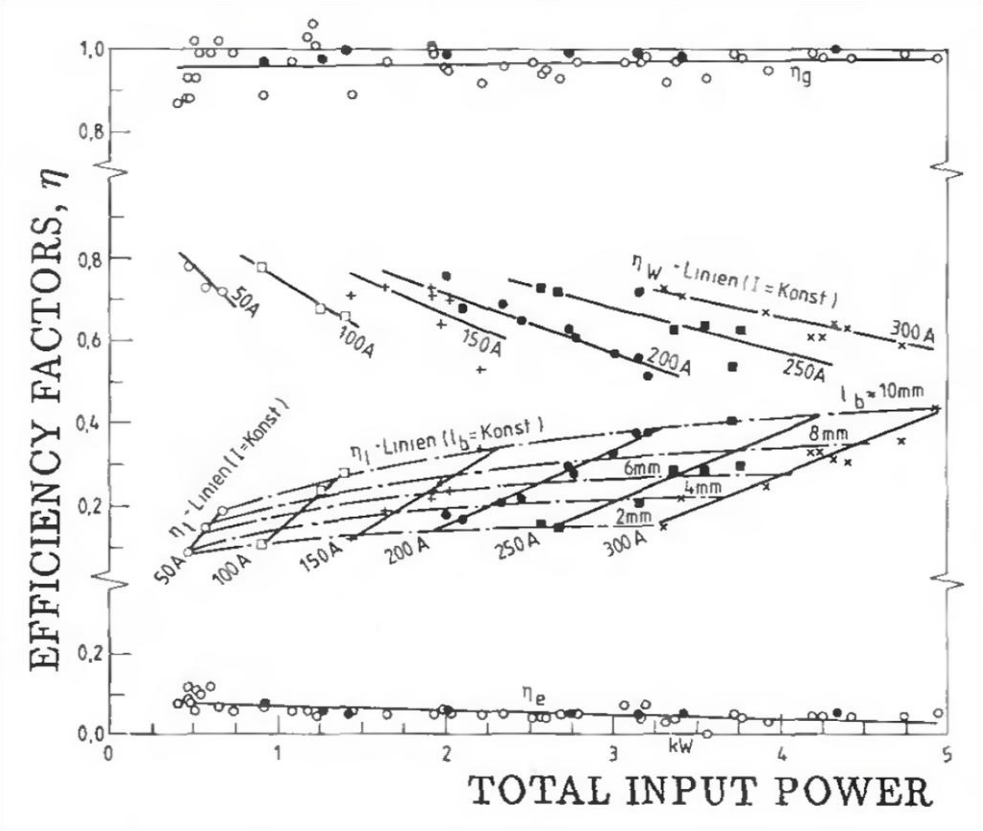

Figure 5-5 Efficiency factors as a function of total input power at atmospheric pressure for argon; property of [Katsaounis 1993]. The electric arc efficiency η_w is shown as a function of electric arc current and electric welder power.

Finally, the electric arc characteristic can be expressed by [Zhang 2008]:

$$U = K_1 + K_2 \cdot I + K_3 \cdot e^{C \cdot I} \tag{5.13}$$

U	Electric arc voltage [V]
I	Electric arc current [A]
K_1, K_2, K_3	Linear functions of arc length [V]
C	Constant
e	Euler number.

The functions K_1, K_2, and K_3, however, were not explicitly given. They must be determined experimentally. Thus, this model was given for completeness only. The electric arc voltage also depends on atmosphere pressure [Katsaounis 1993]. This property, however, was not relevant for the following experiments as glovebox atmosphere pressure was approximately constant, i.e. varying by ± 25 Pa.

5.1.3 Model

An experimental relationship to describe the generated mass flow rate in REP was found by [Champagne and Angers 1981] using regression analysis:

$$\dot{m} = 0.12 \frac{U \cdot I}{H_{\mathrm{m}} \cdot D_{\mathrm{re}}^{0.28} \cdot F_{\mathrm{Ar}}^{0.25}} \tag{5.14}$$

$\dot{m}$	Mass flow rate [kg/s]
U	Electric arc voltage [V]
I	Electric arc current [A]
H_{m}	Enthalpy of melt[34], reference zero at 273 K [kJ/kg]
D_{re}	Rotating electrode diameter [m]
F_{Ar}	Argon fraction [-].

However, equation (5.14) was not accounted for in reviewed secondary literature on atomization [Ashgriz 2011, Lawley 1992, Lefebvre 1989, Wozniak 2003, Yule and Dunkley 1994]. A reason might be that it is not dimensionally correct, incomplete, and that its coefficient of determination was 83.5 %. Also, the equation is based on a configuration with approximately constant electric arc length and a constant electric arc efficiency of 12 %.

Anyway, it can be inferred to a fair extent that there is a linear relationship between mass flow rate and inserted electric power. In addition, the rotating electrode material and geometry have direct influence on the mass flow rate.

5.2 Experimental Setup

U8Mo rotating electrodes were atomized at 4 different electric arc currents, namely 35 A, 50 A, 70 A, and 100 A, with 70 A being the point of reference of the INL atomizer [Clark *et al.* 2007]. Since lowering the mass flow rate increases the probability of reaching the DDF atomization regime (chapter 6.1.4), electric arc currents below the reference point were of higher interest. In fact, the DDF is supposed to produce entirely spherical particles shapes in metal melt atomization. Accordingly, the amount of experiments and their repetition was increased towards smaller electric arc currents.

---

[34] The enthalpy of melt refers to the total energy needed to heat a material from a reference zero to a certain temperature above its melting point. It includes and must therefore be distinguished from the (latent) heat of fusion or enthalpy of fusion that describes the amount of energy needed for the phase transition from solid to liquid state.

In addition, two different electric arc currents, namely 70 A and 100 A, were applied to 1.4301 stainless steel for comparison. In this case, a linear relationship according to equation (5.14) was assumed in order to reduce the amount of experiments.

The tungsten electrode and rotating electrode dimensions were the same throughout this study. The varied parameters were alloy, atomized electrode length, electric arc length, and rotational speed. Notably, different rotational speeds were accepted due to the limited amount of U8Mo electrodes and based on the assumption that rotational speed has a negligible influence on mass flow rate.

5.3 Results and Discussion

5.3.1 Arc Welder Operating Range

The operating range and dynamic behaviour of the implemented arc welder is summarised in Figure 5-6.

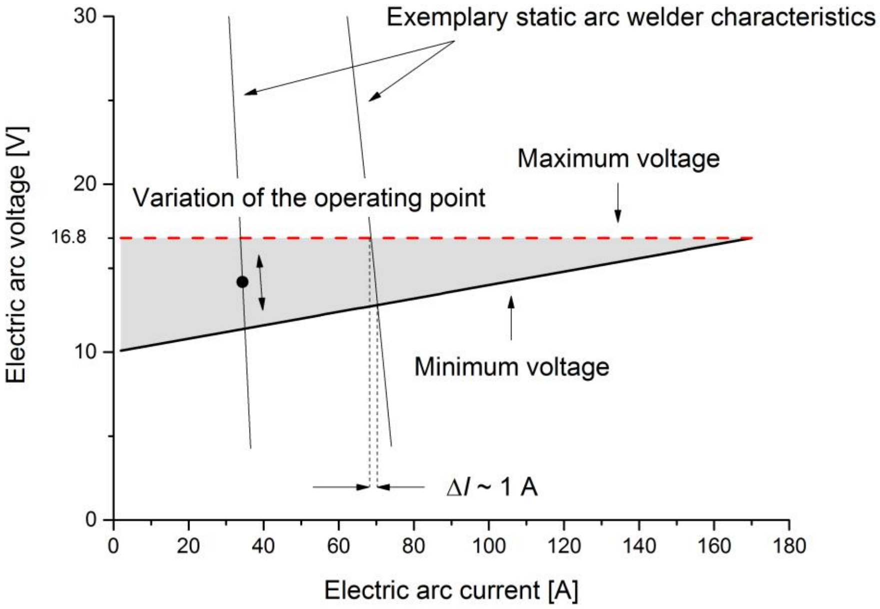

Figure 5-6 Operating range of the implemented arc welder and illustration of the dynamic behaviour of the electric arc operating point due to a variation in electric arc length. The operating point moves along the drooping arc welder characteristic that is predetermined by the electric arc current setting (see also Figure 3-21). The decrease in electric arc current due to an increase in the electric arc length was determined to about 1 A (chapter 4.2).

The minimum voltage curve was calculated from the arc welder current operating range that is 2 A to 170 A (chapter 3.3.6). For calculation, equation (5.12) was used. The results matched exactly the arc welder voltage operating range that is 10.1 V to 16.8 V (chapter 3.3.6). The maximum voltage provided by the arc welder is 16.8 V. In addition, it was found during repeatability experiments[35] that an increase in electric arc length resulted in a decrease in electric arc current of not more than 1 A (chapter 4.2). This is in good agreement with the expected control behaviour of the arc welder (chapter 3.3.6).

5.3.2 Electric Arc Power

It can be seen from Figure 5-7 that the apparent mass flow rate of U8Mo is a linear function of the average electric arc power provided by the arc welder – as implied by equation (5.14).

In addition, it is visible that the slope of the U8Mo fitting line was about 5 times steeper compared to the one of 1.4301 stainless steel. This effect, however, is fairly well explained taking into account equation (5.14) and the ratio of the enthalpies of melt of SAE 1090 steel and U[36] at melting point – 1210 $\mathrm{kJ\,kg^{-1}}$ [Champagne and Angers 1981] and 245 $\mathrm{kJ\,kg^{-1}}$ [Fischer 2000][37], respectively. The calculated ratio was about 5. Accordingly, the absolute variation of the apparent mass flow rate was more pronounced as can be seen from Figure 5-7 when comparing U8Mo and 1.4301. The relative variation of the apparent mass flow rate for a given parameter set increased as well. Namely, experiments U8Mo-552-04, -33, -39, and -42 were conducted with the same input electric arc current of 50 A (Table 5-1). The generated average mass flow rate was 1.21 $\mathrm{g\,s^{-1}}$ with a standard deviation of about ± 0.07 $\mathrm{g\,s^{-1}}$ or 6 %. This value was higher compared to a standard deviation of about 2 % from repeatability experiments (chapter 4.2).

The measurement uncertainty of the U8Mo mass flow rate was generally below 3 % as stated in Table 5-1.

A potential contribution to the increased variation in the mass flow rate is ascribed to the manual torch infeed of the arc-melting system as it induced variation in the electric arc length. This variation caused in turn a change of the electric arc characteristic (Figure 5-2). Accordingly, the operating point of the electric arc varied along the static arc welder characteristic (Figure 5-6). The corresponding changes in electric input power may have been insufficient to provide a constant mass flow rate. In particular, as a variation in electric input power affects the electric arc efficiency and thus heat input to the rotating electrode (Figure 5-5).

---

[35] The manufacturer did not provide detailed information on the static arc welder characteristics.

[36] Uranium and SAE 1090 steel were used for approximation of U8Mo and 1.4301, respectively.

[37] According to the cited author, the enthalpy of melt of liquid uranium is $H_\mathrm{m}(1408\ \mathrm{K}) - H_\mathrm{m}\ (298\ \mathrm{K}) = 58347\ \mathrm{J\,mol^{-1}}$. Thus, uranium has an enthalpy of 245 $\mathrm{kJ\,kg^{-1}}$ at melting point (1408 K) after transition to the liquid state considering the molar mass of uranium of 238 $\mathrm{g\,mol^{-1}}$.

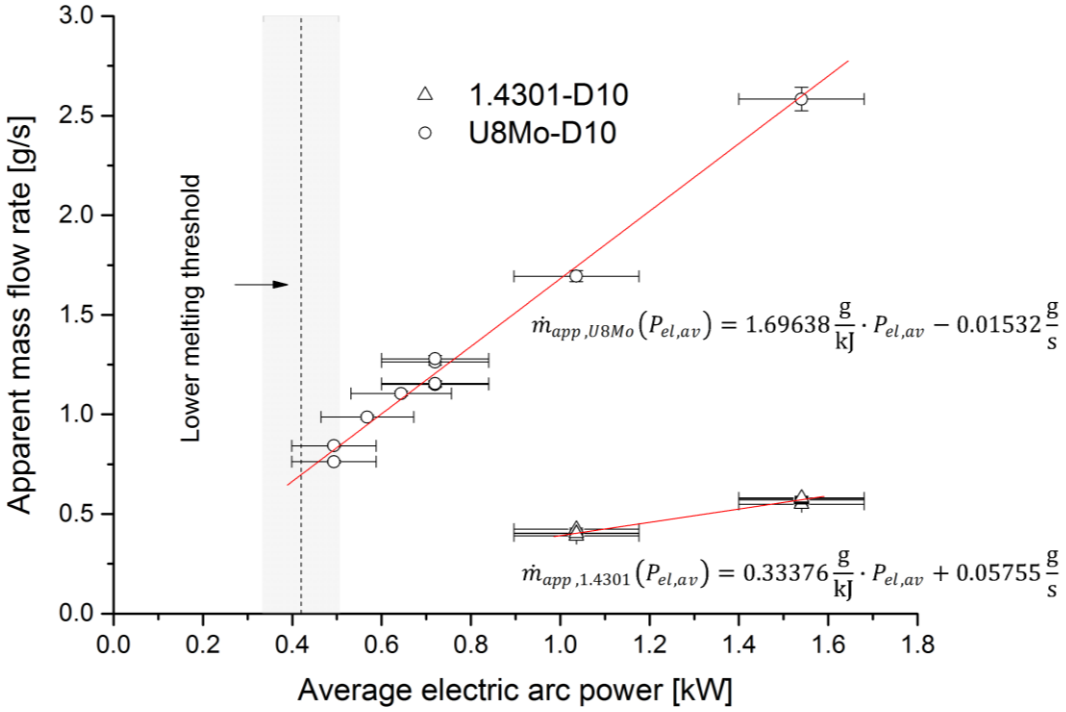

Figure 5-7 Measured apparent mass flow rate as a function of average arc power $P_{el,av}$ for both U8Mo and 1.4301 rotating electrodes with a diameter and length of 10 mm and 30 mm, respectively. While y-error bars represent the measurement uncertainty, x-error bars account for minimum and maximum electric arc power for a given electric arc current. The linear fitting graphs (red) and functions were obtained by using York's[38] method of regression as well as assuming 0 correlation between x and y errors. The standard errors of the fitting graph slopes for U8Mo and 1.4301 stainless steel were ± 0.23872 and ± 0.06681, respectively. The standard errors of the intercepts were 0.17796 and 0.0875, respectively. The dashed, vertical line represents the region where U8Mo melting became impossible, corresponding to an average arc power and set electric arc current of 0.42 kW and 30 A, respectively; the grey area accounts for the uncertainty of ± 0.08 kW due to the variation in electric arc length. Uncertainties within symbol size if not visible.

---

[38] York D, Unified equations for the slope, intercept, and standard error of the best straight line, American Journal of Physics, Volume 72, Issue 3, pp. 367-375 (2004); OriginLab 9.1.0. This method did not report the coefficient of determination R^2.

Table 5-1 Calculated average electric arc power and apparent mass flow rate of U8Mo in ascending order with respect to arc power as well as corresponding absolute and relative uncertainties.

Batch	Calculated average arc power $P_{\text{el,av}}$ [kW]	Absolute uncertainty $\pm\ uc$ [kW]	Relative uncertainty $\pm\ uc$ [%]	Apparent mass flow rate $\dot{m}_{\text{app}}$ [g/s]	Absolute measurm. uncertainty $\pm\ uc$ [g/s]	Relative measurm. uncertainty $\pm\ uc$ [%]
U8Mo-552-08	0.494	0.095	19.1	0.762	0.006	0.852
U8Mo-552-06	0.494	0.095	19.1	0.843	0.007	0.889
U8Mo-552-38	0.568	0.104	18.3	0.987	0.011	1.09
U8Mo-552-36	0.644	0.113	17.5	1.10	0.012	1.07
U8Mo-552-04	0.720	0.120	16.7	1.15	0.014	1.25
U8Mo-552-33	0.720	0.120	16.7	1.15	0.013	1.17
U8Mo-552-39	0.720	0.120	16.7	1.26	0.016	1.27
U8Mo-552-42	0.720	0.120	16.7	1.28	0.016	1.24
U8Mo-552-30	1.04	0.140	13.5	1.69	0.028	1.64
U8Mo-552-29	1.54	0.140	9.1	2.58	0.059	2.30

Furthermore, a deadband was observed (Figure 5-8) between arc ignition and full rotating electrode melting (i.e. the arc covering the entire front surface of the rotating electrode) that delayed atomization. This effect is ascribed to the time needed to heat up the rotating electrode from ambient temperature to its melting point. The deadband reached about 4 s, 3 s, and 2 s at 35 A, 50 A, and 70 A, respectively, being almost negligible around 100 A. It is thus a function of heat input. As a result, the apparent mass flow rate systematically underestimated the "real" mass flow rate (Figure 5-9). Depending on the initial gap between the two electrodes, the deadband varied. Therefore, the reported values should be interpreted as a bench mark only, notably as no further and detailed investigation with respect to this observation was carried out.

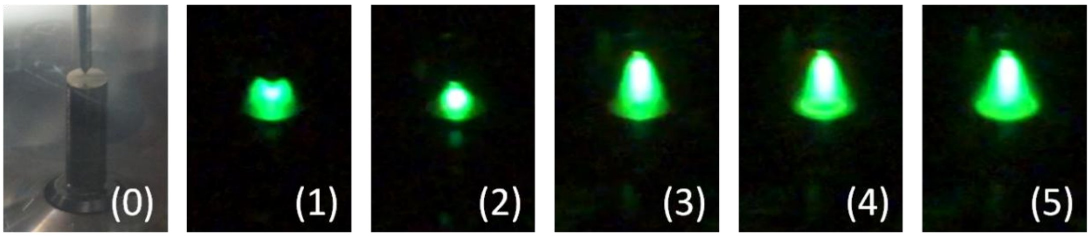

Figure 5-8 Sequence of pictures recorded at the beginning of atomization of the U8Mo rotating electrode 552-10 with a diameter of 10 mm at 70 A. From left to right: (0) U8Mo rotating electrode and tungsten electrode in idle position, (1) electric arc ignition with 2 mm gap at 0 s, (2) electric arc of 2 mm length at ~ 0 s, (3) manual increase of the electric arc length to around 10 mm and development of a melt pool at 1 s, (4) partial coverage of the rotating electrode at 2 s, (5) fully covered rotating electrode diameter at 3 s and beginning reduction of the electrode length (fully developed atomization). The welder starting-ramp included temporary operation at 50 % electric arc current (35 A) for about 0.5 s.

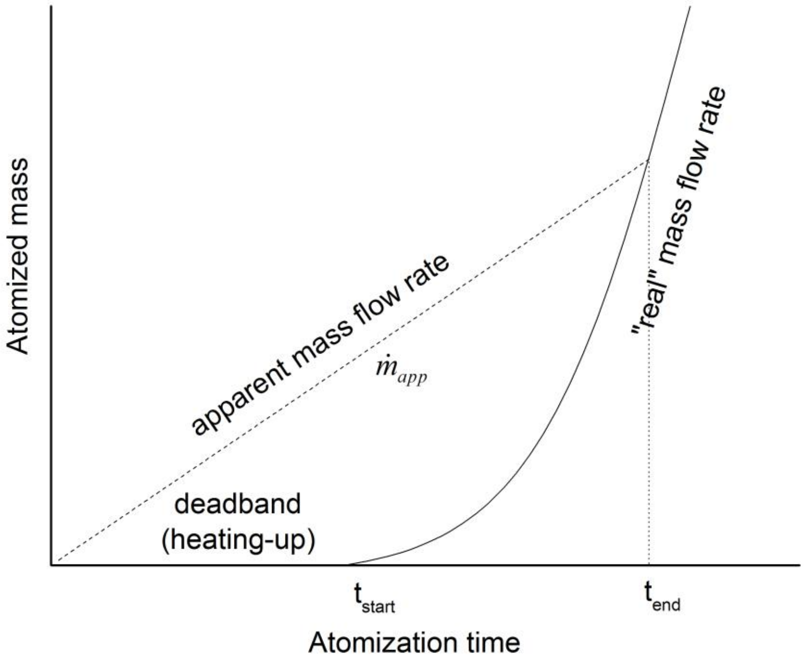

Figure 5-9 Illustration of the difference in apparent and “real” mass flow rate.

Another observation made during this study was that melting of U8Mo by an electric arc became increasingly difficult, if not impossible below 0.42 kW ± 0.08 kW (30 A) – an observation made on two different occasions by two different operators (Figure 5-7). It is suggested that the heat input to the rotating electrode was levelled by energy losses caused by thermal conduction, forced convection, and thermal radiation at this electric arc power. As a consequence, the mass flow rate in REP has a lower threshold.

In addition, generating a weld pool that equally spreads over the entire rotating electrode became increasingly difficult at low electric arc currents (~ 35 A). Occasionally, only a part of the electrode was atomized. This partial atomization was particularly problematic when the tungsten electrode was not centred as it led to audible imbalance (i.e. vibration) of the rotating electrode. The latter in turn may cause fracture of the rotating electrode or damage to the spindle roller bearings.

5.3.3 Rotating Electrode Length

In order to protect atomizer spindle bearings, atomization at maximum rotational speed was conducted with rotating electrodes cut from about 30 mm to 20 mm consumable length (around 43 g and 30 g, respectively).

It was found that the apparent mass flow rate decreased at 35 A and 50 A significantly by about 32 % and 21 %, respectively, with regard to the mean obtained by atomizing the longer electrodes (Figure 5-10). However, this effect was not found at higher arc current intensities, namely 70 A and 100 A.

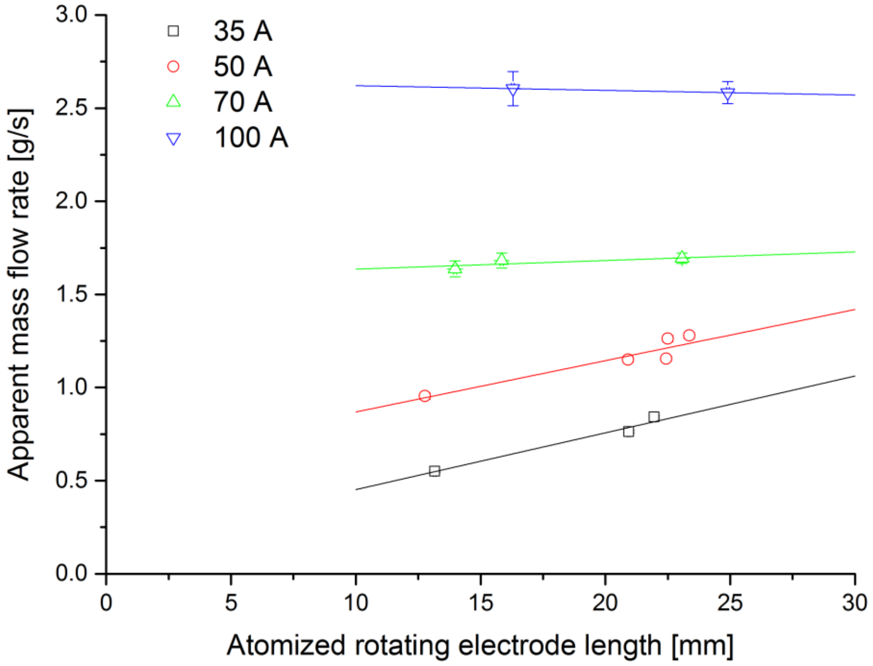

Figure 5-10 Apparent mass flow rate as a function of atomized rotating electrode length for different electric arc currents. Straight lines were included for trend visualisation. Uncertainties within symbol size if not visible.

While for the longer electrodes the apparent positive correlation between apparent mass flow rate and atomized electrode length at 35 A and 50 A may still be ascribed to effects stated before, the results obtained for the short electrodes stand out. Although only two experiments were conducted with short electrodes at 35 A and 50 A, a trend seems apparent as the measurement uncertainties are small compared to the observed effect. Due to the small amount of experimental data, no fitting curve was calculated.

The aforementioned difference between apparent and "real" mass flow rate (Figure 5-9) explains the observation. It can be inferred that, based on the "real" mass flow rate, a shorter rotating electrode (and thus shorter atomization time) will result in a smaller apparent mass flow rate due to the deadband (Figure 5-11). The effect, though, decreases with increasing electric arc current. As a result, apparent and "real" mass flow rate converged at higher electric arc currents and the overall effect became weak as suggested by the experimental observations (Figure 5-10).

Also, the difference in thermal resistance of a standard and short U8Mo rotating electrode may have influenced the mass flow rate. The behaviour of the mass flow rate, however, is not straightforward. Besides the length of the rotating electrode, the heat flow depends on the geometry of the rotating electrode stub, the thermal contact between rotating electrode stub, collet, collet chuck, and high frequency spindle shaft and their respective thermal conductivities.

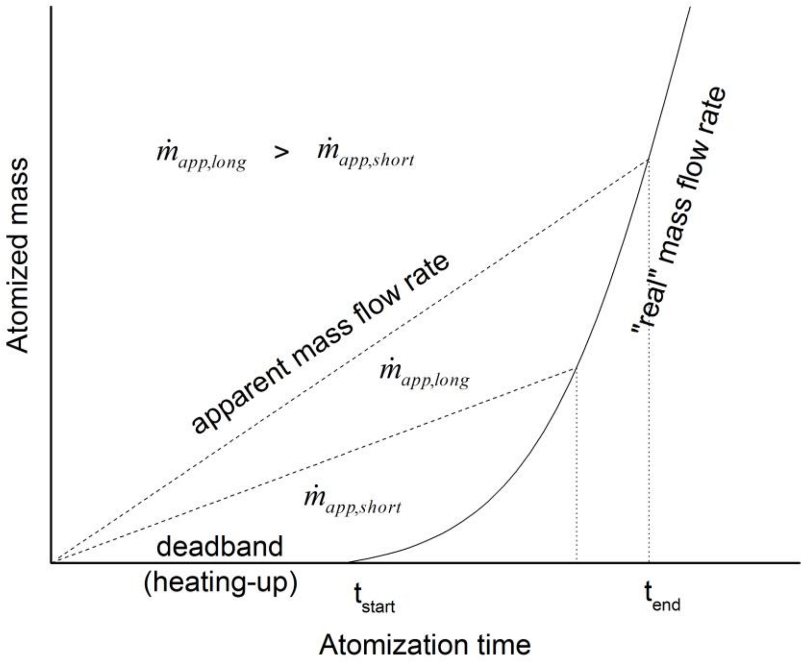
$\dot{m}_{app,long}$ > $\dot{m}_{app,short}$
Atomized mass
apparent mass flow rate
"real" mass flow rate
$\dot{m}_{app,long}$
$\dot{m}_{app,short}$
deadband
(heating-up)
t_{start}
t_{end}
Atomization time

Figure 5-11 Illustration of influence of rotating electrode length on the apparent mass flow rate. For cylindrical rotating electrodes, the atomized mass is proportional to the atomized length. The slopes represent the corresponding mass flow rate.

5.3.4 Rotating Electrode Diameter

Rotating electrode diameters were varied (10 mm, 14 mm, and 20 mm) to verify the impact of rotating electrode diameter and thus electric arc current density on the mass flow rate. According to [Champagne and Angers 1981] and their empiric model (5.14), the following relationship between mass flow rate and rotating electrode diameter was found:

$$\dot{m} \sim \frac{1}{D_{\mathrm{re}}^{0.28}} \ . \tag{5.15}$$

The same authors calculated the apparent mass flow rate as was done in this work, equation (5.1). However, they did not specify in detail how atomization time was measured, i.e. starting from electric arc ignition or the start of melting. It is thus not clear if the atomization deadband (Figure 5-9) was taken into account.

Since the rotating electrode diameter influences particle shape and mean size, the reported relationship was briefly tested using 1.4301 stainless steel due to the absence of U8Mo electrodes with greater a diameter.

Indeed, a negative correlation was found as can be seen from Figure 5-12 and Table 5-2. The number of conducted experiments, however, was low and results scatter, not allowing for quantification of the trend. Furthermore, the observed effect was superimposed by an increase in the heating deadband as discussed in chapter 5.3.2. Namely, an increase in the rotating electrode diameter not only decreases the electric arc current density, but also increases the total mass of the rotating electrode. As a consequence, heating time was increased.

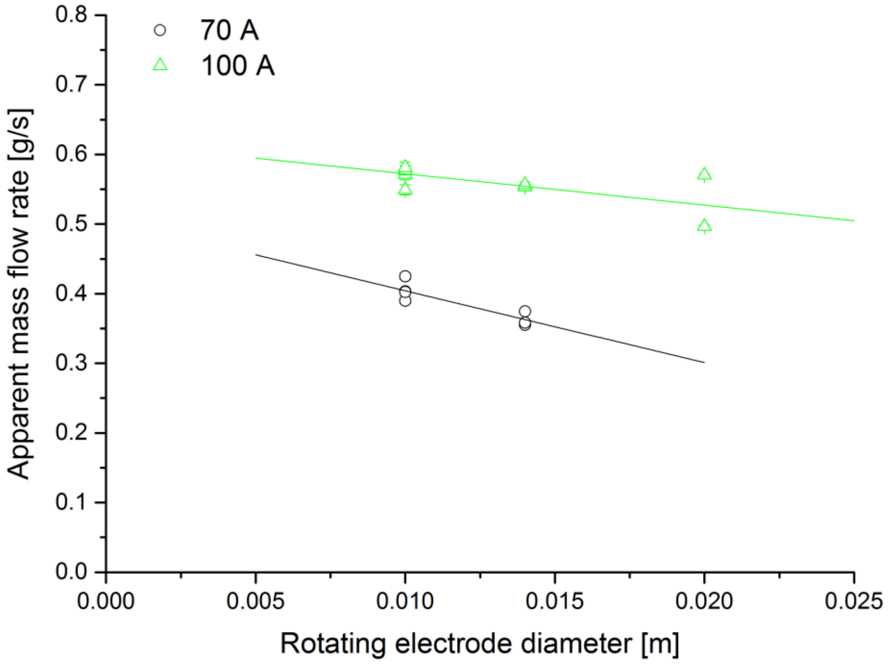

Figure 5-12 Apparent mass flow rate as a function of rotating electrode diameter for 1.4301 stainless steel for different arc current intensities. Straight lines were included for trend visualisation. Uncertainties within symbol size if not visible.

Another observation made during this study was the increased variation of the apparent mass flow rate with respect to the rotating electrode having a diameter of 20 mm (Figure 5-12). In fact, these experiments were conducted by a different operator, implying that variation depends on operator and training. Although this observation does not affect repeatability by definition, it gives an idea of the degree of process reproducibility. In comparison with the relative standard deviation of the INL atomizer of about 26 % (chapter 5.4), the relative standard deviation at a diameter of 20 mm was below 10 % with respect to the mean and therefore still low. This standard deviation was close to the uncertainty in average arc power, which was about 14 % at 100 A (Table 5-1).

Table 5-2 Experimental mass flow rates of both 1.4301 stainless steel for different diameters and arc current intensities. The tungsten electrode had a diameter and tip length of 3.2 mm and 2 mm, respectively.

Batch	Arc current [A]	Rotating electrode diameter [mm]	Apparent mass flow rate [g/s]	Relative measurement uncertainty [-]
Inox-014	70	10.0	0.390	0.010
Inox-015	70	10.0	0.425	0.010
Inox-016	70	10.0	0.403	0.010
Inox-018	70	10.0	0.403	0.010
Inox-019	70	14.0	0.374	0.004
Inox-020	70	14.0	0.355	0.005
Inox-021	70	14.0	0.358	0.005
Inox-022	100	14.0	0.554	0.006
Inox-023	100	14.0	0.557	0.006
Inox-024	100	14.0	0.557	0.006
Inox-025	100	10.0	0.549	0.013
Inox-026	100	10.0	0.571	0.013
Inox-027	100	10.0	0.577	0.013
Inox-028	100	10.0	0.581	0.012
Inox-040	100	20.0	0.497	0.003
Inox-041	100	20.0	0.570	0.003

5.3.5 Impurities

A positive correlation between apparent mass flow rate and carbon content was found for samples of different atomized powder batches (Figure 5-13). The observed effect may originate from melting point depression of the pure substance due to impurities in the alloy. Indeed, soluble impurities disturb the regular crystalline structure as they generally have a different atomic or ionic size and hence do not fit into the crystal lattice. Thereby, the bonds betweens atoms are weakened and the energy needed to disrupt the crystal lattice (i.e. melt the metal) is reduced [Hart *et al.* 2012]. Considering equation (5.14) and a fairly consistent heat input, the mass flow rate had to increase accordingly.

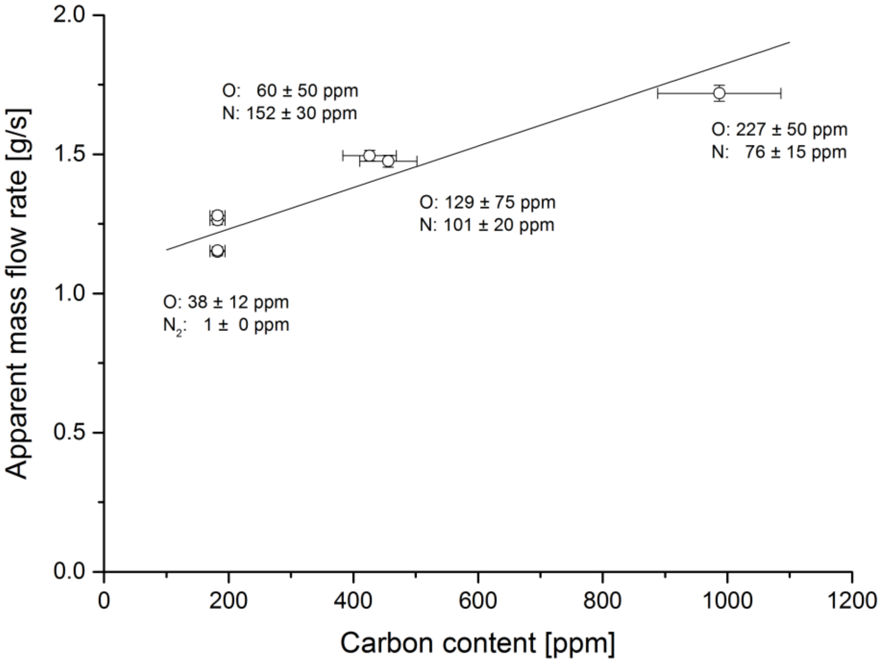

Figure 5-13 Apparent mass flow rate as a function of the carbon content that was measured in samples of atomized powder. In addition, nitrogen and oxygen concentrations are given for every carbon concentration. The nitrogen content of the smallest value is given as molecular value. The tested rotating electrodes had a diameter and atomized length of 10 mm and 23 mm, respectively, and were atomized at 50 A. A straight line was included for trend visualisation. Uncertainties within symbol size if not visible.

Carbon contamination of the powder due to sublimated and subsequently condensed carbon coming from the carbon brushes of the rotary electrical connector (chapter 3.3.14 and Figure 3-3) cannot be excluded but is considered unlikely. After all, the rotary electrical connector is sealed (chapter 3.3.17) and not connected to the powder collection chamber (Figure 3-3). In fact, carbon pollution is ascribed to the different batches of raw uranium, coming from either INL or CERCA, and the casting process where different types of crucibles (copper, graphite, ceramics) where used.

It is pointed out that the examined carbon contents were all below the maximum limits stated in the related fuel specifications [Gery 2011, Harbonnier 2002, Vanvor and Zill 2003]. As a consequence, the observed variation cannot be controlled by applying current fuel specification standards.

Nitrogen did not seem to have any influence on the mass flow rate (Figure 5-13).

Oxygen is considered an impurity, too, but its role has to be assessed carefully. While the mass flow rate seems to increase with its content as well, its retraceability in the range of ppm is more complex. U8Mo is corrodible [Wilkinson 1962a], especially at elevated temperatures, and therefore may oxidise during transport, storage, casting, rotating electrode cutting (conducted under air), atomization, powder storage, and preparation for chemical analysis (under air). As a consequence, every intermediate step may change the oxygen content – even the analysis itself. Furthermore, rotating electrodes were mechanically polished before atomization, thereby randomly changing the oxygen content. In summary, it is thus not clear, to what extent oxygen was already dissolved in the alloy, nor to what extent the surface of the rotating electrodes was oxidised, nor to what extent powder was oxidised during atomization or afterwards.

Another contribution to the variation in mass flow rate observed in chapter 5.3.2 may have originated from the purchased U8Mo rotating electrodes. There is evidence that atomized U8Mo rotating electrodes were inhomogeneous. That is, unmelted macroscopic pieces were found in some rotating electrode rests as well as in the powder, indicating the presence of material with a higher melting point than U8Mo, presumably molybdenum (Figure 5-14).

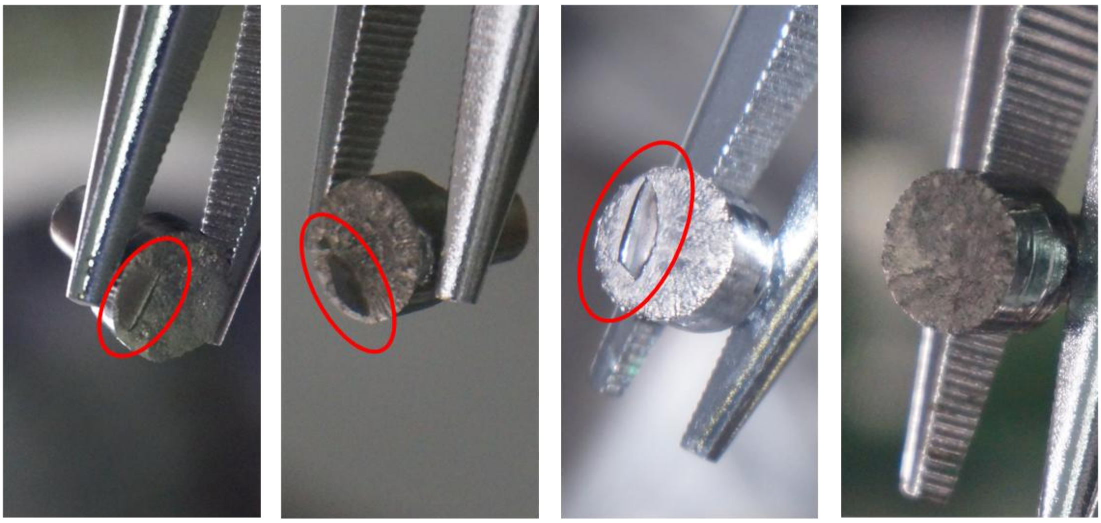

Figure 5-14 Sequence of rotating electrodes 552-13, -14, -04, and -33 (left to right) originating from INL after in-house atomization. Electrode rests of 552-13, -14, and -04 show inclusions, reaching about 5 mm in length (electrode diameter of 10 mm). A shadow zone on the outer rim is visible on 552-13, indicating a different fluid flow behind the inclusion, and thus perturbation of the general mass flow on the electrode surface, therefore influencing the governing droplet formation mechanism. For comparison, an electrode surface (552-33) without visible macroscopic inclusions is presented.

This observation was supported by information on the casting process of the purchased U8Mo rotating electrodes. Molybdenum foils had a thickness of 0.25 mm and were melted three times [Moore and Archibald 2014]. Compared to the equivalent standard melting process of CERCA, the reported value of three cycles is small. Considering the melting temperature of molybdenum of about 2623 °C, the presence of molybdenum pieces would impede the melting process and hence affect the mass flow rate. At lower arc powers, this perturbation should be even more pronounced, since the provided excess temperature is smaller.

5.3.6 Model Evaluation

Mass flow rates were calculated from applied parameter sets using model (5.14). It can be seen from Figure 5-15 as well as Table 5-3 and Table 5-4 that the model (5.14) correlates to the experimental data obtained by atomizing rotating electrodes with different materials and diameters. In general, mass flow rates of 1.4301 were underestimated while mass flow rates of the reference U8Mo rotating electrode (3.3.12, red circles) were overestimated. It is reminded, though, that enthalpies of melt of SAE 1090 steel and uranium were used for approximation of 1.4301 and U8Mo (chapter 5.3.2), respectively, as well as average values for electric arc power.

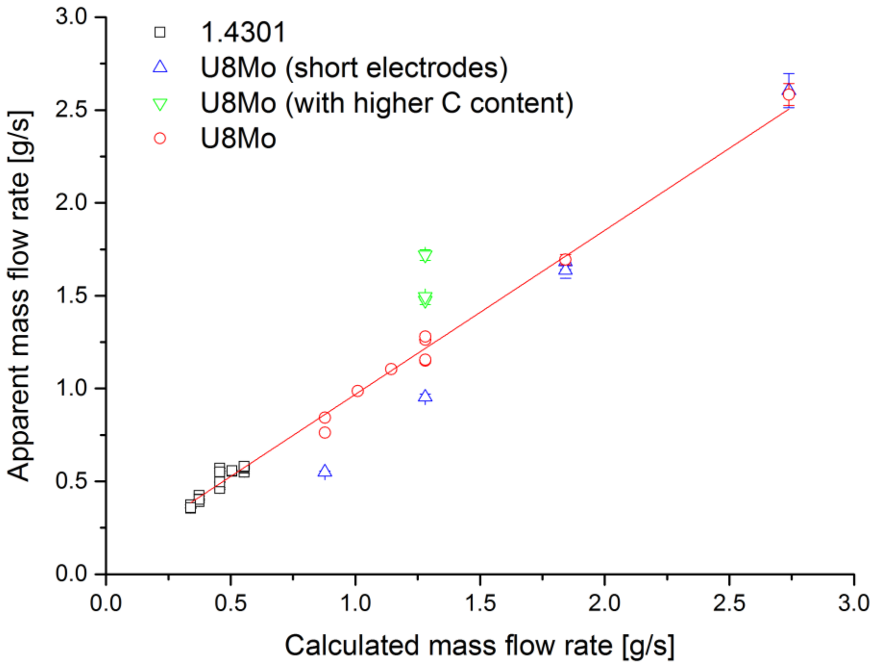

Figure 5-15 Agreement between experimental and calculated mass flow rates using equation (5.14). The reference U8Mo rotating electrodes are presented in red circles; rotating electrodes with higher carbon content are presented in green inversed triangles; shorter rotating electrodes are presented in blue triangles; black squares represent 1.4301 stainless steel. Uncertainties within symbol size if not visible. The red fitting graph has a slope and intercept of 0.88379 and 0.08451, respectively; the corresponding standard deviation is 0.02739 and 0.03074, respectively. The coefficient of determination R^2 is 95 %.

It stands out that the representation of short rotating electrodes at low arc current intensities was worse than the average, which is ascribed to effects stated in chapter

5.3.3. In addition, U8Mo mass flow rates were less well represented with increasing carbon content as discussed in chapter 5.3.5.

Table 5-3 Comparison of calculated and apparent mass flow rates obtained for U8Mo rotating electrodes of 10 mm and 30 mm diameter and length, respectively, and non-rotating tungsten electrode of 3.2 mm diameter and 2 mm tip length. U8Mo originated from different batches – 0914 and 552. For approximation, average electric power and enthalpy of melt of uranium were used.

Batch	Arc current intensity I [A]	Rotating electrode diameter D_{re} [m]	Calculated mass flow rate $\dot{m}_{\mathrm{c}}$ [g/s]	Apparent mass flow rate $\dot{m}_{\mathrm{app}}$ [g/s]
U8Mo-552-06	35	0.010	0.878	0.843
U8Mo-552-08	35	0.010	0.878	0.762
U8Mo-552-12	35	0.010	0.878	0.550
U8Mo-552-38	40	0.010	1.01	0.987
U8Mo-552-36	45	0.010	1.14	1.10
U8Mo-0914-1	50	0.010	1.28	1.72
U8Mo-0914-3	50	0.010	1.28	1.48
U8Mo-0914-4	50	0.010	1.28	1.49
U8Mo-552-04	50	0.010	1.28	1.15
U8Mo-552-14	50	0.010	1.28	0.95
U8Mo-552-33	50	0.010	1.28	1.15
U8Mo-552-39	50	0.010	1.28	1.26
U8Mo-552-42	50	0.010	1.28	1.28
U8Mo-552-10	70	0.010	1.84	1.68
U8Mo-552-16	70	0.010	1.84	1.64
U8Mo-552-30	70	0.010	1.84	1.69
U8Mo-552-11	100	0.010	2.74	2.60
U8Mo-552-29	100	0.010	2.74	2.58

Table 5-4 Comparison of calculated and apparent mass flow rates obtained for 1.4301 rotating electrodes of 30 mm length and non-rotating tungsten electrode of 3.2 mm diameter and 2 mm tip length. For approximation, average electric power and enthalpy of melt of SAE 1090 steel were used.

Batch	Arc current intensity I [A]	Rotating electrode diameter D_{re} [m]	Calculated mass flow rate $\dot{m}_{\mathrm{c}}$ [g/s]	Apparent mass flow rate $\dot{m}_{\mathrm{app}}$ [g/s]
Inox-014	70	0.010	0.373	0.390
Inox-015	70	0.010	0.373	0.425
Inox-016	70	0.010	0.373	0.403
Inox-018	70	0.010	0.373	0.403
Inox-019	70	0.014	0.340	0.374
Inox-020	70	0.014	0.340	0.355
Inox-021	70	0.014	0.340	0.358
Inox-022	100	0.014	0.505	0.554
Inox-023	100	0.014	0.505	0.557
Inox-024	100	0.014	0.505	0.557
Inox-025	100	0.010	0.555	0.549
Inox-026	100	0.010	0.555	0.571
Inox-027	100	0.010	0.555	0.577
Inox-028	100	0.010	0.555	0.581
Inox-043	100	0.020	0.457	0.461
Inox-040	100	0.020	0.457	0.497
Inox-041	100	0.020	0.457	0.570
Inox-042	100	0.020	0.457	0.550

5.4 Comparison

The only comparable and available data regarding the generated mass flow rate of UMo in REP, notably U8Mo, were reported by INL [Moore and Archibald 2014]. For 7 experiments, the same rotating electrode batch, namely 552, was used. Only difference apart from the atomizer design was the atomized mass that reached about 80 % of the average rotating electrode mass of 51.2 g, thus 41 g, compared to an average of 31 g atomized for this study. Rotational speeds were varied in both studies.

For comparison, their apparent mass flow rates were calculated using both the reported average rotating electrode mass and times needed for atomization.

While the deviation of the mean value of their experimental results might be explained by the different welder and drive configuration, the variation of their results with respect to the mean ($1.4\,g\,s^{-1}$) stands out (Figure 5-16), resulting in a standard deviation of $0.36\,g\,s^{-1}$or 26 %. The observed influences on the mass flow rate stated in this work may have contributed to this variation as well as the atomizer design, notably the brush arrangement as suggested by [Moore and Archibald 2014].

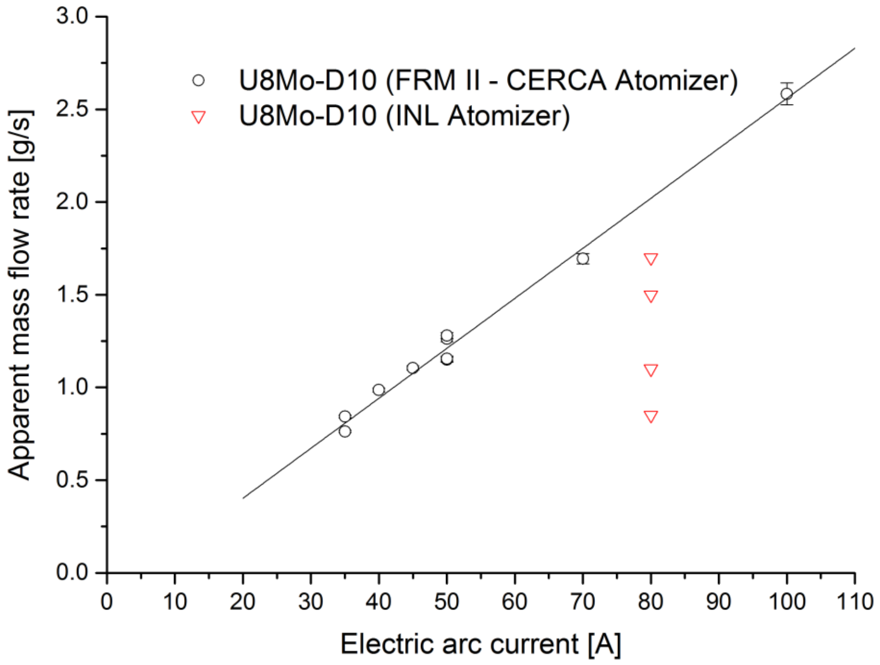

Figure 5-16 Comparison of the apparent mass flow rates obtained by the FRMII-CERCA atomizer and INL atomizer as a function of electric arc current. Overlapping points occur at $1.7\,g\,s^{-1}$ and $1.1\,g\,s^{-1}$ with respect to INL results and around $1.15\,g\,s^{-1}$ and $1.27\,g\,s^{-1}$ with respect to FRM II/CERCA results. Uncertainties within symbol size if not visible. A straight line with respect to the apparent mass flow rate generated by the FRM II/CERCA atomizer was included for better trend visualisation.

5.5 Conclusion

The mass flow rate of U8Mo generated in REP was quantified and its linear dependency on electric arc power within the observed range was validated. As a consequence, the U8Mo mass flow rate may now be estimated from inert experiments using 1.4301 as a surrogate material, if the same experimental setup is applied. It was also validated that the mass flow rate is a square function of the electric arc current given the welder configuration and the relation between voltage-current characteristic of the electric arc in argon.

For U8Mo rotating electrodes with a diameter and length of 10 mm and 30 mm, respectively, the following dependency of the apparent mass flow rate on average electric arc power was found:

$$\dot{m}_{\mathrm{app,U8Mo}} = 1.70\,\frac{\mathrm{g}}{\mathrm{kJ}} \cdot P_{\mathrm{el,av}} - 0.02\,\frac{\mathrm{g}}{\mathrm{s}}\ . \tag{5.16}$$

The slope and intercept had a standard deviation of ± 0.24 g kJ^{-1} and ± 0.18 g s^{-1}, respectively. The lowest generated U8Mo mass flow rate was 0.8 g s^{-1} at 0.5 kW average electric arc power (or 35 A electric arc current). The highest generated U8Mo mass flow rate in this study was 2.6 g s^{-1} at 1.5 kW average electric arc power (or 100 A electric arc current).

Furthermore, a lower melting threshold at about 0.42 kW average electric arc power (or 30 A electric arc current) was found. The threshold is due to inherent heat losses due to thermal conduction, forced convection, and thermal radiation. Only above this value, melting of the tested U8Mo rotating electrodes started. As a consequence, reducing the mass flow rate in order to promote atomization in the DDF regime is limited to this threshold.

The slightly increased relative variation of mass flow rate compared to experiments with 1.4301 stainless steel is ascribed to superimposing effects with respect to the melting of the rotating electrode: increased uncertainty in induced heat caused by manual torch operation the use of U8Mo, alloy inhomogeneity, and heating-up prior to melting (heating deadband). Namely, a standard deviation of about 6 % was found for an average U8Mo mass flow rate of 1.2 g s^{-1}. In order to decrease the observed absolute variation, the elimination of the potential causes is recommended as follows:

Regarding the uncertainty and variation of induced heat to the rotating electrode, it is suggested to use an electronically controlled (automated) motor to keep the electrode gap and thus arc voltage constant, fostering in turn constant power supply and hence melting rate. Although the observed variation was relatively small, the recommended modification will further increase repeatability and, in particular, reproducibility. The motor may move either the torch or the rotating electrode.

Inhomogeneities in the rotating electrode alloy, presumably molybdenum foils from the alloying process, were discovered and their potential influence on mass flow rate including increased variation discussed. In this respect, homogeneity can be promoted and controlled by increasing the number of re-melting procedures and by means of radiography prior to atomization, respectively.

The observed deadband after electric arc ignition can be reduced by using two different arc current intensities during atomization – a small one for heating-up and a higher one for melting. Indeed, this function is an integrated option of the currently implemented arc welder (chapter 3.3.6). Improving time measurement by the use of a high-speed camera that withstands arc light emission is an alternative option.

A positive correlation between apparent mass flow rate and atomized length at low arc current intensities was observed and attributed to the heating deadband and the resulting measurement artefact. The effect was weakened as the rotating electrode length or electric arc current was increased.

A negative correlation between mass flow rate and rotating electrode diameter was confirmed with 1.4301 stainless steel. As increasing the diameter is beneficial in terms of both particle shape and mean size, further studies using U8Mo rotating electrodes of larger diameters are suggested in order to quantify the effect. In this respect, the potential influence of the tungsten electrode diameter and tip should be considered as well.

A positive correlation between mass flow rate and the carbon content in U8Mo was observed. Further investigation into this effect is suggested, as it may have an impact on the atomization regime and thus particle shape. In particular, reduction of the carbon content may be used to reduce the mass flow rate in order to foster operation in the DDF regime. Also, quantification of this effect may extend the existing theoretical model and necessitate the adjustment of present fuel specifications.

The evaluated mass flow rate model represented fairly well experimental data and exhibited a coefficient of determination of 95 % with respect to experimental data. It thus may be used to estimate the mass flow rate from input parameters during the further development process. However, it does not take into account the purity of the rotating electrode material, leaving hence room for extension and improvement.

The present prototype atomizer equipment showed a stable level of result repeatability regarding the mass flow rate, thereby constituting a significant progress regarding process industrialisation.

Finally, the quantification of the U8Mo mass flow rate generated by the electric arc in REP allowed for determination of the governing atomization regime (chapter 6).

6

Atomization Regime

Control of the atomization regime or droplet formation mechanism is detrimental to the shape of the atomized particles – sphere, ellipsoid, filament, or flake. The particle shape, in turn, is a detrimental aspect of powder quality and influences the particle size distribution as well as process efficiency. In the following chapter the relationship between atomization process input-parameters, UMo, and the atomization regime are investigated. The ultimate goal is to identify a parameter set that allows for the production of spherical or near-spherical particles with respect to UMo. Therefore, a generally accepted empirical model to estimate process input parameters (mass flow rate, rotational speed, rotating electrode diameter, material properties) as well as experimental results of the preceding chapter were used.

6.1 Background

In centrifugal atomization, three droplet formation mechanisms can be distinguished: direct droplet formation, ligament disintegration, and sheet disintegration as reported by [Hinze and Milborn 1950], filmed by [Fraser *et al.* 1963], and investigated for multiple elemental metals, alloys, metal carbides, and oxides by [Champagne and Angers 1980][39] and [Hodkin *et al.* 1973][40], Figure 6-1. Furthermore, some authors [Wozniak 2003] distinguish between laminar and turbulent sheet disintegration (Figure 6-3). The schematic of the droplet formation mechanisms (Figure 6-3) also illustrates the predominant size distribution of the droplets that is echoed in the particle size distribution.

---

[39] Zinc, copper, steel, iron, and aluminium.

[40] UC, UO_2, ZrO_2, Al_2O_3, B_4C, and ZrB_2.

6.1.1 Direct Droplet Formation (DDF)

A bimodal particle size distribution is observed in this atomization regime [Champagne and Angers 1981, Champagne and Angers 1984, Hodkin *et al.* 1973, Lawley 1992, Lefebvre 1989, Wozniak 2003, Yule and Dunkley 1994]. In particular, both modes (or peaks) are about equal with respect to a number distribution, that is the number of secondary particles corresponds to the number of main particles [Champagne and Angers 1981, Champagne and Angers 1984]. This proportion results from the droplet formation mechanism where one satellite droplet is produced for every main drop as recorded in Figure 6-1, illustrated in Figure 6-3, and stated by [Champagne and Angers 1981, Champagne and Angers 1984, Lawley 1992, Wozniak 2003, Yule and Dunkley 1994]. The phenomenon occurring in the DDF is caused by the Rayleigh-Taylor instability which occurs at the interface between fluids of different densities (e.g. liquid metal and argon) that move relative to one another [Taylor 1950]. It acts on the liquid torus that is formed on the outer rim of the rotating electrode at relatively low rates of liquid supply, therefore giving rise to protuberances. These protuberances in turn are subjected to the opposing forces of surface tension and centrifugal force, eventually causing the formation of an ellipsoidal drop. As the “large” drop is thrown off, a “small” drop is formed from the “neck” or “thread” [Lawley 1992]. The secondary particles, however, constitute only a small percentage of the total mass as they are relatively small compared to the main particles (Figure 6-3). In fact, the secondary particle mass fraction may drop to 1.5 % depending on the parameter set [Champagne and Angers 1981]. The production of two droplets by the proposed mechanism is somewhat contradicted by observations of [Tanasawa *et al.* 1978] for normal liquids. The author compared photograms of dripping water to droplets forming at the outer rim revealing that the “neck” or “thread” disintegrates into several smaller droplets (Figure 6-2). On the one hand, the difference in observation may be due to the different means of visualisation: photogram [Tanasawa *et al.* 1978] and filming [Champagne and Angers 1984]. In particular, filming of liquid melts necessitates high-speed equipment that withstands the electric arc light emission. On the other hand, the difference in atomized liquids and thus difference in liquid properties such as surface tension, dynamic viscosity, and density may have influenced the break-up of the “neck” or “thread”. Also, two different centrifugal atomization techniques were used: REP and rotating disk atomization.

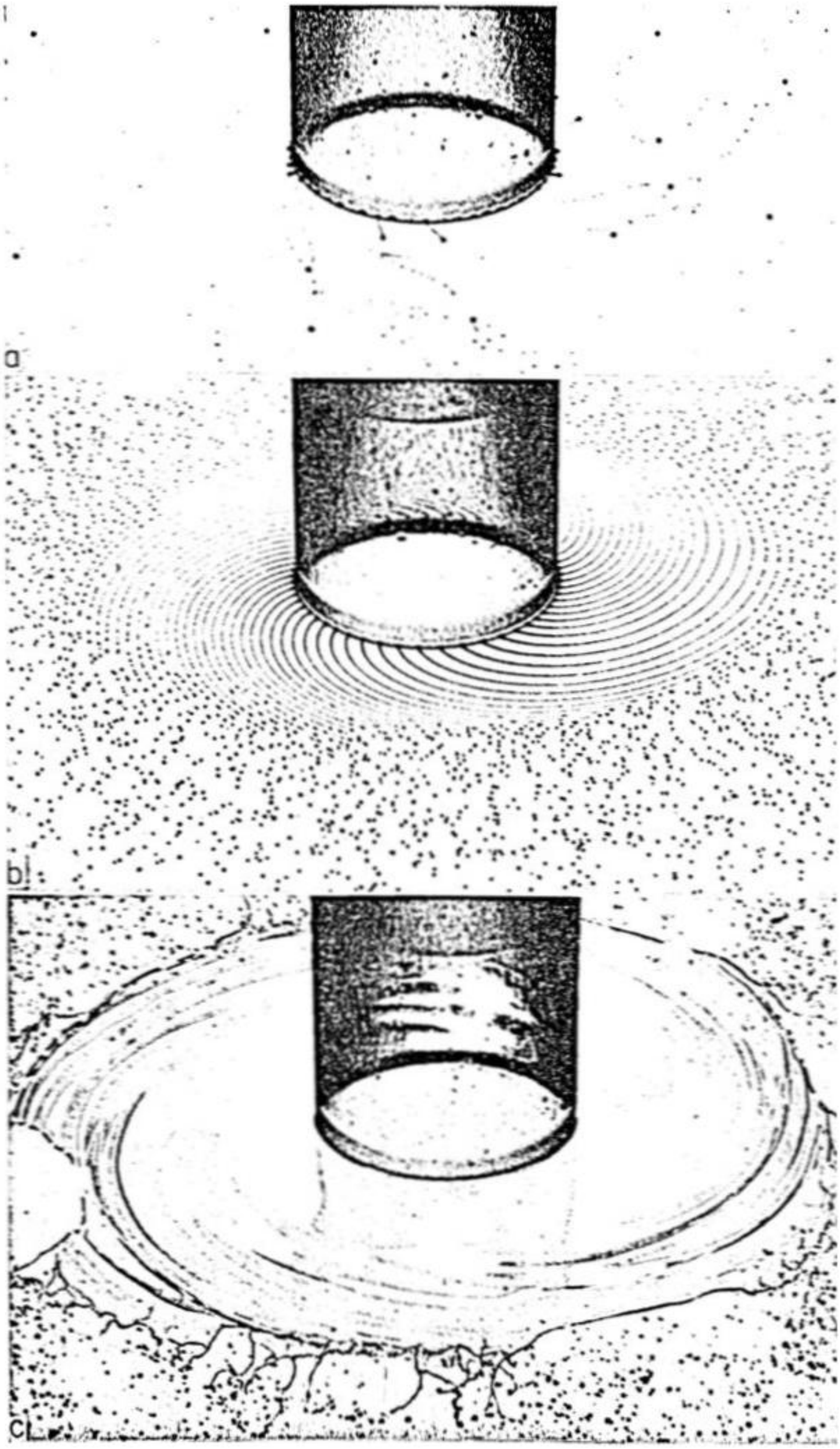

Figure 6-1 Droplet formation mechanisms in centrifugal atomization as filmed by [Fraser *et al.* 1963], top down: direct droplet formation, ligament disintegration, and film disintegration.

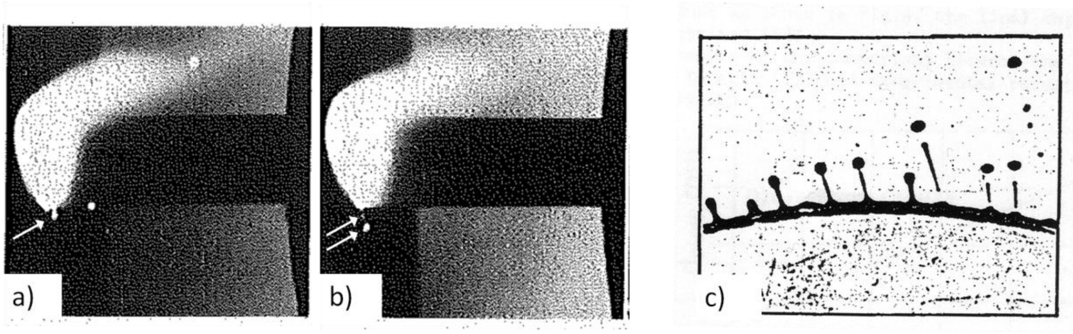

Figure 6-2 Formation of a large main droplet (a) and of a small secondary droplet (b) from the "neck" or "thread" during REP atomization of SAE 1090 steel in the DDF regime [Champagne and Angers 1984]. Formation of a large main droplet and break-up of the "neck" or "thread" into multiple secondary droplets (c) during rotating disk atomization of normal liquids (e.g. water) [Tanasawa *et al.* 1978].

In terms of productivity, this regime is characterized by a relatively small mass flow rate [Wozniak 2003] and thus small production of powder per unit time.

According to [Champagne and Angers 1984], atomized particles in the DDF are entirely spherical in shape. This is contradicted by [Yule and Dunkley 1994] who state that more ellipsoids are found for the ligament formation regime than for the DDF, thus implying that ellipsoids are also part of powder produced in the DDF. Eventually, [Hodkin *et al.* 1973] found that about 80 % of the powder produced through REP[41] in the DDF was spherical in shape; the irregular rest, though, was ascribed to the insufficient dimensions of their collection chamber. Besides the atomization regime, the atmosphere has influence on the particle shape. In particular, an increased oxygen concentration may lead to melt oxidation prior to droplet break-up and spheroidisation [Lawley 1992], consequently resulting in ellipsoids, filaments or irregular particles. For instance, it was found that tin alloy particles were more spherical in shape with decreasing oxygen content [Plookphol *et al.* 2011].

---

[41] The authors did not use the expression REP; instead, the term consumable anode process is used.

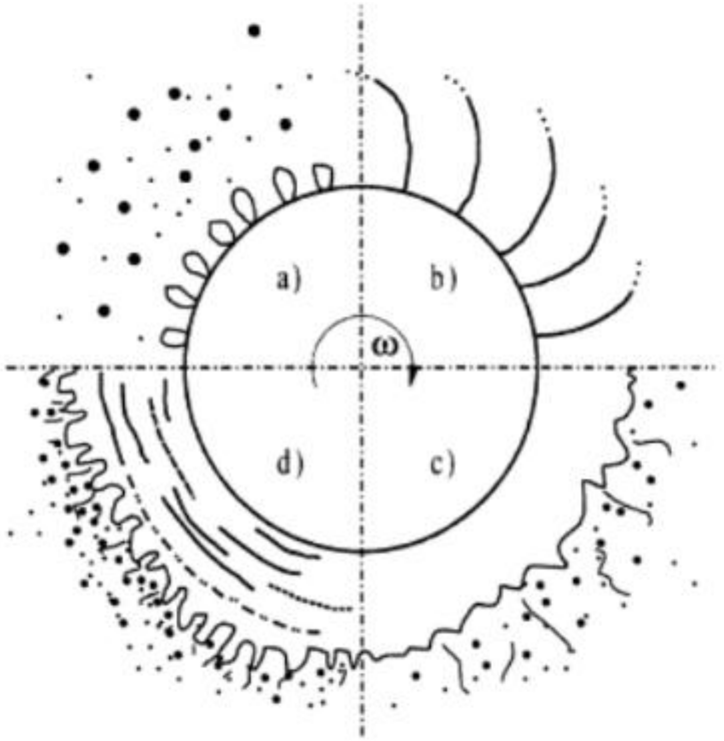

Figure 6-3 Schematic illustration of the different atomization regimes according to [Wozniak 2003]: a) direct droplet formation (DDF), b) ligament disintegration (LD), and c) laminar as well as d) turbulent film disintegration (FD). The illustration additionally accounts for the size distribution and shape of droplets produced in each regime, which is echoed in the resulting particle size distribution.

6.1.2 Ligament Disintegration (LD)

In the ligament disintegration regime (LD) the protuberances develop higher amplitudes [Lawley 1992]. The liquid (melt) forms unstable ligaments that pass the outer rim of the rotating electrode and break up into multiple fine droplets of similar size due to oscillation [Hodkin *et al.* 1973, Wozniak 2003]. The regime was recorded as well as illustrated in Figure 6-1 [Fraser *et al.* 1963] and Figure 6-3 [Wozniak 2003], respectively. The number of ligaments increases up to a certain number for a given rotational speed and electrode diameter as the mass flow rate is increased [Hodkin *et al.* 1973]. Further increase of the mass flow rate, though, results in a constant number of ligaments with increasing thickness [Hodkin *et al.* 1973].

As stated by [Champagne and Angers 1984], the transition from DDF to LD is gradual. The number of secondary particles increases (Figure 6-3), and the resulting particle size distribution changes. The dispersion of the particles in LD is, however, ambiguous. While [Wozniak 2003] indicates an almost monodisperse distribution (Figure 6-3), [Lawley 1992] summarises that the mass fractions of the modes become similar and that the distribution remains bimodal; eventually, [Yule and Dunkley 1994] state that the particle size distribution becomes increasingly polydisperse from DDF to film disintegration. The latter, though, may indicate the presence of multiple modes or a relatively broad distribution or both.

The LD regime is interesting from an industrial perspective due to its high productivity, i.e. production of powder per unit time [Wozniak 2003]. Although the proportion of ellipsoids is higher compared to the DDF [Yule and Dunkley 1994], spherical particles can be produced through centrifugal atomization in the LD. This, however, depends essentially on the superheat of the liquid melt. Particularly in REP, the LD regime can cause the production of ellipsoids or even manifested filaments as superheat is limited and particle solidification may occur before ligament break-up and full spheroidisation.

Starting from DDF, this regime is reached by an increase in mass flow rate and/or rotational speed as well as decrease of the rotating electrode diameter.

6.1.3 Film Disintegration (FD)

The film disintegration regime (Figure 6-1 and Figure 6-3) is reached if mass flow rate and/or rotational speed are further increased coming from LD; or, if the rotating electrode diameter is decreased. According to [Hodkin *et al.* 1973] the transition starts when the maximum of both number and thickness of ligaments is reached. In this respect it was reported that the ligaments gradually disappear for atomization of organic liquids, indicating the presence of a transition range [Champagne and Angers 1984]. The film disintegration can be divided into a laminar and turbulent regime (Figure 6-3 [Wozniak 2003]).

As stated by [Hodkin *et al.* 1973] this disintegration process is less regular and controlled in comparison to both the DDF and LD; the role of aerodynamics is increased, notably with increasing peripheral speed. Particles are less regular in shape and size than for both the DDF and LD. The range of the resulting particle size distribution was reported to be relatively broad [Wozniak 2003] and may resemble two-fluid atomization [Yule and Dunkley 1994]. It is thus avoided in applications where a narrow size distribution is demanded, although it offers high productivity.

[Fraser *et al.* 1963] presented an extensive number of recorded images showing differently developed films or sheets.

6.1.4 Model

A detailed study of [Champagne and Angers 1980, Champagne and Angers 1981, Champagne and Angers 1984] with respect to different REP-atomized metal powders and atomization mechanisms resulted in an empirical model for prediction of the atomization regime and hence particle shape from operating parameters and material properties, equations (6.1) and (6.2):

$$X = \frac{O_p}{M_p} = \left\{\frac{\text{Operating parameters}}{\text{Material properties}}\right\} \tag{6.1}$$

$$X = \frac{Q_\mathrm{l}\,\omega^{0.6}}{D_\mathrm{re}^{0.68}} \Big/ \frac{\sigma^{0.88}}{\rho_\mathrm{l}^{0.71}\,\mu_\mathrm{l}^{0.17}} \tag{6.2}$$

X	Characteristic number describing the atomization regime [-][42]
Q_l	Volume flow rate [m^3/s]
ω	Angular velocity [rad/s]
D_re	Rotating electrode diameter [m]
σ	Surface tension [N/m]
ρ_l	Liquid density [kg/m^3]
μ_l	Dynamic viscosity [kg/(m·s)].

From equation (6.2), it can be inferred that the transition from DDF to LD and eventually FD is promoted by increasing the volume flow rate and/or rotational speed, or by decreasing the rotating electrode diameter for a given material.

The theoretical transition from DDF to LD occurs at $X = 0.07$ while transition from LD to FD occurs at $X = 1.33$ [Champagne and Angers 1984]. Both values were derived semi-empirically by dimensionless analysis. They constitute averaged values. The authors graphically summarised their results in a diagram as can be seen from Figure 6-4. The model is generally accepted in reviewed secondary literature [Lawley 1992, Neikov *et al.* 2009, Yule and Dunkley 1994].

In the present study, the mass flow rate was measured (chapter 5). The relationship between volume and mass flow rate is given by:

$$\dot{m} = Q_\mathrm{l}\rho_\mathrm{l} \tag{6.3}$$

$\dot{m}$ Mass flow rate (kg/s).

Combination of equations (6.2) and (6.3) results in:

$$X = \frac{\dot{m}\,\omega^{0.6}}{\rho_\mathrm{l} D_\mathrm{re}^{0.68}} \Big/ \frac{\sigma^{0.88}}{\rho_\mathrm{l}^{0.71}\,\mu_\mathrm{l}^{0.17}} \ . \tag{6.4}$$

---

[42] X was derived by dimensionless analysis that generally results in dimensionless quantities. However, X is not dimensionless as parameter exponents were rounded to two decimal digits.

With respect to the lack of relevant thermophysical data of UMo in reviewed literature, thermophysical data of metallic uranium were used for calculations [Burkes *et al.* 2010, Creasy 2012, Ferreira *et al.* 2011, Phillips *et al.* 2010, Rest 2009].

Other models exist and are summarised in [Ashgriz 2011, Lefebvre 1989, Wozniak 2003]. In particular, equations for the critical mass flow rate for regime transition derived by [Tanasawa *et al.* 1978] are mentioned. Their application is less convenient, though, since the given models describe either the DDF to LD or the LD to FD transition. In contrast, equation (6.4) can be applied to each regime. Also, the models yield different results depending on the parameter set and atomizer configuration [Wozniak 2003].

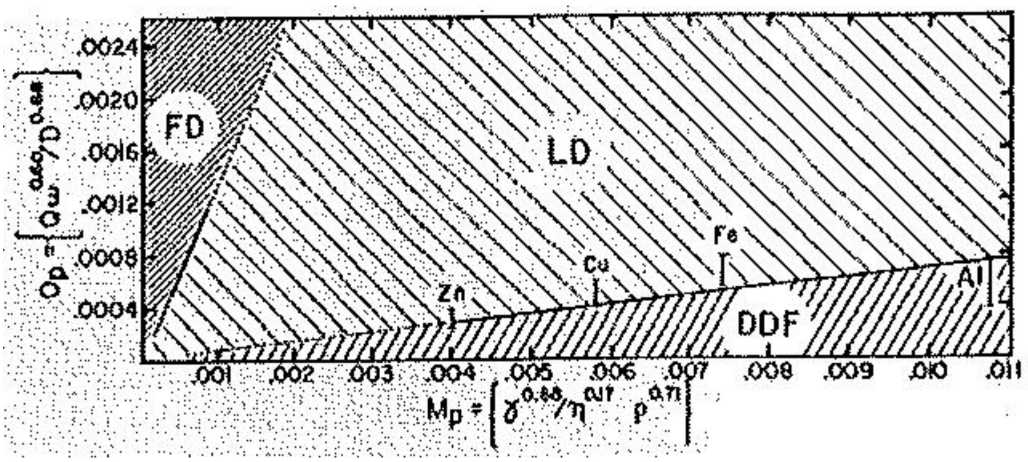

Figure 6-4 Atomization regimes (DDF, LD, and FD) as a function of material properties and operating parameters taken from the original publication [Champagne and Angers 1984]. Investigated materials were zinc, copper, iron, steel, and aluminium. Parameter sets with identical *X* are situated on the straight line $O_p = X \cdot M_p$. The vertical interval bars correspond to experimental results and indicate a transition range from DDF to LD. The theoretical transition from DDF to LD occurs at $X = 0.07$, while transition from LD to FD occurs at $X = 1.33$. Zinc and aluminium constitute the lower and upper limit, respectively, of the experimentally validated data regarding metal melts. The dotted lines represent extrapolations of both transition lines.

However, some general particularities of all models – including (6.4) – have to be mentioned as they have influence on the experimental setup and analysis carried out in this work:

+ *X* is not dimensionless.

+ The models were empirically derived, mostly using dimensionless analysis (e.g. the Buckingham theorem [Champagne and Angers 1984, Hinze and Milborn 1950]) and its inherent shortcomings like the uncertainty of parameters, the increasing or stable confidence with increasing number of parameters, and dependence on the experimental setup. Thus, the models are often based on a specific atomizer configuration and the range of the applied parameter set.

- The transition between the regimes is not distinct but gradual, and the range varies with respect to the atomized material and thus material properties (Figure 6-4).
- Hysteresis is an effect that is not accounted for by the different models but actually present at the transition from DDF to LD according to [Wozniak 2003]. That is, the position of transition depends on the point of departure.
- The coefficient of transition from the DDF to LD, $X = 0.07$, suggests a linear behaviour for a given material. It is, however, an approximation as can be inferred from Figure 6-4 and the different transition ranges as well as different starting points. It is based on the regression analysis of an experimental parameter that had a coefficient of multiple determination of 86 % [Champagne and Angers 1984].
- The X-model is based on the investigation of four elemental metals (except steel) while U8Mo is an alloy with a melting range of about 100 K [Wilkinson 1962a].
- By comparing Figure 6-5 to Figure 6-4, it can be seen that experiments involving U8Mo or pure uranium are situated beyond the experimentally validated limits of equation (6.4), corresponding to zinc and aluminium, respectively. Recent publications on atomization of UMo, U_3Si_x, and other uranium-based alloys did not address this information gap; that is, the corresponding X value was not reported [Clark *et al.* 2010, Clark *et al.* 2007, Kim *et al.* 1992, Kim *et al.* 1997a, Kim *et al.* 1997b, Kim *et al.* 2007, Moore and Archibald 2014, Oh *et al.* 2006, Olivares *et al.* 2012, Park 1999]. As a consequence, the effect of different parameter sets on the atomization regime with respect to centrifugal atomization of U8Mo in general and REP in particular is investigated in this chapter.

6.2 Experimental Setup

With respect to the fuel specifications [Gery 2011, Harbonnier 2002, Vanvor and Zill 2003], though, spherical fuel particles are requested (chapter 2.4). Consequently, the target region was either the DDF regime or the transition region between DDF and LD or the early LD in order to produce spherical or spheroidal (ellipsoidal) particles.

The rotational speed, electric arc current, and rotating electrode diameter were varied from 20’000 rpm to 50’000 rpm, 35 A to 100 A, and 10 mm to 20 mm, respectively. In particular, 50’000 rpm constitutes the maximum rotational speed of the current atomizer configuration (chapter 3.3.13) while 30 A was determined as lower threshold of the electric arc current (chapter 5.3.2) with respect to the reference rotating electrode with 10 mm diameter. The glovebox exhibited approximately ambient pressure (chapter3.3.3). The argon atmosphere contained between 2 and 7 ppm of oxygen as well as moisture.

The operating parameters were so combined as to vary around $X = 0.07$ by at least ± 0.04 in order to determine both the regime where favourable powder is produced and the transition range with respect to U8Mo. The variation range of ± 0.04 was based on graphical measurement of the transition ranges plotted in Figure 6-4. In fact, it can be seen that for the experimentally tested materials the transition from DDF to LD started not earlier than for $X \sim 0.035$ (aluminium) and ended not later than for $X \sim 0.1$ (zinc, copper, iron) [Champagne and Angers 1984]. Both the upper and lower threshold is included in Figure 6-5 (red dotted lines). For comparison, similar parameter sets were applied to 1.4301 stainless steel.

Due to changes in the research and development program [Breitkreutz 2015] during the experiments, the initial alloy composition was changed from U8Mo to U7Mo.

6.3 Results and Discussion

6.3.1 Particle Shape and Model Evaluation

A graphical map of all[43] conducted experiments is given in Figure 6-5 with respect to experimentally validated data on atomization regime transition.

As expected from the experimental setup, different particle shapes were found in analyzed powder samples with respect to U8Mo and U7Mo while the 1.4301 stainless steel powder consisted of almost entirely spherical particles. The results with regard to 1.4301 stainless steel are in agreement with results obtained from REP atomization of SAE 1090 steel [Champagne and Angers 1984].

All U8Mo and U7Mo experiments[44] are listed in Table 6-1 in order to compare the predominant particle shape and number of modes to the calculated X value. For the calculation of X the results of chapter 5 and material properties summarised in Table 6-2 were used.

---

[43] Only experiments that complied with the experimental setup were considered.

[44] Except 552-13/17/18 as their mass flow rate was not measured.

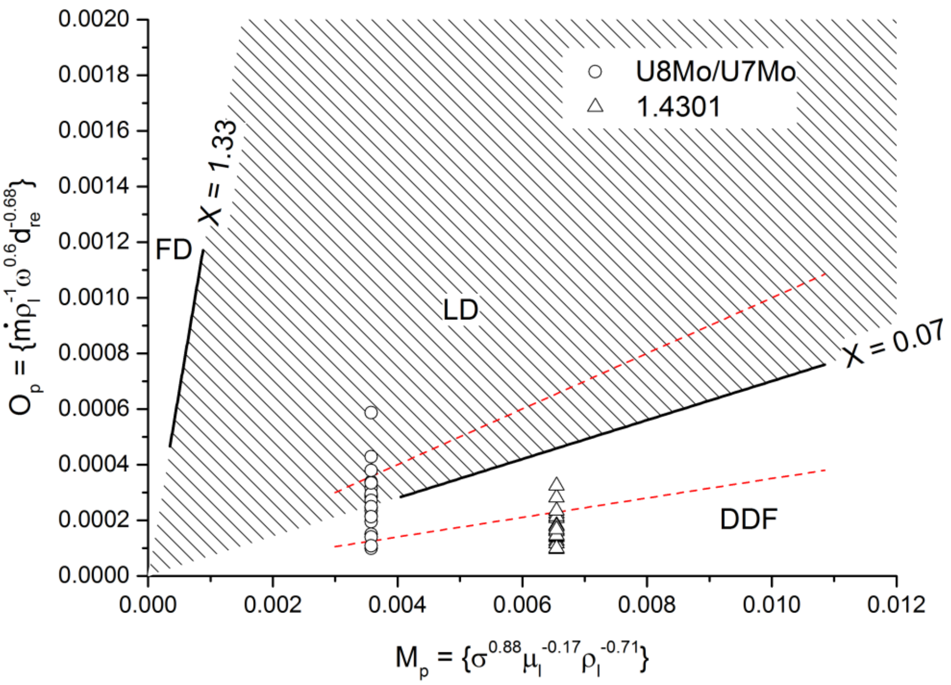

Figure 6-5 X-diagram showing the conducted U8Mo/U7Mo and 1.4301 stainless steel experiments with respect to the atomization regimes. The bold black lines, corresponding to $X = 0.07$ and $X = 1.33$, represent the theoretical (and averaged) transition between regimes as determined by [Champagne and Angers 1984] and [Hinze and Milborn 1950], respectively. The red dotted lines represent the assumed transition range that was obtained from graphical measurement of the transition ranges of Zn, Cu, Fe, and Al plotted in Figure 6-4. The lower threshold was determined to $X = 0.035$, the upper threshold to $X = 0.1$.

From Table 6-1 several conclusions may be drawn:

Within the analysed size ranges (< 180 µm), a clear trend was observed: with decreasing X the fraction of spherical particles increased as predicted by [Champagne and Angers 1984]. In samples with the label "S", about 90 % of the population was spherical.

Below $X \sim 0.068$, particles were almost entirely spheres (Figure 6-6). Below $X \sim 0.82$, spheres and ellipsoids became predominant (Figure 6-7). Above $X \sim 0.82$, manifested filaments appeared (Figure 6-8). Batches 552-16, 552-10, 552-11, and 552-12 were produced from short rotating electrodes and therefore another parameter set. According to the findings in chapter 5.3.3, shorter electrodes tended to underestimate the "real" mass flow rate, thus leading to an underestimation of the "true" X value. Batch 552-14 may have yielded the same results between 45 µm and 125 µm as batches 552-33 and 552-36, but final comparison was not possible as the analysed size ranges were different.

Table 6-1 Experimental values for *X* (equation (6.4)) of atomized U8Mo/U7Mo powder and corresponding particle shape that was observed in extracted powder samples. Particle shapes were determined by visual observation using optical or electron microscopy and visual counting. Most samples were embedded and sectioned for microscopy except U8Mo-552-33/36. As a result, filaments may have appeared as ellipsoids or spheres. Occasional occurrence of a certain particle shape was not taken into account; the applied ratio was about 1:10. A change of alloy or rotating electrode length was noted in the column "remarks".

Batch	Atomization regime parameter	Predominant particle shape [sphere (S), ellipsoid (E), filament (F)]			Remarks	Number of modes
	X [-]	Particle diameter < 45 µm	45 - 125 µm	45 - 180 µm		
U8Mo-552-11	0.164	S+E	/	S+E	short	2
U8Mo-552-29	0.120	S+E+F	/	S+E+F		2
U8Mo-552-10	0.106	S+E	/	S+E	short	2
U8Mo-0914-1	0.095	S+E+F	S+E+F	/		1
U8Mo-552-30	0.093	S+E+F	/	S+E		2
U7Mo-1114-3-4.5	0.088	/	S+E	/	U7Mo	1
U8Mo-0914-4	0.082	S	S+E	/		1
U8Mo-0914-3	0.081	/	/	/		1
U7Mo-1114-03	0.080	S	S+E	S+E*	U7Mo	1
U7Mo-1114-3-1.6	0.079	S	S+E	S+E*	U7Mo	1
U8Mo-552-16	0.076	S+E+F	/	S+E	short	2
U8Mo-552-39	0.070	/	/	/		2
U8Mo-552-33	0.068	S	S	/		2
U8Mo-552-36	0.065	S	S	/		2
U8Mo-552-14	0.060	S	/	S+E	short	3
U8Mo-552-42	0.059	/	/	/		2
U8Mo-552-38	0.054	/	/	/		2
U8Mo-552-04	0.042	S	/	S		1
U8Mo-552-06	0.039	-	/	S+E		1
U8Mo-552-12	0.030	S	/	S+E	short	2
U8Mo-552-08	0.028	S	/	S		1

short: short rotating electrode

* size range 125 - 180 µm

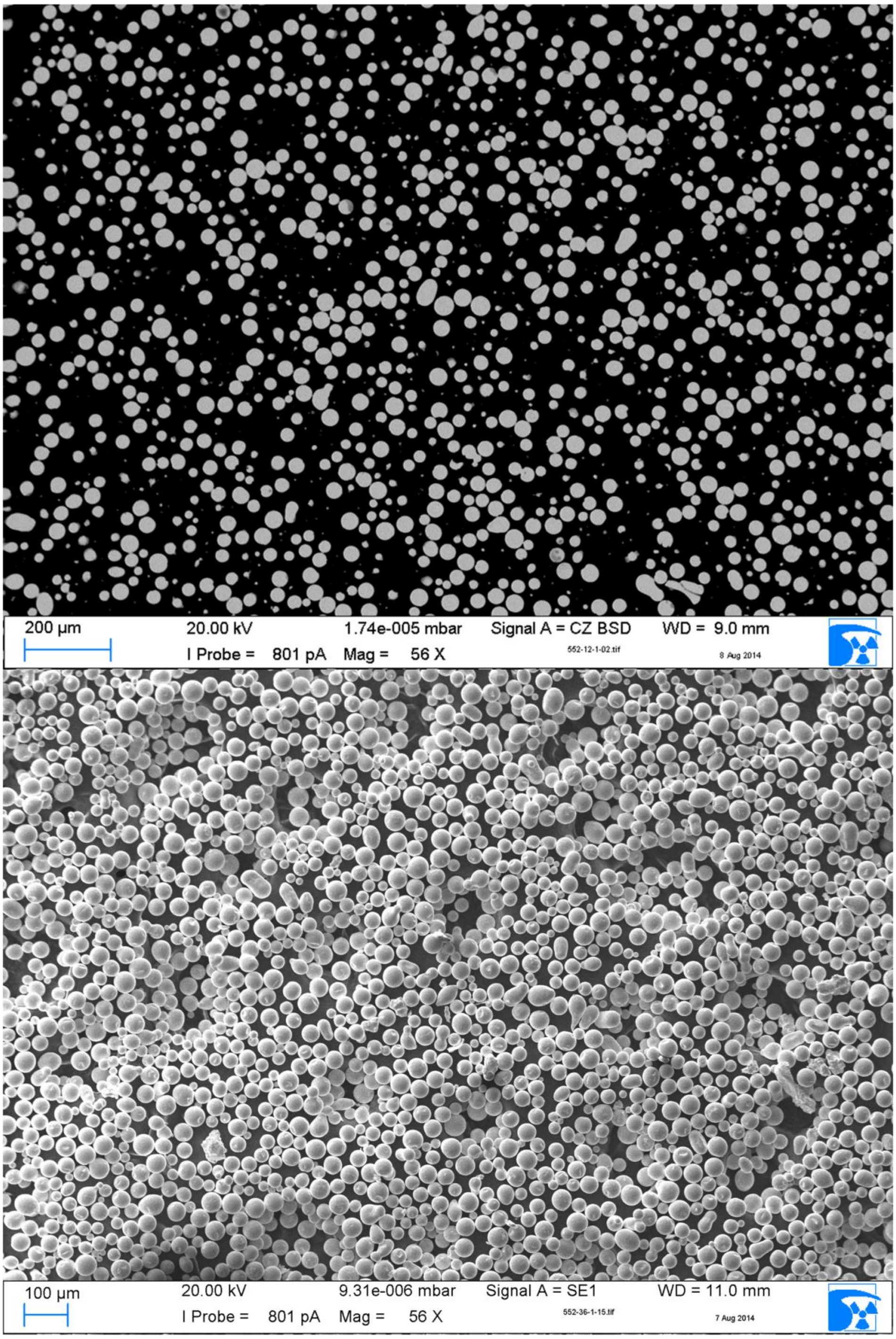
200 µm
20.00 kV
1.74e-005 mbar
Signal A = CZ BSD
WD = 9.0 mm
I Probe = 801 pA
Mag = 56 X
552-12-1-02.tif
8 Aug 2014
100 µm
20.00 kV
9.31e-006 mbar
Signal A = SE1
WD = 11.0 mm
I Probe = 801 pA
Mag = 56 X
552-36-1-15.tif
7 Aug 2014

Figure 6-6 SEM micrographs of samples originating from batches U8Mo-552-12 (top) and U8Mo-552-36 (bottom) showing sectioned and full particles, respectively, with smallest diameter < 45 µm. Batch U8Mo-552-12 was embedded and polished. Both powder samples predominantly consisted of spherical particles; similar samples were marked with “S” with respect to Table 6-1.

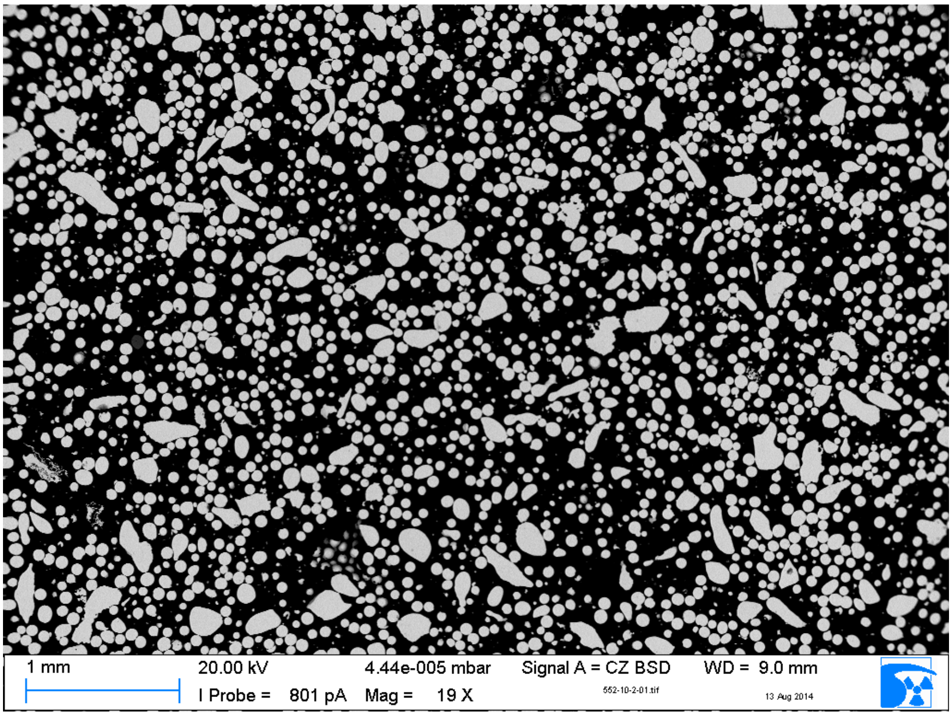
1 mm
20.00 kV
4.44e-005 mbar
Signal A = CZ BSD
WD = 9.0 mm
I Probe = 801 pA
Mag = 19 X
552-10-2-01.tif
13 Aug 2014

Figure 6-7 SEM micrograph of an embedded and polished sample of batch U8Mo-552-10 showing sectioned particles with smallest diameter between 45 μm and 180 μm using back-scattered electrons (BSE). Particle shapes varied between sphere and ellipsoid. Similar samples were typically marked with "S+E" with respect to Table 6-1.

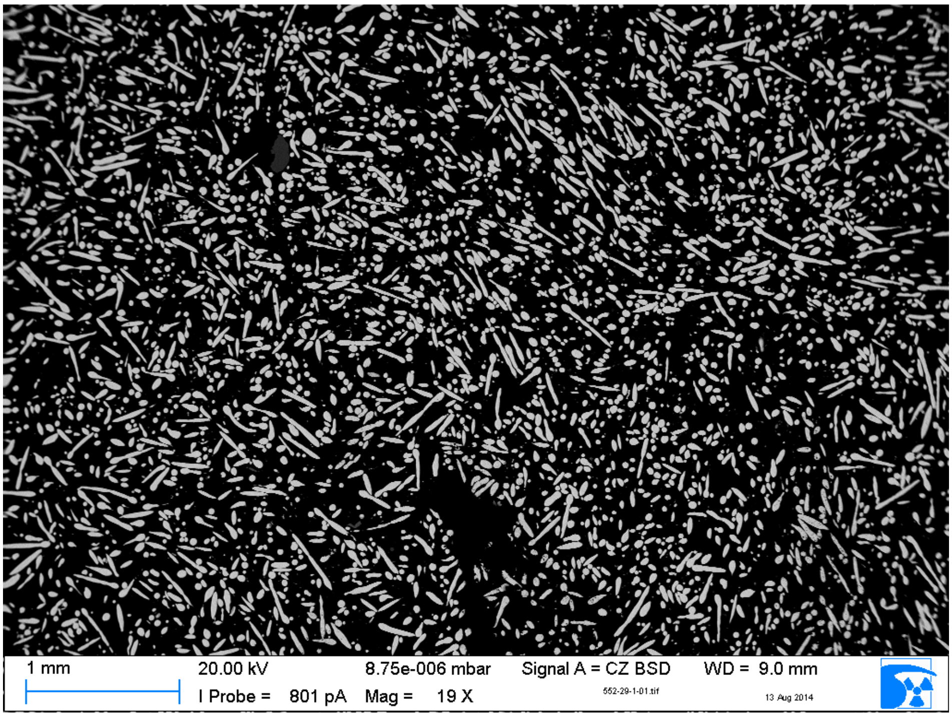
1 mm
20.00 kV
8.75e-006 mbar
Signal A = CZ BSD
WD = 9.0 mm
I Probe = 801 pA
Mag = 19 X
552-29-1-01.tif
13 Aug 2014

Figure 6-8 SEM micrograph of an embedded and polished sample of batch U8Mo-552-29 showing sectioned particles with smallest diameter < 45 μm using back-scattered electrons (BSE). Particle shapes varied between sphere, ellipsoid, and filament (needle). Similar samples were typically marked with "S+E+F" with respect to Table 6-1. The presence of spherical and ellipsoidal particles, though, must be considered carefully as they might represent cross-sections of filaments.

Manifested filaments were observed in batches 552-16, 552-29, 552-30 as well as 0914-01. Their presence is a definite indicator of atomization in the ligament disintegration regime. According to [Hodkin *et al.* 1973] "particles freeze before spheroidisation and are subsequently detached" as the "sheets[45] or[46] ligaments extend beyond the hot zone of the arc".

Another remarkable observation with respect to the manifested filaments was their sudden presence in the sieved powder samples compared to the gradual increase of ellipsoids with increasing X value. This can be explained by the powder screening technique, namely dry sieving: for a filament, the cross-sectional diameter perpendicular to its longest axis is small (in about the size of the diameter of a potential sphere after ligament break-up). The filament thus may fall through the mesh grid if it has the right orientation although its equivalent diameter is much larger [Yule and Dunkley 1994]. This is important as filaments increase not only the number of small particles, but also their mass fraction, hence giving a false impression of the "true" particle size distribution with regard to spherical particles.

In the observed ranges, neither flakes nor fringe nor particles with plastic deformation (due to impingement with the chamber walls) were found. Thus, it can be inferred that the dimensions of the collection chamber and the resulting cooling path was sufficient with respect to the applied operating parameters and materials. It is noted, though, that particles were occasionally found on the collection chamber walls. Irregular particles were systematically found in size ranges > 355 µm (Figure 6-9), though were not part of the investigated target size range. Their presence is ascribed to insufficient particle solidification before impingement on the collection chamber wall, inhomogeneity of the rotating electrode alloy, and atomization of U8Mo through REP (chapters 7.2.3, 8.2.3).

Evaluation of the number of modes of the size distributions (Table 6-1) was inconclusive. While the variation of modes of the particle size distributions above $X \sim 0.082$ was influenced by the presence, thickness, and amount of filaments, the distribution of modes below $X \sim 0.068$ contradicted expected behaviour (chapter 6.1). Limitations of the screening technique as discussed in chapter 4.3 might have contributed to this observation. However, the particle size distributions of U8Mo and U7Mo (chapter 7.2.3) never showed a distinct main mode as observed for 1.4301 stainless steel (Figure 4-1).

---

[45] Some authors use the term sheet disintegration instead of film disintegration.

[46] In the original publication it is written "of" instead of "or", but "sheets or ligaments" were discussed before; the description "sheet of ligaments" is not a common term.

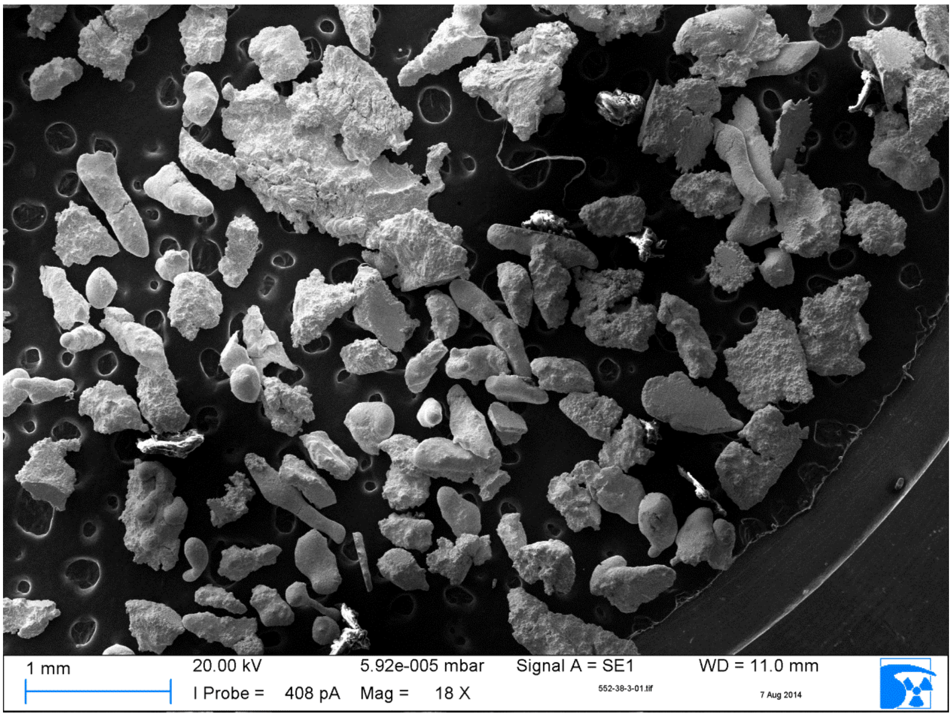

Figure 6-9 SEM micrograph using secondary electrons (SE) of a sample of batch U8Mo-552-38 showing particles with smallest diameter > 355 μm.

The results presented in Table 6-1 suggest that the droplet formation mechanism converges towards the DDF regime with decreasing X. In particular, samples almost entirely consisting of spherical particles in the target size range were found below $X = 0.068$. Compared to the predicted regime transition around $X = 0.07$, it can be inferred that the model applies to REP atomization of U8Mo as well (Figure 6-5).

6.3.2 Surrogate Material

Initially, 1.4301 stainless steel was used to validate the general mechanical function of the atomizer and its unique design at inert test and commissioning level due to its advantages (chapter 4.1)

Evaluation of the interaction of atomizer operating parameters and U8Mo revealed, though, that 1.4301 stainless steel is neither a representative estimator with respect to the mass flow rate (Figure 5-7) nor atomization regime (Figure 6-5).

If extensive inert testing should be part of the prospective development with respect to the industrial pilot, the experience made during this work suggests using a surrogate material that is more representative regarding both the droplet formation mechanism and mass flow rate. As a consequence, a brief study of potential surrogate materials for replacement of 1.4301 stainless steel was conducted in support of future work, in particular paying attention to the parameter M_p (Table 6-2).

Table 6-2 Material properties parameter M_p, calculated for various liquid metals; thermophysical material properties were taken from literature [Champagne and Angers 1981, Fischer 2000, Paradis *et al.* 2014, "Smithells Metals Reference Book" 1992, "Thermophysical properties of materials for nuclear engineering" 2008, Yule and Dunkley 1994]. For some materials, two values are given due to inconsistencies in the reviewed literature.

Material	Dynamic viscosity	Surface tension	Liquid density	Enthalpy of melt	Material properties parameter
	μ_l [kg/(m·s)]	σ [N/m]	ϱ_l [kg/m^3]	H_m [kJ/kg]	M_p $\{\sigma^{0.88}\mu_l^{-0.17}\varrho_l^{-0.71}\}$
Aluminium	0.0045	0.855	2390	1150	0.00872
	0.0013	0.86	2380	1050	0.01085
Cobalt	0.00418	1.873	7740	1233	0.00764
Copper	0.0045	1.3	7990	713	0.00535
	0.004	1.355	8000	670	0.00566
Gold	0.005	1.14	17300	238	0.00271
Lead	0.00263	0.46	10590	74	0.00192
Magnesium	0.00125	0.55	1590	1217	0.00982
Mild steel	0.005	1.5	7000		0.00655
Nickel	0.0049	1.778	7890	1163	0.00701
Platinum	0.00482	1.8	18900	388	0.00382
	0.0071	1.8	18900	388	0.00358
SAE 1090 steel	0.0055	1.546	7015	1210	0.00661
Silver	0.00388	0.903	9300	376	0.00358
Tin	0.00197	0.57	6970	134	0.00328
Titanium	0.0052	1.65	4100	1500	0.01034
Uranium	0.0065	1.65	17320	245	0.00358
Zinc	0.0068	0.8	6550	317	0.00374
	0.0038	0.782	6570	317	0.00405

From Table 6-2 and calculation of M_p it can be inferred that platinum is presumably the best surrogate for uranium with respect to the parameter M_p as well as the single material properties[47] – and thus a good approximation for U8Mo. The M_p of silver matched the one of uranium, too, but its single material properties differed more. In contrast, the single material properties of gold were close to the one of uranium, but its M_p was considerably smaller. Zinc and tin are also options due to their similar M_p.

Another advantage arising from the use of the stated candidates is their enthalpy of melt that is similar to that of uranium – at least significantly closer than the enthalpy of melt of SAE 1090 steel and thus 1.4301 stainless steel (Table 6-2). Taking into account the relationship between mass flow rate and the enthalpy of melt represented by equation (5.14), it follows that using silver, platinum, zinc, tin, or gold instead of 1.4301 stainless steel should result in a significantly better approximation of the mass flow rate of U8Mo for a given arc welder parameter set (electric arc current, voltage).

---

[47] Surface tension and liquid density have direct influence on the mean particle size.

In terms of rotational speed and thus centrifugal force, however, the inferior mechanical properties of some potential candidates with respect to 1.4301 stainless steel and U8Mo must be considered (Table 6-3). Availability, market price, and particularly fabrication options (turning, casting etc.) are additional influencing factors in the choice of an alternative surrogate material. Thus, 1.4301 stainless steel was a well-suited surrogate, though not the best possible.

As a result, platinum is suggested as surrogate material for pilot development. Due to observations discussed in chapter 7.2.3, a platinum alloy with a similar melting range as U8Mo should be preferred, notably for REP, provided the material properties and M_p are still close to those of uranium.

Table 6-3 Mechanical properties of the alternative surrogate materials ["Smithells Metals Reference Book" 1992, "Thermophysical properties of materials for nuclear engineering" 2008]. Tensile strength depends on material purity, alloying elements, condition, and heat treatment.

Material	Tensile strength [MPa]
1.4301	500
Gold	130-220
Platinum	125-205
Silver	170-330
Tin	14.5
UMo	409-972
Zinc	120-150

6.4 Comparison

Operating parameters and obtained particle shapes with respect to atomization of UMo have been recently reported by KAERI [Kim *et al.* 1997b, Kim *et al.* 2007, Oh *et al.* 2006] , INL [Clark *et al.* 2007, Moore and Archibald 2014], and CCHEN [Olivares *et al.*

2012]. KAERI uses the rotating (spinning) disk (or cup) process, while INL and CCHEN are using REP.

For comparison, mass flow rates and the quantity *X* were calculated from reported data [Moore and Archibald 2014]. As can be seen from Table 6-4, the INL atomizer operates in a similar range[48] as the machine presented in this work (Table 6-5). The production of spherical particles was reported accordingly [Clark *et al.* 2007]. The powders generally show monomodal size distributions [Moore and Archibald 2014]. Due to the strong variation in mass flow rate despite a constant parameter setting, it is assumed, that systematic atomization in the proximity of the DDF is compromised due the INL atomizer design (Table 6-4).

In fact, the variation of *X* values of the INL atomizer indicates partial atomization in regimes where filaments were found in this study (Table 6-1). However, the presence of filaments was never reported. A reason might be the general presence of mechanical vibration and resonance due to the design and reported resonances at around 40'000 rpm [Clark *et al.* 2010]. These vibrations may promote a forced break-up of the ligaments before solidification, therefore yielding spherical particles. In this context, recent investigations of this phenomenon with respect to centrifugal atomization have to be mentioned. The development of a vibrating spinning disk atomizer for control of droplet size in the ligament regime by means of forced vibration was reported [Zainoun 2004a, Zainoun 2004b]. In the mentioned studies, vibration was generated by a piezoelectric cell.

CCHEN reported atomization experiments with U7Mo at 36'000 rpm, between 40 A to 80 A, and rotating electrode diameters between 6 mm to 10 mm [Olivares *et al.* 2012]. However, atomization times were not reported, making it impossible to calculate mass flow rates and the corresponding *X*. The presented powder consisted of spheroids, filaments, and irregular particles, though.

---

[48] This includes argon atmosphere with < 5 ppm oxygen.

Table 6-4 Operating parameters of the INL atomizer and corresponding X-values. Data for calculation of the mass flow rates and X were recovered from [Moore and Archibald 2014], namely electric arc current, estimated rotational speed, estimated atomized mass, and atomization time.

Batch	Arc current intensity	Mass flow rate	Rotational speed	Rotating electrode diameter	Atomization regime
U8Mo	I [A]	$\dot{m}_{\mathrm{app}}$ [g/s]	n [rpm]	D_{re} [mm]	X [-]
552-01	80	1.7	37'000	10	0.089
552-37	80	1.5	42'000	10	0.085
552-41	80	1.1	45'000	10	0.065
552-15	80	1.7	45'000	10	0.100
552-20	80	1.1	45'500	10	0.065
552-09	80	0.85	46'000	10	0.051
552-34	80	1.7	46'000	10	0.102

Table 6-5 Operating parameters of the FRM II/CERCA atomizer for $X \leq 0.068$.

Batch	Arc current intensity	Apparent mass flow rate	Rotational speed	Rotating electrode diameter	Atomization regime parameter
U8Mo	I [A]	$\dot{m}_{\mathrm{app}}$ [g/s]	n [rpm]	D_{re} [mm]	X [-]
552-33	50	1.15	45'000	10	0.068
552-36	45	1.10	45'000	10	0.065
552-39	50	1.26	40'000	10	0.070
552-38	40	0.987	40'000	10	0.054
552-42	50	1.28	30'000	10	0.059
552-06	35	0.843	30'000	10	0.039
552-04	50	1.15	20'000	10	0.042
552-08	35	0.762	20'000	10	0.028
552-14*	50	0.953	50'000	10	0.060
552-13*	50	-	40'000	10	-
552-12*	35	0.550	40'000	10	0.030

* short rotating electrode

KAERI reported atomization of U_3Si, U_3Si_2, U2Mo, U7Mo, and U10Mo. Atomization experiments were conducted under argon [Kim *et al.* 2007], argon/helium mixture, and helium atmosphere [Oh *et al.* 2006] with respect to UMo, as did [Champagne and Angers 1981]. Mass flow rates between 1.9 kg min^{-1} to 6.2 kg min^{-1} with respect to UMo were investigated [Kim *et al.* 1997b], and rotational speeds of up to 32'000 rpm were reported [Kim *et al.* 1997a]. Generally, the molten UMo had 200 K superheat and particles were atomized in a collection chamber of 2.5 m in diameter [Kim *et al.* 2007]. However, the rotating disk diameter has not been reported, making the calculation of an X-value impossible. The presented U7Mo powder consisted of spherical particles [Kim *et al.* 2007, Oh *et al.* 2006]. While [Oh *et al.* 2006] reported monomodal particle size distributions, [Kim *et al.* 1997b] presented UMo particles of spherical and ellipsoidal shape with diameters between 120 μm and 140 μm. The same author showed a bimodal particle size distribution of UMo[49] where the number of secondary particles was more than twice the number of main particles. It was also reported that particles below 45 μm were lengthened or had a flaky shape. Thus, both reports indicate atomization in the ligament formation regime.

6.5 Conclusion

It was found that atomization of U8Mo yielded almost entirely spherical particles in the target size ranges (< 40 μm, < 125 μm, and < 180 μm) below $X \sim 0.068$ and an argon atmosphere with less than 10 ppm of oxygen and moisture, respectively. Thus, a reference point was determined for the production of the favoured spherical particle shape.

In addition, undesired filaments (manifested ligaments) were found above $X \sim 0.082$, thus giving a reference point of parameter combinations that have to be avoided.

Irregular particles were found in irrelevant size ranges above 355 μm.

Both the present study and comparison with related publications indicate that the operating range of the FRM II/CERCA atomizer promotes U8Mo atomization in the ligament formation regime, though in proximity of or in transition to the direct droplet formation regime. This is a fairly favourable condition as it combines high productivity (LD regime), a relatively high number of small particles (LD regime), and avoids excessive superficial oxidation of the hot rotating electrode in a "slow" process (DDF regime) while producing spherical or near-spherical particles.

---

[49] It was not stated to which alloy composition – U2Mo or U10Mo – the presented particle size distribution and micrograph belonged.

The predicted transition from the DDF to LD regime at $X \sim 0.07$ was confirmed for REP atomization of U8Mo and 1.4301 stainless steel. As a result, the X-model may serve as useful reference point for operating parameter choice. Also, the use of uranium thermophysical properties as approximation for U8Mo provided reasonable results that were in good agreement with predictions.

For the future development efforts, visualisation of the atomization mechanism by means of a high-speed (video) camera that resists the luminous intensity of the electric arc is recommended if detailed investigation of the atomization regime is planned. Also, the use of platinum as inert surrogate materials for potential inert pilot development is suggested after brief evaluation of potential surrogate metals. It must be taken into account, though, that the suggested materials are still pure metals and not alloys, therefore not exhibiting a melting range as U8Mo. Thus, platinum alloys should be evaluated for their potential as surrogate material.

7

Particle Size and Process Efficiency

Having investigated in the preceding chapter the conditions needed to obtain spherical or near-spherical particles with respect to UMo, process parameters have to be so adjusted as to reach the desired particle size for fuel element production. In this chapter, experimentally obtained yield efficiencies and particle size distributions with respect to U8Mo and operating parameters are evaluated. The knowledge of the particle size distribution allows for better evaluation of the yield efficiency with respect to a specific threshold diameter as it reveals what shape the particle size distribution has within a certain size range – be it narrow or broad, with extreme values or constant. This is essential information as the particle size distribution influences the packing density and the irradiation behaviour of the fuel element, i.e. it is an important parameter for the irradiation performance of UMo fuel. Ultimately, the experimental results are compared to existing models for particle mean size prediction

7.1 Background

7.1.1 Powder Screening

For this study, an electromechanical dry sieving machine was chosen for powder screening as the necessary equipment could be directly integrated into both the production laboratory and atomizer glovebox without impact on nuclear safety and corresponding obligations. In addition, the equipment allows for subsequent powder screening right after atomization instead of costly and time-consuming shipping of the uraniferous fuel powder to appropriately equipped laboratories.

Due to the screening technique, the particles are sorted into classes with respect to their diameter. Thus, all particles with a diameter between 125 μm and 180 μm are part of the same particle size class if for examples the mesh sizes 125 μm and 180 μm are used for sieving.

Table 7-1 summarises the mesh sizes used for dry sieving of UMo and 1.4301 stainless steel. Sieve or mesh sizes are regulated by standards (ISO 565:1990 and ISO 3310-1:2000) and generally follow geometric series. That is, mesh sizes grow by a chosen factor (progression ratio), for instance ~ √2. Hence, particles with greater diameter are collected in greater classes (mesh size intervals), consequently increasing the potential number of collected particles. This approach, thus, mitigates the rising impact of particle mass on the sieving results with increasing diameters [Yule and Dunkley 1994] as linearly increasing particle diameters cause the particle mass to increase by d^3. If, for instance, the number of particles in the region of coarse particles is small, a particle that passes the mesh or not may change significantly the mass fraction in the concerned class. Another advantage arising from the use of geometric series is of particular utility for atomized powders since they are often log Gaussian (log-normal) distributed: when applying a constant progression ratio, the x-axis for broad particle size distributions may be presented on a logarithmic scale, thus resulting in equal interval width on the (logarithmic scale) x-axis [Yule and Dunkley 1994].

Table 7-1 Sieve mesh sizes used for particle size screening in agreement with the main mesh series of ISO 565. Stainless steel analytic sieving meshes according to ISO 3310-1 were used.

Apperture width [μm]	355	250	180	125	90	63	45	32	20

For all sieving procedures, the same machine and sieving parameter setup was used. An oscillation amplitude of about 1 mm was combined with a sieving time of 6 min. This setup was implemented after initial calibration experiments with a 1.4301 stainless steel powder. According to the calibration, the standard deviation in every size class and in the median $D_{m,0.5}$ (of the particle size distribution) was less than 10 % and below 1 %, respectively. Longer sieving times as well as higher or lower amplitudes did not yield improved precision of the sieving results. In general, dry sieving has an accuracy of 2 % in the median $D_{m,0.5}$ [Yule and Dunkley 1994]. Additional uncertainties due to sampling (e.g. removal of a representative sample from one powder batch) were avoided as the entire powder batch was sieved and analysed.

One sieving cycle included prior weighing of each empty sieve, the sieving process itself, weighing of each sieve to determine the retained powder mass fraction in each size class, and posterior sieve cleaning. Generally, nine sieves were used for granulometry. The entire sieving cycle required about one man-hour.

Sieving yields reliable and comparable results for spherical or near-spherical particles. Particles with other shapes, e.g. flakes, rods, pronounced ellipsoids, fibres (filaments), or crystals may cause misleading results. For instance, an irregular particle may pass the sieve mesh due to its smallest diameter while its (comparable) equivalent diameter is greater.

Thus, in this work only samples with spherical or near-spherical particles in the target size range were analysed with respect to their particle size distribution ($X \leq 0.068$). For completeness it is mentioned that [Yule and Dunkley 1994] gave a brief introduction to the obstacles of the interpretation of particle size distributions of non-spherical particles and presented an overview of equivalent diameters, shape factors, and other related parameters.

7.1.2 Particle Size Distribution

The normalised mass size distribution *m(D)* is [Yule and Dunkley 1994]:

$$m(D) = \lim_{\substack{\Delta D \to 0 \\ m_t \to \infty}} \left\{ \frac{\text{Mass of particles between } D - \frac{\Delta D}{2} \text{ and } D + \frac{\Delta D}{2}}{m_\mathrm{t} \Delta D} \right\} \tag{7.1}$$

$m(D)$	Normalised mass distribution [µm^{-1}]
D	Particle diameter [µm]
m_t	Total mass [g].

Equation (7.1) describes the mass fraction of particles within a size interval or class with a width of ΔD and size-class boundaries $D - D/2$ and $D + D/2$. In dry sieving, the size interval widths between two neighbouring meshes are not uniform for standardised mesh series (chapter 7.1.1). Therefore, the resulting particle size-class widths are not uniform as well. As discussed in chapter 7.1.1, they generally increase with increasing mesh size. Consequently, the mass fraction in each size class must be divided by the corresponding size-class width ΔD for normalisation.

The same particle size distributions may be presented in different ways as shown in Figure 7-1 for an exemplary curve. A disambiguation is needed as the plots may address different demands or are more or less representative of the applied particle size-measurement technique.

Particle size distributions are often presented as can be seen in Figure 7-1 a). However, this form should be generally avoided when presenting a particle size distribution obtained through sieving as it ignores the different interval widths of the particle size classes. As a consequence, the shape of the particle size distribution, namely the skewness, is misrepresented. This becomes evident when considering Figure 7-1 b).

In Figure 7-1 b) the same data with respect to the mass fraction are presented, though plotted in a histogram that accounts for the different class interval widths. This type of presentation is mainly used when someone is interested in the mass fraction of the total powder mass with regard to a certain size class. However, an interpretation of this diagram has to consider that the mass fraction is represented by the column height and not column surface.

If, however, the "true" shape of the particle size distribution obtained by sieving is requested (for comparison, atomization regime evaluation etc.), data are preferably presented as in Figure 7-1 c). Here, each mass fraction is normalised by the corresponding size class width [Yule and Dunkley 1994]. For example, the powder mass fraction found on the 45 μm sieve mesh is divided by 18 μm – the corresponding class interval width from 45 μm to 63 μm. This normalisation thus accounts for the deforming effects caused by the geometric series applied to the particles size classes. Comparison of Figure 7-1 b) and Figure 7-1 c) reveals that the particle size distribution based on the mass fraction underestimates the fines while overestimating the coarse particles with regard to the true shape of the particle size distribution [Yule and Dunkley 1994]. In addition, the position of the mode (peak) or minimum may be altered. Furthermore, the normalised particle size distribution accounts for the modes that are present with regard to the classes. In the given example, the bimodal distribution is not visible in the particle size distribution based on the mass fraction, although it is the same particle size distribution.

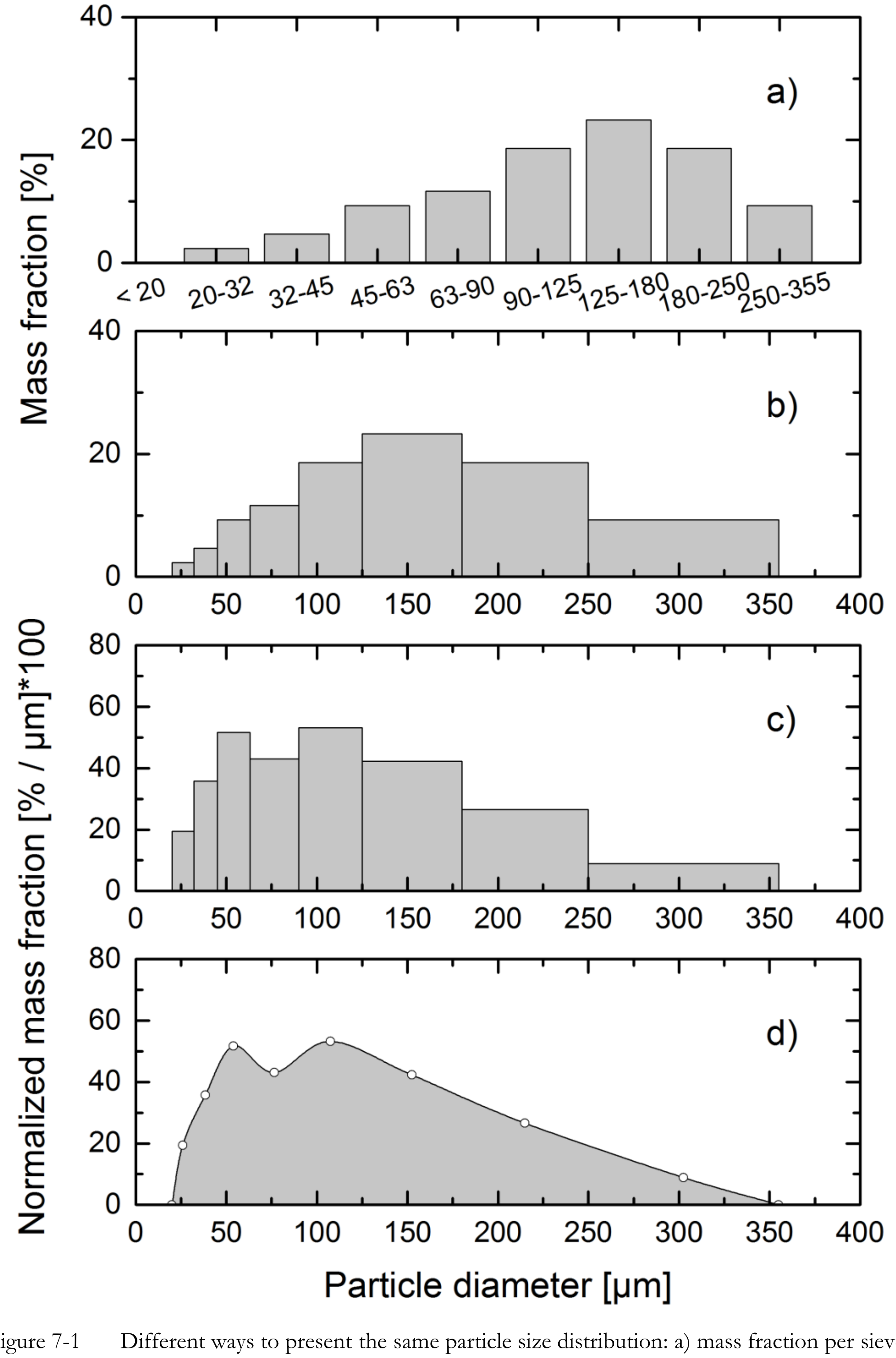

Figure 7-1 Different ways to present the same particle size distribution: a) mass fraction per sieve class as column plot, b) mass fraction per particle-diameter class-range as a histogram, c) normalised mass fraction per particle-diameter class-range as a histogram, and d) normalised mass fraction per particle-diameter class-range as a continuous plot.

Figure 7-1 d) represents a continuous particle size distribution resulting from a continuous measurement technique where every particle and its corresponding size are registered. Presenting data obtained from sieving in this type of diagram may imply monotonicity of the distribution within the size classes, although the "true" curve progression (within a class) is not known. The potential existence of extreme values is thus neglected. As a consequence, this type of data presentation necessitates additional information on the true progression of the curve. In summary, the histogram shown in Figure 7-1 c) represents best particle size distributions obtained by sieving.

Another frequently used diagram type in the analysis of particle size distributions is the cumulative undersize (mass, volume, or number) fraction or percentage distribution (Figure 7-2). It is obtained through consecutive cumulation (addition) of the fractions per class below a certain diameter and defined as the integral over the size distribution [Yule and Dunkley 1994]:

$$m_{\mathrm{cus}}(D) = 100 \int_{D_{\mathrm{min}}}^{D} m(D_{\mathrm{p}})dD_{\mathrm{p}} \tag{7.2}$$

m_{cus}	Cumulative undersize mass fraction [%]
D	Threshold diameter [µm]
D_{p}	Particle Diameter [µm]
D_{min}	Smallest or minimum diameter [µm]
$m(D)$	Mass distribution [µm^{-1}].

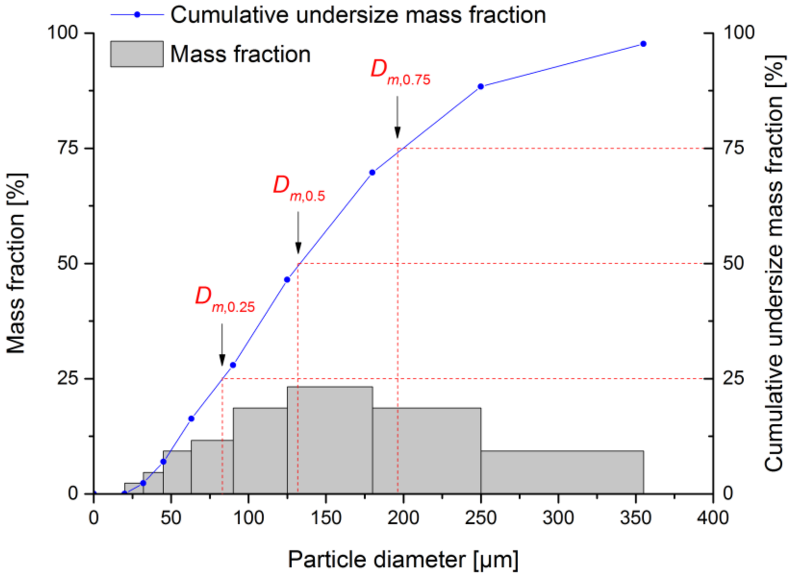

Figure 7-2 Same particle size distribution as in Figure 7-1 b), presented in a histogram and in cumulative undersize form with quantile diameters.

From the cumulative undersize distribution approximated quantile diameters $D_{\mathrm{m},x}$ can be inferred at which x percent of the sample mass m has a smaller diameter [Lawley 1992, Yule and Dunkley 1994]. In the given sample of Figure 7-2, for instance, 50 % of the powder mass has a smaller diameter than $D_{\mathrm{m},0.5}$, and 25 % of the powder mass has a smaller diameter than $D_{\mathrm{m},0.25}$. In the reverse way, this diagram type is used to determine the yield (efficiency) with respect to a specific threshold diameter or interval.

7.1.3 Characteristic values

Characteristic values are used for the description of particle size distributions [Ashgriz 2011, Lawley 1992, Lefebvre 1989, Yule and Dunkley 1994] in order to allow for comparison and modelling.

Atomized powders are generally well described by a log Gaussian (log-normal) distribution [Lawley 1992, Yule and Dunkley 1994]. However, particle size distributions in this work were generally not log-normal but polymodal. Thus, other, more general relations than those for log Gaussian distributions were used.

In general, the mean diameter can be written in moments:

$$D_{pq} = \left[\int_{D_{\min}}^{D_{\max}} D^p n(D) dD \,/ \int_{D_{\min}}^{D_{\max}} D^q n(D) dD \right]^{\frac{1}{p-q}} \tag{7.3}$$

$n(D)$	Number distribution [μm^{-1}], see def. of m(D), eq. (7.1)
D	Particle diameter [µm]
p, q	Moment order; $p, q \in \mathbb{N}$ and $p > q$
$D_{\min}$	Smallest particle diameter [µm]
$D_{\max}$	Largest particle diameter [µm].

Frequently used mean diameters are [Lefebvre 1989]:

D_{10}	Arithmetic mean diameter, describing the mean of a number of particles: particle counting	(7.4)
D_{30}	Number-volume mean diameter, describing a real powder with the same volume as a theoretical powder entirely consisting of particles with D_{30}: volume control	(7.5)
D_{32}	Sauter or surface area moment mean diameter, describing particles with the same surface area to volume ratio as the entire powder: mass transfer and chemical reaction	(7.6)
D_{43}	De Brouckere or volume (mass) moment mean diameter: combustion equilibrium.	(7.7)

These mean diameters were mentioned for completeness and disambiguation as they are often confounded or treated equally although they generally have different values (Figure 7-3) and characterise different applications [Yule and Dunkley 1994]. An extensive list of mean diameters with corresponding applications is given in [Lefebvre 1989].

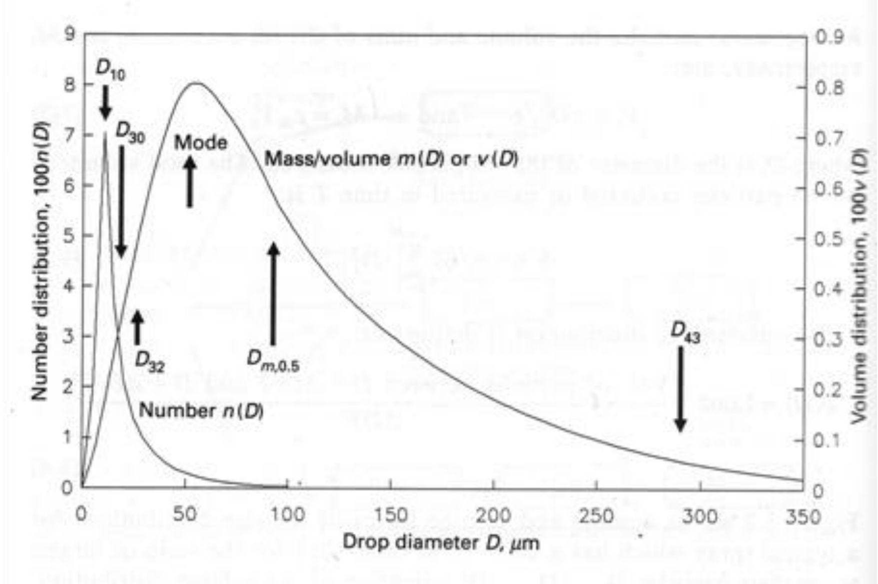

Figure 7-3 Number distribution *n(D)*, left y-axis, and volume (mass) distribution *v(D)*, right y-axis, and relative position of different mean diameters. Volume and mass distribution are equal if the particles have no voids. Property of [Yule and Dunkley 1994].

In this work, however, the following graphic-based definitions were used as they can be derived directly from the cumulative undersize distribution (Figure 7-2):

Quantile diameter:

$D_{\mathrm{m},x}$ Diameter, at which 100x percent of the sample mass m has a smaller diameter. (7.8)

Mass median diameter (2-quantile diameter):

$D_{\mathrm{m},0.5}$ Diameter, at which 50 % of the sample mass m has a smaller diameter. (7.9)

Mass mean diameter [Folk 1966]:

$$D_{\mathrm{m,m}} = \frac{D_{\mathrm{m},0.05} + D_{\mathrm{m},0.15} + D_{\mathrm{m},0.25} + \ldots D_{\mathrm{m},0.85} + D_{\mathrm{m},0.95}}{10} \,. \tag{7.10}$$

Inclusive graphic standard deviation (IGSD) [Folk 1966]:

$$\sigma_{\mathrm{ig}} = \frac{D_{\mathrm{m},0.70}+D_{\mathrm{m},0.80}+D_{\mathrm{m},0.90}+D_{\mathrm{m},0.97}-D_{\mathrm{m},0.03}-D_{\mathrm{m},0.10}-D_{\mathrm{m},0.20}-D_{\mathrm{m},0.30}}{9.1} \tag{7.11}$$

The log-normal standard deviation is given for completeness as it is frequently used in the description of atomized powders that are mostly log-normal [Lawley 1992]:

$$\sigma_{\ln} = \frac{D_{\mathrm{m},0.84}}{D_{\mathrm{m},0.5}} \text{ or } \sigma_{\ln} = \frac{\mathrm{D}_{\mathrm{m},0.5}}{D_{\mathrm{m},0.16}} \ . \tag{7.12}$$

Mode diameter:

D_{mode} Diameter, at which the particle size distribution takes its maximum. (7.13)

Range (spread):

$$R_{\mathrm{m},0.1} = D_{\mathrm{m},0.9} - D_{\mathrm{m},0.1} \tag{7.14}$$

Relative span [Yule and Dunkley 1994]:

$$Sp_{\mathrm{r,m},0.1} = \frac{D_{\mathrm{m},0.9} - D_{\mathrm{m},0.1}}{D_{\mathrm{m},0.5}} \tag{7.15}$$

The definitions summarised by [Folk 1966] are based on the study of monomodal and highly bimodal sediments [Folk and Ward 1957] and were found more appropriate for this work, notably as obtained powders were bimodal and did not show pronounced log Gaussian distributions as predicted by [Lawley 1992, Yule and Dunkley 1994].

It is noted that the cumulative undersize mass fraction of the relevant U8Mo batches reached generally 85 % for particles with a diameter < 355 µm. That is, some values for the graphic-based definitions were linearly extrapolated, namely $D_{\mathrm{m},0.90}$, $D_{\mathrm{m},0.95}$, and $D_{\mathrm{m},0.97}$.

7.1.4 Efficiencies

In the following chapter, definitions used in this work are provided for the coarse-to-fine ratio as well as different yield efficiencies with respect to the usable powder, the total powder obtained from atomization, and the entire process.

Total powder yield efficiency:

$$\eta_{\mathrm{t}} = \frac{m_{\mathrm{re}} - m_{\mathrm{re,rest}}}{m_{\mathrm{re}}} \approx \frac{m_{\mathrm{p}}}{m_{\mathrm{re}}} \tag{7.16}$$

η_{t}	Yield efficiency of total powder
m_{re}	Mass of the rotating electrode
$m_{\mathrm{re,rest}}$	Mass of the rotating electrode after atomization (rest)
m_{p}	Total powder mass obtained through atomization.

The total powder mass was measured after powder collection from the collection chamber. The collection procedure, however, may cause losses.

Usable powder yield efficiency:

$$\eta_{\mathrm{u}} = \frac{m_{\mathrm{i}}}{m_{\mathrm{p}}} \tag{7.17}$$

η_{u}	Yield efficiency of usable powder
m_{i}	Mass of powder in a specific size interval i
m_{p}	Total powder mass obtained through atomization.

Process yield efficiency:

$$\eta_{\mathrm{p}} = \frac{m_{\mathrm{i}}}{m_{\mathrm{re}}} \tag{7.18}$$

η_{p}	Yield efficiency of the atomization process
m_{i}	Mass of powder in a specific size interval
m_{re}	Mass of the rotating electrode.

Coarse-to-fine ratio:

$$r = \frac{m_{\mathrm{c}}}{m_{\mathrm{f}}} \tag{7.19}$$

r	Coarse-to-fine ratio
m_{c}	Mass of coarse particles in a specific size interval, e.g. 45-125 µm

m_f	Mass of fine powder in a specific size interval, e.g. 0-45 µm Note: The intervals of the coarse and fine particles do not overlap.

7.1.5 Models

In atomization, multiple models exist to predict the mean particle size from the atomizer type, its operating parameters, and material properties – extensive summaries were given in [Ashgriz 2011, Lefebvre 1989]. In centrifugal atomization, these models are subdivided with respect to the governing atomization regime (chapter 6.1). For this work, models with respect to REP or rotating (spinning) and (vaneless) disks (cups) without teeth were considered. However, most models were derived from experiments with normal liquids[50] and not for metal melts such as liquid U8Mo.

DDF Regime

For the prediction of a mean particle diameter from operating parameters and material properties in the DDF regime, two different types of models exist: physical and semi-empirical. Nevertheless, all models state more or less the same relationships.

Based on the balance of forces between surface tension and centrifugal force on a liquid (spherical) drop on the outer rim of a disk or the rotating electrode (see also chapter 6.1, DDF), the following model can be derived according to considerations of [Muraszew 1948] and [Dunkley and Aderhold 2007] for metal melts:

$$a_\mathrm{c} \cdot m_\mathrm{sphere} = \sigma \pi D_\mathrm{d} \tag{7.20}$$

$$\omega^2 \frac{D_\mathrm{re}}{2} \cdot \frac{4}{3} \rho_\mathrm{l} \pi \left(\frac{D_\mathrm{d}}{2}\right)^3 = \sigma \pi D_\mathrm{d} \tag{7.21}$$

$$D_\mathrm{d} = \frac{1}{\omega} \sqrt{\frac{12\,\sigma}{\rho_\mathrm{l}\, D_\mathrm{re}}} \tag{7.22}$$

a_c	Centrifugal acceleration [m/s^2]
m_sphere	Mass of a sphere [kg]
σ	Surface tension [N/m]
D_d	Mean droplet diameter [m]
ω	Angular velocity [rad/s]
D_re	Rotating electrode or disk diameter [m]
ρ_l	Liquid density [kg/m^3].

---

[50] Liquid under normal conditions.

A similar, more general model, was proposed by [Jones 1960]:

$$D_{\mathrm{m,0.5}} = \frac{\mathrm{C}}{\omega}\sqrt{\frac{1}{D_{\mathrm{re}}}} \tag{7.23}$$

$D_{\mathrm{m,0.5}}$ Mass median diameter [m]

C Constant depending on the atomizer configuration and material.

According to [Yule and Dunkley 1994] this model is valid for metal melts and may also be applied to the ligament disintegration regime.

On these grounds, the following semi-empirical models for rotating discs and normal liquids were found by [Walton and Prewett 1949] and [Matsumoto *et al.* 1974], respectively:

$$D_{32} = \frac{3.8}{\omega}\sqrt{\frac{\sigma}{\rho_{\mathrm{l}}\, D_{\mathrm{re}}}} \text{ and} \tag{7.24}$$

$$D_{32} = 1.6 D_{\mathrm{re}}\left(\frac{8\sigma}{\rho_{\mathrm{l}}\, {D_{\mathrm{re}}}^{3}\omega^{2}}\right)^{0.523} \tag{7.25}$$

D_{32} Sauter mean diameter [m].

Another semi-empirical model was reported by [Tanasawa *et al.* 1978] based on experiments with disks and cups for normal liquids:

$$D_{32} = \frac{2.83}{\omega}\left(\frac{\sigma}{D_{\mathrm{re}}\rho_{\mathrm{l}}}\right)^{0.5}\left(1 + 0.003\frac{Q_{\mathrm{l}}\rho_{\mathrm{l}}}{D_{\mathrm{re}}\mu_{\mathrm{l}}}\right) \tag{7.26}$$

μ_{l} Dynamic viscosity [kg/(ms)]

Q_{l} Volume flow rate [m^3/s].

The latter model is remarkable due to the consideration of the liquid flow, expressed through the dynamic viscosity and mass flow rate $Q_{\mathrm{l}}\rho_{\mathrm{l}}$ – both are generally omitted in the other DDF models.

In addition, the same authors reported semi-empirical models for the ligament and film disintegration regime:

LD Regime

$$D_{32} = 0.748 \frac{Q_\mathrm{l}^{0.1}\sigma^{0.5}}{D_\mathrm{re}^{0.5}\rho_\mathrm{l}^{0.4}\mu_\mathrm{l}^{0.1}\omega^{1.0}} \;. \tag{7.27}$$

FD Regime

$$D_{32} = 98 \frac{Q_\mathrm{l}^{0.5}\sigma^{0.4}}{D_\mathrm{re}^{0.8}\rho_\mathrm{l}^{0.4}\omega^{1.0}} \;. \tag{7.28}$$

Metal Melts

All presented equations are based on experiments with normal liquids. However, some authors have analyzed centrifugal atomization of metal melts. Particularly, [Kim *et al.* 1992, Kim *et al.* 2007] reported the use of a model that was initially derived by [Champagne and Angers 1980] for REP through dimensionless regression analysis of their experimental data (semi-empirical), only differing in the coefficient for experiments involving U_3Si_2 / UMo. Champagne and Angers seem to be the only researchers to have reported models with respect to REP and atomization of liquid metals:

$$D_{32} = \mathrm{C} \cdot \frac{Q_\mathrm{l}^{0.12}\sigma^{0.43}}{D_\mathrm{re}^{0.64}\rho_\mathrm{l}^{0.43}\omega^{0.98}} \tag{7.29}$$

C	Constant: 4.63 [Champagne and Angers 1980]; 3.65 [Kim *et al.* 2007]
R^2	99.3 %.

Ultimately, [Champagne and Angers 1981] reported an entire list of models with respect to different mean diameters of interest of which the most important are given below:

$$D_{32} = \mathrm{C} \cdot \frac{Q_\mathrm{l}^{0.02}\sigma^{0.50}}{D_\mathrm{re}^{0.58}\rho_\mathrm{l}^{0.50}\omega^{1.03}} \tag{7.30}$$

C	3.3
R^2	99.2 %

$$D_{43} = \mathrm{C} \cdot \frac{Q_\mathrm{l}^{0.06}\sigma^{0.46}}{D_\mathrm{re}^{0.58}\rho_\mathrm{l}^{0.46}\omega^{1.00}} \tag{7.31}$$

C	3.65

R^2 99.3 %.

These models do not differentiate between atomization regimes and were not accounted for in reviewed secondary literature [Ashgriz 2011, Crowe 2005, German 2009, Lawley 1992, Lefebvre 1989, Neikov *et al.* 2009, Wozniak 2003, Yule and Dunkley 1994], except [Liu 2000]. Importantly, metallic melts of mostly elemental elements (Cu, Zn, Al, and Fe) were investigated except SAE 1090 steel. Apart from the latter that has a melting range of about 50 K, all tested materials had a distinct melting point.

For completeness, it is mentioned that [Kim *et al.* 1997a] reported another model based on regression analysis:

$$D_{\mathrm{m},0.5} = \mathrm{C}\,\frac{Q_\mathrm{l}^{0.41}}{\omega^{1.12}} \tag{7.32}$$

C Constant, not reported.

The relatively high exponent of Q_l suggests operation in the LD regime of the KAERI atomizer as most commonly accepted models apply an exponent of about 0.1 to the volume flow rate or even neglect its influence in the DDF. Though, KAERI reported neither the disk diameter nor the constant nor the coefficient of determination.

A calculation showing the influence of rotational speed and rotating electrode diameter on the particle mean diameter was conducted based on model (7.22). The results were used for dimensioning of the high-frequency spindle (chapter 3.3.13) and plotted in Figure 3-31.

7.2 Results and Discussion

7.2.1 Yield Efficiency and Parameter Sets

The yield efficiency with respect to the total powder was in average 66 % and 72 % for short and standard rotating electrodes, respectively.

As the rotating electrode diameter was constant (10 mm) for all analysed experiments with $X < 0.68$, and as the mass flow rate is negligible in the DDF with regard to the mean particle size (see models), the rotational speed was supposed to be the only influencing parameter in terms of yield and yield efficiency of usable powder. Namely, an increase in the fines with increasing rotational speed was expected according to the models listed in chapter 7.1.5. Indeed, this behaviour was generally observed as can be seen from Figure 7-4. Both the absolute yield and yield efficiency of usable powder per batch with respect to the relevant threshold diameters of 40 μm and 125 μm were plotted. The corresponding operating parameters are summarised in Table 7-2. However, other influences apparently have affected the yield and yield efficiency, which will be discussed in the following paragraphs:

The differences in the absolute yield of usable powder for identical rotational speeds are readily explained. The atomized rotating electrode length and thus mass is controlled visually.

In average, 20 g and 30 g were atomized with respect to short and standard rotating electrodes, respectively. However, short rotating electrodes yielded almost the same absolute mass of usable powder in the size categories < 40 μm and < 125 μm as the standard electrodes for a given rotational speed, for instance 40'000 rpm. This effect was due to a change of the particle size distribution (Figure 7-12) and had significant impact on the corresponding yield efficiency of usable powder for a given rotational speed (e.g. 40'000 rpm). Below 125 μm, it was about 50 % and 75 % for standard and short rotating electrodes, respectively. Below 40 μm, the usable powder yield efficiency was about 4 % and 20 %, respectively. Hence, a correlation between the electrode length (for a given diameter) and the yield efficiency in both size categories is suspected. There are two potential explanations for the observed phenomenon – one thermodynamic, the other mechanical:

On the one hand, the mass flow rate increases until thermal equilibrium is reached (Figure 5-11), and an increase in mass flow rate yields higher a mean particle diameter according to the LF regime models (chapter 7.1.5). It could thus be suspected that the mass flow rate at the end of atomization was higher for standard than for short rotating electrodes and consequently yielded coarser particles. However, the stated exponents of the volume flow rate of the commonly accepted models vary between 0.02 and 0.1, thus are supposed to have had little influence. On the other hand, a mechanical phenomenon must be taken into account as well, namely increased vibration of the standard rotating electrode towards the design limit of the high-frequency spindle. In fact, all U8Mo electrodes were atomized as-cast due to the lack of appropriate machining (turning) capacities. As a consequence, their circular runout was lower than the spindle manufacturer's recommendation of 0.02 mm (Table 3-2). Indeed, slight audible vibration of the rotating electrode was encountered around 40'000 rpm to 45'000 rpm for the standard rotating electrode. In particular, this vibration was observed for unevenly cut rotating electrode tops.

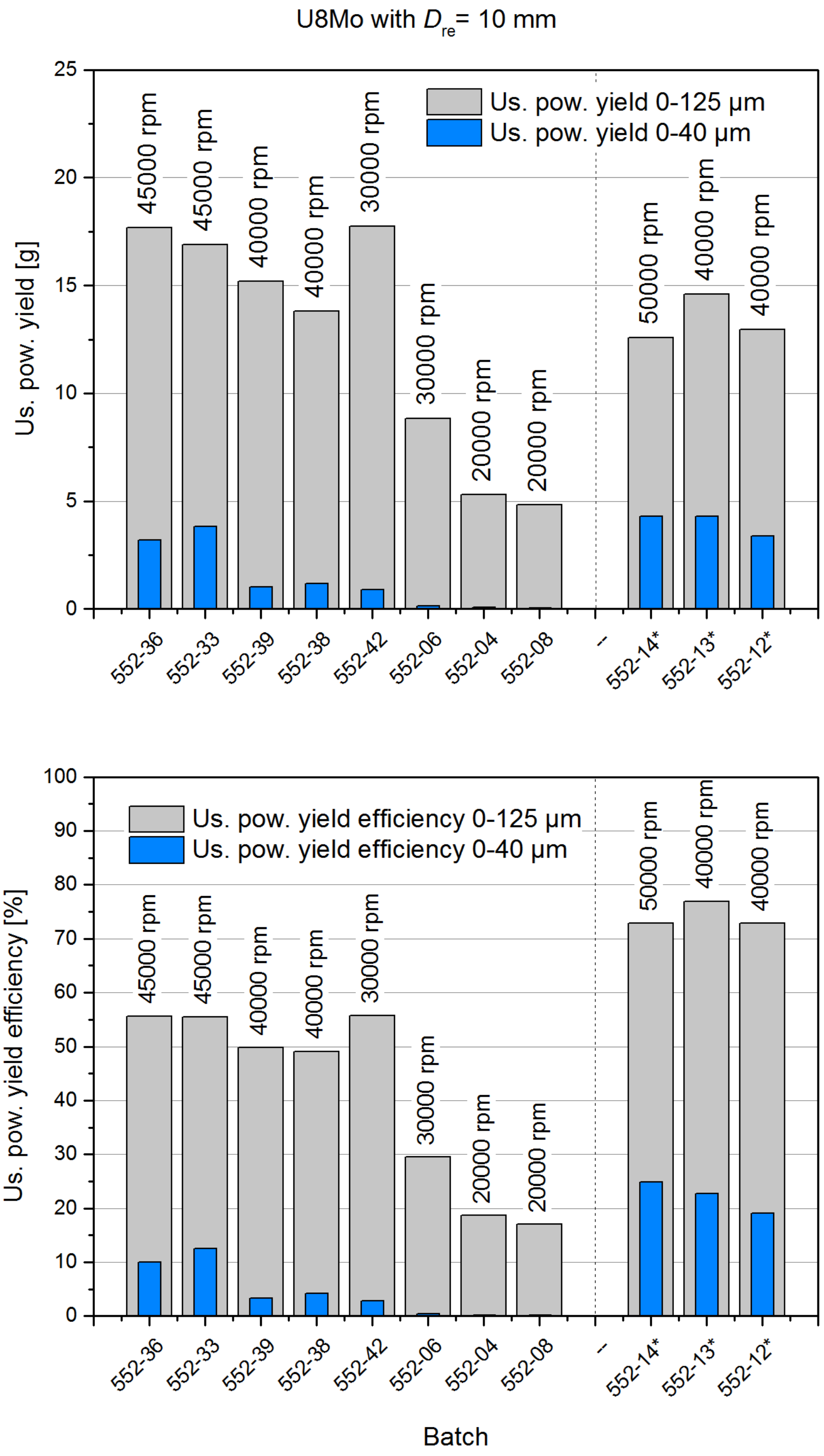

Figure 7-4 Yield and yield efficiency of usable U8Mo powder from rotating electrodes with 10 mm diameter in descending order with respect to particles < 125 µm. The sort rotating electrodes are shown separately and are marked with an asterix. All experiments were atomized with $X < 0.68$.

The vibration vanished entirely after atomization of about 10 mm of the rotating electrode corresponding to about 13 g of U8Mo. The mass of particles with a diameter > 125 µm obtained from atomization of short and standard U8Mo rotating electrodes at 40’000 rpm was about 5 g and 15 g, respectively. The difference, 10 g, is similar to the mass difference between a short and standard rotating electrode, which was 13 g (Table 7-2). This rationale suggests that the coarse particles were mainly produced at the beginning of the atomization process – thus contradicting with thermal effects. As both rationales are contradictory with respect to the time when the coarse particles were produced, a method to verify the thermal or mechanical hypothesis is proposed for further research: atomization of a standard rotating electrode, but only to the amount of powder that corresponds to a short rotating electrode.

Furthermore, batches 552-06 and 552-42 were atomized at the same rotational speed, had the same diameter and the same length, but batch 552-42 showed almost doubled yield efficiency < 125 µm (Figure 7-4). Only difference with respect to the parameter set was the applied electric arc current of 35 A (552-06) and 50 A (552-42), resulting in mass flow rates of 0.843 $g s^{-1}$ and 1.28 $g s^{-1}$ (Figure 7-5), respectively. Thus, the mass flow rate was increased by 50 % (factor 1.5). With regard to the models, however, the contrary behaviour – an increase of the coarse particles by a factor of 1.05 – would be expected when applying the highest[51] reported exponent of 0.12 to the difference in the volume flow rate. A similar behaviour was observed for 1.4301 stainless steel where the yield efficiency was increased by 50 % for an increase in mass flow rate of about 40 % at 30’000 rpm (Figure 7-6). As a result, the influence of the mass flow rate is not regarded as the only cause regarding the observed behaviour. It is noted that an audible oscillation harmonic with a low frequency was encountered around 30’000 rpm ± 3’000 rpm for both 1.4301 stainless steel and U8Mo with regard to the entire atomization system consisting of the atomizing unit and the glovebox. It is suspected that this harmonic in combination with the increase in mass flow rate caused the significant increase in yield efficiency at 30’000 rpm. Besides this phenomenon, it can be inferred from the experiments plotted in Figure 7-6 that the mass flow rate has no significant influence on the yield efficiency of usable powder.

---

[51] Model (7.32) with an exponent of 0.41 was not considered due to the absence of verifiable data regarding its derivation.

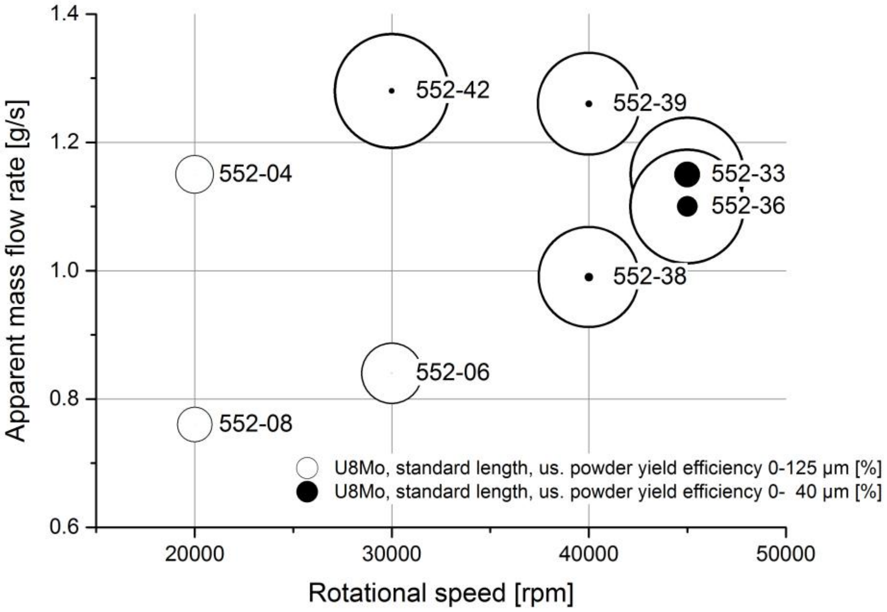

Figure 7-5 Yield efficiency of usable powder as a function of apparent mass flow rate and rotational speed for standard U8Mo rotating electrodes plotted in a bubble chart. The usable powder yield efficiency is proportional to the bubble diameter. The usable powder yield efficiencies of both categories (0-40 μm and 0-125 μm) have the same scaling factor.

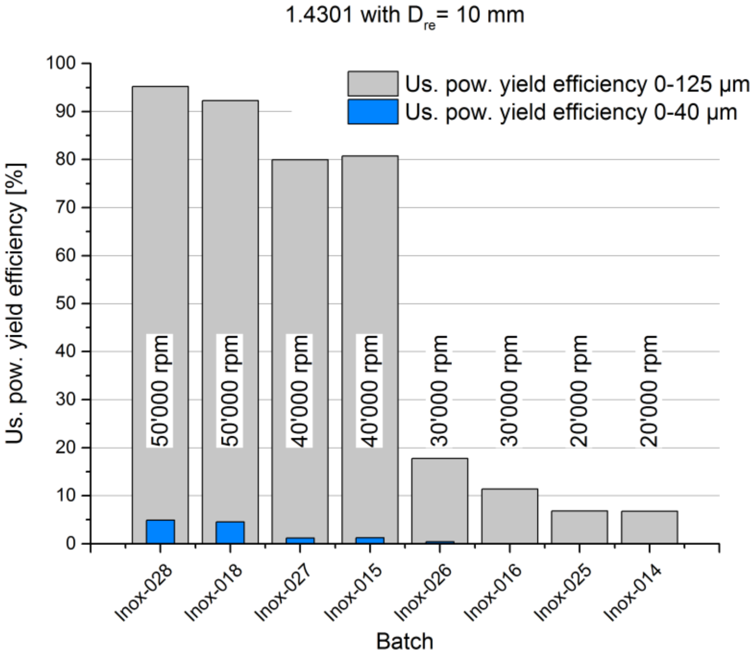

Figure 7-6 Yield efficiencies of usable powder for 1.4301 stainless steel.

The process yield efficiency – the ultimate measure of how much powder with respect to the entire rotating electrode is usable – is summarised in Figure 7-7. Short rotating electrodes had higher yield efficiencies with respect to both target diameter ranges. Furthermore, the coarse-to-fine ratio became smaller with increasing rotational speed and shorter rotating electrodes. In this respect, it is reminded that for the industrial production a coarse-to-fine ratio of about between 1 and 2.33 is aimed (Table 2-2). Closest experiments with respect to this value were batches 552-36, -33, -12, -13, and -14 with coarse-to-fine ratios of 4.6, 3.4, 2.8, 2.4, and 1.9, respectively (Table 7-2): Ultimately, it can be inferred that atomization should be carried out between 40'000 rpm and 50'000 rpm or higher with respect to a rotating electrode diameter of 10 mm.

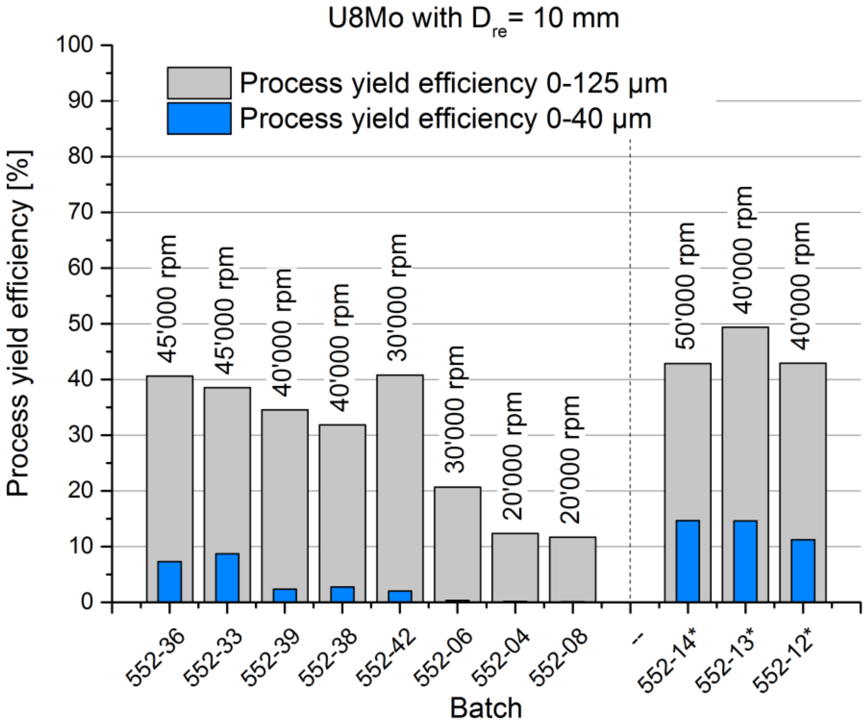

Figure 7-7 Process yield efficiency for U8Mo rotating electrodes with respect to rotational speed.

Table 7-2 List of experiments that yielded predominantly spherical powder ($X \lesssim 0.068$) and corresponding operating parameters, sorted into descending order with respect to rotational speed and then electric arc current. Short rotating electrodes are presented separately. All rotating electrodes had a diameter of 10 mm.

Batch	Yield 0-125 μm	Yield 0-40 μm	Us. pow. yield efficiency 0-125 μm	Us. pow. yield efficiency 0-40 μm	Rotational speed	Electric arc current	Apparent mass flow rate	H_2O	O_2	Rotating electrode mass	Powder mass	Atom. time	Atom. regime parameter X	Coarse-to-fine ratio
U8Mo	[g]	[g]	[%]	[%]	[rpm]	[A]	[g/s]	[ppm]	[ppm]	[g]	[g]	[s]	[-]	[-]
552-33	16.90	3.81	55.5	12.5	45'000	50	1.15	< 6	< 6	43.86	30.46	26.4	0.068	3.4
552-36	17.68	3.18	55.6	10.0	45'000	45	1.10	< 7	< 7	43.55	31.79	28.8	0.065	4.6
552-39	15.19	1.03	49.8	3.4	40'000	50	1.26	< 7	< 7	43.99	30.52	24.2	0.070	13.8
552-38	13.81	1.18	49.1	4.2	40'000	40	0.987	< 7	< 7	43.35	28.15	28.5	0.054	10.7
552-42	17.74	0.88	55.8	2.8	30'000	50	1.28	< 7	< 7	43.55	31.82	24.8	0.059	19.2
552-06	8.84	0.14	29.5	0.5	30'000	35	0.843	< 5	< 5	42.77	29.96	35.4	0.039	64.3
552-04	5.29	0.06	18.6	0.2	20'000	50	1.15	< 6	< 6	42.85	28.40	24.7	0.042	92.8
552-08	4.83	0.05	17.0	0.2	20'000	35	0.762	< 6	< 6	41.37	28.44	37.3	0.028	95.2
552-14*	12.58	4.30	72.9	24.9	50'000	50	0.953	< 6	< 6	29.35	17.26	18.2	0.060	1.9
552-13*	14.59	4.31	76.9	22.7	40'000	50	-	< 6	< 6	29.56	18.97	-	-	2.4
552-12*	12.96	3.38	72.8	19.0	40'000	35	0.550	< 6	< 6	30.20	17.79	32.5	0.030	2.8

7.2.2 Production Capacity

Under optimum conditions, one rotating electrode was atomized within half an hour including rotating electrode mounting and powder collection, resulting in a potential total of 16 electrodes per working day and operator. Considering an average mass of 40 g U8Mo per standard rotating electrode and a (atomization) process efficiency of 40 %, a potential total of 256 g U8Mo per day and operator may be fabricated. According to the prototype requirements, the annual production capacity is to meet 1 kg year^{-1} (chapter 2.9). That is, 25 % of the target annual production can be produced within one day with the current atomizer design.

Both U8Mo and U7Mo rotating electrodes were cast with a preliminary efficiency of 80 % and a production capacity of 2 standard rotating electrodes per day.

Taking into account the aforementioned process yield efficiency of atomization, the entire fabrication process of the implemented production facility including induction casting and REP atomization had an overall process efficiency of 32 %. Reprocessing of both the rotating electrode rest and rejected powder would substantially increase the overall process efficiency, though.

7.2.3 Particle Size Distribution

Rotational Speed

A shift to the fines of the particle size distribution including the modes was observed for increased rotational speeds with respect to U8Mo (Figure 7-8 and Figure 7-9). This observation agrees with the findings of [Champagne and Angers 1984] and the stated models. Despite the shift to the fines, a tail of coarse particles persisted, though with varying size.

Between $X \sim 0.042$ and $X \sim 0.068$, Figure 7-9, the particle size distributions of batches 552-33/39/42 were bimodal, and the modes were sharper and higher as for batches 552-06 and -08. The shape of the particle size distributions, notably the proportion of the modes, suggests that multiple secondary particles were produced for one main particle, thus implying atomization in the ligament disintegration regime. The corresponding characteristic values are given in Table 7-3, from which can be seen that $D_{m,0.35}$ decreased with increasing rotational speed as expected. Both the median and mean diameters, however, behaved in an ambiguous manner, which is associated with the strong variation and spread of both the particle size range and inclusive graphic standard deviation.

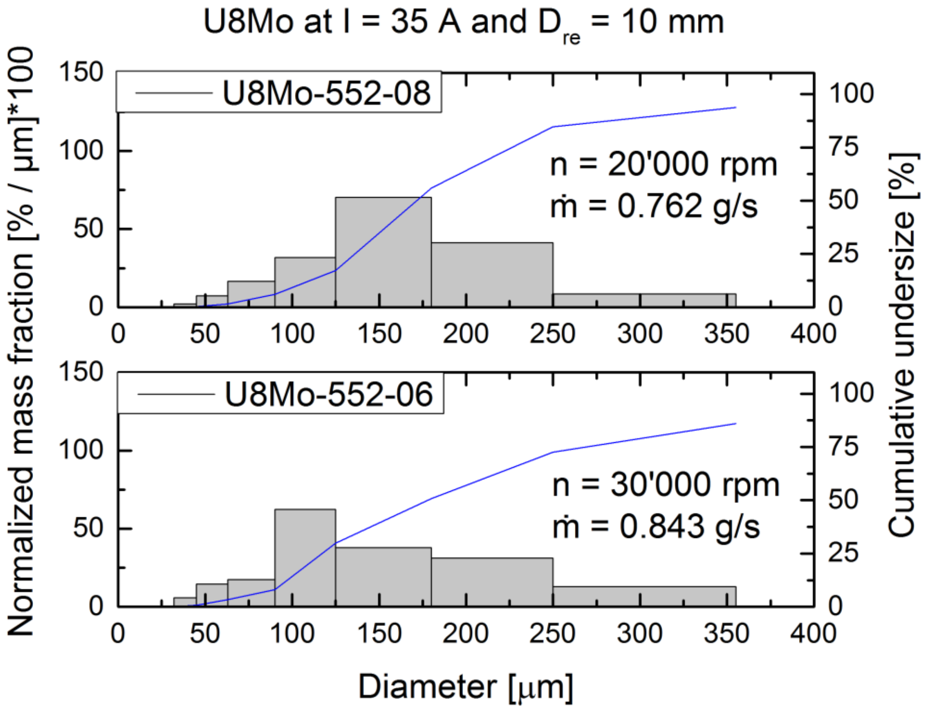

Figure 7-8 Particle size distributions of U8Mo for $X < 0.042$ showing the influence of rotational speed.

Table 7-3 Table of characteristic values obtained from U8Mo particle size distributions divided into groups of constant electric arc current and sorted in an ascending order with respect to rotational speed.

Model	Electric arc current [A]	Rotational speed [rpm]	$D_{m,0.30}$ [µm]	Median [µm]	Mean [µm]	IGSD [µm]	Range$_{0.1}$ [µm]
U8Mo-552-08	35	20000	143	172	188	78	209
U8Mo-552-06	35	30000	125	178	205	109	293
U8Mo-552-42	50	30000	100	119	181	125	361
U8Mo-552-39	50	40000	88	122	150	90	228
U8Mo-552-33	50	45000	70	89	194	165	444

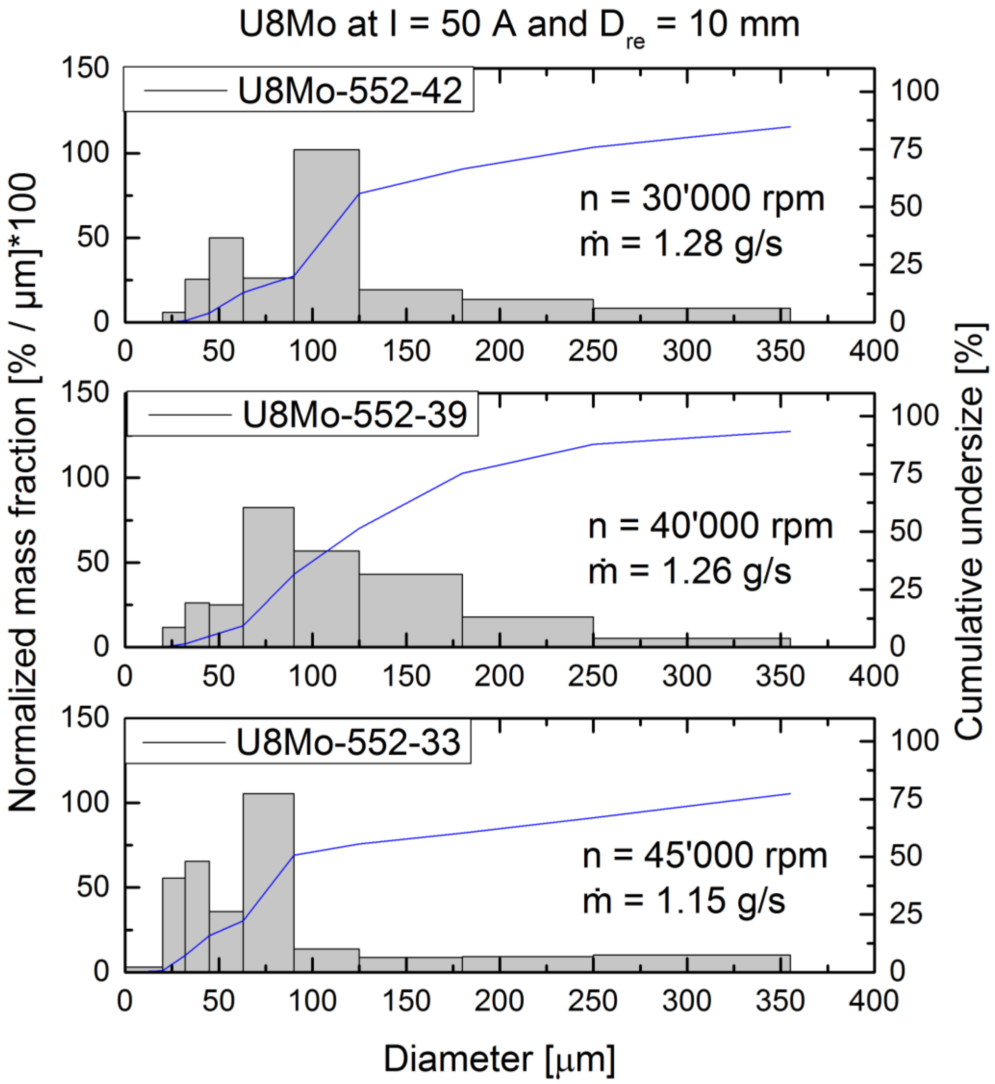

Figure 7-9 Particle size distributions of U8Mo between $X \sim 0.042$ and $X \sim 0.068$ showing the influence of rotational speed and mass flow rate.

For 1.4301 stainless steel, generally a bimodal particle size distribution ($X < 0.04$) was observed with a narrow size distribution and a pronounced mode on the main particle side with respect to mass, Figure 7-10. The curve progression suggests atomization in the DDF regime according to [Champagne and Angers 1984].

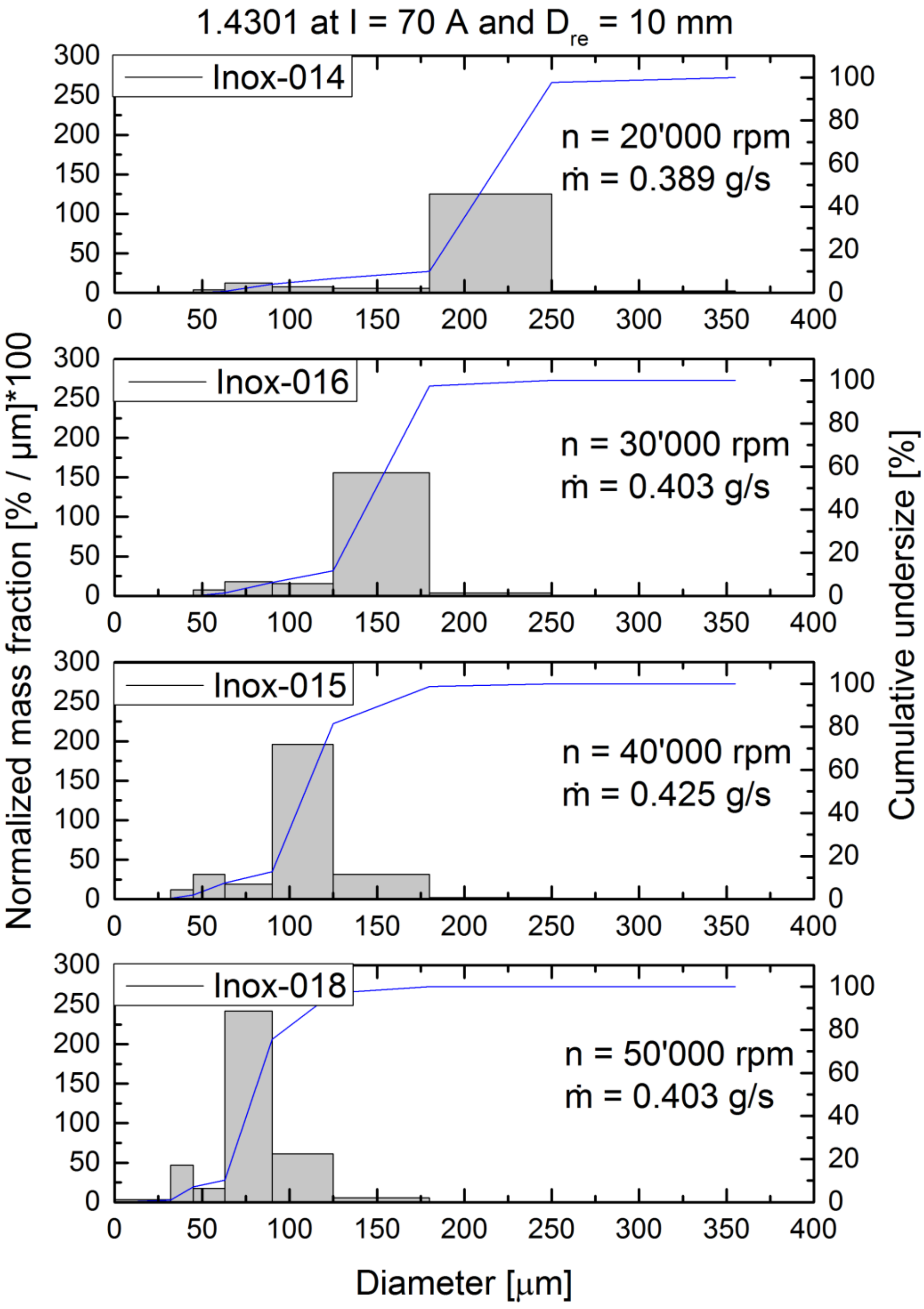

Figure 7-10 Influence of rotational speed on the particle size distribution of 1.4301 stainless steel and typical curve progression with bimodal shape ($X = 0.019$ to $X = 0.034$ for Inox-014 to 018, respectively).

In comparison to U8Mo, it can be seen that the variation of the inclusive graphic standard deviations and particle size range were significantly smaller (Table 7-4), and that $D_{m,0.3}$, the median, and the mean decreased with increasing rotational speed as expected. It is noted that the particle size range is comparable to data of [Champagne and Angers 1984] that showed similar values. In contrast to U8Mo, the diameters of 1.4301 stainless steel particles were entirely smaller than 355 µm for every presented batch as can be seen from the cumulative undersize distribution. Furthermore, it can be seen from Figure 7-10 that the particle size distribution and modes shifted to the fines for increased rotational speeds.

Table 7-4 Table of characteristic values obtained from 1.4301 particle size distributions divided into groups of constant electric arc current and sorted in an ascending order with respect to rotational speed.

Model	Electric arc current [A]	Rotational speed [rpm]	$D_{m,0.30}$ [µm]	Median [µm]	Mean [µm]	IGSD [µm]	$\text{Range}_{0.1}$ [µm]
Inox-014	70	20000	196	212	205	34	64
Inox-016	70	30000	137	150	146	26	61
Inox-015	70	40000	99	109	110	28	77
Inox-018	70	50000	71	79	81	21	52
Inox-025	100	20000	197	213	206	39	65
Inox-026	100	30000	134	147	142	29	79
Inox-027	100	40000	98	108	108	27	74
Inox-028	100	50000	72	82	84	26	65

Rotating Electrode Length

The particle size distributions of the “short” rotating electrodes were also bimodal, Figure 7-11.

However, both modes were sharper with respect to particle size distributions obtained from longer rotating electrodes and same parameter sets. The comparison of the particle size distribution of short and standard rotating electrodes (Figure 7-12) atomized at identical rotational speeds and similar electric arc currents is of particular interest due to the results presented in chapter 7.2.1.

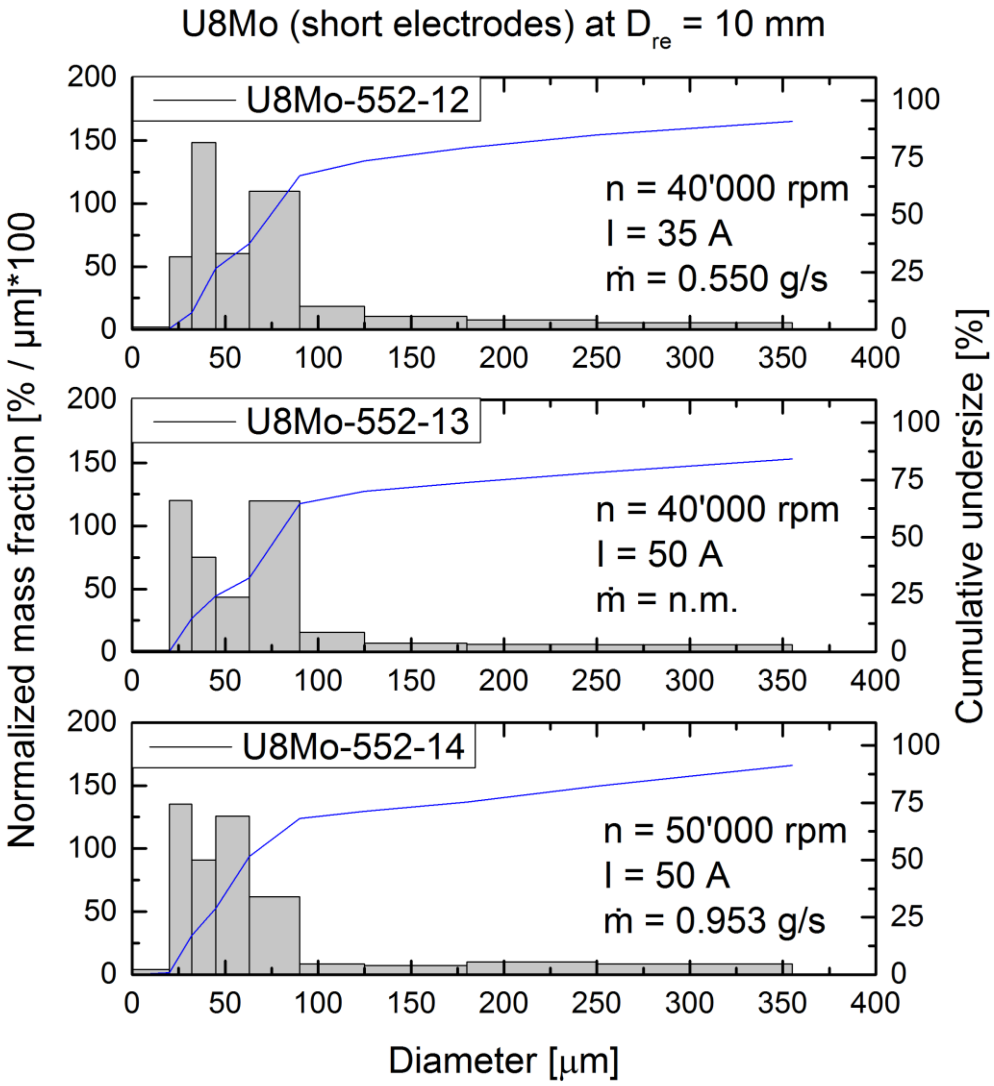

Figure 7-11 Particle size distribution of "short" U8Mo rotating electrodes. Top and middle particle size distribution resulted from the same rotational speeds, middle and bottom from the same electric arc currents.

It was found that the mode stayed in the same size class but increased for shorter rotating electrodes. In addition, there was a shift from coarser particles > 90 µm to finer particles < 45 µm around the mode. Accordingly, the entire shape of the particle size distribution was changed as opposed to a simple shift to the fines. Like for rotating electrodes with standard length, a rather long and flat tail of coarse particles was observed, though it was significantly less pronounced in size. As discussed in chapter 7.2.1, a thermal or mechanical effect related to the rotating electrode length is suspected to have influenced the different tail sizes.

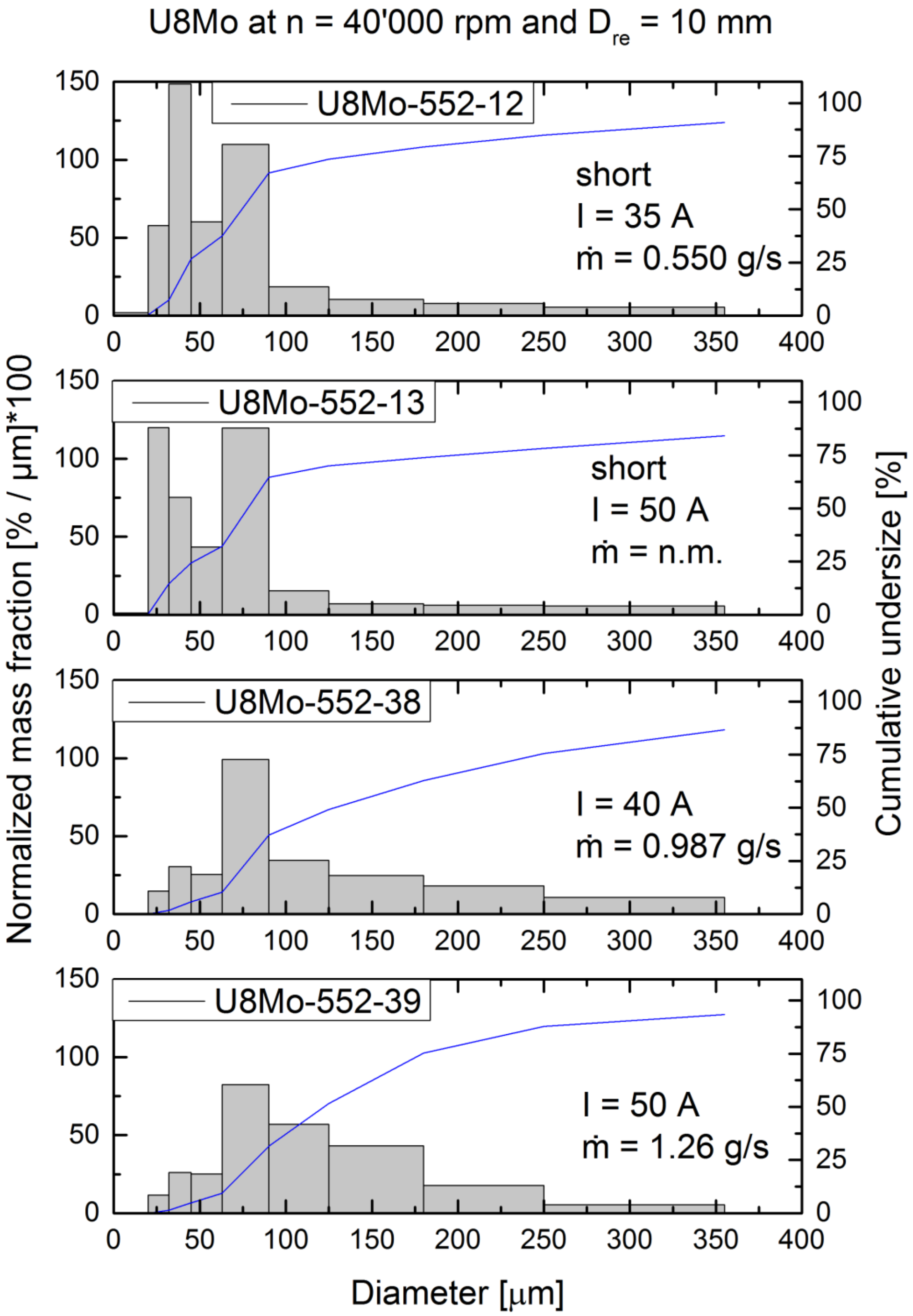

Figure 7-12 Comparison of particle size distributions obtained from “short” (552-12 and 552-13) and standard rotating electrodes (552-38 and 552-39) at the same rotational speed. For both the “short” and standard rotating electrodes similar electric arc currents were applied.

Mass Flow Rate

The role of the mass flow rate was inconclusive when comparing batches 552-38 and 552-39, atomized at 40’000 rpm (Figure 7-12), with batches 552-33 and -36, atomized at 45’000 rpm (Figure 7-13), as well as batches 552-06 and -42, atomized at 30’000 rpm (Figure 7-14), and batches 552-04 and -08, atomized at 20’000 rpm (Figure 7-15).

While at 20’000 rpm an influence neither on the shape of the particle size distribution nor on the yield efficiency was found, at 30’000 rpm a shift from the coarse particles around the mode to the fines as well as the development of a second mode was observed for an increased mass flow rate. The observed effect is related to an oscillation harmonic at around 30’000 rpm ± 3’000 rpm rotational speed, chapter 7.2.1. At 40’000 rpm, an increase in the mass flow rate resulted in coarser particles. However, the yield efficiency was not affected by the shift.

Concerning 1.4301 stainless steel, the apparent mass flow rate did show slight an influence on the particle size distribution, Figure 7-16. An increase of the apparent mass flow rate by about 40 % resulted in a decreased particle size range and less coarse particles, although atomization was conducted in the DDF regime (Table 7-2).

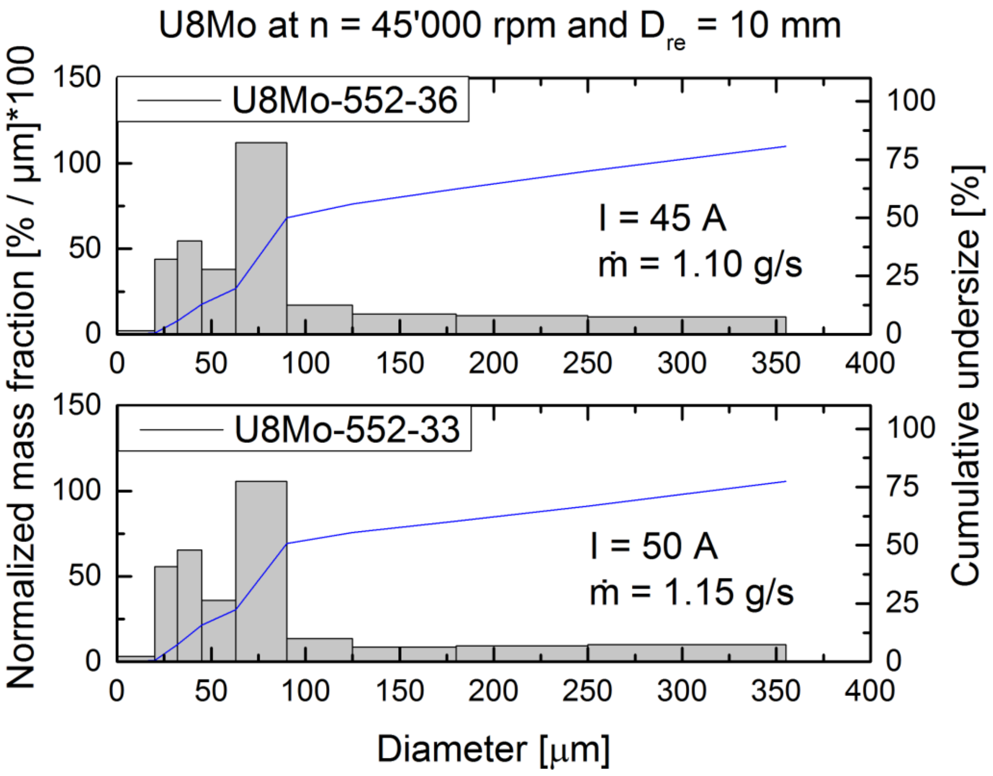

Figure 7-13 Influence of the apparent mass flow rate on U8Mo particle size distribution.

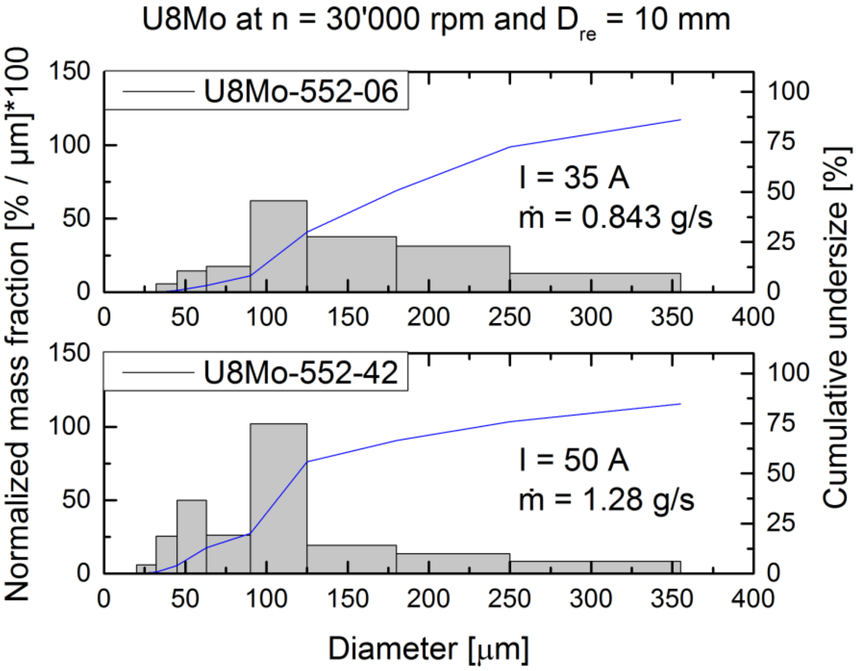

Figure 7-14 Influence of the apparent mass flow rate on U8Mo particle size distribution between $X \sim 0.042$ and $X \sim 0.068$.

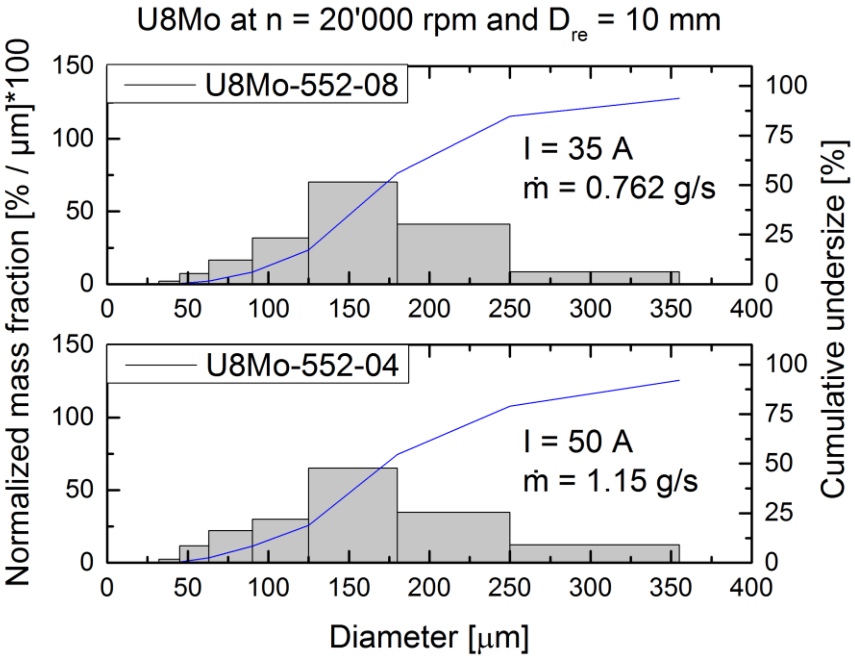

Figure 7-15 Influence of the apparent mass flow rate on U8Mo particle size distribution below $X \sim 0.042$.

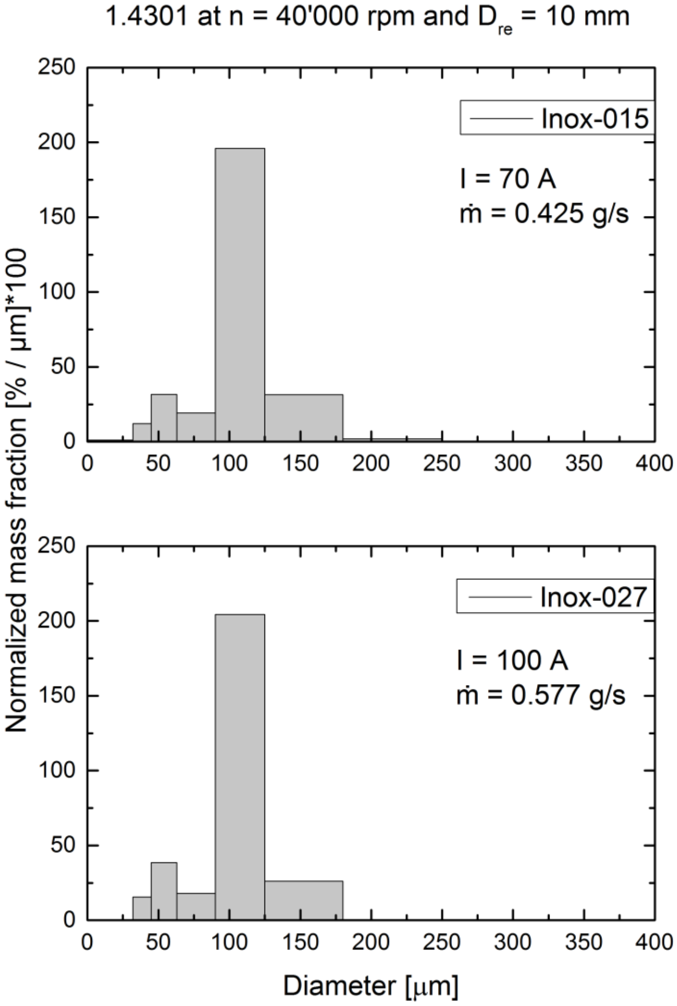

Figure 7-16 Influence of the apparent mass flow rate on the particle size distribution of 1.4301 stainless steel in the DDF for batches Inox-015 and Inox-027 having values of $X \sim 0.032$ and 0.043, respectively.

Rotating Electrode Diameter

A study with 1.4301 stainless steel showed that there is a considerable influence of the rotating electrode diameter on the particle size distribution as was expected from the models. That is, an increase in diameter resulted in a shift of the particle size distribution and mode to the fines (Figure 7-17). A coarse particle tail was observed for 1.4301 stainless steel with respect to the atomization of the rotating electrode with 14 mm diameter.

The diameter of U7Mo rotating electrodes was also increased from 10 mm to 15 mm and 20 mm in order to show general feasibility with respect to the atomizer design limits and REP, of which 4 out of 6 experiments were successful. Two experiments, namely U-7Mo-1114-3-1.6 (D_{re} = 15 mm) and U7Mo-1114-03 (D_{re} = 20 mm), could be compared to the 552 batch, namely 552-29 (30’000 rpm, 2.58 g s^{-1}), as they were carried out at comparable rotational speeds, 30’000 rpm, and similar mass flow rates of 2.24 g s^{-1} and 2.77 g s^{-1}, respectively. However, batch 552-29 showed manifested filaments (Table 6-1), making a comparison of the obtained particle size distributions useless according to considerations stated in chapter 7.1.1. In addition, a different alloy, namely U7Mo, was used with higher a carbon content than reported for batch 552. Carbon, though, was shown to have influence on the mass flow rate, Figure 5-13. Thus, the apparent mass flow rates are not comparable.

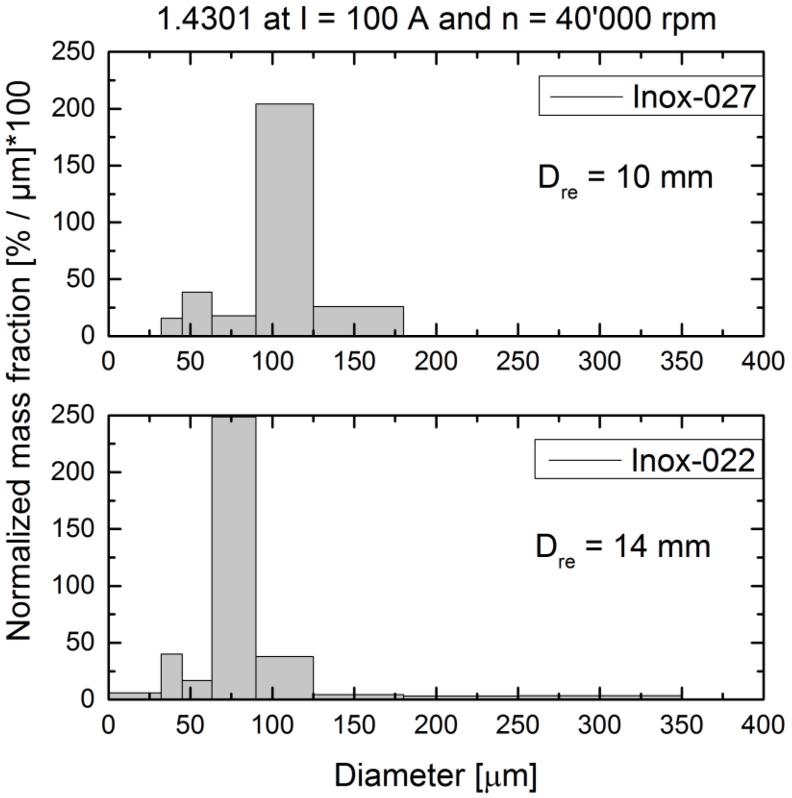

Figure 7-17 Typical influence of the rotating electrode diameter on the particle size distribution of 1.4301 stainless steel. Inox-22 shows a tail on the coarse particle side of the global mode.

Material and Process Interaction

As only particles with a diameter < 180 µm are of industrial interest, larger particles were not investigated by means of microscopy. However, the systematic presence of a significant amount of scrap on the 355 µm mesh (between 6 % and 23 %) after sieving (Table 7-5) and the rather long and flat tails at elevated rotational speeds, i.e. 40’000-50’000 rpm (Figure 7-10, Figure 7-11, Figure 7-12, Figure 7-13), were remarkable. In particular, as no such particles and tail was observed for 1.4301 stainless steel except for increased diameters (Figure 7-17). In addition, the amount of scrap affected strongly the characteristic values of the particle size distributions. As a consequence, these particles were studied in order to reduce rejects and to improve the significance of the information provided by the characteristic values.

It was found that the scrap consisted of highly irregular particles with a rough, fragmented surface and large filaments (Figure 7-18). The presence of the latter in combination with the screening technique, i.e. dry sieving, may explain the observation that the amount of scrap varied inconsistently with rotational speed and electric arc current (Table 7-5) as filaments tend to pass the sieve mesh despite their larger equivalent diameter.

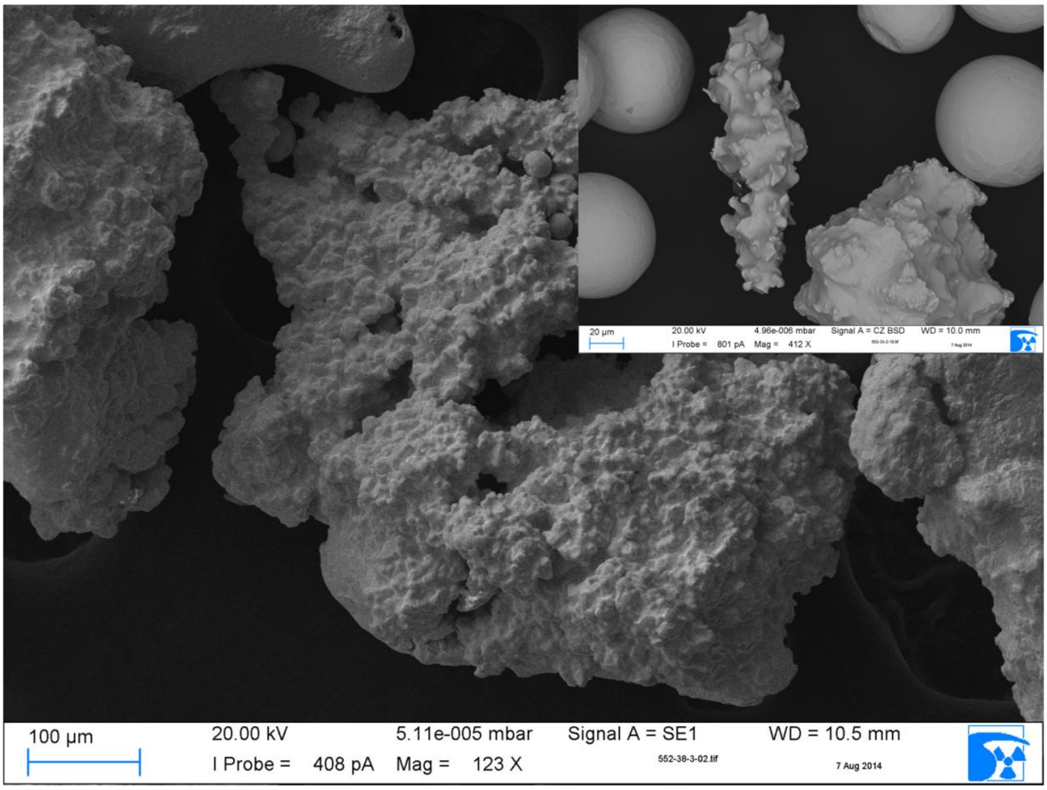

Figure 7-18 Irregular particles typically found on the sieve mesh > 355 µm (image: batch 552-38), occasionally occurring in smaller size classes (batch 552-33, < 125 µm).

It is suggested that the earlier reported inhomogeneity of the purchased rotating electrodes, namely unmelted molybdenum foils (Figure 5-14), provided a significant contribution to the presence of coarse and irregular particles. In fact, molybdenum has a higher melting point than U8Mo. It was thus potentially ejected with the liquid U8Mo melt or slurry prior to full melting.

REP atomization of Ti-Y alloy led to similar particle size distributions as obtained in the present study, notably a prominent tail on the coarse particle side after sieving was found [Naka *et al.* 1987]. However, the authors did not discuss the presented particle size distribution and potential causes. Centrifugal atomization of AZ91 magnesium alloy by the rotating disk process also resulted in the formation of irregular particles [Angers *et al.* 1997]. The reported particle size distributions are similar to those obtained for REP atomization of U8Mo in this work. The formation of the irregular particles was ascribed to partial melt solidification on the rotating disk and subsequent break up [Angers *et al.* 1997]. The authors proposed disk preheating as a remedy to this fragmentation mechanism.

Table 7-5 Amount of scrap per batch of atomized U8Mo.

Batch U8Mo	Rotational speed [rpm]	Electric arc current [A]	Apparent mass flow rate [g/s]	Scrap mass fraction > 355 μm [%]
552-33	45'000	50	1.15	23
552-36	45'000	45	1.10	19
552-39	40'000	50	1.26	7
552-38	40'000	40	0.987	13
552-42	30'000	50	1.28	15
552-06	30'000	35	0.843	14
552-04	20'000	50	1.15	8
552-08	20'000	35	0.762	6
552-14*	50'000	50	0.953	9
552-13*	40'000	50	-	16
552-12*	40'000	35	0.550	9

* short rotating electrode

However, REP and PREP atomization of Ti-6Al-4V, which has a small melting range of about 56 K, resulted in particle size distributions without tail [Isonishi *et al.* 1989, Roberts and Loewenstein 1980]. Although a small third mode was reported [Isonishi *et al.* 1989], it is not similar to the tail that was observed in this work for REP atomization of U8Mo. These results are in agreement with experimental results of this work regarding 1.4301 stainless steel as well as earlier reports regarding SAE 1090 steel [Champagne and Angers 1984]. Both metal alloys exhibit melting ranges of about 50 K, respectively.

Similar to the observations made during atomization of AZ91 [Angers *et al.* 1997], a thermal effect and fragmentation mechanism is suspected to have additionally contributed to the coarse particle tail of REP-atomized U8Mo powders presented in this work. Namely, the presence of irregular particles is partially ascribed to U8Mo having a melting range between liquidus and solidus of about 100 K[52] in combination with the limitations of REP in providing superheat [Lawley 1992]. As mentioned before, in REP the liquid melt is ejected instantaneously due to centrifugal force – in particular at high rotational speeds. It can be inferred from Figure 7-19 that the process of melting and atomization was not uniform with respect to the radial position on the electrode top due to the changing morphology. In fact, it must be taken into account that with increasing radial distance from the rotating electrode centre the electric arc becomes cooler while the centrifugal force and heat loss (due to thermal radiation) rise.

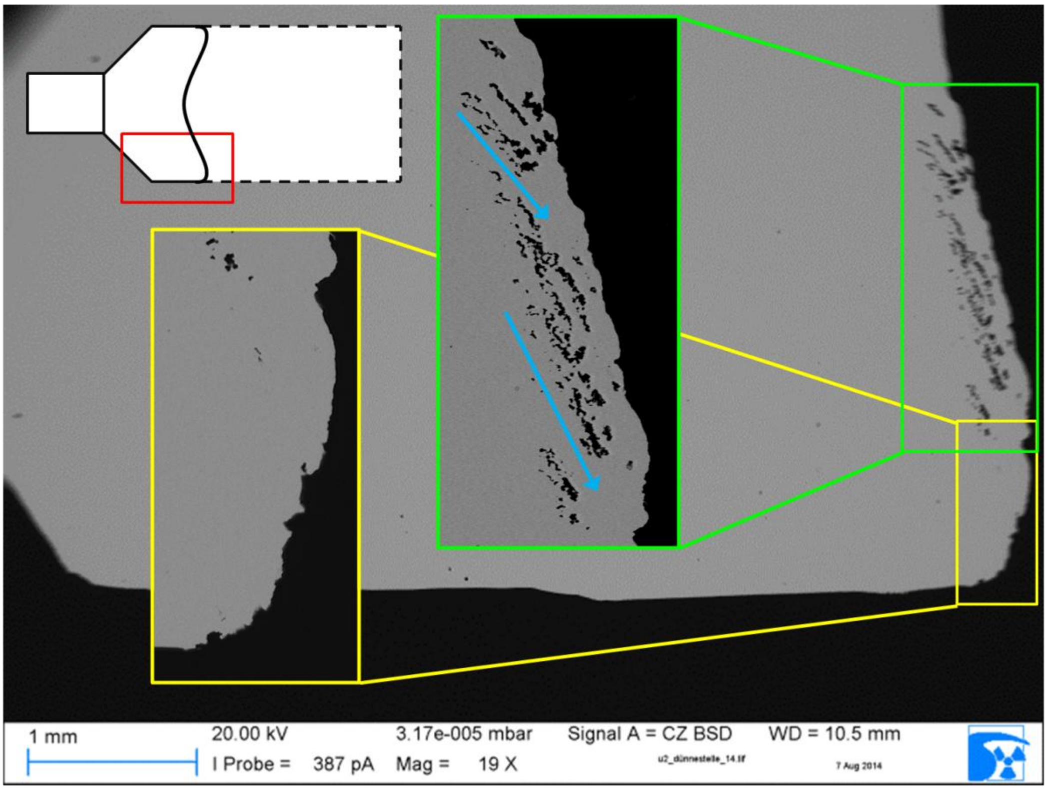

Figure 7-19 Micrograph of a sectioned U8Mo rotating electrode rest (552-39). The red rectangle shows the position of the micrograph relative to the rotating electrode before (dashed line) and after atomization. The green rectangle is a focused detail view of the melting and atomization zone, showing the conical form towards the electrode centre as well as the spongy morphology of the solidified rotating electrode top between centre and rim. The yellow rectangle is a focused detail view of the rim and tear-off zone. About 1 mm radial from the rim the conical shape reaches its maximum and the alloy is homogenous again. The blue arrows indicate the direction of traction and breakaway.

Although these conditions are process-inherent and thus were identical for already successfully REP-atomized elemental metals, the role of alloys having a melting range, e.g. U8Mo, becomes more important. In fact, the alloy at the centre receives more energy and experiences smaller centrifugal force. Consequently, it has more time to both fluidify and heat up on the way to the rim than in the zone between centre and rim.

---

[52] For comparison: [Kim *et al.* 2007] reported a superheat of about 200 K, though it was not stated which temperature – solidus or liquidus – served as basis.

There, the centrifugal force already acts on not entirely molten material, consequently causing the spongy morphology. Comparison of Figure 7-18 and Figure 7-20 shows the similarity of particles of irregular shape and the spongy zone. With reference to chapter 8.2.3, it is suggested that the spongy zone consisted of partially molten and solid crystals of U8Mo.

The discrepancy in heating time reaches its extreme at the outer rim. Though here the morphology was homogenous again like in the electrode centre, the reason was probably another. While in the centre the material was entirely molten prior to removal – thus leaving a homogenous morphology – the material at the outer rim did not even start melting. An extreme example of the latter is given in Figure 7-21.

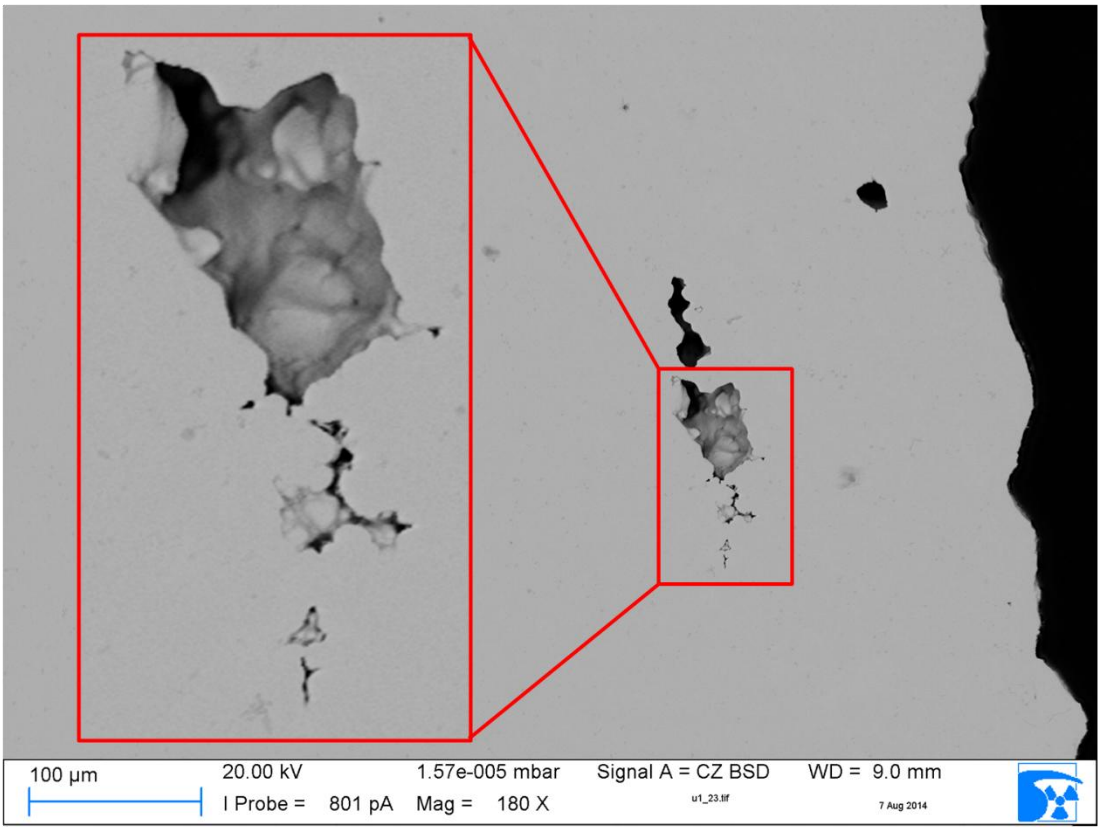

Figure 7-20 Micrograph of a sectioned U8Mo rotating electrode rest (552-38) showing the morphology of the spongy zone (enlarged in red rectangle) similar to the one presented in Figure 7-19. The morphology is similar to the irregular, fragmented particles shown in Figure 7-18.

Furthermore, it is visible in Figure 7-19 that the rim was not smooth but highly irregular, indicating inconsistent droplet tear-off and potential particle breakaway (fragmentation).

A more uniform heat distribution may be obtained with a flat tungsten electrode tip pointing, Figure 3-24. The conical shape of the rotating electrode top is a rough reproduction of the conical shape of the tungsten electrode tip and influenced by the temperature profile of the electric arc [Matthes and Schneider 2012] as well as the electric arc length since the latter affects the heat input [Katsaounis 1993]. However, the conical shape of the rotating electrode top varied inconsistently which is ascribed to the manual control of the electric arc length. While a flat tungsten electrode tip may result in a more uniform heat distribution and shallow penetration, a tapered tip that causes a conical rotating electrode top is beneficial to the production of small particles (Figure 3-24). In fact, it is known that slip of the liquid may occur on a flat disk, while in a cup the liquid is accelerated more as it has to move up the inner the wall of the cup, therefore yielding finer particles. Nevertheless, a flat tungsten electrode tip and thus more uniform heat distribution may compensate for the melting range of U8Mo.

For completeness, it is mentioned that the U8Mo rotating electrodes did not show porosity or spongy morphology after cross-sectional cutting which was done in preparation of every atomization run. In addition, it can be inferred from Figure 7-19 that the spongy melting zone was mainly torn in the direction of the centrifugal force suggesting that the porosity was caused during atomization due to centrifugal force.

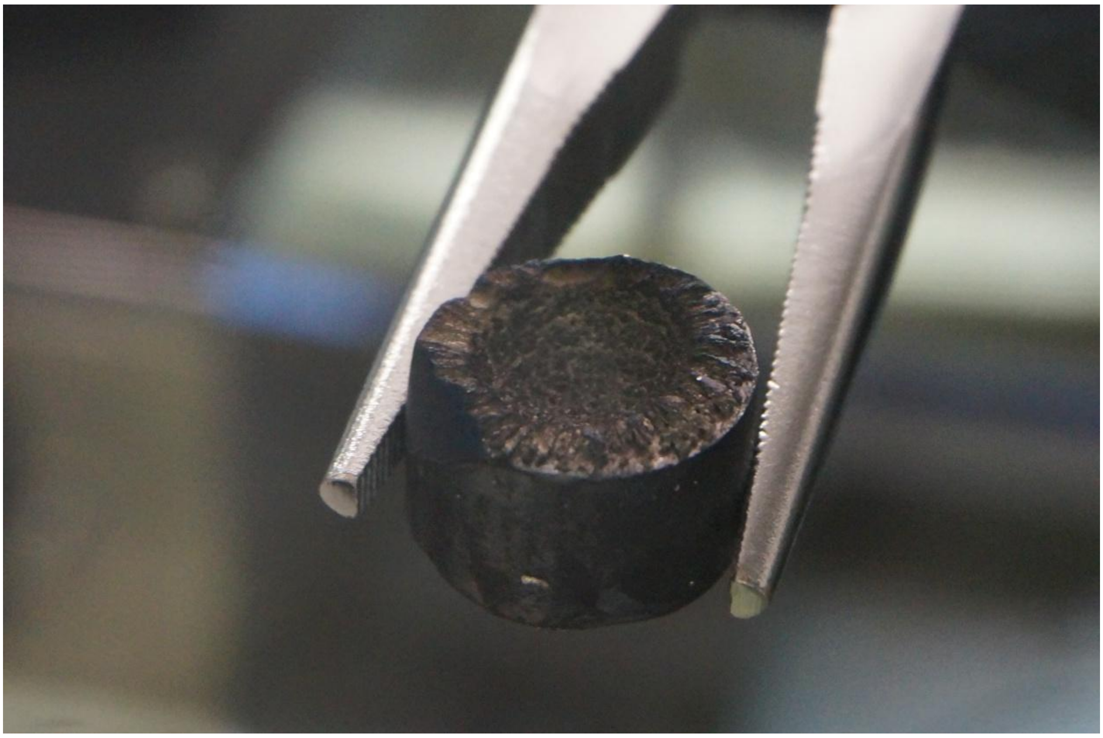

Figure 7-21 Example of partial atomization, i.e. centre erosion, of batch U7Mo-1114-2-1.2 at 25’000 rpm, 50 A, and 20 mm diameter.

The described process conditions may have given rise to three types of particles: regular particles from the liquid phase, not entirely molten and thus fragmented particles from the mushy zone, and particles broken off the partially solid rim.

Another minor contribution to the tail seems to have come from flakes produced from relatively large liquid drops and their impact on the collection chamber wall prior to solidification (Figure 8-28). These “flat” disks, however, were not observed in the relevant size classes < 180 µm.

Ultimately, it is suggested that the combination of the melting range of U8Mo, the inhomogeneity of the purchased rotating electrodes, and the characteristics of REP gave rise to the observed irregular particles. These irregular particles have in turn potentially contributed to the spread of the particle size distribution besides the expected polydispersity due to atomization in the vicinity of the transition from the LD to the DDF regime. The more, as at elevated speeds rather long, flat and persisting tails were found. Another contribution to the tails may have originated from manifested filaments as their presence was observed on sieve meshes > 355 µm.

7.2.4 Model Evaluation

A brief comparison of the relevant models of chapter 7.1.5 with experimental results obtained from atomization of U8Mo and 1.4301 stainless steel was conducted in order to determine the models’ precision and suitability for mean particle size prediction with respect to U8Mo. Measure of precision was the coefficient of determination R^2 that was obtained by linear regression analysis and is summarised in Table 7-6. All calculated and measured diameters are summarised in Table 7-7 and Table 7-8 for 1.4301 stainless steel and U8Mo, respectively. For comparison with external data, it is noted that the characteristic diameters were calculated from the corresponding cumulative undersize distribution and therefore were slightly dependant on the chosen mesh series. As in this work the same mesh series was used for sieving, results are comparable without reservation.

In general, it was found that the coefficient of determination with respect to the experimental data of U8Mo was similar for all applied models regardless of their original application, i.e. for normal liquids or metal melts. Adding data of 1.4301 generally increased the overall coefficient of determination. The increase is explained by the relatively high coefficients of determination obtained for 1.4301 stainless steel atomization: about 96 % with respect to $D_{m,0.3}$ as well as $D_{m,0.5}$, and about 90 % for $D_{m,m}$.

In particular, $D_{m,0.3}$ (particles with a diameter $\leq D_{m,0.3}$ account for 30 % of the total powder mass) was represented best by the models. The coefficient of determination reached 85 % and 92 % with regard to experimental data of U8Mo as well as combined U8Mo and 1.4301 stainless steel. The uncertainty of the experimental $D_{m,0.3}$ was below 1 % with reference to chapter 7.1.1.

The coefficient of determination for the median reached 69 % and 85 % with regard to experimental data of U8Mo as well as combined U8Mo and 1.4301 stainless steel. The uncertainty of the experimental $D_{m,0.5}$ was below 1 % with reference to chapter 7.1.1.

The mass mean diameter was poorly represented having coefficients of determination around 28 % and 50 % with regard to experimental data of U8Mo as well as combined U8Mo and 1.4301 stainless steel.

Table 7-6 Coefficients of determination R2 of representative models (chapter 7.1.5) with respect to characteristic diameters of atomized 1.4301 stainless steel (Table 7-7) and U8Mo (Table 7-8) powders. R2 was obtained through linear regression analysis. The highest values are highlighted in red.

Model	Coefficient of determination with respect to					
	U8Mo			U8Mo and 1.4301		
	$D_{m,0.3}$	$D_{m,0.5}$	$D_{m,m}$	$D_{m,0.3}$	$D_{m,0.5}$	$D_{m,m}$
	R^2 [%]	R^2 [%]	R^2 [%]	R^2 [%]	R^2 [%]	R^2 [%]
Jones	83.73	68.03	25.31	83.51	84.52	49.46
Muraszew	83.73	68.03	25.31	89.26	72.29	18.94
Champagne 1980	85.39	68.74	28.06	91.95	76.20	22.03
Champagne, D_{32}, 1981	83.94	68.02	25.66	90.46	73.91	20.15
Champagne, D_{43}, 1981	84.67	68.46	26.67	91.22	75.02	21.05
Matsumoto	83.54	67.76	25.17	89.85	73.06	19.54
Tanasawa DDF	84.28	68.22	26.11	90.33	73.78	20.22
Tanasawa LD	85.11	68.59	27.52	91.13	75.30	22.02

The decreasing precision with increasing consideration of mass in the creation of the characteristic diameters is mainly explained with the presence of irregular particles on the coarse particle side and an additional contribution from the observed tails (chapter 7.2.2). Best agreement of modelled and experimental data was found for the model "Champagne 1980", equation (7.29). The corresponding linear regression analysis is therefore plotted in detail in Figure 7-22 and Figure 7-23 for combined U8Mo and 1.4301 stainless steel as well as U8Mo, respectively.

As can be seen from Table 7-8, the outliers with respect to U8Mo were the short electrodes of batches 552-12 and -14 as well as the standard electrode of batch 552-06. While the deviations with respect to the short electrodes may be ascribed to an underestimated “real” mass flow rate (chapter 5.3.3) and a different particle size distribution due to thermal and/or mechanical effects (chapter 7.2.1), the deviation of batch 552-06 could be a statistical outlier.

The adjusted model with respect to the linear regression analysis of U8Mo (Figure 7-23) can be written as:

$$D_{32} = 5.56 \cdot \frac{Q_{\mathrm{l}}^{0.12}\sigma^{0.43}}{D_{\mathrm{re}}^{0.64}\rho_{\mathrm{l}}^{0.43}\omega^{0.98}}, R^2 \approx 85\ \% \tag{7.33}$$

The adjusted model with respect to the linear regression analysis of combined U8Mo and 1.4301 stainless steel (Figure 7-22) can be written as.

$$D_{32} = 4.95 \cdot \frac{Q_{\mathrm{l}}^{0.12}\sigma^{0.43}}{D_{\mathrm{re}}^{0.64}\rho_{\mathrm{l}}^{0.43}\omega^{0.98}}, R^2 \approx 92\ \% \tag{7.34}$$

In both adjusted models, only the constant was changed with respect to the original model (7.29). Notably, the constant of model (7.34) is similar to the original constant of 4.63 [Champagne and Angers 1980]. For the same model, also a constant of 3.65 was reported [Kim *et al.* 2007].

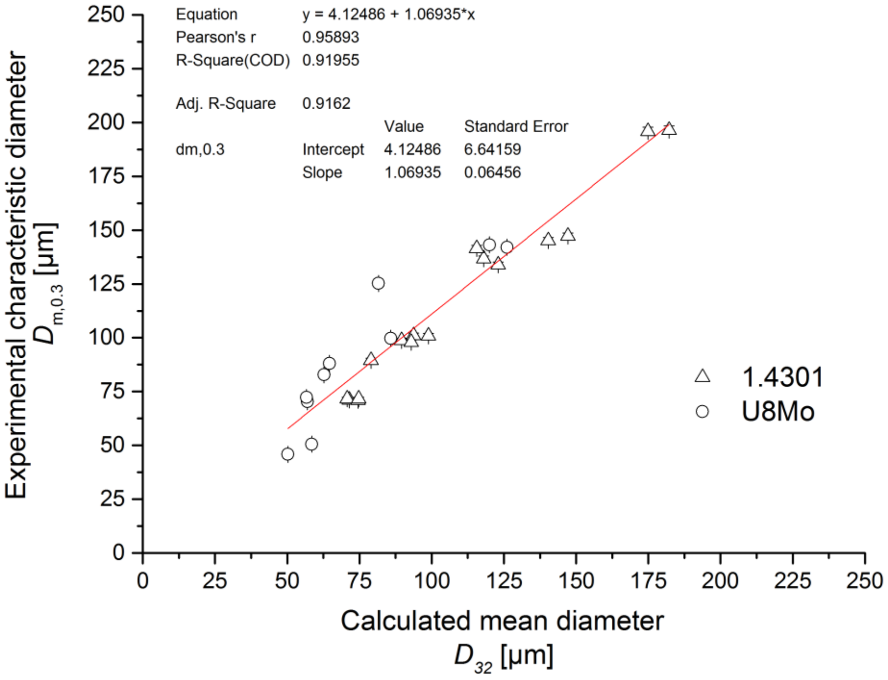

Figure 7-22 Linear regression analysis of experimental and calculated characteristic diameters of U8Mo and 1.4301 stainless steel powders taken from Table 7-8 and Table 7-7, respectively. Uncertainties within symbol size if not visible. D_{32} was calculated using model "Champagne 1980", equation (7.29).

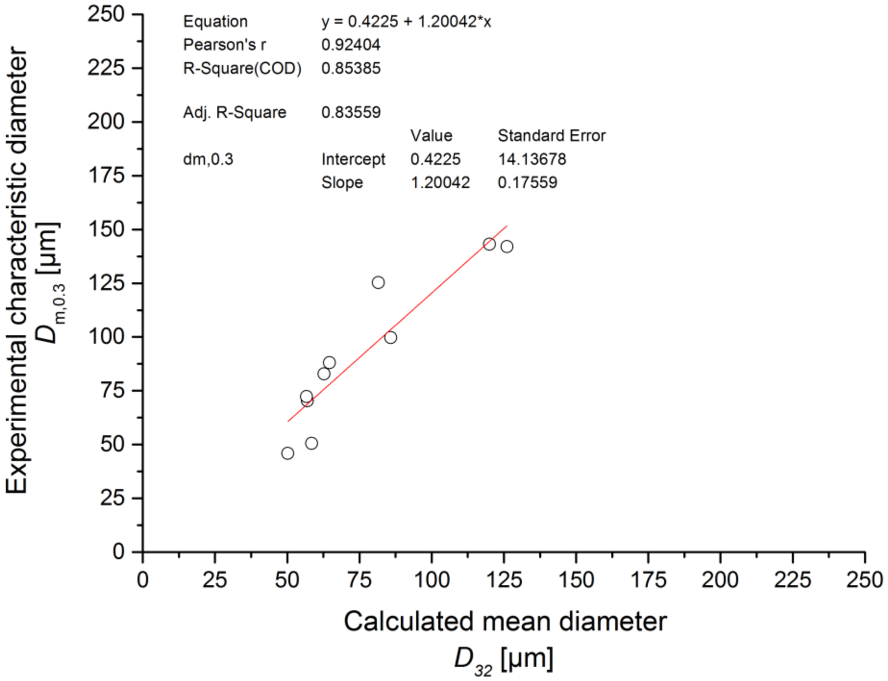

Figure 7-23 Linear regression analysis of experimental and calculated characteristic diameters of U8Mo powder taken from Table 7-8. Uncertainties within symbol size if not visible. D_{32} was calculated using model "Champagne 1980", equation (7.29).

Table 7-7 Characteristic diameters from the cumulative undersize distribution and calculated mean diameters of 1.4301 stainless steel using models from chapter 7.1.5. Uncertainties of experimental characteristic diameters are below 1 % (chapter 7.1.1). Thermophysical properties of mild steel (Table 6-2) were used for calculation.

Batch	Experimental characteristic diameters			Jones	Muraszew	Champagne 1980	Champagne 1981	Champagne 1981	Matsumoto	Tanasawa DDF	Tanasawa LD
	$D_{m,0.3}$ [µm]	$D_{m,0.5}$ [µm]	$D_{m,m}$ [µm]	$D_{m,0.5}$ [rad/(s m$^{0.5}$)]	D_p [µm]	D_{32} [µm]	D_{32} [µm]	D_{43} [µm]	D_{32} [µm]	D_{32} [µm]	D_{32} [µm]
Inox-014	196	212	205	0.00477	242	175	190	190	264	202	255
Inox-015	99	109	110	0.00239	121	90	93	95	128	101	128
Inox-016	137	150	146	0.00318	161	118	125	127	173	135	170
Inox-018	71	79	81	0.00191	97	72	74	76	101	81	102
Inox-019	145	162	172	0.00404	205	140	156	156	218	170	214
Inox-020	101	111	120	0.00269	136	94	103	104	143	113	142
Inox-021	72	79	99	0.00202	102	71	76	78	106	85	107
Inox-022	71	79	94	0.00202	102	75	77	80	106	85	111
Inox-023	147	167	172	0.00404	205	147	157	160	218	171	223
Inox-024	101	112	115	0.00269	136	99	104	106	143	114	149
Inox-025	197	213	206	0.00477	242	182	191	194	264	204	263
Inox-026	134	147	142	0.00318	161	123	126	129	173	136	176
Inox-027	98	108	108	0.00239	121	93	94	97	128	102	132
Inox-028	72	82	84	0.00191	97	75	74	78	101	82	106
Inox-040	142	160	178	0.00338	171	116	128	129	178	142	184
Inox-041	90	103	140	0.00225	114	79	84	87	116	95	125

Table 7-8 Characteristic diameters from the cumulative undersize distribution and calculated mean diameters for U8Mo using models from chapter 7.1.5. Uncertainties of experimental characteristic diameters are below 1 % (chapter 7.1.1). Uranium instead of U8Mo thermophysical material properties were used for calculation.

Batch	Experimental characteristic diameters			Jones	Muraszew	Champagne 1980	Champagne 1981	Champagne 1981	Matsumoto	Tanasawa DDF	Tanasawa LD
U8Mo	$D_{m,0.3}$ [µm]	$D_{m,0.5}$ [µm]	$D_{m,m}$ [µm]	$D_{m,0.5}$ [rad/(s m$^{0.5}$)]	D_p [µm]	D_{32} [µm]	D_{32} [µm]	D_{43} [µm]	D_{32} [µm]	D_{32} [µm]	D_{32} [µm]
552-04	142	173	194	0.00477	161	126	127	132	173	139	184
552-06	125	178	205	0.00318	108	82	83	86	113	91	119
552-08	143	172	188	0.00477	161	120	126	129	173	136	177
552-12	51	74	122	0.00239	81	58	61	63	84	68	86
552-14	46	62	121	0.00191	65	50	49	52	66	55	72
552-33	70	89	194	0.00212	72	57	55	59	74	62	82
552-36	72	90	183	0.00212	72	57	55	59	74	62	82
552-38	83	128	175	0.00239	81	63	62	65	84	69	91
552-39	88	122	150	0.00239	81	65	62	66	84	70	93
552-42	100	119	181	0.00318	108	86	84	89	113	93	124

7.3 Comparison

INL provided a particle size distribution of spherical UMo powder [Clark *et al.* 2007] that was not complete and therefore not valid for comparison; namely, the progression above 106 µm was not reported. A later submitted report on U8Mo atomization [Moore and Archibald 2014] provided several cumulative undersize distributions. However, comparison was not possible as the predominant particle shape was not analyzed.. It is hence not clear, whether the presented particle size distributions are distorted by the presence of filaments. In addition, only a part of the entire particle size range, i.e. up to 212 µm, was covered. Nevertheless, the results indicate the presence of a tail as observed in this work. The total powder yield efficiency was reported to 77-80 %.

KAERI [Kim *et al.* 1997b] reported two bimodal size distributions of UMo based on the normalised number of particles. The authors suggested that one particle size distribution was obtained from atomization in the LD regime while the other resulted from atomization in the DDF regime. The latter interpretation must be considered with caution as the particles below 45 µm had reportedly a "lengthened or flake-like" shape [Kim *et al.* 1997b] and hence did not comply with requirements; though, no representative picture was shown. Characteristic values were not reported. Regarding yield, the atomized mass per batch reached 4 kg and was only limited due to criticality concerns [Kim *et al.* 1997b]. However, the yield efficiency was not reported.

Another report from KAERI suggested that at "large" disk diameters and "high" rotational speeds [Oh *et al.* 2006] less than 5 % of the powder had a greater diameter than 300 µm. However, no statement on the obtained particle shape was made, thus not excluding that the gain in yield came at the price of manifested filaments. The reported particle size distributions were presented as functions of helium-argon mixtures, and it was stated that at 100 % He the particle shape was more spherical. This, however, came at the price of a significantly coarser particle size distribution: the increase of the helium content from 20 % to 100 % resulted in a shift of the mode from about 125 µm to about 250 µm while having the same range (~ 300 µm). Interestingly, the presence of a large and flat tail as observed in this work for REP atomization of U8Mo or for rotating disk atomization of AZ91 magnesium alloy [Angers *et al.* 1997] was not reported. In combination with the results obtained in this work and data provided by INL, the hypothesis of a correlation between the presence of a tail, REP, and the use of U8Mo is thus strengthened.

CCHEN reported yield efficiencies with respect to usable powder [Olivares *et al.* 2012]. The presented particles, however, were highly irregular in shape, oxidised, and consisted of filaments and fragmented particles.

7.4 Conclusion

The analysed particle size distributions ($X \leq 0.068$) were generally bimodal with few exceptions. The usable powder yield efficiency for standard rotating electrodes (10 mm diameter and 30 mm consumable length) reached about 56 % (18 g) and 12.5 % (4 g) with regard to particles of a diameter smaller than 125 µm and 40 µm, respectively, at 45’000 rpm and 50 A. The resulting coarse-to-fine ratio was located between 4.6 and 3.4. The corresponding process yield efficiency was about 40 %.

Higher usable powder yield efficiencies were achieved for short rotating electrodes of 10 mm diameter and 20 mm consumable length. That is, usable powder yield efficiency reached about 77 % (15 g) and 25 % (4 g) in the target size ranges < 125 µm and < 40 µm, respectively. The corresponding rotational speeds varied from 40’000 rpm to 50’000 rpm, the applied electric arc current was 50 A. The resulting coarse-to-fine ratio was located between 2.4 and 1.9. Particle size distributions exhibited median diameters as low as 62 µm. Thus, particle size distributions were found that comply with the fuel specifications in terms of shape, particle size, and desired coarse-to-fine ratio (1 to 2.33), even without posterior blending (chapter 2.4). The corresponding process yield efficiency was generally slightly higher than for standard rotating electrodes with values of about 40 % to 50 %. The improvement in yield efficiency of usable powder with decreasing rotating electrode length is ascribed to thermal and/or mechanical effects. As both effects differ in the moment of when the coarse particles are produced, atomization of several standard rotating electrodes to the length of a short electrode is suggested in order to validate or falsify one of the presented hypotheses.

The target annual production capacity of the prototype is 1 kg per year (chapter 2.9). The production capacity of the current atomizer design allows for a potential U8Mo fuel powder production of 256 g per working day and operator. As a result, the implemented atomizer may cover 25 % of the annual production within one working day.

While an increase in rotational speed resulted in a shift of the particle size distribution to the fines with sharper modes and higher yield efficiency, the role of the mass flow rate was inconclusive. Similar to the rotational speed, an increase of the rotating electrode diameter caused a shift to the fines and thus higher yield efficiencies.

A tail on the coarse particle side was observed for atomization of U8Mo that is typical for atomization in the ligament formation regime. The rather long tail persisted at increased rotational speeds, though was relatively constant and flat in size. An increase of the rotating electrode diameter of 1.4301 stainless steel also revealed the presence of a tail, though less pronounced than for U8Mo. A significant amount of powder (6 % to 23 %), notably at rotational speeds where the yield efficiency of usable powder was best (45’000 rpm), had a diameter above 355 µm. The micrographic analysis revealed that these particles consisted of filaments and highly irregular particles with fragmented and rough surface. Their presence is mainly ascribed to a material and process interaction caused by the following effects: (i) inhomogeneities of purchased U8Mo rotating electrodes, (ii) the limited superheat in REP because of instantaneous melt ejection due to centrifugal force, (iii) a non-uniform input heat distribution in REP, and (iv) the melting range of U8Mo alloy.

The characteristic values of the particle size distributions of U8Mo were affected by the observations stated in the two preceding paragraphs and thus of low significance except for $D_{\mathrm{m},0.3}$.

Comparison of the experimental results was difficult due to incomplete published data with respect to atomization of U2Mo, U7Mo, U8Mo, and U10Mo. However, the results obtained in this study with respect to yield efficiency as well as the presence of tails/scrap are in accordance with other REP atomized powders. The presented particle size distributions are similar to those obtained from rotating disk atomization (KAERI). However, it seems that the particles coming from rotating disk atomizers show irregular shapes below 50 µm in contrast to the particles produced in this work that were spherical in shape.

Several models predicting mean particle size were compared to characteristic diameters of particle size distributions generated during this work. It was found that all models, regardless of their original application, yielded similar results. Best agreement with respect to atomized U8Mo and 1.4301 stainless steel powder was obtained for the model reported by [Champagne and Angers 1980] with adjusted constant and for particles with a diameter ≤ $D_{\mathrm{m},0.3}$, thus particles that constitute 30 % of the total powder mass.

$$D_{32} = 4.95 \cdot \frac{Q_{\mathrm{l}}^{0.12} \sigma^{0.43}}{D_{\mathrm{re}}^{0.64} \rho_{\mathrm{l}}^{0.43} \omega^{0.98}} \tag{7.35}$$

The corresponding coefficient of determination was 92 %.

In summary, it is suggested to produce powder from short rotating electrodes with a diameter of 10 mm as the coarse-to-fine ratio is more favourable with respect to standard size rotating electrodes and as the process yield efficiency is similar. Rotational speeds between 45'000 rpm or 50'000 rpm are recommended depending on the rotating electrode length and diameter. Notably, design limits of the high frequency spindle have to be respected (Table 3-1 and Table 3-2).

As REP is sensitive to the circular runout of the workpiece, the acquisition of appropriate turning and cutting machines for the preparation of the rotating electrode prior to atomization is recommended. This will reduce vibration-induced effects on the atomization mechanism and allow for higher rotational speeds and/or diameters.

In terms of powder screening, purchase or adjustment of the existing CERCA laser granulometry for more precise analysis of the particle size distributions is an option, notably with regard to the fines and the limits of dry sieving. For the future, the (optical) microscopic examination of all size classes is recommended in order to determine both the particle shape present in the tails and the significance of the particle size distributions above a diameter of 180 µm.

As the particle size distributions are the result of the atomization regime, it is called once again for high-speed video equipment that allows for better understanding and traceability of the atomization mechanism and thus production results.

The tip and diameter of the tungsten electrode was not varied in this study. However, it is known to be influential in standard TIG welding. For REP, it is supposed that a flat tip may improve the heat distribution on the top surface of the rotating electrode in order to reduce the amount of scrap. It is reminded, though, that a tapered tip yields a conical pool on the rotating electrode top that promotes the production of finer powder.

8

Particle Morphology and Chemistry

The atomized UMo powder will serve as nuclear fuel. It is therefore ought to become a structural member of fuel plates and fuel elements that will in turn be subject to irradiation and thermal cycles. As the particle chemistry, surface morphology, and microstructure has influence on the mechanical, thermal, and irradiation behaviour of the fuel powder, a characterisation of the particle properties is given in the following chapter.

8.1 Background

8.1.1 Phase Diagrams

U8Mo is an uranium alloy with 8 wt.-% molybdenum. Both elements are entirely soluble in the liquid phase, but have limited solubility in the solid phase. As can be seen from Figure 8-1, uranium and molybdenum form a peritectic system. U8Mo has a liquidus-solidus gap that amounts to about 100 K. That is, solidification of the melt starts at the liquidus and ends at the solidus line in contrast to pure elements that exhibit at discrete melting point. The zone in between the solidus and liquidus is referred to as melting range.

Carbon is an impurity that had influence on the microstructure of powder samples analysed in this work. Therefore, the binary phase diagram of the U-C system is presented here, too (Figure 8-2). Both uranium and carbon are entirely soluble in the liquid phase, but have limited solubility in the solid phase. In the relevant concentration range of carbon, both elements form a eutectic system. The eutectic is situated at 500 ppm carbon by weight.

In addition, isothermal ternary phase diagrams of the U-Mo-C system at 1000 °C and 1400 °C are given in Figure 8-3 and Figure 8-4, respectively. The temperature range roughly encloses the prevailing temperatures expected for REP atomization of U8Mo and U7Mo. It is noted that in the ternary U-Mo-C system at 1000 °C, only UC and γ-U(Mo) are indicated as stable phases although the existence of a ternary alloy γ-U(Mo,C) would be expected with respect to the binary systems.

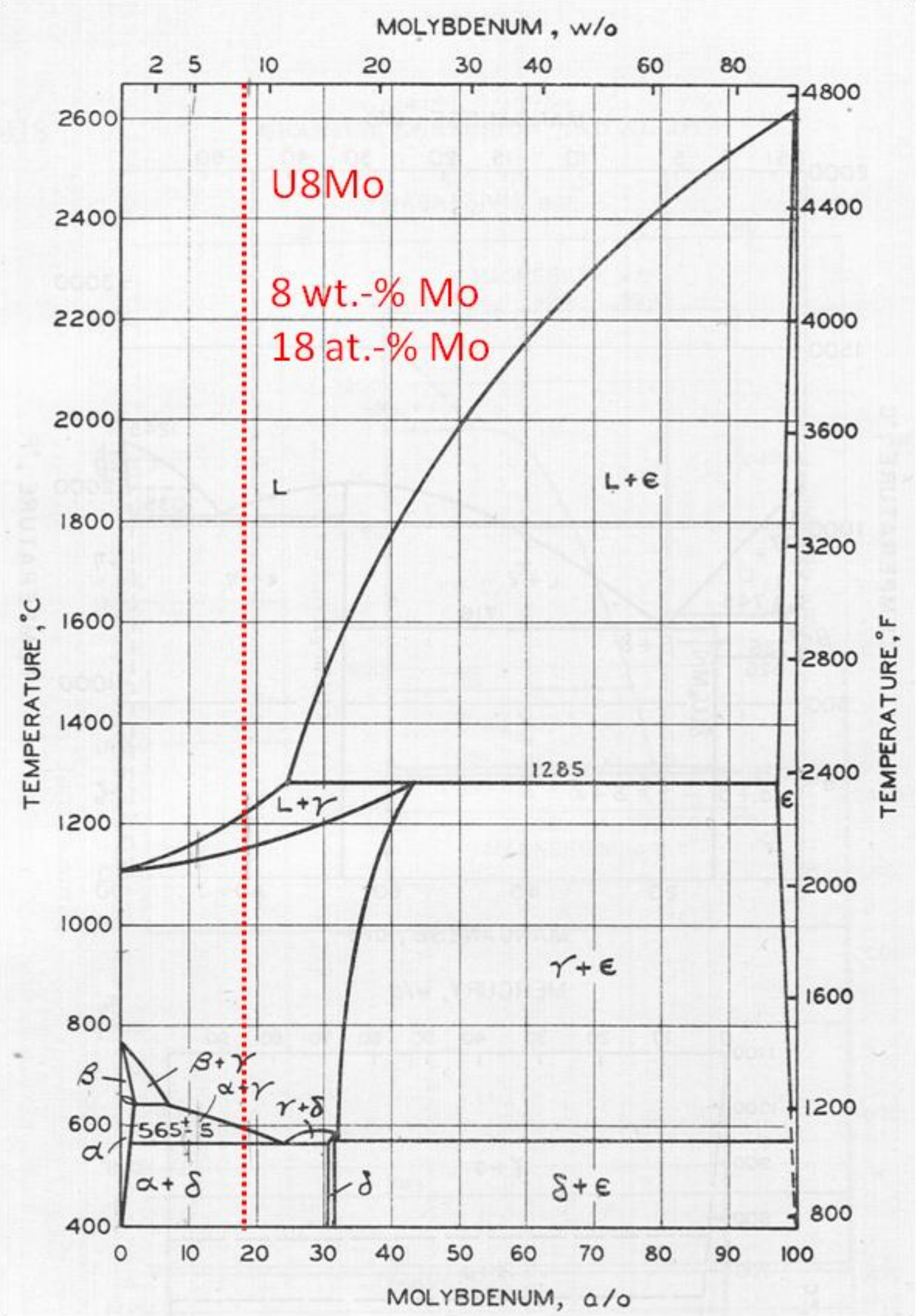

Figure 8-1 Equilibrium phase diagram of the binary U-Mo system; property of [Wilkinson 1962a]. The red dotted line marks the composition of U8Mo.

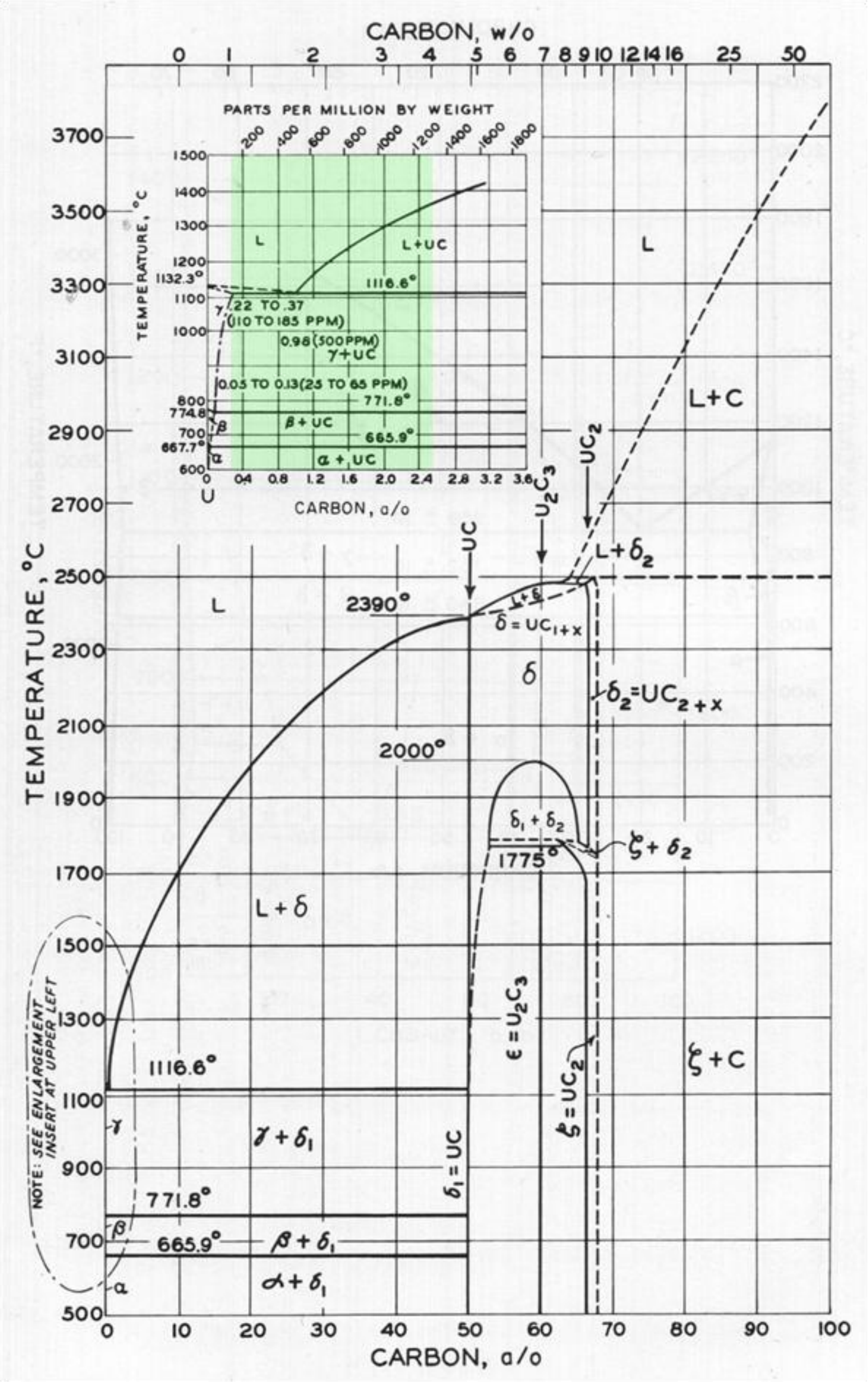

Figure 8-2 Equilibrium phase diagram of the binary U-C system; property of [Wilkinson 1962a]. The green area marks the range of carbon impurities present in the analyzed samples.

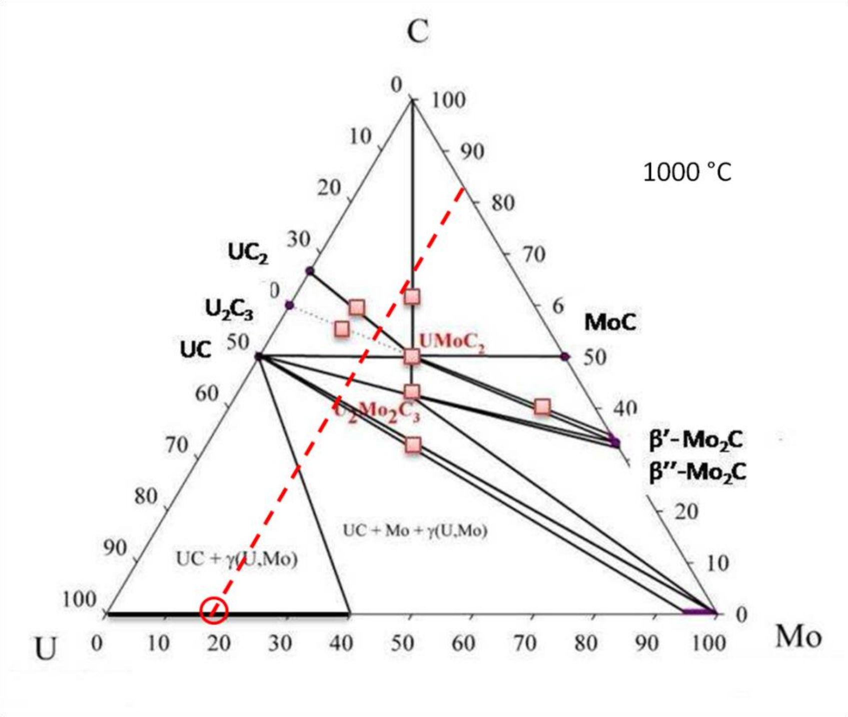
C
1000 °C
UC₂
U₂C₃
UC
UMoC₂
U₂Mo₂C₃
MoC
β'-Mo₂C
β''-Mo₂C
UC + γ(U,Mo)
UC + Mo + γ(U,Mo)
U
Mo
0
10
20
30
40
50
60
70
80
90
100

Figure 8-3 Isothermal section of the U-Mo-C ternary phase diagram at 1000 °C; property of [Peniel *et al.* 2012]. The red dotted line shows a molybdenum concentration of about 18 at.-%. The red circle marks roughly the alloy compositions used in this work.

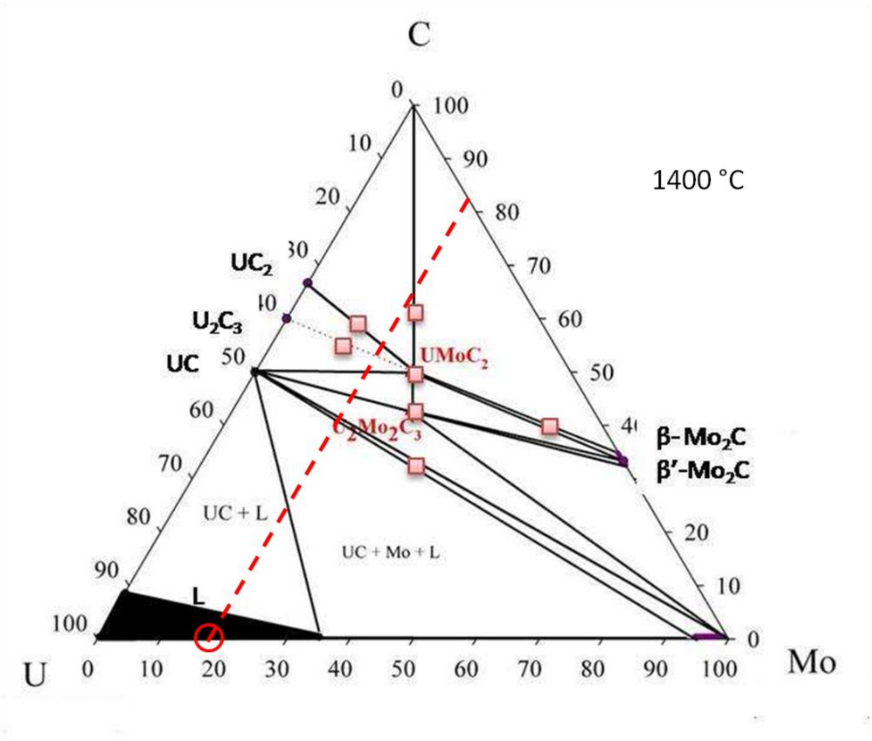
C
1400 °C
UC₂
U₂C₃
UC
UMoC₂
U₂Mo₂C₃
β-Mo₂C
β'-Mo₂C
UC + L
UC + Mo + L
L
U
Mo
0
10
20
30
40
50
60
70
80
90
100

Figure 8-4 Isothermal section of the U-Mo-C ternary phase diagram at 1400 °C; property of [Peniel *et al.* 2012]. The red dotted line shows a molybdenum concentration of about 18 at.-%. The red circle marks roughly the alloy composition used in this work.

8.1.2 Primary Crystallisation in Alloys

Crystallisation and the resulting microstructure in metals depend on nucleation in the melt during cooling, in particular of both the number of crystallisation nuclei and the crystallisation speed [Merkel and Thomas 2003]. Both parameters in turn depend on the level of supercooling[53] of the melt (Figure 8-5). In general, the microstructure is refined with an increased supercooling or solidification rate [Bargel *et al.* 2000]. Uniform heat removal in all directions and spatial freedom will promote the growth of equiaxed grains, while directed heat removal and spatial restrictions may promote the growth of columnar grains or dendrites [Bargel *et al.* 2000].

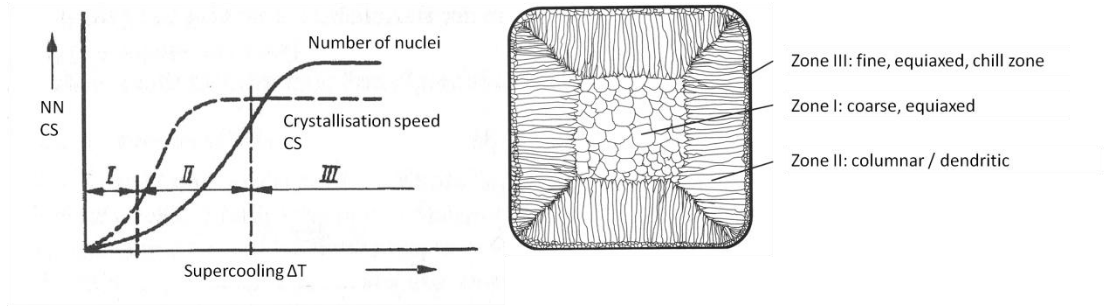

Figure 8-5 Left: Number of nuclei (NN) and crystallisation speed (CS) as a function of supercooling ΔT; property of [Merkel and Thomas 2003]. Right: corresponding schematic microstructure in a geometrically simple ingot; property of [Bergmann 2003].

Alloys consist by definition of at least two elements [Bargel *et al.* 2000]. During cooling of an alloy from liquid to solid state, a difference in the elemental solubility in the melt and initially crystallised solid solutions (mixed crystals) may lead to constitutional supercooling. An exemplary cooling process causing constitutional supercooling is given for a binary A-B system with initial concentration c_0 of the component B (Figure 8-6). The first crystallising solid solutions have a lower solubility of B (T_0, c_1) than the melt, Figure 8-6 a). Thus, the concentration of the component B increases in the melt at the solid-liquid interface, Figure 8-6 b). With respect to the alloy U8Mo, the first crystallising solid solutions in the U-Mo binary system (Figure 8-1) have a higher concentration in molybdenum.

---

[53] A liquid is considered supercooled if it does not solidify although its temperature is beneath the freezing point.

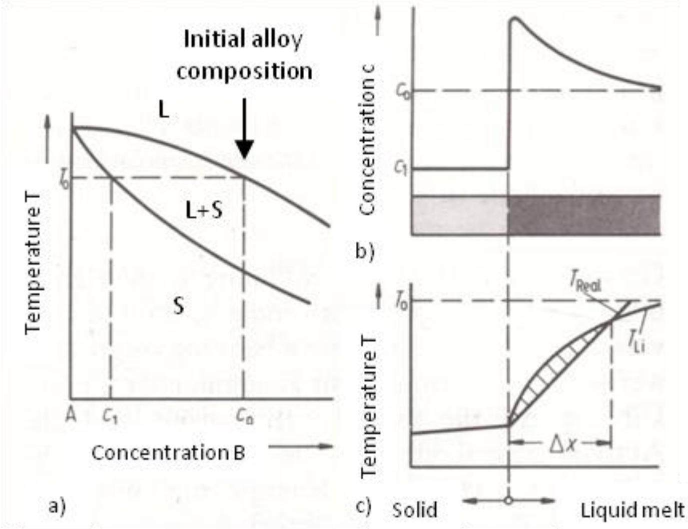

Figure 8-6 Constitutional supercooling in binary alloys as a function of chemical composition and temperature gradient in the melt: a) different composition of liquid melt and first crystallising solids (reduced in component B), b) difference in concentration of B in the liquid melt at the solid-liquid interface, and c) decrease in the liquidus temperature T_{Li} of the remaining melt due to the increased concentration in B at the solid-liquid interface, resulting in supercooled zones Δx due to the real temperature gradient within the melt; property of [Bargel *et al.* 2000].

As a consequence, the liquidus temperature in the vicinity of the solid-liquid interface decreases, Figure 8-6 c). Zones Δx of the liquid melt where the real temperature T_{Real} curve is situated underneath the liquidus T_{Li} of the melt, as shown in Figure 8-6 c), are constitutionally supercooled. Thus, the liquid melt is still liquid although its temperature is beneath the freezing point. The level of constitutional supercooling depends on both the temperature gradient within the melt and the decomposition of the constituents of the alloy melt. Depending on the extent of the constitutionally supercooled zone, different microstructures are yielded – equiaxed, columnar, dendritic (Figure 8-7).

While equiaxed, polycrystalline structures with random grain orientation have quasi-isotropic properties and do not show microsegregation, columnar structures are anisotropic and show poor[54] ductility [Bargel *et al.* 2000].

---

[54] Exception is a directional solidification where columnar structures show excellent properties in axial direction [Bargel *et al.* 2000].

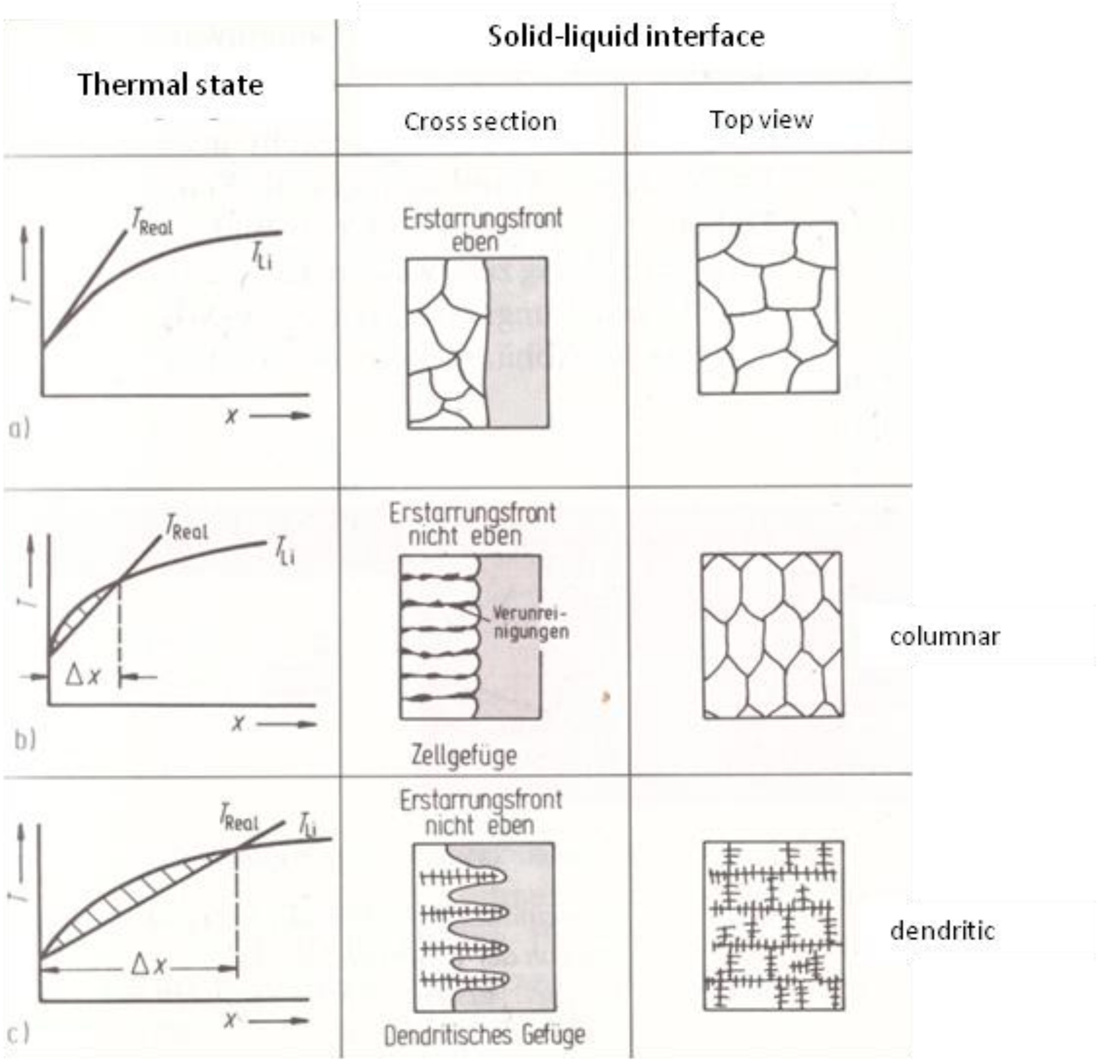
Thermal state
Solid-liquid interface
Cross section
Top view
T_Real
T_Li
T
x
a)
Erstarrungsfront eben
Erstarrungsfront nicht eben
Verunrei-nigungen
Zellgefüge
Δx
b)
columnar
Erstarrungsfront nicht eben
Dendritisches Gefüge
c)
dendritic

Figure 8-7 Primary crystallisation microstructure of alloys as a function of constitutional supercooling Δx: a) steep temperature gradient, mono- or polycrystalline structure, no microsegregation, b) moderate temperature gradient, impurities at grain boundaries, c) gentle temperature gradient, higher concentration of impurities or alloying components, typical for cubically crystallising metals, different chemical composition of dendrites and remaining melt, in the latter: accumulation of inclusions, pores, and microsegregation; property of [Bargel *et al.* 2000].

Dendrites may occur in any solidifying metal melt [Bergmann 2003] and their development depends on the level of supercooling within the melt. In alloys, however, this type of grain growth is highly promoted due to constitutional supercooling. In particular, this grain structure is typical for cubically crystallising alloys [Bargel *et al.* 2000] – such as γ-U(Mo). Dendrites may manifest in different forms depending on the level of supercooling (Figure 8-8). Typical forms are fir-tree-like or needle-like. Grain growth happens in preferred crystallization directions along the cube edges <100>[55].

---

[55] This symbol summarises all direction vectors in a cubic crystal system: [100], [010], [001], [-100], [0-10], [00-1].

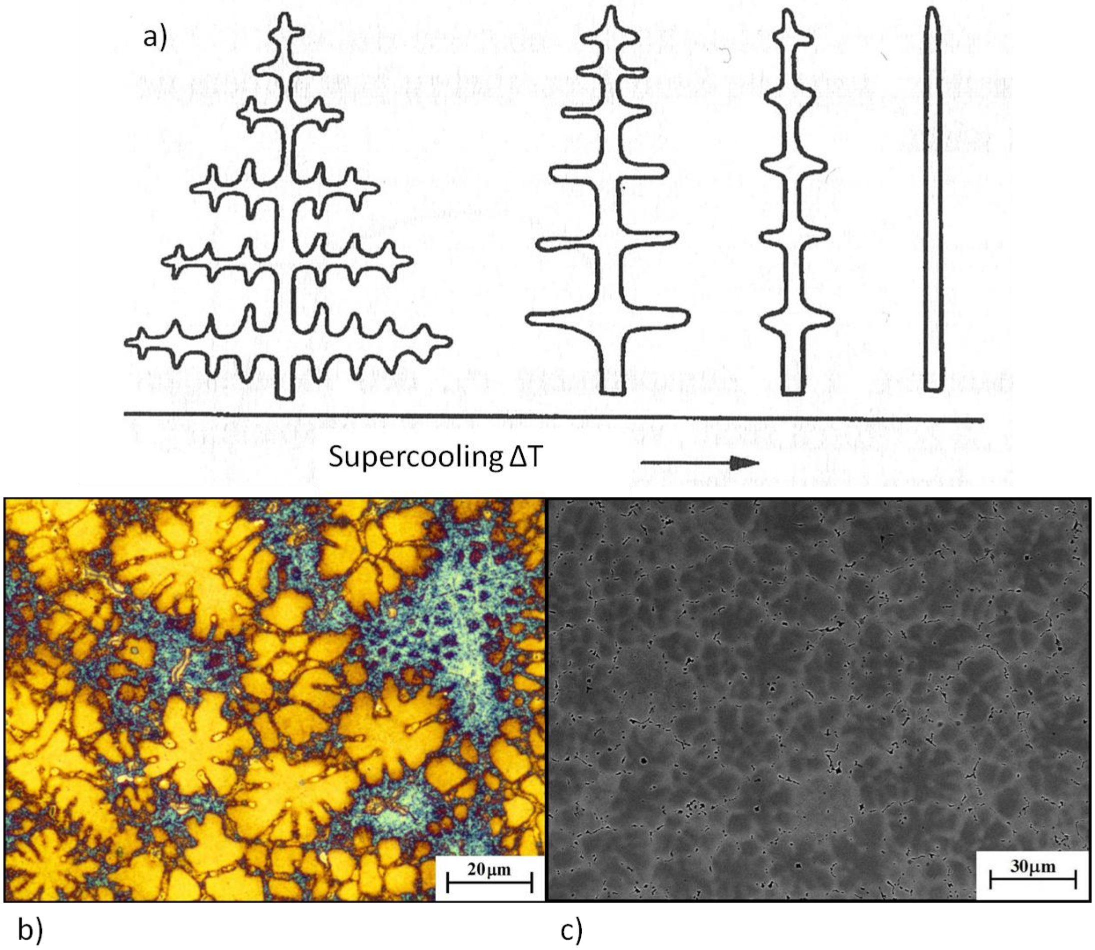

Figure 8-8 Dendrites: a) dendrite manifestation as a function of supercooling ΔT (property of [Merkel and Thomas 2003]), b) and c) optical and SEM micrograph, respectively, of dendrites in UMo bulk material that was melted, quenched, not homogenised, and not annealed; both property of [Dodenhöft 2013])

The solidified remaining melt in dendritic structures has a different chemical composition than the dendrites, exhibits microsegregation (chapter 8.1.3), and consists of inclusions and pores. It has thus generally poor mechanical properties [Bargel *et al.* 2000]. However, heat treatment close to the solidus temperature (diffusion annealing) may “cure” these defects [Bargel *et al.* 2000, Bergmann 2003, Merkel and Thomas 2003].

8.1.3 Microsegregation

Phase diagrams generally describe thermodynamic equilibrium conditions. In practice, the equilibrium structure of the solid solution is not achieved as technical cooling rates are too high in order to allow for diffusion to balance concentration [Bargel *et al.* 2000]. As a consequence, the composition within a grain is not uniform but changes with increasing distance from the core. This phenomenon is referred to as microsegregation[56] or coring and is described in Figure 8-9.

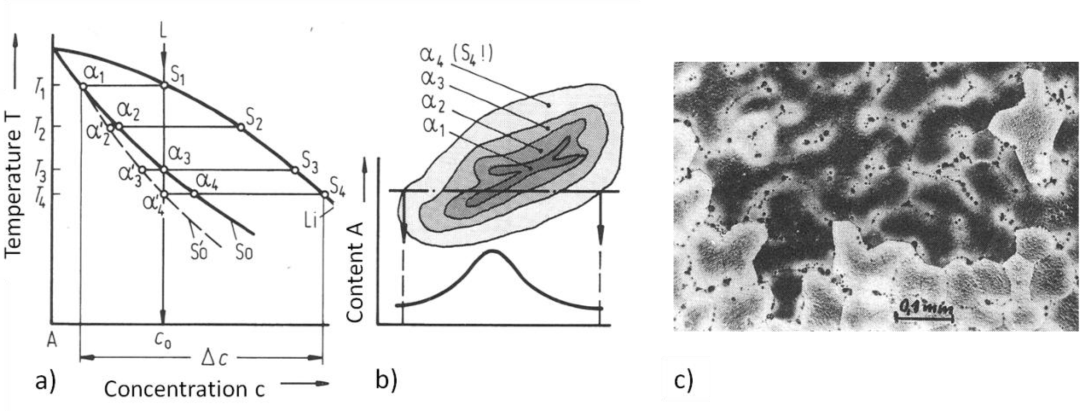

Figure 8-9 Microsegregation in alloys: a) exemplary phase diagram of binary system showing the concentration of the liquid melt S_i, the solid solution α_i, and the average solid solution α_i' during cooling, b) schematic structure of the corresponding grain showing microsegregation and corresponding concentration of component A; both property of [Bargel *et al.* 2000]. Exemplary micrograph of microsegregation in a CuZn solid solution, c); property of [Merkel and Thomas 2003].

In thermodynamic equilibrium cooling, the first precipitated solid solutions α_1 (T_1) have enough time to adjust to subsequently precipitated solid solutions α_2 (T_2) by precipitating the component A and incorporating component B. As a consequence, all solid solutions exhibit the composition α_2 at T_2. Beyond equilibrium, however, solidification is kinetically controlled and the first precipitated α_1 do not reach the composition of α_2. Hence, the precipitated solid solution α_2 will form a layer around α_1, resulting in a concentration gradient throughout the grain diameter and an average grain composition α_2'.

Extremely high cooling rates, though, inhibit the coring or microsegregation according to [Bargel *et al.* 2000]. In fact, a potential feature of rapid solidification processes such as atomization is to provide such high cooling rates.

8.1.4 Classification of Particles and Impurities

The particle shape may affect compaction procedures and therefore tap density [Yule and Dunkley 1994]. Particle shapes and irregularities occurring in atomization were classified by [Yule and Dunkley 1994] and summarised in Figure 8-10. In addition, some examples of typical particle irregularities are given in Figure 8-11. Internal porosity or voids (gas or vacuum) may cause unintentional dimensional change during sintering or rolling (of the fuel) and reduce tap density [Yule and Dunkley 1994]; reduction of fatigue strength and initiation of particle cracking may also occur as observed in titanium powders [Eylon *et al.* 1980a]. Irregular particles may cause problems with respect to packing reproducibility if their amount is significantly increased [Eylon *et al.* 1980b].

---

[56] Disambiguation: microsegregation (German: Kristallseigerung); precipitation (German: Segregatbildung, Ausscheidung, Absonderung).

Minor constituents of the powder that are not intentionally added to the alloy are considered impurities. The impurities of atomized powder generally depend on the purity grade of the raw material as well as subsequent processing steps, e.g. alloying, cleaning, melting, casting, cutting, second cleaning, atomization, sieving, and sample preparation. Impurities gain in importance if the powder is ought to become a structural member as they may affect mechanical, thermal, and irradiation properties. Non-metallic inclusions generally act as zones of stress concentration and may cause fatigue cracks [Lawley 1992]. This, however, is compensated for as the atomized fuel particles are generally embedded in a comparably soft Al matrix.

Impurities are divided into three categories according to [Yule and Dunkley 1994]:

+ exogenous, resulting from contamination of the powder or particle with external particulate matter during melting (casting or atomization) or after atomization;

+ dissolved, resulting from melting, and with influence on the atomization process (mass flow rate and particle size due to a change of surface tension, density, or viscosity) as well as particle quality (grain size, porosity, hardness, tensile strength, irradiation behaviour);

+ superficial, mostly resulting from corrosion during atomization, notably oxidation, and contamination.

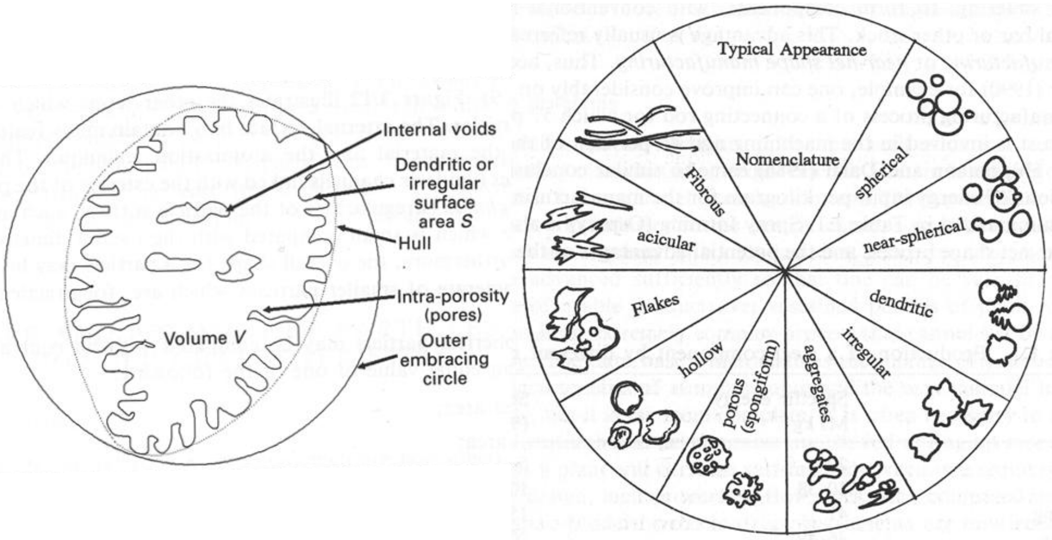
Internal voids
Dendritic or irregular surface area S
Hull
Intra-porosity (pores)
Volume V
Outer embracing circle
Typical Appearance
Nomenclature
spherical
near-spherical
dendritic
irregular
aggregates
porous (spongiform)
hollow
Flakes
acicular
Fibrous

Figure 8-10 Nomenclature for irregular particles (left) and particle shape (right); property of [Yule and Dunkley 1994].

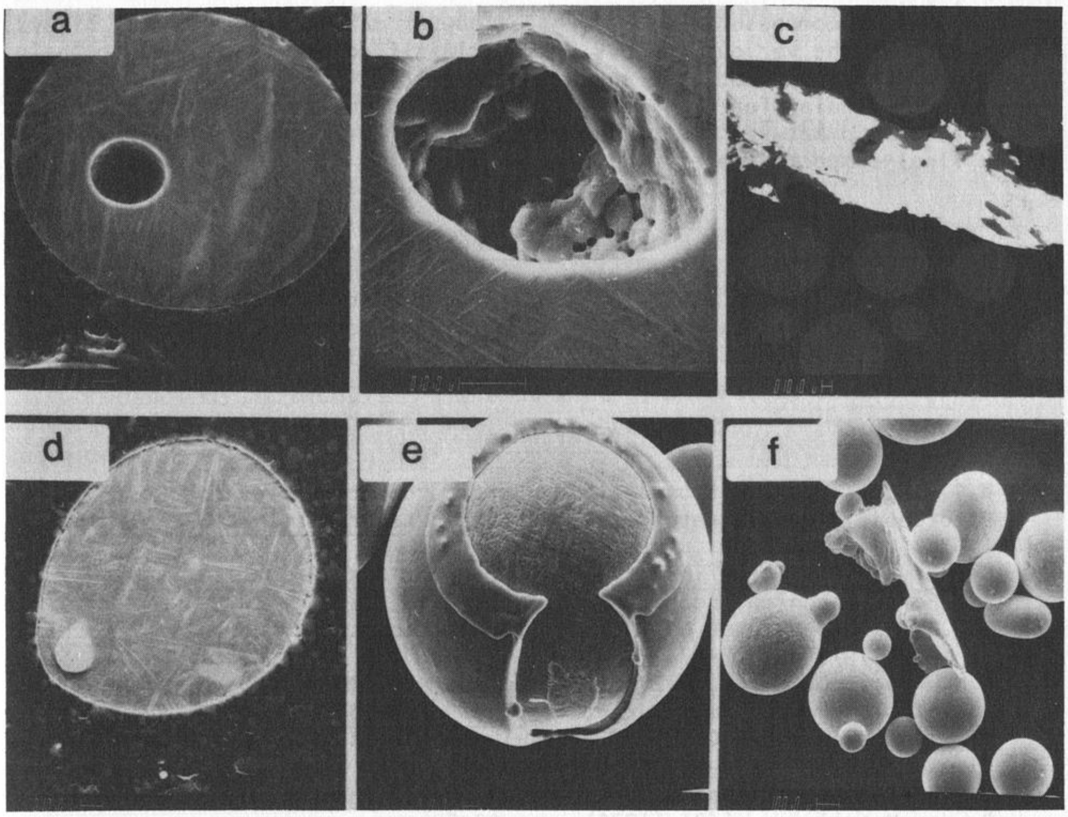

Figure 8-11 Typical morphological irregularities of atomized particles (here: titanium alloy): a) gas pore (internal void), b) shrinkage pore (internal void), c) irregular exogenous particle (tungsten), d) embedded inclusion, e) outer shell, and f) irregular particle (same alloy) and satellite particles; property of [Eylon *et al.* 1980b].

8.2 Results and Discussion

8.2.1 Powder Chemistry

Atomized UMo powder for fuel element fabrication has to comply with fuel specifications regarding alloy composition and impurities (chapter 2.4).

In general, particles larger than the production-relevant size classes (> 180 µm) were chemically analysed as the amount of powder in the target size ranges was limited. The production-relevant size classes (< 180 µm) were reserved and processed for microscopy. According to chapter 3.1.1, the chemical composition is independent of the particle size in the investigated size ranges. In fact, REP (and PREP) can reproduce the ingot chemical composition.

The purity grade of the raw material coming from INL and CERCA as well as prealloyed U8Mo (CERCA) is summarised in Table 8-1. The raw uranium provided by INL and CERCA showed different impurity levels with respect to certain elements.

In addition, it may be inferred that the alloying process at CERCA did not significantly change the impurity levels of single elements compared to the raw material. That is, all concentrations stayed within the range of the measurement uncertainty. This constant level of purity may also be assumed for the rotating electrode alloying and casting process of INL [Moore and Archibald 2014]. The impurity level of the uranium of INL was thus representative of the U8Mo rotating electrodes of batch 552 coming from INL.

The macroscopic alloy composition of UMo, i.e. the mass percentage of uranium and molybdenum, was predefined during the alloying process. After the final fabrication step of atomization, the bulk-powder alloy-composition complied fully with fuel specifications (chapter 2.4) as can be seen in Table 8-2. The molybdenum content of batch 0914, however, was lower than the demanded 8 % ± 0.5 %, which is ascribed to material reprocessing and blending (see below).

The impurities complied each with the fuel specification limits as well (chapter 2.4). Though, it was found that the carbon content varied with different casting configurations, namely the type of crucible, stopper, and mould.

As carbon is suspected to have influence on the mass flow rate during atomization (chapter 5.3.5), the particle microstructure (chapter 8.2.3), and may promote the development of carbides, a detailed explanation of sources of contamination is given below in order to improve control of these impurities. Particularly, carbides affect mechanical properties of atomized particles [Yule and Dunkley1994].

Table 8-1 Excerpt of the chemical composition of feedstock material from INL and CERCA used in this work. Blank places indicate not analyzed elements or provided uncertainties.

	INL U		CERCA U		CERCA U8Mo	
Element	Result [ppm]	± *uc* [ppm]	Result [ppm]	± *uc* [ppm]	Result [ppm]	± *uc* [ppm]
Al	59		33	10	48	14
C	182	12	944	20	960	20
Cu	4.5					
Fe	95		51	15	39	12
H			5.6	0.6	3.6	0.4
Mg	< 1					
Mo	< 1		100	30	7.5 %	0.4 %
N	1	0.3	35	7	28	6
Ni	< 1					
O	38	12	253	30	282	30
Si	70		40	12	37	11
W	< 1					
Zn	< 2					

Batch 0914-1 was reprocessed from rotating electrode rests of INL batch 552. It was melted in a graphite crucible (with graphite stopper) and cast into a graphite mould. Batches 0914-3 and -4 were reprocessed from the same batch, but melted in alumina crucibles (with alumina stoppers) and cast into copper moulds. As a consequence, the carbon content was decreased by about 50 % with respect to batch 0914-1. Therefore, graphite crucibles and moulds were confirmed as sources of carbon contamination. However, the carbon content of both batches was still higher than for the raw material. This may be due to contamination with carbon during handling and operation. A potential source of carbon was the general presence of graphite dust in the induction furnace and its glovebox as well as in the atomizer glovebox, causing the contamination of gloves, tools, raw material, and product. In addition, it is noted that the use of a graphite mantle as induction coupling-agent for ceramic crucibles is mandatory with respect to the implemented induction furnace. Thus, graphite was always present in the induction furnace. This is also true for the atomizer glovebox, since the atomizer uses carbon brushes (chapter 3.3.14). However, the carbon brushes are separated from the powder collection chamber and the sieving equipment. Furthermore, the graphite dust seal (chapter 3.3.17) hinders the dissemination of sublimated carbon from the carbon brushes.

Batch 0914-6 is an exception to the rule regarding carbon content: although it was cast in alumina, the carbon concentration was significantly increased in comparison to batches 0914-3 and -4. In fact, the raw material came from reprocessing and blending of rotating electrode rests of INL batch 552 and CERCA batch F1U8Mo. The latter was originally CERCA raw material that was melted in a graphite crucible and cast into a graphite mould, therefore exhibiting elevated carbon content. Reprocessing and blending is also made responsible for the decreased molybdenum content as both batch 552 (not entirely alloyed molybdenum foils, Figure 5-14) and F1U8Mo had less than 8.0 % alloyed molybdenum content.

Batches 1114-3 and -3-1/6 were prepared from CERCA raw material with inherently higher carbon content (Table 8-1). Both batches were melted in an alumina crucible and cast into a copper mould.

The use of alumina ceramics (> 97 % Al_2O_3, 0.3 % SiO_2, 0.1 % Fe_2O_3, rest CaO) increased the aluminium content of the atomized powder by about 200 ppm. The silicon content was decreased. Both the aluminium and silicon concentration were much smaller than the corresponding limits of the fuel specification (Table 8-2).

Table 8-2 Chemical composition of atomized powder from different U8Mo/U7Mo batches produced from in-house cast rotating electrodes. For comparison, the corresponding limits according to fuel specification G183 [Gery 2011] are given. Uranium and molybdenum concentrations are given in percent.

	G183	U8Mo								U7Mo			
Element	Max. value	0914-1		0914-3		0914-4		0914-6		1114-3		1114-3-1/6	
		Result	± Δ	Result	± Δ	Result	± Δ	Result	± Δ	Result	± Δ	Result	± Δ
	[ppm]	[ppm]	[ppm]	[ppm]	[ppm]	[ppm]	[ppm]	[ppm]	[ppm]	[ppm]	[ppm]	[ppm]	[ppm]
O	7000	227	50	60	50	129	75	184	18	149	15	211	67
C	2000	987	99	456	46	426	43	873	87	1060	106	1337	134
N	2500	76	15	152	30	101	20	73	15	59	12	37	7
H	500	14	1	14	1	10	1	11	1	6	2	8	1
Al	5000							103	31	176	53	233	71
Si	2000							23	8	26	10	< 21	
W	-							< 30		< 30		< 30	
Fe	1500							231	70	13	4	7	3
Ni	500							22	7	25	8	24	8
Zn	1000							< 11		< 11		< 11	
Cu	500									3	1	3	1
Mg	2000							3	1	< 5		< 6	
Mo								6.6 %	0.4 %	7.3 %	0.4 %	6.5 %	0.4 %
U		91.6 %	0.1 %	91. 7 %	0.1 %	91.4 %	0.1 %	91.6 %	0.1 %	92.7 %	0.1 %	92.4 %	0.1 %

8.2.2 Surface Morphology

REP-atomized U8Mo that was produced in the vicinity of the direct droplet regime and that had particle diameters below 125 µm was mostly spherical in shape, free of (adhering) satellite particles, and had no shells. Particle surfaces were generally regular, smooth, and without pores, although concave deformation (dents) were regularly found (Figure 8-12).

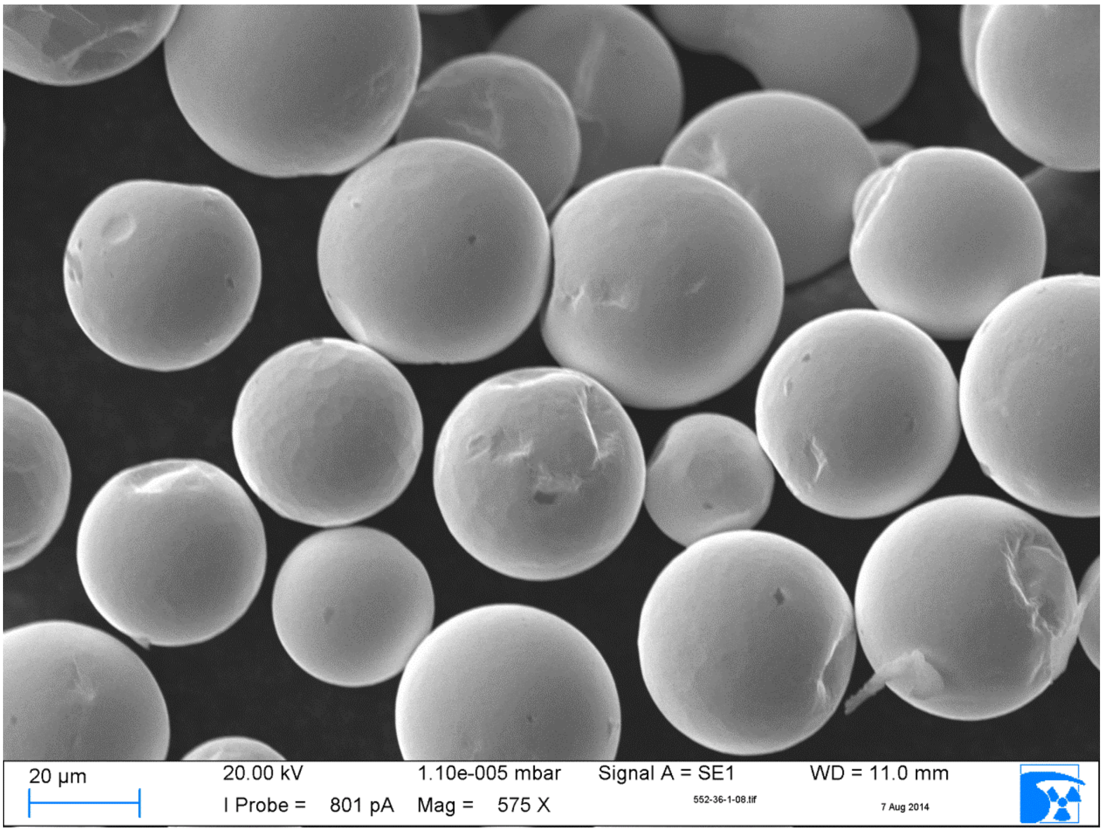

Figure 8-12 Typical spherical U8Mo powder produced from batch 552 by REP.

Particles with diameters in the relevant size ranges (< 40 µm, < 125 µm, and < 180 µm) generally exhibited an equiaxed and faceted surface morphology (Figure 8-13 and Figure 8-14) which reflects the mechanism of grain growth in the surface zone (Figure 8-5, zone 3). In fact, the fine grain structure indicates that rapid solidification conditions prevailed. The latter promotes a high nucleation rate (Figure 8-5). Since the heat loss on the surface is uniform and grain growth not restricted, equiaxed grains developed (Figure 8-5).

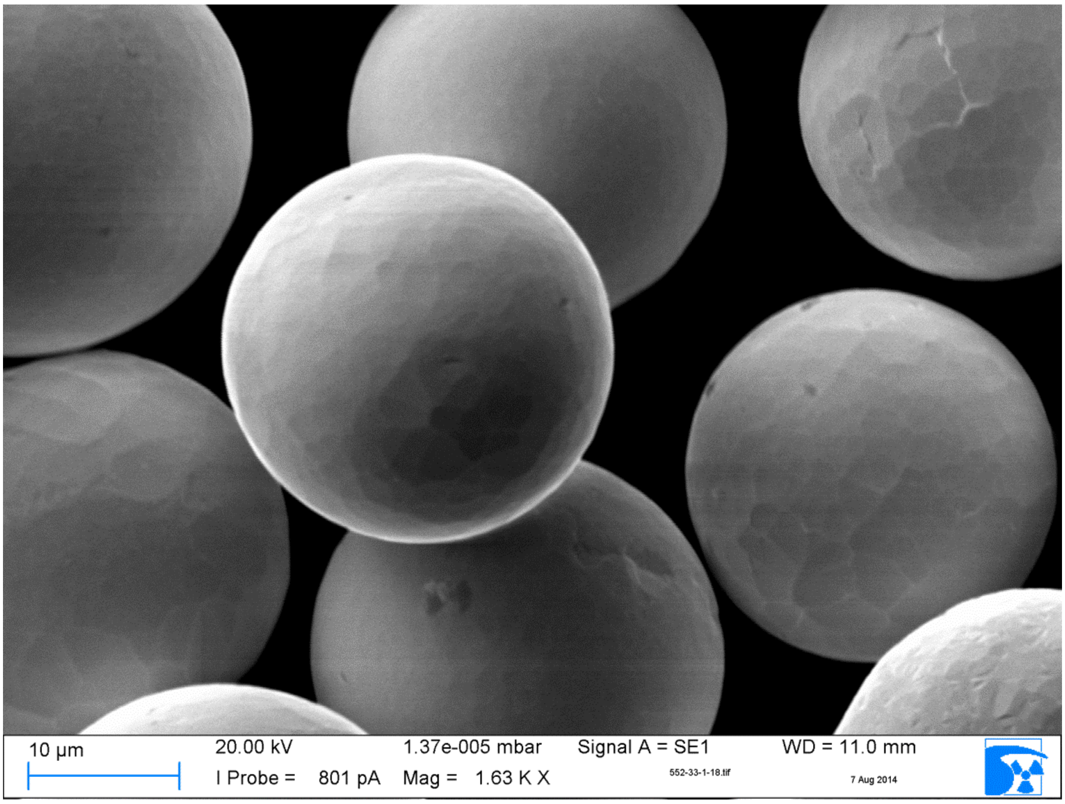
10 µm
20.00 kV
I Probe = 801 pA
1.37e-005 mbar
Mag = 1.63 K X
Signal A = SE1
552-33-1-18.tif
WD = 11.0 mm
7 Aug 2014

Figure 8-13 Batch 552-33: Typical spherical particles in the size class < 45 µm.

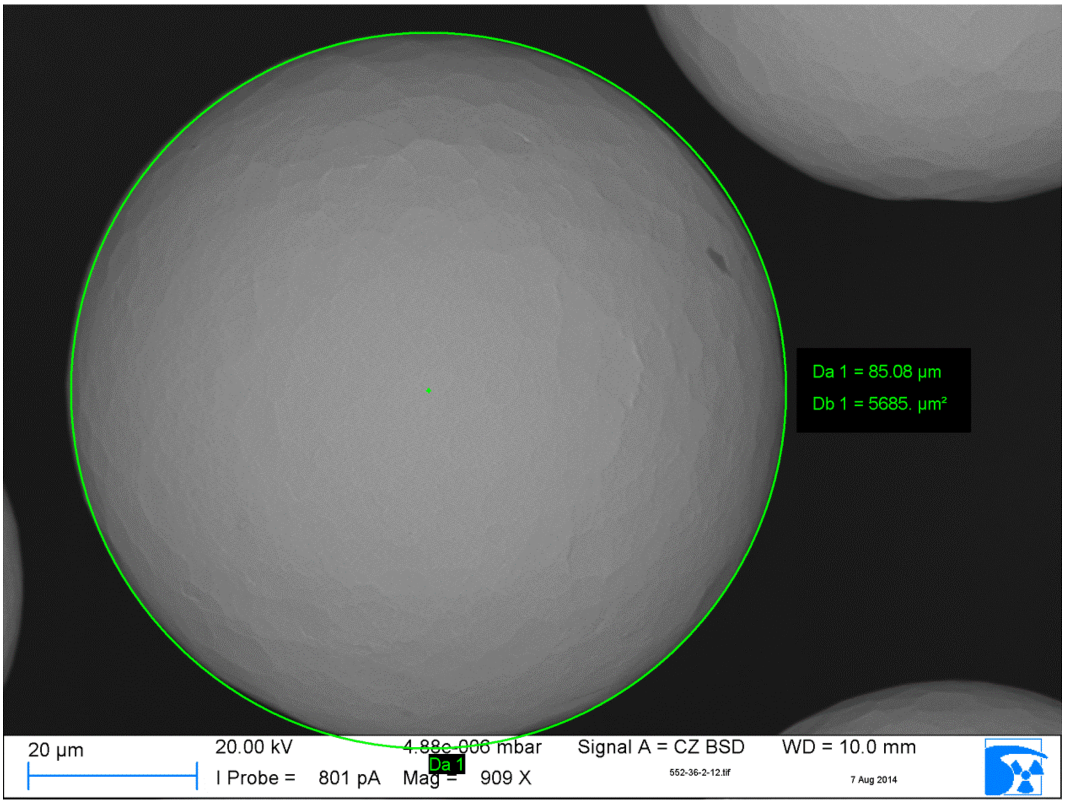
Da 1 = 85.08 µm
Db 1 = 5685. µm²
Da 1
20 µm
20.00 kV
I Probe = 801 pA
4.88e-006 mbar
Mag = 909 X
Signal A = CZ BSD
552-36-2-12.tif
WD = 10.0 mm
7 Aug 2014

Figure 8-14 Batch 552-36: Typical spherical particles in the size class from 45 µm to 125 µm with a diameter D_{a1} of ~ 85 µm and a cross-section area D_{b1} of ~ 5685 µm^2.

The grain size generally varied between 1 µm and 10 µm as can be seen in the exemplary Figure 8-15. The surface morphology consisting of equiaxed grains was occasionally less pronounced which is ascribed to slight surface oxidation (Figure 8-20 and Figure 8-22).

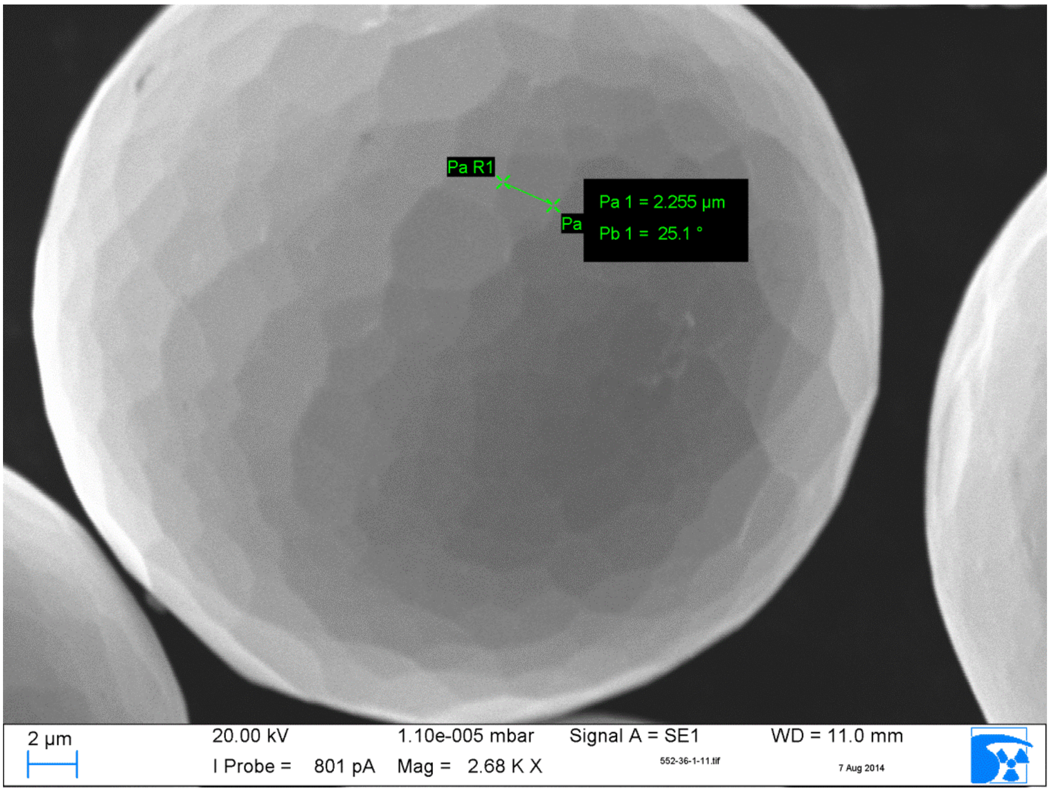

Figure 8-15 Batch 552-36 (< 45 µm): enlarged faceted particle surface showing equiaxed grains. P_{a1} is indicating the typical grain size.

The surface deformations, namely concave dents, were regularly found on spherical particles (Figure 8-16). For the shown particle with a diameter of about 100 µm, the longitudinal length of the dent is about 40 µm. Its depth is a few µm. Similar "concave" surface deformations or dents were already stated by [Hodkin *et al.* 1973] for atomization of tantalum. Also, dents were reported on PREP atomized Ti-6Al-4V particles [Isonishi *et al.* 1989].

It is suggested that the observed dents were a result of instantaneous cooling of the particle surface prior to cooling shrinkage of the particle volume. In fact, the particle surface solidified rapidly and first while the inner particle volume was still in a liquid state, thereby fixing the apparent volume of the particle. The volume of U8Mo, however, shrinks with both the transition from liquid to solid state and decreasing temperature [Wilkinson 1962a]. In order to compensate the loss in volume, material from the rim was torn towards the particle inner, therefore causing the solidified surface to locally collapse. It is suggested that this deformation mechanism applied to all particles.

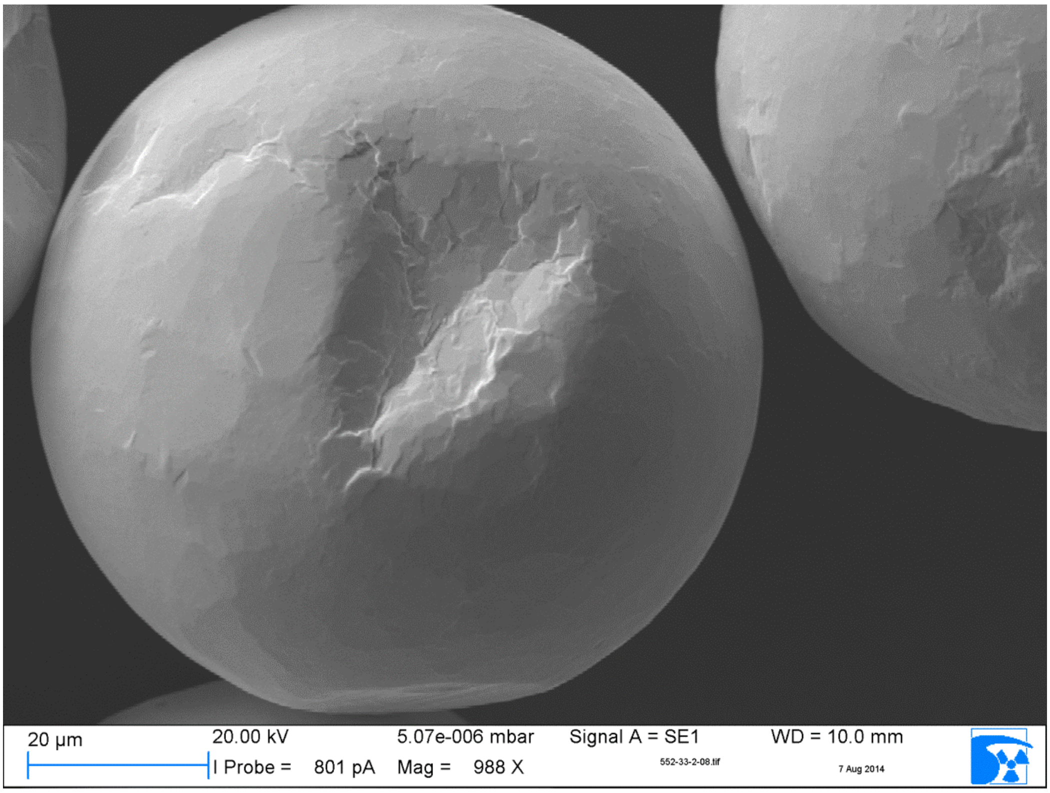

Figure 8-16 Batch 552-33: Typical concave deformation (dent) on the surface of spherical particles that is ascribed to cooling shrinkage and rapid solidification. The diameter of the dent is about 40 µm.

8.2.3 Microstructure

General

As indicated by the faceted surface morphology, a polycrystalline microstructure was found within sectioned particles of batches 552 (Figure 8-17). The grain size was consistent throughout the particle diameter. The relatively high number of grains suggests that nucleation was enhanced due to high supercooling of the melt (chapter 8.1.2) as is the case in rapid solidification processes [Lawley 1992, Yule and Dunkley 1994].

However, back-scattered electron (BSE) imaging showed brighter zones in between the grains (Figure 8-17, bottom), thus implying a compositional difference (segregation). This zone typically extended from 0.5 µm to 1.5 µm which is relatively large compared to the observed grain size of 1 µm to 10 µm. Elemental analysis by energy-dispersive X-ray spectroscopy (EDX) was limited due to the beam footprint of 2 µm · 2 µm which was too large for significant resolution. However, optical microscopy of corroded samples of embedded and sectioned particles revealed that the general grain structure of the REP-atomized U8Mo particles consists of dendrites (Figure 8-18 and Figure 8-19). This result is in agreement with observations made for quenched bulk UMo [Dodenhöft 2013].

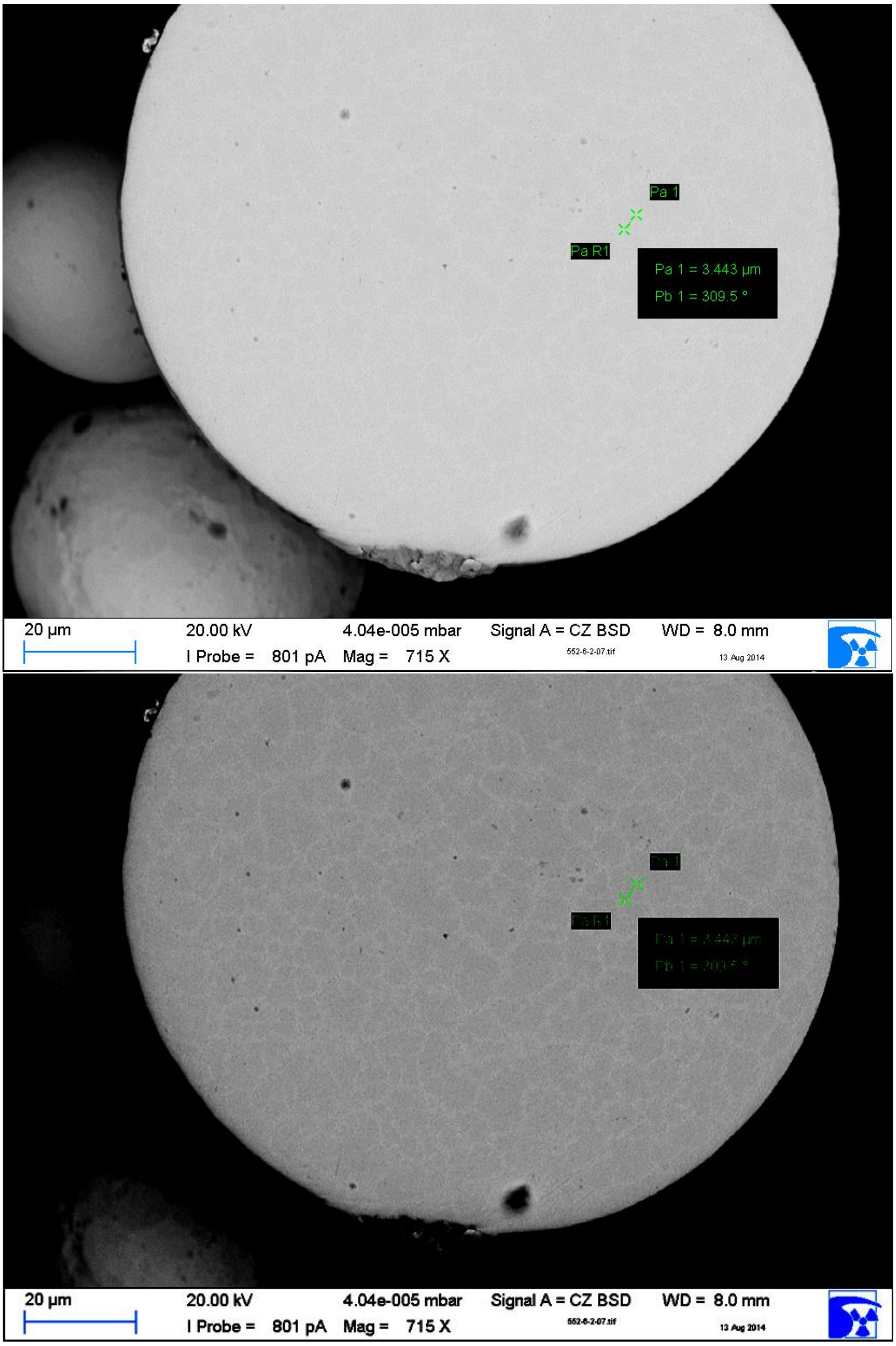
Pa 1
Pa R1
Pa 1 = 3.443 µm
Pb 1 = 309.5 °
20 µm
20.00 kV
I Probe = 801 pA
4.04e-005 mbar
Mag = 715 X
Signal A = CZ BSD
552-6-2-07.tif
WD = 8.0 mm
13 Aug 2014

Figure 8-17 Batch 552-06 (< 180 µm): Typical polycrystalline microstructure found in sectioned REP-atomized U8Mo particles. Top: original micrograph; bottom: same micrograph with edited contrast to make grain boundaries visible. The black particle above the broken U8Mo-particle rim is an impurity on the sample surface. P_{a1} is indicating the typical grain size.

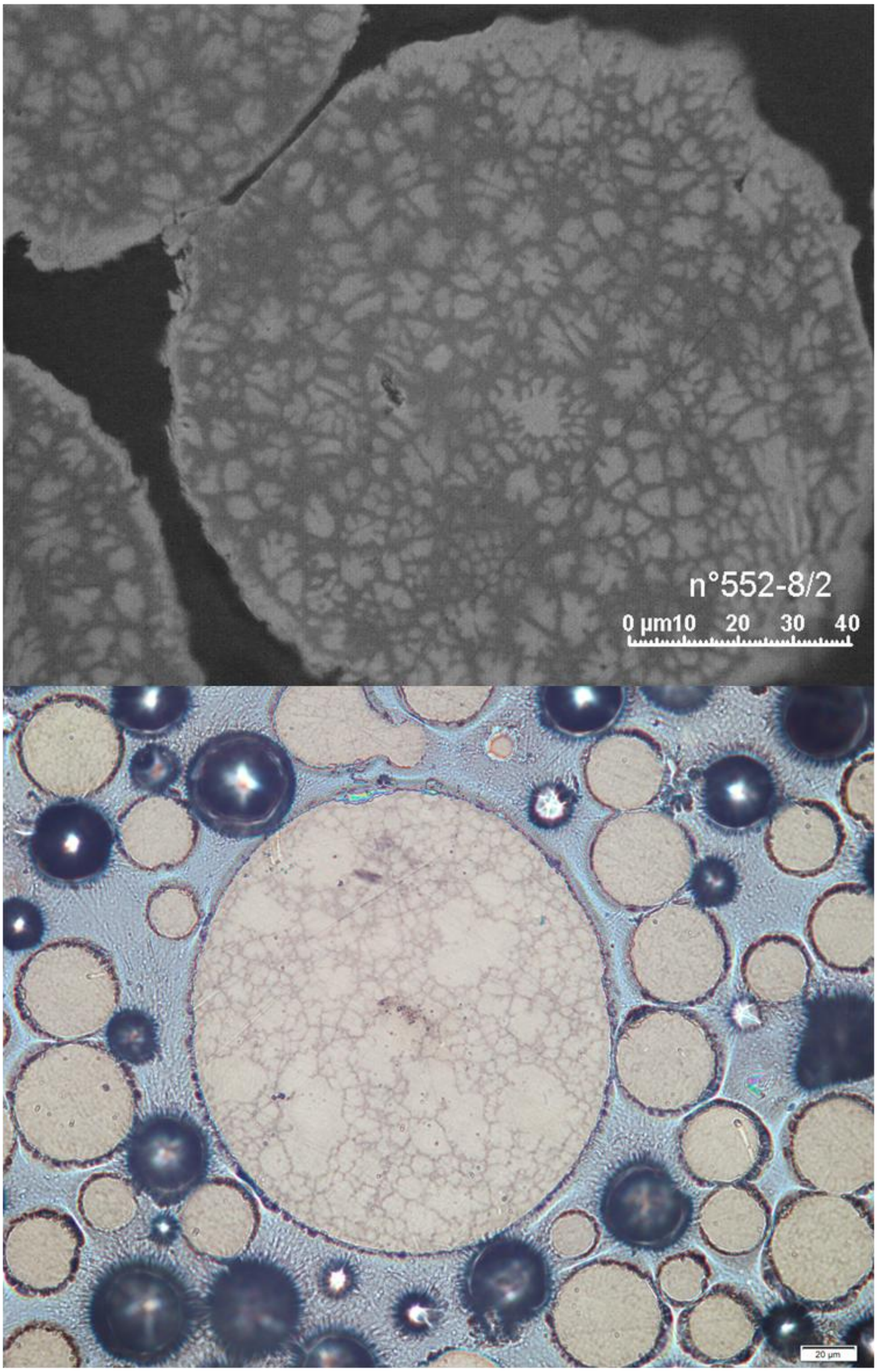

Figure 8-18 Dendritic particle grain structure in sectioned samples of batches 555-08 (top) and 552-12 (bottom) observed with optical microscopy. The samples were exposed to water and air during sample polishing and storage, respectively. The grain structure is present in coarse and fine particles. Light-reflecting voids in sample 552-12 were caused by particle break-out from the resin matrix during polishing.

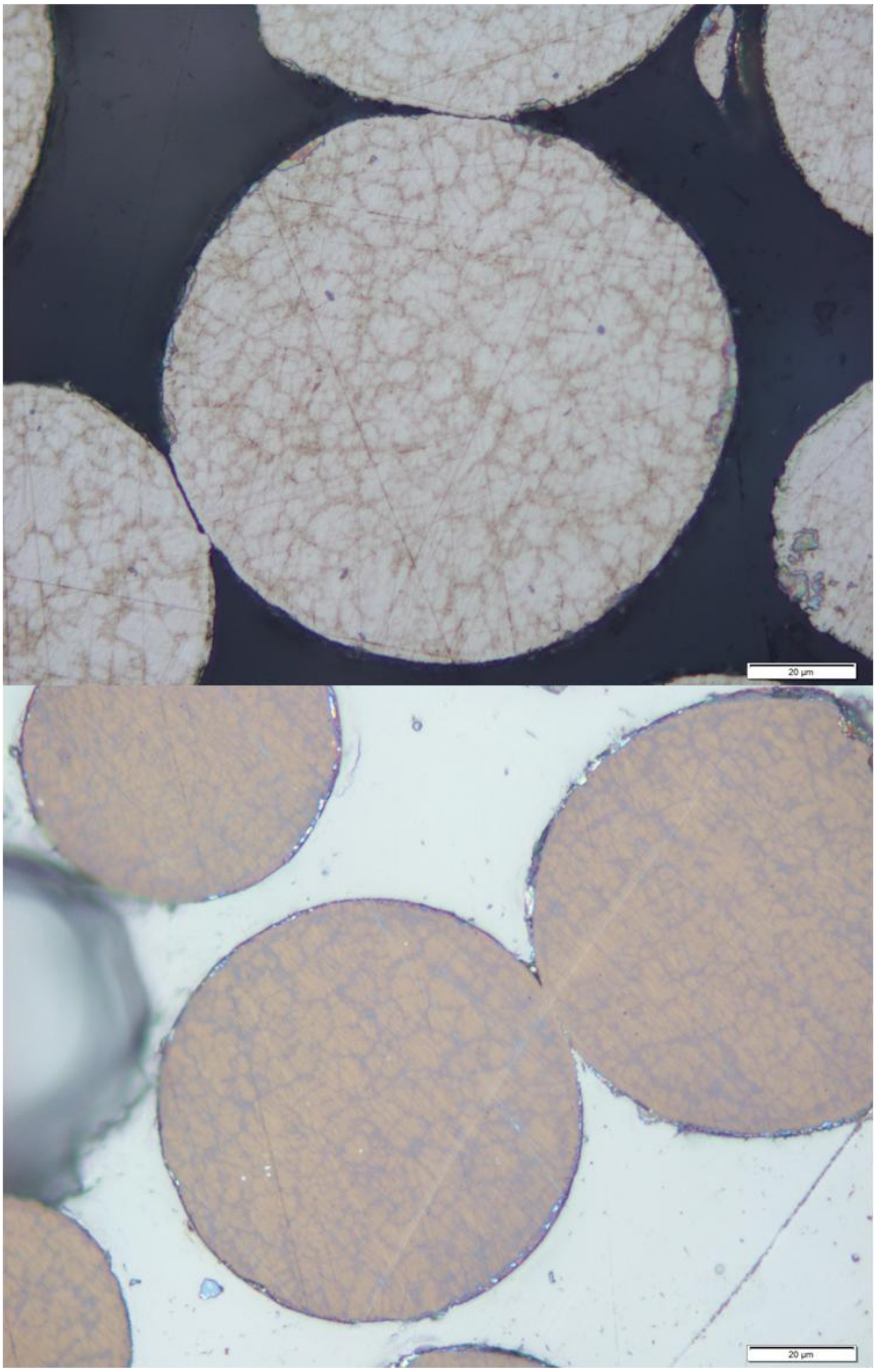

Figure 8-19 Optical micrographs of sectioned samples of batches 552-29 (top) and 552-30 (bottom) confirming the generally dendritic microstructure. The samples were exposed to water and air during sample polishing and storage, respectively.

The dendritic grain structure explains the presence of a segregation zone despite rapid solidification since microsegregation is known to occur in the solidified remaining melt between dendrite spacings (chapter 8.1.2). According to the binary phase diagram of the U-Mo system (Figure 8-1), the solidified remaining melt has to be poorer in molybdenum and richer in uranium. This explains the preferred corrosion of the intergranular zone observed after polishing with water and storage under air since uranium corrodibility increases with decreasing molybdenum content [Wilkinson 1962a].

The fine and dendritic structure is explained with both rapid solidification and constitutional supercooling. On the one hand, rapid solidification conditions prevailed as the fine droplets (< 125 µm) had a high surface-area-to-volume ratio. This promoted rapid temperature loss via forced convection and thermal radiation in the order of 10^2-$10^4\,\mathrm{K\,s^{-1}}$ [Lawley 1992, Yule and Dunkley 1994]. Thus, the nucleation rate was relatively high, therefore causing a fine grain structure as described in Figure 8-5. On the other hand, U8Mo is an alloy where constitutional supercooling may occur. In combination with the relatively gentle temperature gradient within the melt caused by the limited amount of superheat in REP, supercooled zones Δx may have occurred as described in Figure 8-6 and Figure 8-7, hence resulting in the growth of dendrites.

Microsegregation within the grains (coring) was not observed using SEM. The absence of coring is considered one of the features of REP (chapter 3.1.1) and related rapid solidification [Bargel *et al.* 2000].

Internal void porosities between dendrite spacings induced by cooling shrinkage were not observed – neither for optical microscopy nor for SEM.

Impurities

Figure 8-20 shows a rougher surface than generally observed for atomized U8Mo particles which is ascribed to slight surface oxidation; see also Figure 8-22. The oxygen content is supposed to increase with decreasing particle size due to the increase in total surface area of the powder [Lawley 1992]. Occasionally, the oxide layer (< 1 µm) broke and detached during mechanical polishing of embedded particles. In order to confirm the nature of the surface layer and to exclude a smearing effect[57], an EDX line scan on a detached piece was performed (Figure 8-21). Elemental analysis revealed that the detached material mainly consisted of uranium, molybdenum and oxygen. While the fraction of uranium as well as molybdenum was small compared to the particle, the oxygen fraction exceeded the uranium content and reached its maximum with respect to both the particle and resin. The elevated values of oxygen and carbon content are ascribed to sample surface oxidation and the polishing process that caused carbon removal from the resin and deposition onto UMo particles.

---

[57] The U8Mo particles are harder than the resin matrix. As consequence, the resin is removed faster, leaving prominent UMo that is subsequently smeared into the resin during the polishing process.

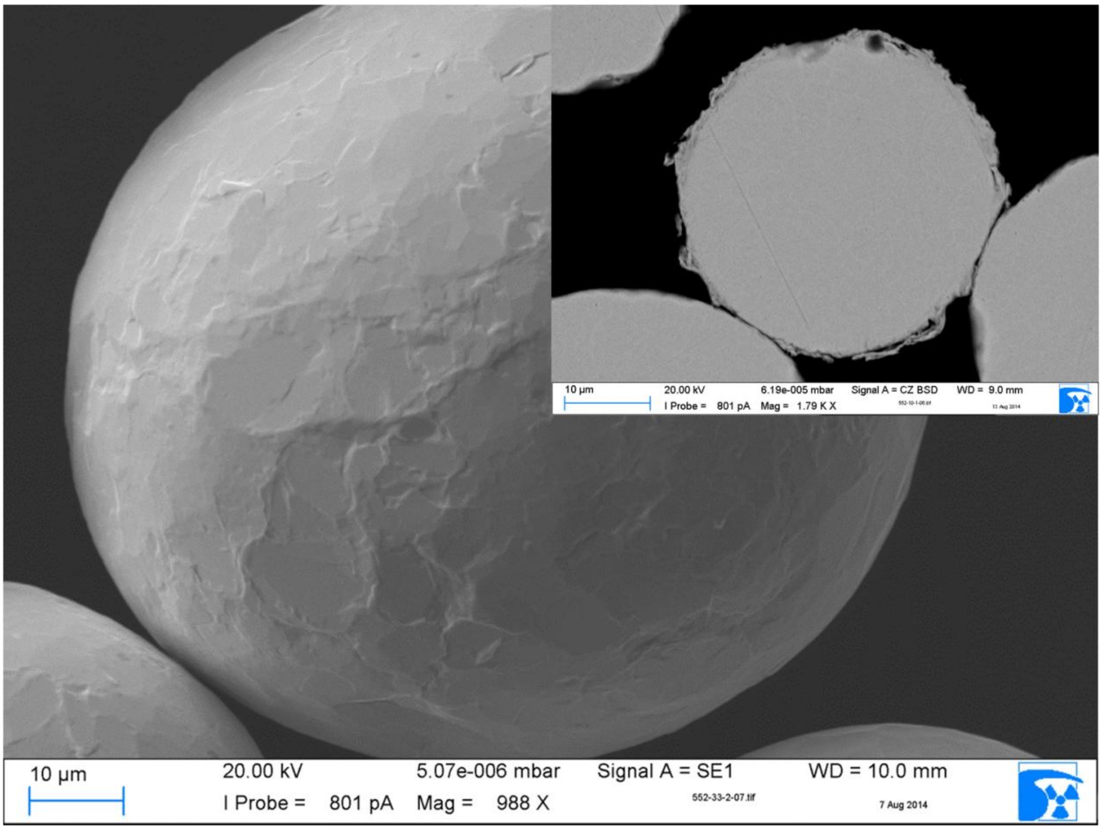
10 µm
20.00 kV
6.19e-005 mbar
Signal A = CZ BSD
WD = 9.0 mm
I Probe = 801 pA
Mag = 1.79 K X
552-10-1-06.tif
13 Aug 2014
10 µm
20.00 kV
5.07e-006 mbar
Signal A = SE1
WD = 10.0 mm
I Probe = 801 pA
Mag = 988 X
552-33-2-07.tif
7 Aug 2014

Figure 8-20 Superficial oxide layer of a particle from batch 552-33. Small window: example of detached material after mechanical polishing, batch 552-10.

Exogenous impurities were observed in some of the 552 batches (Figure 8-22). The impurities were identified as plastics presumably originating from a spattle that was used for powder collection from the collection chamber wall. As a consequence, a stainless steel spattle was substituted for the plastic spattle. In the subsequent samples, these impurities were not observed anymore. It is noted that the particles were placed on an adhesive graphite pad that was not visible in the spectral mapping of carbon as the beam was focused on another height.

No tungsten inclusions in REP-atomized particles or powders resulting from tungsten cathode erosion as discussed by [Eylon *et al.* 1980a, Eylon *et al.* 1980b, Roberts and Loewenstein 1980] were observed. As indicated by the chemical analysis, the amount of tungsten was generally < 30 ppm.

Dissolved impurities were not observed in batch 552 using SEM. Though, this type of impurities was found with increasing carbon content in batches 0914 and 1114.

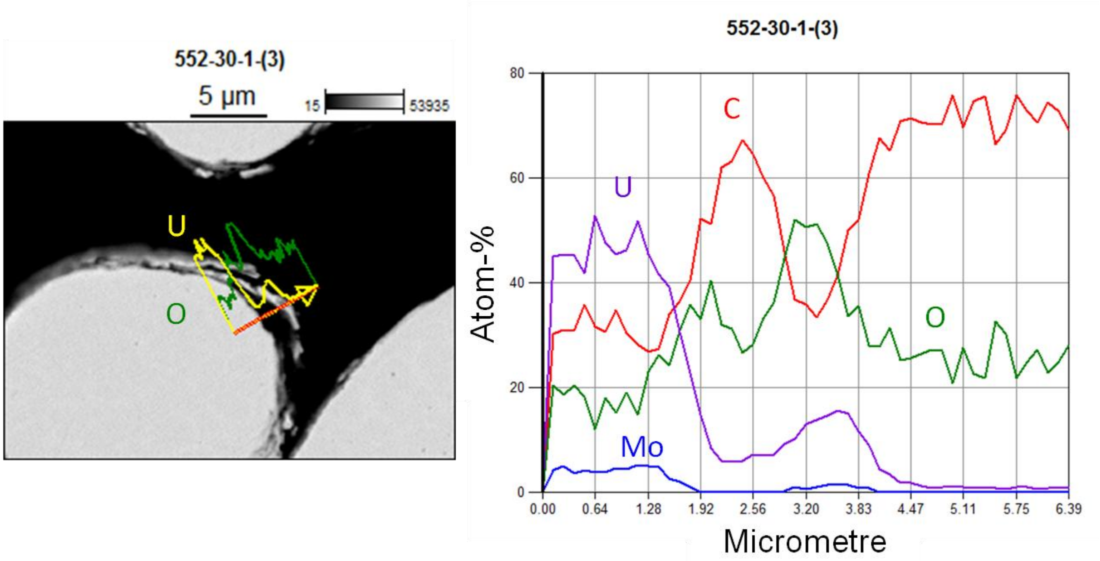

Figure 8-21 EDX line scan traversing a sectioned particle, the resin, and detached material. Left: oxygen (green) and uranium (yellow) concentration curve. Right: oxygen (green), uranium (purple), carbon (red), and molybdenum (blue) curve. The oxygen content (in at.-%) reaches its global maximum in the vicinity of the detached piece. Both the uranium and molybdenum fraction show a local peak in this zone as well. It is suggested that the detached material originates from a thin oxide film (< 1 µm) containing both uranium and molybdenum.

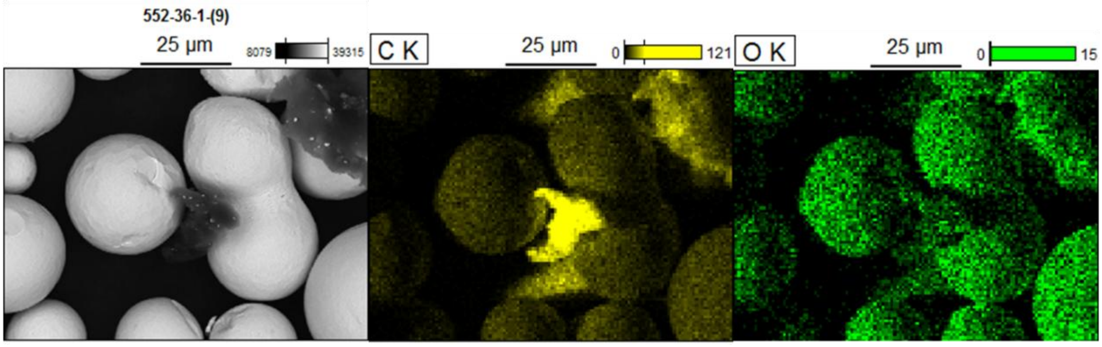

Figure 8-22 Impurities (left: dark grey) found in U8Mo (552-36) powder were identified as remains of plastics (middle: yellow) using spectral mapping. In addition, slight particle surface oxidation (right: green) was detected.

Generally, dissolved impurities manifested in two size classes as observed with SEM (Figure 8-23): On the one hand, large, regular structured impurities, often quadratic or star-like, of diameters between 1 µm to 2 µm were found. They were randomly spread over the particle diameter. On the other hand, fine impurities were observed that were mainly arranged in “dotted lines” along the grain boundaries in the zone of solidified remaining melt (Figure 8-24). In the same figure, fine precipitations within the grain, but to a lower amount, are discernible. Both results are in agreement with observations of [Bonnin *et al.* 2014] that found precipitated U(C,O) in and around grains. In contrast to the large impurities, the fines were consistently distributed over the entire particle diameter.

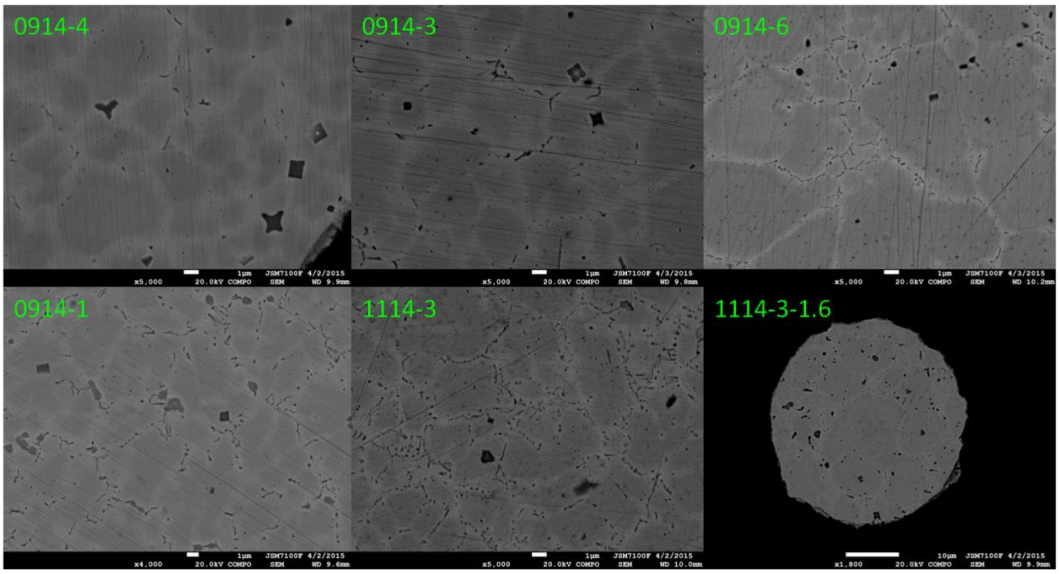
0914-4
0914-3
0914-6
0914-1
1114-3
1114-3-1.6

Figure 8-23 Sequence of micrographs showing impurities as a function of carbon content (see Table 8-2) in ascending order from left to right and top down. All images were taken from particles within the same size class, namely 45 µm to 125 µm. While large inclusions (~ 1 µm) were found in all samples, the number of fine inclusions and their accumulation at grain boundaries increased with increasing carbon content.

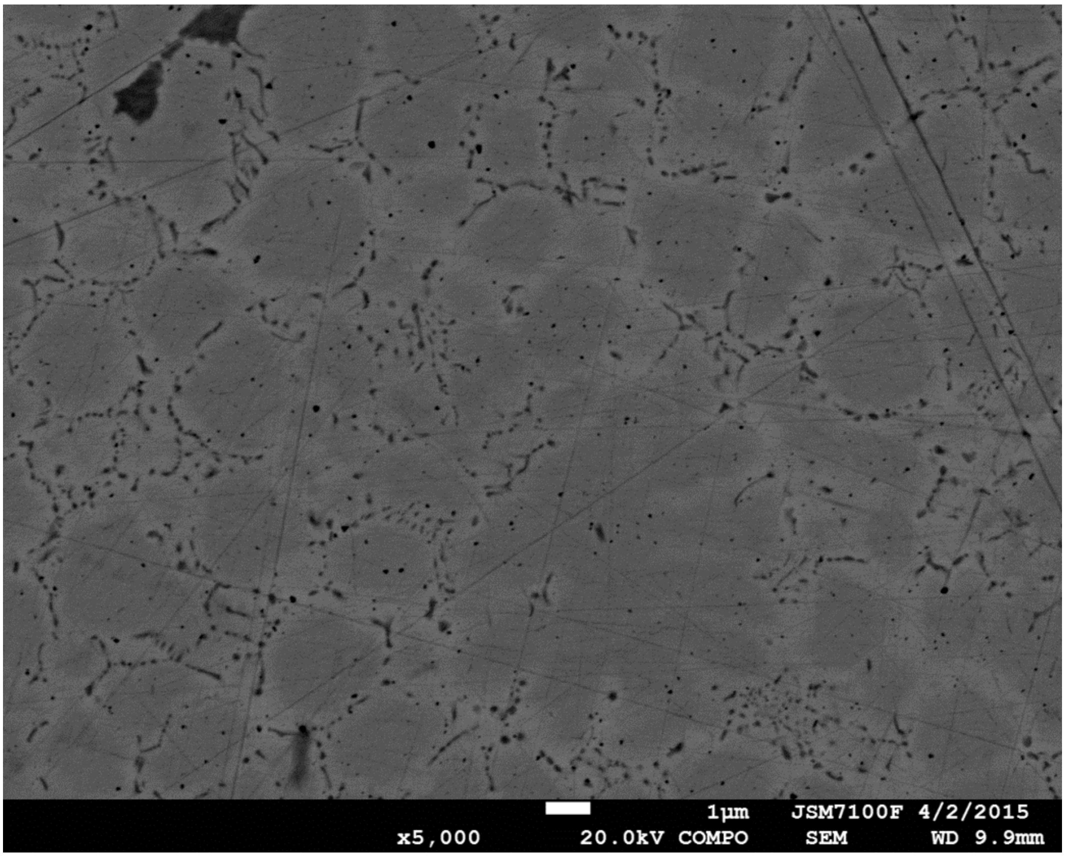
1µm
JSM7100F 4/2/2015
x5,000
20.0kV COMPO
SEM
WD 9.9mm

Figure 8-24 Batch 1114-3 (< 125 µm): enlarged image of a carbon-rich particle showing the general arrangement of fine impurities along the grain boundaries (light grey) in the zone of the solidified remaining melt as well as some precipitation within the grains (dark grey).

The arrangement of low melting point as well as insoluble impurities at grain boundaries is in agreement with literature [Bargel *et al.* 2000, Bergmann 2003].

In order to determine their nature, an EDX point and shoot scan was executed on typical large impurities (Figure 8-25) with respect to the beam footprint. Although the carbon content was exaggerated, presumably due to pollution with resin during sample polishing and generally limited resolution of carbon in EDX, the scan still allowed for qualitative conclusions.

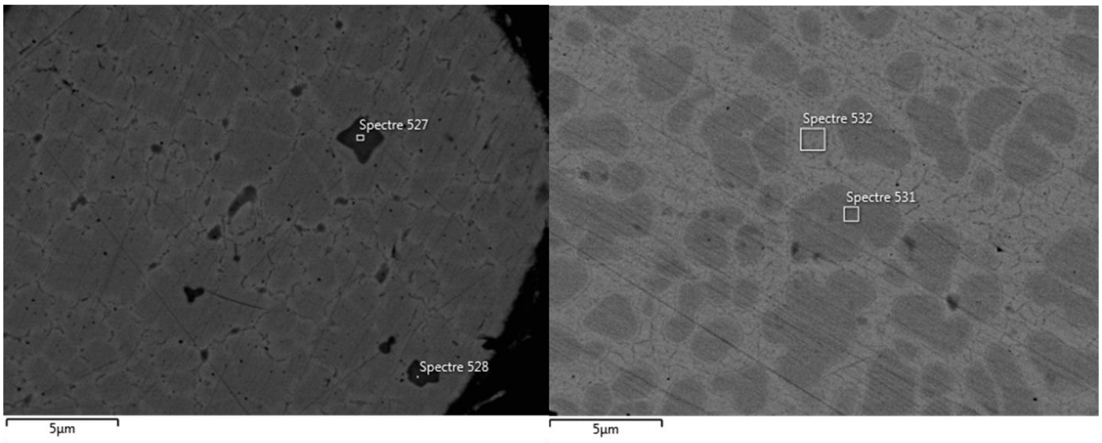

Spectrum	Element	Fraction [wt.-%]	Fraction [at.-%]
527	U	76.66	14.22
	Mo	-	-
	C	23.34	85.78
528	U	77.91	15.11
	Mo	-	-
	C	22.09	84.89
531	U	71.95	14.67
	Mo	6.86	3.47
	C	17.46	70.53
532	U	75.83	16.20
	Mo	5.00	2.65
	C	19.17	81.15

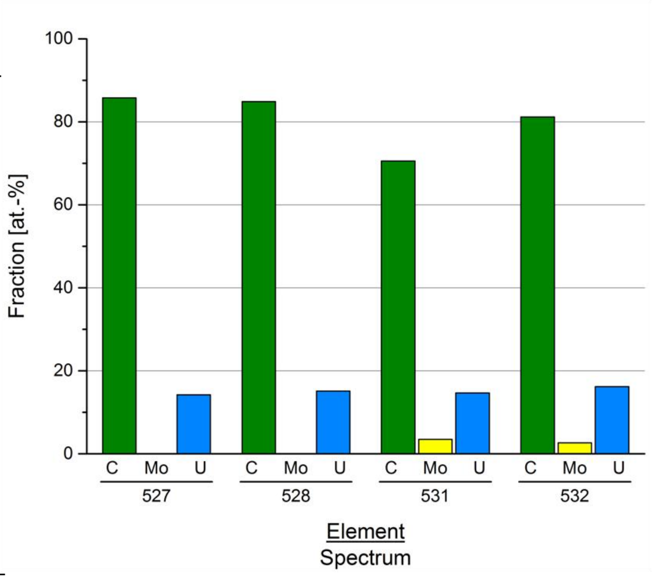

Figure 8-25 EDX point and shoot scan of typical inclusions and microstructure found in batches 0914 and 1114 (here: batch 0914-1, BSE micrograph).

For instance, spectra 527 and 528, which pointed at typical inclusions, showed mainly uranium and carbon. Furthermore, the carbon content was highest in these zones compared to that of spectra 531 and 532 that pointed at a grain and at an intergranular zone, respectively. It is hence suggested that the observed impurities consisted of a uranium carbide phase, presumably UC or U(C), as reported earlier [Schenk *et al.* 2014]. This is in agreement with results of [Palancher *et al.* 2012] who identified UC and traces of oxygen in the grains of rotating-disk-atomized U7Mo. In any case, the amount of carbon was limited, thus limiting the grain growth of uranium carbide.

Furthermore, it can be inferred from Figure 8-25 that the carbon content inside the grain was lowest. The used analytical methods, though, neither excluded nor confirmed the presence of a ternary U(Mo,C) phase. However, the scans confirmed that the intergranular zone was poorer in molybdenum (about 2 percentage points) and richer in uranium as reported earlier [Schenk *et al.* 2014]. The segregation was also indicated by the contrast differences in the microstructure observed for almost carbon-free 552 batches (Figure 8-17 and Figure 8-18).

Another influence of the carbon content on the microstructure was observed in batch 1114 (Figure 8-26). Some particles of batch 1114 showed lamellar, eutectic-like microstructures in the zone of the solidified remaining melt. It is reminded that uranium and carbon form a eutectic at 500 ppm of carbon by weight and 1116.6 °C in the binary system (Figure 8-2).

Although the influence of the increased carbon content on the microstructure was evident (Figure 8-23 and Figure 8-26), its influence on the grain size was inconclusive (Figure 8-27). Compared to the fine and generally consistent microstructure of almost carbon-free 552 batches, some particles of carbon-richer batch 0914-4 showed an inconsistent microstructure containing coarse and fine grains. Then again, particles from the carbon-richest batch 1114 exhibited a fine microstructure. The contradictory behaviour is mainly ascribed to (i) a potential difference in carbon concentration of a single particle compared to the average concentration in the bulk powder (ii) and the carbon concentration in the U(C,O) grains. In fact, the U(C) liquidus temperature increases with increasing carbon content and may exceed prevailing process temperatures (Figure 8-2 and Figure 8-4); the more as the amount of superheat in REP is limited. It hence is difficult to infer from the binary and ternary phase diagrams, whether U(C,O) grains present in the raw material (ingot) were entirely melted during induction casting and/or atomization or not.

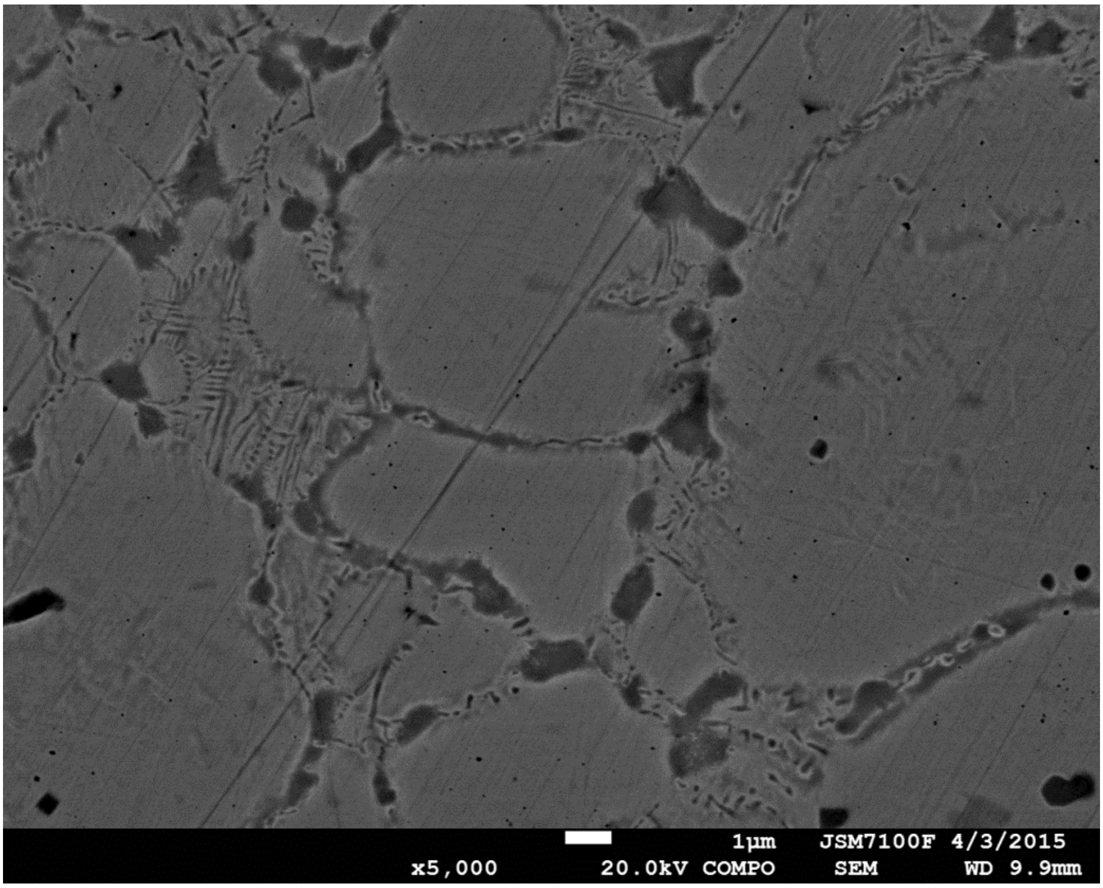

Figure 8-26 Batch 1114-1 (< 125 µm): lamellar structures observed in sectioned particles.

As a consequence, U(C,O) may have been present in atomized liquid droplets in a solid, partially, or entirely molten state. The resulting effect on microstructure, though, is different in each case irrespective of bulk powder or particle carbon concentration. This problem was already addressed to some extent by [Bonnin *et al.* 2014]. The authors suggested that "also U(C,O) particles were melted" at process temperatures of about 1400 °C. With respect to the grain size, however, [Bonnin *et al.* 2014] suggested that there is a positive correlation between γ-U(Mo) grain diameter and the presence of dissolved U(C,O) impurity phases. The investigations were carried out on a rotating-disk-atomized U7Mo particle with a UC content of ~ 1 wt.-% [Palancher *et al.* 2012].

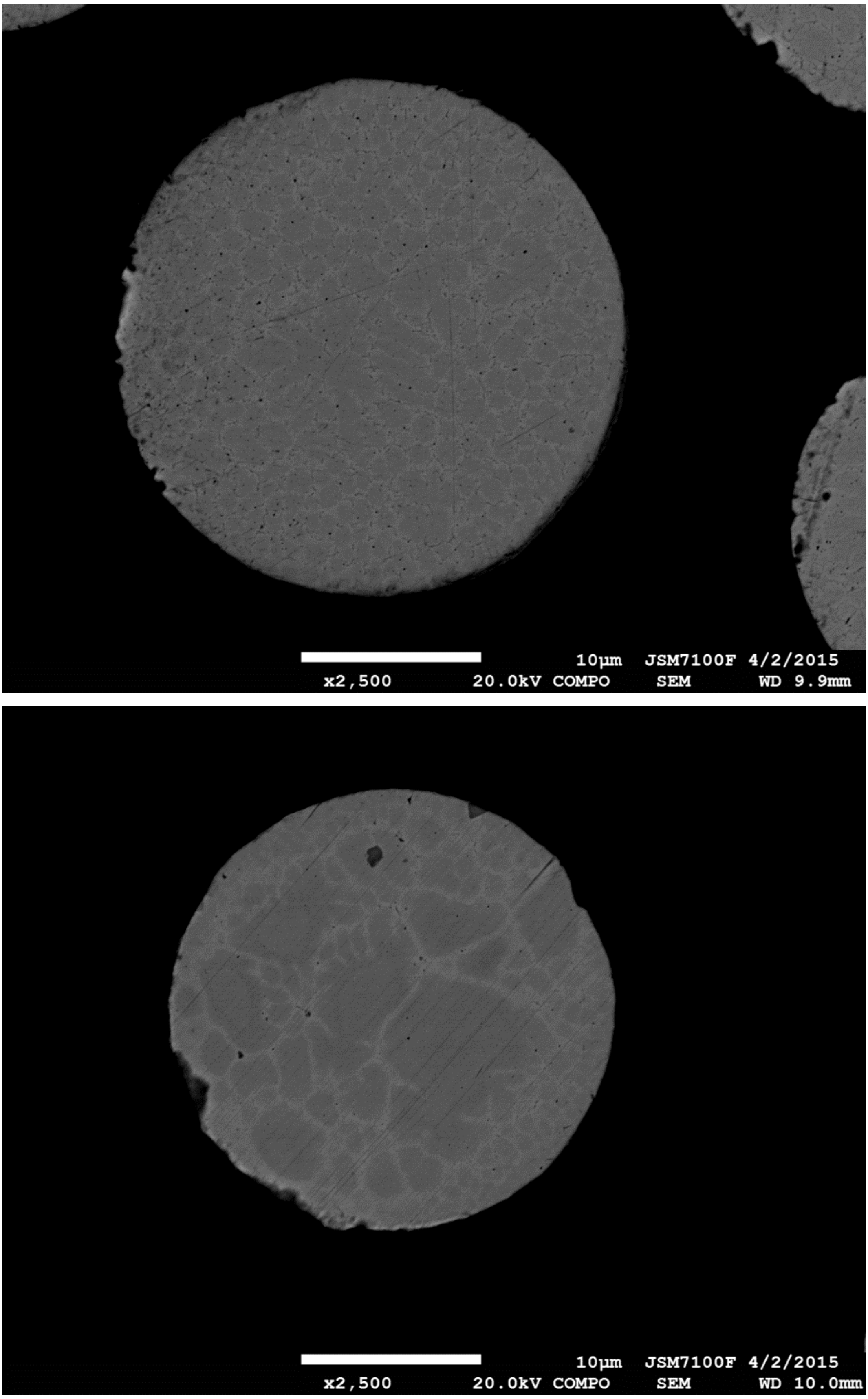
10µm JSM7100F 4/2/2015
x2,500 20.0kV COMPO SEM WD 9.9mm
10µm JSM7100F 4/2/2015
x2,500 20.0kV COMPO SEM WD 10.0mm

Figure 8-27 Different microstructures in the same size class. Top: batch 1114-3 (< 45 µm); bottom: batch 0914-4 (< 45 µm). Batch 1114-3 was 2.5 times richer in carbon according to the chemical analysis.

8.2.4 Irregular Particles

As mentioned in chapter 6.3.1, irregular particles were generally found in size classes > 355 µm (Figure 8-28). The mass fraction of irregular particles in this size class varied from 6 % to 25 % with regard to the atomized U8Mo powder (Table 7-5). Nevertheless, irregular particles were occasionally present in relevant size classes below 125 µm.

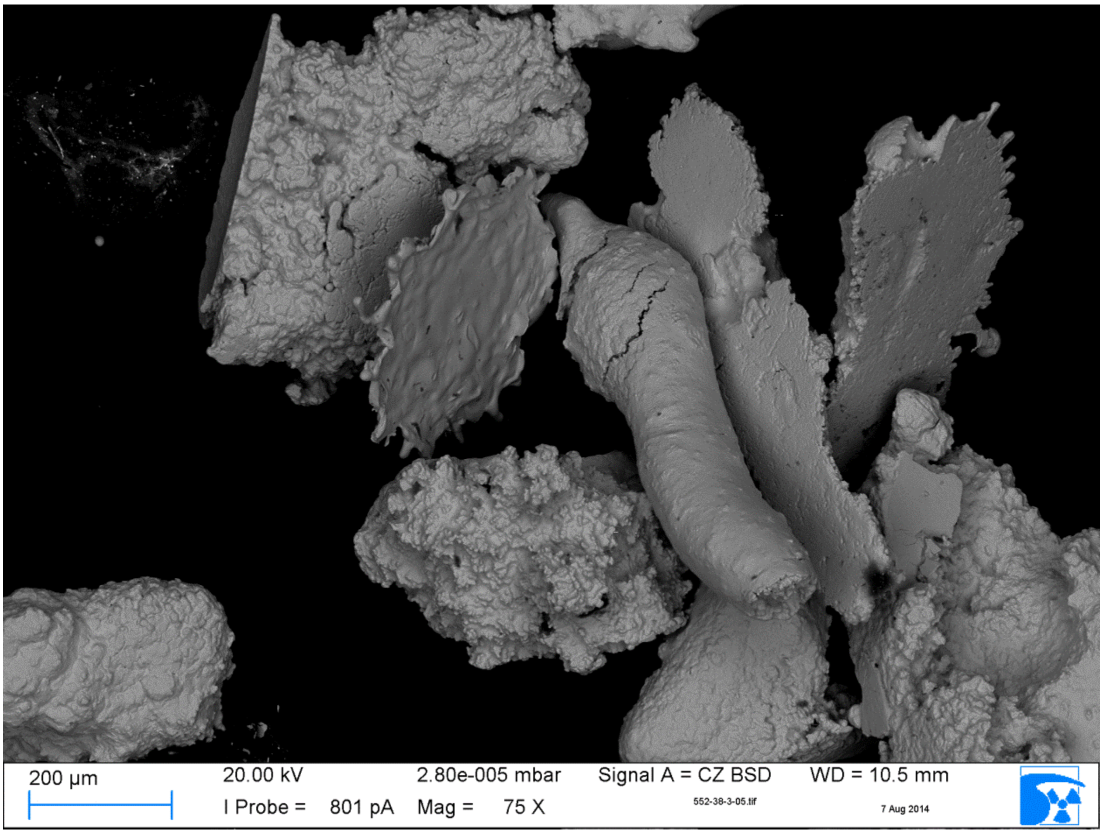

Figure 8-28 Batch 552-38: agglomeration of typical particles found > 355 µm, that consist of filaments, flattened drops, and highly irregular particles with rough surfaces that are partially flattened due to impact on the collection chamber wall prior to solidification.

Apparently, irregular particles had a similar microstructure compared to spherical particles (Figure 8-29). In addition, they were consistently composed of UMo (Figure 8-30). However, EDX line scans revealed that the molybdenum fraction was almost doubled in the irregular particles (Figure 8-31). This is explained by the nature of their creation: premature ejection of molybdenum-rich alloy droplets either from the mushy zone (chapter 7.2.3, material and process interaction) or due to alloy inhomogeneity of the rotating electrode (Figure 5-14).

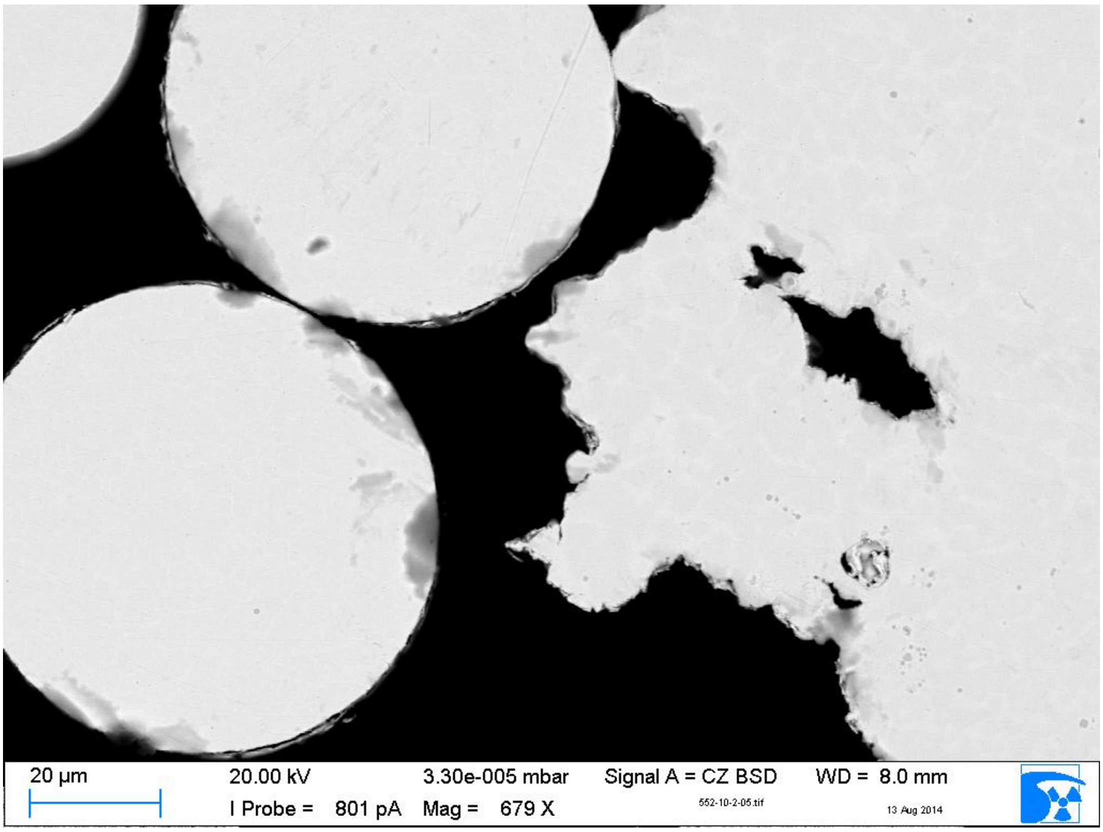
20 µm
20.00 kV
3.30e-005 mbar
Signal A = CZ BSD
WD = 8.0 mm
I Probe = 801 pA
Mag = 679 X
552-10-2-05.tif
13 Aug 2014

Figure 8-29 Micrograph of sectioned particles of batch 552-10 showing particles < 125 µm. The microstructure of the irregular particle is similar to the one of spherical particles.

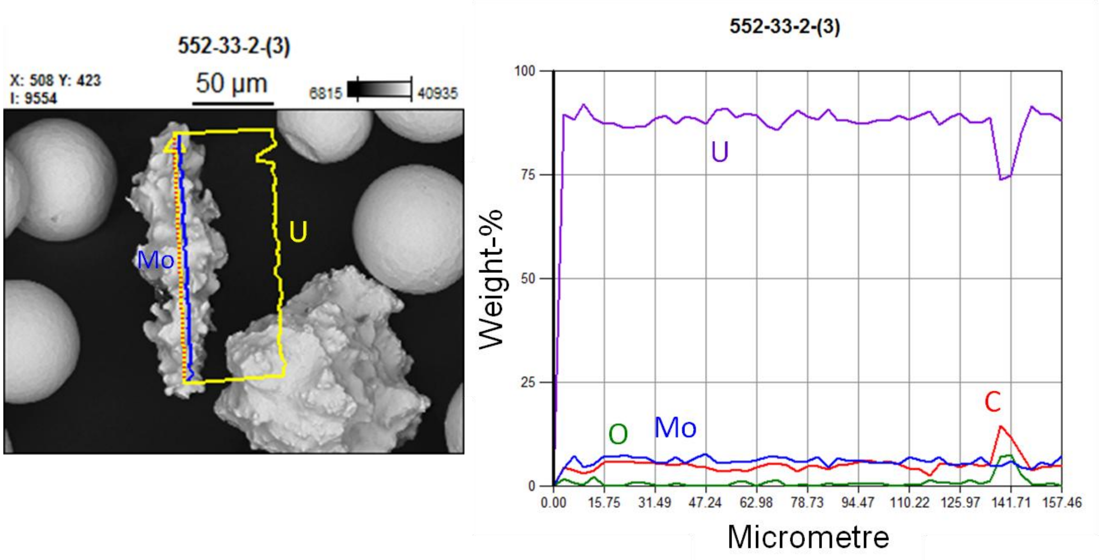

Figure 8-30 EDX line scan of a typical irregular particle confirming its consistent composition of uranium (left picture: yellow; right picture: purple) and molybdenum (blue).

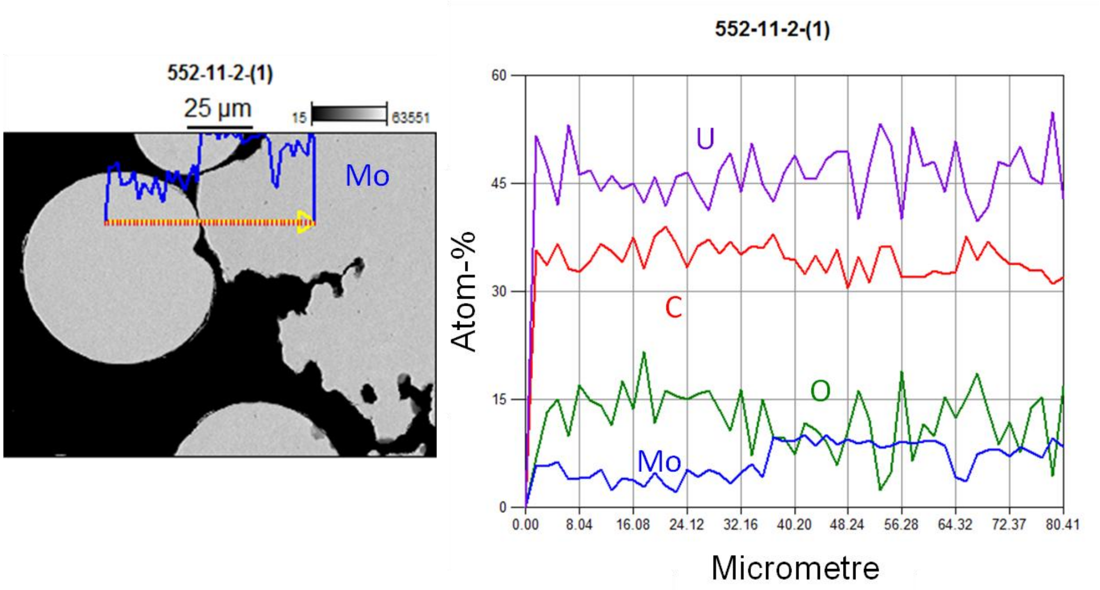

Figure 8-31 EDX line scan traversing a sectioned regular sphere (left) and a sectioned irregular particle (right). The molybdenum fraction (blue) is roughly doubled in the irregular particle.

In general, no internal voids or porosities were found in a total of more than 24 UMo batches and more than 60 corresponding samples[58] that were embedded, sectioned, and analysed using SEM or optical microscopy (see exemplary Figure 8-32). This was in agreement with features of REP-atomized powders reported by [Lawley 1992, Yule and Dunkley 1994]. Only on one occasion an internal spherical void was found, namely in batch 552-11 (Figure 8-33). The internal void was presumably caused by argon entrapment [Eylon *et al.* 1980b] as suggested in Figure 8-11.

---

[58] Generally, each powder batch was divided into two, sometimes three size classes for microscopic analysis.

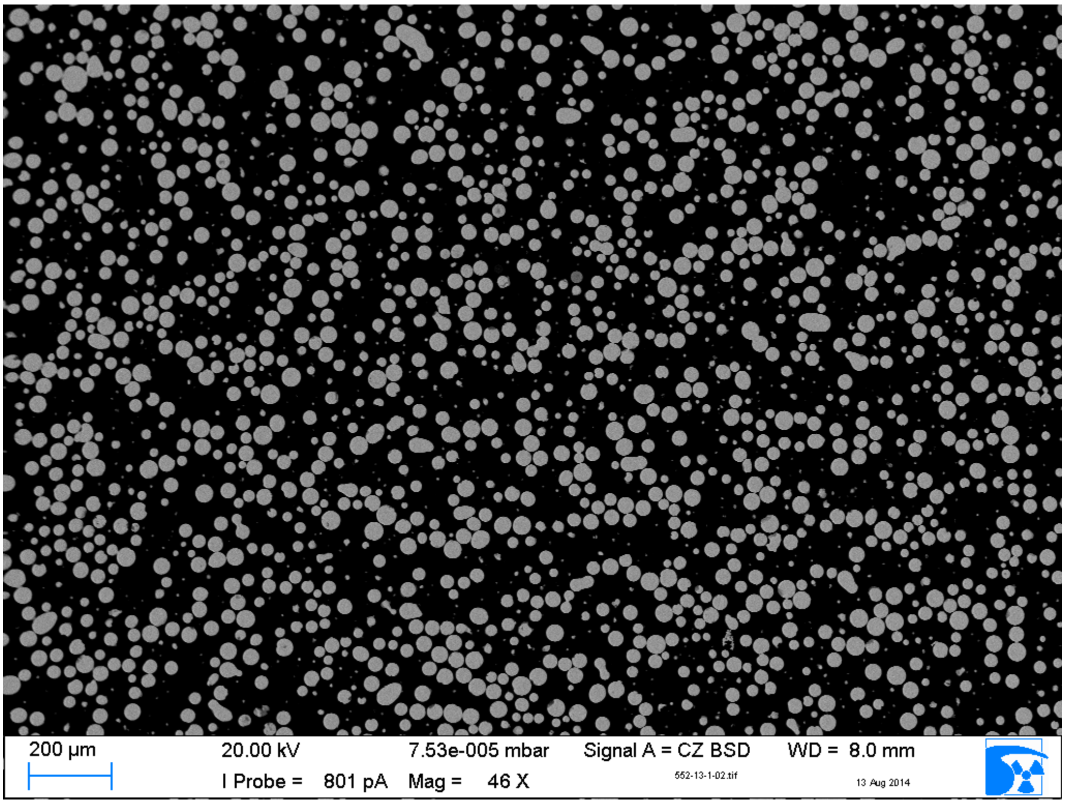
200 µm
20.00 kV
I Probe = 801 pA
7.53e-005 mbar
Mag = 46 X
Signal A = CZ BSD
552-13-1-02.tif
WD = 8.0 mm
13 Aug 2014

Figure 8-32 Typical SEM micrograph of embedded and sectioned U8Mo particles, batch 552-13 (< 45 µm). The particles were generally free of internal voids.

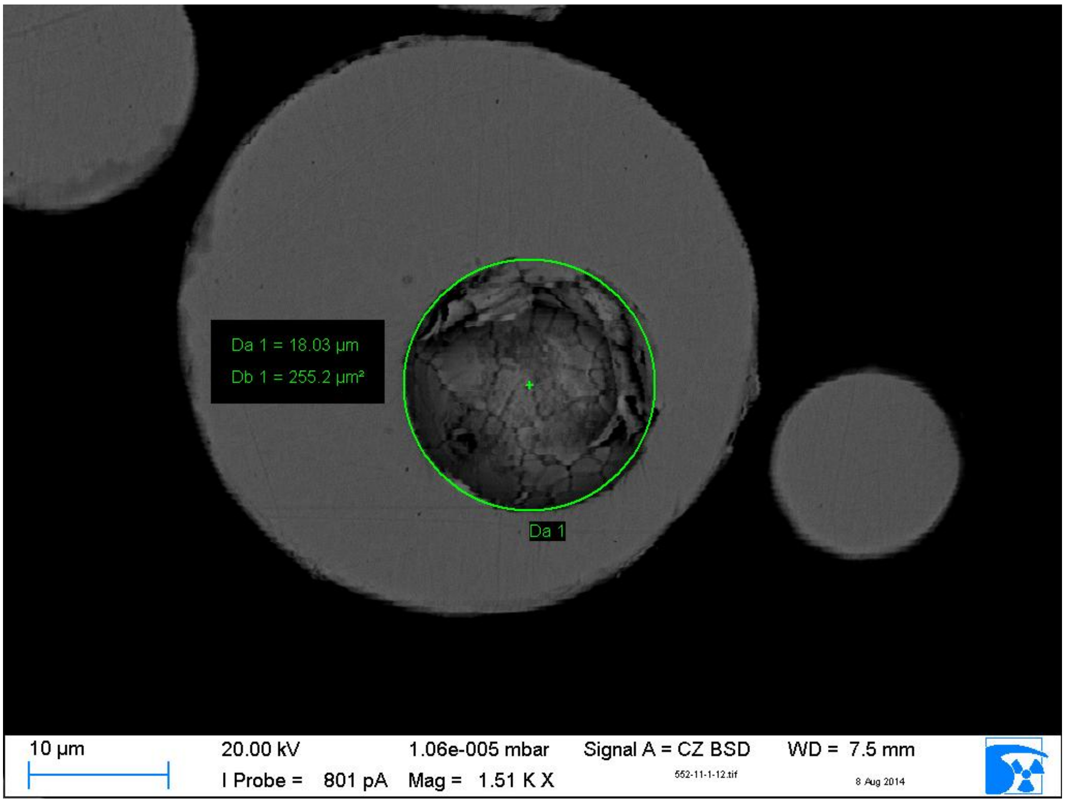
Da 1 = 18.03 µm
Db 1 = 255.2 µm²
Da 1
10 µm
20.00 kV
I Probe = 801 pA
1.06e-005 mbar
Mag = 1.51 K X
Signal A = CZ BSD
552-11-1-12.tif
WD = 7.5 mm
8 Aug 2014

Figure 8-33 Internal void found in batch 552-11 (< 45 µm), presumably due to gas entrapment.

8.3 Comparison

Atomized particles of CCHEN were highly irregular in shape as well as oxidised, thus indicating less precision in process control, notably atmosphere control [Olivares *et al.* 2012].

INL reported generally spherical particle shapes. The presence of some flattened areas on larger particles was ascribed to particle impact on the collection chamber wall prior to solidification. Also, irregular clumping of a small powder fraction was reported, though examples were not reported. It was ascribed to either insufficient droplet separation during atomization or posterior droplet collision [Clark *et al.* 2007]. KAERI reported that "most" of the large particles were spherical or near-spherical in shape and had smooth surfaces with few attached satellite particles [Oh *et al.* 2006]. However, particles < 45 µm exhibited flaky or lengthened geometries [Kim *et al.* 1997b]. Neither INL nor KAERI reported faceted or oxidised surfaces. Similar to observations made in this work, deformations of the particle surface ("wrinkles") were observed for U_3Si_2 particles [Kim *et al.* 1992, Kim *et al.* 1997a]. Micrographs of REP-atomized UMo powder from INL suggest the presence of cooling-based shrinkage dents as well [Clark *et al.* 2007].

The grain structure of rotating-disk-atomized particles was reported to be equiaxed for U2Mo and U10Mo with a grain size of about 5 µm [Kim *et al.* 1997b, Kim *et al.* 2007], which corresponds to observations made on REP-particles [Clark *et al.* 2007]. Experiments by [Oh *et al.* 2006] involving U7Mo, however, resulted in equiaxed grains in the particle centre and columnar grain structures at the particle periphery. According to Figure 8-7, columnar grain structures are found for smaller supercooled zones, indicating less constitutional supercooling or a steeper temperature gradient within the liquid droplet. While the chemical composition was similar to the one used in this work (i.e. U7Mo), the temperature gradient may have been steeper due to an inherently higher amount of superheat compared to REP or increased thermal conductivity of the quenching medium. In fact, their atmosphere was gradually changed from argon to helium. It is noted that the thermal conductivity of argon and helium is $0.02\,W\,m^{-1}\,K^{-1}$ and $0.15\,W\,m^{-1}\,K^{-1}$, respectively [Lawley 1992]. In addition, it was reported that the grain structure refined as the particles became finer since the surface-area-to-volume ratio increases for smaller spherical particles and enhances heat removal. INL reported a polycrystalline, consistent, and equiaxed microstructure for REP-atomized particles [Clark *et al.* 2007] which was ascribed to the limited amount of superheat and rapid solidification. It is suggested, that this observation should be extended by the results of this work, namely dendrite development due to constitutional supercooling. Another type of grain size distribution in rotating-disk-atomized U7Mo was reported by [Bonnin *et al.* 2014]. The particles exhibited a heterogeneous grain size distribution with small grains below 2 µm on the one hand and large grains above 5 µm on the other hand.

Segregation in centrifugally atomized UMo-particles was first reported by [Kim *et al.* 1997b] and later quantified [Kim *et al.* 2007]: the amount of molybdenum at the grain boundaries was 2 to 3 percentage points lower than in the grain. Microsegregation within the grain was not observed. Both observations are in agreement with the results of this work.

Furthermore, KAERI reported internal voids due to gas entrapment whose amount increased with particle size and had a significant impact on tap density [Kim *et al.* 1992, Kim *et al.* 1997b]. Pores with a diameter of 30 µm in sectioned particles with a diameter of 50 µm were shown [Kim *et al.* 1997b]. In contrast, REP-atomized particles of both INL and FRM II/CERCA are considered free of internal voids.

According to [Bonnin *et al.* 2014], surface oxidation of disk-atomized U7Mo particles amounted to 0.3 wt.-% while dissolved impurities U(C,O) reached 1 wt.-%. Both concentrations were about one order higher than the measured values of the bulk powder produced in this work.

The γ-phase of U8Mo is stable above 565 °C as shown in the corresponding phase diagram (Figure 8-1). According to X-ray diffraction measurements of INL and KAERI, the metastable γ-U was retained at room temperature in centrifugally atomized U2Mo, U7Mo, and U10Mo particles due to rapid solidification [Clark *et al.* 2007, Kim *et al.* 1997b, Oh *et al.* 2006]. The same results are expected for REP-atomized U8Mo. As the REP-atomized U8Mo powder produced during this work will be subject to diffusion annealing close to the solidus temperature (~ 1135 °C) and thus above the γ-phase transition of U8Mo, the as-atomized phase was not investigated in detail.

8.4 Conclusion

The chemistry of the fabricated bulk powder including alloy composition and impurity limits complied fully with the fuel specifications for UMo powder. This result was achieved irrespective of the origin and thus impurity of the processed raw material, coming from either INL or CERCA.

Production chains including the use of graphite crucibles, stopper rods, and moulds for rotating electrode casting added up to 800 ppm of carbon to the final product of atomized powder. The added amount was reduced to about 300 ppm if alumina crucibles, stoppers, and copper moulds were used. The remaining added amount of carbon is ascribed to prior graphite contamination of the production facility and the use of graphite mantles as induction coupling agents for the alumina crucible. The alumina/copper configuration added about 200 ppm of aluminium to the atomized powder. The amount of Cu found in the atomized powder was about 3 ppm.

REP-atomized U8Mo particles were mostly spherical in shape for parameter sets resulting in $X < 0.068$. Spherical REP-atomized U8Mo/U7Mo particles were free of satellites and shells. The surface area of most spherical particles was regular, smooth, and faceted, showing equiaxed grains and no intra-porosity. However, a surface deformation, namely a concave dent, was regularly found on spherical particles and is ascribed to cooling shrinkage. It is suggested that every particle underwent this deformation. The dent of an exemplary particle with a 100 µm diameter had a longitudinal diameter of about 40 µm and a depth of a few µm.

Produced particle surface areas are considered oxygen-free. Most particles in relevant size classes below 125 µm exhibited a manifested inner microstructure on the particle surface. The cleanliness was achieved through atomization under an inert argon atmosphere that exhibited an oxygen and moisture concentration below 10 ppm, respectively. The oxygen content of the bulk powder was below 250 ppm according to chemical analysis.

The microstructure of U8Mo particles atomized from INL-cast rotating electrodes was in general polycrystalline, fine, and consistent throughout the entire particle diameter. Though, a dendritic grain structure was evidenced. The "grain" sizes varied from 1 µm to 10 µm. The dendritic microstructure is ascribed to a combination of rapid solidification, constitutional supercooling, and moderate superheat due to REP. The particles were generally free of internal voids, porosity, inclusions or impurities. Indeed, REP-atomized U8Mo particles of batch 552 exhibited no precipitations. However, segregation in the solidified remaining melt between the dendrites was evidenced. That is, the molybdenum concentration in the grain was about 2 percentage points higher than in the intergranular zone.

The microstructure of U8Mo- and U7Mo-particles atomized from in-house cast rotating electrodes was also polycrystalline and dendritic. Nevertheless, it was affected by the increased carbon content that amounted to about 1300 ppm at maximum. That is, fine and large (~ 1 µm) precipitations were found, mostly at grain boundaries but also in the grains. The impurities are considered U(C) phases as (i) large impurities consisted mainly of uranium and carbon, and (ii) as their presence increased with carbon content. This observation is in agreement with investigation of [Palancher *et al.* 2012] that identified UC and traces of oxygen in similar particles. In some carbon-rich U7Mo particles produced in the course of this work, lamellar, eutectic-like structures were observed. In addition, an inconsistent particle grain size distribution and large grains were evidenced in some carbon-rich batches. Investigations of [Bonnin *et al.* 2014] suggest a positive correlation between grain diameter and the presence of impurities of the U(C,O) type.

The solidified remaining melt between dendrites is considered to have poorer mechanical properties (chapter 8.1.2) due to observed microsegregation and observed accumulation of impurities. Dendrite development may be attenuated by increasing the temperature gradient and/or decreasing the concentration of alloying components and/or impurities. Both approaches, however, are limited by the limited amount of superheat in REP and the currently accepted minimum molybdenum content of the alloy, respectively. Another option, namely diffusion annealing (homogenisation), may "cure" microsegregation, promotes diffusion of soluble impurities from the grain boundaries to the grain inner, and coagulates insoluble impurities such as carbides and oxides [Bargel *et al.* 2000]. Also, diffusion annealing generally results in coarser grain structures [Bargel *et al.* 2000, Bergmann 2003]. Although fine, homogeneous, and polycrystalline microstructures are preferred from a mechanical point of view as they offer more strength, ductility, and quasi-isotropy [Bergmann 2003], coarser grain structures are considered to exhibit advantageous irradiation behaviour. Investigations of [Ye *et al.* 2015, Zweifel 2015] suggest that insoluble noble fission gases such as xenon and krypton concentrate at grain boundaries of irradiated fuel and precipitate towards the interdiffusion layer (IDL) between UMo and the aluminium matrix. Here, they concentrate in large bubbles of micrometre size [Zweifel 2015]. The fission gas accumulation is made responsible for fuel swelling, cracking and subsequent release of fission products [Van Den Berghe and Lemoine 2014]. Latest investigations suggest that coarse grain structures limit U8Mo/U7Mo recrystallisation kinetics during irradiation and suppress swelling [Kim *et al.* 2014]. As a consequence, diffusion annealing is currently being implemented in the U8Mo/U7Mo fuel powder production process [Breitkreutz 2015]. It is noted, though, that insoluble impurities (e.g. carbides) are known to impede the movement of grain boundaries and thus grain growth up to a certain temperature (e.g. 1000 °C for steels) [Bargel *et al.* 2000]. As a remedy, diffusion annealing at temperatures close to the U8Mo/U7Mo solidus or use of high purity raw uranium in combination with graphite-free rotating electrode casting is recommended.

III

Summary

9

Summary, Outlook, and Conclusion

In the course of this work, a prototype atomizer was designed, dimensioned, constructed, assembled, commissioned, and parameterised. The atomizer principle is based on the rotating electrode process (REP), a centrifugal atomization technique for high purity metals and specialty alloys. In addition, U8Mo/U7Mo fuel powder was fabricated using different system parameters. The produced powder was characterised using granulometry, chemical analysis, and microscopy. The following chapter summarises both the engineering and experimental results of this work with respect to the earlier defined system and process requirements.

9.1 Summary

9.1.1 Nuclear Operating Licence

The prototype atomizer as a part of the UMo production facility was granted the nuclear operating licence by the French nuclear regulator ASN in 2013 on the basis of the here presented prototype concept. The licence is valid until 2017 and allows for the production of a total of 2 kg of ^{235}U.

9.1.2 Design

The prototype atomizer is based on the rotating electrode process (REP, chapter 3.1.1). It consists of (i) a tungsten arc welder for melting and (ii) a belt-drive system including motor and high frequency spindle for rotation of the rotating electrode (chapter 3.1.3). An external infrastructure to operate the atomizer was build-up (chapter 3.2).

Operation of the REP atomizer is semi-automatic. In particular, control of process parameters was automated. On the one hand, movement of the rotating electrode is controlled by a frequency inverter. Also, variation in length of the electric arc is inherently compensated for by the arc welder. Both belt tensioning system and the rotary electrical connector are self-adjusting. Finally, glovebox atmosphere was controlled by a gas purifier. On the other hand, loss in rotating electrode length due to its atomization is compensated for by a manually controlled tungsten electrode infeed. Rotating electrode mounting and powder collection is a manual operation as well. The rotational speed is controlled using a potentiometer or computer. Using a computer additionally allows for the change of frequency inverter parameter settings. Rotational speed and electric arc current are monitored and displayed. Due to the differential design and system architecture (chapter 3.1.3), all atomizer components (chapter 3.3) are individually accessible and exchangeable.

9.1.3 Dimensioning

The REP atomizer is a lab-scale prototype (chapter 3.1.2). It is dimensioned for the atomization of a standard rotating electrode of cylindrical form with usable length and diameter of 30 mm and 10 mm, respectively, at 40’000 rpm. The corresponding mass of a U8Mo rotating electrode is about 40 g. The maximum rotational speed of the current design is 50’000 rpm, but the high frequency spindle may operate at 60’000 rpm, corresponding to a radial rim speed of about $26\,\mathrm{m\,s^{-1}}$ and $31\,\mathrm{m\,s^{-1}}$, respectively, with regard to the standard rotating electrode diameter of 10 mm (chapter 3.3.13). Electric arc current may be varied from 2 A to 170 A (chapter 3.3.6). For experimental prototype operation and accessibility, a vertical rotation axis was chosen (chapter 3.1.2). The powder collection chamber has a diameter of 600 mm (chapter 3.3.27). The entire prototype atomizer is designed for operation in highly pure argon. It is integrated into a shielding gas system that provides argon atmospheres with less than 7 ppm of oxygen and moisture, respectively (chapter 3.1.3).

9.1.4 General Parameterisation

Both uranium-molybdenum and stainless steel powders were fabricated during experimental operation. For parameterisation, as-cast U8Mo, U7Mo, and machined 1.4301 stainless steel rotating electrode were used. Besides the standard type, short UMo rotating electrode versions with 20 mm usable length as well as rotating electrodes with a diameter of 14 mm and 20 mm were atomized. While electric arc currents were varied from 30 A to 100 A, the applied rotational speeds were varied from 20’000 rpm to 50’000 rpm. The argon atmosphere generally exhibited less than 7 ppm of moisture and oxygen, respectively. More than 60 atomization runs were performed during development and experimental phase. This comprises about 24 atomization runs involving U8Mo/U7Mo alloys.

The volume flow rate generated by melting of the rotating electrode is one of the most important process parameters in REP atomization besides rotating electrode diameter and rotational speed. It influences the atomization regime and therefore both the particle shape and particle size distribution. The generated U8Mo/U7Mo/1.4301 stainless steel mass flow rates were determined from the ratio of atomized powder mass and atomization time, while the electric arc current was used to control its magnitude (chapter 5.3). The measurement and quantification of the mass flow rate allowed for modelling of the atomization regime and thus particle shape estimation (chapter 6.3.1).

A linear dependency of the apparent mass flow rate on electric arc power was found for atomization of U8Mo and 1.4301 stainless steel standard rotating electrodes, equation (5.16). In addition, it was found that the effective electric arc current is limited to a lower threshold of 30 A ± 5 A with respect to a standard U8Mo rotating electrode. As a consequence, the lowest generated mass flow rate was about $0.8\,\mathrm{g\,s^{-1}}$ (chapter 5.3.2). Furthermore, a melting and thus atomization deadband following arc ignition was observed (chapter 5.3.2). It causes a deviation of the apparent from the real mass flow rate, but decreases with increasing electric arc current. The variation of the mass flow rate at same parameter settings is mainly ascribed to variation in electric arc length due to the manual operation of the welder torch infeed. In fact, electric arc heat input decreases with increasing arc length although the arc welder automatically adjusts the arc voltage. At low electric arc currents, a positive correlation of apparent mass flow rate and atomized rotating electrode length was observed (chapter 5.3.3). That is, the mass flow rate is supposed to increase with increasing rotating electrode length, which is ascribed to the difference in apparent and real mass flow rate. Increasing the diameter of the rotating electrode resulted in smaller mass flow rates, thus confirming earlier studies of other researchers on REP (chapter 5.3.4). Furthermore, it was found that the mass flow rate positively correlates with the carbon concentration in U8Mo (chapter 5.3.5). Also, it is suspected that the observed inhomogeneities of the purchased rotating electrodes affect the mass flow rate and thus atomization regime and particle size distributions (5.3.5).

Parameter sets ($X \sim 0.068$) were found where the atomizer prototype yielded almost entirely U8Mo particles of spherical shape within the target size ranges (chapter 6.3.1). Also, parameter sets were identified that produced primarily filaments ($X \sim 0.082$).

Analysed particle shapes (chapter 6.3.1) and particle size distributions (chapter 7.2.3) indicate that the atomizer operates in the ligament formation regime or in the transition range to the direct droplet formation regime.

9.1.5 Surrogate Material

1.4301 stainless steel is a low-cost, readily available surrogate material for the "cold" validation phase of the atomizer prototype with similar relevant physical properties as uranium. It provided a reasonable orientation for "cold" commissioning and hot experiment planning. Improvement regarding the reproduction of the atomization regime, mass flow rate, and melting range with respect to U8Mo/U7Mo may be optimised, though. Therefore, potential surrogate materials for further "cold" testing during development were theoretically evaluated in this work. It was found that platinum amongst others might represent best relevant material properties with respect to uranium atomization, in particular the atomization regime parameter X and enthalpy of melt (chapter 6.3.2). In order to account for the melting range of UMo alloys and rotating electrode fabrication, platinum alloys with a similar melting range in an as-cast condition should be investigated. At present, a troy ounce (~ 31.1 g) of platinum is worth about 830 € or 940 $.

9.1.6 Maintenance

Due to the chosen prototype design, overall maintenance effort of the atomizer prototype was very low. Wear parts of the atomizer include the tungsten electrode, carbon brushes, graphite dust seal, drive belt, and collet (collet chuck). Experimental operation showed that only carbon brushes and collet have to be exchanged regularly in contrast to other wear parts. In particular, the carbon brush wear necessitates regular brush length control as well as removal of the wear product (metallic graphite powder) from the reservoir. A maintenance interval of 15 atomization runs is recommended as brush wear is extensive under high purity argon atmospheres. The collet should be controlled for plastic deformation in the same interval and exchanged if necessary.

The thread of the powder seal screw has to be regularly cleaned (brushed) from fine powder particles.

The argon purification system of the atomizer glovebox naturally saturates in the course of glovebox operation. Reactor regeneration of the gas purifier was executed every two months, generally causing an atomizer downtime of 16 hours or two working days.

9.1.7 Repeatability

In powder metallurgy, repeatability can be related to particle and powder properties such as morphology (shape, surface, microstructure etc.), chemical composition, and degree of impurities as well as type of particle size distribution, mean diameters, and process efficiency. In this work, repeatability was verified using 1.4301 stainless steel rotating electrodes as (i) the amount of purchased U8Mo rotating electrodes was limited and (ii) their chemical composition sometimes inhomogeneous (chapter 4.2). It was found that the prototype REP atomizer reproduced particle median and mean diameters with a standard deviation of 1 % and 3 %, respectively. The average mode was reproduced with a standard deviation of 6 %. Notably, same parameter sets resulted in particle size distributions with a similar curve progression. In addition, same parameter sets yielded particles of the same shape with brilliant and smooth surfaces. Atomization efficiency, a manually controlled process parameter, had a standard deviation of 9 % for a trained operator. Some U8Mo atomizations were repeated once in order to confirm parameter settings. The results indicate that the observations made for 1.4301 stainless steel also apply to atomization of U8Mo.

9.1.8 Powder Quality

In terms of powder quality, about 60 samples coming from 24 fabricated UMo batches were analysed.

The atomization regime parameter X was found to be a good estimator for the production of spherical U8Mo particles (chapter 6.1.4). A parameter range from $X = 0.028$ to $X = 0.164$ was investigated with the implemented atomizer design (6.3.1). For $X \leq 0.068$, about 90 % of the atomized particles were spherical. The corresponding particle size distributions exhibited median diameters as low as 62 μm, depending on rotational speed and rotating electrode diameter. Thus, best U8Mo/U7Mo atomization results with respect to powder quality, in particular spherical particle shape, are obtained for parameter setups that result in an atomization regime parameter of $X \leq 0.068$ and argon atmospheres below 7 ppm of oxygen and moisture, respectively (Table 6-1).

Particle size distributions of the fabricated powders were generally mono- or bimodal, primarily depending on the prevailing atomization regime. According to the shapes of the obtained particle size distributions, the atomizer operates (i) in the ligament formation regime for $X \geq 0.082$ and (ii) in the transition zone from the ligament formation regime to the direct droplet formation regime for $X \leq 0.068$ (chapter 7.2.3). For atomization of U8Mo and U7Mo, it was found that particle size distributions exhibited a persistent tail on the coarse particle side, which was more pronounced for standard than for short rotating electrodes. The general presence of the tails is ascribed to a combination of alloy inhomogeneity in the rotating electrodes, U8Mo melting range, inherently limited superheat in REP, and radial decrease of electric arc heat in contrast to radial increase of centrifugal force (7.2.3). The increased intensity of the tails for standard rotating electrodes, however, is ascribed to a mechanical and/or thermal effect related to the rotating electrode length that affects the atomization mechanism: namely, increase in resonance due to poor circular runout and/or increase in mass flow rate due to heat-up of the standard rotating electrode (7.2.1).

The chemical analysis of the bulk powder showed full conformity with fuel specifications including impurities (chapter 8.2.1). The alloy composition of the ingot was reproduced in the powder for both U7Mo and U8Mo. The amount and degree of impurities was mainly dependant on ingot source and production steps including casting and atomization amongst others. It was found that substituting alumina (crucible) and copper (mould) for graphite parts in induction casting substantially reduced carbon contamination while the amount of copper, aluminium, and silicon maintains below fuel specification limits.

Optical and scanning electron microscopy revealed that spherical REP-atomized particles were generally satellite-free, without internal voids, free of inclusions, and free of shells (chapter 8.2.2). The surface area was generally smooth, without intra-porosity, and faceted. Concave dents, though, were observed on almost every particle and are ascribed to cooling shrinkage. The particle surfaces were practically oxygen-free due to the high purity argon atmosphere in the atomizer glovebox with low oxygen and moisture contents.

The microstructure of REP-atomized U8Mo particles from purchased (INL) rotating electrodes was consistently fine and polycrystalline since rapid solidification conditions prevailed (chapter 8.2.3). It was found, though, that the grains of REP-atomized particles had a dendritic form, which is explained by REP-inherent moderate superheat and constitutional supercooling in metal alloys such as U7Mo and U8Mo. In this respect, segregation in the intergranular zone of the solidified rest melt was found, too. Accordingly, the amount of molybdenum in the grain was higher by about two percentage points than in the intergranular zone. The latter, in turn, was richer in uranium. In the course of general attempts to increase grain size by posterior diffusion annealing in order to improve irradiation behaviour, the dendritic and segregated microstructure is going to be cured and does therefore not affect powder quality.

Particles made from in-house fabricated U8Mo and U7Mo rotating electrodes with increased carbon contamination (> 200 ppm) showed increased U(C) precipitation in the zone of the solidified rest melt (chapter 8.2.3). It was found that the amount of precipitated U(C) positively correlated with bulk powder carbon-content. In addition, large and inconsistent grain sizes were observed in some carbon rich particles suggesting a correlation of grain diameter and presence of impurities, notably carbon. With respect to the projected diffusion annealing and the desired increase in grain size, the presence of insoluble U(C) impurities may necessitate higher annealing temperatures than applicable for pure U8Mo (chapter 8.4).

Particles of highly irregular shape and increased molybdenum concentration as well as manifested filaments were primarily found in non-target size classes with diameters > 355 µm. Their presence is mainly ascribed to a material and process interaction caused by the following effects: (i) inhomogeneities of purchased U8Mo rotating electrodes, (ii) the limited superheat in REP because of instantaneous melt ejection due to centrifugal force, (iii) a non-uniform input heat distribution in REP, and (iv) the melting range of U8Mo alloy.

9.1.9 Process Efficiency

The highest process yield efficiencies η_p (i.e. usable powder out of invested rotating electrode mass) were obtained for $X \leq 0.068$ and atomization of short rotating electrodes. They varied between 40 % and 50 % (chapter 7.2.1). The corresponding parameter set was: (i) rotational speeds between 40’000 rpm and 50’000 rpm, (ii) electric arc currents between 35 A and 50 A, (iii) electrode diameter of 10 mm and usable length of 20 mm, and (iv) argon atmospheres of less than 7 ppm of oxygen and moisture, respectively. The corresponding coarse-to-fine ratios varied between 2.4 and 1.9. These values are in agreement with the fuel specifications (chapter 2.4) that demand a coarse-to-fine ratio between 1 and 2.33. The parameter sets and results are summarised in Table 7-2.

It was found that standard rotating electrodes had lower process yield efficiencies for same parameter sets regarding atomization of U7Mo and U8Mo. The highest process yield efficiencies for standard rotating electrodes amounted to 40 % with coarse-to-fine ratios from 4.6 to 3.4. They were obtained at 45’000 rpm and 45 A to 50 A.

The usable powder efficiency η_p (i.e. usable powder out of atomized powder) was significantly higher for short than for standard rotating electrodes. For instance, atomization of short rotating electrodes in usable powder yield-efficiencies of 77 % (15 g) and 23 % (4 g) in the target size ranges of < 125 µm and < 40 µm, respectively. The experiments were conducted at 40’000 rpm and 50 A. In contrast, the usable powder yield efficiency of atomized standard rotating electrodes reached 50 % and 3 %, respectively.

The difference between short and standard rotating electrodes is ascribed of the observed tailing of the particle size distributions and its increase in intensity with increasing rotating electrode length as discussed in the paragraph “powder quality” in chapter 9.

The amount of scrap (particles with diameter above 355 µm) varied between 6 % to 23 % for atomization of U8Mo and U7Mo. The variation did not correlate with input parameters. A potential reason is the presence of filaments in the scrap that is known to affect dry sieving results strongly.

9.1.10 Production Capacity

One standard rotating electrode was atomized within half an hour including rotating electrode mounting and powder collection, resulting in a total of 16 electrodes per day (chapter 7.2.2). This value corresponds to a potential total of 256 g of usable U8Mo per day, taking into account the observed atomization process yield-efficiency of around 40 %. With respect to the prototype production-capacity requirements, the implemented atomizer is thus capable of providing one quarter of the target annual fuel production of the prototype in one working day.

9.1.11 Modelling

The extent to which existing centrifugal atomization models agree with experimental results of this work was also investigated, namely for the mass flow rate, atomization regime, and mean particle size.

Mass Flow Rate

In contrast to the models describing atomization regime and mean particle size, the applied equation for mass flow rate modelling was not echoed in secondary literature. In fact, reviewed secondary literature on REP does not state any model regarding this parameter. However, the experimental results confirmed model predictions with a coefficient of determination of about 95 % (chapter 5.3.6). As for the other models, uranium instead of U8Mo/U7Mo material properties were used for modelling as they have not been published yet. Also, exact determination of the heat input for modelling was affected by the variation in electric arc length due to manual torch operation.

Besides, a function relating the apparent mass flow rate of U8Mo to the electric arc power was found, equation (5.16). The function is based on experimentally obtained apparent mass flow rates from atomization of standard rotating electrodes of U8Mo as well as 1.4301.

Atomization Regime

Modelling of the atomization regime requires information on thermophysical material properties, rotational speed, rotating electrode diameter, and mass flow rate. As the mass flow rate is not a direct process input parameter in REP such as rotational speed and rotating electrode diameter, it had to be experimentally measured prior to modelling (chapter 5).

The evaluated semi-empirical model proved to be a good estimate in order to produce the desired spherical particles and to avoid filaments in the target size range. According to the model, transition from the ligament formation to the direct droplet formation regime in REP occurs below an atomization regime parameter of $X \sim 0.07$. Although this value gave a generally good orientation and proved to yield entirely spherical particles with respect to atomization of 1.4301 stainless steel, the shape of the atomized U8Mo/U7Mo particles and the particle size distributions did not entirely agree with predictions. That is, for atomization parameter values of $0.028 \leq X \leq 0.068$ about 90 % of the particles were spherical in shape with the rest being ellipsoids or irregular (chapter 6.3.1). In addition, corresponding particle size distributions exhibited shapes that are generally ascribed to the ligament formation regime, namely polydisperse monomodality or bimodality with equally high main and secondary particle modes (chapter 7.2.3). The deviation is ascribed to the following potential influences: (i) the use of uranium material properties for calculation in absence of the relevant UMo material properties, (ii) the basis for the model, namely REP atomization of elemental metals (except steel), (iii) the substantial melting range of U8Mo and U7Mo alloys, (iv) the limited superheat in REP, and (v) the inhomogeneity of purchased U8Mo rotating electrodes.

Mean Particle Size

Multiple models describing mean particle size in centrifugal atomization in general and REP in particular exist, whereof 8 were compared in this work. It was found that the models yielded similar results for same parameter sets, irrespective of their derivation from physical relations or semi-empirical derivation from atomization of normal liquids or metal melts. Best agreement between experimental data and models was achieved for particle mean diameter $D_{\mathrm{m},0.3}$ with a coefficient of determination of 85 % (chapter 7.2.4). The corresponding particles account for 30 % of the total powder mass. Other characteristics of the U8Mo and U7Mo particle size distributions such as mean, median, and standard deviation were less representative as they were strongly affected by the reported tails and scrap. For comparison, $D_{\mathrm{m},0.3}$ and $D_{\mathrm{m},0.5}$ (the median) of 1.4301 stainless steel powder exhibited coefficients of determination of 96 %, respectively. As for the modelling of the atomization regime, the same potential influences apply to modelling of the mean particle size.

9.1.12 Rotating Electrodes

It was found that purchased U8Mo rotating electrodes exhibited alloy inhomogeneities on at least four occasions out of 25. That is, large pieces of molybdenum foils used for alloying were found in rotating electrode rests after atomization (chapter 5.3.5). The presence of undissolved molybdenum indicates an insufficient number of alloying cycles. As all purchased rotating electrodes belonged to the same production batch (U8Mo-552), it is suggested that more than the recognised rotating electrodes were affected. However, in-house fabricated U8Mo and U7Mo rotating electrodes did not exhibit alloy inhomogeneity.

It was shown that rotating electrode alloy homogeneity is a detrimental parameter with respect to UMo fuel-powder production by REP. The observed inhomogeneities are suspected to have significantly affected the powder quality, notably particle shapes, particle size distributions, and the alloy composition of UMo particles (chapter 7.2.3 and chapter 8.2.4).

Carbon concentration of the rotating electrodes strongly varied with the origin of raw uranium (chapter 8.2.1). While uranium coming from INL had carbon concentrations of about 200 ppm, uranium coming from CERCA showed concentrations of around 900 ppm. In-house induction casting in its initial configuration using graphite crucibles, stopper rods, and moulds added up to 800 ppm of carbon. This amount was reduced to 300 ppm using alumina crucibles and stoppers as well as copper moulds. The new configuration added about 200 ppm of aluminium to the bulk powder and thus a negligible amount with respect to fuel specifications.

9.2 Outlook

A general overview of potential modifications, improvements, and suggestions with respect to engineering and atomizer performance is given in the following paragraphs.

In the case of validation of REP for industrial UMo fuel production, an atomizer design with horizontal rotation axis should be considered in order to allow for instantaneous powder recovery without operator intervention. This design, however, will reduce the number of potential alternative processes to be implemented based on the current atomizer design, e.g. centrifugal shot casting, rotating disk atomization, rapid spinning cup atomization and other.

Production capacities of REP may be increased in several ways: (i) increase in the number of atomization units, (ii) increase in rotating electrode length or (iii) increase in rotating electrode diameter. The first option is a matter of production space and man power. The second option is a common solution in industry. However, due to the mechanical limits of the rotating high frequency spindle, notably its roller bearings, an increase in rotating electrode length will either necessitate additional machining for higher circular runout or require a more robust spindle. Another option used in industry with respect to REP is the so-called “long bar” configuration, where a rotating seal-and-bearing assembly allows the electrode to be moved into the collection chamber as it is being atomized. Therefore, the spindle is fixed onto a mobile carrier. The third and last option may demand modification of the spindle as well. As a benefit, an increase in rotating electrode length or diameter will also increase the powder yield efficiency (i.e. the powder produced from one rotating electrode) that reached 72% in the current configuration.

Automation of the tungsten electrode infeed is recommended in order to allow for constant electric arc power supply, heat input, and thus melting rate. The latter is detrimental with respect to the atomization regime. As a result, process repeatability would be additionally increased. This modification would further increase operational safety as manual operator intervention during atomization would become obsolete. In the aforementioned long bar configuration the automated infeed would be provided by the mobile spindle with the tungsten electrode static.

To further decrease mean particle size, the following options should be considered: increase of rotational speed and/or increase of rotating electrode diameter. The current spindle is dimensioned for a maximum rotational speed of 60’000 rpm. In order to reach this rotational speed, the current (exchangeable) motor pulley has to be replaced by a pulley with greater a diameter. However, design limits regarding the rotating electrode dimensions and circular runout must be respected to avoid damage to the high frequency spindle.

The powder seal screw, a simple and removable gap ring seal, proved viable in providing access for rotating electrode mounting and sufficient in terms of protecting the high frequency spindle against atomized particles. To improve its handling, the pitch of the thread should be increased in order to avoid fine particle retention in the thread and subsequent fretting or stalling of the screw. Also, the number of rotations to fix the screw may be reduced to one or two turns in order to facilitate and accelerate the mounting process. An alternative bayonet fitting may substitute the powder seal screw.

To improve sealing of the spindle shaft and bearings against fine particles, the high frequency spindle is equipped with a pressurised gas inlet. Although not compatible with negative pressure operation of the current atomizer glovebox, this option should be considered for industrial operation. In addition, the pressurised gas would flow along the longitudinal axis of the rotating electrode. It could therefore promote ligament break-up in the ligament formation regime and thus production of spherical particles.

Another method to promote ligament break-up and effective particle size control besides the aforementioned pressurised gas flow could be ultra-sound or mechanically induced oscillation as applied in ultrasonic atomization or vibrating electrode atomization, respectively. Both methods are used to fabricate spherical particles.

Main maintenance effort is associated with the carbon brush arrangement due to extensive brush wear in high purity atmospheres. In addition, the wear product – a mixture of graphite and metal powder – is a potential contaminant for fabricated fuel powder although a sealing system exists and is effective. However, wear product removal has been found to be a frequent, time consuming, and delicate operation as graphite powder is greasy and the reservoir fixed with screws. As a consequence, a quick release solution using clamps or other tools should be considered.

If the challenge of simultaneous negative pressure operation of the glovebox and feed of the glovebox with pressurised gas – as discussed for the high frequency spindle seal – can be solved, substitution of plasma arc (non-transferred or twin-torch) for tungsten arc melting should be considered. This would supersede the carbon brush arrangement and its associated maintenance effort as well as carbon contamination potential. Instead, a protective earth (e.g. a copper leaf spring) may be connected to the spindle shaft and rotating electrode in order to avoid arcing or danger to the operator due to electrostatic charging.

Automation of rotating electrode mounting, notably insertion and clamping, may reduce preparation time and effort. Hydraulic and electric clamping systems are industrial standard. Also, other mounting systems than collet chucks may reduce maintenance and component costs.

Monitoring electric arc voltage in addition to electric arc current may provide better control and traceability of the mass flow rate and thus atomization regime. With respect to the observed melting deadband, atomizer operation with two different electric arc currents – one for heating (below the arc current threshold) and the other for melting – may remedy measurement fallacies associated with determination of the mass flow rate. This operating option is already available in the implemented system.

A high speed camera for video filming of the atomization process would provide better insight into the governing atomization mechanism, the mass flow rate, and droplet formation.

A partial atomization of standard-length rotating electrodes is suggested to determine the origin of the influence of rotating electrode length on process efficiency. Besides same parameter sets, the atomized mass of a standard rotating electrode must equal the atomized mass of a short rotating electrode in order to obtain comparable results. If the influence of length can be traced back to poor circular runout of the as-cast rotating electrodes, appropriate remedy would be provided by atomization of shorter rotating electrodes or an intermediate processing step in between casting and atomization, for instance turning. A thermal effect could be remedied using adaptive electric arc current, i.e. reduction of electric arc power with increasing rotating electrode temperature.

Impurities, notably carbon, were found to affect the mass flow rate as well as particle microstructure. It is therefore recommended to investigate the effect further with respect to the atomization process and to adapt fuel specifications and the mass flow rate model if necessary.

The presence of oxygen in the process atmosphere affects the purity of the powder, particle surface properties, and particle spheroidisation. Therefore, the oxygen and moisture concentrations were kept below 10 ppm, respectively. With regard to process industrialisation, however, a study on the minimum acceptable oxygen and moisture concentration may reduce operation costs of the atomizer glovebox. In particular, as the present safety limit regarding oxygen concentration is 4 % (40'000 ppm). The currently implemented gas purifier, however, extracts system-inherently the maximum possible amount of oxygen and moisture.

Optical analysis of all size classes (target as well as non-target) with respect to particle shape will increase validity of the particle size distributions and provide more insight into the origin of the tailing effect.

A small electromagnetic vibrator or imbalance motor as used in conveyor systems may be installed for support of powder recovery from the powder collection chamber.

Although particles above the target size threshold of 180 µm are currently not considered for fuel plate production, this powder should be reprocessed for rotating electrode fabrication at pre-alloying or induction casting stage. As a result, process efficiency would be increased.

9.3 Conclusion

A prototype production facility for the fabrication of UMo fuel powder was successfully planned, implemented, and tested in the course of the FRM II/CERCA UMo atomizer project. The key component of the production facility is a prototype UMo REP atomizer. The engineering of the atomizer, experimental machine parameterisation, and characterisation of the fabricated U8Mo/U7Mo powder is subject of this work.

The prototype atomizer was granted the nuclear operating licence, was implemented on an industrial production site in France, and proved compatibility with nuclear and operational safety regulations. Experimental atomizer parameterisation proved that fabricated UMo fuel powder fully complied with fuel specifications. Hence, UMo fuel powder can be fabricated for irradiation tests.

More than 60 experimental atomization runs were performed during this study, out of which 24 runs were conducted involving UMo. The prototype design demonstrated throughout the experiments to perform stable and reliably. Notably, repeatable production results were obtained – a key property with regard to industrialisation. In addition, the process proved to yield high purity powder for a highly reactive material. As a consequence, both REP and the presented atomizer design can be considered for industrialisation. In particular, the prototype atomizer may serve as basis for the industrial pilot to reduce development time and costs as it performs reliably, safely, and exceeds prototype requirements with respect to production capacity.

IV

Appendix

A

Dimensioning

A1 HF Spindle Design Point

The applied model refers to equation (7.22). In absence of U8Mo thermophysical properties, uranium properties were used (Table 6-2).

$$D_\mathrm{d} = \frac{1}{\omega}\sqrt{\frac{12\,\sigma}{\rho_\mathrm{l}\,D_\mathrm{re}}} \tag{9.1}$$

σ	Surface tension [N/m]
D_d	Mean droplet diameter [m]
ω	Angular velocity [rad/s]
D_re	Rotating electrode or disk diameter [m]
ρ_l	Liquid density [kg/m^3]

$$D_\mathrm{d} = \frac{1}{2\pi \cdot 40'000\ \mathrm{rpm}}\sqrt{\frac{12\ \cdot 1.65\ \dfrac{\mathrm{N}}{\mathrm{m}}}{17'320\ \dfrac{\mathrm{kg}}{\mathrm{m}^3}\cdot 0.01\ \mathrm{m}}} \tag{9.2}$$

$$D_\mathrm{d} \approx 81\ \mathrm{\mu m} \tag{9.3}$$

Thus, the calculated mean droplet diameter of 81 µm lies in the target size range of < 125 µm.

A2 Brushes

A2.1 Maximum Radial Speed of the Shaft Extension Screw

$$v_{\mathrm{ses,max}} = \omega_{\mathrm{max,spindle}} \cdot \frac{D_{\mathrm{ses}}}{2} \tag{9.4}$$

$v_{\mathrm{ses,max}}$	Max. radial speed of the shaft extension screw [m/s]
$\omega_{\mathrm{max,spindle}}$	Max. angular velocity of the high frequency spindle [rad/s]
D_{ses}	Shaft extension screw diameter [m]

$$v_{\mathrm{ses,max}} = 2\pi \cdot 50'000\ \mathrm{rpm} \cdot \frac{0.011\ \mathrm{m}}{2} \tag{9.5}$$

$$v_{\mathrm{ses,max}} \approx 29\ \frac{\mathrm{m}}{\mathrm{s}} \tag{9.6}$$

A2.2 Perimeter of the Shaft Extension Screw

$$p_{\mathrm{ses}} = \pi \cdot D_{\mathrm{ses}} \tag{9.7}$$

p_{ses}	Perimeter of the shaft extension screw [mm]

$$p_{\mathrm{ses}} = \pi \cdot 0.011\ \mathrm{m} \tag{9.8}$$

$$p_{\mathrm{ses}} \approx 35\ \mathrm{mm} \tag{9.9}$$

An available standard circular arc length of a carbon brush was ~ 9 mm, thus enough space to accommodate 3 brushes was inferred.

A2.3 Maximum Electric Arc Current Density for 3 Brushes

$$i_{\mathrm{max}} = \frac{I}{3 \cdot S_{\mathrm{brush}}} \tag{9.10}$$

$$i_{\mathrm{max}} = \frac{I}{3 \cdot b \cdot h} \tag{9.11}$$

i_{max}	Max. arc current density [A/cm^2]
I	Max. arc current [A]
S_{brush}	Shaft extension screw-brush contact surface [mm^2]
b	Circular arc length of brush contact surface [mm]

h	Height of brush contact surface [mm]

$$i_{\mathrm{max}} = \frac{100\ \mathrm{A}}{3 \cdot 9\ \mathrm{mm} \cdot 12\ \mathrm{mm}} \tag{9.12}$$

$$i_{\mathrm{max}} \approx 31 \frac{\mathrm{A}}{\mathrm{cm}^2} \tag{9.13}$$

A3 Motor Pulley Diameter

$$\frac{n_{\mathrm{motor}}}{n_{\mathrm{spindle}}} = \frac{D_{\mathrm{pu,spindle}}}{D_{\mathrm{pu,motor}}} \tag{9.14}$$

n_{motor}	Maximum motor rotational speed [rpm]
n_{spindle}	Maximum HF spindle rotational speed [rpm]
$D_{\mathrm{pu,spindle}}$	Fixed HF spindle pulley diameter [mm]
$D_{\mathrm{pu,motor}}$	Motor pulley diameter [mm]

$$D_{\mathrm{pu,motor}} = \frac{n_{\mathrm{spindle}}}{n_{\mathrm{motor}}} D_{\mathrm{pu,spindle}} \tag{9.15}$$

$$D_{\mathrm{pu,motor}} = \frac{50'000\ \mathrm{rpm}}{10'000\ \mathrm{rpm}} \cdot 22\ \mathrm{mm} \tag{9.16}$$

$$D_{\mathrm{pu,motor}} = 110\ \mathrm{mm} \tag{9.17}$$

A motor pulley with 120 mm diameter was chosen in order to account for belt slip of around 3’000 rpm to 5’000 rpm.

A4 Belt

A4.1 Belt Length

Theoretical belt length [Wittel *et al.* 2009]:

$$L' = 2e' + \frac{\pi}{2}\left(D_{\mathrm{pu,motor}} + D_{\mathrm{pu,spindle}}\right) + \frac{\left(D_{\mathrm{pu,motor}} - D_{\mathrm{pu,spindle}}\right)^2}{4e'} \tag{9.18}$$

L'	Theoretical belt length [mm]

e'	Minimum shaft centre distance [mm]
$D_{\mathrm{pu,spindle}}$	Fixed HF spindle pulley diameter [mm]
$D_{\mathrm{pu,motor}}$	Motor pulley diameter [mm]

$$L' = 2 \cdot 400\ \mathrm{mm} + \frac{\pi}{2} \cdot (120\ \mathrm{mm} + 22\ \mathrm{mm}) + \frac{(120\ \mathrm{mm} - 22\ \mathrm{mm})^2}{4 \cdot 400} \tag{9.19}$$

$$L' \approx 1029\ \mathrm{mm}. \tag{9.20}$$

Available belt lengths are generally standardised, thus a belt with 1060 mm length was chosen. The minimum shaft centre distance accounts for the diameter of the powder collection chamber of 300 mm and the radius of the motor housing of ~ 95 mm.

A4.2 Maximum Belt Speed

$$v_{\mathrm{belt,max}} = \omega_{\mathrm{max,spindle}} \cdot \frac{D_{\mathrm{pu,motor}}}{2} \tag{9.21}$$

$v_{\mathrm{belt,max}}$	Max. radial speed of the shaft extension screw [m/s]
$\omega_{\mathrm{max,spindle}}$	Max. angular velocity of the high frequency spindle [rad/s]
$D_{\mathrm{pu,motor}}$	Spindle pulley diameter [mm]

$$v_{\mathrm{belt,max}} = 2\pi \cdot 10'000\ \mathrm{rpm} \cdot \frac{0.120\ \mathrm{m}}{2} \tag{9.22}$$

$$v_{\mathrm{belt,max}} \approx 63\,\frac{\mathrm{m}}{\mathrm{s}} \tag{9.23}$$

A4.3 Belt Lengthening

Belt lengthening [Wittel *et al.* 2009] due to an elongation of 0.6 % for operational pre-tension:

$$\varepsilon_1 := \frac{\Delta l_1}{l_0} = \frac{l_1 - l_0}{l_0} \tag{9.24}$$

ε_1	Belt elongation after pre-tension [%]
l_1	Belt length after pre-tension [mm]
l_0	Belt length (tensionless) [mm]

$$\Delta l_1 = 0.006 \cdot 1060\ \mathrm{mm} \tag{9.25}$$

$$\Delta l_1 \approx 6\ \mathrm{mm}. \tag{9.26}$$

Expected total elongation considering centrifugal force:

$$\varepsilon_{\mathrm{t,exp}} = \varepsilon_1 + \varepsilon_2 \tag{9.27}$$

$\varepsilon_{\mathrm{t,exp}}$ Expected total elongation [%]
ε_2 Elongation due to centrifugal force [%]

$$\varepsilon_{\mathrm{t,exp}} = 0.6\,\% + 1.5\ \% \tag{9.28}$$

$$\varepsilon_{\mathrm{t,exp}} = 2.1\ \%. \tag{9.29}$$

Typical values of belt elongation vary between 0.5 % and 1 % for belt speeds of 50 $\mathrm{m\,s^{-1}}$ and 70 $\mathrm{m\,s^{-1}}$ according to [Wittel *et al.* 2009]. The elongation of 1.5 % was suggested by the belt supplier and corresponded to a worst case scenario.

Total belt lengthening due centrifugal force:

$$\Delta l_t = \ \varepsilon_{\mathrm{t,exp}} \cdot l_0 \tag{9.30}$$

Δl_t Total belt lengthening [mm]

$$\Delta l_t = 0.021 \cdot 1060\ \mathrm{mm} \tag{9.31}$$

$$\Delta l_t \approx 22\ \mathrm{mm}. \tag{9.32}$$

Thus, in the worst case, a belt lengthening amounting up to 16 mm due to centrifugal force may occur, considering belt lengthening due to pre-tension of6 mm. As a consequence, it was decided to design and construct a belt-tensioning system.

A4.4 Spring Rate of the Belt

The manufacturer stated that for a belt elongation ≤ 1 % Hooke's law applies and that the belt has no pre-tension. The pull force of the belt at 1 % elongation is 400 N.

$$\mathrm{k_b} = \frac{F_{0.01}}{\Delta l_{0.01}} \tag{9.33}$$

$\mathrm{k_b}$ Belt spring rate [N/mm]
$F_{0.01}$ Pull force of the belt at 1 % elongation [N]
$\Delta l_{0.01}$ Belt lengthening due at 1 % elongation [mm]
$\varepsilon_{0.01}$ Elongation of 1 %

$$\mathrm{k_b} = \frac{F_{0.01}}{\varepsilon_{0.01} l_0} \tag{9.34}$$

$$\mathrm{k_b} = \frac{400\ \mathrm{N}}{0.01 \cdot 1060\ \mathrm{mm}} \tag{9.35}$$

$$\mathrm{k_b} \approx 38\ \frac{\mathrm{N}}{\mathrm{mm}} \tag{9.36}$$

A5 Winch

$$F_{\mathrm{pt}} = \mathrm{k_b} \Delta l_1 \tag{9.37}$$

$\mathrm{k_b}$	Belt spring rate [N/mm]
F_{pt}	Required pull force for operational belt pre-tension [N]

$$F_{\mathrm{pt}} = 38\ \frac{\mathrm{N}}{\mathrm{mm}} \cdot 6\ \mathrm{mm} \tag{9.38}$$

$$F_{\mathrm{pt}} = 228\ \mathrm{N} \tag{9.39}$$

A6 Tension Spring

A tension spring with a Hooke's range up to 254 N and a spring rate of 5.62 N mm^{-1} was chosen in order to reach the operational pull force of 228 N within both the linear range and a reasonable elongation of around 40 mm. The spring keeps the pull force of the spring high as the belt tension decreases due to centrifugal force and allows the belt to re-establish the initial condition at idle state.

A6.1 Minimum Belt Pre-Tension

$$F_{\mathrm{b,pt,min}} = \mathrm{k_b} \varepsilon_{\mathrm{min}} l_0 \tag{9.40}$$

$\mathrm{k_b}$	Belt spring rate [N/mm]
$F_{\mathrm{b,pt,min}}$	Minimum pull force for belt pre-tension [N]
$\varepsilon_{\mathrm{min}}$	Minimum elongation: 0.3 %

$$F_{\mathrm{b,pt,min}} = 38\ \frac{\mathrm{N}}{\mathrm{mm}} \cdot 0.003 \cdot 1060\ \mathrm{mm} \tag{9.41}$$

$$F_{\mathrm{b,pt,min}} \approx 121\ \mathrm{N} \tag{9.42}$$

A6.2 Operational Belt Pre-Tension

See Appendix A5.

A6.3 Change in Shaft Centre Distance

Belt lengthening due to centrifugal force may reach 16 mm under worst case conditions (Appendix A4.3.). Accordingly, the change in shaft centre distance is:

$$\Delta e \approx \frac{\Delta l}{2} \tag{9.43}$$

$\Delta\ e$ Change in shaft centre distance [mm]
$\Delta\ l$ Belt lengthening [mm]

$$\Delta e \approx \frac{16\ \mathrm{mm}}{2} \tag{9.44}$$

$$\Delta e \approx 8\ \mathrm{mm}. \tag{9.45}$$

A6.4 Decrease of Belt Tension (Worst Case)

As the shaft centre distance increases during operation by 8 mm in the worst case, the spring length after belt pre-tension must decrease by the same value (Appendix A6.3). Accordingly, the spring pull and thus belt tension must decrease during operation:

$$F_{\mathrm{b,op,wc}} = F_{\mathrm{pt}} - \mathrm{k}\Delta e \tag{9.46}$$

k Spring rate [N/mm]
$F_{\mathrm{b,rp,wc}}$ Pull force of the belt during operation (worst case) [N]

$$F_{\mathrm{b,op,wc}} = 228\ \mathrm{N} - 5.62\ \frac{\mathrm{N}}{\mathrm{mm}} \cdot 8\ \mathrm{mm} \tag{9.47}$$

$$F_{\mathrm{b,op,wc}} \approx 183\ \mathrm{N}. \tag{9.48}$$

Thus, even under worst case conditions with a belt elongation of 1.5 %, the pull force of the spring is still higher than the necessary minimum pull force (120 N) of the belt (Appendix A6.1).

A6.5 Spring Length after Belt Pre-Tension (Operational)

$$s_{\mathrm{max}} = s_0 + \frac{F_{\mathrm{pt}} - F_0}{k} \tag{9.49}$$

s_{max}	Maximum spring length
s_0	Idle spring length [mm]
k	Spring rate [N/mm]
F_0	Inherent spring pre-tension [N]

$$s_{\mathrm{max}} = 88.9\ \mathrm{mm} + \frac{228\ \mathrm{N} - 23\ \mathrm{N}}{5.62\ \frac{\mathrm{N}}{\mathrm{mm}}} \tag{9.50}$$

$$s_{\mathrm{max}} \approx 125\ \mathrm{mm} \tag{9.51}$$

A7 Motor Carrier

The static friction force must be overcome by the tension spring or belt in order to move the motor carrier:

$$F_{\mathrm{f,st}} = g\mu_{\mathrm{st}}m_{motor+carrier} \tag{9.52}$$

$F_{\mathrm{f,st}}$	Static friction force [N]
$m_{motor+carrier}$	Combined mass of motor carrier and motor [kg]
g	Gravitational acceleration [N/kg]
μ_{st}	Static friction coefficient [-]

$$F_{\mathrm{f,st}} = 30\ \mathrm{kg}\ \cdot 9.81\ \frac{\mathrm{N}}{\mathrm{kg}} \cdot 0.1 \tag{9.53}$$

$$F_{\mathrm{f,st}} \approx 30\ \mathrm{N}. \tag{9.54}$$

B

Granulometry

B1 Stainless Steel

B1.1 Inox-002

Experiment	**Inox-002**	Date	**19.03.2014**
Editor	**R. Schenk**	Operator	**R.Schenk**

Atomization parameters

Rotation speed [rpm]	Potentiometer voltage [V]	Arc current [A]	Humidity [ppm]	Oxygen [ppm]	Consumable type	Consumable fabrication	Consumable mass [g]	Consumable length [mm]	Consumable diameter [mm]	Cons. liquid* density [kg/m^3]	Cathode type
40'000	7.78	70	< 10	< 5	1.4301	machined	20.78	30	10.00		WC20

Atomization results

Powder mass [g]	Consumable rest mass [g]	Atomization efficieny [%]	Atomisation time [s]	Apparent mass flow rate [g/s]	Recovery loss [g]
11.93	8.53	57.41	-	-	0.32

Sieving parameters & results

Sieving time [min]	Set sieving amplitude	Oscillation amplitude [mm]	Sieving loss [g]
6	50	1	-0.01

Powder distribution

Mesh size [µm]	Mesh weight before sieving [g]	Powder mass [g]	Mesh weight after sieving [g]	Corrected powder mass [g]	Mass fraction [%]	Normalized mass fraction [% / µm]*100	Cumulative powder mass [g]	Cumulative undersize [%]
0	73.86	0.00	73.86	0.00	0	0	0.00	0
32	193.42	0.19	193.44	0.21	2	12	0.00	0
45	188.43	1.09	188.43	1.09	9	51	0.19	2
63	196.22	0.15	196.20	0.13	1	5	1.28	11
90	196.68	10.37	196.63	10.32	87	248	1.43	12
125	198.77	0.14	198.77	0.14	1	2	11.80	99
180	201.63	0.00	201.60	- 0.03	0	0	11.94	100
250	200.84	0.00	200.84	0.00	0	0	11.94	100
355	201.01	0.00	201.01	0.00	0	*	11.94	100
Total	1650.86	11.94	1650.78	11.86	100			

B1.2 Inox-003

Experiment	**Inox-003**	Date	**19.03.2014**
Editor	**R. Schenk**	Operator	**R.Schenk**

Atomization parameters

Rotation speed [rpm]	Potentiometer voltage [V]	Arc current [A]	Humidity [ppm]	Oxygen [ppm]	Consumable type	Consumable fabrication	Consumable mass [g]	Consumable length [mm]	Consumable diameter [mm]	Cons. liquid* density [kg/m^3]	Cathode type
40'000	7.78	70	< 10	< 5	1.4301	machined	20.79	30	10.00		WC20

Atomization results

Powder mass [g]	Consumable rest mass [g]	Atomization efficieny [%]	Atomisation time [s]	Apparent mass flow rate [g/s]	Recovery loss [g]
12.52	8.17	60.22	-	-	0.10

Sieving parameters & results

Sieving time [min]	Set sieving amplitude	Oscillation amplitude [mm]	Sieving loss [g]
6	50	1	-0.31

Powder distribution

Mesh size [µm]	Mesh weight before sieving [g]	Powder mass [g]	Mesh weight after sieving [g]	Corrected powder mass [g]	Mass fraction [%]	Normalized mass fraction [% / µm]*100	Cumulative powder mass [g]	Cumulative undersize [%]
0	73.86	0.03	73.86	0.03	0	1	0.00	0
32	193.44	0.20	193.45	0.21	2	12	0.03	0
45	188.43	1.32	188.48	1.37	10	57	0.23	2
63	196.20	0.20	196.22	0.22	2	6	1.55	12
90	196.63	10.97	196.64	10.98	86	244	1.75	14
125	198.77	0.11	198.74	0.08	1	2	12.72	99
180	201.60	0.00	201.61	0.01	0	0	12.83	100
250	200.84	0.00	200.81	- 0.03	0	0	12.83	100
355	201.01	0.00	200.96	- 0.05	0	*	12.83	100
Total	1650.78	12.83	1650.77	12.82	100			

B1.3 Inox-005

Experiment	**Inox-005**	Date	**19.03.2014**
Editor	**R. Schenk**	Operator	**R.Schenk**

Atomization parameters

Rotation speed [rpm]	Potentiometer voltage [V]	Arc current [A]	Humidity [ppm]	Oxygen [ppm]	Consumable type	Consumable fabrication	Consumable mass [g]	Consumable length [mm]	Consumable diameter [mm]	Cons. liquid* density [kg/m^3]	Cathode type
40'000	7.78	70	< 10	< 5	1.4301	machined	20.80	30	10.00		WC20

Atomization results

Powder mass [g]	Consumable rest mass [g]	Atomization efficieny [%]	Atomisation time [s]	Apparent mass flow rate [g/s]	Recovery loss [g]
14.60	6.20	70.19	-	-	0.00

Sieving parameters & results

Sieving time [min]	Set sieving amplitude	Oscillation amplitude [mm]	Sieving loss [g]
6	50	1	2.91

Powder distribution

Mesh size [µm]	Mesh weight before sieving [g]	Powder mass [g]	Mesh weight after sieving [g]	Corrected powder mass [g]	Mass fraction [%]	Normalized mass fraction [% / µm]*100	Cumulative powder mass [g]	Cumulative undersize [%]
0	73.86	0.00	73.84	- 0.02	0	0	0.00	0
32	193.45	0.25	193.41	0.21	2	16	0.00	0
45	188.48	1.50	188.40	1.42	13	71	0.25	2
63	196.22	0.28	196.18	0.24	2	9	1.75	15
90	196.64	9.46	196.63	9.45	81	231	2.03	17
125	198.74	0.20	198.72	0.18	2	3	11.49	98
180	201.61	0.00	201.64	0.03	0	0	11.69	100
250	200.81	0.00	200.81	0.00	0	0	11.69	100
355	200.96	0.00	200.98	0.02	0	*	11.69	100
Total	1650.77	11.69	1650.61	11.53	100			

B1.4 Inox-006

Experiment	**Inox-006**	Date	**19.03.2014**
Editor	**R. Schenk**	Operator	**R.Schenk**

Atomization parameters

Rotation speed [rpm]	Potentiometer voltage [V]	Arc current [A]	Humidity [ppm]	Oxygen [ppm]	Consumable type	Consumable fabrication	Consumable mass [g]	Consumable length [mm]	Consumable diameter [mm]	Cons. liquid* density [kg/m^3]	Cathode type
40'000	7.78	70	< 10	< 5	1.4301	machined	20.76	30	10.00		WC20

Atomization results

Powder mass [g]	Consumable rest mass [g]	Atomization efficieny [%]	Atomisation time [s]	Apparent mass flow rate [g/s]	Recovery loss [g]
14.21	6.44	68.45	-	-	0.11

Sieving parameters & results

Sieving time [min]	Set sieving amplitude	Oscillation amplitude [mm]	Sieving loss [g]
6	50	1	0.49

Powder distribution

Mesh size [µm]	Mesh weight before sieving [g]	Powder mass [g]	Mesh weight after sieving [g]	Corrected powder mass [g]	Mass fraction [%]	Normalized mass fraction [% / µm]*100	Cumulative powder mass [g]	Cumulative undersize [%]
0	73.84	0.05	73.84	0.05	0	1	0.00	0
32	193.41	0.25	193.40	0.24	2	14	0.05	0
45	188.40	1.35	188.40	1.35	10	55	0.30	2
63	196.18	0.34	196.18	0.34	2	9	1.65	12
90	196.63	11.32	196.61	11.30	83	236	1.99	15
125	198.72	0.41	198.71	0.40	3	5	13.31	97
180	201.64	0.00	201.60	- 0.04	0	0	13.72	100
250	200.81	0.00	200.81	0.00	0	0	13.72	100
355	200.98	0.00	200.97	- 0.01	0	*	13.72	100
Total	1650.61	13.72	1650.52	13.63	100			

B1.5 Inox-008

Experiment	**Inox-008**	Date	**19.03.2014**
Editor	**R. Schenk**	Operator	**R.Schenk**

Atomization parameters

Rotation speed [rpm]	Potentiometer voltage [V]	Arc current [A]	Humidity [ppm]	Oxygen [ppm]	Consumable type	Consumable fabrication	Consumable mass [g]	Consumable length [mm]	Consumable diameter [mm]	Cons. liquid* density [kg/m^3]	Cathode type
40'000	7.78	70	< 10	< 5	1.4301	machined	20.78	30	10.00		WC20

Atomization results

Powder mass [g]	Consumable rest mass [g]	Atomization efficieny [%]	Atomisation time [s]	Apparent mass flow rate [g/s]	Recovery loss [g]
14.32	6.41	68.91	32.1	0.448	0.05

Sieving parameters & results

Sieving time [min]	Set sieving amplitude	Oscillation amplitude [mm]	Sieving loss [g]
6	50	1	0.14

Powder distribution

Mesh size [µm]	Mesh weight before sieving [g]	Powder mass [g]	Mesh weight after sieving [g]	Corrected powder mass [g]	Mass fraction [%]	Normalized mass fraction [% / µm]*100	Cumulative powder mass [g]	Cumulative undersize [%]
0	73.84	0.00	73.84	0.00	0	0	0.00	0
32	193.40	0.30	193.48	0.38	2	16	0.00	0
45	188.40	1.34	188.50	1.44	9	52	0.30	2
63	196.18	0.30	196.27	0.39	2	8	1.64	12
90	196.61	12.01	196.68	12.08	85	242	1.94	14
125	198.71	0.23	198.72	0.24	2	3	13.95	98
180	201.60	0.00	201.68	0.08	0	0	14.18	100
250	200.81	0.00	200.89	0.08	0	0	14.18	100
355	200.97	0.00	201.06	0.09	0	*	14.18	100
Total	1650.52	14.18	1651.12	14.78	100			

B1.6 Inox-009

Experiment	**Inox-009**	Date	**19.03.2014**
Editor	**R. Schenk**	Operator	**R.Schenk**

Atomization parameters

Rotation speed [rpm]	Potentiometer voltage [V]	Arc current [A]	Humidity [ppm]	Oxygen [ppm]	Consumable type	Consumable fabrication	Consumable mass [g]	Consumable length [mm]	Consumable diameter [mm]	Cons. liquid* density [kg/m^3]	Cathode type
40'000	7.78	70	< 10	< 5	1.4301	machined	20.77	30	10.00		WC20

Atomization results

Powder mass [g]	Consumable rest mass [g]	Atomization efficieny [%]	Atomisation time [s]	Apparent mass flow rate [g/s]	Recovery loss [g]
13.44	7.38	64.71	31.5	0.425	-0.05

Sieving parameters & results

Sieving time [min]	Set sieving amplitude	Oscillation amplitude [mm]	Sieving loss [g]
6	50	1	-0.13

Powder distribution

Mesh size [µm]	Mesh weight before sieving [g]	Powder mass [g]	Mesh weight after sieving [g]	Corrected powder mass [g]	Mass fraction [%]	Normalized mass fraction [% / µm]*100	Cumulative powder mass [g]	Cumulative undersize [%]
0	73.84	0.05	73.85	0.06	0	1	0.00	0
32	193.48	0.25	193.45	0.22	2	14	0.05	0
45	188.50	1.34	188.46	1.30	10	55	0.30	2
63	196.27	0.49	196.21	0.43	4	13	1.64	12
90	196.68	10.77	196.65	10.74	79	227	2.13	16
125	198.72	0.67	198.72	0.67	5	9	12.90	95
180	201.68	0.00	201.64	- 0.04	0	0	13.57	100
250	200.89	0.00	200.85	- 0.04	0	0	13.57	100
355	201.06	0.00	201.02	- 0.04	0	*	13.57	100
Total	1651.12	13.57	1650.85	13.30	100			

B1.7 Inox-010

Experiment	**Inox-010**	Date	**19.03.2014**
Editor	**R. Schenk**	Operator	**R.Schenk**

Atomization parameters

Rotation speed [rpm]	Potentiometer voltage [V]	Arc current [A]	Humidity [ppm]	Oxygen [ppm]	Consumable type	Consumable fabrication	Consumable mass [g]	Consumable length [mm]	Consumable diameter [mm]	Cons. liquid* density [kg/m^3]	Cathode type
40'000	7.78	70	< 10	< 5	1.4301	machined	20.79	30	10.00		WC20

Atomization results

Powder mass [g]	Consumable rest mass [g]	Atomization efficieny [%]	Atomisation time [s]	Apparent mass flow rate [g/s]	Recovery loss [g]
14.00	6.74	67.34	33.1	0.424	0.05

Sieving parameters & results

Sieving time [min]	Set sieving amplitude	Oscillation amplitude [mm]	Sieving loss [g]
6	50	1	0.12

Powder distribution

Mesh size [µm]	Mesh weight before sieving [g]	Powder mass [g]	Mesh weight after sieving [g]	Corrected powder mass [g]	Mass fraction [%]	Normalized mass fraction [% / µm]*100	Cumulative powder mass [g]	Cumulative undersize [%]
0	73.85	0.04	73.83	0.02	0	1	0.00	0
32	193.45	0.27	193.44	0.26	2	15	0.04	0
45	188.46	1.24	188.49	1.27	9	50	0.31	2
63	196.21	0.44	196.21	0.44	3	12	1.55	11
90	196.65	11.26	196.64	11.25	81	232	1.99	14
125	198.72	0.63	198.75	0.66	5	8	13.25	95
180	201.64	0.00	201.64	0.00	0	0	13.88	100
250	200.85	0.00	200.83	- 0.02	0	0	13.88	100
355	201.02	0.00	201.00	- 0.02	0	*	13.88	100
Total	1650.85	13.88	1650.83	13.86	100			

B1.8 Inox-011

Experiment	**Inox-011**	Date	**19.03.2014**
Editor	**R. Schenk**	Operator	**R.Schenk**

Atomization parameters

Rotation speed [rpm]	Potentiometer voltage [V]	Arc current [A]	Humidity [ppm]	Oxygen [ppm]	Consumable type	Consumable fabrication	Consumable mass [g]	Consumable length [mm]	Consumable diameter [mm]	Cons. liquid* density [kg/m^3]	Cathode type
40'000	7.78	70	< 10	< 5	1.4301	machined	20.77	30	10.00		WC20

Atomization results

Powder mass [g]	Consumable rest mass [g]	Atomization efficieny [%]	Atomisation time [s]	Apparent mass flow rate [g/s]	Recovery loss [g]
15.20	5.70	73.18	34.9	0.432	-0.13

Sieving parameters & results

Sieving time [min]	Set sieving amplitude	Oscillation amplitude [mm]	Sieving loss [g]
6	50	1	-0.04

Powder distribution

Mesh size [µm]	Mesh weight before sieving [g]	Powder mass [g]	Mesh weight after sieving [g]	Corrected powder mass [g]	Mass fraction [%]	Normalized mass fraction [% / µm]*100	Cumulative powder mass [g]	Cumulative undersize [%]
0	73.83	0.05	73.83	0.05	0	1	0.00	0
32	193.44	0.27	193.43	0.26	2	14	0.05	0
45	188.49	1.45	188.45	1.41	10	53	0.32	2
63	196.21	0.54	196.20	0.53	4	13	1.77	12
90	196.64	12.18	196.64	12.18	80	228	2.31	15
125	198.75	0.75	198.69	0.69	5	9	14.49	95
180	201.64	0.00	201.64	0.00	0	0	15.24	100
250	200.83	0.00	200.84	0.01	0	0	15.24	100
355	201.00	0.00	201.00	0.00	0	*	15.24	100
Total	1650.83	15.24	1650.72	15.13	100			

B1.9 Inox-012

Experiment	**Inox-012**	Date	**19.03.2014**
Editor	**R. Schenk**	Operator	**R.Schenk**

Atomization parameters

Rotation speed [rpm]	Potentiometer voltage [V]	Arc current [A]	Humidity [ppm]	Oxygen [ppm]	Consumable type	Consumable fabrication	Consumable mass [g]	Consumable length [mm]	Consumable diameter [mm]	Cons. liquid* density [kg/m^3]	Cathode type
40'000	7.78	70	< 10	< 5	1.4301	machined	20.75	30	10.00		WC20

Atomization results

Powder mass [g]	Consumable rest mass [g]	Atomization efficieny [%]	Atomisation time [s]	Apparent mass flow rate [g/s]	Recovery loss [g]
14.84	5.92	71.52	-	-	-0.01

Sieving parameters & results

Sieving time [min]	Set sieving amplitude	Oscillation amplitude [mm]	Sieving loss [g]
6	50	1	0.04

Powder distribution

Mesh size [µm]	Mesh weight before sieving [g]	Powder mass [g]	Mesh weight after sieving [g]	Corrected powder mass [g]	Mass fraction [%]	Normalized mass fraction [% / µm]*100	Cumulative powder mass [g]	Cumulative undersize [%]
0	73.83	0.05	73.85	0.07	0	1	0.00	0
32	193.43	0.30	193.46	0.33	2	16	0.05	0
45	188.45	1.36	188.43	1.34	9	51	0.35	2
63	196.20	0.50	196.23	0.53	3	13	1.71	12
90	196.64	11.85	196.66	11.87	80	229	2.21	15
125	198.69	0.74	198.73	0.78	5	9	14.06	95
180	201.64	0.00	201.64	0.00	0	0	14.80	100
250	200.84	0.00	200.85	0.01	0	0	14.80	100
355	201.00	0.00	200.99	- 0.01	0	*	14.80	100
Total	1650.72	14.80	1650.84	14.92	100			

B1.10 Inox-013

Experiment	**Inox-013**	Date	**19.03.2014**
Editor	**R. Schenk**	Operator	**R.Schenk**

Atomization parameters

Rotation speed [rpm]	Potentiometer voltage [V]	Arc current [A]	Humidity [ppm]	Oxygen [ppm]	Consumable type	Consumable fabrication	Consumable mass [g]	Consumable length [mm]	Consumable diameter [mm]	Cons. liquid* density [kg/m^3]	Cathode type
40'000	7.78	70	< 10	< 5	1.4301	machined	20.74	30	10.00		WC20

Atomization results

Powder mass [g]	Consumable rest mass [g]	Atomization efficieny [%]	Atomisation time [s]	Apparent mass flow rate [g/s]	Recovery loss [g]
12.30	7.85	59.31	-	-	0.59

Sieving parameters & results

Sieving time [min]	Set sieving amplitude	Oscillation amplitude [mm]	Sieving loss [g]
6	50	1	0.13

Powder distribution

Mesh size [µm]	Mesh weight before sieving [g]	Powder mass [g]	Mesh weight after sieving [g]	Corrected powder mass [g]	Mass fraction [%]	Normalized mass fraction [% / µm]*100	Cumulative powder mass [g]	Cumulative undersize [%]
0	73.85	0.00	73.88	0.03	0	0	0.00	0
32	193.46	0.18	193.44	0.16	1	11	0.00	0
45	188.43	1.04	188.41	1.02	9	47	0.18	1
63	196.23	0.56	196.20	0.53	5	17	1.22	10
90	196.66	9.89	196.63	9.86	81	232	1.78	15
125	198.73	0.50	198.75	0.52	4	7	11.67	96
180	201.64	0.00	201.62	- 0.02	0	0	12.17	100
250	200.85	0.00	200.87	0.02	0	0	12.17	100
355	200.99	0.00	201.00	0.01	0	*	12.17	100
Total	1650.84	12.17	1650.80	12.13	100			

B1.11 Inox-014

Experiment **Inox-014**
Editor **R. Schenk**
Date **08.09.2014**
Operator **C. Moyroud**

Atomization parameters

Rotation speed [rpm]	Potentiometer voltage [V]	Arc current [A]	Humidity [ppm]	Oxygen [ppm]	Consumable type	Consumable fabrication	Consumable mass [g]	Consumable length [mm]	Consumable diameter [mm]	Cons. liquid* density [kg/m^3]	Cathode type
20'000	3.95	70	< 3	< 15	1.4301	machined	20.77	30	10.00		WC20

Atomization results

Powder mass [g]	Consumable rest mass [g]	Atomization efficieny [%]	Atomisation time [s]	Apparent mass flow rate [g/s]	Recovery loss [g]
14.66	6.01	70.58	37.9	0.4	0.10

Sieving parameters & results

Sieving time [min]	Set sieving amplitude	Oscillation amplitude [mm]	Sieving loss [g]
6	50	1	-0.03

Powder distribution

Mesh size [µm]	Mesh weight before sieving [g]	Powder mass [g]	Mesh weight after sieving [g]	Corrected powder mass [g]	Mass fraction [%]	Normalized mass fraction [% / µm]*100	Cumulative powder mass [g]	Cumulative undersize [%]
0	70.72	0.00	70.73	0.01	0	0	0.00	0
32	193.65	0.00	193.63	- 0.02	0	0	0.00	0
45	188.56	0.10	188.59	0.13	1	4	0.00	0
63	196.33	0.49	196.36	0.52	3	12	0.10	1
90	196.86	0.40	196.88	0.42	3	8	0.59	4
125	198.91	0.47	198.92	0.48	3	6	0.99	7
180	201.80	12.88	201.82	12.90	88	125	1.46	10
250	200.97	0.35	201.01	0.39	2	2	14.34	98
355	201.15	0.00	201.17	0.02	0	*	14.69	100
Total	1648.95	14.69	1649.11	14.85	100			

B1.12 Inox-015

Experiment	**Inox-015**	Date	**08.09.2014**
Editor	**R. Schenk**	Operator	**C. Moyroud**

Atomization parameters

Rotation speed [rpm]	Potentiometer voltage [V]	Arc current [A]	Humidity [ppm]	Oxygen [ppm]	Consumable type	Consumable fabrication	Consumable mass [g]	Consumable length [mm]	Consumable diameter [mm]	Cons. liquid* density [kg/m^3]	Cathode type
40'000	7.78	70	< 3	< 16	1.4301	machined	20.75	30	10.00		WC20

Atomization results

Powder mass [g]	Consumable rest mass [g]	Atomization efficieny [%]	Atomisation time [s]	Apparent mass flow rate [g/s]	Recovery loss [g]
15.54	5.24	74.89	36.5	0.4	-0.03

Sieving parameters & results

Sieving time [min]	Set sieving amplitude	Oscillation amplitude [mm]	Sieving loss [g]
6	50	1	0.12

Powder distribution

Mesh size [µm]	Mesh weight before sieving [g]	Powder mass [g]	Mesh weight after sieving [g]	Corrected powder mass [g]	Mass fraction [%]	Normalized mass fraction [% / µm]*100	Cumulative powder mass [g]	Cumulative undersize [%]
0	70.74	0.05	70.74	0.05	0	1	0.00	0
32	193.61	0.24	193.70	0.33	2	12	0.05	0
45	188.59	0.88	188.63	0.92	6	32	0.29	2
63	196.36	0.80	196.36	0.80	5	19	1.17	8
90	196.88	10.58	196.87	10.57	69	196	1.97	13
125	198.90	2.66	198.91	2.67	17	31	12.55	81
180	201.81	0.21	201.82	0.22	1	2	15.21	99
250	200.99	0.00	200.97	- 0.02	0	0	15.42	100
355	201.15	0.00	201.14	- 0.01	0	*	15.42	100
Total	1649.03	15.42	1649.14	15.53	100			

B1.13 Inox-016

Experiment	**Inox-016**	Date	**08.09.2014**
Editor	**R. Schenk**	Operator	**C. Moyroud**

Atomization parameters

Rotation speed [rpm]	Potentiometer voltage [V]	Arc current [A]	Humidity [ppm]	Oxygen [ppm]	Consumable type	Consumable fabrication	Consumable mass [g]	Consumable length [mm]	Consumable diameter [mm]	Cons. liquid* density [kg/m^3]	Cathode type
30'000	5.98	70	< 3	< 15	1.4301	machined	20.84	30	10.00		WC20

Atomization results

Powder mass [g]	Consumable rest mass [g]	Atomization efficieny [%]	Atomisation time [s]	Apparent mass flow rate [g/s]	Recovery loss [g]
15.09	5.71	72.41	37.5	0.4	0.04

Sieving parameters & results

Sieving time [min]	Set sieving amplitude	Oscillation amplitude [mm]	Sieving loss [g]
6	50	1	0.38

Powder distribution

Mesh size [µm]	Mesh weight before sieving [g]	Powder mass [g]	Mesh weight after sieving [g]	Corrected powder mass [g]	Mass fraction [%]	Normalized mass fraction [% / µm]*100	Cumulative powder mass [g]	Cumulative undersize [%]
0	70.72	0.00	70.75	0.03	0	0	0.00	0
32	193.83	0.00	193.81	- 0.02	0	0	0.00	0
45	188.77	0.20	188.76	0.19	1	8	0.00	0
63	196.37	0.71	196.40	0.74	5	18	0.20	1
90	197.08	0.81	197.08	0.81	6	16	0.91	6
125	199.02	12.62	199.04	12.64	86	156	1.72	12
180	201.78	0.37	201.85	0.44	3	4	14.34	97
250	201.00	0.00	201.00	0.00	0	0	14.71	100
355	201.14	0.00	201.13	- 0.01	0	*	14.71	100
Total	1649.71	14.71	1649.82	14.82	100			

B1.14 Inox-018

Experiment	**Inox-018**	Date	**08.09.2014**
Editor	**R. Schenk**	Operator	**C. Moyroud**

Atomization parameters

Rotation speed [rpm]	Potentiometer voltage [V]	Arc current [A]	Humidity [ppm]	Oxygen [ppm]	Consumable type	Consumable fabrication	Consumable mass [g]	Consumable length [mm]	Consumable diameter [mm]	Cons. liquid* density [kg/m^3]	Cathode type
50'000	9.54	70	< 3	< 15	1.4301	machined	20.79	30	10.00		WC20

Atomization results

Powder mass [g]	Consumable rest mass [g]	Atomization efficieny [%]	Atomisation time [s]	Apparent mass flow rate [g/s]	Recovery loss [g]
14.91	5.79	71.72	37.3	0.4	0.09

Sieving parameters & results

Sieving time [min]	Set sieving amplitude	Oscillation amplitude [mm]	Sieving loss [g]
6	50	1	0.72

Powder distribution

Mesh size [µm]	Mesh weight before sieving [g]	Powder mass [g]	Mesh weight after sieving [g]	Corrected powder mass [g]	Mass fraction [%]	Normalized mass fraction [% / µm]*100	Cumulative powder mass [g]	Cumulative undersize [%]
0	70.72	0.14	70.72	0.14	1	3	0.00	0
32	193.79	0.87	193.83	0.91	6	47	0.14	1
45	188.74	0.45	188.77	0.48	3	18	1.01	7
63	196.38	9.27	196.37	9.26	65	242	1.46	10
90	197.02	3.03	197.08	3.09	21	61	10.73	76
125	199.03	0.43	199.02	0.42	3	6	13.76	97
180	201.82	0.00	201.78	- 0.04	0	0	14.19	100
250	200.99	0.00	201.00	0.01	0	0	14.19	100
355	201.10	0.00	201.14	0.04	0	*	14.19	100
Total	1649.59	14.19	1649.71	14.31	100			

B1.15 Inox-019

Experiment	**Inox-019**	Date	**08.09.2014**
Editor	**R. Schenk**	Operator	**R. Schenk**

Atomization parameters

Rotation speed [rpm]	Potentiometer voltage [V]	Arc current [A]	Humidity [ppm]	Oxygen [ppm]	Consumable type	Consumable fabrication	Consumable mass [g]	Consumable length [mm]	Consumable diameter [mm]	Cons. liquid* density [kg/m^3]	Cathode type
20'000	3.95	70	< 4	< 15	1.4301	machined	39.37	30	14.00		WC20

Atomization results

Powder mass [g]	Consumable rest mass [g]	Atomization efficieny [%]	Atomisation time [s]	Apparent mass flow rate [g/s]	Recovery loss [g]
30.92	8.64	78.54	82.1	0.4	-0.19

Sieving parameters & results

Sieving time [min]	Set sieving amplitude	Oscillation amplitude [mm]	Sieving loss [g]
6	50	1	0.08

Powder distribution

Mesh size [µm]	Mesh weight before sieving [g]	Powder mass [g]	Mesh weight after sieving [g]	Corrected powder mass [g]	Mass fraction [%]	Normalized mass fraction [% / µm]*100	Cumulative powder mass [g]	Cumulative undersize [%]
0	70.73	0.00	70.73	0.00	0	0	0.00	0
32	193.63	0.16	193.60	0.13	1	4	0.00	0
45	188.59	0.45	188.60	0.46	1	8	0.16	1
63	196.36	0.91	196.33	0.88	3	11	0.61	2
90	196.79	0.55	196.80	0.56	2	5	1.52	5
125	198.89	19.59	198.84	19.54	64	115	2.07	7
180	201.81	6.94	201.77	6.90	23	32	21.66	70
250	200.96	1.93	200.98	1.95	6	6	28.60	93
355	201.14	0.31	201.13	0.30	1	*	30.53	99
Total	1648.90	30.84	1648.78	30.72	100			

B1.16 Inox-020

Experiment	**Inox-020**	Date	**08.09.2014**
Editor	**R. Schenk**	Operator	**C. Moyroud**

Atomization parameters

Rotation speed [rpm]	Potentiometer voltage [V]	Arc current [A]	Humidity [ppm]	Oxygen [ppm]	Consumable type	Consumable fabrication	Consumable mass [g]	Consumable length [mm]	Consumable diameter [mm]	Cons. liquid* density [kg/m^3]	Cathode type
30'000	5.8	70	< 4	< 15	1.4301	machined	39.40	30	14.00		WC20

Atomization results

Powder mass [g]	Consumable rest mass [g]	Atomization efficieny [%]	Atomisation time [s]	Apparent mass flow rate [g/s]	Recovery loss [g]
26.63	12.67	67.59	75.2	0.4	0.10

Sieving parameters & results

Sieving time [min]	Set sieving amplitude	Oscillation amplitude [mm]	Sieving loss [g]
6	50	1	0.03

Powder distribution

Mesh size [µm]	Mesh weight before sieving [g]	Powder mass [g]	Mesh weight after sieving [g]	Corrected powder mass [g]	Mass fraction [%]	Normalized mass fraction [% / µm]*100	Cumulative powder mass [g]	Cumulative undersize [%]
0	70.73	0.10	70.72	0.09	0	1	0.00	0
32	193.63	0.45	193.65	0.47	2	13	0.10	0
45	188.59	0.88	188.56	0.85	3	18	0.55	2
63	196.34	0.60	196.33	0.59	2	8	1.43	5
90	196.85	18.74	196.86	18.75	70	201	2.03	8
125	198.89	3.98	198.91	4.00	15	27	20.77	78
180	201.78	0.81	201.80	0.83	3	4	24.75	93
250	200.96	0.57	200.97	0.58	2	2	25.56	96
355	201.14	0.47	201.15	0.48	2	*	26.13	98
Total	1648.91	26.60	1648.95	26.64	100			

B1.17 Inox-021

Experiment	**Inox-021**	Date	**08.09.2014**
Editor	**R. Schenk**	Operator	**C. Moyroud**

Atomization parameters

Rotation speed [rpm]	Potentiometer voltage [V]	Arc current [A]	Humidity [ppm]	Oxygen [ppm]	Consumable type	Consumable fabrication	Consumable mass [g]	Consumable length [mm]	Consumable diameter [mm]	Cons. liquid* density [kg/m^3]	Cathode type
40'000	7.78	70	< 4	< 15	1.4301	machined	39.37	30	14.00		WC20

Atomization results

Powder mass [g]	Consumable rest mass [g]	Atomization efficieny [%]	Atomisation time [s]	Apparent mass flow rate [g/s]	Recovery loss [g]
28.02	11.28	71.17	78.4	0.4	0.07

Sieving parameters & results

Sieving time [min]	Set sieving amplitude	Oscillation amplitude [mm]	Sieving loss [g]
6	50	1	0.37

Powder distribution

Mesh size [µm]	Mesh weight before sieving [g]	Powder mass [g]	Mesh weight after sieving [g]	Corrected powder mass [g]	Mass fraction [%]	Normalized mass fraction [% / µm]*100	Cumulative powder mass [g]	Cumulative undersize [%]
0	70.75	0.38	70.73	0.36	1	4	0.00	0
32	193.81	0.79	193.77	0.75	3	22	0.38	1
45	188.76	0.55	188.72	0.51	2	11	1.17	4
63	196.40	20.45	196.36	20.41	74	274	1.72	6
90	197.08	2.34	197.10	2.36	8	24	22.17	80
125	199.04	0.76	199.02	0.74	3	5	24.51	89
180	201.85	0.65	201.79	0.59	2	3	25.27	91
250	201.00	1.08	200.97	1.05	4	4	25.92	94
355	201.13	0.65	201.14	0.66	2	*	27.00	98
Total	1649.82	27.65	1649.60	27.43	100			

B1.18 Inox-022

Experiment	**Inox-022**	Date	**11.09.2014**
Editor	**R. Schenk**	Operator	**R. Schenk**

Atomization parameters

Rotation speed [rpm]	Potentiometer voltage [V]	Arc current [A]	Humidity [ppm]	Oxygen [ppm]	Consumable type	Consumable fabrication	Consumable mass [g]	Consumable length [mm]	Consumable diameter [mm]	Cons. liquid* density [kg/m^3]	Cathode type
40'000	7.78	100	< 2	< 9	1.4301	machined	39.43	30	14.00		WC20

Atomization results

Powder mass [g]	Consumable rest mass [g]	Atomization efficieny [%]	Atomisation time [s]	Apparent mass flow rate [g/s]	Recovery loss [g]
29.09	10.23	73.78	52.8	0.6	0.11

Sieving parameters & results

Sieving time [min]	Set sieving amplitude	Oscillation amplitude [mm]	Sieving loss [g]
6	50	1	0.79

Powder distribution

Mesh size [µm]	Mesh weight before sieving [g]	Powder mass [g]	Mesh weight after sieving [g]	Corrected powder mass [g]	Mass fraction [%]	Normalized mass fraction [% / µm]*100	Cumulative powder mass [g]	Cumulative undersize [%]
0	70.73	0.54	70.73	0.54	2	6	0.00	0
32	193.65	1.47	193.76	1.58	5	40	0.54	2
45	188.59	0.85	188.72	0.98	3	17	2.01	7
63	196.36	19.00	196.36	19.00	67	249	2.86	10
90	196.89	3.74	197.01	3.86	13	38	21.86	77
125	198.97	0.68	198.97	0.68	2	4	25.60	90
180	201.80	0.60	201.81	0.61	2	3	26.28	93
250	201.01	1.00	201.01	1.00	4	3	26.88	95
355	201.16	0.42	201.16	0.42	1	*	27.88	99
Total	1649.16	28.30	1649.53	28.67	100			

B1.19 Inox-023

Experiment	**Inox-023**	Date	**11.09.2014**
Editor	**R. Schenk**	Operator	**C. Moyroud**

Atomization parameters

Rotation speed [rpm]	Potentiometer voltage [V]	Arc current [A]	Humidity [ppm]	Oxygen [ppm]	Consumable type	Consumable fabrication	Consumable mass [g]	Consumable length [mm]	Consumable diameter [mm]	Cons. liquid* density [kg/m^3]	Cathode type
20'000	3.95	100	< 3	< 15	1.4301	machined	39.39	30	14.00		WC20

Atomization results

Powder mass [g]	Consumable rest mass [g]	Atomization efficieny [%]	Atomisation time [s]	Apparent mass flow rate [g/s]	Recovery loss [g]
29.11	10.35	73.90	52.2	0.6	-0.07

Sieving parameters & results

Sieving time [min]	Set sieving amplitude	Oscillation amplitude [mm]	Sieving loss [g]
6	50	1	0.14

Powder distribution

Mesh size [µm]	Mesh weight before sieving [g]	Powder mass [g]	Mesh weight after sieving [g]	Corrected powder mass [g]	Mass fraction [%]	Normalized mass fraction [% / µm]*100	Cumulative powder mass [g]	Cumulative undersize [%]
0	70.73	0.00	70.74	0.01	0	0	0.00	0
32	193.65	0.07	193.61	0.03	0	2	0.00	0
45	188.58	0.32	188.59	0.33	1	6	0.07	0
63	196.34	1.18	196.36	1.20	4	15	0.39	1
90	196.91	0.68	196.88	0.65	2	7	1.57	5
125	198.92	15.89	198.90	15.87	55	100	2.25	8
180	201.80	9.62	201.81	9.63	33	47	18.14	63
250	201.00	1.17	200.99	1.16	4	4	27.76	96
355	201.14	0.04	201.15	0.05	0	*	28.93	100
Total	1649.07	28.97	1649.03	28.93	100			

B1.20 Inox-024

Experiment	**Inox-024**	Date	**11.09.2014**
Editor	**R. Schenk**	Operator	**R. Schenk**

Atomization parameters

Rotation speed [rpm]	Potentiometer voltage [V]	Arc current [A]	Humidity [ppm]	Oxygen [ppm]	Consumable type	Consumable fabrication	Consumable mass [g]	Consumable length [mm]	Consumable diameter [mm]	Cons. liquid* density [kg/m^3]	Cathode type
30'000	5.98	100	< 3	< 12	1.4301	machined	39.41	30	14.00		WC20

Atomization results

Powder mass [g]	Consumable rest mass [g]	Atomization efficieny [%]	Atomisation time [s]	Apparent mass flow rate [g/s]	Recovery loss [g]
28.70	10.80	72.82	51.4	0.6	-0.09

Sieving parameters & results

Sieving time [min]	Set sieving amplitude	Oscillation amplitude [mm]	Sieving loss [g]
6	50	1	0.42

Powder distribution

Mesh size [µm]	Mesh weight before sieving [g]	Powder mass [g]	Mesh weight after sieving [g]	Corrected powder mass [g]	Mass fraction [%]	Normalized mass fraction [% / µm]*100	Cumulative powder mass [g]	Cumulative undersize [%]
0	70.73	0.10	70.72	0.09	0	1	0.00	0
32	193.76	0.42	193.79	0.45	1	11	0.10	0
45	188.72	1.39	188.74	1.41	5	27	0.52	2
63	196.36	0.85	196.38	0.87	3	11	1.91	7
90	197.01	18.28	197.02	18.29	65	185	2.76	10
125	198.97	6.02	199.03	6.08	21	39	21.04	74
180	201.81	0.79	201.82	0.80	3	4	27.06	96
250	201.01	0.34	200.99	0.32	1	1	27.85	98
355	201.16	0.09	201.10	0.03	0	*	28.19	100
Total	1649.53	28.28	1649.59	28.34	100			

B1.21 Inox-025

Experiment	**Inox-025**	Date	**11.09.2014**
Editor	**R. Schenk**	Operator	**R. Schenk**

Atomization parameters

Rotation speed [rpm]	Potentiometer voltage [V]	Arc current [A]	Humidity [ppm]	Oxygen [ppm]	Consumable type	Consumable fabrication	Consumable mass [g]	Consumable length [mm]	Consumable diameter [mm]	Cons. liquid* density [kg/m^3]	Cathode type
20'000	3.95	100	< 3	< 18	1.4301	machined	20.78	30	10.00		WC20

Atomization results

Powder mass [g]	Consumable rest mass [g]	Atomization efficieny [%]	Atomisation time [s]	Apparent mass flow rate [g/s]	Recovery loss [g]
13.71	6.99	65.98	25.1	0.5	0.08

Sieving parameters & results

Sieving time [min]	Set sieving amplitude	Oscillation amplitude [mm]	Sieving loss [g]
6	50	1	0.16

Powder distribution

Mesh size [µm]	Mesh weight before sieving [g]	Powder mass [g]	Mesh weight after sieving [g]	Corrected powder mass [g]	Mass fraction [%]	Normalized mass fraction [% / µm]*100	Cumulative powder mass [g]	Cumulative undersize [%]
0	70.73	0.00	70.73	0.00	0	0	0.00	0
32	193.63	0.00	193.65	0.02	0	0	0.00	0
45	188.59	0.07	188.58	0.06	1	3	0.00	0
63	196.36	0.45	196.34	0.43	3	12	0.07	1
90	196.88	0.42	196.91	0.45	3	9	0.52	4
125	198.92	0.38	198.92	0.38	3	5	0.94	7
180	201.82	11.59	201.80	11.57	86	122	1.32	10
250	201.01	0.64	201.00	0.63	5	4	12.91	95
355	201.17	0.00	201.14	- 0.03	0	*	13.55	100
Total	1649.11	13.55	1649.07	13.51	100			

B1.22 Inox-026

Experiment	**Inox-026**	Date	**11.09.2014**
Editor	**R. Schenk**	Operator	**R. Schenk**

Atomization parameters

Rotation speed [rpm]	Potentiometer voltage [V]	Arc current [A]	Humidity [ppm]	Oxygen [ppm]	Consumable type	Consumable fabrication	Consumable mass [g]	Consumable length [mm]	Consumable diameter [mm]	Cons. liquid* density [kg/m^3]	Cathode type
30'000	5.98	100	< 3	< 20	1.4301	machined	20.79	30	10.00		WC20

Atomization results

Powder mass [g]	Consumable rest mass [g]	Atomization efficieny [%]	Atomisation time [s]	Apparent mass flow rate [g/s]	Recovery loss [g]
13.85	6.73	66.62	24.6	0.6	0.21

Sieving parameters & results

Sieving time [min]	Set sieving amplitude	Oscillation amplitude [mm]	Sieving loss [g]
6	50	1	-0.83

Powder distribution

Mesh size [µm]	Mesh weight before sieving [g]	Powder mass [g]	Mesh weight after sieving [g]	Corrected powder mass [g]	Mass fraction [%]	Normalized mass fraction [% / µm]*100	Cumulative powder mass [g]	Cumulative undersize [%]
0	70.73	0.00	70.73	0.00	0	0	0.00	0
32	193.64	0.09	193.63	0.08	1	5	0.00	0
45	188.60	0.42	188.59	0.41	3	16	0.09	1
63	196.35	0.77	196.36	0.78	5	19	0.51	3
90	196.82	1.18	196.79	1.15	8	23	1.28	9
125	198.90	11.97	198.89	11.96	82	148	2.46	17
180	201.79	0.25	201.81	0.27	2	2	14.43	98
250	200.99	0.00	200.96	- 0.03	0	0	14.68	100
355	201.15	0.00	201.14	- 0.01	0	*	14.68	100
Total	1648.97	14.68	1648.90	14.61	100			

B1.23 Inox-027

Experiment	**Inox-027**	Date	**11.09.2014**
Editor	**R. Schenk**	Operator	**R. Schenk**

Atomization parameters

Rotation speed [rpm]	Potentiometer voltage [V]	Arc current [A]	Humidity [ppm]	Oxygen [ppm]	Consumable type	Consumable fabrication	Consumable mass [g]	Consumable length [mm]	Consumable diameter [mm]	Cons. liquid* density [kg/m^3]	Cathode type
40'000	7.78	100	< 3	< 20	1.4301	machined	20.80	30	10.00		WC20

Atomization results

Powder mass [g]	Consumable rest mass [g]	Atomization efficieny [%]	Atomisation time [s]	Apparent mass flow rate [g/s]	Recovery loss [g]
14.74	5.80	70.87	26.0	0.6	0.26

Sieving parameters & results

Sieving time [min]	Set sieving amplitude	Oscillation amplitude [mm]	Sieving loss [g]
6	50	1	0.92

Powder distribution

Mesh size [µm]	Mesh weight before sieving [g]	Powder mass [g]	Mesh weight after sieving [g]	Corrected powder mass [g]	Mass fraction [%]	Normalized mass fraction [% / µm]*100	Cumulative powder mass [g]	Cumulative undersize [%]
0	70.74	0.00	70.72	- 0.02	0	0	0.00	0
32	193.70	0.28	193.67	0.25	2	16	0.00	0
45	188.63	0.96	188.59	0.92	7	39	0.28	2
63	196.36	0.67	196.32	0.63	5	18	1.24	9
90	196.87	9.88	196.89	9.90	71	204	1.91	14
125	198.91	1.98	198.99	2.06	14	26	11.79	85
180	201.82	0.05	201.81	0.04	0	1	13.77	100
250	200.97	0.00	201.01	0.04	0	0	13.82	100
355	201.14	0.00	201.15	0.01	0	*	13.82	100
Total	1649.14	13.82	1649.15	13.83	100			

B1.24 Inox-028

Experiment	**Inox-028**	Date	**11.09.2014**
Editor	**R. Schenk**	Operator	**R. Schenk**

Atomization parameters

Rotation speed [rpm]	Potentiometer voltage [V]	Arc current [A]	Humidity [ppm]	Oxygen [ppm]	Consumable type	Consumable fabrication	Consumable mass [g]	Consumable length [mm]	Consumable diameter [mm]	Cons. liquid* density [kg/m^3]	Cathode type
50'000	9.54	100	< 3	< 20	1.4301	machined	20.76	30	10.00		WC20

Atomization results

Powder mass [g]	Consumable rest mass [g]	Atomization efficieny [%]	Atomisation time [s]	Apparent mass flow rate [g/s]	Recovery loss [g]
15.87	5.09	76.45	27.0	0.6	-0.20

Sieving parameters & results

Sieving time [min]	Set sieving amplitude	Oscillation amplitude [mm]	Sieving loss [g]
6	50	1	0.10

Powder distribution

Mesh size [µm]	Mesh weight before sieving [g]	Powder mass [g]	Mesh weight after sieving [g]	Corrected powder mass [g]	Mass fraction [%]	Normalized mass fraction [% / µm]*100	Cumulative powder mass [g]	Cumulative undersize [%]
0	70.73	0.24	70.73	0.24	2	5	0.00	0
32	193.60	0.87	193.63	0.90	6	42	0.24	2
45	188.60	1.00	188.59	0.99	6	35	1.11	7
63	196.33	8.18	196.34	8.19	52	192	2.11	13
90	196.80	4.82	196.85	4.87	31	87	10.29	65
125	198.84	0.59	198.89	0.64	4	7	15.11	96
180	201.77	0.07	201.78	0.08	0	1	15.70	100
250	200.98	0.00	200.96	- 0.02	0	0	15.77	100
355	201.13	0.00	201.14	0.01	0	*	15.77	100
Total	1648.78	15.77	1648.91	15.90	100			

B1.25 Inox-040

Experiment	**Inox-040**	Date	**25.03.2015**
Editor	**R. Schenk**	Operator	**R. Schauer**

Atomization parameters

Rotation speed [rpm]	Potentiometer voltage [V]	Arc current [A]	Humidity [ppm]	Oxygen [ppm]	Consumable type	Consumable fabrication	Consumable mass [g]	Consumable length [mm]	Consumable diameter [mm]	Cons. liquid* density [kg/m^3]	Cathode type
20'000	4.96	100	< 2	< 10	1.4301	machined	78.61	30	20.00		WC20 snubnose

Atomization results

Powder mass [g]	Consumable rest mass [g]	Atomization efficieny [%]	Atomisation time [s]	Apparent flow rate [g/s]	Recovery loss [g]	Calc. Atomized length [mm]
56.31	21.98	71.64	114.0	0.5	0.32	10.42

Sieving parameters & results

Sieving time [min]	Set sieving amplitude	Oscillation amplitude [mm]	Sieving loss [g]
6	50	1	0.93

Powder distribution

Mesh size [µm]	Mesh weight before sieving [g]	Powder mass [g]	Mesh weight after sieving [g]	Corrected powder mass [g]	Mass fraction [%]	Normalized mass fraction [% / µm]*100	Cumulative powder mass [g]	Cumulative undersize [%]
0	70.71	0.00	70.71	0.00	0	0	0.00	0
20	194.39	0.00	194.36	- 0.03	0	0	0.00	0
32	194.10	0.19	194.06	0.15	0	3	0.00	0
45	192.42	0.90	192.38	0.86	2	9	0.19	0
63	191.73	1.09	191.61	0.97	2	7	1.09	2
90	195.52	4.55	195.51	4.54	8	23	2.18	4
125	193.29	33.13	193.44	33.28	60	108	6.73	12
180	195.58	10.52	195.51	10.45	19	27	39.86	72
250	204.68	2.42	204.65	2.39	4	4	50.38	91
355	201.83	2.86	201.74	2.77	5	*	52.80	95
Total	1834.25	55.66	1833.97	55.38	100			

B1.26 Inox-041

Experiment	**Inox-041**	Date	**25.03.2015**
Editor	**R. Schenk**	Operator	**R. Schauer**

Atomization parameters

Rotation speed [rpm]	Potentiometer voltage [V]	Arc current [A]	Humidity [ppm]	Oxygen [ppm]	Consumable type	Consumable fabrication	Consumable mass [g]	Consumable length [mm]	Consumable diameter [mm]	Cons. liquid* density [kg/m^3]	Cathode type
30'000	5.98	100	< 3	< 12	1.4301	machined	78.63	30	20.00		WC20 snubnose

Atomization results

Powder mass [g]	Consumable rest mass [g]	Atomization efficieny [%]	Atomisation time [s]	Apparent flow rate [g/s]	Recovery loss [g]	Calc. Atomized length [mm]
61.23	17.61	77.87	107.0	0.6	-0.21	11.23

Sieving parameters & results

Sieving time [min]	Set sieving amplitude	Oscillation amplitude [mm]	Sieving loss [g]
6	50	1	0.16

Powder distribution

Mesh size [µm]	Mesh weight before sieving [g]	Powder mass [g]	Mesh weight after sieving [g]	Corrected powder mass [g]	Mass fraction [%]	Normalized mass fraction [% / µm]*100	Cumulative powder mass [g]	Cumulative undersize [%]
0	70.71	0.00	70.72	0.01	0	0	0.00	0
20	194.36	0.26	194.36	0.26	0	4	0.00	0
32	194.06	1.40	194.06	1.40	2	18	0.26	0
45	192.38	2.19	192.36	2.17	4	20	1.66	3
63	191.61	14.63	191.72	14.74	24	89	3.85	6
90	195.51	31.97	195.77	32.23	53	150	18.48	30
125	193.44	1.89	193.32	1.77	3	6	50.45	83
180	195.51	1.12	195.53	1.14	2	3	52.34	86
250	204.65	1.85	204.64	1.84	3	3	53.46	88
355	201.74	5.49	201.76	5.51	9	*	55.31	91
Total	1833.97	60.80	1834.24	61.07	100			

B1.27 Inox-042

Experiment	**Inox-042**	Date	**27.03.2015**
Editor	**R. Schenk**	Operator	**R. Schauer**

Atomization parameters

Rotation speed [rpm]	Potentiometer voltage [V]	Arc current [A]	Humidity [ppm]	Oxygen [ppm]	Consumable type	Consumable fabrication	Consumable mass [g]	Consumable length [mm]	Consumable diameter [mm]	Cons. liquid* density [kg/m^3]	Cathode type
40'000	7.82	100	< 2	< 20	1.4301	machined	26.72	10	20.00		WC20 snubnose

Atomization results

Powder mass [g]	Consumable rest mass [g]	Atomization efficieny [%]	Atomisation time [s]	Apparent flow rate [g/s]	Recovery loss [g]	Calc. Atomized length [mm]
16.68	9.26	62.42	31.8	0.6	0.78	3.21

Sieving parameters & results

Sieving time [min]	Set sieving amplitude	Oscillation amplitude [mm]	Sieving loss [g]
6	50	1	0.58

Powder distribution

Mesh size [µm]	Mesh weight before sieving [g]	Powder mass [g]	Mesh weight after sieving [g]	Corrected powder mass [g]	Mass fraction [%]	Normalized mass fraction [% / µm]*100	Cumulative powder mass [g]	Cumulative undersize [%]
0	73.87	0.00	73.87	0.00	0	0	0.00	0
20	191.00	0.13	191.04	0.17	1	7	0.00	0
32	193.72	1.38	193.66	1.32	8	65	0.13	1
45	188.66	2.37	188.54	2.25	14	80	1.51	9
63	196.34	5.50	196.32	5.48	33	124	3.88	24
90	197.07	0.86	196.96	0.75	5	15	9.38	57
125	198.98	0.87	198.93	0.82	5	10	10.24	62
180	201.76	0.92	201.76	0.92	6	8	11.11	68
250	200.96	1.46	200.96	1.46	9	8	12.03	73
355	201.13	2.94	201.12	2.93	18	*	13.49	82
Total	1843.49	16.43	1843.16	16.10	100			

B1.28 Inox-043

Experiment	**Inox-043**	Date	**31.03.2015**
Editor	**R. Schenk**	Operator	**R. Schauer**

Atomization parameters

Rotation speed [rpm]	Potentiometer voltage [V]	Arc current [A]	Humidity [ppm]	Oxygen [ppm]	Consumable type	Consumable fabrication	Consumable mass [g]	Consumable length [mm]	Consumable diameter [mm]	Cons. liquid* density [kg/m^3]	Cathode type
50'000	9.55	100	< 3	< 25	1.4301	machined	26.64	10	20.00		WC20 snubnose

Atomization results

Powder mass [g]	Consumable rest mass [g]	Atomization efficieny [%]	Atomisation time [s]	Apparent flow rate [g/s]	Recovery loss [g]	Calc. Atomized length [mm]
14.65	12.08	54.99	31.6	0.5	-0.09	2.68

Sieving parameters & results

Sieving time [min]	Set sieving amplitude	Oscillation amplitude [mm]	Sieving loss [g]
6	50	1	0.90

Powder distribution

Mesh size [µm]	Mesh weight before sieving [g]	Powder mass [g]	Mesh weight after sieving [g]	Corrected powder mass [g]	Mass fraction [%]	Normalized mass fraction [% / µm]*100	Cumulative powder mass [g]	Cumulative undersize [%]
0	73.87	0.00	73.80	- 0.07	0	0	0.00	0
20	191.04	0.99	191.03	0.98	7	59	0.00	0
32	193.66	2.15	193.63	2.12	15	119	0.99	7
45	188.54	3.78	188.52	3.76	27	151	3.14	23
63	196.32	0.83	196.34	0.85	6	22	6.92	50
90	196.96	0.56	196.99	0.59	4	12	7.75	56
125	198.93	0.99	198.83	0.89	7	13	8.31	60
180	201.76	1.13	201.78	1.15	8	12	9.30	67
250	200.96	1.41	200.97	1.42	10	10	10.43	75
355	201.12	2.04	201.14	2.06	15	*	11.84	85
Total	1843.16	13.88	1843.03	13.75	100			

B2 UMo

B2.1 U7Mo-1114-02

Experiment	**U7Mo-1114-02**	Date	**26.02.2015**
Editor	**R. Schenk**	Operator	**R.Schenk**

Atomization parameters

Rotation speed [rpm]	Potentiometer voltage [V]	Arc current [A]	Humidity [ppm]	Oxygen [ppm]	Consumable type	Consumable fabrication	Consumable mass [g]	Consumable length [mm]	Consumable diameter [mm]	Cons. liquid* density [kg/m^3]	Cathode type
30'000	20	80-90	<3	<3	U7Mo	cast	88.59		20.00		WC20

Atomization results

Powder mass [g]	Consumable rest mass [g]	Atomization efficieny [%]	Atomisation time [s]	Apparent flow rate [g/s]	Recovery loss [g]	Calc. Atomized length [mm]
78.90	9.67	89.06	16.6 25.24	1.9	0.02	14.52

Sieving parameters & results

Sieving time [min]	Set sieving amplitude	Oscillation amplitude [mm]	Sieving loss [g]
6	50	1	0.96

Powder distribution

Mesh size [µm]	Mesh weight before sieving [g]	Powder mass [g]	Mesh weight after sieving [g]	Corrected powder mass [g]	Mass fraction [%]	Normalized mass fraction [% / µm]*100	Cumulative powder mass [g]	Cumulative undersize [%]
0	70.73	0.05	70.72	0.04	0	0	0.00	0
20	194.37	0.52	194.37	0.52	1	6	0.05	0
32	194.09	3.56	194.15	3.62	5	35	0.57	1
45	192.39	6.46	192.37	6.44	8	46	4.13	5
63	191.70	10.19	191.75	10.24	13	48	10.59	14
90	195.54	4.75	195.56	4.77	6	17	20.78	27
125	193.28	4.39	193.28	4.39	6	10	25.53	33
180	195.62	5.07	195.60	5.05	7	9	29.92	38
250	204.72	6.81	204.69	6.78	9	8	34.99	45
355	201.79	36.05	201.83	36.09	46	*	41.80	54
Total	1834.23	77.85	1834.32	77.94	100			

B2.2 U7Mo-1114-03

Experiment	**U7Mo-1114-03**	Date	**27.02.2015**
Editor	**R. Schenk**	Operator	**R.Schenk**

Atomization parameters

Rotation speed [rpm]	Potentiometer voltage [V]	Arc current [A]	Humidity [ppm]	Oxygen [ppm]	Consumable type	Consumable fabrication	Consumable mass [g]	Consumable length [mm]	Consumable diameter [mm]	Cons. liquid* density [kg/m^3]	Cathode type
30'000	20	90	<3	<3	U7Mo	cast	96.08		20.00		WC20

Atomization results

Powder mass [g]	Consumable rest mass [g]	Atomization efficieny [%]	Atomisation time [s]	Apparent flow rate [g/s]	Recovery loss [g]	Calc. Atomized length [mm]
85.66	10.27	89.15	31.0	2.8	0.15	15.79

Sieving parameters & results

Sieving time [min]	Set sieving amplitude	Oscillation amplitude [mm]	Sieving loss [g]
6	50	1	-2.48

Powder distribution

Mesh size [µm]	Mesh weight before sieving [g]	Powder mass [g]	Mesh weight after sieving [g]	Corrected powder mass [g]	Mass fraction [%]	Normalized mass fraction [% / µm]*100	Cumulative powder mass [g]	Cumulative undersize [%]
0	70.72	0.01	70.73	0.02	0	0	0.00	0
20	194.37	0.27	194.41	0.31	0	3	0.01	0
32	194.15	0.83	194.13	0.81	1	7	0.28	0
45	192.37	2.16	192.41	2.20	2	14	1.11	1
63	191.75	5.04	191.72	5.01	6	21	3.27	4
90	195.56	9.99	195.53	9.96	11	32	8.31	9
125	193.28	12.88	193.30	12.90	15	27	18.30	21
180	195.60	14.25	195.58	14.23	16	23	31.18	35
250	204.69	12.94	204.69	12.94	15	14	45.43	52
355	201.83	29.76	201.83	29.76	34	*	58.37	66
Total	1834.32	88.13	1834.33	88.14	100			

B2.3 U-7Mo-1114-3-1.6

Experiment	**U-7Mo-1114-3-1.6**	Date	**10.02.2014**
Editor	**R. Schenk**	Operator	**R. Schenk**

Atomization parameters

Rotation speed [rpm]	Potentiometer voltage [V]	Arc current [A]	Humidity [ppm]	Oxygen [ppm]	Consumable type	Consumable fabrication	Consumable mass [g]	Consumable length [mm]	Consumable diameter [mm]	Cons. liquid* density [kg/m^3]	Cathode type
30'000	-	60	< 3	< 4	U7Mo	cast	80.84	-	15.00		WC20

Atomization results

Powder mass [g]	Consumable rest mass [g]	Atomization efficieny [%]	Atomisation time [s]	Apparent mass flow rate [g/s]	Recovery loss [g]	Calc. atomized length [mm]
73.40	7.31	90.80	32.8	2.2	0.13	24.05

* Pin rupture at shoulder level during atomization

Sieving parameters & results

Sieving time [min]	Set sieving amplitude	Oscillation amplitude [mm]	Sieving loss [g]
6	50	1	-0.53

Powder distribution

Mesh size [µm]	Mesh weight before sieving [g]	Powder mass [g]	Mesh weight after sieving [g]	Corrected powder mass [g]	Mass fraction [%]	Normalized mass fraction [% / µm]*100	Cumulative powder mass [g]	Cumulative undersize [%]
0	70.73	0.00	70.75	0.02	0	0	0.00	0
20	194.37	0.00	194.44	0.07	0	0	0.00	0
32	194.10	0.16	194.14	0.20	0	2	0.00	0
45	192.38	0.68	192.43	0.73	1	5	0.16	0
63	191.74	2.39	191.81	2.46	3	12	0.84	1
90	195.63	9.39	195.68	9.44	13	37	3.23	4
125	193.37	23.79	193.38	23.80	32	59	12.62	17
180	195.63	21.94	195.69	22.00	30	43	36.41	50
250	204.66	9.16	204.76	9.26	12	12	58.35	79
355	201.68	5.89	201.74	5.95	8	*	67.51	92
Total	1834.29	73.40	1834.82	73.93	100			

B2.4 U-7Mo-1114-3-4.5

Experiment	**U-7Mo-1114-3-4.5**	Date	**10.02.2014**
Editor	**R. Schenk**	Operator	**R. Schenk**

Atomization parameters

Rotation speed [rpm]	Potentiometer voltage [V]	Arc current [A]	Humidity [ppm]	Oxygen [ppm]	Consumable type	Consumable fabrication	Consumable mass [g]	Consumable length [mm]	Consumable diameter [mm]	Cons. liquid* density [kg/m^3]	Cathode type
25'000	5	100	< 3	< 4	U7Mo	cast	73.68	-	20.00		WC20

Atomization results

Powder mass [g]	Consumable rest mass [g]	Atomization efficieny [%]	Atomisation time [s]	Apparent mass flow rate [g/s]	Recovery loss [g]	Calc. atomized length [mm]
68.15	4.90	92.49	20.2	3.4	0.63	12.66

Sieving parameters & results

Sieving time [min]	Set sieving amplitude	Oscillation amplitude [mm]	Sieving loss [g]
6	50	1	#WERT!

* Pin rupture at shoulder level during atomization

Powder distribution

Mesh size [µm]	Mesh weight before sieving [g]	Powder mass [g]	Mesh weight after sieving [g]	Corrected powder mass [g]	Mass fraction [%]	Normalized mass fraction [% / µm]*100	Cumulative powder mass [g]	Cumulative undersize [%]
0	70.75	0.00	-	#WERT!	0	0	0.00	0
20	194.44	0.04	-	#WERT!	0	0	0.00	0
32	194.14	0.31	-	#WERT!	0	3	0.04	0
45	192.43	0.83	-	#WERT!	1	7	0.35	1
63	191.81	2.78	-	#WERT!	4	15	1.18	2
90	195.68	5.35	-	#WERT!	8	22	3.96	6
125	193.38	7.60	-	#WERT!	11	20	9.31	14
180	195.69	9.13	-	#WERT!	13	19	16.91	25
250	204.76	9.06	-	#WERT!	13	13	26.04	38
355	201.74	33.37	-	#WERT!	49	*	35.10	51
Total	1834.82	68.47	0.00	#WERT!	100			

B2.5 U8Mo-0914-1

Experiment	**U8Mo-0914-1**	Date	**04.02.2014**
Editor	**R. Schenk**	Operator	**R. Schenk**

Atomization parameters

Rotation speed [rpm]	Potentiometer voltage [V]	Arc current [A]	Humidity [ppm]	Oxygen [ppm]	Consumable type	Consumable fabrication	Consumable mass [g]	Consumable length [mm]	Consumable diameter [mm]	Cons. liquid* density [kg/m^3]	Cathode type
40'000	7.88	50	< 13	< 14	U8Mo	cast	43.05	30	10.00		WC20

Atomization results

Powder mass [g]	Consumable rest mass [g]	Atomization efficieny [%]	Atomisation time [s]	Apparent mass flow rate [g/s]	Recovery loss [g]	Calc. atomized length [mm]
30.41	12.10	70.64	18.0	1.7	0.54	22.78

Sieving parameters & results

Sieving time [min]	Set sieving amplitude	Oscillation amplitude [mm]	Sieving loss [g]
6	50	1	0.35

Powder distribution

Mesh size [µm]	Mesh weight before sieving [g]	Powder mass [g]	Mesh weight after sieving [g]	Corrected powder mass [g]	Mass fraction [%]	Normalized mass fraction [% / µm]*100	Cumulative powder mass [g]	Cumulative undersize [%]
0	70.73	0.00	70.73	0.00	0	0	0.00	0
20	194.40	0.17	194.37	0.14	1	5	0.00	0
32	194.05	0.58	194.10	0.63	2	15	0.17	1
45	192.35	2.79	192.38	2.82	9	52	0.75	3
63	191.74	7.61	191.74	7.61	26	95	3.54	12
90	195.55	12.01	195.63	12.09	40	115	11.15	37
125	193.29	5.29	193.37	5.37	18	32	23.16	78
180	195.55	0.89	195.63	0.97	3	4	28.45	96
250	204.65	0.35	204.66	0.36	1	1	29.34	99
355	201.69	0.08	201.68	0.07	0	*	29.69	100
Total	1834.00	29.77	1834.29	30.06	100			

B2.6 U8Mo-0914-3

Experiment	**U8Mo-0914-3**	Date	**06.02.2014**
Editor	**R. Schenk**	Operator	**R. Schenk**

Atomization parameters

Rotation speed [rpm]	Potentiometer voltage [V]	Arc current [A]	Humidity [ppm]	Oxygen [ppm]	Consumable type	Consumable fabrication	Consumable mass [g]	Consumable length [mm]	Consumable diameter [mm]	Cons. liquid* density [kg/m^3]	Cathode type
40'000	7.88	50	< 2	< 5	U8Mo	cast	46.41	30	10.00		WC20

Atomization results

Powder mass [g]	Consumable rest mass [g]	Atomization efficieny [%]	Atomisation time [s]	Apparent mass flow rate [g/s]	Recovery loss [g]	Calc. atomized length [mm]
30.69	15.74	66.13	20.8	1.5	-0.02	22.57

Sieving parameters & results

Sieving time [min]	Set sieving amplitude	Oscillation amplitude [mm]	Sieving loss [g]
6	50	1	0.27

Powder distribution

Mesh size [µm]	Mesh weight before sieving [g]	Powder mass [g]	Mesh weight after sieving [g]	Corrected powder mass [g]	Mass fraction [%]	Normalized mass fraction [% / µm]*100	Cumulative powder mass [g]	Cumulative undersize [%]
0	70.73	0.00	70.73	0.00	0	0	0.00	0
20	194.38	0.00	194.40	0.02	0	0	0.00	0
32	194.07	0.06	194.05	0.04	0	2	0.00	0
45	192.37	0.65	192.35	0.63	2	12	0.06	0
63	191.74	2.69	191.74	2.69	9	33	0.71	2
90	195.58	5.98	195.55	5.95	20	56	3.40	11
125	193.29	9.80	193.29	9.80	32	58	9.38	31
180	195.60	6.14	195.55	6.09	20	29	19.18	63
250	204.67	2.84	204.65	2.82	9	9	25.32	83
355	201.71	2.40	201.69	2.38	8	*	28.16	92
Total	1834.14	30.56	1834.00	30.42	100			

B2.7 U8Mo-0914-4

Experiment	**U8Mo-0914-4**	Date	**09.02.2014**
Editor	**R. Schenk**	Operator	**R. Schenk**

Atomization parameters

Rotation speed [rpm]	Potentiometer voltage [V]	Arc current [A]	Humidity [ppm]	Oxygen [ppm]	Consumable type	Consumable fabrication	Consumable mass [g]	Consumable length [mm]	Consumable diameter [mm]	Cons. liquid* density [kg/m^3]	Cathode type
40'000	7.88	50	< 1	< 19	U8Mo	cast	43.03	30	10.00		WC20

Atomization results

Powder mass [g]	Consumable rest mass [g]	Atomization efficieny [%]	Atomisation time [s]	Apparent mass flow rate [g/s]	Recovery loss [g]	Calc. atomized length [mm]
35.52	7.45	82.55	23.8	1.5	0.06	26.19

Sieving parameters & results

Sieving time [min]	Set sieving amplitude	Oscillation amplitude [mm]	Sieving loss [g]
6	50	1	0.12

Powder distribution

Mesh size [µm]	Mesh weight before sieving [g]	Powder mass [g]	Mesh weight after sieving [g]	Corrected powder mass [g]	Mass fraction [%]	Normalized mass fraction [% / µm]*100	Cumulative powder mass [g]	Cumulative undersize [%]
0	70.75	0.00	70.73	- 0.02	0	0	0.00	0
20	194.40	0.08	194.38	0.06	0	2	0.00	0
32	194.06	0.39	194.07	0.40	1	8	0.08	0
45	192.37	1.28	192.37	1.28	4	20	0.47	1
63	191.74	5.98	191.74	5.98	17	63	1.75	5
90	195.58	8.20	195.58	8.20	23	66	7.73	22
125	193.37	8.35	193.29	8.27	24	43	15.93	45
180	195.57	4.11	195.60	4.14	12	17	24.28	69
250	204.64	2.88	204.67	2.91	8	8	28.39	80
355	201.69	4.16	201.71	4.18	12	*	31.27	88
Total	1834.17	35.43	1834.14	35.40	100			

B2.8 U8Mo-0914-6

Experiment	**U8Mo-0914-6**	Date	**09.02.2014**
Editor	**R. Schenk**	Operator	**R. Schenk**

Atomization parameters

Rotation speed [rpm]	Potentiometer voltage [V]	Arc current [A]	Humidity [ppm]	Oxygen [ppm]	Consumable type	Consumable fabrication	Consumable mass [g]	Consumable length [mm]	Consumable diameter [mm]	Cons. liquid* density [kg/m^3]	Cathode type
40'000	7.88	50	< 1	< 16	U8Mo	cast	41.52	30	10.00		WC20

Atomization results

Powder mass [g]	Consumable rest mass [g]	Atomization efficieny [%]	Atomisation time [s]	Apparent mass flow rate [g/s]	Recovery loss [g]	Calc. atomized length [mm]
33.06	8.48	79.62	23.6	1.4	-0.02	24.32

Sieving parameters & results

Sieving time [min]	Set sieving amplitude	Oscillation amplitude [mm]	Sieving loss [g]
6	50	1	1.09

Powder distribution

Mesh size [µm]	Mesh weight before sieving [g]	Powder mass [g]	Mesh weight after sieving [g]	Corrected powder mass [g]	Mass fraction [%]	Normalized mass fraction [% / µm]*100	Cumulative powder mass [g]	Cumulative undersize [%]
0	70.76	0.00	70.75	- 0.01	0	0	0.00	0
20	194.40	0.00	194.40	0.00	0	0	0.00	0
32	194.06	0.20	194.06	0.20	1	5	0.00	0
45	192.36	1.32	192.37	1.33	4	23	0.20	1
63	191.77	5.80	191.74	5.77	18	66	1.52	5
90	195.74	10.92	195.58	10.76	34	97	7.32	23
125	193.48	9.26	193.37	9.15	29	52	18.24	56
180	195.58	2.96	195.57	2.95	9	13	27.50	85
250	204.64	1.10	204.64	1.10	3	3	30.46	94
355	201.72	0.75	201.69	0.72	2	*	31.56	98
Total	1834.51	32.31	1834.17	31.97	100			

B2.9 U8Mo-552-04

Experiment	**U8Mo-552-04**	Date	**10.07.2014**
Editor	**R. Schenk**	Operator	**R.Schenk**

Atomization parameters

Rotation speed [rpm]	Potentiometer voltage [V]	Arc current [A]	Humidity [ppm]	Oxygen [ppm]	Consumable type	Consumable fabrication	Consumable mass [g]	Consumable length [mm]	Consumable diameter [mm]	Cons. liquid* density [kg/m^3]	Cathode type
20'000	4.98	50	< 6	< 4	U-8Mo	Arc-melter cast	42.85	30	10.00		WC20

Atomization results

Powder mass [g]	Consumable rest mass [g]	Atomization efficieny [%]	Atomisation time [s]	Apparent flow rate [g/s]	Recovery loss [g]	Calc. Atomized length [mm]
28.40	14.44	66.28	24.7	1.2	0.01	20.91

Sieving parameters & results

Sieving time [min]	Set sieving amplitude	Oscillation amplitude [mm]	Sieving loss [g]
6	50	1	0.90

Powder distribution

Mesh size [µm]	Mesh weight before sieving [g]	Powder mass [g]	Mesh weight after sieving [g]	Corrected powder mass [g]	Mass fraction [%]	Normalized mass fraction [% / µm]*100	Cumulative powder mass [g]	Cumulative undersize [%]
0	70.65	0.00	70.68	0.03	0	0	0.00	0
20	194.19	0.00	194.19	0.00	0	0	0.00	0
32	193.75	0.09	193.74	0.08	0	2	0.00	0
45	192.21	0.59	192.21	0.59	2	12	0.09	0
63	191.62	1.67	191.57	1.62	6	22	0.68	2
90	193.56	2.94	193.33	2.71	10	30	2.35	8
125	193.08	10.04	193.06	10.02	36	65	5.29	19
180	195.59	6.82	195.36	6.59	24	35	15.33	55
250	204.47	3.66	204.45	3.64	13	12	22.15	79
355	201.52	2.24	201.50	2.22	8	*	25.81	92
Total	1830.64	28.05	1830.09	27.50	100			

B2.10 U8Mo-552-06

Experiment **U8Mo-552-06** Date **10.07.2014**
Editor **R. Schenk** Operator **R.Schenk**

Atomization parameters

Rotation speed [rpm]	Potentiometer voltage [V]	Arc current [A]	Humidity [ppm]	Oxygen [ppm]	Consumable type	Consumable fabrication	Consumable mass [g]	Consumable length [mm]	Consumable diameter [mm]	Cons. liquid* density [kg/m^3]	Cathode type
30'000	6.89	35	< 5	< 5	U-8Mo	Arc-melter cast	42.77	30	10.00		WC20

Atomization results

Powder mass [g]	Consumable rest mass [g]	Atomization efficieny [%]	Atomisation time [s]	Apparent flow rate [g/s]	Recovery loss [g]	Calc. Atomized length [mm]
29.96	12.94	70.05	35.4	0.8	-0.13	21.95

Sieving parameters & results

Sieving time [min]	Set sieving amplitude	Oscillation amplitude [mm]	Sieving loss [g]
6	50	1	0.37

Powder distribution

Mesh size [µm]	Mesh weight before sieving [g]	Powder mass [g]	Mesh weight after sieving [g]	Corrected powder mass [g]	Mass fraction [%]	Normalized mass fraction [% / µm]*100	Cumulative powder mass [g]	Cumulative undersize [%]
0	70.68	0.00	70.68	0.00	0	0	0.00	0
20	194.17	0.00	194.18	0.01	0	0	0.00	0
32	193.74	0.22	193.72	0.20	1	6	0.00	0
45	192.21	0.77	192.19	0.75	3	14	0.22	1
63	191.57	1.40	191.59	1.42	5	18	0.99	3
90	193.33	6.45	193.31	6.43	22	62	2.39	8
125	193.06	6.16	193.06	6.16	21	38	8.84	30
180	195.36	6.47	195.38	6.49	22	31	15.00	51
250	204.45	3.99	204.46	4.00	13	13	21.47	73
355	201.50	4.13	201.50	4.13	14	*	25.46	86
Total	1830.07	29.59	1830.07	29.59	100			

B2.11 U8Mo-552-08

Experiment	**U8Mo-552-08**	Date	**10.07.2014**
Editor	**R. Schenk**	Operator	**R.Schenk**

Atomization parameters

Rotation speed [rpm]	Potentiometer voltage [V]	Arc current [A]	Humidity [ppm]	Oxygen [ppm]	Consumable type	Consumable fabrication	Consumable mass [g]	Consumable length [mm]	Consumable diameter [mm]	Cons. liquid* density [kg/m^3]	Cathode type
20'000	4.98	35	< 6	< 5	U-8Mo	Arc-melter cast	41.37	30	10.00		WC20

Atomization results

Powder mass [g]	Consumable rest mass [g]	Atomization efficieny [%]	Atomisation time [s]	Apparent flow rate [g/s]	Recovery loss [g]	Calc. Atomized length [mm]
28.44	12.93	68.75	37.3	0.8	0.00	20.93

Sieving parameters & results

Sieving time [min]	Set sieving amplitude	Oscillation amplitude [mm]	Sieving loss [g]
6	50	1	0.43

Powder distribution

Mesh size [µm]	Mesh weight before sieving [g]	Powder mass [g]	Mesh weight after sieving [g]	Corrected powder mass [g]	Mass fraction [%]	Normalized mass fraction [% / µm]*100	Cumulative powder mass [g]	Cumulative undersize [%]
0	69.82	0.00	69.82	0.00	0	0	0.00	0
20	194.18	0.00	194.18	0.00	0	0	0.00	0
32	193.72	0.08	193.73	0.09	0	2	0.00	0
45	192.19	0.37	192.18	0.36	1	7	0.08	0
63	191.59	1.25	191.58	1.24	4	16	0.45	2
90	193.31	3.13	193.34	3.16	11	32	1.70	6
125	193.06	10.85	193.05	10.84	39	70	4.83	17
180	195.38	8.12	195.35	8.09	29	41	15.68	56
250	204.46	2.53	204.43	2.50	9	9	23.80	85
355	201.50	1.75	201.48	1.73	6	*	26.33	94
Total	1829.21	28.08	1829.14	28.01	100			

B2.12 U8Mo-552-10

Experiment	**U8Mo-552-10**	Date	**16.07.2014**
Editor	**R. Schenk**	Operator	**R.Schenk**

Atomization parameters

Rotation speed [rpm]	Potentiometer voltage [V]	Arc current [A]	Humidity [ppm]	Oxygen [ppm]	Consumable type	Consumable fabrication	Consumable mass [g]	Consumable length [mm]	Consumable diameter [mm]	Cons. liquid* density [kg/m^3]	Cathode type
50'000	9.54	70	< 7	< 11	U-8Mo	Arc-melter cast	29.85	20	10.00		WC20

Atomization results

Powder mass [g]	Consumable rest mass [g]	Atomization efficieny [%]	Atomisation time [s]	Empirical mass flow rate [g/s]	Recovery loss [g]	Calc. Atomized length [mm]
21.39	8.32	71.66	12.8	1.7	0.14	15.85

Sieving parameters & results

Sieving time [min]	Set sieving amplitude	Oscillation amplitude [mm]	Sieving loss [g]
6	50	1	-0.30

Powder distribution

Mesh size [µm]	Mesh weight before sieving [g]	Powder mass [g]	Mesh weight after sieving [g]	Corrected powder mass [g]	Mass fraction [%]	Normalized mass fraction [% / µm]*100	Cumulative powder mass [g]	Cumulative undersize [%]
0	69.81	0.29	69.84	0.32	1	7	0.00	0
20	194.20	6.81	194.23	6.84	32	267	0.29	1
32	193.85	2.51	194.01	2.67	12	91	7.10	33
45	192.14	2.89	192.17	2.92	14	75	9.61	45
63	191.50	4.47	191.59	4.56	21	78	12.50	59
90	195.30	0.79	195.32	0.81	4	11	16.97	80
125	193.07	0.83	193.05	0.81	4	7	17.76	83
180	195.33	0.84	195.35	0.86	4	6	18.59	87
250	204.38	0.83	204.42	0.87	4	4	19.43	91
355	201.47	1.02	201.48	1.03	5	*	20.26	95
Total	1831.05	21.28	1831.46	21.69	100			

B2.13 U8Mo-552-11

Experiment	**U8Mo-552-11**	Date	**16.07.2014**
Editor	**R. Schenk**	Operator	**R.Schenk**

Atomization parameters

Rotation speed [rpm]	Potentiometer voltage [V]	Arc current [A]	Humidity [ppm]	Oxygen [ppm]	Consumable type	Consumable fabrication	Consumable mass [g]	Consumable length [mm]	Consumable diameter [mm]	Cons. liquid* density [kg/m^3]	Cathode type
50'000	9.54	100	< 7	< 10	U-8Mo	Arc-melter cast	29.56	30	10.00		WC20

Atomization results

Powder mass [g]	Consumable rest mass [g]	Atomization efficieny [%]	Atomisation time [s]	Apparent flow rate [g/s]	Recovery loss [g]	Calc. Atomized length [mm]
22.03	7.42	74.53	8.5	2.6	0.11	16.29

Sieving parameters & results

Sieving time [min]	Set sieving amplitude	Oscillation amplitude [mm]	Sieving loss [g]
6	50	1	0.05

Powder distribution

Mesh size [µm]	Mesh weight before sieving [g]	Powder mass [g]	Mesh weight after sieving [g]	Corrected powder mass [g]	Mass fraction [%]	Normalized mass fraction [% / µm]*100	Cumulative powder mass [g]	Cumulative undersize [%]
0	69.84	0.15	69.83	0.14	1	3	0.00	0
20	194.32	2.67	194.23	2.58	12	100	0.15	1
32	194.01	2.82	193.87	2.68	13	98	2.82	13
45	192.17	3.35	192.18	3.36	15	84	5.64	25
63	191.59	6.55	191.59	6.55	29	109	8.99	40
90	195.32	2.65	195.30	2.63	12	34	15.54	70
125	193.05	2.02	193.05	2.02	9	17	18.19	82
180	195.35	0.99	195.36	1.00	4	6	20.21	91
250	204.42	0.44	204.42	0.44	2	2	21.20	95
355	201.49	0.58	201.49	0.58	3	*	21.64	97
Total	1831.56	22.22	1831.32	21.98	100			

B2.14 U8Mo-552-12

Experiment	**U8Mo-552-12**	Date	**11.07.2014**
Editor	**R. Schenk**	Operator	**R.Schenk**

Atomization parameters

Rotation speed [rpm]	Potentiometer voltage [V]	Arc current [A]	Humidity [ppm]	Oxygen [ppm]	Consumable type	Consumable fabrication	Consumable mass [g]	Consumable length [mm]	Consumable diameter [mm]	Cons. liquid* density [kg/m^3]	Cathode type
40'000	7.82	35	< 6	< 6	U-8Mo	Arc-melter cast	30.20	30	10.00		WC20

Atomization results

Powder mass [g]	Consumable rest mass [g]	Atomization efficieny [%]	Atomisation time [s]	Apparent flow rate [g/s]	Recovery loss [g]	Calc. Atomized length [mm]
17.79	12.32	58.91	32.5	0.6	0.09	13.16

Sieving parameters & results

Sieving time [min]	Set sieving amplitude	Oscillation amplitude [mm]	Sieving loss [g]
6	50	1	0.13

Powder distribution

Mesh size [µm]	Mesh weight before sieving [g]	Powder mass [g]	Mesh weight after sieving [g]	Corrected powder mass [g]	Mass fraction [%]	Normalized mass fraction [% / µm]*100	Cumulative powder mass [g]	Cumulative undersize [%]
0	69.82	0.07	69.83	0.08	0	2	0.00	0
20	194.17	1.22	194.17	1.22	7	58	0.07	0
32	193.73	3.40	193.79	3.46	19	149	1.29	7
45	192.18	1.91	192.18	1.91	11	60	4.69	27
63	191.58	5.22	191.58	5.22	30	110	6.60	37
90	193.34	1.14	193.30	1.10	6	18	11.82	67
125	193.05	1.03	193.06	1.04	6	11	12.96	74
180	195.35	0.96	195.34	0.95	5	8	13.99	79
250	204.43	1.04	204.44	1.05	6	6	14.95	85
355	201.48	1.62	201.49	1.63	9	*	15.99	91
Total	1829.13	17.61	1829.18	17.66	100			

B2.15 U8Mo-552-13

Experiment	**U8Mo-552-13**	Date	**11.07.2014**
Editor	**R. Schenk**	Operator	**R.Schenk**

Atomization parameters

Rotation speed [rpm]	Potentiometer voltage [V]	Arc current [A]	Humidity [ppm]	Oxygen [ppm]	Consumable type	Consumable fabrication	Consumable mass [g]	Consumable length [mm]	Consumable diameter [mm]	Cons. liquid* density [kg/m^3]	Cathode type
40'000	7.82	50	< 6	< 4	U-8Mo	Arc-melter cast	29.56	30	10.00		WC20

Atomization results

Powder mass [g]	Consumable rest mass [g]	Atomization efficieny [%]	Atomisation time [s]	Apparent flow rate [m^3/s]	Recovery loss [g]	Calc. Atomized length [mm]
18.97	10.72	64.17	-	#DIV/0!	-0.13	13.87

Sieving parameters & results

Sieving time [min]	Set sieving amplitude	Oscillation amplitude [mm]	Sieving loss [g]
6	50	1	-1.84

Powder distribution

Mesh size [µm]	Mesh weight before sieving [g]	Powder mass [g]	Mesh weight after sieving [g]	Corrected powder mass [g]	Mass fraction [%]	Normalized mass fraction [% / µm]*100	Cumulative powder mass [g]	Cumulative undersize [%]
0	69.83	0.05	69.82	0.04	0	1	0.00	0
20	194.17	3.00	194.18	3.01	14	120	0.05	0
32	193.79	2.04	193.80	2.05	10	75	3.05	15
45	192.18	1.63	192.18	1.63	8	43	5.09	24
63	191.58	6.74	191.57	6.73	32	120	6.72	32
90	193.30	1.13	193.31	1.14	5	15	13.46	65
125	193.06	0.82	193.04	0.80	4	7	14.59	70
180	195.34	0.91	195.34	0.91	4	6	15.41	74
250	204.44	1.24	204.42	1.22	6	6	16.32	78
355	201.49	3.29	201.48	3.28	16	*	17.56	84
Total	1829.18	20.85	1829.14	20.81	100			

B2.16 U8Mo-552-14

Experiment	**U8Mo-552-14**	Date	**11.07.2014**
Editor	**R. Schenk**	Operator	**R.Schenk**

Atomization parameters

Rotation speed [rpm]	Potentiometer voltage [V]	Arc current [A]	Humidity [ppm]	Oxygen [ppm]	Consumable type	Consumable fabrication	Consumable mass [g]	Consumable length [mm]	Consumable diameter [mm]	Cons. liquid* density [kg/m^3]	Cathode type
50'000	9.6	50	< 6	< 5	U-8Mo	Arc-melter cast	29.35	30	10.00		WC20

Atomization results

Powder mass [g]	Consumable rest mass [g]	Atomization efficieny [%]	Atomisation time [s]	Apparent flow rate [g/s]	Recovery loss [g]	Calc. Atomized length [mm]
17.26	12.00	58.81	18.2	1.0	0.09	12.77

Sieving parameters & results

Sieving time [min]	Set sieving amplitude	Oscillation amplitude [mm]	Sieving loss [g]
6	50	1	-0.56

Powder distribution

Mesh size [µm]	Mesh weight before sieving [g]	Powder mass [g]	Mesh weight after sieving [g]	Corrected powder mass [g]	Mass fraction [%]	Normalized mass fraction [% / µm]*100	Cumulative powder mass [g]	Cumulative undersize [%]
0	69.82	0.14	69.83	0.15	1	4	0.00	0
20	194.18	2.87	194.18	2.87	16	135	0.14	1
32	193.80	2.09	193.89	2.18	12	91	3.01	17
45	192.18	4.00	192.18	4.00	23	126	5.10	29
63	191.57	2.95	191.59	2.97	17	62	9.10	51
90	193.31	0.53	193.30	0.52	3	9	12.05	68
125	193.04	0.71	193.05	0.72	4	7	12.58	71
180	195.34	1.25	195.35	1.26	7	10	13.29	75
250	204.42	1.59	204.43	1.60	9	9	14.54	82
355	201.48	1.54	201.49	1.55	9	*	16.13	91
Total	1829.14	17.67	1829.29	17.82	100			

B2.17 U8Mo-552-16

Experiment	**U8Mo-552-16**		Date	**16.07.2014**
Editor	**R. Schenk**		Operator	**R.Schenk**

Atomization parameters

Rotation speed [rpm]	Potentiometer voltage [V]	Arc current [A]	Humidity [ppm]	Oxygen [ppm]	Consumable type	Consumable fabrication	Consumable mass [g]	Consumable length [mm]	Consumable diameter [mm]	Cons. liquid* density [kg/m^3]	Cathode type
30'000	5.98	70	< 7	< 10	U-8Mo	Arc-melter cast	29.49	30	10.00		WC20

Atomization results

Powder mass [g]	Consumable rest mass [g]	Atomization efficieny [%]	Atomisation time [s]	Apparent flow rate [g/s]	Recovery loss [g]	Calc. Atomized length [mm]
19.16	10.50	64.97	11.6	1.6	-0.17	13.98

Sieving parameters & results

Sieving time [min]	Set sieving amplitude	Oscillation amplitude [mm]	Sieving loss [g]
6	50	1	0.17

Powder distribution

Mesh size [µm]	Mesh weight before sieving [g]	Powder mass [g]	Mesh weight after sieving [g]	Corrected powder mass [g]	Mass fraction [%]	Normalized mass fraction [% / µm]*100	Cumulative powder mass [g]	Cumulative undersize [%]
0	69.83	0.00	69.85	0.02	0	0	0.00	0
20	194.23	0.66	194.21	0.64	3	29	0.00	0
32	193.87	4.15	193.85	4.13	22	167	0.66	3
45	192.18	2.85	192.17	2.84	15	83	4.81	25
63	191.59	1.77	191.53	1.71	9	34	7.66	40
90	195.30	6.23	195.30	6.23	33	93	9.43	49
125	193.05	0.94	193.04	0.93	5	9	15.66	82
180	195.36	0.62	195.37	0.63	3	5	16.60	87
250	204.42	0.63	204.42	0.63	3	3	17.22	90
355	201.49	1.26	201.46	1.23	7	*	17.85	93
Total	1831.32	19.11	1831.20	18.99	100			

B2.18 U8Mo-552-29

Experiment	**U8Mo-552-29**	Date	**16.04.2014**
Editor	**R. Schenk**	Operator	**R.Schenk**

Atomization parameters

Rotation speed [rpm]	Potentiometer voltage [V]	Arc current [A]	Humidity [ppm]	Oxygen [ppm]	Consumable type	Consumable fabrication	Consumable mass [g]	Consumable length [mm]	Consumable diameter [mm]	Cons. liquid* density [kg/m^3]	Cathode type
30'000	5.98	100	< 4	< 11	U-8Mo	Arc-melter cast	43.90	30	10.00		WC20

Atomization results

Powder mass [g]	Consumable rest mass [g]	Atomization efficieny [%]	Atomisation time [s]	Apparent flow rate [g/s]	Recovery loss [g]	Calc. Atomized length [mm]
33.90	10.06	77.22	13.1	2.6	-0.06	24.91

Sieving parameters & results

Sieving time [min]	Set sieving amplitude	Oscillation amplitude [mm]	Sieving loss [g]
6	50	1	-0.12

Powder distribution

Mesh size [µm]	Mesh weight before sieving [g]	Powder mass [g]	Mesh weight after sieving [g]	Corrected powder mass [g]	Mass fraction [%]	Normalized mass fraction [% / µm]*100	Cumulative powder mass [g]	Cumulative undersize [%]
0	69.81	0.05	69.82	0.06	0	1	0.00	0
20	194.15	0.51	194.16	0.52	2	13	0.05	0
32	193.79	3.54	193.79	3.54	10	80	0.56	2
45	192.15	4.90	192.16	4.91	14	80	4.10	12
63	191.54	4.46	191.55	4.47	13	49	9.00	27
90	195.29	14.90	195.28	14.89	44	125	13.46	40
125	193.01	3.20	193.03	3.22	9	17	28.36	84
180	195.31	1.13	195.33	1.15	3	5	31.56	93
250	204.41	0.59	204.41	0.59	2	2	32.69	96
355	201.46	0.66	201.47	0.67	2	*	33.28	98
Total	1830.92	33.94	1831.00	34.02	100			

B2.19 U8Mo-552-30

Experiment	**U8Mo-552-30**	Date	**16.04.2014**
Editor	**R. Schenk**	Operator	**R.Schenk**

Atomization parameters

Rotation speed [rpm]	Potentiometer voltage [V]	Arc current [A]	Humidity [ppm]	Oxygen [ppm]	Consumable type	Consumable fabrication	Consumable mass [g]	Consumable length [mm]	Consumable diameter [mm]	Cons. liquid* density [kg/m^3]	Cathode type
40'000	7.8	70	< 7	< 12	U-8Mo	Arc-melter cast	43.47	30	10.00		WC20

Atomization results

Powder mass [g]	Consumable rest mass [g]	Atomization efficieny [%]	Atomisation time [s]	Apparent flow rate [g/s]	Recovery loss [g]	Calc. Atomized length [mm]
30.56	12.12	70.30	18.5	1.7	0.79	23.07

Sieving parameters & results

Sieving time [min]	Set sieving amplitude	Oscillation amplitude [mm]	Sieving loss [g]
6	50	1	-0.05

Powder distribution

Mesh size [µm]	Mesh weight before sieving [g]	Powder mass [g]	Mesh weight after sieving [g]	Corrected powder mass [g]	Mass fraction [%]	Normalized mass fraction [% / µm]*100	Cumulative powder mass [g]	Cumulative undersize [%]
0	69.82	0.17	69.81	0.16	1	3	0.00	0
20	194.16	7.56	194.20	7.60	25	206	0.17	1
32	193.79	5.49	193.85	5.55	18	138	7.73	25
45	192.16	2.28	192.14	2.26	7	41	13.22	43
63	191.55	8.20	191.50	8.15	27	99	15.50	51
90	195.28	1.25	195.30	1.27	4	12	23.70	78
125	193.03	0.89	193.07	0.93	3	5	24.95	82
180	195.33	1.02	195.33	1.02	3	5	25.84	85
250	204.41	1.28	204.38	1.25	4	4	26.86	88
355	201.47	2.42	201.47	2.42	8	*	28.14	92
Total	1831.00	30.56	1831.05	30.61	100			

B2.20 U8Mo-552-33

Experiment **U8Mo-552-33** Date **23.07.2014**
Editor **R. Schenk** Operator **R.Schenk**

Atomization parameters

Rotation speed [rpm]	Potentiometer voltage [V]	Arc current [A]	Humidity [ppm]	Oxygen [ppm]	Consumable type	Consumable fabrication	Consumable mass [g]	Consumable length [mm]	Consumable diameter [mm]	Cons. liquid* density [kg/m^3]	Cathode type
45'000	8.7	50	< 6	< 3	U-8Mo	Arc-melter cast	43.86	30	10.00		WC20

Atomization results

Powder mass [g]	Consumable rest mass [g]	Atomization efficieny [%]	Atomisation time [s]	Apparent flow rate [g/s]	Recovery loss [g]	Calc. Atomized length [mm]
30.46	13.37	69.45	26.4	1.2	0.03	22.44

Sieving parameters & results

Sieving time [min]	Set sieving amplitude	Oscillation amplitude [mm]	Sieving loss [g]
6	50	1	0.04

Powder distribution

Mesh size [µm]	Mesh weight before sieving [g]	Powder mass [g]	Mesh weight after sieving [g]	Corrected powder mass [g]	Mass fraction [%]	Normalized mass fraction [% / µm]*100	Cumulative powder mass [g]	Cumulative undersize [%]
0	69.84	0.19	69.84	0.19	1	3	0.00	0
20	194.21	2.03	194.23	2.05	7	56	0.19	1
32	193.85	2.59	193.86	2.60	9	65	2.22	7
45	192.18	1.97	192.19	1.98	6	36	4.81	16
63	191.57	8.67	191.56	8.66	28	105	6.78	22
90	195.32	1.45	195.30	1.43	5	14	15.45	51
125	193.03	1.46	193.00	1.43	5	9	16.90	56
180	195.32	1.98	195.33	1.99	7	9	18.36	60
250	204.41	3.22	204.40	3.21	11	10	20.34	67
355	201.48	6.88	201.48	6.88	23	*	23.56	77
Total	1831.21	30.44	1831.19	30.42	100			

B2.21 U8Mo-552-36

Experiment	**U8Mo-552-36**	Date	**22.07.2014**
Editor	**R. Schenk**	Operator	**R.Schenk**

Atomization parameters

Rotation speed [rpm]	Potentiometer voltage [V]	Arc current [A]	Humidity [ppm]	Oxygen [ppm]	Consumable type	Consumable fabrication	Consumable mass [g]	Consumable length [mm]	Consumable diameter [mm]	Cons. liquid* density [kg/m^3]	Cathode type
45'000	8.7	45	< 7	< 4	U-8Mo	Arc-melter cast	43.55	30	10.00		WC20

Atomization results

Powder mass [g]	Consumable rest mass [g]	Atomization efficieny [%]	Atomisation time [s]	Apparent flow rate [g/s]	Recovery loss [g]	Calc. Atomized length [mm]
31.79	11.75	73.00	28.8	1.1	0.01	23.40

Sieving parameters & results

Sieving time [min]	Set sieving amplitude	Oscillation amplitude [mm]	Sieving loss [g]
6	50	1	0.22

Powder distribution

Mesh size [µm]	Mesh weight before sieving [g]	Powder mass [g]	Mesh weight after sieving [g]	Corrected powder mass [g]	Mass fraction [%]	Normalized mass fraction [% / µm]*100	Cumulative powder mass [g]	Cumulative undersize [%]
0	69.84	0.13	69.84	0.13	0	2	0.00	0
20	194.23	1.67	194.24	1.68	5	44	0.13	0
32	193.83	2.25	193.86	2.28	7	55	1.80	6
45	192.21	2.16	192.19	2.14	7	38	4.05	13
63	191.59	9.59	191.58	9.58	30	112	6.21	20
90	195.33	1.88	195.31	1.86	6	17	15.80	50
125	193.08	2.04	193.04	2.00	6	12	17.68	56
180	195.39	2.43	195.37	2.41	8	11	19.72	62
250	204.46	3.37	204.45	3.36	11	10	22.15	70
355	201.54	6.13	201.54	6.13	19	*	25.52	81
Total	1831.50	31.65	1831.42	31.57	100			

B2.22 U8Mo-552-38

Experiment	**U8Mo-552-38**	Date	**22.07.2014**
Editor	**R. Schenk**	Operator	**R.Schenk**

Atomization parameters

Rotation speed [rpm]	Potentiometer voltage [V]	Arc current [A]	Humidity [ppm]	Oxygen [ppm]	Consumable type	Consumable fabrication	Consumable mass [g]	Consumable length [mm]	Consumable diameter [mm]	Cons. liquid* density [kg/m^3]	Cathode type
40'000	7.8	40	< 7	< 3	U-8Mo	Arc-melter cast	43.35	30	10.00		WC20

Atomization results

Powder mass [g]	Consumable rest mass [g]	Atomization efficieny [%]	Atomisation time [s]	Apparent flow rate [g/s]	Recovery loss [g]	Calc. Atomized length [mm]
28.15	15.23	64.94	28.5	1.0	-0.03	20.70

Sieving parameters & results

Sieving time [min]	Set sieving amplitude	Oscillation amplitude [mm]	Sieving loss [g]
6	50	1	0.32

Powder distribution

Mesh size [µm]	Mesh weight before sieving [g]	Powder mass [g]	Mesh weight after sieving [g]	Corrected powder mass [g]	Mass fraction [%]	Normalized mass fraction [% / µm]*100	Cumulative powder mass [g]	Cumulative undersize [%]
0	69.84	0.00	69.84	0.00	0	0	0.00	0
20	194.24	0.50	194.21	0.47	2	15	0.00	0
32	193.86	1.11	193.85	1.10	4	30	0.50	2
45	192.19	1.29	192.18	1.28	5	26	1.61	6
63	191.58	7.51	191.57	7.50	27	99	2.90	10
90	195.31	3.40	195.32	3.41	12	35	10.41	37
125	193.04	3.81	193.03	3.80	14	25	13.81	49
180	195.37	3.54	195.32	3.49	13	18	17.62	63
250	204.45	3.14	204.41	3.10	11	11	21.16	75
355	201.54	3.74	201.48	3.68	13	*	24.30	87
Total	1831.42	28.04	1831.21	27.83	100			

B2.23 U8Mo-552-39

Experiment	**U8Mo-552-39**	Date	**22.07.2014**
Editor	**R. Schenk**	Operator	**R.Schenk**

Atomization parameters

Rotation speed [rpm]	Potentiometer voltage [V]	Arc current [A]	Humidity [ppm]	Oxygen [ppm]	Consumable type	Consumable fabrication	Consumable mass [g]	Consumable length [mm]	Consumable diameter [mm]	Cons. liquid* density [kg/m^3]	Cathode type
40'000	7.8	50	< 7	< 3	U-8Mo	Arc-melter cast	43.99	30	10.00		WC20

Atomization results

Powder mass [g]	Consumable rest mass [g]	Atomization efficieny [%]	Atomisation time [s]	Apparent flow rate [g/s]	Recovery loss [g]	Calc. Atomized length [mm]
30.52	13.42	69.38	24.2	1.3	0.05	22.50

Sieving parameters & results

Sieving time [min]	Set sieving amplitude	Oscillation amplitude [mm]	Sieving loss [g]
6	50	1	1.02

Powder distribution

Mesh size [µm]	Mesh weight before sieving [g]	Powder mass [g]	Mesh weight after sieving [g]	Corrected powder mass [g]	Mass fraction [%]	Normalized mass fraction [% / µm]*100	Cumulative powder mass [g]	Cumulative undersize [%]
0	69.84	0.00	69.84	0.00	0	0	0.00	0
20	194.22	0.41	194.23	0.42	1	12	0.00	0
32	193.85	1.00	193.84	0.99	3	26	0.41	1
45	192.20	1.33	192.20	1.33	5	25	1.41	5
63	191.59	6.57	191.57	6.55	22	83	2.74	9
90	195.32	5.88	195.32	5.88	20	57	9.31	32
125	193.03	6.99	193.06	7.02	24	43	15.19	52
180	195.36	3.69	195.36	3.69	13	18	22.18	75
250	204.43	1.67	204.43	1.67	6	5	25.87	88
355	201.50	1.94	201.51	1.95	7	*	27.54	93
Total	1831.34	29.48	1831.36	29.50	100			

B2.24 U8Mo-552-42

Experiment	**U8Mo-552-42**	Date	**22.07.2014**
Editor	**R. Schenk**	Operator	**R.Schenk**

Atomization parameters

Rotation speed [rpm]	Potentiometer voltage [V]	Arc current [A]	Humidity [ppm]	Oxygen [ppm]	Consumable type	Consumable fabrication	Consumable mass [g]	Consumable length [mm]	Consumable diameter [mm]	Cons. liquid* density [kg/m^3]	Cathode type
30'000	5.98	50	< 7	< 4	U-8Mo	Arc-melter cast	43.55	30	10.00		WC20

Atomization results

Powder mass [g]	Consumable rest mass [g]	Atomization efficieny [%]	Atomisation time [s]	Apparent flow rate [g/s]	Recovery loss [g]	Calc. Atomized length [mm]
31.82	11.81	73.07	24.8	1.3	-0.08	23.36

Sieving parameters & results

Sieving time [min]	Set sieving amplitude	Oscillation amplitude [mm]	Sieving loss [g]
6	50	1	0.02

Powder distribution

Mesh size [µm]	Mesh weight before sieving [g]	Powder mass [g]	Mesh weight after sieving [g]	Corrected powder mass [g]	Mass fraction [%]	Normalized mass fraction [% / µm]*100	Cumulative powder mass [g]	Cumulative undersize [%]
0	69.84	0.00	69.84	0.00	0	0	0.00	0
20	194.23	0.23	194.22	0.22	1	6	0.00	0
32	193.87	1.05	193.85	1.03	3	25	0.23	1
45	192.18	2.86	192.20	2.88	9	50	1.28	4
63	191.59	2.24	191.59	2.24	7	26	4.14	13
90	195.30	11.36	195.32	11.38	36	102	6.38	20
125	193.05	3.37	193.03	3.35	11	19	17.74	56
180	195.36	3.02	195.36	3.02	10	14	21.11	66
250	204.42	2.80	204.43	2.81	9	8	24.13	76
355	201.48	4.85	201.50	4.87	15	*	26.93	85
Total	1831.32	31.78	1831.34	31.80	100			

List of Figures

Figure 1-1 Sectioned schematic view of the primary circuit of FRM II (left) and fuel element during replacement (right); both pictures property of TUM.......... 2

Figure 1-2 Top view (left) and sectioned view (right) of the FRM II fuel element [Breitkreutz 2011].......... 3

Figure 1-3 Fuel plate section showing the meat and cladding zones [Schmid 2011]. 4

Figure 1-4 Implemented prototype UMo fuel powder production facility including induction furnace (left) and atomizer (right).......... 8

Figure 3-1 Physical principle of the rotating electrode process (REP) [Schenk *et al.* 2013].......... 20

Figure 3-2 CAD model of the atomizing unit of the REP atomizer (the collection chamber is transparent).......... 24

Figure 3-3 Schematic of the prototype atomizer system architecture. 25

Figure 3-4 Schematic showing equilibrium conditions of the belt-tensioning system – at motor standstill and during atomizer operation. 27

Figure 3-5 Atomizer installation during cold commissioning. 31

Figure 3-6 Atomizer infrastructure during hot operation in the UMo laboratory. 32

Figure 3-7 Installation schematic of the atomizer facility for hot operation including the atomizing unit, auxiliary equipment, supply requirements, and interfaces.......... 33

Figure 3-8 Exploded CAD model of the atomizing unit consisting of (1) infeed linear guide rails, (2) cover hood, (3) powder seal screw, (4) powder collection chamber, (5) quick release clamps, (6) motor, (7) motor pulley, (8) belt, (9) rotating (U8Mo) electrode, (10) collet and collet chuck, (11) high frequency spindle, (12) spindle clamps and spacer, (13) spindle pulley, (14) shaft extension screw, (15) welding torch, (16) torch adapter, (17) drill adapter, (18) cantilever, (19) linear slider, (20) drill rig, (21) static (tungsten) electrode, (22) graphite dust seal, (23) carbon brushes, (24) brass pipes, (25) brass collector ring, (26) screw insulation, (27) insulator with retention depot, (28) winch with handle bar, (29) tension spring, (30) linear guide rails, (31) motor carrier, (32) hybrid bearings, (33) bump stop, (34) atomizer framework, and (35) belt-drive protection cover. 35

Figure 3-9 Inside view of the atomizer glovebox before hot commissioning, showing the atomizing unit, sieving machine for powder granulometry, and weighing scales. 36

Figure 3-10 Outside view of the atomizer glovebox in the UMo laboratory before hot commissioning [Schenk *et al.* 2014]. 37

Figure 3-11 Inside and outside view of the large vacuum lock (the small vacuum lock is visible on the right picture, though partially hidden behind the drill rig). 38

Figure 3-12 Rotary vane vacuum pump of the atomizer glovebox. 40

Figure 3-13 Passive pressure relief valve to protect the glovebox from excessive positive pressure. 40

Figure 3-14 Example of HEPA filters installed for argon double-filtration inside and outside the atomizer glovebox. 41

Figure 3-15 Exemplary KF40 flange fittings and feed-throughs at the atomizer glovebox backside. 42

Figure 3-16 Gas purifier for glovebox atmosphere control and reprocessing. 43

Figure 3-17 Control panel of the gas purifier. 46

Figure 3-18 CAD model of the atomizer framework. 46

Figure 3-19 Back (left) and front view (right, showing operator interface) of the electric arc welder with food pedal for arc ignition. 49

Figure 3-20 Typical voltage-current output characteristic curves of the two basic power source types (arc welders), constant voltage (CV) and constant current (CC) arc welder, and electric arc operating points. The operating point is the intersection of a characteristic of an electric arc and a static characteristic of the arc welder; taken from ["Welding theory and application" 1993]. 51

Figure 3-21 Left: Typical static voltage-current characteristics of a traditional CC machine. Right: Typical static voltage-current characteristics of a true constant-current arc welders with low current (LC) and high current (HC) option; both taken from ["Welding theory and application" 1993]. 52

Figure 3-22 Welding torch (black bar) of the tungsten inert gas arc welder. 54

Figure 3-23 Tungsten electrode mounted on the arc welder torch through a brass clamp screw...55

Figure 3-24 Schematic showing the influence of the tip angle. Both electrodes have paraxial tip pointing. 56

Figure 3-25 Assembly showing the torch adapter (16) that carries the welder torch (15). In addition, the linear slider (19) that runs on the linear guide rails (1) is mounted on the adapter. The numbers correspond to Figure 3-8. 57

Figure 3-26 CAD model of the torch adapter (left) with front view (right) and cutaway at thread level. The red arrow points to the second screw intake to open the clamp...58

Figure 3-27 Drill rig (20) with cantilever (18) and drill adapter (17). The green arrows indicate moving directions. 59

Figure 3-28 Standard rotating electrode dimensions for the REP prototype atomizer. 61

Figure 3-29 Examples of U8Mo and U7Mo rotating electrodes. Left: INL arc-melter cast U8Mo rotating electrode after mechanical polishing. Middle: short rotating U8Mo electrode mounted on the collet chuck. Right: in-house cast U7Mo rotating electrode with 20 mm diameter. 61

Figure 3-30 High frequency spindle of the atomizer prototype. Left: Spindle as mounted on the atomizing unit. Right: CAD model of the spindle, showing collet chuck (10), two spindle clamps (12, yellow) and spacer (12, red), pulley (13), and shaft extension screw (14)..............................63

Figure 3-31 Estimated particle mean diameter D_d as a function of rotational speed n and rotating electrode diameter D_{re} using REP model (7.22). The resonance frequency and manufacturer's maximum rotation speed are marked black and red, respectively. The prototype atomizer design-point is marked with a green needle...63

Figure 3-32 Mounting of a U8Mo rotating electrode on the collet chuck.................65

Figure 3-33 Mounting position of the inductive rotary sensor with respect to the high frequency spindle...66

Figure 3-34 Shaft extension screw as mounted (left) and in schematic view (right). 68

Figure 3-35 Metallic carbon brushes with spring and electric contact. Bottom: type N91...72

Figure 3-36 Carbon brush mounted on the brass pipe which is closed by a screwable cap at the left end...73

Figure 3-37 Brass collector ring (25) as part of the rotary electrical connector, mounted on the atomizer (left) with carbon brushes and brass pipes. Right: CAD model in sectional view with screw insulation (26)...........74

Figure 3-38 Graphite dust seal (22) as mounted on the collector ring......................75

Figure 3-39 CAD model of the insulator and retention depot..................................76

Figure 3-40 Parameterisation diagram of the VFD software. (O) is the rotation offset, (B) is the backlash...77

Figure 3-41 Extricable VFD control panel, situated underneath the atomizer glovebox bottom plate. 78

Figure 3-42 Asynchronous induction motor with cooling fan (not visible), mounted on the mobile motor carrier. 79

Figure 3-43 Inside view of the motor carrier showing the motor shaft, pulley, and belt (yellow)..81

Figure 3-44 Belt-drive arrangement showing motor, motor carrier, belt, and high frequency spindle. 82

Figure 3-45 Motor carrier mounted to the hybrid bearings and linear guide rails....83

Figure 3-46 Metric division scale on motor carrier backside indicating belt elongation and pre-tension. 84

Figure 3-47 Winch with handle bar and tension spring (under load) pulling the motor carrier. 86

Figure 3-48 Powder collection chamber in operational condition with closed quick release clamps before atomization, after atomization with U8Mo powder, and as sectioned CAD model, showing both the chamber geometry and high frequency spindle positioning..................................88

Figure 3-49 Mounted powder seal screw on the atomizer prototype and as a sectioned CAD model for construction. 89

Figure 4-1 Average particle size distribution of 11 atomized stainless steel (1.4301) rotating electrodes with 10 mm diameter and 30 mm consumable length atomized at 40’000 rpm and 70 A, and corresponding standard deviation (red error bars) from Table 4-2. 95

Figure 4-2 Optical micrograph of typical 1.4301 stainless steel atomized powder produced under argon atmosphere using REP. The powder was produced at 35’000 rpm, 60 A, and under argon atmosphere; the electrode had a diameter of 10 mm [Schenk *et al.* 2013]. 96

Figure 5-1 Left: Image of a TIG welding electric arc (property of EWM AG). Right: Schematic of a TIG welding electric arc using direct current (DC) with reverse polarity, i.e. welding with the tungsten electrode positive (DCEP) and the work negative (property of [Correy 1982]). For REP, the inverse polarity with tungsten electrode negative (DCEN) and the work positive is used. 104

Figure 5-2 Electric arc voltage in argon at atmospheric pressure as a function of electric arc current and electric arc length. The voltage-current electric arc characteristic shows a non-linear behaviour with a minimum towards an electric arc current of about 85 A; property of [Katsaounis 1993]..105

Figure 5-3 Electric field strength as a function of electric arc length at atmospheric pressure; property of [Katsaounis 1993]...106

Figure 5-4 Calculated electric arc gain or sensitivity $\mathrm{d}U/\mathrm{d}l$ as a function of electric arc voltage and electric arc current (1 inch = 25.4 mm); property of [Bjorgvinsson *et al.* 1993].. 106

Figure 5-5 Efficiency factors as a function of total input power at atmospheric pressure for argon; property of [Katsaounis 1993]. The electric arc efficiency η_w is shown as a function of electric arc current and electric welder power.. 107

Figure 5-6 Operating range of the implemented arc welder and illustration of the dynamic behaviour of the electric arc operating point due to a variation in electric arc length. The operating point moves along the drooping arc welder characteristic that is predetermined by the electric arc current setting (see also Figure 3-21). The decrease in electric arc current due to an increase in the electric arc length was determined to about 1 A (chapter 4.2). 109

Figure 5-7 Measured apparent mass flow rate as a function of average arc power $P_{el,av}$ for both U8Mo and 1.4301 rotating electrodes with a diameter and length of 10 mm and 30 mm, respectively. While y- error bars represent the measurement uncertainty, x-error bars account for minimum and maximum electric arc power for a given electric arc current. The linear fitting graphs (red) and functions were obtained by using York's method of regression as well as assuming 0 correlation between x and y errors. The standard errors of the fitting graph slopes for U8Mo and 1.4301 stainless steel were ± 0.23872 and ± 0.06681, respectively. The standard errors of the intercepts were 0.17796 and 0.0875, respectively. The dashed, vertical line represents the region where U8Mo melting became impossible, corresponding to an average arc power and set electric arc current of 0.42 kW and 30 A, respectively; the grey area accounts for the uncertainty of ± 0.08 kW due to the variation in electric arc length. Uncertainties within symbol size if not visible. 111

Figure 5-8 Sequence of pictures recorded at the beginning of atomization of the U8Mo rotating electrode 552-10 with a diameter of 10 mm at 70 A. From left to right: (0) U8Mo rotating electrode and tungsten electrode in idle position, (1) electric arc ignition with 2 mm gap at 0 s, (2) electric arc of 2 mm length at ~ 0 s, (3) manual increase of the electric arc length to around 10 mm and development of a melt pool at 1 s, (4) partial coverage of the rotating electrode at 2 s, (5) fully covered rotating electrode diameter at 3 s and beginning reduction of the electrode length (fully developed atomization). The welder starting-ramp included temporary operation at 50 % electric arc current (35 A) for about 0.5 s. 112

Figure 5-9 Illustration of the difference in apparent and "real" mass flow rate. ..113

Figure 5-10 Apparent mass flow rate as a function of atomized rotating electrode length for different electric arc currents. Straight lines were included for trend visualisation. Uncertainties within symbol size if not visible. 114

Figure 5-11 Illustration of influence of rotating electrode length on the apparent mass flow rate. For cylindrical rotating electrodes, the atomized mass is proportional to the atomized length. The slopes represent the corresponding mass flow rate. 115

Figure 5-12 Apparent mass flow rate as a function of rotating electrode diameter for 1.4301 stainless steel for different arc current intensities. Straight lines were included for trend visualisation. Uncertainties within symbol size if not visible..........116

Figure 5-13 Apparent mass flow rate as a function of the carbon content that was measured in samples of atomized powder. In addition, nitrogen and oxygen concentrations are given for every carbon concentration. The nitrogen content of the smallest value is given as molecular value. The tested rotating electrodes had a diameter and atomized length of 10 mm and 23 mm, respectively, and were atomized at 50 A. A straight line was included for trend visualisation. Uncertainties within symbol size if not visible. 118

Figure 5-14 Sequence of rotating electrodes 552-13, -14, -04, and -33 (left to right) originating from INL after in-house atomization. Electrode rests of 552-13, -14, and -04 show inclusions, reaching about 5 mm in length (electrode diameter of 10 mm). A shadow zone on the outer rim is visible on 552-13, indicating a different fluid flow behind the inclusion, and thus perturbation of the general mass flow on the electrode surface, therefore influencing the governing droplet formation mechanism. For comparison, an electrode surface (552-33) without visible macroscopic inclusions is presented. 119

Figure 5-15 Agreement between experimental and calculated mass flow rates using equation (5.14). The solid line represents a perfect agreement. The reference U8Mo rotating electrodes are presented in red circles; rotating electrodes with higher a carbon content are presented in green inversed triangles; shorter rotating electrodes are presented in blue triangles;

black squares represent 1.4301 stainless steel. Uncertainties within symbol size if not visible. The fitting graph has a slope and intercept of 0.88379 and 0.08451, respectively; the corresponding standard deviation is 0.02739 and 0.03074, respectively. The coefficient of determination R^2 is 95 %. 120

Figure 5-16 Comparison of the apparent mass flow rates obtained by the FRMII-CERCA atomizer and INL atomizer as a function of electric arc current. Overlapping points occur at 1.7 g s^{-1} and 1.1 g s^{-1} with respect to INL results and around 1.15 g s^{-1} and 1.27 g s^{-1} with respect to FRM II/CERCA results. Uncertainties within symbol size if not visible. A straight line with respect to the apparent mass flow rate generated by the FRM II/CERCA atomizer was included for better trend visualisation. 123

Figure 6-1 Droplet formation mechanisms in centrifugal atomization as filmed by [Fraser *et al.* 1963], top down: direct droplet formation, ligament disintegration, and film disintegration. 129

Figure 6-2 Formation of a large main droplet (a) and of a small secondary droplet (b) from the “neck” or “thread” during REP atomization of SAE 1090 steel in the DDF regime [Champagne and Angers 1984]. Formation of a large main droplet and break-up of the “neck” or “thread” into multiple secondary droplets (c) during rotating disk atomization of normal liquids (e.g. water) [Tanasawa *et al.* 1978]. 130

Figure 6-3 Schematic illustration of the different atomization regimes according to [Wozniak 2003]: a) direct droplet formation (DDF), b) ligament disintegration (LD), and c) laminar as well as d) turbulent film disintegration (FD). The illustration additionally accounts for the size distribution and shape of droplets produced in each regime, which is echoed in the resulting particle size distribution. 131

Figure 6-4 Atomization regimes (DDF, LD, and FD) as a function of material properties and operating parameters taken from the original publication [Champagne and Angers 1984]. Investigated materials were zinc, copper, iron, steel, and aluminium. Parameter sets with identical X are situated on the straight line $Op = X \cdot Mp$. The vertical interval bars correspond to experimental results and indicate a transition range from DDF to LD. The theoretical transition from DDF to LD occurs at X = 0.07, while transition from LD to FD occurs at X = 1.33. Zinc and aluminium constitute the lower and upper limit, respectively, of the experimentally validated data regarding metal melts. The dotted lines represent extrapolations of both transition lines. 134

Figure 6-5 X-diagram showing the conducted U8Mo/U7Mo and 1.4301 stainless steel experiments with respect to the atomization regimes. The bold black lines, corresponding to $X = 0.07$ and $X = 1.33$, represent the theoretical (and averaged) transition between regimes as determined by [Champagne and Angers 1984] and [Hinze and Milborn 1950], respectively. The red dotted lines represent the assumed transition range that was obtained from graphical measurement of the transition ranges of Zn, Cu, Fe, and Al plotted in Figure 6-4. The lower threshold was determined to $X = 0.035$, the upper threshold to $X = 0.1$. 137

Figure 6-6 SEM micrographs of samples originating from batches U8Mo-552-12 (top) and U8Mo-552-36 (bottom) showing sectioned and full particles, respectively, with smallest diameter < 45 µm. Batch U8Mo-552-12 was embedded and polished. Both powder samples predominantly consisted of spherical particles; similar samples were marked with “S” with respect to Table 6-1. 139

Figure 6-7 SEM micrograph of an embedded and polished sample of batch U8Mo-552-10 showing sectioned particles with smallest diameter between 45 µm and 180 µm using back-scattered electrons (BSE). Particle shapes varied between sphere and ellipsoid. Similar samples were typically marked with “S+E” with respect to Table 6-1. 140

Figure 6-8 SEM micrograph of an embedded and polished sample of batch U8Mo-552-29 showing sectioned particles with smallest diameter < 45 µm using back-scattered electrons (BSE). Particle shapes varied between sphere, ellipsoid, and filament (needle). Similar samples were typically marked with “S+E+F” with respect to Table 6-1. The presence of spherical and ellipsoidal particles, though, must be considered carefully as they might represent cross-sections of filaments. 140

Figure 6-9 SEM micrograph using secondary electrons (SE) of a sample of batch U8Mo-552-38 showing particles with smallest diameter > 355 µm. ...142

Figure 7-1 Different ways to present the same particle size distribution: a) mass fraction per sieve class as column plot, b) mass fraction per particle-diameter class-range as a histogram, c) normalised mass fraction per particle-diameter class-range as a histogram, and d) normalised mass fraction per particle-diameter class-range as a continuous plot. 153

Figure 7-2 Same particle size distribution as in Figure 7-1 b), presented in a histogram and in cumulative undersize form with quantile diameters. 154

Figure 7-3 Number distribution *n(D)*, left y-axis, and volume (mass) distribution *v(D)*, right y-axis, and relative position of different mean diameters. Volume and mass distribution are equal if the particles have no voids. Property of [Yule and Dunkley 1994]. 156

Figure 7-4 Yield and yield efficiency of usable U8Mo powder from rotating electrodes with 10 mm diameter in descending order with respect to particles < 125 µm. The sort rotating electrodes are shown separately and are marked with an asterix. All experiments were atomized with $X < 0.68$. 164

Figure 7-5 Yield efficiency of usable powder as a function of apparent mass flow rate and rotational speed for standard U8Mo rotating electrodes plotted in a bubble chart. The usable powder yield efficiency is proportional to the bubble diameter. The usable powder yield efficiencies of both categories (0-40 µm and 0-125 µm) have the same scaling factor........ 166

Figure 7-6 Yield efficiencies of usable powder for 1.4301 stainless steel. 166

Figure 7-7 Process yield efficiency for U8Mo rotating electrodes with respect to rotational speed. 167

Figure 7-8 Particle size distributions of U8Mo for $X < 0.042$ showing the influence of rotational speed. 170

Figure 7-9 Particle size distributions of U8Mo between $X \sim 0.042$ and $X \sim 0.068$ showing the influence of rotational speed and mass flow rate........ 171

Figure 7-10 Influence of rotational speed on the particle size distribution of 1.4301 stainless steel and typical curve progression with bimodal shape ($X = 0.019$ to $X = 0.034$ for Inox-014 to 018, respectively). 172

Figure 7-11 Particle size distribution of “short” U8Mo rotating electrodes. Top and middle particle size distribution resulted from the same rotational speeds, middle and bottom from the same electric arc currents........ 174

Figure 7-12 Comparison of particle size distributions obtained from “short” (552-12 and 552-13) and standard rotating electrodes (552-38 and 552-39) at the same rotational speed. For both the “short” and standard rotating electrodes similar electric arc currents were applied. 175

Figure 7-13 Influence of the apparent mass flow rate on U8Mo particle size distribution. 176

Figure 7-14 Influence of the apparent mass flow rate on U8Mo particle size distribution between $X \sim 0.042$ and $X \sim 0.068$. 177

Figure 7-15 Influence of the apparent mass flow rate on U8Mo particle size distribution below $X \sim 0.042$. 177

Figure 7-16 Influence of the apparent mass flow rate on the particle size distribution of 1.4301 stainless steel in the DDF for batches Inox-015 and Inox-027 having values of $X \sim 0.032$ and 0.043, respectively. 178

Figure 7-17 Typical influence of the rotating electrode diameter on the particle size distribution of 1.4301 stainless steel. Inox-22 shows a tail on the coarse particle side of the global mode. 179

Figure 7-18 Irregular particles typically found on the sieve mesh > 355 μm (image: batch 552-38), occasionally occurring in smaller size classes (batch 552-33, < 125 μm). 180

Figure 7-19 Micrograph of a sectioned U8Mo rotating electrode rest (552-39). The red rectangle shows the position of the micrograph relative to the rotating electrode before (dashed line) and after atomization. The green rectangle is a focused detail view of the melting and atomization zone, showing the conical form towards the electrode centre as well as the spongy morphology of the solidified rotating electrode top between centre and rim. The yellow rectangle is a focused detail view of the rim and tear-off zone. About 1 mm radial from the rim the conical shape reaches its maximum and the alloy is homogenous again. The blue arrows indicate the direction of traction and breakaway. 182

Figure 7-20 Micrograph of a sectioned U8Mo rotating electrode rest (552-38) showing the morphology of the spongy zone (enlarged in red rectangle) similar to the one presented in Figure 7-19. The morphology is similar to the irregular, fragmented particles shown in Figure 7-18. 183

Figure 7-21 Example of partial atomization, i.e. centre erosion, of batch U7Mo-1114-2-1.2 at 25’000 rpm, 50 A, and 20 mm diameter. 184

Figure 7-22 Linear regression analysis of experimental and calculated characteristic diameters of U8Mo and 1.4301 stainless steel powders taken from Table 7-8 and Table 7-7, respectively. Uncertainties within symbol size if not visible. D_{32} was calculated using model "Champagne 1980", equation (7.29). 188

Figure 7-23 Linear regression analysis of experimental and calculated characteristic diameters of U8Mo powder taken from Table 7-8. Uncertainties within symbol size if not visible. D_{32} was calculated using model "Champagne 1980", equation (7.29). 188

Figure 8-1 Equilibrium phase diagram of the binary U-Mo system; property of [Wilkinson 1962a]. The red dotted line marks the composition of U8Mo. 197

Figure 8-2 Equilibrium phase diagram of the binary U-C system; property of [Wilkinson 1962a]. The green area marks the range of carbon impurities present in the analyzed samples. 198

Figure 8-3 Isothermal section of the U-Mo-C ternary phase diagram at 1000 °C; property of [Peniel *et al.* 2012]. The red dotted line shows a molybdenum concentration of about 18 at.-%. The red circle marks roughly the alloy compositions used in this work. 199

Figure 8-4 Isothermal section of the U-Mo-C ternary phase diagram at 1400 °C; property of [Peniel *et al.* 2012]. The red dotted line shows a molybdenum concentration of about 18 at.-%. The red circle marks roughly the alloy composition used in this work. 199

Figure 8-5 Left: Number of nuclei (NN) and crystallisation speed (CS) as a function of supercooling ΔT; property of [Merkel and Thomas 2003]. Right: corresponding schematic microstructure in a geometrically simple ingot; property of [Bergmann 2003]. 200

Figure 8-6 Constitutional supercooling in binary alloys as a function of chemical composition and temperature gradient in the melt: a) different composition of liquid melt and first crystallising solids (reduced in component B), b) difference in concentration of B in the liquid melt at the solid-liquid interface, and c) decrease in the liquidus temperature T_{Li} of the remaining melt due to the increased concentration in B at the solid-liquid interface, resulting in supercooled zones Δx due to the real temperature gradient within the melt; property of [Bargel *et al.* 2000]. 201

Figure 8-7 Primary crystallisation microstructure of alloys as a function of constitutional supercooling Δx: a) steep temperature gradient, mono- or polycrystalline structure, no microsegregation, b) moderate temperature gradient, impurities at grain boundaries, c) gentle temperature gradient, higher concentration of impurities or alloying components, typical for cubically crystallising metals, different chemical composition of dendrites and remaining melt, in the latter: accumulation of inclusions, pores, and microsegregation; property of [Bargel *et al.* 2000]...............202

Figure 8-8 Dendrites: a) dendrite manifestation as a function of supercooling ΔT (property of [Merkel and Thomas 2003]), b) and c) optical and SEM micrograph, respectively, of dendrites in UMo bulk material that was melted, quenched, not homogenised, and not annealed; both property of [Dodenhöft 2013]) 203

Figure 8-9 Microsegregation in alloys: a) exemplary phase diagram of binary system showing the concentration of the liquid melt S_i, the solid solution α_i, and the average solid solution α_i' during cooling, b) schematic structure of the corresponding grain showing microsegregation and corresponding concentration of component A; both property of [Bargel *et al.* 2000]. Exemplary micrograph of microsegregation in a CuZn solid solution, c); property of [Merkel and Thomas 2003]. 204

Figure 8-10 Nomenclature for irregular particles (left) and particle shape (right); property of [Yule and Dunkley 1994]. 206

Figure 8-11 Typical morphological irregularities of atomized particles (here: titanium alloy): a) gas pore (internal void), b) shrinkage pore (internal void), c) irregular exogenous particle (tungsten), d) embedded inclusion, e) outer shell, and f) irregular particle (same alloy) and satellite particles; property of [Eylon *et al.* 1980b]..206

Figure 8-12 Typical spherical U8Mo powder produced from batch 552 by REP..211

Figure 8-13 Batch 552-33: Typical spherical particles in the size class < 45 µm.....212

Figure 8-14 Batch 552-36: Typical spherical particles in the size class from 45 µm to 125 µm with a diameter D_{a1} of ~ 85 µm and a cross-section area D_{b1} of ~ 5685 µm^2. 212

Figure 8-15 Batch 552-36 (< 45 µm): enlarged faceted particle surface showing equiaxed grains. P_{a1} is indicating the typical grain size...........................213

Figure 8-16 Batch 552-33: Typical concave deformation (dent) on the surface of spherical particles that is ascribed to cooling shrinkage and rapid solidification. The diameter of the dent is about 40 µm. 214

Figure 8-17 Batch 552-06 (< 180 µm): Typical polycrystalline microstructure found in sectioned REP-atomized U8Mo particles. Top: original micrograph; bottom: same micrograph with edited contrast to make grain boundaries visible. The black particle above the broken U8Mo-particle rim is an impurity on the sample surface. P_{a1} is indicating the typical grain size. 215

Figure 8-18 Dendritic particle grain structure in sectioned samples of batches 555-08 (top) and 552-12 (bottom) observed with optical microscopy. The samples were exposed to water and air during sample polishing and storage, respectively. The grain structure is present in coarse and fine particles. Light-reflecting voids in sample 552-12 were caused by particle break-out from the resin matrix during polishing. 216

Figure 8-19 Optical micrographs of sectioned samples of batches 552-29 (top) and 552-30 (bottom) confirming the generally dendritic microstructure. The samples were exposed to water and air during sample polishing and storage, respectively. 217

Figure 8-20 Superficial oxide layer of a particle from batch 552-33. Small window: example of detached material after mechanical polishing, batch 552-10. 219

Figure 8-21 EDX line scan traversing a sectioned particle, the resin, and detached material. Left: oxygen (green) and uranium (yellow) concentration curve. Right: oxygen (green), uranium (purple), carbon (red), and molybdenum (blue) curve. The oxygen content (in at.-%) reaches its global maximum in the vicinity of the detached piece. Both the uranium and molybdenum fraction show a local peak in this zone as well. It is suggested that the detached material originates from a thin oxide film (< 1 µm) containing both uranium and molybdenum. 220

Figure 8-22 Impurities (left: dark grey) found in U8Mo (552-36) powder were identified as remains of plastics (middle: yellow) using spectral mapping. In addition, slight particle surface oxidation (right: green) was detected. 220

Figure 8-23 Sequence of micrographs showing impurities as a function of carbon content (see Table 8-2) in ascending order from left to right and top down. All images were taken from particles within the same size class, namely 45 µm to 125 µm. While large inclusions (~ 1 µm) were found in all samples, the number of fine inclusions and their accumulation at grain boundaries increased with increasing carbon content. 221

Figure 8-24 Batch 1114-3 (< 45 µm): enlarged image of a carbon-rich particle showing the general arrangement of fine impurities along the grain boundaries (light grey) in the zone of the solidified remaining melt as well as some precipitation within the grains (dark grey). 221

Figure 8-25 EDX point and shoot scan of typical inclusions and microstructure found in batches 0914 and 1114 (here: batch 0914-1, BSE micrograph). 222

Figure 8-26 Batch 1114-1 (< 125 µm): lamellar structures observed in sectioned particles. 224

Figure 8-27 Different microstructures in the same size class. Top: batch 1114-3 (< 45 µm); bottom: batch 0914-4 (< 45 µm). Batch 1114-3 was 2.5 times richer in carbon according to the chemical analysis..............................225

Figure 8-28 Batch 552-38: agglomeration of typical particles found > 355 µm, that consist of filaments, flattened drops, and highly irregular particles with rough surfaces that are partially flattened due to impact on the collection chamber wall prior to solidification. 226

Figure 8-29 Micrograph of sectioned particles of batch 552-10 showing particles < 125 µm. The microstructure of the irregular particle is similar to the one of spherical particles. 227

Figure 8-30 EDX line scan of a typical irregular particle confirming its consistent composition of uranium (left picture: yellow; right picture: purple) and molybdenum (blue). 227

Figure 8-31 EDX line scan traversing a sectioned regular sphere (left) and a sectioned irregular particle (right). The molybdenum fraction (blue) is roughly doubled in the irregular particle..228

Figure 8-32 Typical SEM micrograph of embedded and sectioned U8Mo particles, batch 552-13 (< 45 µm). The particles were generally free of internal voids. 229

Figure 8-33 Internal void found in batch 552-11 (< 45 µm), presumably due to gas entrapment. 229

List of Tables

Table 2-1 Excerpt of the most important maximum operating limitations of the powder production facility with respect to criticality and radiation protection [Cadoret 2013]. 12

Table 2-2 Excerpt of desired U8Mo fuel powder characteristics with respect to atomization according to the material supply specification G183 [Gery 2011] 13

Table 2-3 Excerpt of regulated chemical impurities of U8Mo fuel powder according to the material supply specification G183 [Gery 2011]; stated are elements that may occur in the casting and atomization process. 14

Table 3-1 High frequency spindle operating limits according to manufacturer's (Fischer AG) instructions with respect to U8Mo. 64

Table 3-2 Calculation of the maximum circular runout for U8Mo rotating electrodes for a maximum centrifugal force of about 20 N as provided by Fischer AG. 67

Table 4-1 Particle size distributions of atomized 1.4301 stainless steel (Inox) and resulting mean with corresponding standard deviation. Experiments were conducted at 40'000 rpm ± 500 rpm, 70 A, < 10 ppm moisture, < 5 ppm oxygen, with machined rotating electrodes with 10 mm diameter and 30 mm consumable length. Sieving time and amplitude for each powder batch was 6 min and 1 mm, respectively. 97

Table 4-2 Characteristic values of each particle size distribution from Table 4-1 as well as of the corresponding atomization process 98

Table 5-1 Calculated average electric arc power and apparent mass flow rate of U8Mo in ascending order with respect to arc power as well as corresponding absolute and relative uncertainties. 112

Table 5-2 Experimental mass flow rates of both 1.4301 stainless steel for different diameters and arc current intensities. The tungsten electrode had a diameter and tip length of 3.2 mm and 2 mm, respectively................. 117

Table 5-3 Comparison of calculated and apparent mass flow rates obtained for U8Mo rotating electrodes of 10 mm and 30 mm diameter and length, respectively, and non-rotating tungsten electrode of 3.2 mm diameter and 2 mm tip length. U8Mo originated from different batches – 0914 and 552. For approximation, average electric power and enthalpy of melt of uranium were used. 121

Table 5-4 Comparison of calculated and apparent mass flow rates obtained for 1.4301 rotating electrodes of 30 mm length and non-rotating tungsten electrode of 3.2 mm diameter and 2 mm tip length. For approximation, average electric power and enthalpy of melt of SAE 1090 steel were used. 122

Table 6-1 Experimental values for X (equation (6.4)) of atomized U8Mo/U7Mo powder and corresponding particle shape that was observed in extracted powder samples. Particle shapes were determined by visual observation using optical or electron microscopy and visual counting. Most samples were embedded and sectioned for microscopy except U8Mo-552-33/36. As a result, filaments may have appeared as ellipsoids or spheres. Occasional occurrence of a certain particle shape was not taken into account; the applied ratio was about 1:10. A change of alloy or rotating electrode length was noted in the column “remarks”. 138

Table 6-2 Material properties parameter M_p, calculated for various liquid metals; thermophysical material properties were taken from literature [Champagne and Angers 1981, Fischer 2000, Paradis *et al.* 2014, "Smithells Metals Reference Book" 1992, "Thermophysical properties of materials for nuclear engineering" 2008, Yule and Dunkley 1994]. For some materials, two values are given due to inconsistencies in the reviewed literature. 143

Table 6-3 Mechanical properties of the alternative surrogate materials ["Smithells Metals Reference Book" 1992, "Thermophysical properties of materials for nuclear engineering" 2008]. Tensile strength depends on material purity, alloying elements, condition, and heat treatment. 144

Table 6-4 Operating parameters of the INL atomizer and corresponding X-values. Data for calculation of the mass flow rates and X were recovered from [Moore and Archibald 2014], namely electric arc current, estimated rotational speed, estimated atomized mass, and atomization time...146

Table 6-5 Operating parameters of the FRM II-CERCA atomizer for $X \leq 0.068$. 146

Table 7-1 Sieve mesh sizes used for particle size screening in agreement with the main mesh series of ISO 565. Stainless steel analytic sieving meshes according to ISO 3310-1 were used. 150

Table 7-2 List of experiments that yielded predominantly spherical powder ($X \lesssim 0.068$) and corresponding operating parameters, sorted into descending order with respect to rotational speed and then electric arc current. Short rotating electrodes are presented separately. All rotating electrodes had a diameter of 10 mm. 168

Table 7-3 Table of characteristic values obtained from U8Mo particle size distributions divided into groups of constant electric arc current and sorted in an ascending order with respect to rotational speed. 170

Table 7-4 Table of characteristic values obtained from 1.4301 particle size distributions divided into groups of constant electric arc current and sorted in an ascending order with respect to rotational speed. 173

Table 7-5 Amount of scrap per batch of atomized U8Mo. 181

Table 7-6 Coefficients of determination R2 of representative models (chapter 7.1.5) with respect to characteristic diameters of atomized 1.4301 stainless steel (Table 7-7) and U8Mo (Table 7-8) powders. R2 was obtained through linear regression analysis. The highest values are highlighted in red. 186

Table 7-7 Characteristic diameters from the cumulative undersize distribution and calculated mean diameters of 1.4301 stainless steel using models from chapter 7.1.5. Uncertainties of experimental characteristic diameters are below 1 % (chapter 7.1.1). Thermophysical properties of mild steel (Table 6-2) were used for calculation. 189

Table 7-8 Characteristic diameters from the cumulative undersize distribution and calculated mean diameters for U8Mo using models from chapter 7.1.5. Uncertainties of experimental characteristic diameters are below 1 % (chapter 7.1.1). Uranium instead of U8Mo thermophysical material properties were used for calculation.. 190

Table 8-1 Excerpt of the chemical composition of feedstock material from INL and CERCA used in this work. Blank places indicate not analyzed elements or provided uncertainties.. 208

Table 8-2 Chemical composition of atomized powder from different U8Mo/U7Mo batches produced from in-house cast rotating electrodes. For comparison, the corresponding limits according to fuel specification G183 [Gery 2011] are given. Uranium and molybdenum concentrations are given in percent.. 210

Publications

Schenk, R., Petry, W., Stepnik, B., Grasse, M., Bourdat, G., Moyroud, C., Coullomb, C. and Jarousse, C. (2014): "FRM II/CERCA UMo Atomizer Project Progress", Proceedings of the RRFM 2014, Ljubljana, Slovenia.

Schenk, R., Petry, W., Stepnik, B., Jarousse, C., Bourdat, G., Moyroud, C. and Grasse, M. (2013): "FRM II/CERCA UMo Atomizer Project Status", Proceedings of the RRFM 2013, Saint Petersburg, The Russian Federation.

Bibliography

Angers, R., Tremblay, R. and Dubé, D. (1997): "Formation of irregular particles during centrifugal atomization of AZ91 alloy", **33**, Materials Letters, 1-2, pp. 13-18.

Ashgriz, N. (2011): "Handbook of Atomization and Sprays: Theory and Applications", Springer US, pp. 215-232, 327-338, 479-496, 479-580, 755-775, 837- 848.

Bargel, H. J., Hilbrans, H. and Schulze, G. (2000): "Werkstoffkunde", 7, Springer Berlin Heidelberg, pp. 8-10, 18-22, 32-53, 67-71, 152-156.

Bergmann, W. (2003): "Werkstofftechnik 1: Struktureller Aufbau von Werkstoffen - Metallische Werkstoffe - Polymerwerkstoffe - Nichtmetallisch-anorganische Werkstoffe", Carl Hanser Verlag GmbH & Company KG, pp. 60-83, 114-120.

Bjorgvinsson, J. B., Cook, G. E. and Andersen, K. (1993): "Microprocessor-based arc voltage control for gas tungsten arc welding using gain scheduling", **29**, IEEE Transactions on Industry Applications, 2, pp. 250-255.

Bonnin, A., Wright, J. P., Tucoulou, R. and Palancher, H. (2014): "Impurity precipitation in atomized particles evidenced by nano x-ray diffraction computed tomography", Applied Physics Letters, pp. 105.

Bose, B. K. (1981): "Adjustable speed AC drive systems", IEEE Press, New York.

Boulanger, M. (2012): "Rapport de verification de conformite de machine", 2425250/11.1.1, Bureau Veritas, Valence.

Bourgeois, B. L. (1989): "Soudage à l'arc: Procédés avec fil électrode fusible, procédés avec électrode réfractaire", **3**, Publications de la soudure autogène, Institut de Soudure, Paris.

Breitkreutz, H. (2011): "Coupled Neutronics and Thermal Hydraulics of High Density Cores for FRM II", Fakultät für Physik, FRM II, Technische Universität München, Garching, Garching.

Breitkreutz, H. (2015): "FDEG meeting report".

Burkes, D. E., Papesch, C. A., Maddison, A. P., Hartmann, T. and Rice, F. J. (2010): "Thermo-physical properties of DU–10 wt.% Mo alloys", **403**, Journal of Nuclear Materials, 1–3, pp. 160-166.

Cadoret, G. (2013): "INB 63 - Dossier de sûreté UMo", PEPS-F 2011 DC 13, D, AREVA, Lyon.

Carazzetti, P. (2009): "Electrical breakdown at low pressure for planar microelectromechanical systems with gaps", **8**, Journal of Micro/Nanolithography, MEMS, and MOEMS, 3.

Champagne, B. and Angers, R. (1980): "Fabrication of powders by the rotating electrode process", **16**, International Journal of Powder Metallurgy, Princeton, NJ, pp. 359.

Champagne, B. and Angers, R. (1981): "Size Distribution of Powders Atomized by the Rotating Electrode Process", **12**, Metal Powder Industries Federation, Princeton NJ, pp. 83-104.

Champagne, B. and Angers, R. (1984): "REP Atomization Mechanisms", **16**, Powder Metallurgy International, 3, pp. 125.

Champion, G., Allenou, J., Pasturel, M., Noël, H., Charollais, F., Anselmet, M.-C., Iltis, X. and Tougait, O. (2013): "Magnesiothermic Reduction Process Applied to the Powder Production of U(Mo) Fissile Particles", **15**, Advanced Engineering Materials, 4, pp. 257-261.

Clark, C. R., Knighton, G. C., Fielding, R. S. and Hallinan, N. P. (2010): "INL Laboratory Scale Atomizer", INL/EXT-10-17574, Idaho National Laboratory, Idaho Falls.

Clark, C. R., Meyer, M. K. and Strauss, J. T. (1998): "Fuel Powder Production from Ductile Uranium Alloys", International Meeting on Reduced Enrichment for Research and Test Reactors, Sao Paulo, Brazil.

Clark, C. R., Muntifering, B. R. and Jue, J. F. (2007): "Production and Characterization of Atomized U-Mo Powder by the Rotating Electrode Process", INL/CON-07-13156, Idaho National Laboratory, Idaho Falls.

Correy, T. B. (1982): "What makes an electric welding arc perform its required function", Pacific Northwest Laboratory, Battelle Memorial Institute, Richland, Washington.

Creasy, J. T. (2012): "Thermal properties of Uranium-Molybdenum alloys: phase decomposition effects of heat treatments", Master's thesis, Texas A&M University, Texas.

Crowe, C. T. (2005): "Multiphase Flow Handbook", CRC Press,Taylor & Francis, Boca Raton, pp. 1-41, ch. 8.

Davies, J. (1990): "Conduction and Induction Heating", P. Peregrinus Limited, London, UK.

"Décret no. 2007-1557" (2014), NOR: DEVQ0762539D, Journal officiel de la République française, Paris, Version consolidée.

Denet, N. (2010): "Options de sûreté pour la mise en place d'une installation prototype de fabrication d'alliage d'uranium hautement enrichi et de molybdène", PEPL-F 2010 DC 56, B, AREVA, Lyon.

Dodenhöft, M. (2013): "Metallografische Präparation von Uran-Molybdän", Bachelorarbeit, Fakultät für Physik, FRM II, Technische Universität München, Garching, pp. 22, 34, 52.

Dunkley, J. J. and Aderhold, D. (2007): "Centrifugal atomisation of metal powders", Advances in Powder Metallurgy & Particulate Materials-2007, Metal Powder Industries Federation.

Durazzo, M., Neto, R. M. L. and Marques, J. R. O. (2014): "Fabrication Procedures for Manufacturing UMo-Al Dispersion Fuel at IPEN", RERTR 2014, Vienna.

Emendörfer, D. and Höcker, K. H. (1982): "Theorie der Kernreaktoren. Band 1: Der stationäre Reaktor", Bibliographisches Institut, Mannheim, pp. 108.

Eylon, D., Mahajan, Y., Ontko, N. R. and Froes, F. H. (1980a): "Fatigue crack initiation of titanium alloy powder compacts", Powder metallurgy of titanium powders, Conference proceedings, AIME, Las Vegas, pp. 93-102.

Eylon, D., Omlor, R. E., Bacon, R. J. and Froes, F. H. (1980b): "Morphological and microstructural evaluation of various titanium alloy powders", Powder metallurgy of titanium powders, Conference proceedings, AIME, Las Vegas, pp. 71-81.

Fahrenwaldt, H. J., Schuler, V. and Twrdek, J. (2014): "Praxiswissen Schweißtechnik", 5, Springer Vieweg, pp. 18-42.

Ferreira, R. a. N., Camarano, D. M., Miranda, O., Grossi, P. A., Carneiro, L. C. S., Vicente, C. J. M., Queiroz, C. M., Pedrosa, T. A. and Ferraz, W. B. (2011): "Thermophysical Properties Determination of Uranium-Molybdenum Fuel by the Flash Laser Method", 2011 International Nuclear Atlantic Conference - INAC 2011, Belo Horizonte, MG, Brazil.

Fischer, E. A. (2000): "Density of liquid uranium and derived equation of state", Wissenschaftliche Berichte FZKA 6387, Institut für Kern- und Energietechnik, Projekt Nukleare Sicherheitsforschung, Forschungszentrum Karlsruhe, Technik und Umwelt, Karlsruhe.

Folk, R. L. (1966): "A Review of Grain-size Parameters", **6**, Sedimentology, Blackwell Publishing Ltd, 2, pp. 73-93.

Folk, R. L. and Ward, W. C. (1957): "Brazos river bar: A study in the significance of grain size parameters", **27**, Journal of Sedimentary Petrology, 1, pp. 3-26.

Fraser, R. P., Dombrowski, N. and Routley, J. H. (1963): "The filming of liquids by spinning cups", **18**, Chemical Engineering Science, 6, pp. 323-337.

German, R. M. (2009): "Handbook of Mathematical Relations in Particulate Materials Processing", Wiley, New York, pp. 34-35, 252.

Gery, C. (2011): "Poudre UMo atomisée", G183, Rév. 0, CERCA, Romans.

Harbonnier, G. (2002): "Spécification matière - Uranium", G 160, Rév. 6, CERCA, Romans.

Hart, H., Craine, L. E., Hart, D. J. and Vinod, T. K. (2012): "Organic Chemistry: A Short Course", 13, CH 2270, Houghton-Mifflin, Clemson University, Boston.

Hayward, M. L. (1990): "Environmental hardening of equipment operating in an automated test bed enclosure", Special Isotope Separation Program, Lawrence Livermore National Laboratory, Livermore, California.

Hinze, J. O. and Milborn, H. (1950): "Atomization of Liquids by Means of a Rotating Cup", **17**, ASME Journal of Applied Mechanics, pp. 145.

Hodkin, D. J., Sutcliffe, P., Hardon, P. G. and Russel, L. E. (1973): "Centrifugal Shot Casting: A New Atomization Process for the Preparation of High-Purity Alloy Powders", **16**, Powder Metallurgy, London, 32, pp. 277.

Holden, A. N. (1958): "Physical metallurgy of uranium", Addison-Wesley Pub. Co., Reading, Mass.

Huber, T. K., Breitkreutz, H., Petry, W., Reiter, C., Elgeti, S., Burkes, D. E., Casella, A. J., Casella, A. M., Smith, F. N. and Wachs, D. M. (2015): "The Thermal Properties of Fresh and Spent U-MO Fuels: an Ovierview.", Talk presented at European Research Reactor Conference (RRFM 2015), Bucharest, Romania.

Isonishi, K., Kobayashi, M. and Tokizane, M. (1989): "Production of Ti-6Al-4V Alloy Powders by Plasma Rotating Electrode Process", **75**, Tetsu-to-Hagane, 10, pp. 1913-1920.

Jones, W. D. (1960): "Fundamental Principles of Powder Metallurgy", Edward Amold Ltd., London.

Jungwirth, R. (2011): "Irradiation behaviour of modified high-performance nuclear fuels", Dissertation, Fakultät für Physik, FRM II, Technische Universität München, Garching.

Katsaounis, A. (1993): "Heat Flow and Arc Efficiency at High Pressures in Argon and Helium Tungsten Arcs", **72(9)**, American Welding Society, Welding Journal, pp. 447-454.

Kim, C. K., Kim, K. H., Jang, S. J., Jo, H. D. and Kuk, I. H. (1992): "Characterization of atomized U_3Si_2 powder for research reactor", Proceedings of the 1992 International Meeting on RERTR, Roskilde, Denmark.

Kim, K. H., Lee, D. B., Kim, C. K., Kuk, I. H. and Paik, K. W. (1997a): "Characteristics of U_3Si and U_3Si_2 Powders Prepared by Centrifugal Atomization", **34**, Journal of Nuclear Science and Technology, 12, pp. 1127-1132.

Kim, K. H., Lee, D. B. L., Kim, C. K., Hofman, G. E. and Paik, K. W. (1997b): "Characterization of U-2Mo d U-10Mo alloy powders prepared by centrifugal atomization", **245**, Journal of Nuclear Materials, pp. 179-184.

Kim, K. H., Park, J. M. and Ryu, H. J. (2007): "Use of a centrifugal atomization process in the development of research reactor fuel", **39**, Nuclear Engineering and Technology, 5, pp. 617-626.

Kim, Y. S., Park, J. M., Lee, K. H., Yoo, B. O., Ryu, H. J. and Ye, B. (2014): "In-pile test results of U-silicide or U-nitride coated U-7Mo particle dispersion fuel in Al", **454**, Journal of Nuclear Materials, 1–3, pp. 238-246.

Lancaster, J. F. (1986): "The Physics of Welding", 2, International Institute of Welding, Elsevier Science, pp. 132-134.

Lawley, A. (1992): "Atomization: the production of metal powders", Metal Powder Industries Federation, Princeton, NJ, pp. 1-12, 13-36, 37-48, 49-71, 82-98, 107-111, 153-154.

Lefebvre, A. (1989): "Atomization and Sprays", Taylor & Francis, New York, pp. 79-102, 127-136, 189-193, 222-228.

Liu, H. (2000): "Science and Engineering of Droplets: Fundamentals and Applications", Noyes Publications, Norwich, NY.

"Makrolon® AR" (2014), Produktdatenblatt, Bayer MaterialScience GmbH.

Marchand, E. (2012): "Etudes d'explosions: Station gaz F2L", PRO NTC 12 11023, 02, FBFC Romans sur Isère.

Matsumoto, S., Saito, K. and Takashima, Y. (1974): "Phenomena transition of a liquid atomization from disk", **7**, J. Chem. Eng. Jpn., pp. 13-19.

Matthes, K.-J. and Schneider, W. (2012): "Schweißtechnik", 5, Carl Hanser Verlag, pp. 15-28, 64-90, 127-187.

Merkel, M. and Thomas, K. H. (2003): "Taschenbuch der Werkstoffe", 6, Fachbuchverl. Leipzig im Carl-Hanser-Verlag, pp. 70-75, 101-123.

Moore, G. A. and Archibald, K. E. (2014): "Atomization-Pin and DU8Mo Fuel Powder Fabrication Summary Report", INL/LTD-14-31630, Idaho National Laboratory, Idaho Falls.

Muraszew, A. (1948): "Continuous Fuel-Injection Systems with Rotating Fuel Chamber", **165-166**, Engineering, pp. 316-317.

Naka, S., Marty, M. and Octor, H. (1987): "Oxide-dispersed titanium alloys Ti-Y prepared with the rotating electrode process", J Mater Sci, **22**, Journal of Materials Science, Kluwer Academic Publishers, 3, pp. 887-895.

Neikov, O. D., Murashova, I. B., Yefimov, N. A., Naboychenko, S., Mourachova, I. B., Gopienko, V. G., Frishberg, I. V. and Lotsko, D. V. (2009): "Handbook of Non-Ferrous Metal Powders: Technologies and Applications", Elsevier Science, pp. 129-131.

Oh, S. J., Kim, K. H., Jang, S. J., Lee, D. B., Lee, Y. S., Park, J. M., Park, H. D. and Kim, C. K. (2006): "The development of U-7Mo for large particle powders by centrifugal atomization", 10th International Topical Meeting, RRFM, Sofia, Bulgaria.

Olivares, L., Marin, J., Barrera, M., Gutierrez, C. and Lisboa, J. (2012): "Dispersion feul miniplates based on UMo powder produced by centrifugal atomization", RERTR - Reduced Enrichment for Research and Test Reactors, Warsaw, Poland.

Paine, S. H. and Kittel, J. H. (1955): "Irradiation effects in uranium and its alloys", Proceedings of the international conference on the peaceful uses of atomic energy, New York, United Nations, pp. 745.

Palancher, H., Bonnin, A., Honkimaki, V., Suhonen, H., Cloetens, P., Zweifel, T., Tucoulou, R., Rack, A. and Voltolini, M. (2012): "Coating thickness determination in highly absorbent core-shell systems", **45**, Journal of Applied Crystallography, 5, pp. 906-913.

Paradis, P.-F., Ishikawa, T. and Okada, J. T. (2014): "Thermophysical Properties of Platinum Group Metals in their Liquid Undercooled and Superheated Phases", **58**, Johnson Matthey Technology Review, 3, pp. 124-136.

Park, J.-M. (1999): "Characterization of U-Nb-Zr dispersion fuel prepared by centrifugal atomization process", Journal of Nuclear Materials, 265, pp. 38-43.

Peniel, M., Bekkachi, H. E., Tougait, O., Pasturel, M. and Noël, H. (2012): "An Experimental Investigation of the U-Mo-C Ternary Diagram", **194**, Solid State Phenomena, pp. 26-30.

Phillips, A. M., Mickum, G. S. and Burkes, D. E. (2010): "Thermophysical Properties of U-10MO Alloy", INL/EXT-10-19373, Idaho National Laboratory, Idaho Falls.

Plookphol, T., Wisutmethangoon, S. and Gonsrang, S. (2011): "Influence of process parameters on SAC305 lead-free solder powder produced by centrifugal atomization", **214**, Powder Technology, 3, pp. 506-512.

Ponn, J. and Lindemann, U. (2008): "Konzeptentwicklung und Gestaltung Technischer Produkte", Springer, Berlin Heidelberg.

Rest, J. (2009): "UMo Alloy Fuels Handbook", ANL-09/31, Argonne National Laboratory, Chicago.

Rest, J., Hofman, G. L., Konovalov, I. I. and Maslov, A. A. (1998): "Experimental and Calculated Swelling Behavior of U-10Mo under Low Irradiation Temperatures", Proceedings of the 21st International Topical Meeting on Reduced Enrichment for Research and Test Reactors (RERTR), Sao Paulo.

Roberts, P. R. and Loewenstein, P. (1980): "Titanium alloy powders made by the rotating electrode process", Powder metallurgy of titanium powders, Conference proceedings, AIME, Las Vegas, pp. 21-35.

Röhrmoser, A., Breitkreutz, H. and Petry, W. (2012): "Extended studies of FRM II core conversion with UMo dispersive fuel at a prolonged fuel element", Transactions of the RRFM 2012, Prague, Czech Republic.

Röhrmoser, A., Petry, W. and Wieschalla, N. (2005): "Reduced enrichment program for the FRM-II, status 2004/05", ENS RRFM 2005: 9th international topical meeting on research reactor fuel management. Transactions, Budapest.

Schenk, R., Petry, W., Stepnik, B., Grasse, M., Bourdat, G., Moyroud, C., Coullomb, C. and Jarousse, C. (2014): "FRM II/CERCA UMo Atomizer Project Progress", Proceedings of the RRFM 2014, Ljubljana, Slovenia.

Schenk, R., Petry, W., Stepnik, B., Jarousse, C., Bourdat, G., Moyroud, C. and Grasse, M. (2013): "FRM II/CERCA UMo Atomizer Project Status", Proceedings of the RRFM 2013, Saint Petersburg, The Russian Federation.

Schmid, W. (2011): "Construction of a sputtering reactor for the coating and processing of monolithic U-Mo nuclear fuel", Dissertation, Fakultät für Physik, FRM II, Technische Universität München, Garching.

Sherrod, H. C. (1960): "Electrical characteristics of a plasma arc torch", Department of Electrical Engineering, Rensselaer Polytechnic Institute, Troy, New York.

Slawecki, M. A., Bernstein, G. J. and Coleman, L. F. (1966): "Tests of commutating brushes for use in DC motors operating in a dry argon atmosphere", ANL-7262, Argonne National Laboratory, Chicago.

"Smithells Metals Reference Book" (1992), 7, Butterworth-Heinemann, Oxford.

Snelgrove, J. L., Hofman, G. L., Meyer, M. K., Trybus, C. L. and Wiencek, T. C. (1997): "Development of very-high-density low-enriched-uranium fuels", **178**, Nuclear Engineering and Design, 1, pp. 119-126.

Tanasawa, Y., Miyasaka, Y. and Umehara, M. (1978): "Effect of Shape of Rotating Disks and Cups on Liquid Atomization", Proceedings of the 1st ICLASS, Tokyo, pp. 165.

Taylor, B. N. and Kuyatt, C. E. (1994): "Guidelines for Evaluating and Expressing the Uncertainty of NIST Measurement Results", NIST Technical Note 1297, National Institute of Standards and Technology, Washington.

Taylor, G. I. (1950): "The Instability of Liquid Surfaces When Accelerated in a Direction Perpendicular to their Planes.", **201**, Proc. Roy. Soc. of London, Series A, Mathematical and Physical Sciences, pp. 192.

"Technische Anleitung Nr. 5 - Lagerströme in modernen AC-Antriebssystemen" (2001), ABB Automation Products.

"Thermophysical properties of materials for nuclear engineering" (2008), IAEA, Vienna, pp. 14-18.

Van Den Berghe, S. and Lemoine, P. (2014): "Review of 15 years of high-density low-enriched umo dispersion fuel development for research reactors in Europe", **46**, Nuclear Engineering and Technology, 2, pp. 125-146.

Vanvor, D. and Zill, V. (2003): "FRM-II Brennelemente", KS D 1100/FRM-II, c.

Walton, W. H. and Prewett, W. C. (1949): "The Production of Sprays and Mists of Uniform Drop Size by Means of Spinning Disc Type Sprayers", **62**, Proceedings of the Physical Society, Section B, 6, pp. 341.

"Welding Handbook" (2004), 9, **2 (I)**, Welding Processes, American Welding Society, pp. 1-42, ch. 1.

"Welding theory and application" (1993), TC 9-237, Operator's circular, Department of the Army, Headquarters, Washington, DC, pp. 1-23, ch. 10.

Wilkinson, W. D. (1962a): "Uranium Metallurgy", **II**, Uranium Corrosion and Alloys, Interscience Publishers, New York, pp. 769-771, 819-823, 862-878, 947-980, 1199-1200, 1411, 1420.

Wilkinson, W. D. (1962b): "Uranium Metallurgy", **I**, Uranium Process Metallurgy, Interscience Publishers, New York, pp. 256-274,.

Wittel, H., Muhs, D., Jannasch, D. and Voßiek, J. (2009): "Roloff/Matek Maschinenelemente - Normung, Berechnung, Gestaltung", 19, Vieweg+Teubner Verlag, Wiesbaden, pp. 1-20, 71-88, 217-273, 299-340, 341-372, 475-525, 581-610, 657-676.

Wozniak, G. (2003): "Zerstäubungstechnik: Prinzipien, Verfahren, Geräte", Springer Berlin Heidelberg, pp. 31-50, 73-81.

Ye, B., Bhattacharya, S., Mo, K., Yun, D., Mohamed, W., Pellin, M., Fortner, J., Kim, Y. S., Hofman, G. L., Yacout, A. M., Wiencek, T., Van Den Berghe, S. and Leenaers, A. (2015): "Irradiation behavior study of U–Mo/Al dispersion fuel with high energy Xe", **464**, Journal of Nuclear Materials, pp. 236-244.

Yule, A. J. and Dunkley, J. J. (1994): "Atomization of melts for powder production and spray deposition", Clarendon Press, Oxford, pp. 1-14, 15-46, 47-87, 88-113, 160-162, 205-218, 219-233, 374-375.

Zainoun, N. C., J-M.; Renaudeaux, J-P. (2004a): "Contrôle dimensionnel des aérosols par piézoélectricité", **112**, XXIXème Congrès de la Société de Biomécanique, Mécano - Transduction 2004 (GAMAC), Université Paris XII, Créteil, pp. 140.

Zainoun, N. C., J-M.; Renaudeaux, J-P. (2004b): "Le vibro-générateur d'aérosols homogènes", The 20th French Congress on Aerosols (CFA 2004), Actes de la conférence annuelle ASFERA, Paris.

Zhang, Y. M. (2008): "Real-Time Weld Process Monitoring", Elsevier Science, pp. 15-25.

Zweifel, T. (2015): "Fission Gas Behaviour and Interdiffusion Layer Growth in in-pile and out-of-pile Irradiated U-Mo/Al Nuclear Fuels", Dissertation, Lehrstuhl für Funktionelle Materialien E13, FRM II , Technische Universität München, Garching.

Acknowledgement

I am very fortunate to have many mentors, colleagues, friends, and family whom I can approach for advice and help. I am most grateful to

Prof. Petry for entrusting me with this project, for giving appreciated scientific and personal advice, for his constant support, for the backup in critical situations, and for his winning excitement for challenges.

Prof. Macián for his confidence, encouragement, and advice as well as for being always available when necessary.

Bertrand Stepnik for creating a productive working environment, for managing the laborious licensing procedure and lab reconstruction, and for his scientific input to the experimental results.

Christophe Jarousse for sharing his professional experience and for giving valuable advice in project management and life.

Max Febvre for his genuine interest in and support of my engineering and experimental work, for enriching conversations about engineering, motorcycles, and nature late in the evening.

My colleagues at TUM – Harald Breitkreutz and Wolfgang Schmid for urging me into the project, for the scientific and less scientific discussions, and for being helpful and encouraging. Tobias Zweifel for his valuable support in SEM and metallurgy. Christian Steyer, Malte Kreß, and Raphaël Roset for contributing to my work and making mentoring a pleasure. Christian together with Bruno Baumeister for countless component purchases and excellent sample preparation for microscopic analysis. Christian Reiter for his support in statistics. Elbio Calzada for advice in engineering and life and for raising a laugh whenever we had time to discuss. Lea Canella, Hsin-Yin Chiang, Stefanie Egle, Margitta Franke, Brigitte Gallenberger, Marta Gonzalez, Rainer

Grossmann, Wolfgang Hagn, Bernd Heck, Isabella Heinath, Tobias Hollmer, Tanja Huber, Elisabeth Jörg-Müller, Philipp Jüttner, Rainer Jungwirth, Christoph Morkel, Nathalie Munnikes, Reinhard Obermeier, Sabine Osorio, Manfred Pfaller, Jörg Pulz, Gabriel Reingen, Anton Röhrmoser, Rupert Schauer, Michael Schmidt, Klaus Seebach, Stefan Söllradl, Jörg Stoll, Franz Tralmer, Harald Türck, Silvia Valentin-Hantschel, Franz Wagner, and Peter Wind for support in engineering, IT, fabrication, and administration, for encouragement and the enjoyable time.

My colleagues at AREVA – Christophe Moyroud for his practical solutions during machine assembly and experimental operation, for carrying out numerous experiments and granulometries, and for delicious French cuisine lessons. Michel Grasse for his expertise in powder metallurgy, for raising a laugh and providing me with the “rock and blues” essentials. Gilles Bourdat for carrying out many administrative works and for summarising the operating manuals as well as Christel Coullomb for managing all hot material transfers with accuracy and a smile. Jonathan Clémençon, Patrice Delhomme, Daniel Petitjean, and Gérald Vical for their vital support in lab reconstruction and maintenance. Brigitte Barbaret for the daily ten minutes of German reminiscence. Especially the team of SMN, Norbert Alonso, Bernard Baratier, Patrick Bobichon, Christophe Bouvier, Michel Chabanel, Jean Philippe Coffigny, Patrick Comte, Xavier Cremers, Chantal Divan, Yves Jolivet, Yves Perret, Pierre Poirier, Jean Marc Rochette, and Eric Vioujas for providing hands-on help during assembly, for component fabrication in urgent situations, and coffee machine discussions. Pierre Marcot, Eric Torlini, Gilles Cadoret, and Michel Doucet for their essential support in the licensing process. Gilles Baty, Richard Baudoin, Cédric Blay for tennis sessions, Maurice Bodon, Jean Pierre Boudon, Geneviève Callière, Joseph Chabert, Sébastien Chartier, Pierre Colomb, Isabelle Dressler, Pascal Durand, Gérard Ferraz, Nicolas Frank, Eric Furet for football training and talks, Christophe Géry, David Jan, David Klein, Dominique Geslin, Gérard Harbonnier, Thomas Heulot, Michel Honoré for ensuring my safety, Raphaël Ismalun, Pierre Juvenet, Thierry Kara, Omar Khayame, Pierre Koehl, Marc Lauglaney, Mickaël Loua, Magali Mahé, Adeline Metzger, Gérald Orard for invaluable IT support, Olivier Poulat, Hugo Pugnet, Thierry Rey, Aurélie Sabardeil, and Martine Valette for support, encouragement, and integration.

Daniel M. Wachs and Curtis R. Clark for inviting me twice to INL and for providing me with important insight to the INL atomization and casting process as well as Glenn A. Moore, K. E. Archibald, Tammy L. Trowbridge, and Randall S. Fielding for sharing their experimental results and experience.

Olivier Tougait, Francis Gouttefangeas, and Chantal Moussa for inviting me twice to université de Rennes 1 and for providing me with valuable help in metallurgy.

For those who helped but were forgotten – thank you.

It was a pleasure and enriching to work with all of you.

Morgane Allain, Lucile Delmas, Romain Digonnet, Corentin Dufour, Sonja Kubisz, Gaëtan Perret, Damien Petit, and Pauline Regalia for making France a home.

My parents, Ljudmila and Dieter Schenk, as well as Christine Hug, Gregor Koch, and my sister, Maria Schenk, for their constant faith, support, friendship, and love.